A fertility company that defies the textbooks *p. 620*

Multigenerational effects on development *pp. 634 & 651*

Microbial ecology and evolution *pp. 649 & 663*

Science

$10
6 NOVEMBER 2015
sciencemag.org

AAAS

MAVEN at Mars

Probing a dynamic upper atmosphere *p. 643*

CONTENTS

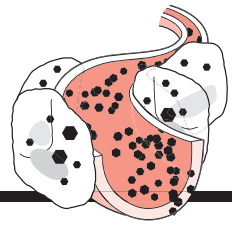

628 & 650
Timing insulin release

6 NOVEMBER 2015 • VOLUME 350 • ISSUE 6261

NEWS

IN BRIEF

610 Roundup of the week's news

IN DEPTH

613 **HOW BURIED WATER MAKES DIAMONDS AND OIL**
A new picture of water in the deep Earth predicts surprising chemistry *By E. Hand*

614 **MICROBES AND CANCER DRUGS**
Gut bacteria boost immunotherapies
By M. Leslie

615 **DATA CHECK: HOW A $30 BILLION HIKE BECOMES $3 BILLION**
The new 2-year U.S. budget deal is frontloaded, with most of the spending increase coming in 2016 *By J. Mervis*

616 **PACIFIC RIM MATHEMATICIANS COAXED FROM THEIR IVORY TOWERS**
Programs to yoke math to industrial needs are booming in the Asia Pacific
By D. Normile

617 **INDIA ORDERS PREMIER LABS TO PAY THEIR OWN WAY**
"Self-finance" directive comes as government pushes indigenous innovation *By S. Ravindran*

618 **USING EVOLUTION TO BETTER IDENTIFY CELL TYPES**
Gene expression patterns show that apparently related cells can have very different evolutionary histories *By E. Pennisi*

619 **VITAMIN C COULD TARGET SOME COMMON CANCERS**
Therapy kills tumor cells with difficult-to-treat mutation *By J. Kaiser*
▸ J. YUN *ET AL*. 10.1126/science.aaa5004

FEATURE

620 **EGGS UNLIMITED**
A company's fertility treatments spark hope and disbelief *By J. Couzin-Frankel*

INSIGHTS

PERSPECTIVES

626 **DENGUE VACCINES AT A CROSSROAD**
Despite modest efficacy, a newly developed vaccine may be key for controlling dengue *By A. Wilder-Smith and D. J. Gubler*

628 **A PANCREATIC CLOCK TIMES INSULIN RELEASE**
Circadian oscillators of beta cells control insulin secretion and glucose homeostasis *By C. Dibner and U. Schibler*
▸ RESEARCH ARTICLE P. 650

629 **LOVE AT SECOND SIGHT FOR CO_2 AND H_2 IN ORGANIC SYNTHESIS**
Catalysts can combine H_2 and CO_2 to create building blocks for high-value products *By J. Klankermayer and W. Leitner*

631 **FRUSTRATING A QUANTUM MAGNET**
Nuclear magnetic resonance reveals the ground state of frustrated magnets
By Y. Furukawa
▸ REPORT P. 655

632 **EVIDENCE GAPS AND ETHICAL REVIEW OF MULTICENTER STUDIES**
Empirical research is needed to guide federal policy *By A.-M. Ervin* et al.

634 **THE EPIGENOME—A FAMILY AFFAIR**
Epigenome disruptions can be transmitted as altered histone modification patterns in sperm
By J. R. McCarrey
▸ RESEARCH ARTICLE P. 651

635 **HOW TO ISOLATE AMERICIUM**
An electrolytic process enables isolation of the radioactive element americium from used nuclear fuel
By C. Soderquist
▸ REPORT P. 652

636 **A NEW DAWN FOR CATARACTS**
Sterols reverse protein aggregation in an eye lens paradigm
By R. A. Quinlan
▸ REPORT P. 674

BOOKS *ET AL.*

638 **HOLDING FAST TO DREAMS**
By F. A. Hrabowski III, reviewed by I. M. Warner and G. Thomas

639 **THE EVOLUTION OF EVERYTHING**
By M. Ridley, reviewed by R. Gawne

639 **SPOOKY ACTION AT A DISTANCE**
By G. Musser

LETTERS

640 **LIFT NIH RESTRICTIONS ON CHIMERA RESEARCH**
By A. Sharma et al.

640 **MAKING SENSE OF THE TROUBLES AT NEON**
By S. V. Ollinger

641 **ONLINE BUZZ: DISASTER PREPAREDNESS**

DEPARTMENTS

609 **EDITORIAL**
Eradicating polio *By Anthony Adams and David M. Salisbury*

710 **WORKING LIFE**
Improving student advising
By Rachel Bernstein

CONTENTS

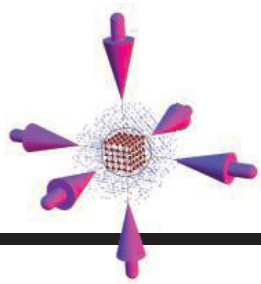

659
Molecules in a lattice of light

6 NOVEMBER 2015 • VOLUME 350 • ISSUE 6261

RESEARCH

IN BRIEF

646 From *Science* and other journals

REVIEW

649 MICROBIOME
Microbiomes in light of traits: A phylogenetic perspective
J. B. H. Martiny et al.
REVIEW SUMMARY; FOR FULL TEXT:
dx.doi.org/10.1126/science.aac9323
▸ REPORT P. 663

RESEARCH ARTICLES

650 METABOLIC HEALTH
Pancreatic β cell enhancers regulate rhythmic transcription of genes controlling insulin secretion
M. Perelis et al.
RESEARCH ARTICLE SUMMARY; FOR FULL TEXT:
dx.doi.org/10.1126/science.aac4250
▸ PERSPECTIVE P. 628

651 EPIGENETICS
Disruption of histone methylation in developing sperm impairs offspring health transgenerationally *K. Siklenka* et al.
RESEARCH ARTICLE SUMMARY; FOR FULL TEXT:
dx.doi.org/10.1126/science.aab2006
▸ PERSPECTIVE P. 634

REPORTS

652 ACTINIDE CHEMISTRY
Electrochemical oxidation of ^{243}Am(III) in nitric acid by a terpyridyl-derivatized electrode *C. J. Dares* et al.
▸ PERSPECTIVE P. 635

655 FRUSTRATED MAGNETISM
Evidence for a gapped spin-liquid ground state in a kagome Heisenberg antiferromagnet *M. Fu* et al.
▸ PERSPECTIVE P. 631

659 QUANTUM SIMULATION
Creation of a low-entropy quantum gas of polar molecules in an optical lattice
S. A. Moses et al.

663 MICROBIOME
The ecology of the microbiome: Networks, competition, and stability
K. Z. Coyte et al.
▸ REVIEW P. 649

667 MOVEMENT CONTROL
Corticomotoneuronal cells are "functionally tuned" *D. M. Griffin* et al.

670 PLANT SCIENCE
Plant pathogenic anaerobic bacteria use aromatic polyketides to access aerobic territory *G. Shabuer* et al.

674 OPHTHALMOLOGY
Pharmacological chaperone for α-crystallin partially restores transparency in cataract models
L. N. Makley et al.
▸ PERSPECTIVE P. 636

678 PROTEIN SYNTHESIS
Operon structure and cotranslational subunit association direct protein assembly in bacteria *Y.-W. Shieh* et al.

680 STRUCTURAL BIOLOGY
Crystal structure of the anion exchanger domain of human erythrocyte band 3
T. Arakawa et al.

684 PLANT EVOLUTION
The *Papaver rhoeas S* determinants confer self-incompatibility to *Arabidopsis thaliana* in planta
Z. Lin et al.

688 PLANT GENETICS
A cucurbit androecy gene reveals how unisexual flowers develop and dioecy emerges *A. Boualem* et al.

691 NONHUMAN GENOMICS
The *Symbiodinium kawagutii* genome illuminates dinoflagellate gene expression and coral symbiosis
S. Lin et al.

Science Staff 606
New Products 699
Science Careers 700

INTRODUCTION

643 MAVEN explores the martian upper atmosphere *B. M. Jakosky*

RESEARCH ARTICLE ABSTRACTS

MAVEN observations of the response of Mars to an interplanetary coronal mass ejection
B. M. Jakosky et al.

Early MAVEN Deep Dip campaign reveals thermosphere and ionosphere variability
S. Bougher et al.

Discovery of diffuse aurora on Mars *N. M. Schneider* et al.

REPORT ABSTRACT

Dust observations at orbital altitudes surrounding Mars
L. Andersson et al.

SEE ALSO
▸ PODCAST

ON THE COVER

Paths of ions escaping Mars' atmosphere due to solar wind radiation. The energy of the particles is illustrated by a brown-to-white gradient. The most energetic ions (white) create a plume, seen at the top. See page 643. For more on the process behind creating this data visualization, see http://scim.ag/maven-cover. *Data visualization: Valerie Altounian/*Science*; Data: X. Fang and the MAVEN science team*

SCIENCE (ISSN 0036-8075) is published weekly on Friday, except the last week in December, by the American Association for the Advancement of Science, 1200 New York Avenue, NW, Washington, DC 20005. Periodicals mail postage (publication No. 484460) paid at Washington, DC, and additional mailing offices. Copyright © 2015 by the American Association for the Advancement of Science. The title SCIENCE is a registered trademark of the AAAS. Domestic individual membership and subscription (51 issues): $153 ($74 allocated to subscription). Domestic institutional subscription (51 issues): $1282; Foreign postage extra: Mexico, Caribbean (surface mail) $55; other countries (air assist delivery) $85. First class, airmail, student, and emeritus rates on request. Canadian rates with GST available upon request, GST #1254 88122. Publications Mail Agreement Number 1069624. **Printed in the U.S.A.**
Change of address: Allow 4 weeks, giving old and new addresses and 8-digit account number. **Postmaster:** Send change of address to AAAS, P.O. Box 96178, Washington, DC 20090–6178. **Single-copy sales:** $10.00 current issue, $15.00 back issue prepaid includes surface postage; bulk rates on request. **Authorization to photocopy** material for internal or personal use under circumstances not falling within the fair use provisions of the Copyright Act is granted by AAAS to libraries and other users registered with the Copyright Clearance Center (CCC) Transactional Reporting Service, provided that $30.00 per article is paid directly to CCC, 222 Rosewood Drive, Danvers, MA 01923. The identification code for *Science* is 0036-8075. *Science* is indexed in the *Reader's Guide to Periodical Literature* and in several specialized indexes.

Published by AAAS

Science
AAAS
1200 New York Avenue, NW, Washington, DC 20005
Bateman House, 82-88 Hills Road, Cambridge, UK CB2 1LQ

Editor-in-Chief Marcia McNutt
Executive Editor Monica M. Bradford **News Editor** Tim Appenzeller
Managing Editor, Research Journals Katrina L. Kelner
Deputy Editors Barbara R. Jasny, Andrew M. Sugden(UK), Valda J. Vinson, Jake S. Yeston

Research and Insights

SR. EDITORS Caroline Ash(UK), Gilbert J. Chin, Lisa D. Chong, Julia Fahrenkamp-Uppenbrink(UK), Pamela J. Hines, Stella M. Hurtley(UK), Paula A. Kiberstis, Marc S. Lavine(Canada), Kristen L. Mueller, Ian S. Osborne(UK), Beverly A. Purnell, L. Bryan Ray, Guy Riddihough, H. Jesse Smith, Jelena Stajic, Peter Stern(UK), Phillip D. Szuromi, Brad Wible, Nicholas S. Wigginton, Laura M. Zahn **ASSOCIATE EDITORS** Brent Grocholski, Keith T. Smith, Sacha Vignieri **ASSOCIATE BOOK REVIEW EDITOR** Valerie B. Thompson **ASSOCIATE LETTERS EDITOR** Jennifer Sills **CHIEF CONTENT PRODUCTION EDITOR** Cara Tate **SR. CONTENT PRODUCTION EDITOR** Harry Jach **CONTENT PRODUCTION EDITORS** Jeffrey E. Cook, Chris Filiatreau, Cynthia Howe, Lauren Kmec, Barbara P. Ordway, Catherine Wolner **SR. EDITORIAL COORDINATORS** Carolyn Kyle, Beverly Shields **EDITORIAL COORDINATORS** Ramatoulaye Diop, Joi S. Granger, Lisa Johnson, Anita Wynn **PUBLICATIONS ASSISTANTS** Aneera Dobbins, Jeffrey Hearn, Dona Mathieu, Le-Toya Mayne Flood, Shannon McMahon, Scott Miller, Jerry Richardson, Rachel Roberts(UK), Alice Whaley(UK), Brian White **EXECUTIVE ASSISTANT** Anna Bashkirova **ADMINISTRATIVE SUPPORT** Janet Clements(UK), Lizanne Newton(UK), Maryrose Madrid, Laura-Nadine Schuhmacher (UK, Intern), Alix Welch (Intern), John Wood(UK)

News

NEWS MANAGING EDITOR John Travis **INTERNATIONAL EDITOR** Richard Stone **DEPUTY NEWS EDITORS** Daniel Clery(UK), Robert Coontz, Elizabeth Culotta, David Grimm, David Malakoff, Leslie Roberts **CONTRIBUING EDITOR** Martin Enserink(Europe) **SR. CORRESPONDENTS** Jeffrey Mervis, Elizabeth Pennisi **NEWS WRITERS** Adrian Cho, Jon Cohen, Jennifer Couzin-Frankel, Carolyn Gramling, Eric Hand, Jocelyn Kaiser, Catherine Matacic, Kelly Servick, Robert F. Service, Erik Stokstad(Cambridge, UK), Emily Underwood **INTERNS** Hanae Armitage, Emily DeMarco, Annick Laurent, Laura Olivieri, Juan David Romero **CONTRIBUTING CORRESPONDENTS** Michael Balter(Paris), John Bohannon, Ann Gibbons, Mara Hvistendahl, Sam Kean, Eli Kintisch, Kai Kupferschmidt(Berlin), Andrew Lawler, Christina Larson(Beijing), Mitch Leslie, Charles C. Mann, Eliot Marshall, Virginia Morell, Dennis Normile(Tokyo), Heather Pringle, Tania Rabesandratana(London), Gretchen Vogel(Berlin), Lizzie Wade(Mexico City) **CAREERS** Donisha Adams, Rachel Bernstein **COPY EDITORS** Julia Cole, Jennifer Levin (Chief) **ADMINISTRATIVE SUPPORT** Jessica Williams

Executive Publisher Rush D. Holt
Publisher Kent R. Anderson **Chief Digital Media Officer** Rob Covey

BUSINESS OPERATIONS AND PORTFOLIO MANAGEMENT DIRECTOR Sarah Whalen **BUSINESS SYSTEMS AND FINANCIAL ANALYSIS DIRECTOR** Randy Yi **MANAGER OF FULFILLMENT SYSTEMS** Neal Hawkins **SYSTEMS ANALYST** Nicole Mehmedovich **ASSISTANT DIRECTOR, BUSINESS OPERATIONS** Eric Knott **MANAGER, BUSINESS OPERATIONS** Jessica Tierney **BUSINESS ANALYSTS** Cory Lipman, Cooper Tilton, Celeste Troxler **FINANCIAL ANALYST** Robert Clark **RIGHTS AND PERMISSIONS ASSISTANT DIRECTOR** Emilie David **PERMISSIONS ASSOCIATE** Elizabeth Sandler **RIGHTS, CONTRACTS, AND LICENSING ASSOCIATE** Lili Kiser

MARKETING DIRECTOR Elise Swinehart **ASSOCIATE DIRECTOR OF ACQUISITION AND RETENTION** Julianne Wielga **MARKETING ASSOCIATE** Elizabeth Sattler **SR. MARKETING EXECUTIVE** Jennifer Reeves **ASSOCIATE DIRECTOR, CREATIVE SERVICES** Tzeitel Sorrosa **ART ASSOCIATE** Seil Lee **JR. ART ASSOCIATE** Kim Huynh **ASSISTANT COMMERCIAL EDITOR** Selby Frame **MARKETING PROJECT MANAGER** Angelissa McArthur **PROGRAM DIRECTOR, AAAS MEMBER CENTRAL** Peggy Mihelich **FULFILLMENT SYSTEMS AND OPERATIONS** membership@aaas.org **MANAGER, MEMBER SERVICES** Pat Butler **SPECIALISTS** LaToya Casteel, Terrance Morrison, Latasha Russell **MANAGER, DATA ENTRY** Mickie Napoleoni **DATA ENTRY SPECIALISTS** JJ Regan, Brenden Aquilino, Fiona Giblin

DIRECTOR, SITE LICENSING Tom Ryan **DIRECTOR, CORPORATE RELATIONS** Eileen Bernadette Moran **SR. PUBLISHER RELATIONS SPECIALIST** Kiki Forsythe **PUBLISHER RELATIONS MANAGER** Catherine Holland **PUBLISHER RELATIONS, EASTERN REGION** Keith Layson **PUBLISHER RELATIONS, WESTERN REGION** Ryan Rexroth **SALES RESEARCH COORDINATOR** Aiesha Marshall **MANAGER, SITE LICENSE OPERATIONS** Iquo Edim **SENIOR PRODUCTION SPECIALIST** Robert Koepke **SENIOR OPERATIONS ANALYST** Lana Guz **FULFILLMENT ANALYST** Judy Lillibridge **ASSOCIATE DIRECTOR, MARKETING** Christina Schlecht **MARKETING ASSOCIATES** Thomas Landreth, Isa Sesay-Bah

WEB TECHNOLOGIES SR. DEVELOPER Chris Coleman **DEVELOPERS** Dan Berger, Jimmy Marks, Ryan Jensen **SR. PROJECT MANAGER** Trista Smith

CREATIVE DIRECTOR, MULTIMEDIA Martyn Green **DIRECTOR OF ANALYTICS** Enrique Gonzales **SR. WEB PRODUCER** Sarah Crespi **WEB PRODUCER** Alison Crawford **VIDEO PRODUCER** Nguyen Nguyen **SOCIAL MEDIA PRODUCER** Meghna Sachdev

DIRECTOR OF OPERATIONS PRINT AND ONLINE Lizabeth Harman **DIGITAL/PRINT STRATEGY MANAGER** Jason Hillman **QUALITY TECHNICAL MANAGER** Marcus Spiegler **PROJECT ACCOUNT MANAGER** Tara Kelly **DIGITAL PRODUCTION MANAGER** Lisa Stanford **ASSISTANT MANAGER DIGITAL/PRINT** Rebecca Doshi **SENIOR CONTENT SPECIALISTS** Steve Forrester, Antoinette Hodal, Lori Murphy, Anthony Rosen **CONTENT SPECIALISTS** Jacob Hedrick, Kimberley Oster

DESIGN DIRECTOR Beth Rakouskas **DESIGN EDITOR** Marcy Atarod **SENIOR DESIGNER** Garvin Grullón **DESIGNER** Chrystal Smith **GRAPHICS MANAGING EDITOR** Alberto Cuadra **SENIOR SCIENTIFIC ILLUSTRATORS** Chris Bickel, Katharine Sutliff **SCIENTIFIC ILLUSTRATOR** Valerie Altounian **SENIOR ART ASSOCIATES** Holly Bishop, Nathalie Cary, Preston Huey **SENIOR PHOTO EDITOR** William Douthitt **PHOTO EDITORS** Leslie Blizard, Christy Steele

DIRECTOR, GLOBAL COLLABORATION, CUSTOM PUBLICATIONS, ADVERTISING Bill Moran **EDITOR, CUSTOM PUBLISHING** Sean Sanders: 202-326-6430 **ASSISTANT EDITOR, CUSTOM PUBLISHING** Tianna Hicklin: 202-326-6463 **ADVERTISING MARKETING MANAGER** Justin Sawyers: 202-326-7061 science_advertising@aaas.org **ADVERTISING MARKETING ASSOCIATE** Javia Flemmings **ADVERTISING SUPPORT MANAGER** Karen Foote: 202-326-6740 **ADVERTISING PRODUCTION OPERATIONS MANAGER** Deborah Tompkins **SR. PRODUCTION SPECIALIST/GRAPHIC DESIGNER** Amy Hardcastle **PRODUCTION SPECIALIST** Yuse Lajiminmuhip **SR. TRAFFIC ASSOCIATE** Christine Hall **SALES COORDINATOR** Shirley Young **ASSOCIATE DIRECTOR, COLLABORATION, CUSTOM PUBLICATIONS/CHINA/TAIWAN/KOREA/SINGAPORE** Ruolei Wu: +86-186 0082 9345, rwu@aaas.org **COLLABORATION/ CUSTOM PUBLICATIONS/JAPAN** Adarsh Sandhu + 81532-81-5142 asandhu@aaas.org **EAST COAST/E. CANADA** Laurie Faraday: 508-747-9395, FAX 617-507-8189 **WEST COAST/W. CANADA** Lynne Stickrod: 415-931-9782, FAX 415-520-6940 **MIDWEST** Jeffrey Dembski: 847-498-4520 x3005, Steven Loerch: 847-498-4520 x3006 **UK EUROPE/ASIA** Roger Goncalves: TEL/FAX +41 43 243 1358 **JAPAN** Katsuyoshi Fukamizu(Tokyo): +81-3-3219-5777 kfukamizu@aaas.org **CHINA/TAIWAN** Ruolei Wu: +86-186 0082 9345, rwu@aaas.org

WORLDWIDE ASSOCIATE DIRECTOR OF SCIENCE CAREERS Tracy Holmes: +44 (0) 1223 326525, FAX +44 (0) 1223 326532 tholmes@science-int.co.uk **CLASSIFIED** advertise@sciencecareers.org **U.S. SALES** Tina Burks: 202-326-6577, Nancy Toema: 202-326-6578 **SALES ADMINISTRATOR** Marci Gallun **EUROPE/ROW SALES** Axel Gesatzki, Sarah Lelarge **SALES ASSISTANT** Kelly Grace **JAPAN** Hiroyuki Mashiki(Kyoto): +81-75-823-1109 hmashiki@aaas.org **CHINA/TAIWAN** Ruolei Wu: +86-186 0082 9345 rwu@aaas.org **MARKETING MANAGER** Allison Pritchard **MARKETING ASSOCIATE** Aimee Aponte

AAAS BOARD OF DIRECTORS RETIRING PRESIDENT, CHAIR Gerald R. Fink **PRESIDENT** Geraldine (Geri) Richmond **PRESIDENT-ELECT** Barbara A. Schaal **TREASURER** David Evans Shaw **CHIEF EXECUTIVE OFFICER** Rush D. Holt **BOARD** Bonnie L. Bassler, May R. Berenbaum, Carlos J. Bustamante, Stephen P.A. Fodor, Claire M. Fraser, Michael S. Gazzaniga, Laura H. Greene, Elizabeth Loftus, Mercedes Pascual

SUBSCRIPTION SERVICES For change of address, missing issues, new orders and renewals, and payment questions: 866-434-AAAS (2227) or 202-326-6417, FAX 202-842-1065. Mailing addresses: AAAS, P.O. Box 96178, Washington, DC 20090-6178 or AAAS Member Services, 1200 New York Avenue, NW, Washington, DC 20005

INSTITUTIONAL SITE LICENSES 202-326-6730 **REPRINTS:** Author Inquiries 800-635-7181 **COMMERCIAL INQUIRIES** 803-359-4578 **PERMISSIONS** 202-326-6765, permissions@aaas.org **AAAS Member Services** 202-326-6417 or http://membercentral.aaas.org/discounts

Science serves as a forum for discussion of important issues related to the advancement of science by publishing material on which a consensus has been reached as well as including the presentation of minority of conflicting points of view. Accordingly, all articles published in *Science*—including editorials, news and comment, and books reviews—are signed and reflect the individual views of the authors and not official points of view adopted by AAAS or the institutions with which the authors are affiliated.

INFORMATION FOR AUTHORS See pages 678 and 679 of the 6 February 2015 issue or access www.sciencemag.org/about/authors

SENIOR EDITORIAL BOARD

Robert H. Grubbs, *California Institute of Technology,* **Gary King,** *Harvard University*
Susan M. Rosenberg, *Baylor College of Medicine,* **Ali Shilatifard,** *Northwestern University*
Feinberg School of Medicine, **Michael S. Turner**, *U. of Chicago*

BOARD OF REVIEWING EDITORS (Statistics board members indicated with **(S)**)

Adriano Aguzzi, *U. Hospital Zürich*
Takuzo Aida, *U. of Tokyo*
Leslie Aiello, *Wenner-Gren Foundation*
Judith Allen, *U. of Edinburgh*
Sonia Altizer, *U. of Georgia*
Sebastian Amigorena, *Institut Curie*
Kathryn Anderson, *Memorial Sloan-Kettering Cancer Center*
Meinrat O. Andreae, *Max-Planck Inst. Mainz*
Paola Arlotta, *Harvard U.*
Johan Auwerx, *EPFL*
David Awschalom, *U. of Chicago*
Clare Baker, *University of Cambridge*
Jordi Bascompte, *University of Zurich*
Facundo Batista, *London Research Inst.*
Ray H. Baughman, *U. of Texas, Dallas*
David Baum, *U. of Wisconsin*
Carlo Beenakker, *Leiden U.*
Kamran Behnia, *ESPCI-ParisTech*
Yasmine Belkaid, *NIAID, NIH*
Philip Benfey, *Duke U.*
Stephen J. Benkovic, *Penn State U.*
May Berenbaum, *U. of Illinois*
Gabriele Bergers, *U. of California, San Francisco*
Bradley Bernstein, *Massachusettes General Hospital*
Peer Bork, *EMBL*
Bernard Bourdon, *Ecole Normale Supérieure de Lyon*
Chris Bowler, *École Normale Supérieure*
Ian Boyd, *U. of St. Andrews*
Emily Brodsky, *U. of California, Santa Cruz*
Ron Brookmeyer, *U. of California Los Angeles* **(S)**
Christian Büchel, *U. Hamburg-Eppendorf*
Joseph A. Burns, *Cornell U.*
Carter Tribley Butts, *U. of California, Irvine*
Gyorgy Buzsaki, *New York U. School of Medicine*
Blanche Capel, *Duke U.*
Mats Carlsson, *U. of Oslo*
Ib Chorkendorff, *U. of Denmark*
David Clapham, *Children's Hospital Boston*
David Clary, *U. of Oxford*
Joel Cohen, *Rockefeller U., Columbia U.*
James J. Collins, *MIT*
Robert Cook-Deegan, *Duke U.*
Alan Cowman, *Walter & Eliza Hall Inst.*
Robert H. Crabtree, *Yale U.*
Roberta Croce, *Vrije Universiteit*
Janet Currie, *Princeton U.*
Jeff L. Dangl, *U. of North Carolina*
Tom Daniel, *U. of Washington*
Frans de Waal, *Emory U.*
Stanislas Dehaene, *Collège de France*
Robert Desimone, *MIT*
Claude Desplan, *New York U.*
Ap Dijksterhuis, *Radboud U. of Nijmegen*
Dennis Discher, *U. of Pennsylvania*
Gerald W. Dorn II, *Washington U. School of Medicine*
Jennifer A. Doudna, *U. of California, Berkeley*
Bruce Dunn, *U. of California, Los Angeles*
William Dunphy, *Caltech*
Christopher Dye, *WHO*
Todd Ehlers, *U. of Tuebingen*
David Ehrhardt, *Carnegie Inst. of Washington*
Tim Elston, *U. of North Carolina at Chapel Hill*
Gerhard Ertl, *Fritz-Haber-Institut, Berlin*
Barry Everitt, *U. of Cambridge*
Ernst Fehr, *U. of Zurich*
Anne C. Ferguson-Smith, *U. of Cambridge*
Michael Feuer, *The George Washington U.*
Toren Finkel, *NHLBI, NIH*
Kate Fitzgerald, *U. of Massachusetts*
Peter Fratzl, *Max-Planck Inst.*
Elaine Fuchs, *Rockefeller U.*
Daniel Geschwind, *UCLA*
Karl-Heinz Glassmeier, *TU Braunschweig*
Ramon Gonzalez, *Rice U.*
Julia R. Greer, *Caltech*
Elizabeth Grove, *U. of Chicago*
Nicolas Gruber, *ETH Zurich*
Kip Guy, *St. Jude's Children's Research Hospital*
Taekjip Ha, *U. of Illinois at Urbana-Champaign*
Christian Haass, *Ludwig Maximilians U.*
Michael Hasselmo, *Boston U.*
Martin Heimann, *Max-Planck Inst. Jena*
Yka Helariutta, *U. of Cambridge*
James A. Hendler, *Rensselaer Polytechnic Inst.*
Janet G. Hering, *Swiss Fed. Inst. of Aquatic Science & Technology*
Kai-Uwe Hinrichs, *U. of Bremen*
Kei Hirose, *Tokyo Inst. of Technology*
David Hodell, *U. of Cambridge*
David Holden, *Imperial College*
Lora Hooper, *UT Southwestern Medical Ctr. at Dallas*
Raymond Huey, *U. of Washington*
Auke Ijspeert, *EPFL Lausanne*
Steven Jacobsen, *U. of California, Los Angeles*
Kai Johnsson, *EPFL Lausanne*
Peter Jonas, *Inst. of Science & Technology (IST) Austria*
Matt Kaeberlein, *U. of Washington*
William Kaelin Jr., *Dana-Farber Cancer Inst.*
Daniel Kahne, *Harvard U.*
Daniel Kammen, *U. of California, Berkeley*
Masashi Kawasaki, *U. of Tokyo*
V. Narry Kim, *Seoul National U.*
Joel Kingsolver, *U. of North Carolina at Chapel Hill*
Robert Kingston, *Harvard Medical School*
Etienne Koechlin, *Ecole Normale Suprieure*
Alexander Kolodkin, *Johns Hopkins U.*
Leonid Kruglyak, *UCLA*
Thomas Langer, *U. of Cologne*
Mitchell A. Lazar, *U. of Pennsylvania*
David Lazer, *Harvard U.*
Thomas Lecuit, *IBDM*
Virginia Lee, *U. of Pennsylvania*
Stanley Lemon, *U. of North Carolina at Chapel Hill*
Ottoline Leyser, *Cambridge U.*
Wendell Lim, *U.C. San Francisco*
Marcia C. Linn, *U. of California, Berkeley*
Jianguo Liu, *Michigan State U.*
Luis Liz-Marzan, *CIC biomaGUNE*
Jonathan Losos, *Harvard U.*
Ke Lu, *Chinese Acad. of Sciences*
Christian Lüscher, *U. of Geneva*
Laura Machesky, *CRUK Beatson Inst. for Cancer Research*
Anne Magurran, *U. of St. Andrews*
Oscar Marin, *CSIC & U. Miguel Hernández*
Charles Marshall, *U. of California, Berkeley*
C. Robertson McClung, *Dartmouth College*
Graham Medley, *U. of Warwick*
Tom Misteli, *NCI*
Yasushi Miyashita, *U. of Tokyo*
Mary Ann Moran, *U. of Georgia*
Richard Morris, *U. of Edinburgh*
Alison Motsinger-Reif, *NC State U.* **(S)**
Thomas Murray, *The Hastings Center*
James Nelson, *Stanford U. School of Med.*
Daniel Neumark, *U. of California, Berkeley*
Kitty Nijmeijer, *U. of Twente*
Pär Nordlund, *Karolinska Inst.*
Helga Nowotny, *European Research Advisory Board*
Ben Olken, *MIT*
Joe Orenstein, *U. of California Berkeley & Lawrence Berkeley National Lab*
Harry Orr, *U. of Minnesota*
Andrew Oswald, *U. of Warwick*
Steve Palumbi, *Stanford U.*
Jane Parker, *Max-Planck Inst. of Plant Breeding Research*
Giovanni Parmigiani, *Dana-Farber Cancer Inst.* **(S)**
Donald R. Paul, *U. of Texas, Austin*
John H. J. Petrini, *Memorial Sloan-Kettering Cancer Center*
Samuel Pfaff, *Salk Institute for Biological Studies*
Joshua Plotkin, *U. of Pennsylvania*
Albert Polman, *FOM Institute AMOLF*
Philippe Poulin, *CNRS*
Jonathan Pritchard, *Stanford U.*
David Randall, *Colorado State U.*
Colin Renfrew, *U. of Cambridge*
Felix Rey, *Institut Pasteur*
Trevor Robbins, *U. of Cambridge*
Jim Roberts, *Fred Hutchinson Cancer Research Ctr.*
Barbara A. Romanowicz, *U. of California, Berkeley*
Amy Rosenzweig, *Northwestern University*
Jens Rostrup-Nielsen, *Haldor Topsoe*
Mike Ryan, *U. of Texas, Austin*
Mitinori Saitou, *Kyoto U.*
Shimon Sakaguchi, *Kyoto U.*
Miquel Salmeron, *Lawrence Berkeley National Lab*
Jürgen Sandkühler, *Medical U. of Vienna*
Alexander Schier, *Harvard U.*
Randy Seeley, *U. of Cincinnati*
Vladimir Shalaev, *Purdue U.*
Robert Siliciano, *Johns Hopkins School of Medicine*
Denis Simon, *Arizona State U.*
Uri Simonsohn, *U. of Pennsylvania*
Alison Smith, *John Innes Centre*
Richard Smith, *U. of North Carolina* **(S)**
John Speakman, *U. of Aberdeen*
Allan C. Spradling, *Carnegie Institution of Washington*
Jonathan Sprent, *Garvan Inst. of Medical Research*
Eric Steig, *U. of Washington*
Paula Stephan, *Georgia State U. and National Bureau of Economic Research*
Molly Stevens, *Imperial College London*
V. S. Subrahmanian, *U. of Maryland*
Ira Tabas, *Columbia U.*
Sarah Teichmann, *Cambridge U.*
John Thomas, *North Carolina State U.*
Shubha Tole, *Tata Institute of Fundamental Research*
Christopher Tyler-Smith, *The Wellcome Trust Sanger Inst.*
Herbert Virgin, *Washington U.*
Bert Vogelstein, *Johns Hopkins U.*
Cynthia Volkert, *U. of Göttingen*
Douglas Wallace, *Dalhousie U.*
David Wallach, *Weizmann Inst. of Science*
Ian Walmsley, *U. of Oxford*
Jane-Ling Wang, *U. of California, Davis*
David A. Wardle, *Swedish U. of Agric. Sciences*
David Waxman, *Fudan U.*
Jonathan Weissman, *U. of California, San Francisco*
Chris Wikle, *U. of Missouri* **(S)**
Ian A. Wilson, *The Scripps Res. Inst.* **(S)**
Timothy D. Wilson, *U. of Virginia*
Rosemary Wyse, *Johns Hopkins U.*
Jan Zaanen, *Leiden U.*
Kenneth Zaret, *U. of Pennsylvania School of Medicine*
Jonathan Zehr, *U. of California, Santa Cruz*
Len Zon, *Children's Hospital Boston*
Maria Zuber, *MIT*

BOOK REVIEW BOARD

David Bloom, *Harvard U.*, **Samuel Bowring,** *MIT,* **Angela Creager,** *Princeton U.,*
Richard Shweder, *U. of Chicago,* **Ed Wasserman,** *DuPont*

EDITORIAL

Eradicating polio

On 20 September 2015, the Global Commission for the Certification of Poliomyelitis Eradication (GCC) declared that type 2 wild poliovirus had been eradicated. The GCC examined reports from 189 of 195 countries around the world and studied separate data [held by the World Health Organization (WHO)] from the remaining countries. According to WHO, nearly 2 million appropriate clinical samples had been tested, and no type 2 wild polioviruses were found. The announcement is the first step toward eradicating all three wild poliovirus types. But this landmark will only be declared when the GCC is confident that there have been no wild virus cases of any type for 3 years.

The last case of type 3 wild poliovirus occurred in northern Nigeria 3 years ago. In theory, declaration of its eradication could happen now. However, the polio programs from 18 African countries have not yet been scrutinized by the African Regional Certification Commission to ensure that no cases have been missed. This assessment will happen 3 years after each country's last case of any wild poliovirus. By the end of 2017, all African countries must have gone successfully through their regional commission's scrutiny, and no wild virus cases must have occurred. If that happens, all countries in the world will submit their data to the GCC and type 3 wild poliovirus eradication can be declared.

That will leave just the type 1 poliovirus, which is still circulating in Pakistan and Afghanistan. To date, the 51 cases of 2015 are far fewer than the 334 cases reported in 2014. This is probably the result of improved access to vaccination in key regions. But there are always fewer cases the year after high numbers are reported, because natural infection reduces the numbers of children susceptible to polio in the following year. The polio programs in both countries must further accelerate their activities. If transmission is interrupted by the end of 2016, then the world can be declared polio-free in 2019.

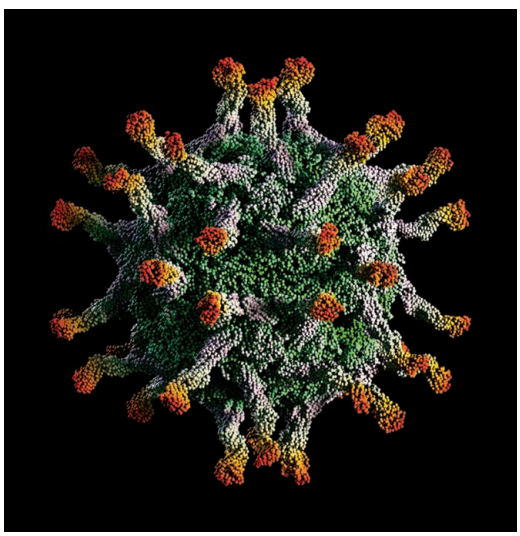

"A second human virus may soon be consigned to history."

One underappreciated consequence of the path toward eradication is that all polioviruses (wild and vaccine strains) in laboratory, research, and manufacturing facilities will have to be destroyed or securely contained. Last month, the WHO Strategic Advisory Group of Experts on immunization reaffirmed April 2016 as the date for the globally synchronized withdrawal of type 2 oral poliovirus vaccine. This first step toward the eventual phased removal of all three vaccine types brings urgency to completing the destruction, and securing the containment, of type 2 wild polioviruses in all facilities. The fewer the places that hold either polioviruses or specimens that could contain polioviruses, the more certain we can be that they will not be released inadvertently. This means that the vaccine industry will have to comply with high levels of assurance of containment in their manufacturing processes. Researchers and institutions holding samples collected from places where there could have been polioviruses must ensure that these are destroyed or secured under appropriate biocontainment levels. Countries will need to submit inventories of all laboratories to the GCC for review, and manufacturers and laboratories planning to retain type 2 polioviruses will need to be inspected for compliance with containment guidelines.

In 1980, smallpox was declared eradicated after a global immunization campaign led by WHO. But 2 years earlier, a year after the last natural smallpox case (in Somalia), there was an inadvertent release of smallpox virus from a research lab in the United Kingdom, from which one person died. While we wait for Pakistan and Afghanistan to stop the spread of type 1, we must prepare to safely and securely contain all polioviruses. A second human virus may soon be consigned to history. Until then, the whole world, especially countries with fragile health systems, remains at risk of this disease.

– Anthony Adams and David M. Salisbury

Anthony Adams is a former professor of public health at the Australian National University and the former Chief Medical Officer of Australia. E-mail: aarr@netspeed.com.au

David M. Salisbury is an associate fellow at the Centre for Global Health Security, Chatham House, London, UK. E-mail: david.salisbury@btinternet.com

A.A. and D.M.S. are writing on behalf of the GCC: Anthony Adams (Chair), Supamit Chunsuttiwat, Arlene King, Rose Gana F. Leke, Yagob Al Mazrou, and David M. Salisbury.

10.1126/science.aad7294

PHOTOS: (TOP RIGHT) SIGRUN ROESEL; (BOTTOM RIGHT) WORLD HEALTH ORGANIZATION; (INSET) MARTIN MCCARTHY/ISTOCKPHOTO.COM

Published by AAAS

NEWS

"Our constitution demands that we possess scientific temper and a commitment to reason, but our government is now moving away from scientific temper and reason."

Molecular biologist Pushpa Bhargava, to BBC Hindi, on his decision to return the Indian government's prestigious Padma Bhushan award in protest of religious extremism.

IN BRIEF

A new glimpse of Enceladus

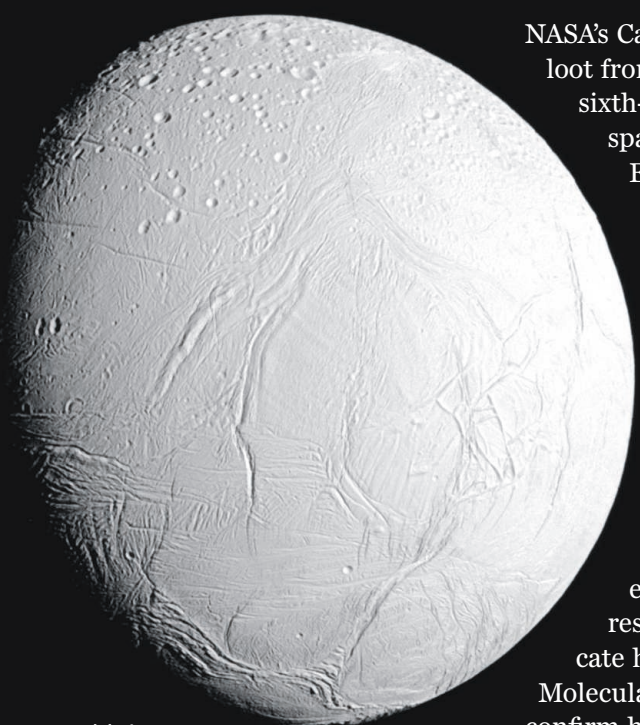

Enceladus, snapped during Cassini's deep dive toward the moon last week.

NASA's Cassini spacecraft has returned some photographic loot from its plunge toward the icy surface of Saturn's sixth-largest moon. The 28 October flyby sent the spacecraft just 49 kilometers above the surface of Enceladus, and through one of its huge geysers. No new images of the geysers are available yet, but the latest snapshots highlight the moon's fractured, cratered surface. Since Cassini began its flybys of Saturn and its moons in 2005, researchers have spotted more than 100 geysers, which spew the contents of Enceladus's subglacial ocean—ice particles, water vapor, and organic molecules—out of fractures in the ice covering the moon's south polar region. Samples from the flyby should give scientists a fuller picture of the plumes' makeup, perhaps even settling a debate over whether its eruptions resemble curtains or columns. And they could indicate how hospitable that buried ocean is for biology. Molecular hydrogen in the plume, for example, would help confirm hydrothermal activity on the sea floor, a potentially important ingredient for life.

AROUND THE WORLD

Chronic fatigue research boost

BETHESDA, MARYLAND | Myalgic encephalomyelitis/chronic fatigue syndrome (ME/CFS), a baffling illness that has attracted few researchers, is receiving far more serious attention from the U.S. National Institutes of Health (NIH). Director Francis Collins announced last week that the NIH Clinical Center will launch a new study of the disease, which will be moved from the Office of Research on Women's Health to the higher profile and better funded National Institute of Neurological Disorders and Stroke. NIH currently spends only $5 million on the disease, which is estimated to affect more than 1 million Americans. ME/CFS patients have applauded the NIH announcement, though the "renewed research focus" does not include new money. Collins promises that will happen soon. "Give us a chance to prove we're serious, because we are," he says. **http://scim.ag/cfsboost**

Language trove goes digital

NEW GUINEA | Though not much larger than the state of Texas, the island of New Guinea is one of the most linguistically diverse places in the world, with more than 1000 distinct languages, many of which have never been analyzed by linguists. Last week, in the journal *PLOS ONE*, linguist Simon Greenhill of the Australian National University in Canberra presented a new online database of words gathered from published surveys, book chapters, and articles, as well as the accounts of early European explorers. TransNewGuinea.org already contains glossaries for more than 1000 languages from 23 different language families, including 145,000 words. Greenhill hopes the linguistic community will use the site to solve long-standing questions about how New Guinean populations expanded and spread their culture.

NOAA rejects email subpoena

WASHINGTON, D.C. | The National Oceanic and Atmospheric Administration (NOAA) last week declined to turn over employees' internal correspondence in response to a 13 October subpoena by the U.S. House of

PHOTO: NASA/JPL-CALTECH/SPACE SCIENCE INSTITUTE

Downloaded from www.sciencemag.org on November 5, 2015

Published by AAAS

Representatives Committee on Science, Space, and Technology. The issue stems from a paper by NOAA scientists published 5 June in *Science* that found corrections to atmosphere and ocean temperature data biases erased an apparent "pause" in global warming that began in 1998, as noted by the Intergovernmental Panel on Climate Change in its fifth assessment report. On 23 October, Democrats on the committee published a letter on their website detailing the committee's multiple interactions with NOAA since June related to the paper's data and methodologies. The letter chastised the chairman, Representative Lamar Smith (R–TX), and science committee Republicans for "furthering a fishing expedition" with the subpoena. In light of NOAA's refusal to turn over internal communications, Smith's office says the chairman is considering next steps.

Fellowships for refugee scholars

BERLIN | The German government will help universities and research organizations hire scientists at risk of persecution in their home countries. On 30 October, the Alexander von Humboldt Foundation and the German Foreign Office announced their plans for the Philipp Schwartz Initiative, which will provide up to 3 years of funding for refugee scientists to work in Germany. The program is named for a Jewish neuropathologist who was forced to leave the University of Frankfurt in 1933. He fled to Switzerland, where he founded the Advisory Office for German Scientists, which helped other refugee researchers to find jobs abroad. He later worked in Turkey and the United States. Budget details are still being negotiated, but the Foundation says it expects to fund 20 scholars in 2016 and 20 more in 2017.

Cancer-killing virus clears FDA

SILVER SPRING, MARYLAND | U.S. regulators last week approved the first therapy that targets and destroys cancer cells with a genetically engineered virus. Talimogene laherparepvec (T-VEC), a modified herpesvirus developed by the pharmaceutical company Amgen, based in Thousand Oaks, California, won approval from the U.S. Food and Drug Administration on 27 October, making it the first so-called oncolytic viral therapy to be cleared for market. The treatment, which targets advanced skin cancer, is delivered as a series of injections directly into melanoma lesions. The virus selectively infects and replicates inside tumor cells. After infection, the cells rupture and release proteins that further provoke the immune system to attack the tumor. Now, the company is exploring using T-VEC in combination with other melanoma drugs to boost their effectiveness.

When it wraps around its prey, an electric eel doubles the shock.

Eels shock prey with a twist

An electric eel can stun its prey with hundreds of volts of electricity, but if it curls up around the victim first it can double that zap, according to a new study. Horizontal strands of nervous tissue running along an electric eel's body generate an electric field inside the animal, with a positive pole near the head and a negative one near the end of the tail, researchers reported last week in *Current Biology*. When they placed eels in a tank and dangled fish wired with electrodes in the water, the creatures used the curling tactic to bring their two poles together and increase the strength of the electric field. The experiments indicate that eels use the curling strategy more when their prey continues to struggle. The largest eels, which generate the most voltage, were less likely to bother with the tactic.

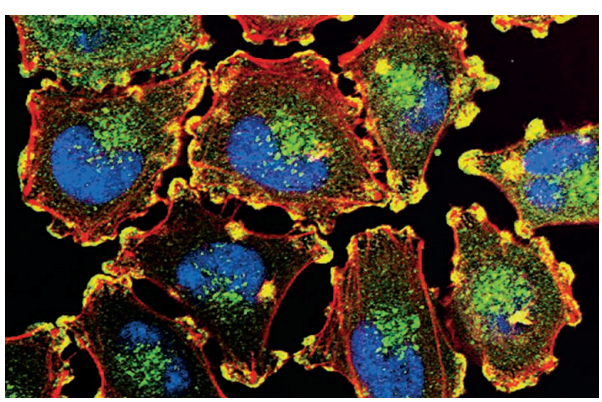

A genetically engineered virus therapy targets melanoma cells (shown).

FINDINGS

Snail sets tiny record

In the rainforests of Borneo, the smallest land snail known to science ekes out a secret existence in limestone cracks. At least, that's where researchers think they live. Scientists have only ever found their shells, translucent granules 0.60 to 0.79 mm high scattered at the base of cliffs. The team behind the discovery has named the minute gastropod *Acmella nana*, and described it—along with 47 other new Bornean snail species—in an article published online this week in *ZooKeys*.

PHOTOS: (TOP TO BOTTOM) © KENNETH C. CATANIA; JULIO C. VALENCIA/NCI CENTER FOR CANCER RESEARCH

Published by AAAS

Acmella nana, with 12-point font for scale.

Thanks to its tiny size, *A. nana* can probably fit into crevices other snails can't reach, vacuuming up bacteria and fungi that grow on wet limestone.

Quicker cure for hepatitis C

Targeting three different vulnerable components of the hepatitis C virus (HCV) may shorten the route to a cure, according to a small study to be presented next week at The Liver Meeting in San Francisco, California. Various combinations of three of the most effective anti-HCV drugs cured all 18 patients within 3 weeks. The approach could save thousands of dollars over the standard 12-week protocol, which attacks two HCV targets and has a $100,000 price tag. The study still needs to be confirmed in a larger trial, and its subjects don't represent most of the estimated 150 million HCV-infected people in the world: They were selected in part based on their positive response after 2 days of the drug treatment. Still, the study "opens a philosophical discussion about how to treat hepatitis C," says Mark Sulkowski, director of the viral hepatitis center at the Johns Hopkins University School of Medicine in Baltimore, Maryland. **http://scim.ag/hcvcure**

NEWSMAKERS

Quake official to stand trial

The official who ran Italy's civil protection department at the time of the deadly 2009 earthquake in L'Aquila will stand trial on charges of manslaughter, a judge ruled last week. **Guido Bertolaso** convened a panel of seven experts to analyze seismic risks days before the quake. Those experts were accused of making unjustifiably reassuring statements that led some people to remain indoors and perish. They were convicted and sentenced to 6 years in prison; all but one were acquitted last November. The new trial, set for 20 November, centers on a phone call before the experts' meeting, in which Bertolaso called it a "media operation" intended to "shut up" a technician from a nearby physics laboratory who had allegedly made alarmist predictions that had panicked the local population. **http://scim.ag/quaketrial**

THE *SCIENCE* NEWS QUIZ

Here's the question that stumped our readers this week: Can you outdo them? **Where did researchers find a skeleton that might unseat the current "first ancestor" of living apes and humans?**

Take the quiz—and find out the answer—here: **http://scim.ag/1XJTJFy**

A worker at a U.S. Army biodefense lab.

Scrutiny for U.S. biosecurity

Spurred by several accidents at federal labs, the White House last week announced new steps to shore up biosafety and biosecurity at facilities that work on risky pathogens and toxins known as select agents. The White House memo comes in response to inadvertent shipments of live anthrax samples and the discovery of old vials of live smallpox, among other incidents. It includes plans for public disclosure of lab accidents, a new anonymous system for reporting mishaps, and a review of the many high-containment labs in the country (**http://scim.ag/biomemo**). The memo came the same week as a report from two conservative Washington, D.C., think tanks finding that the nation's fragmented, $6-billion-a-year biodefense effort should be overseen by the vice president. **http://scim.ag/bidenreport**

BY THE NUMBERS

67%

Portion of the world's population infected with type 1 of the herpes simplex virus (World Health Organization).

15%

Fraction of Americans surveyed who said they are "more convinced that global warming is happening and we should act" as a result of Pope Francis's May encyclical (University of Michigan and Muhlenberg College).

22%

Increase in mortality among white middle-aged U.S. men with a high school degree or less, 1999–2013 (*Proceedings of the National Academy of Sciences*).

PHOTOS: (TOP TO BOTTOM) M. SCHILTHUIZEN/NATURALIS BIODIVERSITY CENTER; PATRICK SEMANSKY/AP PHOTO

Published by AAAS

Diamonds, such as these from South Africa, can grow from carbon injected into Earth's mantle by subducted seawater.

PHOTO: ORASA WELDON/GIA/GEMS & GEMOLOGY/GIFT OF DE BEERS

Downloaded from www.sciencemag.org on November 5, 2015

GEOCHEMISTRY

How buried water makes diamonds and oil

A new picture of water in the deep Earth predicts surprising chemistry

By **Eric Hand**

Diamonds are not only the hardest things around; they're also hard to make. They can only crystallize from carbon in the vise of the deep Earth, and they must make their way to the surface in explosive volcanic eruptions. In some cases, the carbon is inorganic and native to the depths. In others, however, geochemists have assumed it gets there through a complex sequence of events. First, seawater containing traces of organic carbon must be dragged hundreds of kilometers down into the mantle in subducting slabs of ocean crust. Then the carbon-bearing fluids have to escape from the slabs and rise until they infiltrate rocks with different chemical properties, releasing the carbon. Only then can the diamonds grow.

New research suggests a simpler scenario: Diamonds can form in the subducted water whenever it becomes more acidic—even if it doesn't move at all. "It looks to me like an easier way to make them," says Steve Shirey, a diamond expert at the Carnegie Institution for Science in Washington, D.C., who was not involved with the work. "It could mean that they're more prevalent in the Earth."

The theoretical calculation, published this week in *Nature Communications*, is just one consequence of a new picture of water's versatile chemistry in the deep Earth. The Deep Earth Water model, unveiled in a series of papers over the past 2 years by Dimitri Sverjensky, a geochemist at Johns Hopkins University in Baltimore, Maryland, predicts that under extreme pressures, water can dissolve a plethora of ions and host unexpected new reactions. "I'm inventing a new kind of chemistry of water-rock interactions at high pressures," Sverjensky says. "It simply hasn't been possible to model any of these processes in the deep Earth."

Diamond formation is just one such process. Sverjensky and his colleagues also have new experimental results that show how one of the ions expected to be present at depth—acetate, the main component in vinegar—can react to produce long-chain hydrocarbons. Oil, in other words. "If transported up to shallower environments, it conceivably forms a food for a deep biosphere," a microbial ecosystem thought to exist many kilometers deep in the crust, Sverjensky says. This oil-from-rock could even be contributing to shallower oil reservoirs, generally thought to form only from the burial and compaction of organic matter—a provocative suggestion that could reignite old debates.

The model represents "a real shift" in the understanding of deep Earth, says Isabelle Daniel, an experimental mineralogist at Claude Bernard University Lyon 1 in France who helped Sverjensky verify it by crushing tiny samples of minerals and water in high-pressure cells. Rick Carlson, a geochemist at the Carnegie Institution who was not involved in the work, agrees. "The complexity of the reactions and the consequence of what happens [in deep water] hasn't been appreciated until Dimitri's models," he says.

Sverjensky has literally taken geochemistry to new depths. Earlier theories—including the long-dominant Helgeson-Kirkham-Flowers model, published in 1981—predicted water-rock reactions up to pressures of 5 kilobars, about 15 kilometers down. For much of the planet, that's still in the crust. Below that, in the subduction zones that drive much of the mantle's chemistry, geochemists had little way of knowing what was going on, so for simplicity they typically assumed that the deep water carried a bare-bones load of carbon dioxide, methane, and hydrogen.

To understand water's behavior in the mantle, Sverjensky needed to know how one of its key physical parameters would change with depth: its dielectric constant, which determines how readily water dissolves other substances. In 2013, publishing in the *Proceedings of the National*

Published by AAAS

Academy of Sciences with colleagues at the University of Chicago in Illinois, Sverjensky extended knowledge about the dielectric constant to 60 kilobars, or about 200 kilometers—well into the mantle. It was a theoretical result, driven by a branch of computational chemistry called ab initio molecular dynamics, which predicts chemistry based on quantum mechanical first principles. "It's a hard calculation, and it requires a huge amount of computer time," says Craig Manning, an experimental geochemist at the University of California, Los Angeles.

The result suggested that water was a better solvent than expected at high pressures—and that it could hold in solution many more ions, such as carbonate. Previously, many geoscientists thought that the subduction of carbonate-bearing limestone would bury the carbon permanently in the mantle. But Sverjensky's calculations implied that carbonate dissolved in deep water could percolate up through the crust and back to the surface—an important new way for carbon to get back in circulation, where it can ultimately affect (among other things) atmospheric chemistry and climate. "It really tunes the deep carbon cycle," Daniel says.

To check his results experimentally, Sverjensky turned to Daniel, who creates deep-Earth pressures in her laboratory in France. In one key experiment, Daniel and colleagues put water and a single crystal of calcite—limestone—inside a gold-lined metal cylinder, smaller than a human hair. Then they squeezed the cylinder to intense pressures between two diamond-tipped anvils, mimicking the conditions 200 kilometers below the surface. Cameras recording through the transparent diamonds showed the calcite getting smaller and smaller at higher pressures: It was dissolving. And a spectrometer revealed that the dissolved ions were carbonate and bicarbonate. "It's kind of a love story," Daniel says. "The water has a tremendous affinity with the minerals down there."

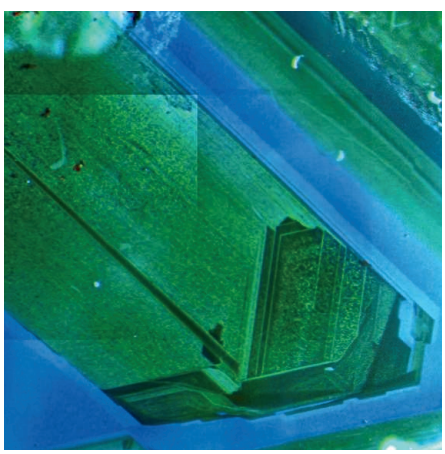

Layers in this diamond from Botswana may be due to changes in acidity of a carbon-bearing fluid.

Sverjensky has now worked out the equations governing the concentrations of more than 200 different chemicals at pressures as high as 60 kilobars and temperatures up to 1000°C. He plans to offer workshops to help other researchers familiarize themselves with the model. In the meantime, he is skimming off some of the creamiest science. In a paper published last year, Sverjensky used his model to show that under the conditions in Earth's mantle, nitrogen can exist in water as N_2, which can easily spew back into the atmosphere through volcanoes. That helps explain why Earth's atmosphere is so much more nitrogen-rich than those of Venus and Mars, where the deep nitrogen is more likely to stay put in mantle rocks as ammonium (NH_4^+).

The new diamond-forming mechanism, meanwhile, could help explain why some diamonds have layered textures: Changes in the acidity of the water could make crystals grow and dissolve in fits and starts. The result might also force researchers to rethink a long-standing assumption that a high proportion of light carbon isotopes in diamond indicates that the carbon originally hailed from organic matter on the sea floor. Changes in acidity can create similar mixes of isotopes, Sverjensky says. "So diamonds with these isotopic signals may have nothing to do with ancient life."

Even more startling may be the model's predictions of deep-Earth oil, which Daniel and her colleagues have now validated in an experiment to be presented at a meeting of the American Geophysical Union in December. The researchers put water and dissolved acetate into their diamond anvil apparatus, and, as they ramped up pressures and temperatures, little oily droplets began emerging from the water.

The result recalls controversial theories from the 1970s, when astrophysicist Thomas Gold and Soviet geoscientists claimed that some of Earth's oil and gas were created by purely geological processes in the planet's interior. Sverjensky says the oil his model predicts would probably be too deep and too scarce to be worth drilling for. But Daniel says the result on its own is exciting. "Previously it was thought that oil was 100% from biotic organisms," she says. "What we see here is just starting with minerals deep in the Earth." ■

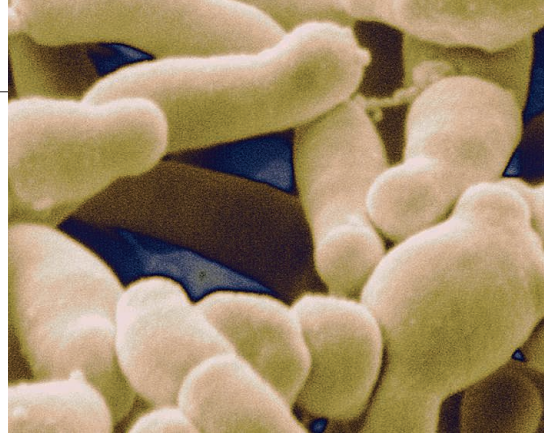

MICROBIOME

Microbes aid cancer drugs

Gut bacteria boost immunotherapies

By **Mitch Leslie**

A new class of cancer treatments that unleash the power of the immune system on tumors may depend on some unlikely allies. Two studies of mice in this week's issue of *Science* demonstrate that the gut microbiome—the swarms of microorganisms dwelling in the intestines—determines how effective these cancer immunotherapies are.

Known as checkpoint inhibitors, the therapies foil one of cancer's devious survival tricks: its ability to turn off the immune response that might otherwise attack tumor cells. Yet despite their promise, the drugs so far only help a minority of people with cancer. Researchers have suspected that genetic differences between patients might explain the varying responses, notes molecular biologist Scott Bultman of the University of North Carolina School of Medicine in Chapel Hill. The new results are encouraging, he says, because "it's easier to change your gut microbiota than your genome."

Checkpoint inhibitors target molecules that are key to cancer's immune-blocking effect. Some tumor cells stimulate CTLA4, a receptor on T cells that dials down their activity; others don a protein called PD-L1 that stifles potential T cell attackers. Ipilimumab, a monoclonal antibody that in 2011 became the first checkpoint inhibitor to receive Food and Drug Administration approval, blocks CTLA4, whereas other therapies, such as nivolumab and pembrolizumab, target PD-L1 or its receptor.

Ipilimumab often triggers colitis, an inflammation of the large intestine, where part of our microbiome lives. This side ef-

PHOTOS: (TOP TO BOTTOM) STEVEN SHIREY; SCIMAT/SCIENCE SOURCE

Published by AAAS

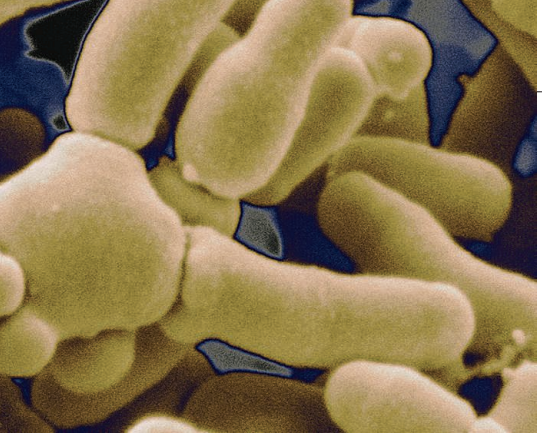

Bifidobacterium may stimulate the immune system's attacks on tumors.

fect suggested that checkpoint inhibitors could interact with the microbiome. To figure out whether they do, oncoimmunologist Laurence Zitvogel of the Gustave Roussy Cancer Campus in Villejuif, France, and colleagues tracked the growth of tumors implanted into mice lacking intestinal bacteria. They found that an antibody that blocks CTLA4 was less powerful in the animals.

The key missing microbes appeared to be bacteria in the *Bacteroides* and *Burkholderia* genera. Feeding those organisms to the microbe-free mice, either in pure form or in *Bacteroides*-rich feces from certain ipilimumab-treated patients, strengthened the animals' response to a CTLA4-inhibiting antibody. "Our immune system can be mobilized by the trillions of bacteria we have in our gut," Zitvogel says.

A second team led by immunologist Thomas Gajewski of the University of Chicago in Illinois came to a similar conclusion after noticing that melanoma tumors grew slower in mice from one supplier than in mice from another. Caging the mice together so that their microbiomes could homogenize erased the difference in tumor growth, indicating that the bacteria in one set of mice had been aiding their immune system. This team pinpointed members of the genus *Bifidobacterium* as an immune helper: Feeding mice a probiotic that contains several *Bifidobacterium* species increased the efficiency of a PD-L1–blocking antibody against tumors.

The fact that the two teams implicated different bacterial groups doesn't worry microimmunologist Christian Jobin of the University of Florida College of Medicine in Gainesville. "Different drugs, different bugs, but the same endpoint," he says.

Exactly how the microbiome bolsters the drugs remains unclear. Still, the discovery "opens up novel ways to potentially augment therapy," says Cynthia Sears, an infectious disease specialist at Johns Hopkins School of Medicine in Baltimore, Maryland. Doctors could, for example, try to beef up antitumor responses with probiotics, although Zitvogel notes that regulatory agencies haven't approved their use for cancer patients. ■

CREDITS: (GRAPHICS) M. ATAROD; DATA SOURCE: U.S. CONGRESS

DATA CHECK

BEHIND THE NUMBERS

How a $30 billion hike becomes $3 billion

By **Jeffrey Mervis**

Get your money this year—because federal spending in 2017 may feel very tight. That message for U.S. scientists is buried in the new 2-year budget agreement that President Barack Obama signed this week.

The Obama administration and the Republican-led Congress struck a surprise deal to prevent the U.S. government from defaulting on its loans and fund operations through the fall of 2017. The agreement adds $50 billion this year and $30 billion next year to caps on discretionary spending imposed by a 2011 law intended to reduce the federal deficit over the next decade (see graph, below). That law, called the Budget Control Act (BCA), led in 2013 to sequestration, those across-the-board, arbitrary cuts that nobody thinks are a good mechanism to determine funding levels.

The $50 billion jump will represent a 5% increase in overall discretionary spending for 2016. In 2017, however, the added $30 billion will boost overall discretionary federal spending by only $3 billion—a 0.3% rise that won't even keep pace with inflation.

What's the catch? The $30 billion is only the increase over the spending levels laid down in the 2011 budget law. It is NOT the amount added to the 2016 spending level. So the deal delivers "basically flat funding in 2017 from a higher baseline," says Matthew Hourihan, a budget analyst for AAAS (publisher of *Science*) in Washington, D.C. But there's a silver lining, he adds: The agreement locks in "a cumulative 4% increase in [discretionary] spending over 2 years. That's not bad."

Although Congress must still decide on 2016 spending levels for science funding agencies, many research groups have already lined up behind the new deal. "We are very encouraged … It provides much needed breathing room," said Washington, D.C.–based United for Medical Research, a coalition that backs increased biomedical research spending, in a statement.

Still, many science advocates say the deal highlights the continuing dysfunction of the federal budget process, which has lurched from crisis to crisis with no end in sight. The agreement was struck behind closed doors by a handful of White House aides and congressional leaders from both parties. Then it was rammed through Congress within a few days on a take-it-or-leave-it basis, passing with unanimous Democratic support despite the opposition of most Republicans, who control both houses of Congress.

The new agreement may be the most anyone could expect in an era of hyperpartisan politics. And it's only a temporary solution. The deal postpones but does not eliminate the BCA spending caps, which will go back into effect in 2018 unless an alternative is found. If not, discretionary spending would dip by $6 billion in 2018, and could trigger another high-stakes spending debate between Congress and the next president.

In the meantime, Congress's appropriations panels must decide by early December on how to allocate the additional $50 billion they've gotten for 2016. (The new agreement requires the increase each year to be spread evenly between the civilian and military sectors, although in a separate account it provides an additional $32 billion for ongoing war activities.) Those decisions are likely to have long-lasting consequences for scientists, because whatever levels lawmakers approve in the coming weeks are likely to be extended through the 2017 fiscal year. (Something similar happened earlier this year, under a 2-year agreement struck in 2013 to avert a similar budget-debt crisis.)

The bottom line: The sighs of relief that have greeted that seemingly hefty $30 billion growth in spending for 2017 may turn to grumbles when researchers realize it translates into just a $3 billion pimple. ■

Different yardsticks

A new U.S. budget deal lifts 2017 discretionary spending by $30 billion above existing budget caps. But that's only $3 billion, or 0.3%, more than in 2016.

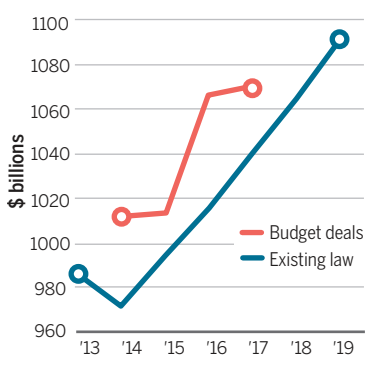

Downloaded from www.sciencemag.org on November 5, 2015

Published by AAAS

In Japan, mathematicians are using topology—the study of surface deformation—to optimize steelmaking.

PHOTO: MICHAEL S. YAMASHITA/CORBIS

SCIENCE IN SOCIETY

Pacific Rim mathematicians coaxed from their ivory towers

Programs to yoke mathematics to industrial needs are booming across the Asia-Pacific region

By **Dennis Normile**

Graeme Wake is an academic mathematician, but he is willing to get his hands dirty. He and a colleague recently devised an algorithm that optimizes fertilizer use in New Zealand pastures. "Cattle and sheep feed on grass, which makes it one of the most important industries for the country," says Wake, a professor emeritus of industrial mathematics at Massey University, Albany, in New Zealand.

For Wake and an increasing number of mathematicians around the Pacific Rim, applying their skills to challenges in industry has become a cause. An "isolationist attitude encouraged a generation ago is changing," Wake says. "Industry is learning that they can get value" from teaming up with mathematicians. In South Korea, when academics explain how math expertise can boost competitiveness, "the government is listening," adds Hyungju Park of Ajou University in Suwon, South Korea. Other nations are joining the bandwagon, resulting in a wave of new institutes, grant programs, and brainstorming sessions in the Asia-Pacific region.

Some trace the movement's roots to 1968, when the Mathematical Institute at the University of Oxford in the United Kingdom organized a study group bringing together mathematicians and corporate representatives. It has percolated through the math community in Europe and North America ever since. But until recently, Asia largely steered clear. At Japanese universities, for example, applied mathematicians have traditionally been members of engineering faculties, allowing those in math departments to remain aloof from practical problems, says Masato Wakayama of Kyushu University in Fukuoka, Japan.

But the walls are crumbling. In 2011, Kyushu University set up an Institute of Mathematics for Industry (IMI), the first of its kind in Asia. Three years later, mathematicians from 11 countries formed the Asia Pacific Consortium of Mathematics for Industry. In June, converts in New Zealand organized their first weeklong mathematics in industry study group, bringing together academics and company representatives. And in July, South Korea inaugurated its Industrial Mathematics Ignition Program, with $2.5 million in grants distributed to 21 academic teams; at a follow-up symposium in Seoul on 21 and 22 October, overseas experts offered advice to the grant winners.

Industry sometimes needs convincing. As one of its first efforts to find corporate partners, Kyushu's IMI tried to place mathematics graduate students as interns at corporations. "We sent 262 letters to leading companies. Only two replied and both refused," Wakayama says. To jump-start the matchmaking, IMI faculty members worked personal connections and have since placed 50 students in internships. Those connections have helped forge collaborations to apply stochastic differential equations to manage financial transactions, group theory to improve computer graphics, and topology—the study of surface deformation—to optimize steelmaking.

The South Korean effort, in contrast, is geared more toward startup companies, which "are showing tremendous interest," says Park. Winners of the new South Korean grants are modeling how drugs reach target organs, developing new approaches to analyzing big datasets, and delving into the complex geometry of computer animation.

The study group held last summer in New Zealand illustrates another way to bridge the gap between math and industry. "A lot of companies don't want to employ high-powered mathematicians, but they have a short-term need for mathematical advice," Wake says. For a $4000 fee, companies presented challenges. Academics volunteering their time brainstormed and developed possible solutions over the course of a week.

Among the companies seeking help in New Zealand was Auror, an Auckland-based startup specializing in antishoplifting software. The company collects industry and police data on shoplifters, their behavioral patterns, the types of products they steal, and daily and seasonal patterns of crime activity. Auror asked mathematicians to turn its data into algorithms to identify where and when repeat offenders are likely to strike. The firm joined the study group because it offered input from 100 or so of the country's top academic mathematicians, something that would have been difficult for a startup to arrange on its own. "We got access to expertise we would not have otherwise had," says Phil Thomson, Auror's CEO.

"Maths are ubiquitous," says Wake, who argues that few endeavors couldn't benefit from mathematical analysis—even growing grass. Wake and his colleague "went deep into systems biology" to turn such things as the chemical kinetics of fertilizer ingredients into equations, which AgKnowledge, a consulting firm in Hamilton, New Zealand, will put to use. By inputing data such as fertilizer cost, soil characteristics, and whether a farm is a dairy or livestock operation, "We'll be able to make decisions about fertilizer use based on the economic outcome and not just guesswork," says Doug Edmeades, AgKnowledge's managing director. "It's impossible to do that without the mathematics." ■

Downloaded from www.sciencemag.org on November 5, 2015

Published by AAAS

SCIENCE POLICY

India orders premier labs to pay their own way

"Self-finance" directive comes as government pushes indigenous innovation

By **Shruti Ravindran**, *in Mumbai, India*

India's Council of Scientific and Industrial Research (CSIR) has boosted the country's economy by fostering a booming generic drug industry and devising new approaches to hybrid crops. Now, the network of 38 national laboratories needs to nurture its own finances. The central government, intent on curbing domestic spending, feels CSIR's $600 million budget is a luxury it can no longer afford and has given the labs 2 to 3 years to "self-finance" half their expenditures by winning grants, licensing discoveries, and collaborating with industry.

The ultimatum, issued quietly at a CSIR meeting in June, is the most dramatic sign of the funding squeeze now gripping science in India. Prime Minister Narendra Modi's government insists it is not hostile to research: Rather, it wants R&D to better serve national interests. In addition to seeking their own funding, CSIR lab chiefs now must send reports to the government about how their centers serve flagship government programs such as schemes to build smart cities, clean the Ganges River, and promote sanitation. CSIR's newly appointed director general, Girish Sahni, says he is fully on board with the directive. "We don't always depend on our parents, do we?" he asks. "We live in challenging times, and this present government has posted these challenges on the bulletin board of the nation."

But the self-financing directive has riled many in India's scientific community. The CSIR labs "were founded to give know-how to Indian industry, and I agree that they should work on solving the country's problems," says Shri Krishna Joshi, a former CSIR director general. "But I fail to understand how frontier R&D institutions can become self-supporting in 2 years, unless they take on routine jobs like testing, which technicians at third-rate labs usually get subcontracted to do."

Since Modi came to power 18 months ago, his government has increased overall spending, by 5.7% this year. But most of the rise went to infrastructure projects—building new highways and upgrading rail lines, for instance—to stimulate economic growth. Meanwhile, it has slashed spending on the environment and social welfare, including health. A study to be published in *The Lancet* next month warns of a "collapse" if the government continues its low levels of investment in public health, among the lowest in the world at 1.3% of gross domestic product. Most science agencies have barely kept pace with inflation. "I'm already working against all odds on a very low budget," one medical researcher says. "Everyone I know is pissed beyond belief."

In science and technology, the sole winners are the Department of Atomic Energy, which is ramping up construction of nuclear reactors, and the Indian Space Research Organisation. Those champions reflect another Modi priority: indigenous innovation, at which India's nuclear and space communities excel thanks to years of coping with international sanctions imposed over the country's nuclear weapons program. Underscoring that, the government this week launched a $153 million program called IMPRINT to support projects, it said, "in areas where the country is heavily dependent on foreign technology." Smart sensors, renewable energy, nanotechnology, and diagnostic imaging are priorities.

4600
Number of scientists at CSIR's 38 centers.

90%
CSIR's share of U.S. patents among India's public R&D organizations.

50%
Fraction of budget CSIR must "self-finance" within 2 to 3 years.

Some scientists worry that the Modi government is not getting sound scientific advice. The prime minister disbanded a scientific advisory council that had served his predecessor. As a result, says C.N.R. Rao, a chemist who served as the previous government's chief scientific adviser, the government now lacks "capable people advising them on policy matters."

The government's moves put CSIR's very future at stake, some say, because the self-financing drive is doomed to fail. India doesn't have a funding ecosystem like that of the United States, where entrepreneurial scientists can seek venture capital and foundation support, says Sidharth Chopra, who studies antibiotic resistance at the Central Drug Research Institute in Lucknow, a CSIR-affiliated lab. "In India, there's nobody, not a single industrialist, who'll give you a dime," he says.

He thinks the government has its priorities wrong. "I'm a big [space] fan, don't get me wrong," Chopra adds. "But the next time you have diarrhea, and don't have antibiotics that work, Mars will be the last thing on your mind."

Defending the CSIR directive, Harsh Vardhan, India's science minister, told *The Hindu* newspaper last week that the government hopes to hasten technology transfer from lab to industry, and to make labs more accountable. "There is no harm in relying on industry to scale up or take forward the research projects underway," he said.

Sahni, CSIR's director, says that researchers should quit griping and get with the program. "It's high time Indian scientists rose to the occasion, and not merely published papers to satisfy their natural curiosity," he says, "but also got together, with their best ideas and technologies, to solve the nation's problems." ■

Shruti Ravindran is a freelance writer.

PHOTO: COUNCIL OF SCIENTIFIC AND INDUSTRIAL RESEARCH, INDIA

CSIR's institute in Jorhat will soon see government funding evaporate.

Downloaded from www.sciencemag.org on November 5, 2015

Published by AAAS

Studies of the marine worm *Platynereis* have confirmed that the nervous system has two origins.

PHOTO: ANTJE FISCHER

DEVELOPMENTAL BIOLOGY

Using evolution to better identify cell types

Gene expression patterns show that apparently related cells can have very different evolutionary histories

By **Elizabeth Pennisi**, *in Santa Fe*

In biology, appearances can be deceiving. Evolutionary biologists know that similarities in form and function are no guarantee that distinct species are actually related: Think bats and birds, or wombats and groundhogs. To classify a creature, scientists now look to its DNA. But many still rely on appearance and function for parsing the cell types that make up these organisms. A small group of biologists is now pushing their colleagues to look instead for evolutionary clues to cells' true nature.

The push grows out of recent evidence that similar-looking cells in the brain and reproductive tract can have entirely different origins. "We need a different, more reliable concept" for classifying cells, says Stefanie Widder, a systems biologist at the University of Vienna. Widder was one of about 20 scientists who gathered this month at the Santa Fe Institute to hammer out an alternative way of defining the identities of cells, based not on their looks but on the pattern of genes they express. Not only do the gene-expression signatures yield a truer picture of the range of cell types in an organism, advocates argue, they also offer clues to how particular cell types have adopted new roles over the course of evolution.

Because almost all cells in a body have the same basic genome, DNA sequence differences themselves can't be used to trace their origins. But each cell type has a distinctive pattern of gene activity, which depends not just on a cell's current function but, biologists believe, on its evolutionary history. The sequencing revolution has led to efficient ways of assessing this repertoire of active genes, and through comparisons of such "transcriptomes," biologists are finding that many cell types are in need of revision.

About 18 months ago, for example, Detlev Arendt, an evolutionary biologist at the European Molecular Biology Laboratory (EMBL) in Heidelberg, Germany, drew on studies of brain evolution in vertebrates, annelid worms, and insects to suggest that all brains originate from two separate places in the embryo. One part arises from the tip of the embryo, he said, and the other from what becomes the animal's trunk. Working with John Marioni, a mathematician at the EMBL-European Bioinformatics Institute in Hinxton, U.K., Arendt tested that idea by looking at gene expression in individual nerve cells in the marine worm *Platynereis dumerilii*. Even though the cells from the two embryo sites look similar, their expression patterns are distinct, he reported at the meeting. For example, the trunk-derived neurons also express genes active in striated muscle cells. The two kinds of neurons must have evolved independently very early in animal history and only later joined forces in the brain.

Similar surprises are waiting in other brains, Arendt says. "It cannot be taken for granted that all cell types categorized as 'neurons' today in a given animal are more related to each other than to other cell types," he concludes. "It is impossible to really understand a nervous system in the absence of knowledge about the distinct evolutionary histories of its constituting cell types."

Günter Wagner, a development evolutionary biologist at Yale University, saw something similar when he studied gene expression patterns in the cells that make up the uterus. He found that one type, the decidual cells that form part of the interface between fetus and mother and are sloughed off after birth with the placenta, are a relatively recent innovation compared with other uterine cells. Many of the cell types making up the uterus appear to have evolved very early in the history of mammals, he said at the meeting. But based on differences in gene expression profiles in decidual cells from across the mammalian family tree, Wagner concluded that they arose about 200 million years ago, with the evolution of placental mammals.

Gene expression is also telling unexpected stories about cell types that look similar in different species. For example, both vertebrates and cnidarians such as jellyfish have striated muscle cells, but researchers have shown that these cells arose independently in the two groups and built the striation using different sets of genes. These studies, as well as other work in mammals, sea urchins, and nematodes over the past decade, indicate that it's just a subset of the gene regulatory network that defines a cell type. This subset is in play in the same cell type across organisms, providing strong evidence of evolutionary connectedness.

"We find that at [any] given time, each cell expresses only 40% of the genes that are expressed in all cells of the same type together," Mihaela Pavlicev, an evolutionary quantitative geneticist at the University of Cincinnati in Ohio, reported at the Santa Fe meeting from her studies of placental cells. The other active genes likely represent "modules" that turn on to impart a particular structure or function to the cell, Arendt has proposed.

Defining these functional modules and distinguishing them from the so-called character-identifying networks is a challenge for researchers who want to use transcriptomics and other genomics data to define cell types. As the meeting in Santa Fe drew to a close, participants outlined a pa-

Downloaded from www.sciencemag.org on November 5, 2015

Published by AAAS

The growth of cell complexity

This analysis from 20 years ago, when cells were classified by how they look, shows how cell type number rises as animals become more complex. Today, more cell types are recognized, making this curve even steeper.

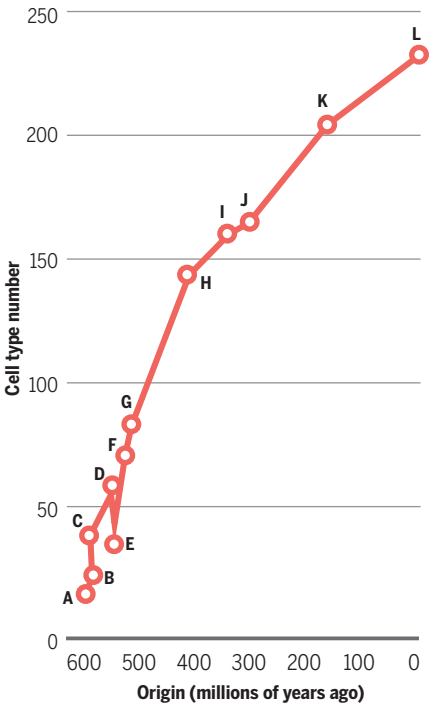

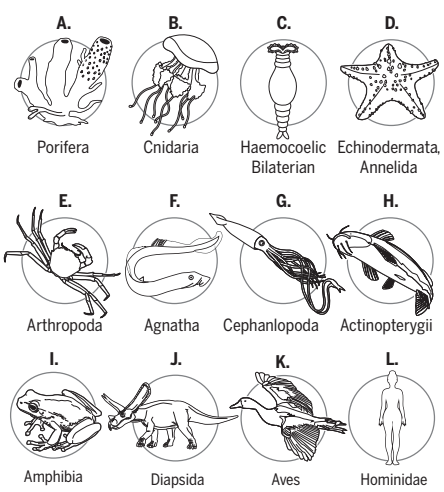

CREDITS: (GRAPHIC) G. GRULLON/*SCIENCE*; (DATA) VALENTINE *ET AL*., *PALEONTOLOGICAL SOCIETY* **20**, (23 SEPTEMBER 1994) © JSTOR; (PHOTO) DU CANE MEDICAL IMAGING LTD./SCIENCE SOURCE

per that they hope will clarify how to classify cells using transcriptomics and will lay out the case for understanding cell types from an evolutionary prospective. "It is like with species: One can study them in a variety of ways but you do not understand them until one understands that they are evolved entities," Wagner says. Pavlicev agrees: "I think [the evolutionary approach] will eventually take over, because it appears to offer strong explanatory power." ■

ONCOLOGY

Vitamin C could target some common cancers

Therapy kills tumor cells with difficult-to-treat mutation

By **Jocelyn Kaiser**

Maybe Linus Pauling was onto something after all. Decades ago the Nobel Prize–winning chemist was relegated to the fringes of medicine after championing the idea that high doses of vitamin C could combat a host of illnesses, including cancer. Now, a study published online this week by *Science* reports that vitamin C can kill tumor cells that carry a common cancer-causing mutation and, in mice, can curb the growth of tumors with the mutation.

If the findings hold up in people, researchers may have found a way to treat a large swath of tumors that has lacked effective drugs. "This has the potential to be one answer to the question everybody's striving for," says molecular biologist Channing Der of the University of North Carolina, Chapel Hill, one of many researchers trying to target cancers with mutations in the so-called RAS gene family.

The failure of two clinical trials of vitamin C pills in cancer patients, conducted in the late 1970s and early 1980s at the Mayo Clinic in Rochester, Minnesota, dampened enthusiasm. Studies later suggested that the vitamin must be given intravenously to reach doses high enough to kill cancer cells, and a few small trials found hints that IV vitamin C treatment extended cancer survival either alone or combined with chemotherapy. But doubters were not swayed. "The atmosphere was poisoned" by the earlier failures, says Mark Levine of the National Institute of Diabetes and Digestive and Kidney Diseases in Bethesda, Maryland, a collaborator on these trials.

A few years ago, Jihye Yun, then a graduate student at Johns Hopkins University (JHU) in Baltimore, Maryland, found that colon cancer cells whose growth is driven by a mutation in the genes *KRAS* or *BRAF* also make unusually large amounts of a protein that transports glucose across the cell membrane (*Science*, 18 September 2009, p. 1555). The transporter, GLUT1, supplies the cells with the high levels of glucose they need to survive. GLUT1 also transports the oxidized form of vitamin C, dehydroascorbic acid (DHA), into the cell, and Yun has now found that DHA can deplete a cell's supply of a chemical needed to sop up free radicals. Because free radicals can harm a cell in various ways, the finding suggested "a vulnerability" if the cells were flooded with DHA, says Lewis Cantley at Weill Cornell Medicine in New York City, where Yun is now a postdoc.

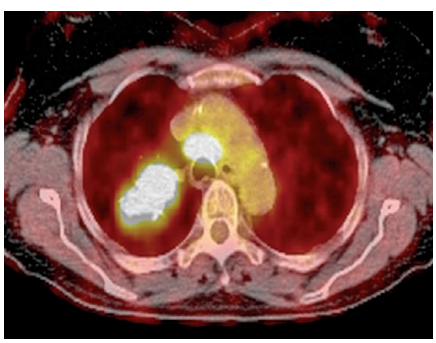

PET scans reveal glucose-hungry tumors, such as this lung mass, that may be treated by vitamin C.

Cantley's lab and collaborators found that large doses of vitamin C did indeed kill cultured cells with *BRAF* or *KRAS* mutations by raising free radical levels, which in turn inactivate an enzyme needed to metabolize glucose, depriving the cells of energy. Then they gave daily high dose injections—equivalent to a person eating 300 oranges—to mice engineered to develop *KRAS*-driven colon tumors. The mice developed fewer and smaller colon tumors compared with control mice.

Cantley hopes to soon start clinical trials that will select cancer patients based on *KRAS* or *BRAF* mutations and possibly GLUT1 status. Bert Vogelstein of JHU, in whose lab Yun noticed the GLUT1 connection, is excited about vitamin C therapy as well, not only as a possible treatment for *KRAS*-mutated colon tumors, which make up about 40% of this cancer type, but also for pancreatic cancer, a typically lethal cancer driven by *KRAS*. "No *KRAS*-targeted therapeutics have emerged despite decades of effort," Vogelstein says.

Others are intrigued but caution that the effects seen in mice may not hold up in humans. Still, because high dose vitamin C is already known to be safe, says cancer researcher Vuk Stambolic of the University of Toronto in Canada, oncologists "can quickly move forward in the clinic." ■

Published by AAAS

Downloaded from www.sciencemag.org on November 5, 2015

EGGS UNLIMITED

A company's fertility treatments spark disbelief as well as hope

By **Jennifer Couzin-Frankel**

PHOTO: STACEY LEE ROBSON

Baby Zain was born after his mother received a controversial new treatment that has the infertility world in an uproar.

On 11 August 2014, an anonymous user of a popular infertility forum typed a message. "I am 47 years old and have been keeping an avid eye on the OvaScience website (they have three new treatments to be available over the next few years)," she wrote. "The treatments are to do with developing egg cell treatments to help the IVF procedure … Does anyone else have any information?"

In the 14 months since, respondents have flooded the forum with more than 3500 replies, many brimming with optimism about the company's promise. One poster writes that she is $300,000 in debt ("yes, that's right, not a typo") from other fertility treatments. Still, she plans to borrow more for a shot at what OvaScience says it can do: coax primitive cells in the ovaries to turn into mature eggs. "I am betting my life that I will have a baby" with this technology, says another, who has liquidated her family's retirement plan in part to buy stock in the company.

OvaScience is preoccupied by an enduring mystery in human biology—why eggs fail—and the palpable hope that we can do something about it. On the company's homepage, a beautiful, smiling woman with red hair tumbling down her shoulders gazes at something off-screen. "A woman's biology is extraordinary," the tagline reads. Venture capitalists fueled OvaScience with $40 million soon after it launched in 2011, and it raised more than $200 million after going public a year later.

If the company's treatments achieve widespread success, it will be transformative. Experiments in the 20th century demonstrated that the ovaries of mammals hold a set number of eggs at birth. Unlike sperm, which the testes churn out into old age, the eggs you're born with are all the eggs you'll ever get—or so say the textbooks.

OvaScience, headquartered in Waltham, Massachusetts, disagrees. So do the fertility specialists offering its first treatment, called AUGMENT, for which the company charges up to $25,000; patients pay thousands more in clinic fees and roughly another $25,000 for the in vitro fertilization (IVF) cycle that must accompany it. The technique relies on mitochondria from putative egg precursor cells to boost the success of IVF, and 17 babies have been born so far. The company is poised to introduce a second treatment using these cells, often

called oocyte stem cells, to directly restore fertility.

To write about OvaScience is an exercise in mental whiplash. There are the reproductive biologists appalled by the company's activities, who say evidence is overwhelming that oocyte stem cells do not exist in adult mammals. There are the regulators in Canada who opened the country's doors to the company, and the U.S. officials who demanded that OvaScience stay away from patients until it has more data. There are bullish analysts buoyed by the company's prospects. And there's the biologist in Boston, Jonathan Tilly, who set this story in motion, first by describing oocyte stem cells and later by co-founding OvaScience. Tilly is combative, determined, and frustrated by ongoing challenges to his research; his scientist colleagues say that at meetings, he sometimes slips away after talks before questioners can jump in.

At the nexus of this unfolding drama are the patients: women who will endure almost any treatment, pay almost any price, and travel almost anywhere to have a baby.

"There's a lot more than science going on, as you probably surmised," David Albertini, a reproductive biologist at the University of Kansas Medical Center in Kansas City, says with a sigh. "There's a lot more than science."

A tonic for faltering eggs?

OvaScience says its AUGMENT treatment, which requires a laparoscopic surgery, draws mitochondria from egg precursor cells and uses them to boost egg health before IVF. There is no consensus on whether it works.

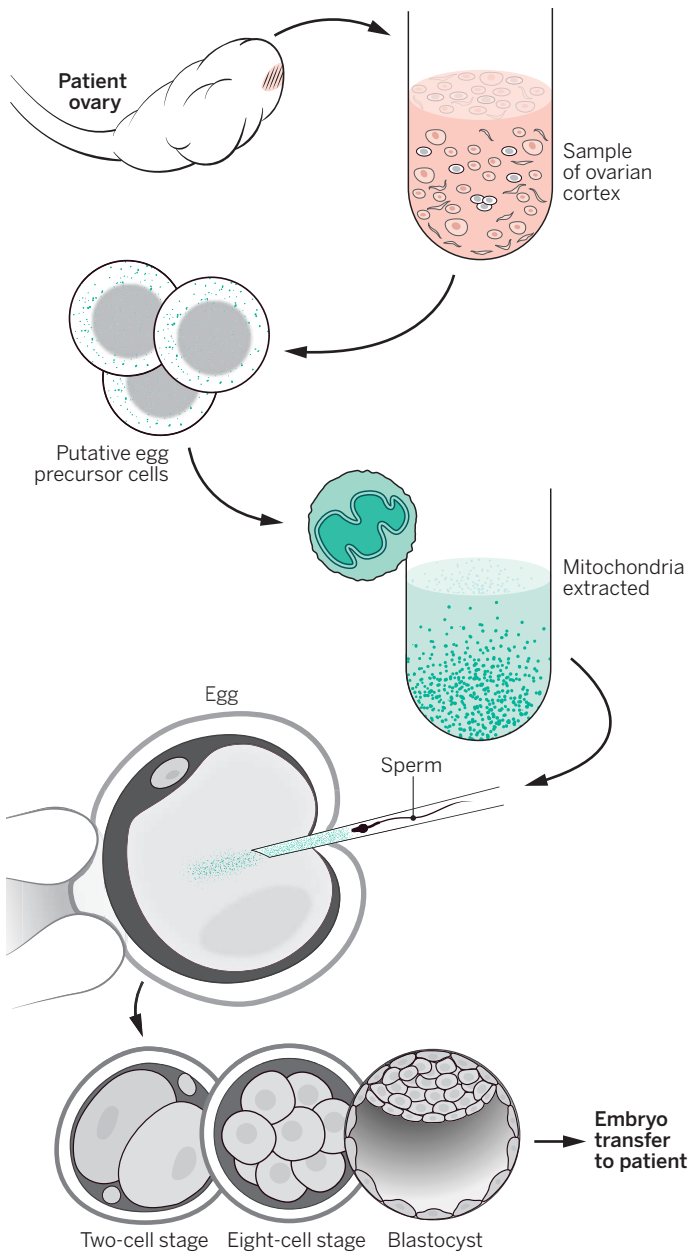

THE SCIENCE, however, is the best place to begin. In 2004, Tilly, then at Massachusetts General Hospital in Boston, dropped a bombshell. Writing in the journal *Nature*, his team described a new type of stem cell in mouse ovaries that they claimed could turn into full-fledged egg cells (*Science*, 12 March 2004, p. 1593). "The mind boggles at the implications," a now-retired leading reproductive biologist, Roger Gosden, told *The New York Times* back then. "The ability to make more eggs would be a revolution in women's health."

In 2005, Tilly reported that in mice, these stem cells were huddled inside bone marrow, and that marrow transplants might restore fertility in the animals (*Science*, 29 July 2005, p. 678). "I used to have patients tell me they were going to go to Mass General to get a bone marrow transplant to get new eggs," recalls David Keefe, an infertility specialist at New York University Langone Medical Center in New York City. "I pointed out, 'This has not been replicated.' At which point many of them would say, 'I would do anything to have my own baby.'"

Experiments the following year by another group challenged this result (*Science*, 16 June 2006, p. 1583). Although Tilly stands by his work, over time he focused on ovarian tissue rather than bone marrow as the best source of the putative stem cells.

Tilly says he's proven the existence of these stem cells by every method imaginable. But skeptics, and there are many, argue that he has relied chiefly on appearance and genetic markers to identify them. Most reproductive biologists insist that the cells be caught in the act of undergoing meiosis, the cell division unique to sperm and eggs in which bits of DNA are swapped between chromosomes. They also want to see that the resulting eggs can be fertilized and create offspring.

In 2009, a lab at Shanghai Jiao Tong University in China, led by reproductive biologist Ji Wu, reported the latter. Her paper in *Nature Cell Biology* described transplanting stem cells from the ovaries of newborn mice into sterilized mice (*Science*, 17 April 2009, p. 320). The animals gave birth to pups. "They got the mice," says Evelyn Telfer, a reproductive biologist at the University of Edinburgh, who has visited Wu's lab and thinks oocyte stem cells likely exist. "I believe there's something" there, she says.

To Tilly's exasperation, most biologists still weren't convinced. "The bar for acceptance was altered once again," he says. "The bar changed to, 'Well, this is just a mouse study.'"

Others perceive it differently. At least four groups tried and failed to find oocyte stem cells that turn into mature eggs. "We immediately repeated the experiment … My lab never got the cells," says Kui Liu, a molecular reproductive biologist at the University of Gothenburg in Sweden. Says Keefe, who collaborated with Lin Liu of Nankai University in Tianjin, China: "I've published three papers showing I see no evidence of these germ line stem cells in monkey, human, or mouse."

In 2013, two preeminent biologists, geneticist David Page of the Whitehead Institute in Cambridge, Massachusetts, and reproductive biologist John Eppig of the Jackson Laboratory in Bar Harbor, Maine, and their colleagues published a study that might help explain the conflicting results. Writing in *Nature Genetics*, they showed that certain

ILLUSTRATION: K. SUTLIFF/*SCIENCE*

Published by AAAS

cells could differentiate into something that looked very much like an oocyte under a microscope and responded similarly to hormones. But these cells didn't enter meiosis, meaning they were, in Eppig's words, "oocyte wannabes" and not the real thing.

Wu, who described the mouse pups, did not respond to calls and emails to comment for this story. But Tilly says his own lab repeated her experiments. It took 9 months before success was in sight—a time during which skeptics would have given up, he points out—but "we made mice as well." He presented the data at a meeting in 2013, but hasn't published because he doubts another paper from his lab will sway skeptics.

Tilly is baffled by the entrenched opposition: "Anyone who continues to question the existence of the cells in light of all this literature is either naïve, or they just have an ulterior motive that's not science-related," he says.

On the opposite side of the chasm is Hugh Clarke, a reproductive biologist at McGill University in Montreal, Canada. Given the evidence to date, Clarke seems bewildered that oocyte stem cells are not only hanging on but enhancing their public profile. "I don't know anybody in the community" of basic scientists who believes in these cells, he says. "I would have thought the debate was worth putting to bed. I thought it was over—but here's OvaScience."

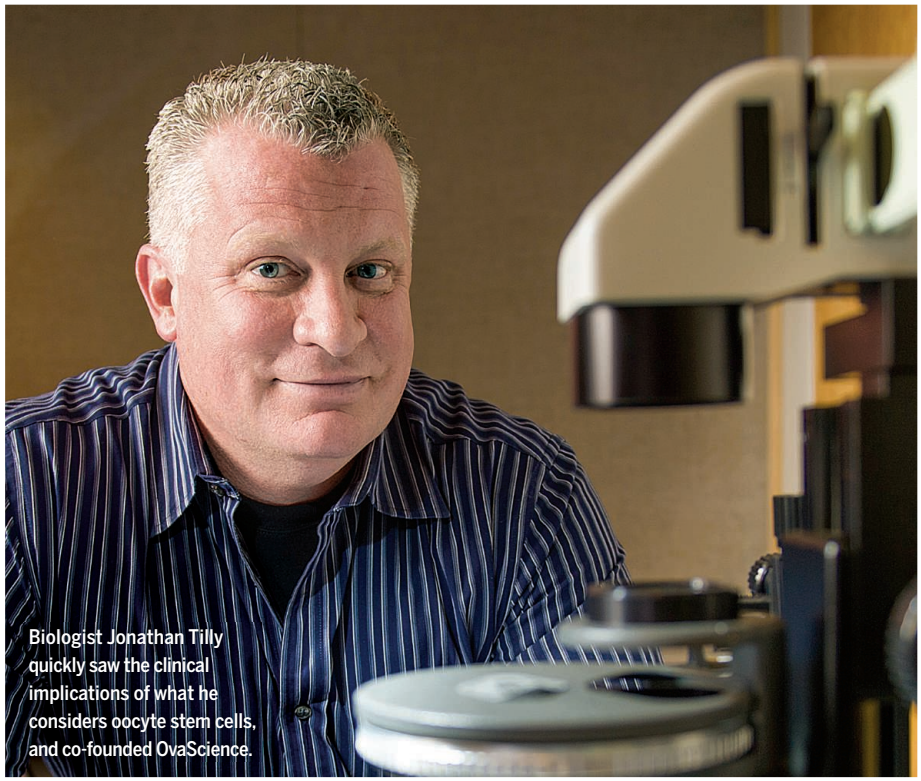

Biologist Jonathan Tilly quickly saw the clinical implications of what he considers oocyte stem cells, and co-founded OvaScience.

PHOTO: SAM OGDEN

THE FIRST OVASCIENCE BABY was born in Toronto, Canada, this past April. Photos of adorable Zain Rajani, with his clutch of dark hair and clenched newborn fists, were beamed around the world.

Baby Zain's mother received OvaScience's AUGMENT treatment. As its name suggests, AUGMENT aims to supplement eggs with extra mitochondria, tiny organelles that swim in the cell's cytoplasm and serve as its energy source. Studies have shown that mitochondria falter in older eggs, and Tilly says he was inspired by an experiment in the late 1990s, in which doctors removed cytoplasm from healthy women's eggs and injected it 30 times into the egg cells of infertile women. Thirteen women got pregnant.

A leader of that work, clinical embryologist Jacques Cohen of Reprogenetics in Livingston, New Jersey, is circumspect about the outcomes. Although "a few more pregnancies" were recorded than might have been otherwise, this was a pilot study, not solid proof of cytoplasm's potency, he says (*Science*, 3 April, p. 14). But Tilly was impressed. "By any criteria, despite the small treatment size, this worked," Tilly says. Success "went from 0% to 43%."

AUGMENT relies on a woman's own mitochondria rather than cytoplasm from donor eggs. To perform the treatment, doctors biopsy tissue from the lining of a woman's ovaries via laparoscopic surgery, normally while she's under general anesthesia. They transport the sample to an OvaScience lab, where company employees isolate what they describe as egg precursor cells, and extract mitochondria from them. Then, during IVF, the doctor injects the mitochondria plus sperm into a woman's eggs, and transfers one or more embryos to her uterus.

Clinics in Canada, Turkey, and the United Arab Emirates began offering AUGMENT in 2014. Recently Panama and Spain joined the list, and Japan and the United Kingdom are poised to do the same.

All 17 AUGMENT babies, born mostly to younger women, so far appear healthy. "Doctors have published a 10-fold increase in pregnancy rates," company CEO Michelle Dipp proclaimed in a conference call with investors in late September. Dipp's numbers come from a paper published in August by doctors in Toronto and Dubai in the *Journal of Fertilization: In Vitro-IVF-Worldwide, Reproductive Medicine, Genetics & Stem Cell Biology*. The Toronto group, led by Robert Casper, cited 34 women who on average had failed two cycles of IVF; the Dubai group, led by Michael Fakih, included 59 women who had on average failed 4.3 IVF cycles. Their past live-birth rate hovered between 1% and 2%, meaning a couple had previously had a baby.

The Toronto team reported an ongoing pregnancy rate after AUGMENT of 26%, or nine out of 34 women, which is where Dipp got her 10-fold increase. At Fakih's clinic, the rate was 18%. Fakih and Casper, who did not respond to inquiries from *Science* for this story, were even more optimistic than Dipp. In their paper, they announced that AUGMENT had yielded 11-fold and 18-fold increases in pregnancy rates, respectively.

Statements like this make Keefe, the New York infertility specialist, almost apoplectic. "It's completely flawed, what they've done," says Keefe, who previously sat on a Food and Drug Administration (FDA) committee that evaluates cell therapies. "They said these patients have failed two cycles of IVF, so their untreated success rate was zero. Then we gave them the treatment and they have a 20%, 25% success rate. It's like saying I threw the coin twice and I didn't get any heads, so then the third time I threw a head—it's like 100 times better."

> ***"It's completely flawed, what they've done."***
>
> **David Keefe**, New York University Langone Medical Center

The published paper notes that the women had poor prognoses, and that pregnancy rates decrease with each subsequent standard IVF cycle. Keefe disputes that. Data "show that the pregnancy rate per IVF cycle doesn't change much up to cycle five," and

Published by AAAS

usually hovers around 30%, he says. That's awfully close to the 26% reported by the Toronto group. To Keefe and some others, the pregnancies were most likely due to garden-variety IVF.

HOVERING BEHIND THE CLINICAL question is a deeper puzzle. How can biologists clash about whether certain cells even exist? The dizzying back-and-forth erupted again last month in *Nature Medicine,* where two groups published similar results but interpreted them differently. Liu of Sweden reported that he couldn't find oocyte stem cells when he hunted them in basically the same way OvaScience does: He used an antibody that latches onto a protein called DDX4, known to be unique to germ stem cells. Another group, led by Erin Wolff, an infertility specialist at the National Institutes of Health (NIH) in Bethesda, Maryland, also failed to find oocyte stem cells in mice, monkeys, and people using DDX4 antibodies, but concluded that some of the cells just don't express DDX4. Wolff, who has worked with Tilly and receives funding from OvaScience through an NIH program for collaboration with industry, argued that the cells likely exist. (Wolff declined to be interviewed for this story.)

OvaScience says technical problems are largely to blame for the confusion. Most of the researchers who can't isolate oocyte stem cells are not using OvaScience's specially designed, proprietary antibody, explains immunologist Arthur Tzianabos, the company's president and chief scientific officer. Tzianabos says the standard DDX4 antibodies ordered from companies simply aren't much good: They detect cells without any DDX4 and miss cells that have it.

Researchers have questioned the reliability of commercial antibodies, but Liu does not think that explains why he and others have been unable to find the precursor cells. "I don't believe everybody got bad antibodies," he says.

Until now, OvaScience has declined to ship its antibody to outside scientists. Telfer in Scotland is hoping it will make an exception for her. Initially a critic of Tilly's work, she says seeing how Wu's Shanghai lab had created mouse pups helped convert her. She also was impressed by data Tilly shared with her, as well as the "openness and diligence" she witnessed in his lab when she dropped by. When people learn she's working on these cells, "they'll say 'You've gone over to the dark side,'" she laughs. "I thought, 'It's too easy just to dismiss this work.'"

Telfer is currently studying whether the cells she suspects are oocyte stem cells go through meiosis. So far she is seeing markers of that cell division—proteins produced by meiosis genes. Reproductive biologist Allan Spradling of the Carnegie Institution for Science in Washington, D.C., dismisses this method of nailing meiosis. "There are brain tumors that switch on" these genes, he says. He argues that a far better strategy would be a technique that tracks a cell's fate in an animal as the cell differentiates and eventually divides. Telfer acknowledges she still needs to record meiosis in action, and is planning those experiments.

OvaScience's Tzianabos says the controversy is unsurprising. "What you're seeing here is the reaction to a shift in a paradigm," he says. "When you're trying to translate a new paradigm, people just don't want to believe."

It's unlikely the divide will be bridged anytime soon. Placebo-controlled trials might satisfy doubters, but OvaScience has no plans to perform them, a position in keeping with the history of infertility treatments. IVF and other therapies did not go through rigorous clinical trials either (*Science*, 15 August 2014, p. 744).

OvaScience doesn't need trials to satisfy most regulators. In Canada, fertility treatments are generally overseen by the provinces, which often "leave it to physicians to self-regulate," says Ubaka Ogbogu, who teaches health law and science policy at the University of Alberta, Edmonton, in Canada. Ogbogu argues that all countries should approach OvaScience as the United States did. In 2013, FDA alerted it that AUGMENT would require the same raft of clinical trials as other novel therapies. OvaScience is in a "low-level dialogue" with FDA, says Tzianabos, but with AUGMENT being adopted elsewhere, the company feels confident about its future.

> ***"When you're trying to translate a new paradigm, people just don't want to believe."***
>
> **Arthur Tzianabos**, OvaScience's president

Investment analysts agree. Once OvaScience gains a toehold in a country, it's often well-positioned to make money. "The end market is attractive," says Zarak Khurshid, an analyst at WedBush Securities in San Francisco, California, who follows the company. "These are very motivated customers. This is a cash pay business, [which] we think supports a very high price point as a result." OvaScience says it charges between $15,000 and $25,000 for each cycle of AUGMENT, and the clinics add an additional fee including surgical costs. So far more than 200 women have started or completed AUGMENT, although only about 35 have paid. OvaScience has a training system for clinics during which the company may absorb costs.

AUGMENT is just the beginning. The company's next two therapies, OvaPrime and OvaTure, rely directly on the so-called egg precursor cells to make a baby. OvaPrime, which the company expects to start offering in one country by the end of the year, involves two laparoscopic surgeries. The first extracts tissue from the ovarian lining, after which the putative precursor cells are isolated. The second surgery inserts the cells into part of a woman's ovary. There, OvaScience expects them to mature, and patients can get pregnant via IVF or, potentially, on their own. OvaTure is similar, except that the precursor eggs will be matured in a lab, then fertilized and transferred.

The OvaScience story underscores how differently researchers read the same data—or lack of it. Hugh Taylor, a reproductive endocrinologist at Yale University, receives funding from OvaScience for endometriosis research and sits on the company's scientific advisory board. The AUGMENT work published so far is "not reaching the highest level of evidence, but it isn't an unreasonable place to start," he says. "When there's a medical problem with no solution, people are desperate. People would say it's unethical to withhold helpful treatment." Taylor would offer his patients AUGMENT as part of a trial if it were available in the United States. "Physicians want proof that it helps," he says. "The underlying biology is less important."

Keefe is on a different planet. "Everybody wants to believe in Santa Claus," he says. He wants OvaScience to halt all treatments until the basic science is resolved. "You're proposing to offer something for $50,000," he says, estimating the total cost of AUGMENT to patients. The company "may be sure" where those putative precusors come from, "but the world is not."

OvaScience disclosed in September that it's selling far fewer cycles of AUGMENT than hoped, a slump the company attributes to mergers and acquisitions of the fertility clinics it serves, which means that new technologies are sometimes put on hold. Analysts remain upbeat. Rohit Vanjani of Oppenheimer & Co. in New York City predicts 8500 cycles of AUGMENT worldwide in 2018.

As for Tilly, now at Northeastern University in Boston, he's pressing ahead with studies of putative oocyte stem cells, including how they behave naturally in the body. "For us, the work pushes forward," he says. "The science will ultimately win out." ■

Published by AAAS

Evidence gaps for ethical oversight p. 632

Transmitting mutations through chromatin p. 634 ▸

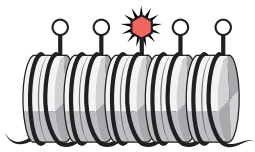

PERSPECTIVES

Public health emergency. During dengue epidemics, hospitals in developing countries—such as this ward in Quezon City, Philippines, in August 2011—can be overwhelmed by sick patients. A new vaccine may help to reduce the number of hospitalizations, easing the public health burden of dengue.

PUBLIC HEALTH

Dengue vaccines at a crossroad

Despite modest efficacy, a newly developed vaccine may be key for controlling dengue

By **Annelies Wilder-Smith**[1] *and* **Duane J. Gubler**[2]

The era when most vaccines provided efficacy well beyond 90% is over. Many of the more recently developed vaccines only provide partial efficacy. Although vaccines are typically licensed on the basis of demonstrated efficacy, the ultimate goal of vaccination goes far beyond efficacy. In addition to averting disease and death at an individual level, vaccination programs should decrease the public health burden of diseases at the population level. What counts is the impact on the reduction of vaccine-preventable disease incidence through direct and indirect protection, which is particularly pertinent for diseases that are of high public health importance.

A case in point is dengue, a flavivirus infection that is transmitted by *Aedes* mosquitoes. Every year, an estimated 390 million people—many of them children between 2 and 16 years—in more than 100 countries are infected with dengue, and over 50% of the world's population lives in areas at risk of infection (see the figure) (*1*). Infection with any of the four serotypes of dengue virus may result in a nonspecific febrile illness (classic dengue fever) or severe dengue manifested by plasma leakage, hemorrhagic tendencies, organ failure, shock, and possibly death. Patients with a second infection with a different serotype are thought to be at increased risk for severe disease (*2*), possibly due to antibody-dependent enhancement (*3*). Fatality rates are around 0.1 to 1% in hospitalized cases.

Dengue often requires hospitalization, thereby challenging already fragile health care systems (*4*). The often unpredictable nature of dengue epidemics further compounds the public health impact (see the photo). The incidence of dengue has increased more than 30-fold in the past 40 years and is being introduced to nonendemic areas such as the United States, Southern Europe, and Australia with increasing frequency. Effective vector

PHOTO: © JOHN JAVELLANA/REUTERS/CORBIS

Downloaded from www.sciencemag.org on November 5, 2015

Published by AAAS

control remains elusive (*5*), underscoring the need for a dengue vaccine.

Seven decades of dengue vaccine research have shown how challenging it is to develop a highly efficacious vaccine that protects against all four serotypes (*6*). But now, the first dengue vaccine is about to be licensed. The vaccine developed by Sanofi Pasteur (CYD-TDV) uses an infectious clone of the live attenuated yellow fever 17D vaccine virus to construct four chimeric viruses, each one engineered to express the surface envelope and premembrane proteins from one of the four dengue serotypes (*7*).

Efficacy results for the CYD-TDV vaccine come from two phase 3 trials in ~30,000 children aged 2 to 16 years, conducted in 10 highly endemic countries in Asia and Latin America (*8, 9*). The pooled data from these two trials showed an overall efficacy of 60% against virologically confirmed dengue of any severity due to any of the four serotypes (*10*). However, efficacy differed by serotype, was higher in individuals with prior dengue infections, and increased with age. Among children aged 9 years and older, efficacy was higher (66%) than in younger children (45%). Efficacy against severe dengue and hospitalization was substantial (93% and 81%, respectively) in children aged 9 years or older, compared with 45% and 56% in children younger than 9 years.

The efficacy results are complex, and the efficacy is modest; and elucidating the reasons for this complexity is warranted. Nonetheless, the efficacy results for severe disease and hospitalizations look promising, especially in older children. Reducing hospitalizations would be a major public health victory in dengue control. Furthermore, reducing overall infections may have a public health impact beyond efficacy by reducing virus circulation, thereby decreasing epidemic transmission.

Whether other dengue vaccine candidates in the pipeline (including inactivated, live attenuated, chimeric recombinant, subunit, and DNA vaccines) (*11*) will have higher overall efficacy remains to be shown. For the moment, CYD-TDV is the only dengue vaccine available. The moderate efficacy observed underscores the need to integrate dengue vaccination with improved vector control if there is to be hope of controlling this disease. This would have the added benefit of helping to control other *Aedes*-transmitted diseases such as chikungunya, zika, and yellow fever.

Of key importance is that a dengue vaccine must be safe (*12*). Long-term safety data are available from the third year of the phase 3 trials and from the third and fourth years of a phase 2b long-term follow-up study of CYD-TDV conducted in Thailand (*10*). Among children aged 9 to 16 years, dengue hospitalizations were reduced for up to 3 years after completion of the three-dose vaccine regimen (*10*). However, the pooled relative risk of dengue hospitalization in the younger vaccinated group was 1.58 during the third year, suggesting a trend to increased risk in vaccinees that was not observed in the fourth year (*10*). Further long-term follow-up of the phase 3 study participants is ongoing. For the time being, the transient reversed risk/benefit ratio observed in the third year in young children excludes this vaccine from being used in children under the age of 9 years.

Because of the higher efficacy and the absence of safety concerns in older children, the age group that would most benefit from the use of this vaccine is hence individuals aged 9 years and older. Indeed, Sanofi Pasteur now seeks licensure for CYD-TDV with an indication for persons in this age group.

The first dengue vaccine does not have the hoped-for high and balanced efficacy over all age groups. The quest to overcome these shortcomings through different vaccine development approaches has intensified. But in the meantime, the question is, can we use this vaccine, and if so, how? The answer will depend on a broader perspective in evaluating vaccines. Because the ultimate goal of vaccination goes beyond efficacy, we need to consider the capacity of a vaccination program to reduce hospitalizations, thus minimizing the pressure on health systems and reducing health inequities. The burden and age distribution of the disease in individual countries will determine the impact of such a program.

Thus, from a public health perspective, available vaccines with demonstrated safety even with only moderate efficacy should be used to help control the ever-growing problem of dengue in countries where dengue poses a major disease burden. In doing so, we should adopt a "learn by doing" approach. Post-licensure surveillance and research will enhance understanding of vaccine effectiveness at the population level, quantify the reduction in vaccine-preventable disease incidence, assess long-term safety, aid in determining the best timing for booster doses, and measure the indirect effect of the vaccine. Integration with other strategies, including improved clinical case management and effective approaches to vector control, will ensure a more substantial public health impact in the long run. Lessons learned from an integrated dengue vaccine introduction will also pave the way for other vaccines that only offer partial efficacy. ■

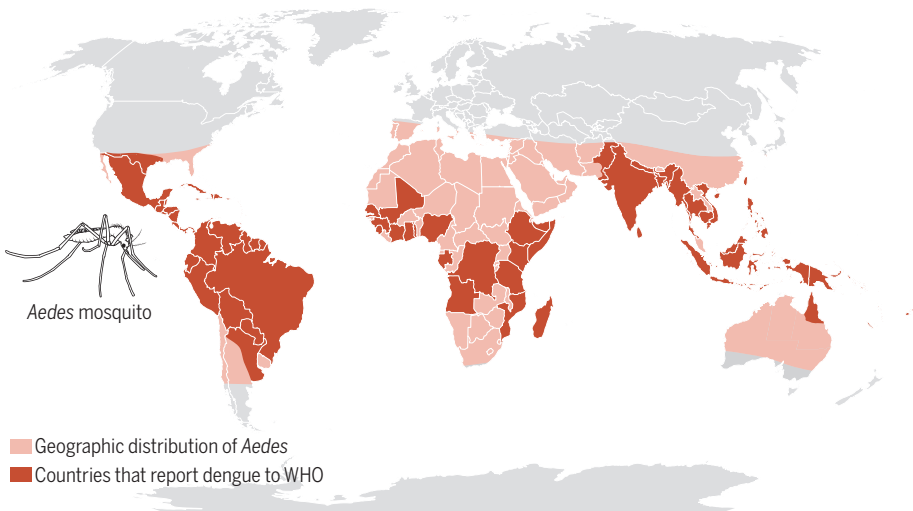

Global dengue. More than 90 countries have reported cases of dengue to the World Health Organization in recent years. The wide geographical distribution of the *Aedes aegypti*, the principal mosquito vector of dengue viruses highlights the potential for further spread. [Map adapted from (*13*)]

MAP: ADAPTED FROM WORLD HEALTH ORGANIZATION BY P. HUEY/*SCIENCE*

[1]*Lee Kong Chian School of Medicine, Nanyang Technological University, Singapore.* [2]*Emerging Infectious Diseases Program, Duke-NUS Graduate Medical School, Singapore.*
E-mail: awilder-smith@ntu.edu.sg

REFERENCES

1. S. Bhatt *et al.*, *Nature* **496**, 504 (2013).
2. S. Yacoub, B. Wills, *BMC Med.* **12**, 147 (2014).
3. S. B. Halstead, *Science* **239**, 476 (1988).
4. C. P. Simmons, J. J. Farrar, N. van Vinh Chau, B. Wills, *N. Engl. J. Med.* **366**, 1423 (2012).
5. A. Wilder-Smith, D. J. Gubler, *Med. Clin. North Am.* **92**, 1377 (2008).
6. S. J. Thomas, A. L. Rothman, *Vaccine* 10.1016/j.vaccine.2015.05.095 (2015).
7. B. Guy, M. Saville, J. Lang, *Hum. Vaccin.* **6**, 696 (2010).
8. M. R. Capeding *et al.*, *Lancet* **384**, 1358 (2014).
9. L. Villar *et al.*, *N. Engl. J. Med.* **372**, 113 (2015).
10. S. R. Hadinegoro *et al.*, *N. Engl. J. Med.* **373**, 1195 (2015).
11. S. J. Thomas, T. P. Endy, *Curr. Opin. Infect. Dis.* **26**, 429 (2013).
12. S. J. Thomas, *N. Engl. J. Med.* **372**, 172 (2015).
13. http://apps.who.int/ithmap/

10.1126/science.aab4047

Published by AAAS

METABOLISM

A pancreatic clock times insulin release

Circadian oscillators of beta cells control insulin secretion and glucose homeostasis

By Charna Dibner[1] and Ueli Schibler[2]

The circadian timing system plays an essential role in the temporal coordination of metabolism in health and disease (*1*). This includes maintaining blood glucose homeostasis, a process that is regulated to a large extent by insulin. Cell-autonomous circadian oscillators—molecular "clocks"—operate in virtually all body cells. On page 650 of this issue, Perelis *et al.* report that the circadian clock specific to islet beta cells in the pancreas controls the release of insulin as a response to blood glucose levels in a manner that is dependent on the time of day (*2*).

Peripheral cellular clocks must be synchronized daily by systemic signals that are controlled by a master pacemaker in the brain's suprachiasmatic nucleus. This maintains phase coherence among the cellular clocks in the body during the entire life span of an animal. However, the clocks of cultured cells or organ explants can be synchronized by activating various signaling pathways and thereafter display circadian cycles of gene expression during several consecutive days (*3*). Hence, at least some tissue-autonomous functions of circadian clocks can be investigated in vitro. Perelis *et al.* provide compelling evidence for pronounced circadian rhythms of the insulin secretory response in isolated pancreatic islets. A reciprocal connection between circadian clocks and metabolism was already demonstrated previously (*4, 5*), as was the existence of islet-autonomous circadian oscillators (*6*). Mice engineered to lack the clock component and transcription factor BMAL1 (brain and muscle Arnt-like protein–1) in all cells suffered from hyperglycemia and deficient glucose-stimulated insulin secretion (*6*). This phenotype was even stronger in mice bearing a beta cell–specific deletion of the *Bmal1* gene, which developed features of type 2 diabetes at an early age.

Perelis *et al.* show that the glucose-induced circadian insulin secretion is islet-autonomous (see the figure). Temporal analysis of transcription in synchronized islets revealed strong circadian oscillations of messenger RNAs (mRNAs) encoding proteins important for beta cell function. In particular, the accumulation of transcripts related to the insulin secretory pathway was severely compromised in beta cells lacking BMAL1. By developing a mouse model in which the islet-specific disruption of *Bmal1* expression can be induced by the drug tamoxifen, Perelis *et al.* observed that perturbation of beta cell clock function during adulthood causes severe glucose intolerance. Hence, the observed phenotypes cannot be attributed to developmental defects in islet differentiation. Collectively, these findings illustrate the interplay between acute control mechanisms (insulin secretion as a consequence of high blood glucose concentration) and "hard-wired" control mechanisms (insulin secretion that is modulated by beta cell–autonomous clocks) in governing glucose homeostasis.

Insulin release is acutely regulated by dietary sugar intake; circadian beta cell clocks modulate the efficacy of this process in a daytime-dependent manner through the circadian regulation of genes involved in secretion. How can the core clock components BMAL1 and CLOCK (circadian locomotor output cycles kaput), which accumulate in most cell types, act in a tissue-specific manner? Perelis *et al.* demonstrate that BMAL1 and CLOCK (also a transcription factor) bind to different enhancer and promoter elements of the genome in mouse islet and liver cells. Most probably, BMAL1-CLOCK occupancy at these cis-acting elements is largely determined by cooperative binding with tissue-specific transcription factors that have affinity to nearby sites, or by cell type–enriched pioneer transcription factors that render binding sites accessible to BMAL-CLOCK. Such mechanisms might also account for previously observed tissue-specific effects of these core clock transcription factors. Thus, mice with a liver-specific *Bmal1* disruption suffer from hypoglycemia during the resting phase (*7*), a phenotype

Beta cell clock. Glucose homeostasis is controlled in part by insulin release from pancreatic beta cells into the bloodstream. Circadian oscillation in insulin secretion and in genes that control secretion suggest that the beta cell clock gates the insulin response in a cell-autonomous manner. In the absence of beta cell clocks, the insulin response is dampened, resulting in hyperglycemia.

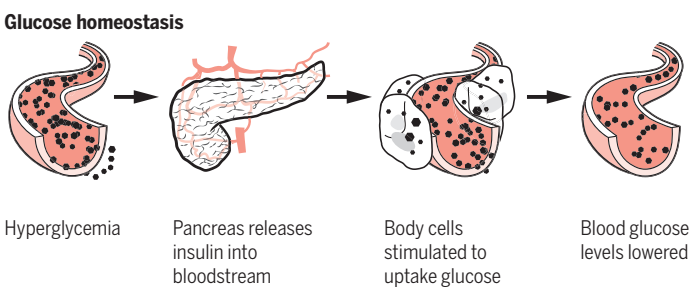

GRAPHIC: V. ALTOUNIAN/*SCIENCE*

[1]Department of Endocrinology, Diabetes, Nutrition, and Hypertension, Diabetes Center, Faculty of Medicine, University of Geneva, CH-1211 Geneva 14, Switzerland. [2]Department of Molecular Biology, Sciences III, University of Geneva, CH-1211 Geneva 4, Switzerland. E-mail: ueli.schibler@unige.ch

Downloaded from www.sciencemag.org on November 5, 2015

Published by AAAS

in glucose homeostasis that is opposite to that of mice with a beta cell–specific *Bmal1* knockout (*2, 6*).

The impact of core clock function in circadian glucose homeostasis shows that the physiological consequences of BMAL1 depletion are dependent on time of day. Indeed, when studying organisms with mutations in core clock genes, one should keep in mind that these genes also perform functions other than keeping the clock ticking. For example, the fertility of mice lacking BMAL1 is dramatically compromised (*8*), yet other genetically arrhythmic mice reproduce normally (*9*).

If future studies confirm that obesity and type 2 diabetes are associated with circadian clock perturbations in humans, they will open new avenues for treating these diseases. In this context, Perelis *et al.* found that an agonist of G_q-type G protein–coupled receptor signaling could reverse the disruption of insulin secretion due to clock perturbation.

"How can the core clock components...act in a tissue-specific manner?"

Moreover, recent drug screens for molecules that modulate the clock revealed potent candidate therapeutic compounds for mitigating metabolic disorders (*10*, *11*).

The study by Perelis *et al.* represents an important milestone in understanding how the clock, pancreatic islet functions, and the etiology of type 2 diabetes may be linked. Decades ago, Unger and Orci formulated the "bihormonal hypothesis" for the cause of diabetes. They proposed that the dysregulation of both insulin (the blood glucose–lowering hormone) and glucagon (the blood glucose–increasing hormone) contributes to the etiology of diabetes (*12*). Future studies aimed at deciphering clock functions in glucagon-producing alpha cells might reveal whether their circadian oscillators also partake in the modulation of blood glucose levels in healthy and diabetic subjects. ■

REFERENCES

1. C. Dibner, U. Schibler, *J. Intern. Med.* **277**, 513 (2015).
2. S. H. Yoo *et al.*, *Proc. Natl. Acad. Sci. U.S.A.* **101**, 5339 (2004).
3. M. Perelis *et al.*, *Science* **350**, aac4250 (2015).
4. F. W. Turek *et al.*, *Science* **308**, 1043 (2005).
5. A. Kohsaka *et al.*, *Cell Metab.* **6**, 414 (2007).
6. B. Marcheva *et al.*, *Nature* **466**, 627 (2010).
7. K. A. Lamia, K. F. Storch, C. J. Weitz, *Proc. Natl. Acad. Sci. U.S.A.* **105**, 15172 (2008).
8. J. D. Alvarez *et al.*, *J. Biol. Rhythms* **23**, 26 (2008).
9. K. Bae *et al.*, *Neuron* **30**, 525 (2001).
10. Z. Chen *et al.*, *Proc. Natl. Acad. Sci. U.S.A.* **109**, 101 (2012).
11. L. A. Solt *et al.*, *Nature* **485**, 62 (2012).
12. R. H. Unger, L. Orci, *Lancet* **305**, 14 (1975).

10.1126/science.aad5412

GRAPHIC: P. HUEY/*SCIENCE*

CHEMISTRY

Love at second sight for CO_2 and H_2 in organic synthesis

Catalysts can combine H_2 and CO_2 to create building blocks for high-value products

By **Jürgen Klankermayer** *and* **Walter Leitner**

Many romantic comedies are based on a couple with opposite personalities who fall in love, lose track of each other, and reunite against all odds, most often with the help of a mediator. This cinematic scenario recaps the recent progress in bringing together two molecular actors, carbon dioxide (CO_2) and hydrogen (H_2), with the help of homogeneous catalysts in solution. Of the pair, CO_2 is the reluctant partner; it is thermodynamically very stable and kinetically inert in typical organic syntheses. However, an energetic partner such as H_2 can bring out its reactivity if their combination is properly directed. Organometallic catalysts have recently opened new possibilities to merge this odd couple of CO_2 and H_2 and, with the support of helpful in-laws (co-reactants), to establish synthetic methods for sustainable chemical processes across the chemical value chain.

The beginning of the relationship goes back as far as 1976, when the addition of 1 equivalent of H_2 to CO_2 to give formic acid was shown to be catalyzed by phosphine complexes of late transition metals such as platinum or palladium. Since then, impressively active catalytic systems have been developed to synthesize formic acid and its salts, as well as formate esters and formamides (*1*). Nonetheless, the intensification of the CO_2-H_2 relationship was hampered by the ineffectiveness of the organometallic mediators to yield functional groups other than formate. Whereas the combination of CO_2 and H_2 found increasing interest in the context of heterogeneous catalytic processes for energy storage (*2*), it seemed that this pair had only a limited future in the area of synthetic chemistry.

Homogeneously catalyzed reactions in which H_2 is activated and then combined with less reluctant partners than CO_2 have been implemented in industrial applications ranging from large-volume production to specialized fine chemicals and pharmaceutical products. Based on the concomitant progress in molecular understanding of such processes, the first organometallic complex transforming CO_2 together with 3 equivalents of H_2 beyond the formate level to methanol and water in homogeneous solution was recently developed (*3*). A complex based on a ruthenium (Ru) center coordinated by the known tridentate triphos ligand played the role of the mediator in this breakthrough. A key feature of this catalyst was the combination of exceptional thermal stability with a precisely controlled coordination geometry.

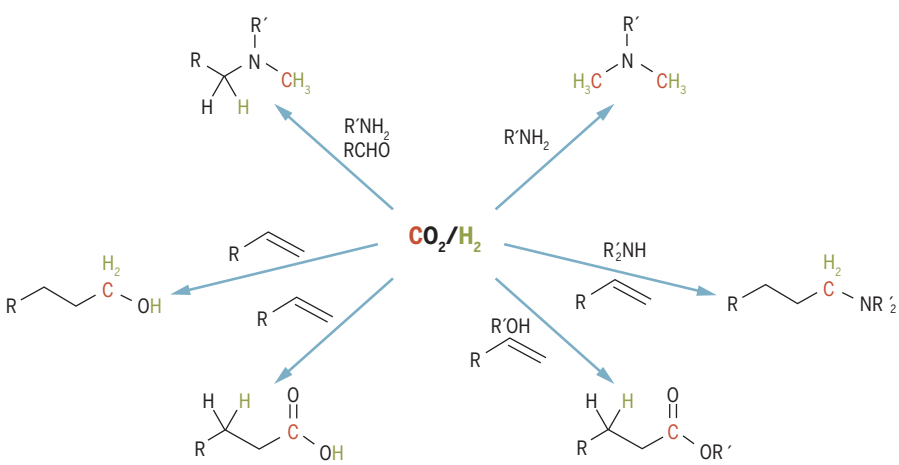

A fruitful couple. Examples of the use of CO_2 and H_2 as C1 building blocks in synthetic pathways to important functional groups; R and R´ are alkyl or aryl groups.

Published by AAAS

Downloaded from www.sciencemag.org on November 5, 2015

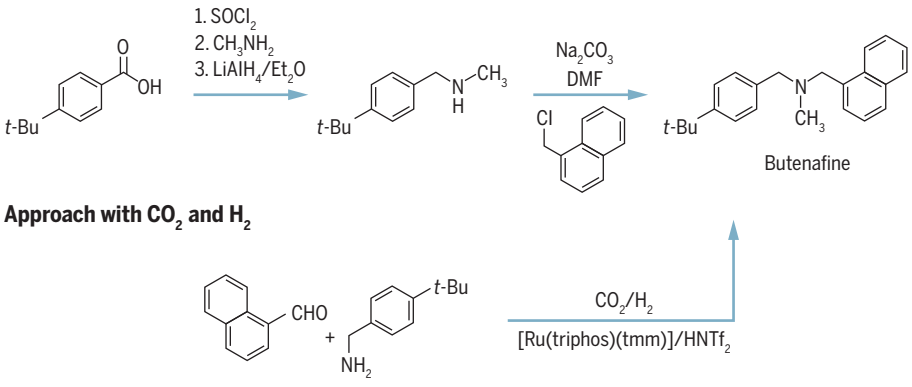

"Green chemistry" at work. The use of CO_2 and H_2 in the synthesis of butenafine saves steps, reduces waste, and avoids potentially hazardous reagents versus the conventional route. Abbreviations: *t*-Bu, *tert*-butyl; Et, ethyl; DMF, dimethylformamide; triphos, 1,1,1-tris(diphenylphosphinomethyl)ethane; tmm, trismethylenemethane ($C_4H_6^{2-}$); Tf, triflate.

The lead structure of this catalyst has enabled the discovery of an effective synthesis of *N*-methylamines via methylation of amines with CO_2 and H_2 (*4*); *N*-methylamines are widely found in biologically active compounds and pharmaceuticals. Since then, this reaction has been developed into a synthetic strategy with a broad substrate scope, including primary and secondary amines as well as imines (*4*–*6*). The latter can even be formed in situ from a primary amine and a carbonyl compound, allowing assembly of tertiary amines with three different substituents at nitrogen in a highly selective multicomponent coupling reaction (*5*). The Ru-triphos catalytic system has been applied also for the methylation of C–H bonds in heteroaromatic substrates (*7*). Unlike the established stoichiometric (and often toxicologically problematic) methylating agents, the synthesis of a methyl group from CO_2 and hydrogen with formation of water as the only by-product is a much cleaner and less wasteful alternative.

The synthetic potential of the CO_2-H_2 couple as source of carbon monoxide (CO) for homogeneously catalyzed carbonylation reactions is also becoming apparent. The interconversion of the two pairs, CO_2-H_2 and CO-H_2O, is known as the water-gas shift (WGS) equilibrium and is well established in heterogeneous catalysis. Homogeneous ruthenium carbonyl complexes have long been known to be able to catalyze this equilibrium in both directions. Only recently has the connection between these two fields been made (*8*). High activity and selectivity have been achieved with an improved version of the Ru-carbonyl catalyst, in particular for the synthesis of primary alcohols from olefins, CO_2, and H_2 (*9*). The $-CH_2OH$ group is assembled via the initial addition of CO and H_2 to the C=C double bond (hydroformylation), followed by further reduction of the resulting aldehyde primary product.

Aldehydes are very reactive intermediates, and their in situ generation opens a whole range of further synthetic applications. For example, they can undergo condensation with secondary amines to form tertiary amines through the incorporation of a $-CH_2-$ group stemming from CO_2 and H_2 (*10*). Depending on the synthetic targets, the overall transformation may be exploited as a possible approach for amination of alkenes or alkylation of amines, respectively.

Whereas these transformations are initiated by the addition of both CO and H_2 to the unsaturated substrate, the intermediates of the initial carbonylation step can also be intercepted with other reaction partners. The synthesis of esters by alkoxy carbonylation of olefins has been demonstrated with CO_2 and alcohols to assemble the carboxylate groups, whereby the alcohol also serves as a hydrogen source for the reduction of CO_2 (*11*). It was shown previously that the mixture of CO and H_2O formed from CO_2 and H_2 via the WGS equilibrium can be also added with the help of rhodium complexes directly to olefins, resulting in formation of free carboxylic acids. Substrates other than olefins can also be used as the alkyl source, providing a wide range of potential synthetic pathways to generate the carboxylic acid function $-C(O)OH$ formally through a hydrocarboxylation (addition of CO_2 and H_2) process (*12*).

The recent progress in catalytic transformations of the combination of CO_2 and H_2 provides novel synthetic tools to generate functional groups and substituents with one carbon atom ("C1 building blocks") found in important high-volume or high-value chemical products (see the first figure). The synthesis of carboxylate, aldehyde, alcohol, methylene, and methyl groups opens unprecedented synthetic pathways. The complexity of the reaction sequences is quite remarkable: They involve a series of bond-forming and bond-breaking events to assemble the C1 building block from CO_2 and several molecules of H_2 at various carbon or heteroatom-based functional groups. Considering this complexity, the activities and selectivities of the catalytic systems are already quite impressive even at this early stage of development. A greater mechanistic understanding of the molecular control factors will help improve the performance and broaden the scope of applications.

The catalytic use of CO_2-H_2 to create C1 units can often provide a "greener" alternative to conventional stoichiometric reagents, resulting in high atom economy with water as the sole by-product. For example, the synthesis of the antifungal agent butenafine can be achieved in one-step reductive amination and *N*-methylation, as compared to the conventional multistep and wasteful process (see the second figure) (*5*). If the H_2 required in these reactions stems from renewable primary energy sources, CO_2-based syntheses have the additional potential to reduce the carbon footprint of the chemical industry (*13*). Although the synthesis of complex molecules has an arguably small volume for the individual case, the generic approach to marry CO_2 and H_2 for the generation of C1 functional groups opens the possibility of harnessing renewable energy across all sectors of the chemical value chain. ■

Institut für Technische und Makromolekulare Chemie, RWTH Aachen University, 52074 Aachen, Germany.
E-mail: jklankermayer@itmc.rwth-aachen.de; leitner@itmc.rwth-aachen.de

REFERENCES

1. P. G. Jessop, F. Joo, C. C. Tai, *Coord. Chem. Rev.* **248**, 2425 (2004).
2. R. Schlögl, *Angew. Chem. Int. Ed.* **54**, 4436 (2015).
3. S. Wesselbaum *et al.*, *Chem. Sci.* **6**, 693 (2015).
4. K. Beydoun, T. vom Stein, J. Klankermayer, W. Leitner, *Angew. Chem. Int. Ed.* **52**, 9554 (2013).
5. K. Beydoun, G. Ghattas, K. Thenert, J. Klankermayer, W. Leitner, *Angew. Chem. Int. Ed.* **53**, 11010 (2014).
6. Y. Li, I. Sorribes, T. Yan, K. Junge, M. Beller, *Angew. Chem. Int. Ed.* **52**, 12156 (2013).
7. Y. Li, T. Yan, K. Junge, M. Beller, *Angew. Chem. Int. Ed.* **53**, 10476 (2014).
8. K.-i. Tominaga, Y. Sasaki, *Catal. Commun.* **1**, 1 (2000).
9. Q. Liu *et al.*, *Chem. Eur. J.* **20**, 6888 (2014).
10. V. K. Srivastava, P. Eilbracht, *Catal. Commun.* **10**, 1791 (2009).
11. L. Wu, Q. Liu, I. Fleischer, R. Jackstell, M. Beller, *Nat. Commun.* **5**, 3091 (2014).
12. T. G. Ostapowicz, M. Schmitz, M. Krystof, J. Klankermayer, W. Leitner, *Angew. Chem. Int. Ed.* **52**, 12119 (2013).
13. G. Centi, E. A. Quadrelli, S. Perathoner, *Energy Environ.* **6**, 1711 (2013).

10.1126/science.aac7997

GRAPHIC: P. HUEY/*SCIENCE*

PHYSICS

Frustrating a quantum magnet

Nuclear magnetic resonance reveals the ground state of frustrated magnets

By **Yuji Furukawa**

Being able to determine the ground state of a frustrated quantum magnet has been a long-sought goal in condensed matter physics. In general, frustration results from the inability to achieve a desired outcome. In solid-state systems, frustration can arise in relation to electron spin, one of an electron's degrees of freedom. The antiferromagnetic (AFM) interaction between electron spins means that the spins minimize their energy by orienting opposite to their neighbors. For example, if spin A was "up," spin B would be "down," antiparallel to spin A. However, introducing the third spin, as in an antiferromagnetically coupled equilateral triangle of electron spins, presents frustration (see the figure, panel A). Here, spin C cannot simultaneously satisfy the up-down interactions with spins A and B. Because spin C cannot achieve its "desired outcome" of being oppositely aligned with both its nearest neighbors, it is "frustrated." On page 655 of this issue, Fu *et al.* (*1*) investigate the ground state of such a system by using nuclear magnetic resonance (NMR) to measure the intrinsic low-energy spin excitation of the ideal frustrated quantum magnet $ZnCu_3(OH)_6Cl_2$.

"...frustration results from the inability to achieve a desired outcome. In solid-state systems, frustration can arise in relation to electron spin..."

Ames Laboratory and Department of Physics and Astronomy, Iowa State University, Ames, IA 50011, USA. E-mail: furukawa@ameslab.gov

Spin frustration is an exciting topic of contemporary research in condensed matter physics (*2*–*4*). The interest in spin frustration was raised in the 1970s by Anderson's prediction of a resonating valence bond (RVB) state (sometimes called a spin liquid state) as an alternative to the classical AFM Néel state for the magnetic ground state of a two-dimensional triangular lattice magnet formed by edge-shared frustrated AFM triangles (*5*). Here, the valence bond is a pair of spins forming an $s = 0$ spin singlet state due to an AFM interaction. In the spin liquid state, the electron spins do not form an ordered pattern, even at a temperature $T = 0$ K, and fluctuate in time; in a spin solid state, by contrast, such a static, ordered pattern does form at a sufficiently low temperature.

Because quantum effects are enhanced in materials with spin $s = ½$, much interest has focused on kagome lattice antiferromagnets, which are formed by corner-shared frustrated AFM triangles and have an even higher degree of spin frustration than triangular lattice antiferromagnets. Although extensive experimental and theoretical investigations have been carried out, the nature of the actual ground-state of the kagome lattice (frustrated quantum magnet) is still not well understood because of the lack of real materials. Three different

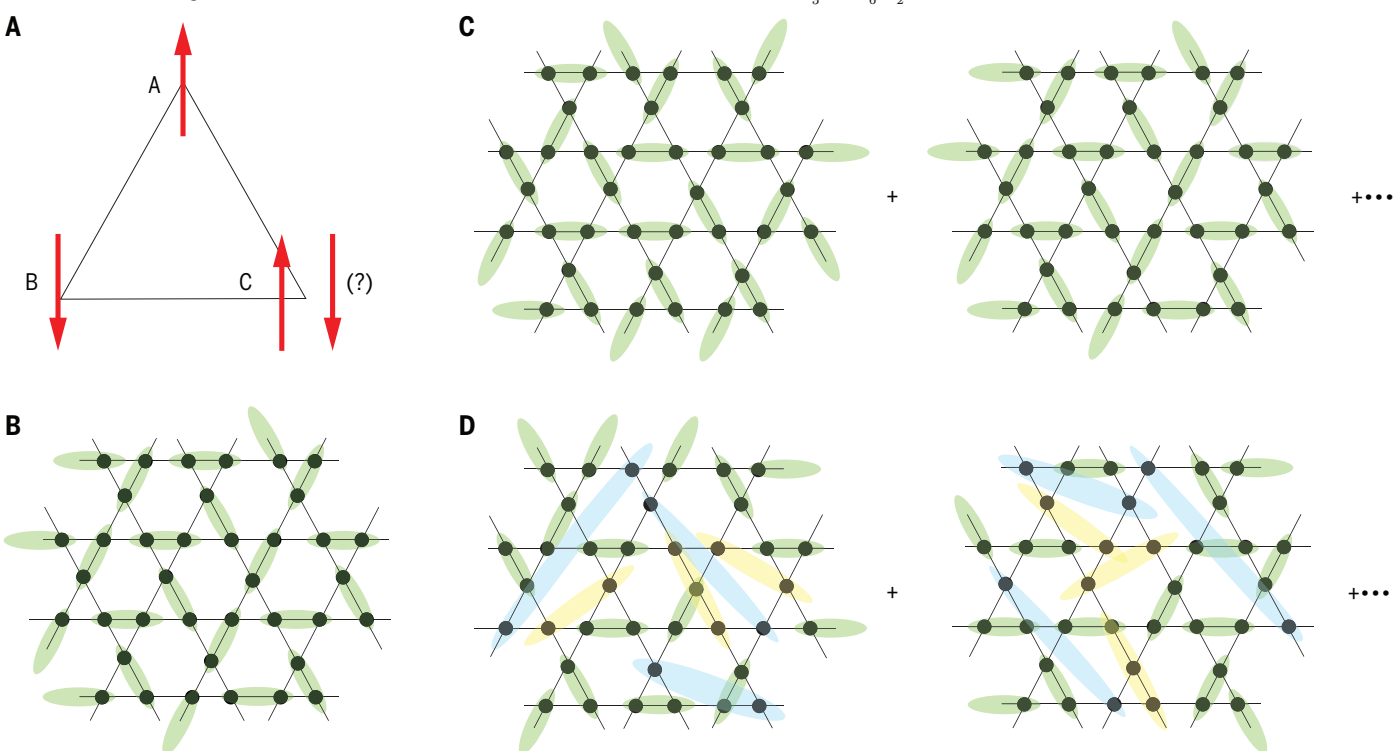

GRAPHIC: N. CARY/*SCIENCE*

Models of frustration. (**A**) Spin frustration on a triangular configuration of three antiferromagnetically coupled spins. (**B**) A valence bond solid (VBS) on a kagome lattice. The green ovals indicate a valence bond, a pair of spins (spin up, spin down) forming an $s = 0$ singlet state. The VBS is static. (**C**) A resonating VBS. The spin singlet pairs change in time, and the state is described by a superposition of many different VBS configurations. The state has a nonzero spin excitation gap. (**D**) A long-range resonating valence bond state. In this state, the spin pairs need not be nearest neighbors; long-range spin pairs are possible. The greater the separation of the pair, the lower the excitation energy, producing a gapless spin excitation.

Downloaded from www.sciencemag.org on November 5, 2015

Published by AAAS

ground states have been proposed theoretically: a valence bond solid (VBS) state with an energy gap in spin excitations (see the figure, panel B) (*6*); a gapped spin liquid (short-range RVB) state (panel C) (*7*); and a gapless spin liquid (long-range RVB) state (panel D) (*8*). A key question is whether the ground state has an energy gap in the spin excitation spectrum.

Fu *et al.* answer this unresolved question by studying a single crystal of a rare mineral, $ZnCu_3(OH)_6Cl_2$ (herbertsmithite), which is an ideal model for the kagome antiferromagnet. Although much experimental work has been carried out since this compound was first synthesized (*9*), the ground state of the compound was not well understood. This is due to the undesirable Cu^{2+} spins (also spin ½) occupying the nonmagnetic Zn^{2+} sites, which prevents the experimental determination of the intrinsic low-energy spin excitation spectrum. Fu *et al.* avoid this problem by using NMR, which can extract the intrinsic magnetic properties. Although NMR has been used to study the compound previously (*10*, *11*), the broad NMR lines typically observed in powder samples hamper precise measurements. Fu *et al.* performed their NMR measurements on a single crystal, yielding much sharper NMR lines than the powder samples could provide. From detailed studies of the single-crystal ^{17}O NMR spectrum, NMR shift, and nuclear spin lattice relaxation time, they were able to conclude that the ground state of the kagome antiferromagnet has a nonzero energy gap, thus excluding model D in the figure.

Fu *et al.* exclude another proposed ground state (the VBS state, model B in the figure) on the basis of the temperature dependence of the x-ray diffraction pattern and the nuclear quadrupole frequency, which is sensitive to lattice distortions. By a process of elimination, they determine that the kagome antiferromagnet possesses a spin liquid ground state with a nonzero spin gap (model C), thus settling the long-outstanding fundamental question and advancing our current understanding of frustrated quantum magnets. ■

REFERENCES

1. M. Fu, T. Imai, T.-H. Han, Y. S. Lee, *Science* **350**, 655 (2015).
2. *Frustrated Spin Systems*, H. T. Diep, Ed. (World Scientific, Singapore, 2005).
3. *Introduction to Frustrated Magnetism*, C. Lacroix, P. Mendels, F. Mila, Eds. (Springer, New York, 2011).
4. L. Balents, *Nature* **464**, 199 (2010).
5. P. W. Anderson, *Mater. Res. Bull.* **8**, 153 (1973).
6. P. Nikolic *et al.*, *Phys. Rev. B* **68**, 214415 (2003).
7. M. Mambrini *et al.*, *Eur. Phys. J. B* **17**, 651 (2000).
8. M. Hermele *et al.*, *Phys. Rev. B* **77**, 224413 (2008).
9. M. P. Shore *et al.*, *J. Am. Chem. Soc.* **127**, 13462 (2005).
10. A. Olariu *et al.*, *Phys. Rev. Lett.* **100**, 087202 (2008).
11. T. Imai *et al.*, *Phys. Rev. Lett.* **100**, 077203 (2008).

10.1126/science.aad3556

RESEARCH ETHICS

Evidence gaps and ethical review of multicenter studies

Empirical research is needed to guide federal policy

By **Ann-Margret Ervin,[1]* Holly A. Taylor,[1,2] Curtis L. Meinert,[1] Stephan Ehrhardt[1]**

Large, multicenter clinical studies are the backbone of evidence-based prevention and health care. Ethical review of multicenter research is usually conducted by the institutional review board (IRB) of each participating institution. However, variation in interpretation of regulations by IRBs is common and can have ethical and scientific implications (*1*, *2*). Recent mandates in the United States aim to reduce the administrative burden and to expedite multicenter research by conducting ethical review with a single, central IRB of record (CIRB). Yet the quality of ethical review must not suffer. We characterize current models of ethical review in the United States and identify research gaps that must be addressed before such policies are instituted.

POLICY

Multicenter studies are designed to expedite participant enrollment but are hampered by the current review process. Requests from disparate IRBs to modify study procedures and consent forms may prevent participation of affected centers or require resubmissions to IRBs of all participating centers. Exclusion of clinical centers or modifications to procedures may unequally distribute the benefits and burdens of research.

In September 2015, 16 federal agencies and departments issued a Notice of Proposed Rulemaking (NPRM) that would amend federal regulations to mandate a CIRB for federally funded multicenter research (*3*). The NPRM public comment period ends 7 December 2015. In 2014, the U.S. National Institutes of Health (NIH) issued a draft policy mandating ethical review by a CIRB for NIH-funded multicenter research (*4*). In July 2015, the U.S. House of Representatives passed the 21st Century Cures Act mandating a change in regulations to facilitate CIRBs (*5*).

ALTERNATIVES TO MULTIPLE IRBS. Federal provisions to streamline ethical review of multicenter studies, including use of CIRBs, have been available for years (*6*, *7*). Various streamlined approaches exist in the United States among industry-funded studies, institutions that frequently collaborate, and within universities that have multiple intrainstitutional IRBs (*8*–*10*). Yet, despite evidence that multiple IRB reviews are burdensome and guidance permitting streamlined approaches, CIRBs are rarely used (*10*).

There are several barriers to widespread adoption of CIRBs. Current regulations state that, "In the conduct of cooperative research projects, each institution is responsible for safeguarding the rights and welfare of human subjects and for complying with this policy." (*7*). Investigators and institutions fear that lack of local IRB review exposes all parties to assertions of noncompliance with federal regulations should there be deficiencies in CIRB review or adverse events (*11*). Under the NPRM, local IRBs are not precluded from conducting ethical review. If local IRBs choose to review despite CIRB review, local IRB review becomes an additional layer, which would extend an already time-intensive process. Guidance on liability for noncompliance when a CIRB is involved must be addressed by an amendment to regulations (*3*, *11*).

> *"Addressing research gaps is critical to successful implementation of CIRBs for multicenter research."*

Unfamiliarity with local context, as well as delineation of responsibilities of local and central IRBs, are barriers to adoption of CIRBs. (*12*) These barriers are touted by institutional stakeholders, including general counsel, research administration officials, and IRB directors to support the perception that more-streamlined approaches may not provide sufficient protection to participants (*2*).

LESSONS LEARNED. Data on responsibilities, procedures, and performance metrics adopted by existing CIRBs are essential for assessing what aspects of CIRBs are amenable to relevant stakeholders and what

[1]*Johns Hopkins Bloomberg School of Public Health, Baltimore, MD, USA.* [2]*Johns Hopkins Berman Institute of Bioethics, Baltimore, MD, USA.* **Corresponding author. E-mail: aervin@jhu.edu*

Published by AAAS

EPIGENETICS

The epigenome—a family affair

Epigenome disruptions can be transmitted as altered histone modification patterns in sperm

By **John R. McCarrey**

Classic dogma has dictated that, in animals, genetic mechanisms in general, and DNA sequence in particular, are responsible for transmission of traits from one generation to the next. However, an increasing number of reports over the past decade have shown that epigenetic mechanisms can also contribute to transgenerational inheritance (*1*). This is important because it implies that effects to which your parents or grandparents were exposed, even if not directly mutagenic, may alter your phenotype or that of your children or grandchildren. Previous studies implicated disruptions in DNA methylation patterns as the molecular basis for this type of epigenetic inheritance (*2*), but on page 651 of this issue, Siklenka *et al.* (*3*) show that disruption of histone modifications, in the apparent absence of any changes in DNA methylation patterns, can also form the basis for transgenerational transmission of epigenetic programming defects that can modify phenotypic characteristics in subsequent generations.

It comes as no surprise that the epigenome is susceptible to disruption given its inherent lability (*4*). Epigenetic programming is, by definition, reversible, different in every cell type, and subject to extensive reorganization during development—especially in the germ line (*5*). Indeed, disruptions of the epigenome have become so commonly recognized that they have been given their own name—"epimutations" (*6*). Two types of epimutations have been postulated: A primary epimutation results from a direct disruption of epigenetic programming (e.g., of DNA methylation or histone modification patterns) that is subsequently propagated as such by epigenetic inheritance, whereas a secondary epimutation is initiated by a genetic effect that then leads to disruption of normal epigenetic programming that can be propagated by either genetic or epigenetic inheritance, or both. The effect described by Siklenka *et al.* was initially induced as a secondary epimutation based on a genetic event—overexpression of a transgene—but was subsequently transmitted as a primary epimutation in mice that had lost the transgene because of the breeding scheme employed.

Department of Biology, University of Texas at San Antonio, San Antonio, TX 78249, USA. E-mail: john.mccarrey@utsa.edu

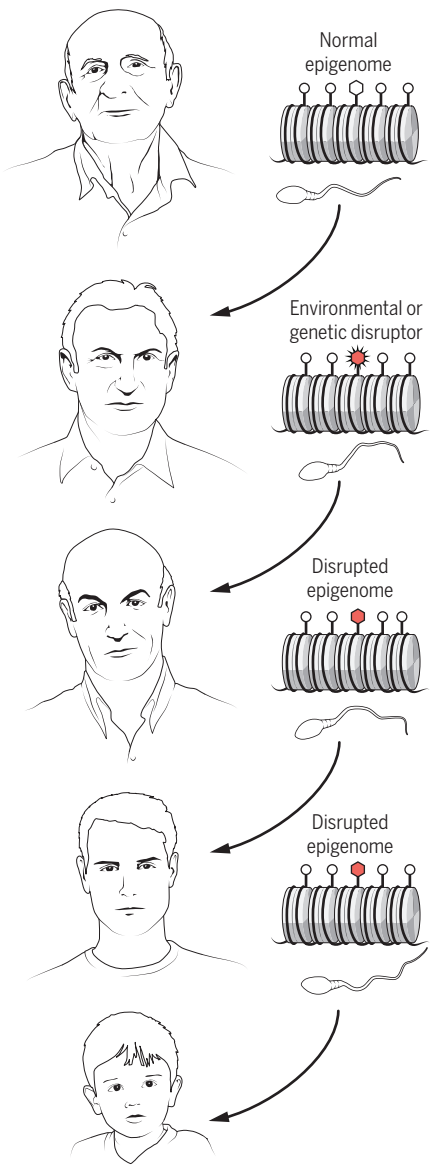

Father to son. Paternal transmission of epigenetic defects to either sons or daughters can occur if an epimutation is introduced into the sperm epigenome in the form of altered DNA methylation or, as depicted here, histone modification patterns (circles and hexagons) on the nucleosomes (disks) that package the genomic DNA (black strand). Such alterations (red covalent modification) can be induced by either aberrant genetic or environmental effects, and if the resulting epimutations escape germline reprogramming, they can then be transmitted to multiple subsequent generations, even in the absence of any further exposure to the original inducing effect.

The transgene used by Siklenka *et al.* altered the function of a histone-modifying enzyme during spermatogenesis to induce aberrant histone methylation patterns in the resulting sperm. Because epigenetic programming regulates gene expression patterns, disruptions in this programming can negatively influence normal development, physiological function, and other key biological pathways, leading to a variety of diseases (*7*). Although Siklenka *et al.* used a genetic approach to disrupt the epigenome, many environmental effects have also been reported to induce epimutations, particularly in the form of altered DNA methylation patterns. Thus, exposure to disruptive chemicals, dietary restrictions, stress, and conditions associated with in vitro fertilization have all been implicated as inducers of epigenetic disruptions, and many of these have been correlated with aberrant phenotypes (*2*).

Although it is not surprising that genetic or environmental effects can modify the epigenome, it is surprising that the resulting epimutations are not corrected by the extensive epigenetic reprogramming—of both DNA methylation and histone modification patterns—that normally occurs during development of the germ line (*5*). As described by Siklenka *et al.*, effects of epimutations observed in a father and his children (paternal inheritance), or in a mother and her children or grandchildren (maternal inheritance), may simply reflect direct effects of exposure to the initial disruptive influence. However, transmission of these same epimutations over additional generations, in the absence of any further exposure to the initial disruptor, requires that heritable information be transmitted from one generation to the next. These are transgenerational epimutations.

Examples of correction of induced epimutations by germline reprogramming have been reported (*8*). However, the growing number of examples of transgenerational transmission of epimutations in mammals indicates that some manage to avoid this correction process. The Siklenka *et al.* study is notable because it implicates histone modification patterns, in addition to the previously implicated disruption of DNA methylation patterns, as a mechanism involved in conveying aberrant epigenetic information from one generation to the next. But perhaps most surprisingly, this study demonstrates that these epimutations can be transmitted paternally (see the figure). This implies that these aber-

GRAPHIC: P. HUEY/*SCIENCE*

Published by AAAS

rant histone modifications must occur in the rare (~1 to 3% in the mouse) regions of the sperm genome that remain complexed with nucleosomes rather than becoming condensed by protamines, which displace most of the histones in sperm nuclei. Thus, these epimutations avoid yet another mechanism that might otherwise erase or correct such abnormalities.

A complete understanding of transgenerational epigenetic inheritance will require answers to many remaining questions: For example, the nature of the initial molecular trigger that leads to transgenerationally transmitted epimutations is unknown. Also unclear is whether transgenerational epimutations result only from alterations induced in certain regions of the genome or during certain stages of development, whether transgenerational epimutations escape epigenetic reprogramming during germline development, or if normal germline reprogramming reinstates these defects during each generation. How stable transgenerational epimutations are in animals and how faithfully they are transmitted via mitosis or meiosis are further open questions, as is the extent to which transgenerational epimutations are reversible or correctable. Until we fully understand these aspects, we must worry not only about disruptions to our genomes, but also about disruptions to our much more malleable epigenomes with respect to the effects that each may impose on the heritable legacy we pass on to subsequent generations. ■

"...it is surprising that the resulting epimutations are not corrected by the extensive epigenetic reprogramming...that normally occurs during development of the germ line."

REFERENCES

1. E. Heard, R. A. Martienssen, *Cell* **157**, 95 (2014).
2. F. Xin, M. Susiarjo, M. S. Bartolomei, *Semin. Cell Dev. Biol.* 10.1016/j.semcdb.2015.05.008 (2015).
3. K. Siklenka *et al.* **350**, aab2006 (2015).
4. J. R. McCarrey, *Mol. Cell. Endocrinol.* **354**, 9 (2012).
5. H. J. Lee, T. A. Hore, W. Reik, *Cell Stem Cell* **14**, 710 (2014).
6. N. C. Whitelaw, E. Whitelaw, *Curr. Opin. Genet. Dev.* **18**, 273 (2008).
7. E. E. Nilsson, M. K. Skinner, *Transl. Res.* **165**, 12 (2015).
8. E. de Waal *et al.*, *Proc. Natl. Acad. Sci. U.S.A.* **109**, 4163 (2012).

10.1126/science.aad5138

PHOTO: COURTESY OF C. SODERQUIST

NUCLEAR FUELS

How to isolate americium

An electrolytic process enables isolation of the radioactive element americium from used nuclear fuel

By **Chuck Soderquist**

Americium is a highly radioactive element found in used nuclear fuel. Because used commercial fuels always contain americium, chemical fuel processing must include separation of this element. Americium is easy to recover concurrently with eight other elements in the fuel (the lanthanide elements) but much more difficult to isolate free of those other eight. On page 652 of this issue, Dares *et al.* report a method that may provide a simple route to isolating americium (*1*).

A key concern about the use of nuclear power is the management of used radioactive fuel. One method for managing used fuel is to place the unprocessed spent fuel into a geologic repository. This is the method the United States has pursued with the Yucca Mountain fuel repository. But the long-term integrity of the fuel in the repository has not been demonstrated to everyone's satisfaction, and the repository never opened. No other country has opened a repository for unprocessed fuel, either, although some are being developed.

An alternative to placing intact fuel in a repository is to chemically separate it into its components. This converts the fuel to a number of simple compounds, intended to simplify the design of the fuel repository and make management of the fuel easier. The idea of separating used nuclear fuel into separate components has been around since the 1950s. Until the 1980s, fuel was reprocessed using chemistry developed in the 1940s and 1950s. These methods generated large volumes of waste, such as the Hanford tank waste in the state of Washington. The purpose was to recover uranium and plutonium, which were quite valuable at the time.

The modern processes under development, including that reported by Dares *et al.*, use chemistry designed to recover every component of the fuel, not just the uranium and plutonium, without generating huge volumes of secondary waste. The goal is to turn the spent fuel into a set of simple compounds that are easier to manage and dispose of (see the figure). The purpose of the modern chemistry is to eliminate the fuel, not to recover the value of the uranium and plutonium. Uranium is cheap, and plutonium has no market value for power generation. The elimination of the used fuel, however, has high value. With the raw fuel gone and the highly hazardous components removed and safely dealt with, the original question of the integrity of the fuel in the repository becomes moot.

Many of the chemical steps involved in fuel separation are not complex in themselves, but the intense radioactivity means that special equipment is required. Every operation must be done by remote control.

Most of the radiotoxicity of used nuclear fuel is caused by the transuranium elements (those heavier than uranium) such as plutonium and americium. All the transuranium elements removed from the fuel can be burned up in a reactor and irrevocably destroyed through conversion into much less toxic fission products. The uranium itself, if made quite pure, has low toxicity. The uranium fission products cesium-137 and strontium-90, which contribute most of the heat and intense radioactivity of the fuel, can be removed and allowed to decay separately (with a ~30-year half-life) to eliminate the heat load in the repository. Once the strontium, cesium, uranium, and transuranium elements have been removed, the remaining fuel is much less radioactive (most of it

Metallic technetium recovered from used nuclear fuel. This piece weighs 44 g and is radioactive (0.74 curie), but the plastic encasing it stops nearly all the radiation, and it is safe to handle with gloves. In contrast to technetium, americium is highly radioactive and cannot be handled as easily.

Published by AAAS

rant histone modifications must occur in the rare (~1 to 3% in the mouse) regions of the sperm genome that remain complexed with nucleosomes rather than becoming condensed by protamines, which displace most of the histones in sperm nuclei. Thus, these epimutations avoid yet another mechanism that might otherwise erase or correct such abnormalities.

A complete understanding of transgenerational epigenetic inheritance will require answers to many remaining questions: For example, the nature of the initial molecular trigger that leads to transgenerationally transmitted epimutations is unknown. Also unclear is whether transgenerational epimutations result only from alterations induced in certain regions of the genome or during certain stages of development, whether transgenerational epimutations escape epigenetic reprogramming during germline development, or if normal germline reprogramming reinstates these defects during each generation. How stable transgenerational epimutations are in animals and how faithfully they are transmitted via mitosis or meiosis are further open questions, as is the extent to which transgenerational epimutations are reversible or correctable. Until we fully understand these aspects, we must worry not only about disruptions to our genomes, but also about disruptions to our much more malleable epigenomes with respect to the effects that each may impose on the heritable legacy we pass on to subsequent generations. ■

"...it is surprising that the resulting epimutations are not corrected by the extensive epigenetic reprogramming...that normally occurs during development of the germ line."

REFERENCES

1. E. Heard, R. A. Martienssen, *Cell* **157**, 95 (2014).
2. F. Xin, M. Susiarjo, M. S. Bartolomei, *Semin. Cell Dev. Biol.* 10.1016/j.semcdb.2015.05.008 (2015).
3. K. Siklenka *et al.* **350**, aab2006 (2015).
4. J. R. McCarrey, *Mol. Cell. Endocrinol.* **354**, 9 (2012).
5. H. J. Lee, T. A. Hore, W. Reik, *Cell Stem Cell* **14**, 710 (2014).
6. N. C. Whitelaw, E. Whitelaw, *Curr. Opin. Genet. Dev.* **18**, 273 (2008).
7. E. E. Nilsson, M. K. Skinner, *Transl. Res.* **165**, 12 (2015).
8. E. de Waal *et al.*, *Proc. Natl. Acad. Sci. U.S.A.* **109**, 4163 (2012).

10.1126/science.aad5138

PHOTO: COURTESY OF C. SODERQUIST

NUCLEAR FUELS

How to isolate americium

An electrolytic process enables isolation of the radioactive element americium from used nuclear fuel

By **Chuck Soderquist**

Americium is a highly radioactive element found in used nuclear fuel. Because used commercial fuels always contain americium, chemical fuel processing must include separation of this element. Americium is easy to recover concurrently with eight other elements in the fuel (the lanthanide elements) but much more difficult to isolate free of those other eight. On page 652 of this issue, Dares *et al.* report a method that may provide a simple route to isolating americium (*1*).

A key concern about the use of nuclear power is the management of used radioactive fuel. One method for managing used fuel is to place the unprocessed spent fuel into a geologic repository. This is the method the United States has pursued with the Yucca Mountain fuel repository. But the long-term integrity of the fuel in the repository has not been demonstrated to everyone's satisfaction, and the repository never opened. No other country has opened a repository for unprocessed fuel, either, although some are being developed.

An alternative to placing intact fuel in a repository is to chemically separate it into its components. This converts the fuel to a number of simple compounds, intended to simplify the design of the fuel repository and make management of the fuel easier. The idea of separating used nuclear fuel into separate components has been around since the 1950s. Until the 1980s, fuel was reprocessed using chemistry developed in the 1940s and 1950s. These methods generated large volumes of waste, such as the Hanford tank waste in the state of Washington. The purpose was to recover uranium and plutonium, which were quite valuable at the time.

The modern processes under development, including that reported by Dares *et al.*, use chemistry designed to recover every component of the fuel, not just the uranium and plutonium, without generating huge volumes of secondary waste. The goal is to turn the spent fuel into a set of simple compounds that are easier to manage and dispose of (see the figure). The purpose of the modern chemistry is to eliminate the fuel, not to recover the value of the uranium and plutonium. Uranium is cheap, and plutonium has no market value for power generation. The elimination of the used fuel, however, has high value. With the raw fuel gone and the highly hazardous components removed and safely dealt with, the original question of the integrity of the fuel in the repository becomes moot.

Many of the chemical steps involved in fuel separation are not complex in themselves, but the intense radioactivity means that special equipment is required. Every operation must be done by remote control.

Most of the radiotoxicity of used nuclear fuel is caused by the transuranium elements (those heavier than uranium) such as plutonium and americium. All the transuranium elements removed from the fuel can be burned up in a reactor and irrevocably destroyed through conversion into much less toxic fission products. The uranium itself, if made quite pure, has low toxicity. The uranium fission products cesium-137 and strontium-90, which contribute most of the heat and intense radioactivity of the fuel, can be removed and allowed to decay separately (with a ~30-year half-life) to eliminate the heat load in the repository. Once the strontium, cesium, uranium, and transuranium elements have been removed, the remaining fuel is much less radioactive (most of it

Metallic technetium recovered from used nuclear fuel. This piece weighs 44 g and is radioactive (0.74 curie), but the plastic encasing it stops nearly all the radiation, and it is safe to handle with gloves. In contrast to technetium, americium is highly radioactive and cannot be handled as easily.

Published by AAAS

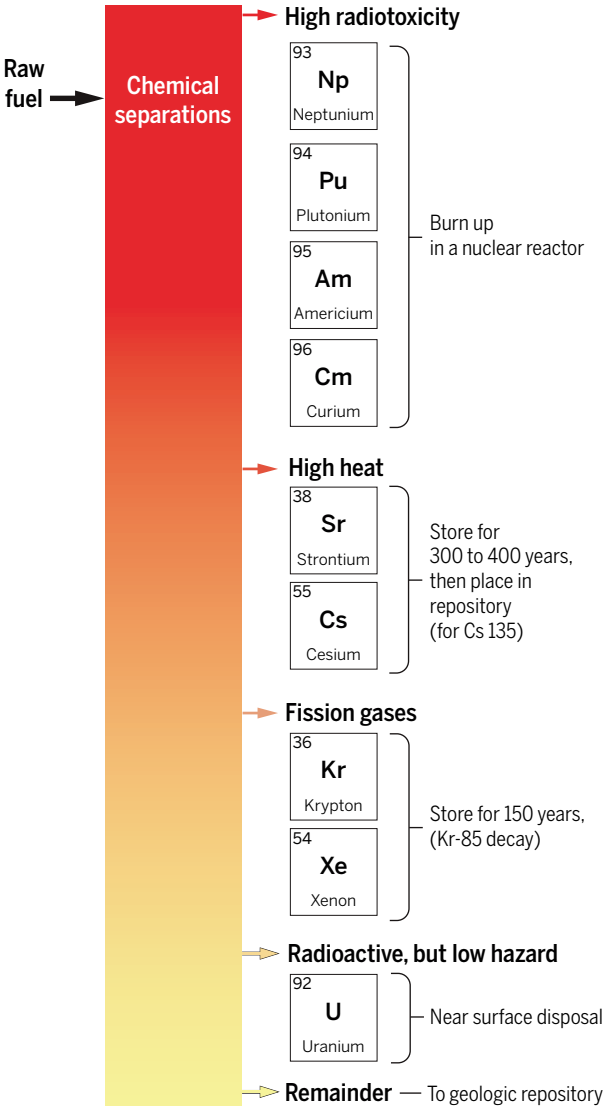

Fuel separation. Spent nuclear fuels contain a mixture of elements that need to be separated for safe disposal. Dares *et al*. report on a method for separating the highly radioactive element americium, which can then be burnt up in a nuclear reactor.

can be handled with a gloved hand) and has much smaller volume than the original fuel. This remainder is roughly as hazardous as the ore originally mined to make the fuel.

Many research groups have recently published new chemical separations of used fuel (*2*–*4*). Most of these processes are designed to work with the traditional PUREX (plutonium uranium redox extraction) process, which recovers uranium and plutonium from used fuel. The UREX+ process has been designed to recover strontium, cesium, the lanthanide elements, technetium (see the photo), uranium, and the transuranic elements (*5*). Other recently published processes do not resemble PUREX at all. One uses sodium carbonate and hydrogen peroxide solution to dissolve the fuel (*6*). Another uses ammonium carbonate and hydrogen peroxide to dissolve the fuel and begin some group separations (*7*). None of them have addressed the problem of how to easily separate americium from the lanthanides.

Dares *et al*. now show that americium can be readily oxidized from Am(III) to Am(V, VI) using simple electrolysis with a chemically modified anode. Am(III) closely resembles the lanthanide elements, but Am(V) and Am(VI) are chemically quite different. This makes an excellent starting point for separations that quickly isolate americium from the lanthanide elements. Used fuel has much more of the lanthanide elements than americium. If americium is to be burned up in a reactor, then it must be quite pure or the lanthanide impurities will absorb neutrons and prevent the americium from burning up.

All processes intended to separate the fuel into its components without generating a large volume of secondary waste need to separate the americium. When they do, they will probably use the electrolytic oxidation approach described by Dares *et al*. Electrolytic oxidation of the americium is versatile and can be used in conjunction with a wide range of processes that separate americium. ■

Pacific Northwest National Laboratory, Richland, WA, USA.
E-mail: chuck.soderquist@pnnl.gov

REFERENCES AND NOTES

1. C. J. Dares *et al*., *Science* **350**, 652 (2015).
2. C. M. Wai, B. J. Mincher, Eds., *Nuclear Energy and the Environment*, *ACS Symposium Series 1046* (American Chemical Society, Washington, DC, 2010).
3. K. L. Nash, G. J. Lumetta, Eds., *Advanced Separation Techniques for Nuclear Fuel Reprocessing and Radioactive Waste Treatment* (Woodhead Publishing, Sawston, UK, 2011).
4. G. J. Lumetta, K. L. Nash, S. B. Clark, J. I. Friese, Eds., *Separations for the Nuclear Fuel Cycle in the 21st Century, ACS Symposium Series 933* (American Chemical Society, Washington, DC, 2006).
5. See chapter 7 in (*3*).
6. K.-W. Kim *et al*., *Nucl. Technol*. **166**, 283 (2009).
7. C. Z. Soderquist *et al*., *I&EC Research* **50**, 1813 (2011).

10.1126/science.aad5131

DRUG DISCOVERY

A new dawn for cataracts

Sterols reverse protein aggregation in an eye lens paradigm

By **Roy A. Quinlan**

Cataract, a clouding of the eye lens, is the major cause of blindness in the world, accounting for about 20 million cases (*1*). Treatment is surgical—the opaque, cataractous lens is replaced with an artificial, plastic one. Many people in the developing world become blind due to cataracts because of a lack of medical resources. A new drug treatment for cataracts based on eye drops would remove this obstacle, as current agents and dietary recommendations are generally ineffective. The findings of Makley *et al*. (*2*) reported on page 674 of this issue, and by Zhao *et al*. (*3*) may substantially boost the cataract pharmacopoeia.

The lens comprises mainly fiber cells. An epithelium, one cell thick, covers the anterior pole of the lens (*4*), and a basement membrane, the capsule, defines the lens perimeter (see the figure). Crystallins contribute much to the refractive properties of the lens. CryAA and cryAB are small heat shock protein chaperones (*5*) that stop lens proteins from forming light-diffracting aggregates. The lens contains some of the oldest proteins in the body (*6*). Cataracts form when the cryAA and cryAB chaperone function is overwhelmed by the age-dependent accumulation of posttranslationally modified lens proteins and lipids (*7*), allowing light-scattering protein aggregates and multilamellar bodies (containing many layers of membrane) to form. Presbyopia—farsightedness caused by the loss of lens elasticity—precedes age-related cataract formation (*8*).

Makley *et al*. and Zhao *et al*. identify sterols that improve lens transparency. Both studies link specific sterols to the reversal of cataract in different animal models and ex vivo lens experiments. Makley *et al*. identified 5-cholesten-3b,25-diol in a small-molecule screen for chemicals that restored the temperature stability of HSP27, a small heat shock protein. It is closely related both structurally and functionally to cryAA and cryAB as protein stabilizing and assembly chaper-

GRAPHIC: N. CARY/*SCIENCE*

Published by AAAS

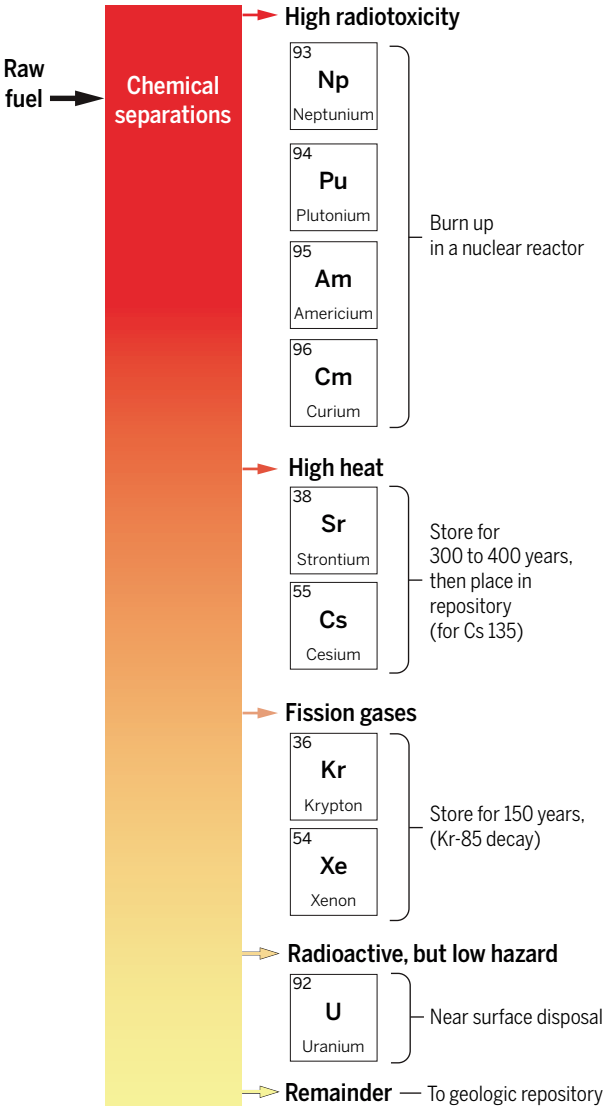

Fuel separation. Spent nuclear fuels contain a mixture of elements that need to be separated for safe disposal. Dares *et al*. report on a method for separating the highly radioactive element americium, which can then be burnt up in a nuclear reactor.

can be handled with a gloved hand) and has much smaller volume than the original fuel. This remainder is roughly as hazardous as the ore originally mined to make the fuel.

Many research groups have recently published new chemical separations of used fuel (*2*–*4*). Most of these processes are designed to work with the traditional PUREX (plutonium uranium redox extraction) process, which recovers uranium and plutonium from used fuel. The UREX+ process has been designed to recover strontium, cesium, the lanthanide elements, technetium (see the photo), uranium, and the transuranic elements (*5*). Other recently published processes do not resemble PUREX at all. One uses sodium carbonate and hydrogen peroxide solution to dissolve the fuel (*6*). Another uses ammonium carbonate and hydrogen peroxide to dissolve the fuel and begin some group separations (*7*). None of them have addressed the problem of how to easily separate americium from the lanthanides.

Dares *et al*. now show that americium can be readily oxidized from Am(III) to Am(V, VI) using simple electrolysis with a chemically modified anode. Am(III) closely resembles the lanthanide elements, but Am(V) and Am(VI) are chemically quite different. This makes an excellent starting point for separations that quickly isolate americium from the lanthanide elements. Used fuel has much more of the lanthanide elements than americium. If americium is to be burned up in a reactor, then it must be quite pure or the lanthanide impurities will absorb neutrons and prevent the americium from burning up.

All processes intended to separate the fuel into its components without generating a large volume of secondary waste need to separate the americium. When they do, they will probably use the electrolytic oxidation approach described by Dares *et al*. Electrolytic oxidation of the americium is versatile and can be used in conjunction with a wide range of processes that separate americium. ■

Pacific Northwest National Laboratory, Richland, WA, USA.
E-mail: chuck.soderquist@pnnl.gov

REFERENCES AND NOTES

1. C. J. Dares *et al*., *Science* **350**, 652 (2015).
2. C. M. Wai, B. J. Mincher, Eds., *Nuclear Energy and the Environment*, *ACS Symposium Series 1046* (American Chemical Society, Washington, DC, 2010).
3. K. L. Nash, G. J. Lumetta, Eds., *Advanced Separation Techniques for Nuclear Fuel Reprocessing and Radioactive Waste Treatment* (Woodhead Publishing, Sawston, UK, 2011).
4. G. J. Lumetta, K. L. Nash, S. B. Clark, J. I. Friese, Eds., *Separations for the Nuclear Fuel Cycle in the 21st Century, ACS Symposium Series 933* (American Chemical Society, Washington, DC, 2006).
5. See chapter 7 in (*3*).
6. K.-W. Kim *et al*., *Nucl. Technol*. **166**, 283 (2009).
7. C. Z. Soderquist *et al*., *I&EC Research* **50**, 1813 (2011).

10.1126/science.aad5131

DRUG DISCOVERY

A new dawn for cataracts

Sterols reverse protein aggregation in an eye lens paradigm

By **Roy A. Quinlan**

Cataract, a clouding of the eye lens, is the major cause of blindness in the world, accounting for about 20 million cases (*1*). Treatment is surgical—the opaque, cataractous lens is replaced with an artificial, plastic one. Many people in the developing world become blind due to cataracts because of a lack of medical resources. A new drug treatment for cataracts based on eye drops would remove this obstacle, as current agents and dietary recommendations are generally ineffective. The findings of Makley *et al*. (*2*) reported on page 674 of this issue, and by Zhao *et al*. (*3*) may substantially boost the cataract pharmacopoeia.

The lens comprises mainly fiber cells. An epithelium, one cell thick, covers the anterior pole of the lens (*4*), and a basement membrane, the capsule, defines the lens perimeter (see the figure). Crystallins contribute much to the refractive properties of the lens. CryAA and cryAB are small heat shock protein chaperones (*5*) that stop lens proteins from forming light-diffracting aggregates. The lens contains some of the oldest proteins in the body (*6*). Cataracts form when the cryAA and cryAB chaperone function is overwhelmed by the age-dependent accumulation of posttranslationally modified lens proteins and lipids (*7*), allowing light-scattering protein aggregates and multilamellar bodies (containing many layers of membrane) to form. Presbyopia—farsightedness caused by the loss of lens elasticity—precedes age-related cataract formation (*8*).

Makley *et al*. and Zhao *et al*. identify sterols that improve lens transparency. Both studies link specific sterols to the reversal of cataract in different animal models and ex vivo lens experiments. Makley *et al*. identified 5-cholesten-3b,25-diol in a small-molecule screen for chemicals that restored the temperature stability of HSP27, a small heat shock protein. It is closely related both structurally and functionally to cryAA and cryAB as protein stabilizing and assembly chaper-

GRAPHIC: N. CARY/*SCIENCE*

Published by AAAS

ones (*5*). In two mouse models of inherited human cataract [mutant cryAA (R49C) and cryAB (R120G), where arginine 49 is replaced with cysteine and arginine 120 with glycine, respectively], 5-cholesten-3b,25-diol reduced cataract severity after only a 2-week eye-drop treatment regime. Similarly, Zhao *et al.* identified mutations in lanosterol synthase as the genetic basis of inherited cataract and found that lanosterol increased lens transparency in a dog model of age-related cataract with a 6-week treatment regime.

Earlier biochemical, genetic, and drug studies indicated an association between cataract and sterols (*7*). Certain bile acids were shown to increase cryAB and cryAA chaperone activity (*9*) and prevent cataract in a selenite model of cataract formation in rats (*10*). Makley *et al.* and Zhao *et al.* advance the field by showing that protein aggregation accompanying cataractogenesis is not an endpoint, but can be quickly reversed with specific sterols.

Makley *et al.* used high-throughput differential scanning fluorimetry to identify 32 compounds active on HSP27, of which 12 were related sterols. As 5a-cholestan-3b-ol-6-one and 5-cholesten-3b,25-diol are derivatives of a common lipid, cholesterol, they were selected for biochemical analysis. 5-Cholesten-3b,25-diol docked into a groove formed at the cryAB dimer interface to stabilize the native state. Both sterols inhibited the potential of R120G cryAB to unfold and form amyloid-like fibrils. Makley *et al.* found that lanosterol performed relatively poorly in binding to HSP27 compared to the identified active compounds, indicating that the structure-function relationship for cataract inhibition by sterols is still an open question. Interestingly, Zhao *et al.* observed that lanosterol dissolved fibers formed by cryAA R116C, R116H, and Y118D mutants (in which arginine 116 is replaced with cysteine or histidine, and tyrosine 118 is replaced with aspartic acid, respectively). Lanosterol also prevented the aggregation of β and γ crystallins in transiently transfected cells. Perhaps lanosterol activates endogenous small heat shock proteins, as evidence from Makley *et al.* suggests that lanosterol does not bind directly to β or γ crystallins.

Lanosterol is a precursor of cholesterol, pointing to cholesterol metabolism as a key factor in cataract formation. This complements clinical observations in certain disorders. Patients with Smith-Lemli-Opitz syndrome have an abnormality in cholesterol metabolism resulting from deficiency of the enzyme 7-dehydrocholesterol reductase; 20% of affected individuals have cataracts. Mevalonic aciduria is caused by a deficiency of mevalonate kinase, which results in a defect in the biosynthesis of cholesterol and isoprenoids; cataract is an ophthalmic feature of this disorder. Cerebrotendinous xanthomatosis patients also present with cataract. This is a fat storage disorder caused by the inability to metabolize certain lipids, including cholesterol. Also, the debate over the increased cataract risk with statin use continues (*11*), but now there is reason for caution. Statins are cholesterol-lowering drugs that inhibit 3-hydroxy-3-methyl-glutaryl-coenzyme A reductase, an enzyme in the cholesterol biosynthesis pathway.

Both cryAB and cryAA bind to cell membranes, possessing high- and low-affinity binding sites (*7*). As lens cells age, more of the soluble crystallin proteins associate with membranes, and cryAA and cryAB become even more membrane-embedded (*7*). Both 5-cholesten-3b,25-diol and lanosterol increase lens protein solubility, but the mechanism was unexplored by Makley *et al.* or Zhao *et al.* The promoter region of the *cryAA* and *cryAB* genes contains sterol responsive element (*12*, *13*), adding a potential transcriptional mechanism to the posttranslational mechanism for integrating chaperone function and cholesterol biosynthesis and metabolism.

There is still much to learn about sterols, small heat shock proteins, and the physiological importance of their interaction and their diverse roles in lens function, presbyopia, and cataractogenesis. Perhaps these chaperones are a new class of sterol sensors, tuned to cholesterol metabolism and cholesterol modifications in the eye lens. Moreover, cryAB functions in many other cellular processes, including the cell division cycle, programmed cell death, cytoskeletal dynamics, and redox balance (*14*). The potential to apply the discovery of Makley *et al.* and Zhao *et al.* to cataract, presbyopia, and protein misfolding diseases that involve these small heat shock proteins and their clients now beckons. ■

Biophysical Sciences Institute, School of Biological and Biomedical Sciences, Durham University, Durham DH1 3LE, UK. E-mail: r.a.quinlan@durham.ac.uk

REFERENCES

1. www.who.int/blindness/causes/priority/en/index1.html
2. L. N. Makley *et al.*, *Science* **350**, 674 (2015).
3. L. Zhao *et al.*, *Nature* **523**, 607 (2015).
4. J. J. Wu *et al.*, *J. R. Soc. Interface* **12**, 20150391 (2015).
5. R. A. Quinlan, R. J. Ellis, *Philos. Trans. R. Soc. Lond. B Biol. Sci.* **368**, 20130091 (2013).
6. Stewart *et al.*, *Mol. Vis.* **19**, 463 (2013).
7. D. Borchman, M. C. Yappert, *J. Lipid Res.* **51**, 2473 (2010).
8. R. J. Truscott, *Exp. Eye Res.* **88**, 241 (2009).
9. S. Song *et al.*, *Cell Stress Chaperones* **16**, 475 (2011).
10. H. P. Qi *et al.*, *Mol. Vis.* **18**, 151 (2012).
11. J. B. Kostis, J. M. Dobrzynski, *J. Cardiovasc. Pharmacol. Ther.* **20**, 346 (2015).
12. F.Y. Lee *et al.*, *J. Biol. Chem.* **280**, 31792 (2005).
13. B. Scheier *et al.*, *Mol. Cell. Endrocrinol.* **123**, 187 (1996).
14. M. D. Perng, R. A. Quinlan, in *The Big Book of Small Heat Shock Proteins*, R. M. Tanguay, L. E. Hightower, Eds. (Springer, 2015) **8**, 401–434

10.1126/science.aad6303

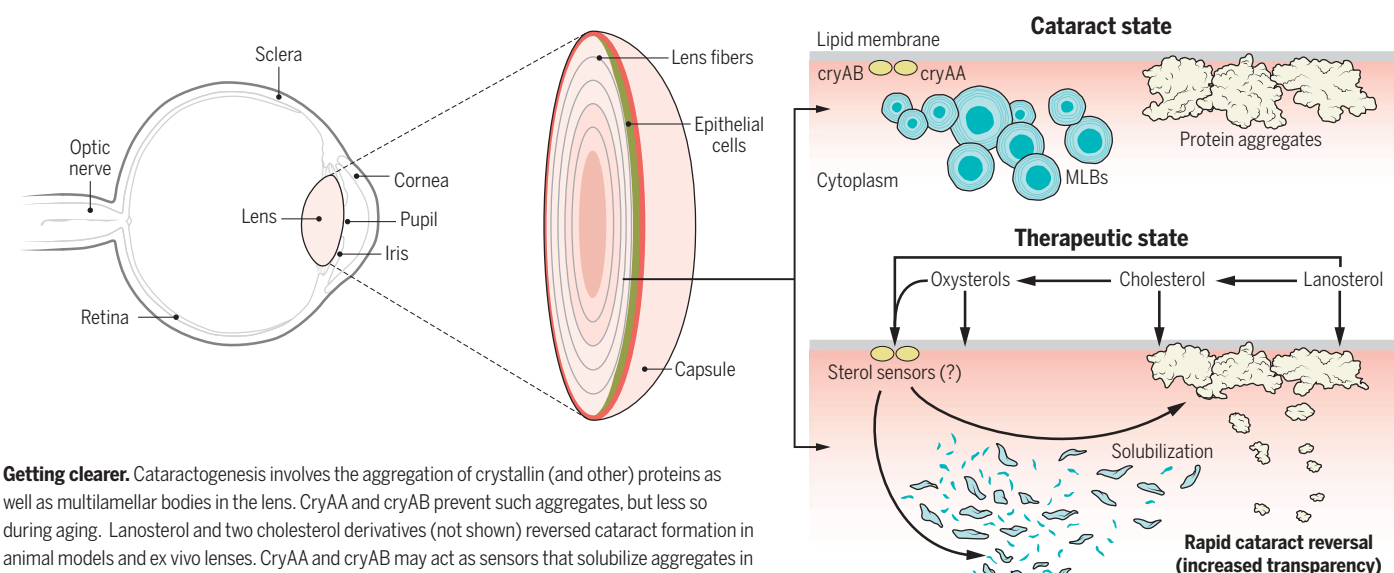

Getting clearer. Cataractogenesis involves the aggregation of crystallin (and other) proteins as well as multilamellar bodies in the lens. CryAA and cryAB prevent such aggregates, but less so during aging. Lanosterol and two cholesterol derivatives (not shown) reversed cataract formation in animal models and ex vivo lenses. CryAA and cryAB may act as sensors that solubilize aggregates in response to such sterols, which will also modulate membrane lipid domains in the lens.

GRAPHIC: P. HUEY/*SCIENCE*

Published by AAAS

BOOKS *et al.*

SCIENCE LIVES

Access for all

A moving memoir offers lessons for increasing diversity in STEM fields

By **Isiah M. Warner* and Gloria Thomas**

Holding Fast to Dreams
Empowering Youth from the Civil Rights Crusade to STEM Achievement
Freeman A. Hrabowski III
Beacon Press, 2015. 208 pp.

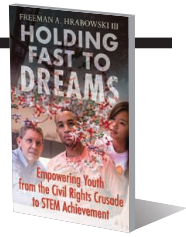

It is not often that one gets to explore and understand the development of a truly impactful national leader through their thoughts, their formative environment, and their education. In *Holding Fast to Dreams*, University of Maryland, Baltimore County (UMBC), President Freeman Hrabowski III takes us on such a journey from his childhood involvement in the civil rights movement to his growing legacy as an advocate for improving access to science, technology, engineering, and mathematics (STEM) higher education. The book juxtaposes the stories of an individual, an institution, and a nation in a manner that is highly instructive.

In the book's opening chapter, we learn about the people who helped shape Hrabowski's early thoughts on education, including his maternal and fraternal grandmothers, who saw education as a powerful tool that could transform lives, as well as his parents, who worked as teachers during his childhood.

Hrabowski grew up in Birmingham, Alabama, during the height of the civil rights movement and describes the impact of being jailed as a young child for participating in the 1963 "Children's Crusade," a march against segregation that generated national headlines and a federal response when local authorities responded with violence. "Being in jail was an awful experience, and the guards made every effort to increase our misery," he recalls. The only solace during his incarceration came when Martin Luther King Jr. arrived midweek and reassured the children that their actions would help make the world a better place for the next generation.

Tragically, one of Hrabowski's friends was among the four young girls who died when the Ku Klux Klan bombed a Birmingham church that same year. It was interesting to learn that he and Angela Davis, the political rights activist and scholar, came from very similar backgrounds, yet took such different paths to the field of higher education.

Hrabowski traces how the educational opportunities he had during his formative years led him to his calling as an educator, recalling, for example, his experience in an integrated summer learning program ("I seemed invisible even to the teachers") and another summer program for high-achieving black students at Tuskegee University ("It was here that I first experienced the power of community and the power of working in groups"). These experiences ultimately inspired his ideas and approaches for improving STEM education.

Holding Fast to Dreams **traces the personal and professional journey of Freeman Hrabowski III, a pioneering leader in American higher education.**

While a young Hrabowski was being jailed for marching in the streets of Birmingham, the foundations of UMBC were being laid. The goal of the founders was to establish a new university that would serve students from all races as an experiment toward inclusive excellence. Hrabowski describes how these events were occurring amid a landscape of legislative acts, including the Civil Rights Act of 1964, the GI Bill, and the Educational Amendments of 1972, all of which helped provide educational expansion and economic opportunities. This progress increased high school and college attainment in America like never before, but many schools, even today, remain essentially segregated and underfunded.

With this personal and national context established, Hrabowski describes the factors that ultimately led to the creation of the now well-known and respected Meyerhoff Scholars Program, which seeks to increase minority scholarship in STEM disciplines. He outlines how the program has been adopted by other institutions and expanded for use in kindergarten through 12th-grade settings.

In Hrabowski's final reflections, he asserts that "success is never final," and he encourages us all to continue telling our stories in an effort to inspire others to take on similar challenges at their own institutions.

Although this book represents a substantial contribution to the fields of higher education and civil rights history independently, it also provides an instructive narrative that is engaging and thought-provoking. For those who may not have lived through the historic and transformative civil rights era, Hrabowski's book will provide insights into this period from a lived experience that is so much more than a simple recounting of facts, dates, and events. Even for those who may have heard parts of these stories before, the compiled compendium of Hrabowski's thoughts and experiences is quite rewarding.

*The authors are in the Office of Strategic Initiatives at Louisiana State University, Baton Rouge, LA 70803, USA. *Corresponding author. E-mail: iwarner@lsu.edu (I.M.W.)*

10.1126/science.aad3007

PHOTO: MARLAYNA DEMOND '11 FOR UMBC

Published by AAAS

CULTURAL ANTHROPOLOGY

The cultural evolution

An ambitious attempt to show that human culture evolves from the bottom up falls flat

By **Richard Gawne**

The Evolution of Everything
How New Ideas Emerge
Matt Ridley
Harper, 2015. 366 pp.

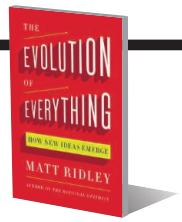

At the heart of the scientific method is the assumption that when something happens, there is a cause. More important, we generally think that with enough sweat and tears we can identify that cause and, if necessary, manipulate it to suit our interests. In *The Evolution of Everything*, Matt Ridley attempts to demonstrate that the complex systems that define the modern world, including our economies, educational systems, population structures, governments, and religions, emerged on their own and did not arise as a result of purposeful human action. Indeed, according to Ridley, when we attempt to exercise control over the systems in question, bad consequences almost inevitably follow. This is an ambitious book, and the author is aware that it will generate controversy.

Ridley claims a Darwinian heritage for the book, noting, "I want to do for every aspect of the human world a little bit of what Charles Darwin did for biology, and get you to see past the illusion of design, to see the emergent, unplanned, inexorable and beautiful process of change that lies underneath." He sets out to undermine what he refers to as "creationist" views of the world that place undue emphasis on the actions of individuals.

Do you believe that human personalities can be shaped by environmental factors such as upbringing or that they simply result from the unfolding of innate genetic tendencies? If you're not willing to accept that individual differences in behavior are genetically predetermined, Ridley suggests that you've adopted a creationist stance. The same goes if you believe that urban planners have played a meaningful role in the structuring of cities or that government interventions have the potential to improve a country's economy.

The positions Ridley attempts to refute may have some flaws, but they do not appeal to supernatural entities, and for this reason the repeated accusations of creationism seem unwarranted. A case in point is the claim that most educational institutions should be classified as creationist because "[t]he curriculum is too prescriptive and slow to change, teachers are encouraged to teach to the exam rather than to the pupils' or their own strengths."

Simply claiming that things change over time does not mean one has proposed an evolutionary theory. Darwin did not declare that species change and call it a day. He provided a testable mechanism to explain how species change. Analogous causal hypotheses are largely absent in Ridley's book.

In recent years, research has shown that group-level behaviors can emerge unplanned from the interactions of individuals, but one of the crucial findings to come out of this work is that some members have a bigger impact on group dynamics than others. Ridley concedes that "individuals can make a difference, of course, and so can political parties or big companies," but few attempts are made to reconcile this fact with the thesis that everything emerges blindly from the bottom up.

On a more fundamental level, the author's message that we should let "incremental, inexorable, inevitable changes" run their course and revolt against the "repeatedly debunked doom-mongering of the scientific elite" is troubling. This, of course, is the same sort of logic that has repeatedly been used to deny the significance of global warming.

Speaking specifically on climate change, Ridley makes a number of remarks that will inflame passions. He deplores the tendency to "latch on to any excuse to blame an extreme weather event on human agency – whether witchdoctoring or man-made global warming" and later adds mockingly that "[N]one must depart from faith (in carbon dioxide) as set out in scripture (the reports of the Intergovernmental Panel on Climate Change). It is the duty of all to condemn heretics (the 'deniers'), venerate saints (Al Gore), heed the prophets (of the IPCC)."

Although it is probably true that we tend to give ourselves too much credit for creating or planning certain things, Ridley often seems to be advocating an extreme swing in the opposite direction that could be mistaken for orthogenesis, particularly when he describes changes as "follow[ing] a narrative," and having their "own spontaneous momentum." In the end, this is a book by an accomplished author whose views have evolved in an unfortunate direction.

The reviewer is a visiting graduate fellow at the Department of Entomology, National Museum of Natural History, Smithsonian Institution, Washington, DC, USA. E-mail: gawner@si.edu

10.1126/science.aad2745

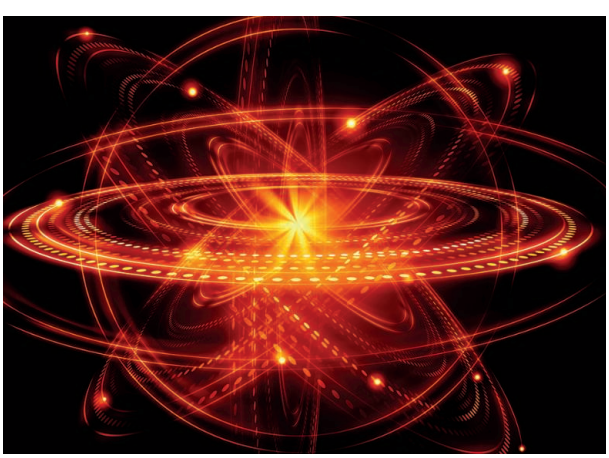

ILLUSTRATION: SERGEY NIVENS/SHUTTERSTOCK

PHYSICS

Spooky Action at a Distance
George Musser
Scientific American/Farrar, Straus and Giroux, 2015. 296 pp.

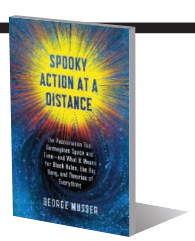

The concept of nonlocality, wherein a particle can influence the behavior of another particle even if they are miles apart, is, according to George Musser, "the mother of all physics riddles." Indeed, the notion that an object can have an effect on another object no matter the distance between them has implications for how we understand everything from black holes to gravity. In just under 300 pages, Musser deftly traces the history of our quest to understand this curious phenomenon, covering an ambitious breadth of challenging topics from string theory to the multiverse to the unification of physics.

10.1126/science.aad6372

Published by AAAS

Downloaded from www.sciencemag.org on November 5, 2015

LETTERS

Edited by **Jennifer Sills**

Lift NIH restrictions on chimera research

MANY OVERSIGHT MECHANISMS exist for research involving human subjects and cells, as well as the transfer of materials into other vertebrates, partly to reassure the public that biomedical research is ethically conducted. In the recently posted notice NOT-OD-15-158, the NIH stated that it "will not fund research in which human pluripotent cells are introduced into non-human vertebrate animal pre-gastrulation–stage embryos while the agency considers a possible policy revision in this area" (*1*). This notice encompasses human pluripotent stem cells (hPSCs), including human induced pluripotent stem cell (hiPSC)–based human/non-human chimera studies. We believe that this notice poses a threat to progress in stem cell biology, developmental biology, and regenerative medicine. We hope the guideline recommendations that emerge from the NIH Workshop on 6 November will accelerate the decision to reinstate NIH funding for this research area, which has tremendous promise. We strongly believe that a continued dialogue between scientists and bioethicists regarding human/non-human chimera studies is critical for advancing human health through basic science.

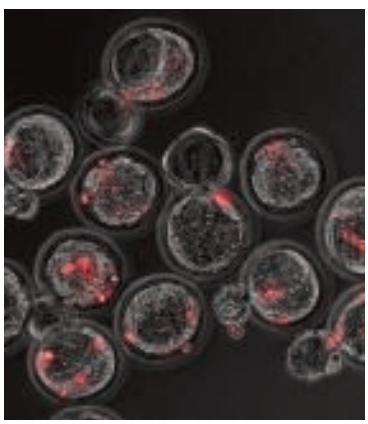

Engraftment of hiPSC (red) into mouse blastocyst-stage embryo

Much of the bioethical concern in regard to human/non-human chimerism arises from the possibility of chimeric animals harboring human neurons and germ cells. Can human neural cells coexist with those from animals and establish "humanized" cerebral anatomy and circuitries? Furthermore, would such chimeras be elevated to a higher metaphysical state and "think" more like us (*2*)? Current scientific data have not supported such possibilities, despite hundreds of xenotransplant studies introducing human neurons into the mouse brain (*3*–*5*). With regard to germline transmission, the National Academy of Medicine and the National Research Council have stated in the Guidelines for Human Embryonic Stem Cell Research that animals in which human pluripotent stem cells (hPSCs) have been introduced during development should not breed and that hPSC chimerism with non-human primates is restricted (*6*).

Research involving hPSC complementation in non-human, pre-gastrulation–stage vertebrate embryos represents a special topic with tremendous potential to elucidate early human development. Development of stem and progenitor cells from pre-gastrulation embryos occurs over the weeks following blastocyst implantation into appropriate hosts. Currently, it is impossible to accurately recapitulate human development in vitro, and there is no ethical method to obtain post-implantation–stage human fetal tissue for isolating tissue and organ stem cells for regenerative medicine. Although early chimera studies involving hESCs/iPSCs and non-human vertebrate animal blastocysts have shown some capacity for contribution to host tissues (*7*–*9*), much work remains to unravel key differences in early development between humans and other vertebrates. If we succeed in inducing significant chimerism between hPSCs and pre-gastrulation–stage embryos from non-human vertebrates, tremendous potential exists to develop humanized disease models for studying drug pharmacology. Similarly, implantation of hPSCs derived from patients with heritable diseases could illuminate genetic disease pathogeneses in an appropriate in vivo context. It may even be possible to generate an unlimited supply of therapeutic replacement organs using porcine or sheep models, an effort that we (H.N.) have undertaken with support from the California Institute for Regenerative Medicine. By eliminating federal funding for this research, the NIH casts a shadow of negativity towards all chimerism studies regardless of whether human cells are involved.

Ultimately, we believe that human/non-human chimerism studies in pre-gastrulation embryos hold tremendous potential to improve our understanding of early development, enhance disease modeling, and promote therapeutic discovery. Given that the objective of the NIH is to enable discoveries that advance human health, the restrictions presented in NOT-OD-15-158 serve to impede scientific progress in regenerative medicine and should be lifted.

Arun Sharma,[1,2] Vittorio Sebastiano,[1,3] Christopher T. Scott,[4] David Magnus,[4] Naoko Koyano-Nakagawa,[5] Daniel J. Garry,[5,6,7] Owen N. Witte,[8] Hiromitsu Nakauchi,[1,9,10] Joseph C. Wu,[1,2,11,12] Irving L. Weissman,[1,13]* Sean M. Wu[1,2,11]*

[1]Institute for Stem Cell Biology and Regenerative Medicine, Stanford University School of Medicine, Stanford, CA 94305, USA. [2]Cardiovascular Institute, Stanford University School of Medicine, Stanford, CA 94305, USA. [3]Department of Obstetrics and Gynecology, Stanford University School of Medicine, Stanford, CA 94305, USA. [4]Center for Biomedical Ethics, Stanford University School of Medicine, Stanford, CA 94305, USA. [5]Lillehei Heart Institute, University of Minnesota, Minneapolis, MN 55455, USA. [6]Stem Cell Institute and Paul and Sheila Wellstone Muscular Dystrophy Center, University of Minnesota, Minneapolis, MN 55455, USA. [7]Cardiovascular Division, Department of Medicine, University of Minnesota, Minneapolis, MN 55455, USA. [8]Broad Stem Cell Research Center and Department of Microbiology, Immunology, and Molecular Genetics, University of California, Los Angeles, Los Angeles, CA 90095, USA. [9]Department of Genetics, Stanford University School of Medicine, Stanford, CA 94305, USA. [10]Center for Stem Cell Biology and Regenerative Medicine, The University of Tokyo, Tokyo, Japan. [11]Division of Cardiovascular Medicine, Department of Medicine, Stanford University School of Medicine, Stanford, CA 94305, USA. [12]Department of Radiology, Stanford University School of Medicine, Stanford, CA 94305, USA. [13]Department of Pathology, Stanford University School of Medicine, Stanford, CA 94305, USA.

*Corresponding author. E-mail: irv@stanford.edu (I.W.); smwu@stanford.edu (S.M.W.)

REFERENCES

1. NIH Notice Number NOT-OD-15-158 (https://grants.nih.gov/grants/guide/notice-files/NOT-OD-15-158.html).
2. H. T. Greely, M. K. Cho, L. F. Hogle, D. M. Satz, *Am. J. Bioeth.* **7**, 27 (2007).
3. O. Brustle *et al.*, *Nat. Biotechnol.* **16**, 1040 (1998).
4. S. C. Zhang, M. Wernig, I. D. Duncan, O. Brustle, J. A. Thomson, *Nat. Biotechnol.* **19**, 1129 (2001).
5. H. Lee *et al.*, *Stem Cells* **25**, 1931 (2007).
6. National Research Council (U.S.), Committee on Guidelines for Human Embryonic Stem Cell Research, Institute of Medicine (U.S.), Board on Health Sciences Policy, *Guidelines for Human Embryonic Stem Cell Research* (National Academies Press, Washington, DC, 2005).
7. O. Gafni *et al.*, *Nature* **504**, 282 (2013).
8. J. Wu *et al.*, *Nature* **521**, 316 (2015).
9. H. Masaki *et al.*, *Development* **142**, 3222 (2015).

Making sense of the troubles at NEON

IN HIS 25 September News Feature "Ecology's tough climb" (p. 1436), J. Mervis detailed the problems that have plagued the National Science Foundation's (NSF's) National Ecological Observatory Network (NEON). The severity of NEON's troubles recently led to a congressional hearing in which James Olds, head of NSF's Biological Sciences Directorate, said that NEON Inc. would be replaced as NEON's contractor

PHOTO: HIROMITSU (HIRO) NAKAUCHI

Downloaded from www.sciencemag.org on November 5, 2015

Published by AAAS

if it didn't get its act together. I served as NEON's lead scientist and observatory director in 2013–2014, and Mervis summarized my own frustrations at NEON as an example of how poorly the project has been managed.

I agree with Mervis's assessment of what has gone wrong at NEON, but some additional clarification might help understand why. Thus far, the spotlight has primarily been on mismanagement by NEON Inc., which prompted the recent removal of its CEO as well as the congressional hearing. But NEON program directors at NSF also bear considerable responsibility for how the project has been run. The authority they hold extends to nearly all levels of the organization, as well as how it can and cannot interact with the external community. To date, their philosophy has been that the Observatory can be most efficiently built by project managers with minimal interference from scientists or members of the community. Applying this approach to a distributed ecological observatory that lacked a detailed blueprint was a mistake that has put NEON under a chronic strain. This underlies a number of NEON Inc.'s present difficulties, its own management failures notwithstanding.

At the 18 September congressional hearing on NEON, Olds told panel members that "NSF is going to be sitting on NEON Inc. over the next three months…and we will know very quickly whether this organization is going to be successful under new leadership" (*1*). Sound management by whatever organization builds NEON is clearly needed to get the project back on track. But NEON's success will equally depend on improvements within NSF and a shift in perspective that puts stewardship of NEON science back in the hands of scientists.

Scott V. Ollinger

Earth Systems Research Center, University of New Hampshire, Durham, NH 03824, USA.
E-mail: scott.ollinger@unh.edu

REFERENCE

1. Committee on Science, Space, and Technology, "Subcommittee on Research and Technology and Subcommittee on Oversight Hearing: NEON Warning Signs: Examining the Management of the National Ecological Observatory Network" (https://science.house.gov/legislation/hearings/subcommittee-research-and-technology-and-subcommittee-oversight-hearing-neon).

ONLINE BUZZ

Disaster Preparedness

In her Editorial "Preparing for the next Katrina" (28 August, p. 905), M. McNutt discussed how far disaster preparedness has come in the past 10 years and how we should continue to move forward. Readers added their warnings and encouragement in the comments section. Excerpts from their comments are below. See the full comments, and add your own, at http://comments.sciencemag.org/content/10.1126/science.aad2209.

A selection of your thoughts:

…We would like to caution against an endorsement of the unqualified benefits of social media in all phases of a disaster. A recent report showed that people who used social media following Hurricane Sandy were more likely to exhibit higher levels of post-traumatic stress reactions when compared to survivors who opted for more traditional information providers [R. Goodwin *et al.*, *J. Psychiatr. Res.* **47**, 1099 (2013)]. A similar pattern of results was observed after the Super Typhoon Hayian with regard to acute stress reactions and psychological distress [R. Goodwin *et al.*, *Psychother. Psychosom.* **84**, 253 (2015)]. Even informed social media can result in "stress contagion," wherein psychological difficulties experienced by some may augment the adverse effects of the event. Social media, in its sheer immediacy and volume, can rapidly overload the user, making it more difficult to coordinate effective behaviors…. Every asset has its liabilities….

Menachem Ben-Ezra, Krzysztof Kaniasty, Robin Goodwin

…The importance of communities being aware of…what they themselves might be able to do is essential. When the seawall cracks or the tsunami strikes, it is an absolute duty of authorities and aid agencies to establish a meaningful engagement with populations so that people are respected….[I]f there truly is a listening process, populations are empowered….

Martin Dawes

Published by AAAS

MAVEN

EXPLORES THE MARTIAN UPPER ATMOSPHERE

by **Bruce M. Jakosky**

After decades of exploration by landers, rovers, and orbiting spacecraft, Mars continues to capture imaginations and reveal surprises. Indeed, the more we learn about Mars, the more we see the connections between its interior, surface, and atmosphere. Answering questions about the potential for habitability, presence of water, and history of its climate requires understanding Mars as a connected system over time.

It was in this context that NASA flew the orbiting Mars Atmosphere and Volatile Evolution (MAVEN) mission *(1)*. Its goal was to explore the modern martian upper atmosphere in unprecedented detail. MAVEN carries a suite of instruments that take measurements while directly traveling through the atmosphere as it orbits the planet, from ~125 to ~6000 km above the rocky surface. MAVEN has been operating in orbit around Mars since 18 September 2014, and the data now allow us to start addressing key science questions that had otherwise been unanswerable.

Artist's rendition of the MAVEN spacecraft over Mars.

Previous Mars missions have provided compelling evidence for abundant liquid water on ancient Mars. This would seem to require a thicker CO_2 atmosphere to provide the necessary greenhouse warming. Where did the CO_2 go? Where did the water go? There do not appear to be sufficient carbon-bearing minerals on the surface or in the subsurface to account for a thick early atmosphere *(2)*, but loss to space is thought to be a viable mechanism for producing the observed changes in climate *(1)*. Measurements by MAVEN shed light on how the upper atmosphere interacts with the Sun and solar wind, and the ability of gases to escape to space—both important processes for understanding planetary atmospheres. Four papers in this issue report some of the initial discoveries and are complemented by a series of companion papers in *Geophysical Research Letters (3)*.

Jakosky *et al*. examine measurements made during the impact of an interplanetary coronal mass ejection onto the Mars system. The sudden and dramatic increase in solar wind density, velocity, and magnetic field intensity lead to enhancements in the production and energization of ions picked up by the solar wind as it streams by, and to an increase in the rate of gas escape to space. Solar storms might have been more abundant and more intense early in solar system history, so this increase may have implications for the early loss of Mars' atmosphere to space.

Bougher *et al*. describe in situ measurements of the Mars thermosphere; the only previous measurements came from profiles obtained during the entry of the two Viking landers in 1976. The thermosphere, spanning roughly 120 to 200 km, connects the lower atmosphere that controls the martian climate to the exosphere that controls gases' escape to space. Its properties are central to understanding the long-term evolution of the atmosphere. The measurements provide detailed information on the composition of the neutral atmosphere and ionosphere, the variability of this region, and the energetics of ion acceleration that leads to loss.

Schneider *et al*. report the discovery of a "diffuse" aurora produced by a solar storm. The diffuse aurora was widespread geographically, as opposed to previously observed "discrete" auroras. The solar electrons responsible for the aurora probably entered the martian atmosphere directly from the solar wind. The auroras reflect active processes that produce ionization and dissociation, which may affect the overall atmospheric escape rate. The lack of a global magnetic field on Mars probably causes the martian auroras to be more a global phenomenon than they are on Earth.

Andersson *et al*. describe the discovery of dust at orbital altitudes surrounding Mars, detected by the effect a dust grain has when it strikes the spacecraft. Dust impacts were detected from the lowest altitudes visited by the spacecraft, around 125 km above the surface, up to ~1000 km altitude. The distribution of the dust points to interplanetary debris in the solar system as the likely source. Such debris is thought to be responsible for producing discrete layers in the ionosphere and for affecting the chemistry and energetics in that region.

Together, these measurements—along with those reported in the companion papers—are beginning to shape a new view of both modern and past processes on Mars. The upper atmosphere of Mars was probably a major contributor to the evolution of Mars' climate, and thereby influenced the stability of liquid water and the potential habitability of Mars by microorganisms. MAVEN is continuing to make measurements as it orbits the Red Planet and will be able to explore the upper atmosphere over a full Mars year and during the changing phases of the solar cycle. The measurements being reported here only scratch the surface of what remains to be learned about the connected Mars system.

REFERENCES

1. B. M. Jakosky and 70 others, The MAVEN mission to Mars, *Space Sci. Rev.* 10.1007/s11214-015-0139-x (2015).
2. C. S. Edwards, B. L. Ehlmann, Carbon sequestration on Mars. *Geology* 10.1130/G36983.1 (2015).
3. B. M. Jakosky, J. M. Grebowsky, J. G. Luhmann, D. A. Brain, Initial results from the MAVEN mission to Mars. *Geophys. Res. Lett.* **42**, 10.1002/2015GL065271 (2015).

10.1126/science.aad3443

Laboratory for Atmospheric and Space Physics and Department of Geological Sciences, University of Colorado, Boulder, CO, USA.

CREDIT: NASA/GSFC

Downloaded from www.sciencemag.org on November 5, 2015

Published by AAAS

MAVEN observations of the response of Mars to an interplanetary coronal mass ejection

B. M. Jakosky,* J. M. Grebowsky, J. G. Luhmann, J. Connerney, F. Eparvier, R. Ergun, J. Halekas, D. Larson, P. Mahaffy, J. McFadden, D. F. Mitchell, N. Schneider, R. Zurek, S. Bougher, D. Brain, Y. J. Ma, C. Mazelle, L. Andersson, D. Andrews, D. Baird, D. Baker, J. M. Bell, M. Benna, M. Chaffin, P. Chamberlin, Y.-Y. Chaufray, J. Clarke, G. Collinson, M. Combi, F. Crary, T. Cravens, M. Crismani, S. Curry, D. Curtis, J. Deighan, G. Delory, R. Dewey, G. DiBraccio, C. Dong, Y. Dong, P. Dunn, M. Elrod, S. England, A. Eriksson, J. Espley, S. Evans, X. Fang, M. Fillingim, K. Fortier, C. M. Fowler, J. Fox, H. Gröller, S. Guzewich, T. Hara, Y. Harada, G. Holsclaw, S. K. Jain, R. Jolitz, F. Leblanc, C. O. Lee, Y. Lee, F. Lefevre, R. Lillis, R. Livi, D. Lo, M. Mayyasi, W. McClintock, T. McEnulty, R. Modolo, F. Montmessin, M. Morooka, A. Nagy, K. Olsen, W. Peterson, A. Rahmati, S. Ruhunusiri, C. T. Russell, S. Sakai, J.-A. Sauvaud, K. Seki, M. Steckiewicz, M. Stevens, A. I. F. Stewart, A. Stiepen, S. Stone, V. Tenishev, E. Thiemann, R. Tolson, D. Toublanc , M. Vogt, T. Weber, P. Withers, T. Woods, R. Yelle

Coupling between the lower and upper atmosphere, combined with loss of gas from the upper atmosphere to space, likely contributed to the thin, cold, dry atmosphere of modern Mars. To help understand ongoing ion loss to space, the Mars Atmosphere and Volatile Evolution (MAVEN) spacecraft made comprehensive measurements of the Mars upper atmosphere, ionosphere, and interactions with the Sun and solar wind during an interplanetary coronal mass ejection impact in March 2015. Responses include changes in the bow shock and magnetosheath, formation of widespread diffuse aurora, and enhancement of pick-up ions. Observations and models both show an enhancement in escape rate of ions to space during the event. Ion loss during solar events early in Mars history may have been a major contributor to the long-term evolution of the Mars atmosphere.

The list of author affiliations is available in the full article online. ***Corresponding author. E-mail: bruce.jakosky@lasp.colorado.edu.** Cite as B. M. Jakosky *et al.*, *Science* **350**, aad0210 (2015). Read the full article at http://dx.doi.org/10.1126/science.aad0210

Ions escaping the martian atmosphere (right) due to solar wind radiation emitted by the Sun (left).

Early MAVEN Deep Dip campaign reveals thermosphere and ionosphere variability

S. Bougher,* B. Jakosky, J. Halekas, J. Grebowsky, J. Luhmann, P. Mahaffy, J. Connerney, F. Eparvier, R. Ergun, D. Larson, J. McFadden, D. Mitchell, N. Schneider, R. Zurek, C. Mazelle, L. Andersson, D. Andrews, D. Baird, D. N. Baker, J. M. Bell, M. Benna, D. Brain, M. Chaffin, P. Chamberlin, J.-Y. Chaufray, J. Clarke, G. Collinson, M. Combi, F. Crary, T. Cravens, M. Crismani, S. Curry, D. Curtis, J. Deighan, G. Delory, R. Dewey, G. DiBraccio, C. Dong, Y. Dong, P. Dunn, M. Elrod, S. England, A. Eriksson, J. Espley, S. Evans, X. Fang, M. Fillingim, K. Fortier, C. M. Fowler, J. Fox, H. Gröller, S. Guzewich, T. Hara, Y. Harada, G. Holsclaw, S. K. Jain, R. Jolitz, F. Leblanc, C. O. Lee, Y. Lee, F. Lefevre, R. Lillis, R. Livi, D. Lo, Y. Ma, M. Mayyasi, W. McClintock, T. McEnulty, R. Modolo, F. Montmessin, M. Morooka, A. Nagy, K. Olsen, W. Peterson, A. Rahmati, S. Ruhunusiri, C. T. Russell, S. Sakai, J.-A. Sauvaud, K. Seki, M. Steckiewicz, M. Stevens, A. I. F. Stewart, A. Stiepen, S. Stone, V. Tenishev, E. Thiemann, R. Tolson, D. Toublanc, M. Vogt, T. Weber, P. Withers, T. Woods, R. Yelle

The Mars Atmosphere and Volatile Evolution (MAVEN) mission, during the second of its Deep Dip campaigns, made comprehensive measurements of martian thermosphere and ionosphere composition, structure, and variability at altitudes down to ~130 kilometers in the subsolar region. This altitude range contains the diffusively separated upper atmosphere just above the well-mixed atmosphere, the layer of peak extreme ultraviolet heating and primary reservoir for atmospheric escape. In situ measurements of the upper atmosphere reveal previously unmeasured populations of neutral and charged particles, the homopause altitude at approximately 130 kilometers, and an unexpected level of variability both on an orbit-to-orbit basis and within individual orbits. These observations help constrain volatile escape processes controlled by thermosphere and ionosphere structure and variability.

The list of author affiliations is available in the full article online. ***Corresponding author. E-mail: bougher@umich.edu.** Cite as Bougher *et al.*, *Science* **350**, aad 0459 (2015). Read the full article at http://dx.doi.org/10.1126/science.aad0459

Published by AAAS

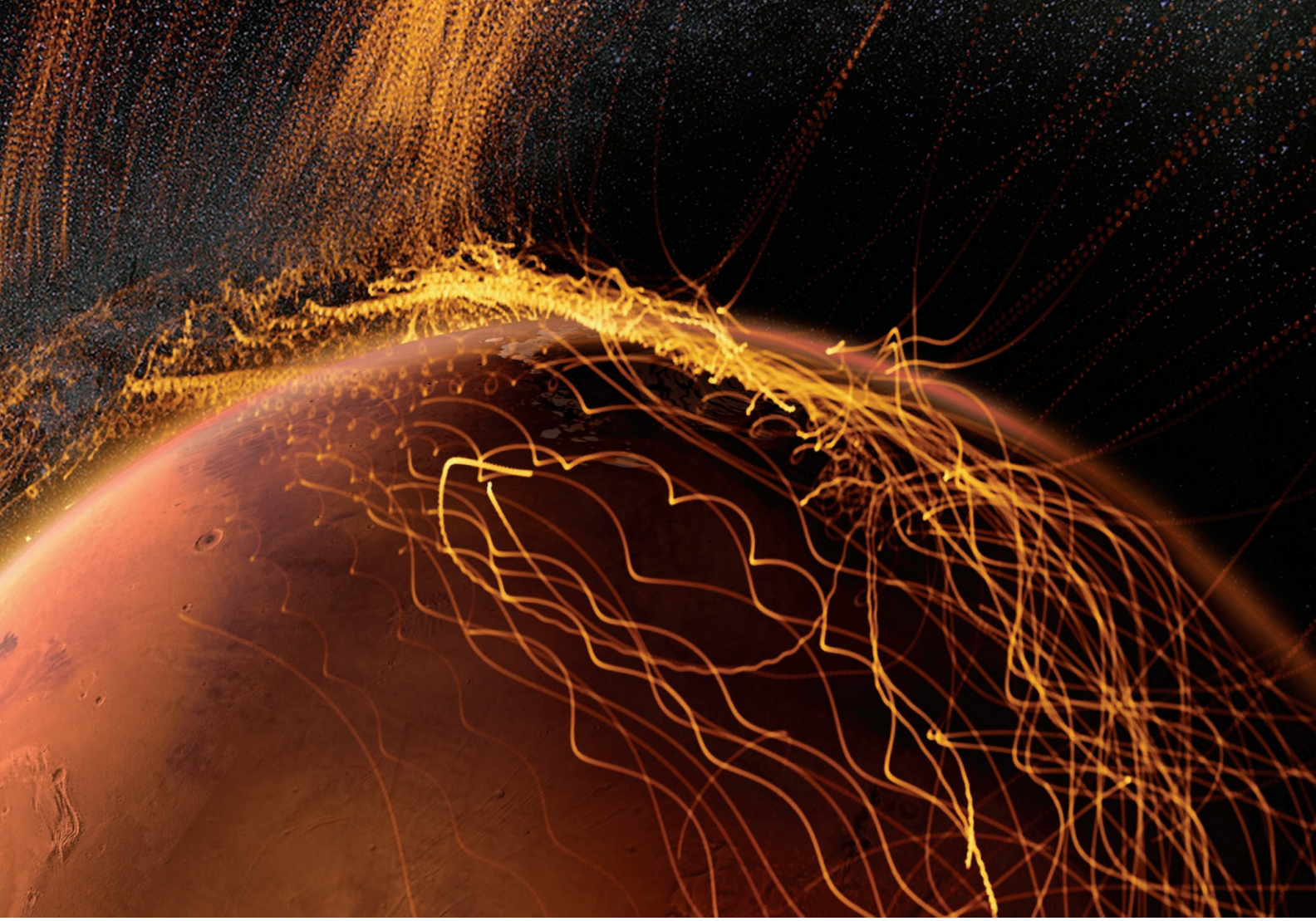

DATA VISUALIZATION: A. CUADRA AND V. ALTOUNIAN/*SCIENCE*; DATA: X. FANG AND THE MAVEN SCIENCE TEAM

Discovery of diffuse aurora on Mars

N. M. Schneider,* J. I. Deighan, S. K. Jain, A. Stiepen, A. I. F. Stewart, D. Larson, D. L. Mitchell, C. Mazelle, C. O. Lee, R. J. Lillis, J. S. Evans, D. Brain, M. H. Stevens, W. E. McClintock, M. S. Chaffin, M. Crismani, G. M. Holsclaw, F. Lefevre, D. Y. Lo, J. T. Clarke, F. Montmessin, B. M. Jakosky

Planetary auroras reveal the complex interplay between an atmosphere and the surrounding plasma environment. We report the discovery of low-altitude, diffuse auroras spanning much of Mars' northern hemisphere, coincident with a solar energetic particle outburst. The Imaging Ultraviolet Spectrograph, a remote sensing instrument on the Mars Atmosphere and Volatile Evolution (MAVEN) spacecraft, detected auroral emission in virtually all nightside observations for ~5 days, spanning nearly all geographic longitudes. Emission extended down to ~60 kilometer (km) altitude (1 microbar), deeper than confirmed at any other planet. Solar energetic particles were observed up to 200 kilo–electron volts; these particles are capable of penetrating down to the 60-km altitude. Given minimal magnetic fields over most of the planet, Mars is likely to exhibit auroras more globally than Earth.

The list of author affiliations is available in the full article online. ***Corresponding author. E-mail: nick.schneider@lasp.colorado.edu.** Cite as Schneider *et al.*, *Science* **350**, aad0313 (2015). Read the full article at http://dx.doi.org/10.1126/science.aad0313

Dust observations at orbital altitudes surrounding Mars

L. Andersson,* T. D. Weber, D. Malaspina, F. Crary, R. E. Ergun, G. T. Delory, C. M. Fowler, M. W. Morooka, T. McEnulty, A. I. Eriksson, D. J. Andrews, M. Horanyi, A. Collette, R. Yelle, B. M. Jakosky

Dust is common close to the martian surface, but no known process can lift appreciable concentrations of particles to altitudes above ~150 kilometers. We present observations of dust at altitudes ranging from 150 to above 1000 kilometers by the Langmuir Probe and Wave instrument on the Mars Atmosphere and Volatile Evolution spacecraft. Based on its distribution, we interpret this dust to be interplanetary in origin. A comparison with laboratory measurements indicates that the dust grain size ranges from 1 to 12 micrometers, assuming a typical grain velocity of ~18 kilometers per second. These direct observations of dust entering the martian atmosphere improve our understanding of the sources, sinks, and transport of interplanetary dust throughout the inner solar system and the associated impacts on Mars' atmosphere.

The list of author affiliations is available in the full article online. ***Corresponding author. E-mail: laila.andersson@lasp.colorado.edu.** Cite as L. Andersson *et al.*, *Science* **350**, aad0398 (2015). Read the full article at http://dx.doi.org/10.1126/science.aad0398

Published by AAAS

PLANETARY SCIENCE

MAVEN observations of the response of Mars to an interplanetary coronal mass ejection

B. M. Jakosky,[1]* J. M. Grebowsky,[2] J. G. Luhmann,[3] J. Connerney,[2] F. Eparvier,[1] R. Ergun,[1] J. Halekas,[4] D. Larson,[3] P. Mahaffy,[2] J. McFadden,[3] D. F. Mitchell,[3] N. Schneider,[1] R. Zurek,[5] S. Bougher,[6] D. Brain,[1] Y. J. Ma,[7] C. Mazelle,[8,9] L. Andersson,[1] D. Andrews,[10] D. Baird,[11] D. Baker,[1] J. M. Bell,[21] M. Benna,[2] M. Chaffin,[1] P. Chamberlin,[2] Y.-Y. Chaufray,[12] J. Clarke,[13] G. Collinson,[2] M. Combi,[6] F. Crary,[1] T. Cravens,[14] M. Crismani,[1] S. Curry,[3] D. Curtis,[3] J. Deighan,[1] G. Delory,[3] R. Dewey,[1] G. DiBraccio,[2] C. Dong,[6] Y. Dong,[1] P. Dunn,[3] M. Elrod,[2] S. England,[3] A. Eriksson,[10] J. Espley,[2] S. Evans,[15] X. Fang,[1] M. Fillingim,[3] K. Fortier,[1] C. M. Fowler,[1] J. Fox,[16] H. Gröller,[17] S. Guzewich,[2] T. Hara,[3] Y. Harada,[3] G. Holsclaw,[1] S. K. Jain,[1] R. Jolitz,[3] F. Leblanc,[12] C. O. Lee,[3] Y. Lee,[6] F. Lefevre,[12] R. Lillis,[3] R. Livi,[3] D. Lo,[17] M. Mayyasi,[13] W. McClintock,[1] T. McEnulty,[1] R. Modolo,[12] F. Montmessin,[12] M. Morooka,[1] A. Nagy,[6] K. Olsen,[6] W. Peterson,[1] A. Rahmati,[14] S. Ruhunusiri,[4] C. T. Russell,[7] S. Sakai,[14] J.-A. Sauvaud,[8,9] K. Seki,[18] M. Steckiewicz,[8,9] M. Stevens,[19] A. I. F. Stewart,[1] A. Stiepen,[1] S. Stone,[17] V. Tenishev,[6] E. Thiemann,[1] R. Tolson,[20] D. Toublanc,[8,9] M. Vogt,[13] T. Weber,[1] P. Withers,[13] T. Woods,[1] R. Yelle[17]

Coupling between the lower and upper atmosphere, combined with loss of gas from the upper atmosphere to space, likely contributed to the thin, cold, dry atmosphere of modern Mars. To help understand ongoing ion loss to space, the Mars Atmosphere and Volatile Evolution (MAVEN) spacecraft made comprehensive measurements of the Mars upper atmosphere, ionosphere, and interactions with the Sun and solar wind during an interplanetary coronal mass ejection impact in March 2015. Responses include changes in the bow shock and magnetosheath, formation of widespread diffuse aurora, and enhancement of pick-up ions. Observations and models both show an enhancement in escape rate of ions to space during the event. Ion loss during solar events early in Mars history may have been a major contributor to the long-term evolution of the Mars atmosphere.

Quantifying the role that escape of gas to space played throughout martian history will help to determine whether it was an important mechanism for driving the climate change observed in the geological record (*1*, *2*). Determining the effects that discrete solar storms have had on the structure of the upper atmosphere, ionosphere, and magnetosphere, and on the loss rate to space, is an important component of this, owing to the increased occurrence of storms in early martian history and their potential contributions to the total loss.

The Mars Atmosphere and Volatile Evolution (MAVEN) mission to Mars was designed to study the upper atmosphere, ionosphere, and magnetosphere of Mars, the response to solar and solar-wind input, and the ability of atmospheric molecules and atoms to escape to space (*3*). MAVEN was launched on 18 November 2013, and went into orbit around Mars on 21 September 2014. After a 2-month commissioning phase, it began its one-Earth-year primary science mission on 16 November 2014. MAVEN is in an elliptical orbit with periapsis altitude of ~150 km and apoapsis altitude of ~6200 km. This orbit allows a combination of in situ measurements throughout the entire region of interest and remote-sensing measurements that provide quasi-global coverage. The nine science instruments provide a combination of measurements of the solar and solar-wind energetic input into the upper atmosphere, the composition and structure of the upper atmosphere and ionosphere, the topology of the interactions of the solar wind with the planet, and the composition and energetics of atomic and molecular ions interacting with and escaping from the system (*3*, *4*).

We report here on observations from MAVEN that show the integrated effects of an interplanetary coronal mass ejection (ICME) with the planet, the consequences for the upper atmosphere, and the impact on escape to space. We both present the observations made by MAVEN of the ICME and Mars atmospheric response, and use the observations to validate a global model of the martian atmosphere interaction with the solar wind during the ICME. The model is then used to estimate the global response of the system, which MAVEN samples only locally during the event. These observations complement studies of the structure of the upper atmosphere and ionosphere and the overall behavior of the martian system, along with the initial look at the chain of events from energetic drivers to response of the upper atmosphere and then leading to escape to space (*4*–*7*).

Energetic inputs into the system

MAVEN has been making observations nearly continuously since November 2014. The strongest solar event observed to date occurred on 8 March 2015. MAVEN measurements during the entire time period from 25 February to 13 March 2015 exhibited disturbed interplanetary conditions, as shown in Fig. 1. The solar irradiance time series from the perspective of Mars (Fig. 1, top panel) shows the flare activity detected by the MAVEN extreme ultraviolet (EUV) detector. The flare event (F4) occurring on 6 March ~05:00 UT was likely associated with the major interplanetary disturbance of this period. Major flares are often related to eruptions of coronal material known as coronal mass ejections (CMEs, best known for causing geomagnetic storms at Earth) (*8*). White light coronagraph images from the Solar Heliospheric Observatory (SOHO) showed that multiple CMEs erupted in the general direction of Mars during this time.

We used orbital ephemerides and Magnetomer (MAG) (*9*) and Solar Wind Ion Analyzer (SWIA) (*10*) measurements to select periods during which we had unambiguous measurements of the upstream solar wind outside of the martian bow shock and foreshock. The solar-wind density, velocity, and interplanetary magnetic field (IMF) were averaged over the upstream interval, for each MAVEN orbit for which they could be determined. The most disturbed period analyzed here spanned about three ~4.5-hour MAVEN orbits.

The upstream solar-wind data set shows four major density enhancements (labeled S1 to S4) associated with a series of ICMEs. During the last of these events (S4) on 8 March, the solar wind reached a peak flow speed of 825 km/s, with a corresponding peak ram pressure of 15 nPa, and magnetic-field strength of ~20 nT, all the highest values observed by MAVEN to date. For comparison, the peak pressure observed at Mars during the Halloween 2003 ICME event was ~33 nT, and the average pressure during this period was ~7 nPa (*11*); the event reported here is one of the strongest ever observed at Mars. The average upstream solar

[1]University of Colorado, Boulder, CO, USA. [2]NASA/Goddard Space Flight Center, Greenbelt, MD, USA. [3]University of California at Berkeley, Berkeley, CA, USA. [4]University of Iowa, Iowa City, IA, USA. [5]Jet Propulsion Laboratory, California Institute of Technology, Pasadena, CA, USA. [6]University of Michigan, Ann Arbor, MI, USA. [7]University of California at Los Angeles, Los Angeles, CA, USA. [8]CNRS–Institut de Recherche en Astrophysique et Planétologie (IRAP), Toulouse, France. [9]University Paul Sabatier, Toulouse, France. [10]Swedish Institute of Space Physics, Uppsala, Sweden. [11]NASA/Johnson Space Center, Houston, TX, USA. [12]Laboratoire atmosphères, milieux et observations spatiales (LATMOS)–CNRS, Paris, France. [13]Boston University, Boston, MA, USA. [14]University of Kansas, Lawrence, KS, USA. [15]Computational Physics, Inc., Boulder, CO, USA. [16]Wright State University, Dayton, OH, USA. [17]University of Arizona, Tucson, AZ, USA. [18]Nagoya University, Nagoya, Japan. [19]Naval Research Laboratory, Washington, DC, USA. [20]North Carolina State University, Raleigh, NC, USA. [21]National Institute of Aerospace, Hampton, VA, USA.
*Corresponding author. E-mail: bruce.jakosky@lasp.colorado.edu

Downloaded from www.sciencemag.org on November 5, 2015

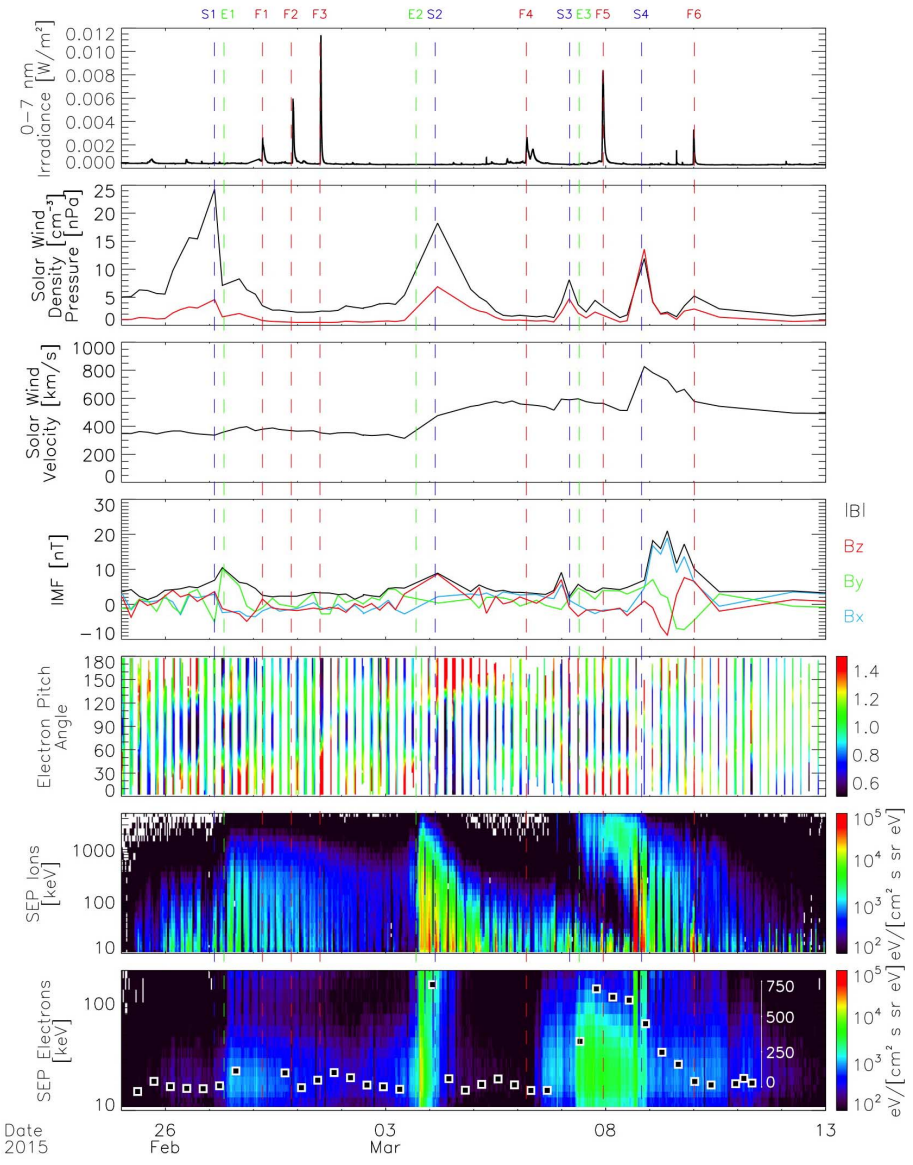

Fig. 1. Energy inputs to the martian system. The seven panels show flare irradiance from EUVM, solar-wind density (black) and ram pressure (red), velocity, and interplanetary magnetic field computed from SWIA and MAG data averaged over the portion of the orbit when the spacecraft was upstream from the bow shock, electron pitch-angle distributions at 110 to 140 eV from SWEA, and energetic ion and electron differential energy flux spectra from SEP. The intensities of CO_2^+ UV doublet auroral emission at 289 nm from the Mars nightside are plotted over the energetic electrons, using the inset scale; values below 50 to 100 Rayleighs are attributed to instrumental noise.

wind values measured by MAVEN from late November 2014 to late March 2015 were ~1 nPa for the ram pressure and 4 nT for the magnetic-field strength. The detailed MAG data from within the induced magnetosphere (discussed below) indicates that at ~15:20 UT 8 March, a strong magnetic rotation and compression associated with the arrival of the major ICME of the interval (event S4) were seen. The IMF returned to a more typical level within 48 hours after this signature. Major ICME events often have durations of up to a few days.

The Solar Wind Electron Analyzer (SWEA) (*12*) instrument measured suprathermal electron pitch-angle distributions (Fig. 1, fourth panel) upstream of the Mars bow shock. These reveal the magnetic topology associated with this series of events. The topology leading up to the final series of events (S3, S4) is complex, with electron beaming reversals and counterstreaming, suggesting that magnetically "closed" topologies are present almost every orbit. Such interplanetary field topologies, which are characteristic of ICME drivers and complex space-weather events, also affect the solar-wind interaction with Mars by altering the details of external field reconnection with the Mars crustal fields.

Solar energetic particle (SEP) events (*13*) (E1 to E3) were seen in conjunction with the multiple ICME passages, as shown in Fig. 1 (last two panels). The highest SEP ion fluxes at lower energies (<1 MeV) peaked around the ICME shock arrival times (S2 and S4), consistent with energetic storm particle (ESP) enhancements that occur when an ICME makes a direct strike. The most energetic ions (>1 MeV) in the strong event (E3) reached Mars at ~08:00 UT 7 March, ahead of the ICME disturbance (S4). This is the classical velocity dispersion, where the most energetic ions arrive first, at least a day before the plasma and field disturbance. The SEP ions gradually diminished in intensity throughout the rest of the ICME disturbance. SEP ion energy deposition in the Mars atmosphere peaked for ICME events S2 and S4, the latter being stronger. The largest energy fluxes occurred below ~300 keV, where most energy is deposited between 100- and 140-km altitude (*14*) and should affect strongly the thermospheric reservoir from which atmospheric escape occurs (*15*). The observed SEP electrons (bottom panel), which arrived early with the most-energetic ions, show a spread in energy at the ICME shock arrival on 8 March and a diminished flux soon after the shock passage.

We used the Wang-Sheeley-Arge (WSA)–ENLIL+Cone model to numerically simulate the interplanetary solar-wind conditions and provide a global heliospheric context for these events at Mars (*16*). Based on the simulation, the 8 March ICME impact of Mars was composed of two individual transients that merged en route to the planet. The first ICME was injected into the inner boundary of the ENLIL solar wind model at 04:49 UT 6 March with an initial radial speed of

900 km/s, whereas the second ICME was injected at 07:12 UT 6 March with a faster speed of 1500 km/s. The southern part of the second ICME interacted with and overtook the first ICME to produce a merged ICME. The model predicted the eastern flank of the merged structure to strike Mars at ~11:40 UT 8 March. Interestingly, the active region that triggered the Mars-directed ICMEs subsequently rotated toward Earth and launched an ICME, to produce one of the strongest geomagnetic storms of the current solar cycle (*17*).

Response of the system

MAVEN observations show that the ICME impact on 8 March 2015 dramatically altered the overall morphology and dynamics of the magnetosphere, affected the ionosphere, and induced auroral emissions from the neutral atmosphere.

Prior to the ICME, SWIA (*10*) measured a solar-wind proton density of 1.8 cm^{-3}, an alpha-particle density of 0.1 cm^{-3}, and flow speed of 505 km/s, corresponding to a ram pressure of 0.9 nPa. MAG (*9*) measured a typical IMF magnitude of ~5 nT. After the passage of the ICME shock, the upstream proton density rose to as high as 11 cm^{-3}, the alpha density to 0.6 cm^{-3}, and the flow speed to 820 km/s, with a ram pressure of 15 nPa, the highest encountered to date during the MAVEN mission. The IMF increased to 14 nT and in succeeding days rose to as high as 20 nT, also the highest value seen so far.

Using these measurements as inputs, we calculated three steady-state cases with a multispecies magnetohydrodynamic (MHD) model (*18*) to provide global context for the observations. The solar-wind conditions are set corresponding to before the ICME arrival (case 1), shortly after the arrival (case 2), and during the later time of the ICME, when the solar-wind dynamic pressure was intensified (case 3). Data-model comparisons are shown in Fig. 2. The orbit prior to arrival of the ICME, with apoapsis near 11:10 UT and periapsis at 13:23 UT, provides a baseline. Given the nominal IMF magnitude and plasma density, but moderately high Mach number of the flow, the observed and modeled magnetospheric boundaries are both asymmetric. The quasi-parallel bow-shock crossing on the outbound portion of the apoapsis segment occurred slightly earlier than expected from its average location (*19*), but the inbound boundaries were close to their nominal positions. MAVEN observed only minor crustal magnetic fields (*20*) of ~10 nT near periapsis, a total magnetic field of ~50 nT in the ionosphere, and few fluctuations.

During the succeeding apoapsis segment, MAVEN encountered extremely unusual plasma, with 10% alpha-particle abundance, a flow speed of 825 km/s with a 150 km/s off-axis component, and a high proton temperature of 130 eV, suggesting

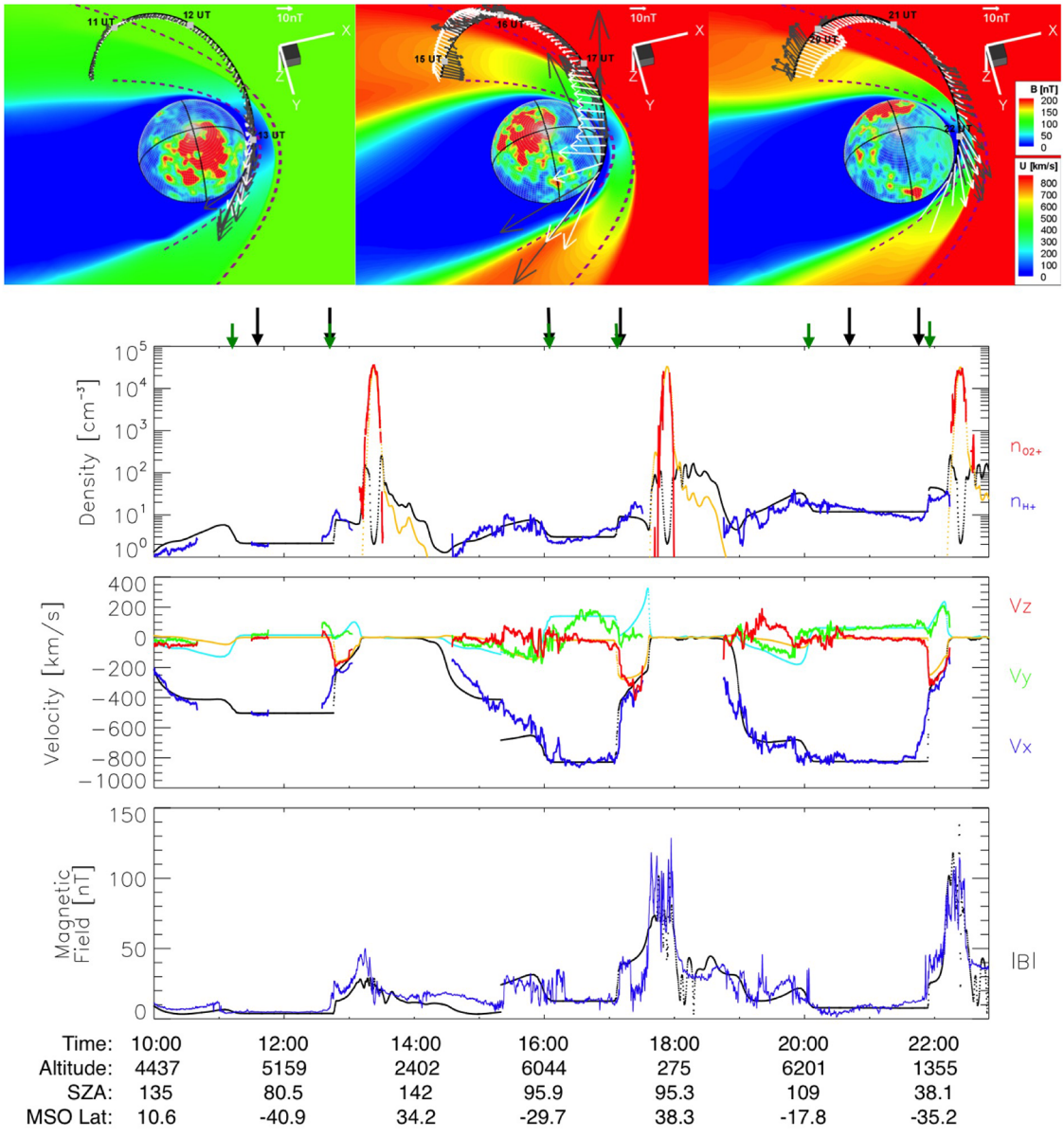

Fig. 2. The response of the martian magnetosphere to the passage of an ICME. The top panel shows predicted magnetospheric structure for three orbits, based on MHD runs utilizing upstream solar-wind conditions. The color contours show plasma flow speed in the equatorial plane (from the south). Black lines indicate the MAVEN orbit, black arrows show measured magnetic fields, and white arrows show model fields. The three-dimensional sphere represents the inner model boundary at 100-km altitude, with colors indicating the crustal magnetic field strength at the time of periapsis. The black dashed lines show nominal ionosphere-magnetosphere boundary and bow shock positions. The bottom three panels show MAG, SWIA, STATIC, and NGIMS (Neutral Gas and Ion Mass Spectrometer) observations (solid lines), with MHD results for comparison (dotted lines). Green and black arrows mark the observed and nominal bow shock locations, respectively.

that MAVEN encountered the sheath region trailing the ICME shock. The combination of high ram pressure and low Mach number conspired to produce boundaries near their normal position, but we observed multiple shock crossings and large magnetic fluctuations during this time period, implying a highly dynamic interaction. Commensurate with the high ram pressure, the average draped field inside the magnetosphere increased to ~90 nT, with a maximum of 130 nT during periapsis. The MHD model matches the overall magnetospheric structure during this period, but the time-stationary model cannot capture the observed variability and fluctuations in magnetic-field direction.

The magnetospheric effects continued and intensified in the succeeding orbit. The magnetic field exhibited large fluctuations, and the draped field remained at ~90 nT. The solar wind flow remained >800 km/s for ~7 hours, and the density increased, producing a solar-wind ram pressure more than an order of magnitude larger than typically observed and resulting in substantial deformation of the bow shock and compression of the entire magnetosphere. The MHD model, which matches the data well during this period, shows these effects globally.

On smaller scales, MAVEN observed sharp isolated magnetic-field enhancements in the martian magnetosheath just after the ICME shock arrival on 8 March. The enhancements are associated with magnetic-field rotations characteristic of magnetic flux ropes (*21*), which are observed to occur in the martian ionosphere and downstream from crustal magnetic fields (*22*, *23*). Suprathermal and Thermal Ion Composition (STATIC) measurements indicate that heavy (i.e., planetary) ions are present in the flux-rope structures, with energies of a few kilo–electron volts. The presence of heavy planetary ions collocated with flux ropes at the 5000-km altitude of the observed structures allows us to infer that the flux ropes formed in the vicinity of the ionosphere. The magnetic-field amplitudes in the flux ropes exceeded 80 nT, which is a few times larger than the typical detached flux ropes seen during nominal solar-wind conditions. Strong-field detached flux ropes observed at high altitudes are unique in the MAVEN observations to date. Moreover, the velocity of the detached flux ropes is estimated to be much faster than usual by a factor of approximately 10, under the assumption that these structures are in magneto-hydrostatic equilibrium (*24*).

The March ICME events also affected the upper atmosphere. MAVEN's Imaging Ultraviolet Spectrograph (IUVS) detected diffuse auroral emissions during the ICME events similar to those observed in December 2014 (*6*). IUVS is a remote-sensing instrument designed to map UV atmospheric emissions with altitude and across the planetary disk (*25*). The most sensitive mode for detection of auroral emission uses limb scans taken near periapsis on Mars' nightside. The vast majority of nightside limb scans show no atmospheric emissions apart from the ubiquitous hydrogen Lyman alpha (*26*) and occasional NO band emissions.

Observations spanning 22 min near periapsis were obtained on alternating orbits at ~9-hour intervals during the period encompassing the ICME. Figure 1 (bottom panel) shows the observed timeline for auroral emission from Mars' nightside during this period. The figure plots emission from the CO_2^+ UV doublet at 289 nm. Fainter emission was also detected from the CO Cameron bands. Both emissions are generated by particle impact on CO_2, which causes ionization, dissociation, and excitation. These emissions have been well studied on Mars' dayside, where they are excited by solar EUV radiation and resulting photoelectrons, and have been observed since the Mariner missions (*27*). The same emissions were observed on the Mars nightside in discrete aurora detected by the SPICAM (Spectroscopy for Investigation of Characteristics of the Atmosphere of Mars) instrument on Mars Express near crustal magnetic fields (*28*), and were seen previously by MAVEN in widespread diffuse aurora far from crustal fields and associated with a solar event (*6*).

IUVS detected three separate episodes of substantial auroral emission. The first occurred on 27 to 28 February and the second in a single orbit on 4 March. On 7 March, emission was observed to rise, peak, and fall over ~50 hours; no data were taken on the orbits immediately preceding the rise or following the decline. Although the seven detections in the third event are limited to ~20-min periods separated by ~9 hours, the repeated detections and relatively smooth variation suggest that it was a widespread, sustained event. The event spanned more than one Mars rotation, indicating that geographic control of this type of auroral emission is weak or nonexistent.

Substantial ion energization and enhancement resulting from the disturbed conditions were observed by SWIA, STATIC, and SEP during the 8 March event, as seen in measurements from a single MAVEN orbit shown in Fig. 3, after the arrival of the ICME shock. Although pickup ions are evident during the entire disturbed period subsequent to the maxima in IMF strength and ram pressure around 14:00 UT, we focus on the orbit spanning ~18:00 to 22:00 on 8 March.

The SWIA instrument (*7*) recorded strong pickup ion enhancements during this orbit (Fig. 3C). The solar wind is evident at high altitudes as a continuous flux of protons with energy per charge of 2 to 5 keV/q and alpha particles with energy per charge of 6 to 9 keV/q. Intermittent periods of higher-energy ion flux (~10 keV and above) appear at high altitudes. The black trace in Fig. 3C illustrates the predicted energy of pickup ions originating from any point directly sunward from the martian subsolar point (*29*) and accelerated entirely by the measured local $\mathbf{V} \times \mathbf{B}$ electric field. The predicted pickup ion energies have good agreement with the observations and correspond to periods where high-energy ion fluxes are observed. This agreement suggests that planetary ions were accelerated to high energies by the local convection electric field.

The STATIC (*30*) instrument also measures ions and can discriminate mass. Figure 3, D and E, show the observed energies [for mass >9 atomic mass units (amu)] and masses of ions during this orbit. Near periapsis, both O_2^+ and CO_2^+ are evident, and as the spacecraft altitude increases, the flux of massive CO_2^+ molecules decreases rapidly, and O^+ fluxes increase. Also present is a probable signature of He^+, most likely produced from charge exchange between solar-wind helium and planetary neutrals, as recently observed by Rosetta (*31*). This population also can be observed during quiet times, but is intensified during this period owing to the high solar-wind flux. Heavy-ion observations at high altitudes are complicated by the substantial solar-wind proton fluxes during the ICME. Internally scattered protons can contaminate higher-mass channels and have been removed via a background subtraction algorithm. Even though the background subtraction errs on the side of subtracting too many counts at high masses, fluxes of high-mass species are distinguishable periodically all the way up to apoapsis, often at energies higher than the predicted pickup ion energy shown in Fig. 3C. A closer look at the period near apoapsis (Fig. 3F) reveals that O^+, O_2^+, and CO_2^+ are all present at energies substantially greater than the solar-wind energy and have been stripped away from the planet.

At even higher energies, the SEP instrument (*13*) detected pick-up oxygen ions that had been produced upstream in the neutral oxygen corona and then accelerated toward Mars; these pick-up ions had energies above ~70 keV. The maximum oxygen pickup ion energy is given by $E_{max} = 2\, m_o\, U_{sw}^2\, \sin^2\theta_{UB}$, where m_o is the mass of atomic oxygen, U_{sw} is the solar-wind speed, and θ_{UB} is the angle between the solar wind and the IMF; after the 8 March ICME arrival, solar-wind velocities in excess of 800 km/s enable acceleration of pickup oxygen to energies as high as 210 keV. Following the method of (*32*), pickup oxygen fluxes are simulated for the first MAVEN apoapsis after the ICME arrival (the orbit prior to the one shown in Fig. 3, A to E, because of more favorable observing geometry during that orbit), and the agreement between the SEP measured and modeled fluxes confirms detection of O^+ by SEP. Figure 3G illustrates MAVEN data for a 45-min time period after 16:20 UT, when MAVEN was in the undisturbed upstream solar wind. For most of this time period, θ_{UB} was ~50°, giving an E_{max} of ~120 keV. The elevated background noise in the SEP data is due to energetic particles associated with the ICME. Oxygen pickup ions detected by SEP during the ICME event have the highest energies observed since MAVEN's arrival at Mars.

Loss to space

We can compare planetary ion fluxes during the ICME event to those observed over many months as a means for assessing the likely impact of the ICME on atmospheric escape rates. In addition, we can calculate the escape rate using MHD models of the interaction of the solar wind with the planet and using measured solar-wind conditions as model inputs. Both show a substantial enhancement in the escape rate during the ICME event.

To determine the measured escape rate, we use STATIC (*30*) observations of heavy-ion fluxes

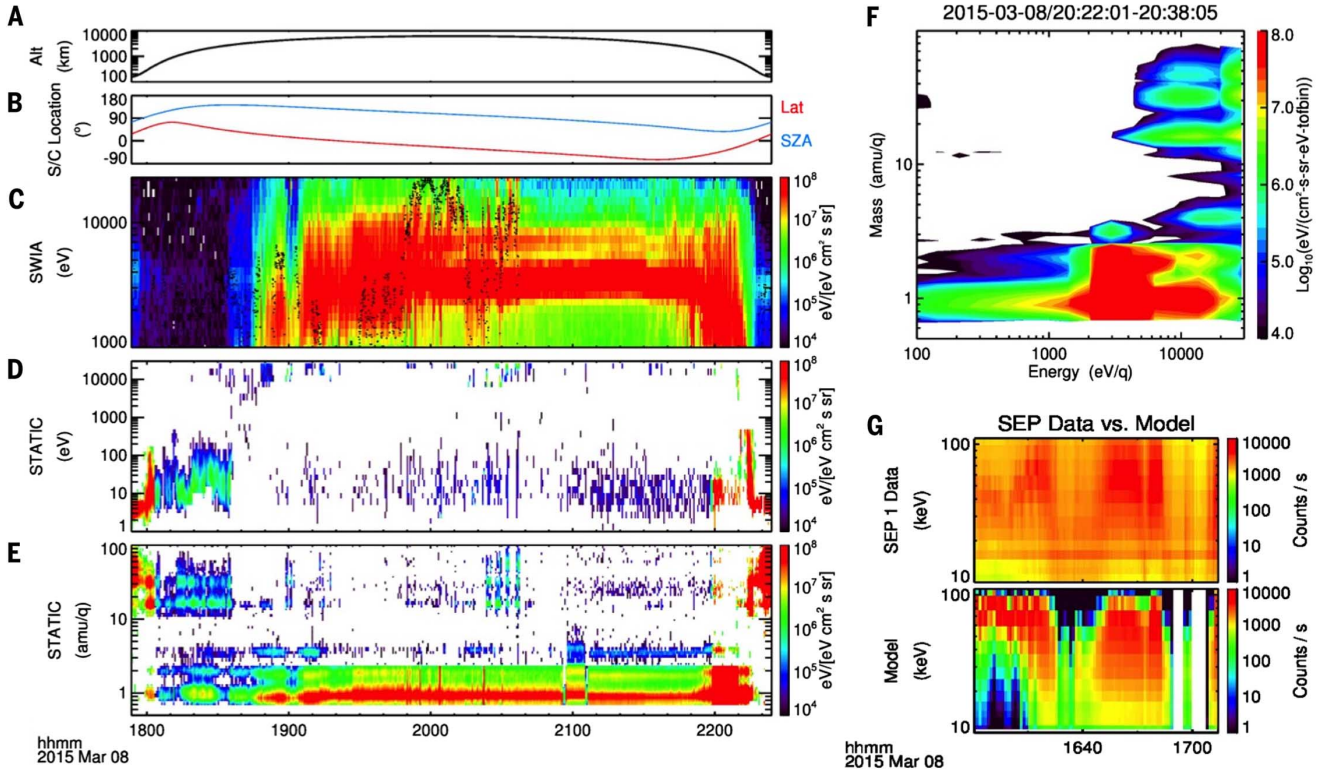

Fig. 3. MAVEN charged-particle observations reveal the presence of pick-up ions during the 8 March 2015 ICME. Observations from a single orbit are shown in (A) to (D). (**A**) Spacecraft altitude. (**B**) Spacecraft location given as latitude and solar zenith angle. (**C**) SWIA observations of ion energy fluxes as a function of energy, with the predicted energy of subsolar pickup ions given by the black trace. (**D**) STATIC observations of high-mass (>9 amu/q) ion energy fluxes as a function of energy. (**E**) STATIC observations of ion energy fluxes as a function of ion mass. (**F**) STATIC observations near periapsis of ion energy fluxes as a function of energy and mass simultaneously, showing both the low-mass solar wind and high-energy, high-mass pickup ions. (**G**) Observed and modeled SEP spectra for ~40 min during the beginning of the ICME passage, on the orbit prior to the one shown in (A) to (D).

during time periods when the spacecraft occupied altitudes between 0.25 and 0.45 planetary radii. At these altitudes, observations cover a large fraction of the sphere enclosing Mars, and the measurements provide a good estimate of the total escape. MAG and SWIA measurements of the IMF and solar-wind velocity, respectively, were used to rotate the spacecraft position into a Mars-Solar-Electric field (MSE) coordinate system, with MSE-x antiparallel to the incident solar-wind flow, MSE-y parallel to the IMF direction projected into the plane perpendicular to the flow, and MSE-z in the direction of the convection electric field given by $-\mathbf{V} \times \mathbf{B}$. Such a coordinate system is frequently used to organize escaping planetary ion fluxes [e.g., (*33*)], which should be strongly influenced by the electric field in the solar wind. Individual observations recorded when the instrument was in "pickup mode" (32 energy bins, 8 mass bins, and 64 look directions) were separated so that ion flux toward and away from the planet were tracked separately. We limit ourselves to energies greater than 25 eV, as the MAVEN data have not been corrected yet for the effects of spacecraft electric potential that can significantly influence the low-energy measurements. Inclusion of low-energy particles will increase both the reported fluxes and escape rates, with the consequence that we present lower limits here. Previous studies (*34*) have shown that reported escape rates depend at least partly on the energy range of ions being considered.

A comparison of fluxes during the ICME event (2015-03-08/16:00 to 2015-03-09/12:00) to median fluxes over a period of approximately 4 months is shown in Fig. 4. Because of uncertainties in the direction of the electric field during the turbulent ICME event, we show the results as a function of solar zenith angle. This comparison is valid independent of the electric-field direction. Most notable is the strong flux of planetary ions away from the planet on the dayside during the ICME, in a region usually dominated by the flow of ions toward the planet. These fluxes are among the strongest observed in this region during the entire mission. Nightside regions sampled during the ICME have fluxes more characteristic for their location, or even lower than is typical.

We cannot reliably provide a global escape rate during the ICME event based on these sparse observations alone, owing to the limited coverage over a short time period. However, it appears that escape rates on the nightside of the planet remained at values during the ICME that were similar to values at other times, and that dayside escape rates of planetary ions were enhanced considerably. Previous measurements of ion escape rates during ICMEs have been reported (*35*) and suggest that total escape rates can be 10 to 100 times greater during solar storm events.

The good agreement described earlier between the MHD model and MAVEN observations during the ICME event gives us confidence to use the model to infer the variations of the ion loss rate during the ICME passage. The integrated ion loss rates are listed in Table 1 using model results of the same three cases described earlier. Before the ICME arrival, the model predicted that the integrated escape rate was of the order of 1.5×10^{24}/s, dominated by O_2^+ ions. As the flow speed of the solar wind increased to more than 800 km/s shortly after the ICME arrival, the solar-wind dynamic pressure was about four times enhanced, and the model predicted that the total ion escape rate would increase to ~10^{25}/s, which is seven times larger than the ion loss rate during nominal conditions. When the solar-wind density and velocity were both enhanced, the corresponding solar-wind dynamic pressure increased to ~15 times, and the escape rate for case 3 reached 3×10^{25}/s, more than an order of magnitude enhancement. The major ions lost to space changed from O_2^+ (in both case 1 and 2) to O^+ ions in case 3. This model prediction is consistent with measurements made by STATIC, which detected a large increase in O^+ ion fluxes during the orbits after the ICME arrival. This increase is likely caused by enhancement of O^+ ion production through augmented electron-impact ionization and charge-exchange reactions

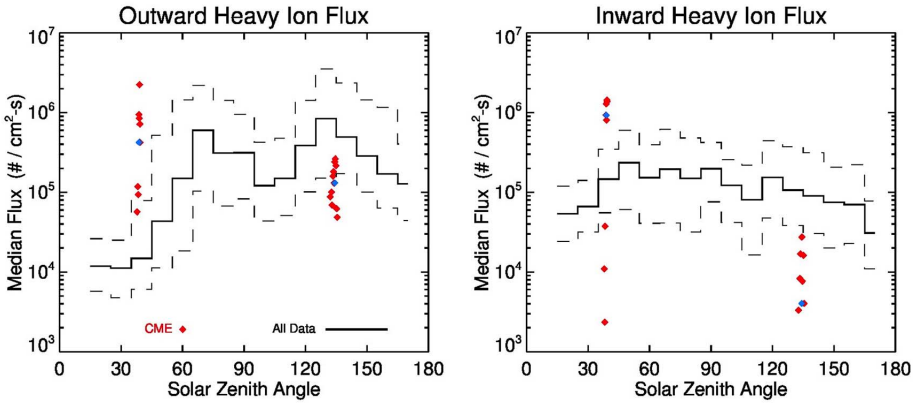

Fig. 4. Comparison of loss during ICME with integrated loss through the mission to date. Planetary heavy ion fluxes (>9 amu) measured by STATIC during the ICME event (red, with median value shown in blue) are shown in comparison to median and first/fourth quartile ion fluxes measured over a ~4 month period (gray traces). Fluxes are evaluated in a spherical shell around Mars from 1.25 to 1.45 R_M (radius of Mars), and the position of MAVEN is rotated into a coordinate system aligned with the solar wind electric field. During the ICME, strong outward flux is observed in regions of typically inward flow.

Table 1. Ion loss rates calculated by the MHD model for the three cases corresponding to three different stages of the ICME. *P*sw is the solar-wind pressure for the model run.

	P_{SW} (nPa)	O^+ (s^{-1})	O_2^+ (s^{-1})	CO_2^+ (s^{-1})	Total (s^{-1})	Total (kg/s)
Case 1	0.9	6.4×10^{23}	7.7×10^{23}	4.9×10^{22}	1.46×10^{24}	0.06
Case 2	3.4	2.6×10^{24}	7.6×10^{24}	3.3×10^{23}	1.06×10^{25}	0.50
Case 3	13.4	1.96×10^{25}	1.32×10^{25}	6.3×10^{23}	3.34×10^{25}	1.27

between solar-wind protons and neutral oxygen atoms, resulting from the intense electron and proton fluxes in the ICME.

Similarly, a multifluid MHD model (*36*, *37*) predicted more than an order-of-magnitude enhancement of the ion loss rates during extreme solar-wind conditions associated with the ICME. The multifluid model results were also used to examine the relative importance of the two major ion loss channels from the planet—energetic-ion loss through the dayside polar plume and cold-ion loss through the nightside plasma-wake region. Escape of ions from the dayside polar plume could be as much as ~30% prior to the ICME arrival. When solar-wind dynamic pressure was drastically intensified, the ratio of escape rates from the polar plume reduced to ~10%, and the cold ions escaping from the plasma wake made up most of the ion loss from the planet.

Both the observations and the model results suggest there are substantial enhancements in the ion loss rates during ICME events. The agreement of the models with the observations reinforces the interpretation and allows a global estimate of the increase of about an order of magnitude to be made. The ion loss reported here is only one means by which gas can be removed from the atmosphere. Particles can also be removed to space as neutrals. Neutral escape may prove to be the dominant loss channel, but observations are more difficult to interpret. These ion loss enhancements can thus be considered a lower limit on the escape enhancement.

The results obtained by MAVEN for this strong ICME event can be compared with previous measurements of ion escape at Mars during disturbed periods. These include case studies (*35*, *38*), and statistical studies during CIR events, solar maximum, and solar minimum periods (*39*–*42*). The compression of the magnetosphere in response to high dynamic pressure is consistent with observations of disturbed conditions presented in the studies cited above. Nearly all of these studies also suggest an increase in ion escape rates during disturbed periods, but differ in the degree to which they change. Our results are consistent with the case study presented by Futaana *et al.* (*35*), which estimated an order-of-magnitude increase in planetary ion fluxes (and thus escape) in response to an ICME event observed by Mars Express. By contrast, our results appear to be inconsistent with a recent statistical reanalysis of Mars Express observations that shows a decrease in escape rates in response to increased solar-wind density (*41*). Though the reason for the discrepancies between previous studies can include differences in data selection and analysis method, it seems likely that different events and different kinds of events induce responses of different magnitude at Mars. Constraining how ICME events influence ion escape is an important component for understanding escape rates from early Mars.

Conclusions and future observations

MAVEN observations show a major impact of the ICME observed in March 2015. The effects through the entire upper-atmosphere–ionosphere–magnetosphere system produced substantially disturbed conditions and appeared to have a major impact on the instantaneous rates of loss of ions to space. Given the likely prevalence of ICME-like conditions earlier in solar-system history (*43*), it is possible that ion escape rates at that time were dominated by storm events. As these early periods may have been the dominant times at which the martian atmosphere experienced loss, the inferred climate change on Mars may have been driven to a large extent by these solar storms.

The MAVEN spacecraft is continuing to collect observations. These ongoing observations will fill in the three-dimensional space surrounding Mars and allow us to better understand the processes occurring in the upper atmosphere and ionosphere and to observe the response to changing external forcing in the form of the changing solar EUV, solar wind, and solar storms. Ongoing observations also will show the response to the changing martian seasons, eventually allowing coverage of a full Mars year and beyond.

REFERENCES AND NOTES

1. M. H. Carr, Water on Mars. *Nature* **326**, 30–35 (1987). doi: 10.1038/326030a0
2. D. J. Des Marais, B. M. Jakosky, B. M. Hynek, Astrobiological implications of Mars surface composition and properties, in *The Martian Surface: Composition, Mineralogy, and Physical Properties*, J. F. Bell III, Ed. (Cambridge Univ. Press, Cambridge, 2008), 599–623.
3. B. M. Jakosky *et al.*, The Mars Atmosphere and Volatile Evolution (MAVEN) Mission. *Space Sci. Rev.* (2015). doi: 10.1007/s11214-015-0139-x
4. B. M. Jakosky, J. M. Grebowsky, J. G. Luhmann, D. A. Brain, Initial results from the MAVEN mission to Mars. *Geophys. Res. Lett.* 10.1002/2015GL065271 (2015).
5. S. Bougher *et al.*, Early MAVEN Deep Dip campaign reveals thermosphere and ionosphere variability. *Science* **350**, aad0459 (2015).
6. N. M. Schneider *et al.*, Discovery of diffuse aurora on Mars. *Science* **350**, aad0210 (2015).
7. L. Andersson *et al.*, Dust observations at orbital altitudes surrounding Mars. *Science* **350**, aad0398 (2015).
8. J. Gosling, The solar flare myth. *J. Geophys. Res.* **98**, 18937–18949 (1993). doi: 10.1029/93JA01896
9. J. E. P. Connerney *et al.*, The MAVEN magnetic field investigation. *Space Sci. Rev.* 10.1007/s11214-015-0169-4 (2015). doi: 10.1007/s11214-015-0169-4
10. J. S. Halekas *et al.*, The solar wind ion analyzer for MAVEN. *Space Sci. Rev.* 10.1007/s11214-013-0029-z (2013). doi: 10.1007/s11214-013-0029-z
11. D. H. Crider *et al.*, Mars Global Surveyor Observations of the Halloween 2003 solar Superstorm's Encounter with Mars. *J. Geophys. Res.* **110**, A09S21 (2005). doi: 10.1029/2004JA010881
12. D. L. Mitchell, C. Mazelle, J. P. McFadden, D. Larson, J. S. Halekas, J. E. P. Connerney, J. Espley, L. Andersson, J. G. Luhmann, R. J. Lillis, M. Fillingim, T. Hara, D. A. Brain, MAVEN observations of the Martian ionosphere and magneotheath [sic]. *Lunar Planet. Sci. Conf.*, abstract 3015, Houston, TX, 2015.
13. D. E. Larson, R. J. Lillis, P. A. Dunn, A. Rahmati, T. E. Cravens, K. Hatch, M. Robinson, D. Glaser, J. Chen, D. W. Curtis, C. Tiu, R. P. Lin, J. G. Luhmann, J. P. McFadden, J. Connerney, J. Halekas, B. M. Jakosky, The Solar Energetic Particle Experiment on MAVEN: First Results. *Lunar Planet. Sci. Conf.*, abstract 2890, Houston, TX, 2015.
14. F. Leblanc, J. G. Luhmann, R. Johnson, E. Chassefiere, Some expected impacts of a solar energetic particle event at Mars. *J. Geophys. Res.* **107**, 1058 (2002). doi: 10.1029/2001JA900178
15. S. W. Bougher, T. E. Cravens, J. Grebowsky, J. Luhmann, The aeronomy of Mars: Characterization by MAVEN of the upper atmospheric reservoir that regulates volatile escape. *Space Sci. Rev.* (2014). doi: 10.1007/s11214-014-0053-7

16. M. L. Mays *et al*., Ensemble modeling of CMEs using the WSA-ENLIL+Cone model. *Sol. Phys.* **290**, 1775–184 (2015). doi: 10.1007/s11207-015-0692-1
17. Y. Kamide, K. Kusano, No major solar flares but the largest geomagnetic storm in the present solar cycle. *Space Weather* **13**, 365–367 (2015). doi: 10.1002/2015SW001213
18. Y. Ma *et al*., Effects of crustal field rotation on the solar wind plasma interaction with Mars. *Geophys. Res. Lett.* **41**, 6563–6569 (2014). doi: 10.1002/2014GL060785
19. D. Vignes *et al*., The solar wind interaction with Mars: Locations and shapes of the bow shock and the magnetic pile-up boundary from the observations of the MAG/ER experiment onboard Mars Global Surveyor. *Geophys. Res. Lett.* **27**, 49–52 (2000). doi: 10.1029/1999GL010703
20. M. H. Acuña *et al*., Magnetic field and plasma observations at Mars: Initial results of the Mars Global Surveyor Mission. *Science* **279**, 1676–1680 (1998). doi: 10.1126/science.279.5357.1676; pmid: 9497279
21. C. T. Russell, R. C. Elphic, Observation of magnetic flux ropes in the Venus ionosphere. *Nature* **279**, 616–618 (1979). doi: 10.1038/279616a0
22. P. A. Cloutier *et al*., Venus-like interaction of the solar wind with Mars. *Geophys. Res. Lett.* **26**, 2685–2688 (1999). doi: 10.1029/1999GL900591
23. D. A. Brain *et al*., Episodic detachment of Martian crustal magnetic fields leading to bulk atmospheric plasma escape. *Geophys. Res. Lett.* **37**, L14108 (2010). doi: 10.1029/2010GL043916
24. T. Hara *et al*., The spatial structure of Martian magnetic flux ropes recovered by the Grad-Shafranov reconstruction technique. *J. Geophys. Res.* **119**, 1262–1271 (2014). doi: 10.1002/2013JA019414
25. W. E. McClintock *et al*., The Imaging Ultraviolet Spectrograph (IUVS) for the MAVEN Mission. *Space Sci. Rev.* 10.1007/s11214-014-0098-7 (2014). doi: 10.1007/s11214-014-0098-7
26. M. S. Chaffin *et al*., Three dimensional structure of the Mars H corona revealed by IUVS on MAVEN. *Geophys. Res. Lett.* 10.1002/2015GL065287 (2015).
27. C. Barth, A. I. Stewart, C. W. Hord, A. L. Lane, Mariner 9 ultraviolet spectrometer experiment: Mars airglow spectroscopy and variations in Lyman alpha. *Icarus* **17**, 457–468 (1972). doi: 10.1016/0019-1035(72)90011-5
28. J.-L. Bertaux *et al*., Discovery of an aurora on Mars. *Nature* **435**, 790–794 (2005). doi: 10.1038/nature03603; pmid: 15944698
29. S. Curry, M. Liemohn, X. Fang, Y. Ma, J. Espley, The influence of production mechanisms on pick-up ion loss at Mars. *J. Geophys. Res.* **118**, 554–569 (2013). doi: 10.1029/2012JA017665
30. J. P. McFadden, R. Livi, J. Luhmann, J. Connerney, D. Mitchell, C. Mazelle, L. Andersson, B. Jakosky, Structure of the martian ionosphere and atmospheric loss: MAVEN STATIC first results. *Lunar Planet. Sci. Conf.*, abstract 2899 (2015).
31. H. Nilsson *et al*., Birth of a comet magnetosphere: A spring of water ions. *Science* **347**, aaa0571 (2015). doi: 10.1126/science.aaa0571; pmid: 25613894
32. A. Rahmati *et al*., Pickup ion measurements by MAVEN: A diagnostic of photochemical oxygen escape from Mars. *Geophys. Res. Lett.* **41**, 4812–4818 (2014). doi: 10.1002/2014GL060289
33. S. Barabash, A. Fedorov, R. Lundin, J. A. Sauvaud, Martian atmospheric erosion rates. *Science* **315**, 501–503 (2007). doi: 10.1126/science.1134358; pmid: 17255508
34. E. Dubinin *et al*., Ion energization and escape on Mars and Venus. *Space Sci. Rev.* **162**, 173–211 (2011). doi: 10.1007/s11214-011-9831-7
35. Y. Futaana *et al*., Mars Express and Venus Express multi-point observations of geoeffective solar flare events in December 2006. *Planet. Space Sci.* **56**, 873–880 (2008). doi: 10.1016/j.pss.2007.10.014
36. D. Najib, A. F. Nagy, G. Tóth, Y. Ma, Three-dimensional, multifluid, high spatial resolution MHD model studies of the solar wind interaction with Mars. *J. Geophys. Res.* **116**, A05204 (2011). doi: 10.1029/2010JA016272
37. C. Dong *et al*., Solar wind interaction with the Mars upper atmosphere: Results from the one-way coupling between the multifluid MHD model and the MTGCM model. *Geophys. Res. Lett.* **41**, 2708–2715 (2014). doi: 10.1002/2014GL059515
38. E. Dubinin *et al*., Ionospheric storms on Mars: Impact of corotating interaction region. *Geophys. Res. Lett.* **36**, L01105 (2009). doi: 10.1029/2008GL036559
39. N. J. T. Edberg *et al*., Pumping out the atmosphere of Mars through solar wind pressure pulses. *Geophys. Res. Lett.* **37**, L03107 (2010). doi: 10.1029/2009GL041814
40. R. Ramstad *et al*., Phobos 2/ASPERA data revisited: Planetary ion escape rate from Mars near the 1989 solar maximum. *Geophys. Res. Lett.* **40**, 477–481 (2013). doi: 10.1002/grl.50149
41. R. Ramstad *et al*., The Martian atmospheric ion escape rate dependence on solar wind and solar EUV conditions: 1. Seven years of Mars Express observations. *J. Geophys. Res.* **120**, 1298–1309 (2015). doi: 10.1002/2015JE004816
42. H. Nilsson *et al*., Heavy ion escape from Mars, influence from solar wind conditions and crustal magnetic fields. *Icarus* **215**, 475–484 (2011). doi: 10.1016/j.icarus.2011.08.003
43. B. Wood, H.-R. Müller, G. P. Zank, J. L. Linsky, S. Redfield, New Mass-loss measurements from Astrospheric Ly-a absorption. *Astrophys. J.* **628**, L143–L146 (2005). doi: 10.1086/432716

ACKNOWLEDGMENTS

The results presented here represent the work of hundreds of scientists and engineers who designed, built, and operated the spacecraft and instruments and carried out the scientific analyses. We are indebted to them beyond words. The MAVEN mission has been funded by NASA through the Mars Exploration Program. Additional support was provided by CNES for the SWEA instrument and analysis, and by the Belgian American Educational Foundation. Part of this research was carried out at the Jet Propulsion Laboratory, California Institute of Technology, under a contract with the National Aeronautics and Space Administration. M. L. Mays and D. Odstrcil provided valuable analysis with the WSA-ENLIL+Cone model. Data from the MAVEN mission have been made available via the Planetary Data System (accessible via http://atmos.nmsu.edu/data_and_services/atmospheres_data/MAVEN/maven_main.html).

15 July 2015; accepted 18 September 2015
10.1126/science.aad0210

PLANETARY SCIENCE

Discovery of diffuse aurora on Mars

N. M. Schneider,[1]* J. I. Deighan,[1] S. K. Jain,[1] A. Stiepen,[1] A. I. F. Stewart,[1] D. Larson,[2] D. L. Mitchell,[2] C. Mazelle,[3,4] C. O. Lee,[2] R. J. Lillis,[2] J. S. Evans,[5] D. Brain,[1] M. H. Stevens,[6] W. E. McClintock,[1] M. S. Chaffin,[1] M. Crismani,[1] G. M. Holsclaw,[1] F. Lefevre,[7] D. Y. Lo,[8] J. T. Clarke,[9] F. Montmessin,[8] B. M. Jakosky[1]

Planetary auroras reveal the complex interplay between an atmosphere and the surrounding plasma environment. We report the discovery of low-altitude, diffuse auroras spanning much of Mars' northern hemisphere, coincident with a solar energetic particle outburst. The Imaging Ultraviolet Spectrograph, a remote sensing instrument on the Mars Atmosphere and Volatile Evolution (MAVEN) spacecraft, detected auroral emission in virtually all nightside observations for ~5 days, spanning nearly all geographic longitudes. Emission extended down to ~60 kilometer (km) altitude (1 microbar), deeper than confirmed at any other planet. Solar energetic particles were observed up to 200 kilo–electron volts; these particles are capable of penetrating down to the 60 km altitude. Given minimal magnetic fields over most of the planet, Mars is likely to exhibit auroras more globally than Earth.

Auroras are hallmarks of energetic particle deposition in planetary upper atmospheres. They can be used to understand composition, structure, and chemistry of the target atmosphere, as well as the energy and flux of particles striking the atmosphere. Auroral emission in planetary atmospheres can be caused by a number of incident particle populations, energized via a variety of processes. Distinguishing between the various auroral phenomena is best achieved via a combination of observations of both the precipitating particles and the emitted photon radiation. Auroras at Earth are well studied by these complementary means (*1*).

At least three distinct types of aurora are present in Earth's atmosphere (*2*). The brightest and most widely discussed is called "discrete aurora," in reference to its spatial confinement within auroral ovals roughly encircling Earth's magnetic poles. This type of aurora is powered by some combination of parallel electric fields and plasma waves that accelerate the precipitating particles. A second type of aurora can occur equatorward of the auroral zones and is caused by particles locked deeper in Earth's magnetic field. Named "diffuse aurora" or "drizzle," it occurs over much wider spatial ranges, without discernible patterns or structure. It also differs from discrete aurora in that it arises from particles scattered into Earth's atmosphere without acceleration. A third type of aurora occurs poleward of the auroral ovals, again from particles (in this case, solar wind electrons) precipitating into the atmosphere without local acceleration (*3*). Though also morphologically diffuse, this type of aurora is called "polar rain aurora" so as to differentiate this type from the diffuse aurora described above. Normally, both forms of morphologically diffuse aurora are fainter than discrete auroras, owing to their lower particle flux and energy. In all three cases, these terrestrial auroras are confined to the polar region with an emission peak in the upper atmosphere or thermosphere.

The collision of energetic particles with planetary atmospheres is nearly unavoidable, so auroras are a widespread planetary phenomenon. Auroras have been detected at all planets with substantial atmospheres, as well as at some moons with atmospheres. These planetary auroras are either discrete, in cases with intrinsic magnetic fields, or diffuse, in cases without.

Mars is an interesting intermediate case, for which parts of the planet retain remanent magnetism that was locked in the crust about 4 billion years ago, whereas the rest of the planet has a negligible intrinsic magnetic field (*4*). Discrete auroras were detected in regions of strong crustal magnetic fields by the SPICAM (Spectroscopy for Investigation of Characteristics of the Atmosphere of Mars) instrument on the European Space Agency's Mars Express orbiter (*5*–*7*). The emission appeared in patches that were tens of kilometers across at altitudes around 130 km. Further analysis (*8*) revealed a total of 20 instances of auroral patches during 10 years of intermittent SPICAM observations. Auroral excitation was attributed to the precipitation of electrons, typically up to 1 keV, likely accelerated by parallel electric fields analogous to Earth's discrete aurora (*9*, *10*).

Discrete auroras provide concrete evidence of particle precipitation into the martian nightside atmosphere in localized regions, and the likely effects of more global precipitation of charged particles during both quiet and solar storm periods have also been considered (*11*–*13*). However, auroral emission caused by global precipitation had never been discussed. Thus, it remained uncertain whether auroral processes were primarily local effects in specific small-scale regions or a widespread planetary process affecting upper atmospheric chemistry, energy balance, and loss processes on a more global scale.

Observations

The Mars Atmosphere and Volatile Evolution (MAVEN) spacecraft entered Mars' orbit in September 2014, on a mission to study the behavior of the upper atmosphere and the escape of its constituent gases to space (*14*). MAVEN orbits Mars on a 4.5-hour elliptical orbit, with a closest approach to Mars' surface at the periapse, with a distance of ~150 km. MAVEN carries nine instruments optimized for the study of the Mars atmosphere, as well as the drivers that control its behavior. The majority of instruments are used to study the electromagnetic fields and particle environment that surround and collide with Mars' upper atmosphere.

MAVEN also carries a remote sensing instrument for the study of Mars' upper atmosphere: the Imaging Ultraviolet Spectrograph (IUVS) (*15*). The instrument captures reflectance and emission spectra of the planet and its atmosphere in the far-ultraviolet (FUV) (110 to 190 nm) and mid-UV (MUV) (180 to 340 nm) regions, ideal for recording well-known atmospheric emissions from CO_2 and its dissociation and ionization products. The instrument is mounted on an articulated payload platform (APP) that can orient IUVS's field of regard relative to Mars, depending on spacecraft location, orientation, and desired viewing geometry. At the periapse, the APP orients IUVS to look to the side of spacecraft motion, allowing IUVS to use a scan mirror to repeatedly map out the vertical structure of the emitting layers while the spacecraft travels ~90° around the planet. IUVS uses different observing modes in other parts of the orbit, but no auroral emissions have yet been detected in those modes.

We report on periapse observations for 42 orbits between orbit 382 (9 December 2014) and orbit 453 (23 December 2014), with gaps during data downlinks, observations by other instruments, and instrument protection commanding. Data were corrected for detector dark current and scaled according to intensity calibration with UV-bright stars, scaled by instrument geometric factors appropriate for extended source observations (*16*). The MUV data presented herein carry a systematic uncertainty of 30%. The data used in this study, archived with the Planetary Data System, can be identified by the orbit numbers above, the label "periapse" in the filename, and "v02_r01" as a version and revision identifier. Cleaned spectra and vertical profiles of individual emissions were obtained through multiple linear regression fits of independent spectral components (*17*), accounting for molecular bands, atomic lines, and reflected solar spectrum background, as

[1]Laboratory for Atmospheric and Space Physics, University of Colorado, Boulder, Boulder, CO 80303, USA. [2]Space Sciences Lab, University of California, Berkeley, Berkeley, CA 94720, USA. [3]Institut de Recherche en Astrophysique et Planétologie (IRAP), CNRS, Toulouse, France. [4]University Paul Sabatier, IRAP, CNRS, Toulouse, France. [5]Computational Physics, Inc, Springfield, VA 22151, USA. [6]Space Science Division, Naval Research Laboratory, Washington, DC 20375, USA. [7]Laboratoire Atmosphères, Milieux, Observations Spatiales, Institut Pierre Simon Laplace, Guyancourt, France. [8]Lunar and Planetary Laboratory, University of Arizona, Tucson, AZ 85721, USA. [9]Center for Space Physics, Boston University, Boston, MA 02215, USA.
*Corresponding author. E-mail: nick.schneider@lasp.colorado.edu

Downloaded from www.sciencemag.org on November 5, 2015

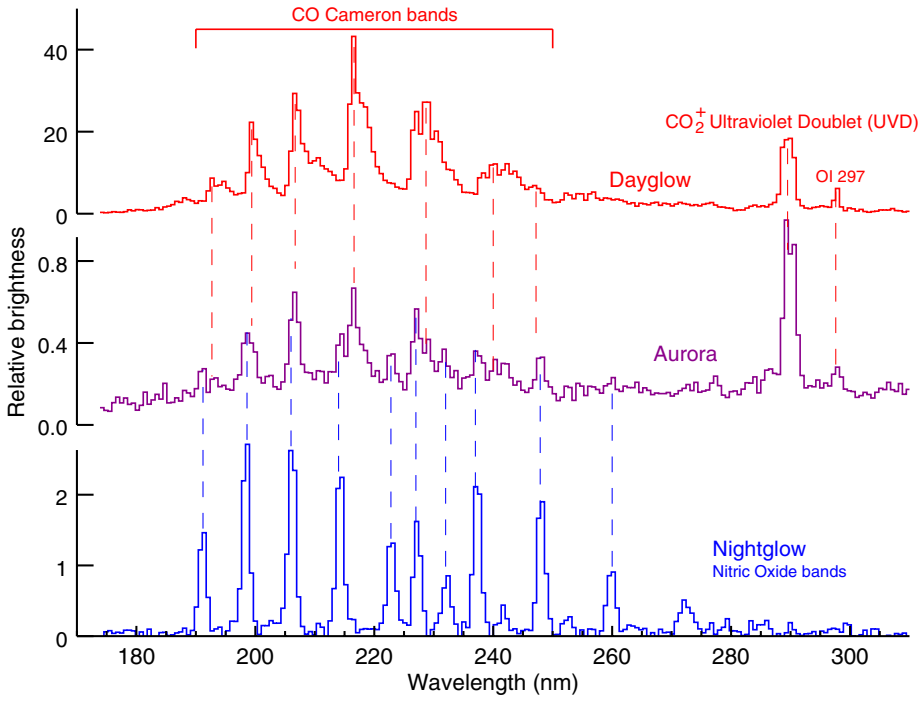

Fig. 1. Three types of Mars spectra observed by IUVS. The top spectrum shows three dayglow emission features from the ionization and dissociation products of CO_2 created by solar EUV radiation (*19*). The bottom spectrum shows a nightside spectrum under conditions where nitric oxide nightglow (*38*, *39*) is produced by atmospheric chemistry; no other emissions are present. Dotted lines from peaks in the top and bottom spectra show that the middle spectrum from the nightside is a combination of features seen in dayglow and nightglow, indicating that particle precipitation is responsible for creating the spectral features of dayglow on the nightside. The differences at 289 nm are most pronounced, as the nitric oxide and Cameron bands have considerable overlap. Spectra were obtained during orbits 114 (top), 437 (middle), and 387 (bottom). OI refers to emission from neutral oxygen.

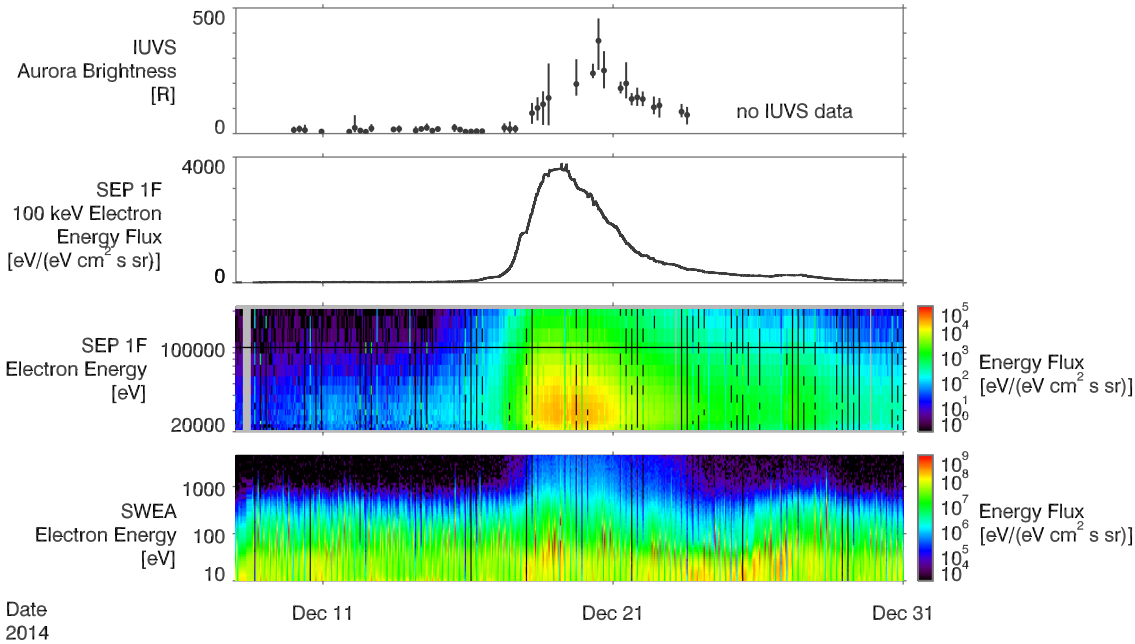

Fig. 2. Time series for auroral emissions and precipitating electron populations. UVD brightnesses measured by IUVS (**top panel**) are compared to the precipitating electrons measured by SEP (**middle panels**) and SWEA (**bottom panel**). The upper SEP panel plots the flux at 100 keV, whereas the lower panel displays all energies. The rise in auroral emission is well correlated with the arrival of the solar energetic particles. Auroral brightnesses in the top panel are averages for entire periapse passes, over the altitude range from 60 to 100 km and over five limb scans spanning 35° of latitude. The maximum and minimum values within each periapse pass are also shown, indicating the intrinsic variability. Emission brightnesses are given in units of rayleighs (R).

well as instrumental resolution and instrumental backgrounds (*18*).

Results

Three types of MUV spectra were observed by IUVS at Mars (Fig. 1). The hallmark of an aurora is the presence of dayside spectroscopic features in selected nightside spectra—in this case, the CO Cameron bands, the CO_2^+ ultraviolet doublet (UVD), and oxygen 297-nm emission (*19*). All emissions ultimately arise from the dissociation and ionization of CO_2, the dominant gas in Mars' atmosphere. In the absence of sunlight, energetic particle excitation is required to produce the emissions. No auroral emission has been detected in the FUV wavelength range, though the search for weak spectral features is ongoing. The auroral emissions are ~100 times weaker than their dayglow counterparts.

Contemporaneous time series for IUVS auroral brightnesses and electron fluxes measured by MAVEN's Solar Energetic Particle (SEP) (*20*) and Solar Wind Electron Analyzer (SWEA) (*21*) instruments show correlated behavior (Fig. 2). Electron fluxes as a function of energy were derived from 3- to 4-keV measurements (SWEA) and from 25- to 200-keV measurements (SEP). The particle data in the bottom three panels of Fig. 2 show quiescent

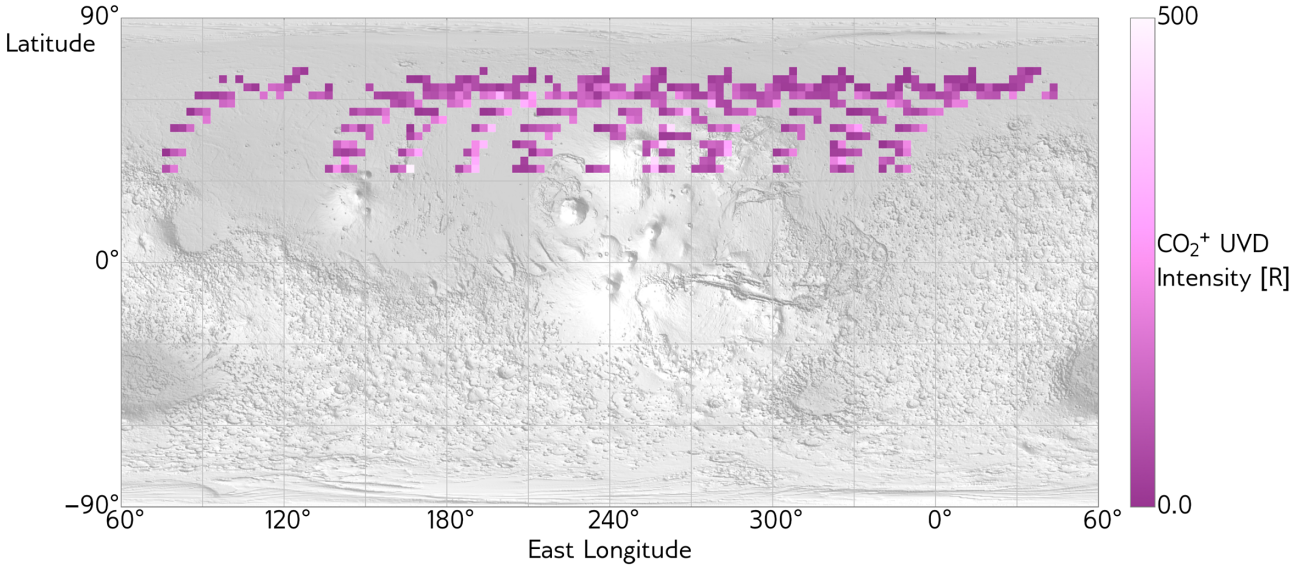

Fig. 3. Geographic distribution of auroral emission. CO_2^+ UVD emission brightnesses superposed on a map of Mars. The extent of emission was limited by the regions observed rather than the occurrence of auroras. All observations were obtained along the same nightside orbit path evident in the pattern of parallel arcs sloping up to the right. Geographic coverage was obtained by the rotation of the planet underneath on subsequent orbits, with longitudes shifting ~66° westward every orbit. It is possible that a large fraction of the nightside exhibited auroral emission during this period.

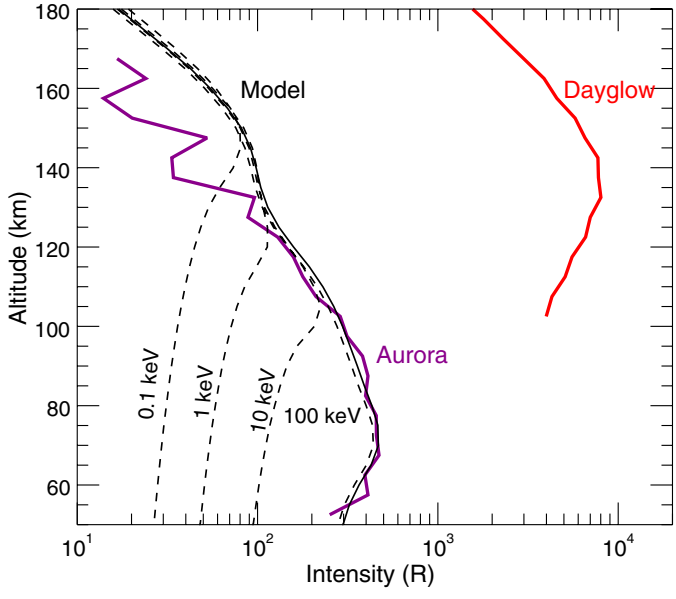

Fig. 4. Observed and modeled vertical brightness profiles for auroral emission. The red curve denotes the CO_2^+ UVD in daylight near the terminator; the purple curve indicates the CO_2^+ UVD during auroras on the nightside. Whereas the photons that excite UVD emission on the dayside are absorbed at altitudes between 120 and 150 km (depending on solar zenith angle), the energetic electrons that excite auroral emission penetrate nearly 60 km lower. The black curve shows the model emission profiles based on the SEP and SWEA data. Dashed lines show truncated energy distributions to illustrate how the maximum energy controls the depth of penetration.

behavior up until 17 December 2014. In the following hours, the solar energetic particle flux increases by two orders of magnitude, and electrons are clearly detected up to the 200-keV limit of the instrument. Data from SWEA measurements also show a comparable rise. Note that when corrected for scale differences and reduced solar energetic particle sensitivity at low energies, the energy distribution decreases smoothly and monotonically over four orders of magnitude. The lack of any peak at intermediate energies is an indication that no local acceleration has occurred. The auroral intensities in the top panel of Fig. 2 follow the same temporal behavior, lasting through the end of the IUVS observations in that period on 23 December. Note that although the onset, rise, and decay of the solar energetic particles and auroral phenomena are consistent, there are clear differences in the detailed structure of the time series. These differences could stem from short-term variability on the 10-min observations for IUVS or spatial structures in either the aurora or particle environment. The correlation between solar energetic particle events and auroral emission is confirmed by at least three additional occurrences observed in February and March 2015 (*22*).

Auroral emissions were detected in all 17 periapse passes during the 5-day period of solar energetic particle enhancement in December 2014, as well as in 97% of 120 vertical scans with appropriate geometry within those passes. The spatial distribution of auroral emission recorded in IUVS observations spanned ~35° in latitude and did not reach Mars' southern hemisphere (Fig. 3). It is probable that the aurora was even more geographically widespread than the large region observed. There is apparently no correlation between the geographic location of the aurora and its brightness. It is possible, however, that local time plays a role in controlling emission. IUVS only sampled a limited range on the nightside, with a relatively fixed ground track during this period from 35°N and ~00:30 local time to 70°N and 5:00 local time. Diffuse emission detected in March 2015 (*23*) occurred near the evening terminator; this finding suggests that narrow confinement in local time is unlikely.

The vertical profile of auroral emission in Mars' atmosphere offers important insights into the deposition of particle energy. The observed average vertical emission profile (Fig. 4) shows a broad emission peak at an apparent altitude of 70 km. This altitude could be interpreted as either the true altitude of emission at the limb or a geometrically projected value for higher-altitude auroras in front of or behind the limb. The latter was the case for SPICAM observations (*4*–*7*), as small patches observed infrequently were unlikely to appear at the limb of the planet. In the IUVS case, the presence of emission at all observed locations and over 5 days continuously provides evidence against substantial patchiness, and the consistency of widely separated individual altitude profiles suggests that projection effects in front of or behind the limb are not important.

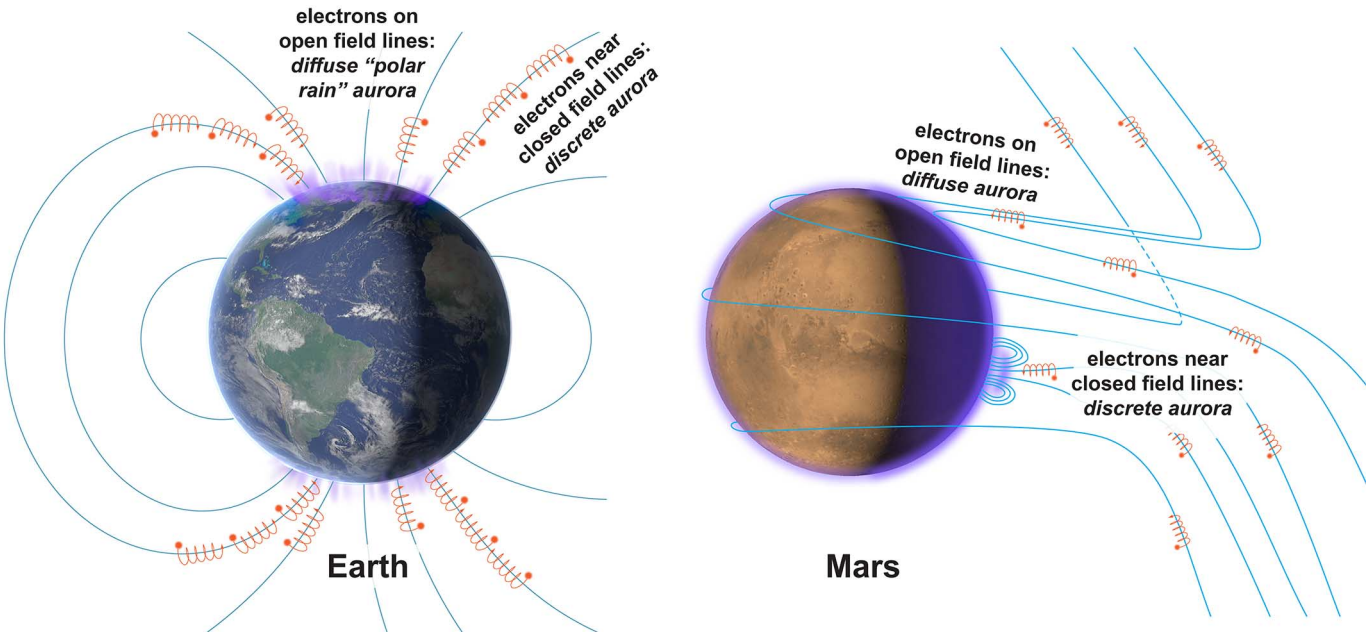

Fig. 5. Comparison of field geometry for diffuse and discrete auroras on Earth and Mars. Mars lacks an internally generated global magnetic field, due to the cooling of its core. Fields surrounding Mars are a combination of small structures locked in the crust billions of years ago (lower right) and solar wind field lines draped around the planet.

The 70-km altitude of the emission peak is compelling evidence for very-high-energy particle precipitation. Both dayglow and SPICAM auroral emissions peak ~60 km higher, where the pressure is lower by a factor of ~10^4. The IUVS aurora must therefore be excited by particles penetrating much deeper than the EUV photons responsible for the airglow or the <1-keV electrons typically responsible for the SPICAM aurora.

Modeling of the auroral emission profile confirms that the energetic particle population detected by SEP and SWEA can produce the observed low-altitude emission peak. As a representative spectrum, we used SEP and SWEA measurements at an altitude of 400 km from the outbound portion of orbit 437. We use SWEA data over its entire energy range from 3 to 5 keV. We then use a power law interpolation between 5 keV and the higher-energy electron spectra measured by SEP from 30 to 200 keV. The overall distribution approximately follows a power law of index 2.2 from ~10 to 200 keV.

We used the Boltzmann three-constituent (B3C) model (*24*) to solve the Boltzmann transport equation for energetic electrons. The B3C model has been used to study the FUV airglow from Earth (*22*, *25*, *26*), Titan (*27*), and Triton (*28*). For the purposes of our study, we adapted this model to the martian atmosphere. The B3C model degrades the energy of the electrons through dissociation, ionization, excitation, and other energy-loss processes and allows us to calculate an omnidirectional vertical electron flux (in units of centimeters^{-2} second^{-1} electron volt^{-1}). The electron flux is then used as input to the Atmospheric Ultraviolet Radiance Integrated Code (AURIC), which was originally developed for terrestrial use (*29*) and recently adapted for use at Mars (*30*), to calculate volume emission rates and column emission rates. Inputs to the B3C model include a mean martian neutral atmosphere (consisting of CO_2, N_2, and O) based on the Mars Climate Database (*31*).

The shape of the emission profile predicted from the full SEP and SWEA electron distributions (black line in Fig. 4) is a good match to the observations. (The measured energy flux has been scaled to match the model-predicted peak UVD brightness to the peak brightness measured by IUVS; future modeling work will be required to confirm the absolute brightness.) The dashed lines in Fig. 4 show the cumulative contributions found by truncating the energy distributions at increasing energies. These energy-dependent profiles demonstrate that electrons with energies less than ~100 eV interact strongly with atmospheric gases through ionization and excitation and are stopped at relatively high altitudes. The ~140-km inflection at this energy is close to the altitude for the lower-energy aurora observed by SPICAM. At high energies, the cross section for interaction decreases, and the particles penetrate deeper. Ultimately, the highest-energy incident electrons create a multitude of secondary electrons at lower energies and altitudes, which efficiently interact with the local gases to cause further ionization and excitation. Only a sufficiently "hard" electron energy distribution, with substantial fluxes of electrons with energies up to at least ~200 keV, can create a single dominant peak at 70 km.

Discussion and conclusions

The discovery of diffuse low-altitude auroras on Mars allows a more complete comparison of auroral phenomena between Mars and Earth (Fig. 5), dictated by their very different magnetic field configurations. The critical distinction lies between field lines that are "closed," meaning connected to the planet on both ends, versus "open" or "draped," with at least one end not connected to the planet. Discrete auroras occur at Earth in the auroral ovals along the edges of closed field lines, where the interaction between Earth's magnetic field and the solar wind accelerates magnetospheric particles to sufficient energies to cause auroras. A similar interaction probably occurs at Mars to cause discrete auroras. Where crustal fields are present, their complex rotating interaction with the variable solar wind allows opportunities for particle acceleration. Over discrete auroras, Mars Express observed particle populations that had been accelerated to energies up to 100 eV, though the local acceleration mechanism remains unclear. Thus, Earth's auroral ovals and Mars' discrete auroral patches probably originate from analogous processes, despite their different appearances.

Diffuse auroras occur differently on the two planets as well. Terrestrial polar rain aurora and the Mars diffuse aurora are both powered by electrons accelerated at the Sun and not locally at the planet. (We note again that Earth's diffuse auroras, which occur deep within the magnetosphere, have no direct counterpart on Mars, so we do not discuss them here.) Electrons can directly collide with Earth's atmosphere along open field lines poleward of the auroral ovals and can strike Mars' atmosphere away from strong closed crustal magnetic fields. Mars' field lines, which are open or draped, allow solar energetic particles to penetrate the atmosphere during solar storms. These particles, which are 100 to 1000 times more energetic than those causing discrete auroras, reach much lower altitudes in the atmosphere. Open and draped field lines often cover much of the planet, though the locations change

as the planet rotates in the variable solar wind (*32*). Mars distorts the solar wind magnetic field, draping field lines that thread through much of the planet's atmosphere, including the nightside (Fig. 5). Diffuse auroras on Mars could therefore occur practically anywhere, and potentially nearly everywhere, on the planet.

The Mars diffuse aurora has much in common with auroras on Venus and some moons of the Jovian planets. Diffuse auroras are not surprising at Venus, which has neither a global magnetic field nor any crustal fields. The Pioneer Venus orbiter first detected auroras from oxygen emission at 130-nm UV wavelengths, where the auroras were attributed to relatively low-energy electrons (*33*, *34*). (No such emission was detected in IUVS observations at Mars.) Venus auroras have also been detected at visible wavelengths through ground-based observations, where they might be caused by solar energetic particles (*35*, *36*), as in this work. Analogously, Jupiter's moons Io and Europa lack intrinsic magnetic fields. In their cases, their tenuous atmospheres are exposed to the energetic particle population of the jovian magnetosphere within which they are embedded. The resulting particle-generated auroral emissions are more globally distributed, and the particles are not locally accelerated (*37*). Enabled by MAVEN and IUVS, the study of Mars' diffuse auroras may therefore have applications to these other solar system objects and potentially also to extrasolar planets without intrinsic magnetic fields.

Diffuse auroras may have additional effects on atmospheric processes. Only a fraction of the deposited energy results in atmospheric excitation and emission. Incident particles also ionize and dissociate atmospheric species, as well as heat the target atmosphere. These effects can lead to increased atmospheric escape rates: Ionized particles at sufficient altitudes can escape via outflow processes, and atmospheric heating can lead to increased thermal escape. Detailed modeling is required to estimate the extent to which atmospheric escape rates increase during diffuse auroral events, as well as which species escape more efficiently. The knowledge that auroras can occur on a more global scale at Mars lends new importance to these studies.

REFERENCES AND NOTES

1. P. E. Sandholt, H. C. Carlson, A. Egeland, *Dayside and Polar Cap Aurora* (Kluwer Academic Publishers, Dordrecht, Netherlands, 2002).
2. P. T. Newell, T. Sotirelis, S. Wing, Diffuse, monoenergetic, and broadband aurora: The global precipitation budget. *J. Geophys. Res.* **114**, A09207 (2009) and references therein.
3. Y. Zhang, L. J. Paxton, A. T. Y. Lui, Polar rain aurora. *Geophys. Res. Lett.* **34**, L20114 (2007). doi: 10.1029/2007GL031602
4. M. H. Acuña *et al*., Global distribution of crustal magnetization discovered by the Mars Global Surveyor MAG/ER experiment. *Science* **284**, 790–793 (1999). doi: 10.1126/science.284.5415.790; pmid: 10221908
5. J.-L. Bertaux *et al*., Discovery of an aurora on Mars. *Nature* **435**, 790–794 (2005). doi: 10.1038/nature03603; pmid: 15944698
6. F. Leblanc *et al*., Origins of the martian aurora observed by Spectroscopy for Investigation of Characteristics of the Atmosphere of Mars (SPICAM) on board Mars Express. *J. Geophys. Res.* **111**, A09313 (2006). doi: 10.1029/2006JA011763
7. F. Leblanc *et al*., Observations of aurorae by SPICAM ultraviolet spectrograph on board Mars Express: Simultaneous ASPERA-3 and MARSIS measurements. *J. Geophys. Res.* **113**, A08311 (2008). doi: 10.1029/2008JA013033
8. J.-C. Gérard *et al*., Concurrent observations of ultraviolet aurora and energetic electron precipitation with Mars Express. *J. Geophys. Res.* **120**, 6749–6765 (2015). doi: 10.1002/2015JA021150
9. R. Lundin *et al*., Plasma acceleration above martian magnetic anomalies. *Science* **311**, 980–983 (2006). doi: 10.1126/science.1122071; pmid: 16484488
10. D. A. Brain *et al*., On the origin of aurorae on Mars. *Geophys. Res. Lett.* **33**, L01201 (2006). doi: 10.1029/2005GL024782
11. J. L. Fox, J. F. Brannon, H. S. Porter, Upper limits to the nightside ionosphere of Mars. *Geophys. Res. Lett.* **20**, 1339–1342 (1993). doi: 10.1029/93GL01349
12. F. Leblanc, J. G. Luhmann, R. E. Johnson, E. Chassefiere, Some expected impacts of a solar energetic particle event at Mars. *J. Geophys. Res.* **107**, 1058 (2002). doi: 10.1029/2001JA900178
13. R. J. Lillis, D. A. Brain, Nightside electron precipitation at Mars: Geographic variability and dependence on solar wind conditions. *J. Geophys. Res.* **118**, 3546–3556 (2013). doi: 10.1002/jgra.50171
14. B. Jakosky *et al*., The Mars Atmosphere and Volatile Evolution (MAVEN) mission. *Space Sci. Rev.* 10.1007/s11214-015-0139-x (2015). doi: 10.1007/s11214-015-0139-x
15. W. E. McClintock *et al*., The Imaging Ultraviolet Spectrograph (IUVS) for the MAVEN Mission. *Space Sci. Rev.* 10.1007/s11214-014-0098-7 (2014). doi: 10.1007/s11214-014-0098-7
16. M. Snow, A. Reberac, E. Quémerais, J. Clarke, W. E. McClintock, T. N. Woods, "A new catalog of ultraviolet stellar spectra for calibration," in *Cross-Calibration of Far UV Spectra of Solar System Objects and the Heliosphere*, E. Quémerais, M. Snow, R.-M. Bonnet, Eds. (ISSI Scientific Report Series, Springer, New York, 2013), pp. 191–226.
17. M. H. Stevens *et al*., New observations of molecular nitrogen in the martian upper atmosphere by IUVS on MAVEN. *Geophys. Res. Lett.* 10.1002/2015GL065319 (2015).
18. M. H. Stevens *et al*., The production of Titan's ultraviolet nitrogen airglow. *J. Geophys. Res.* **116**, A05304 (2011). doi: 10.1029/2010JA016284
19. S. K. Jain *et al*., The structure and variability of Mars upper atmosphere as seen in MAVEN/IUVS dayglow observations. *Geophys. Res. Lett.* 10.1002/2015GL065419 (2015).
20. D. E. Larson, R. J. Lillis, P. A. Dunn, A. Rahmati, T. E. Cravens, K. Hatch, M. Robinson, D. Glaser, J. Chen, D. W. Curtis, C. Tiu, R. P. Lin, J. G. Luhman, J. P. McFadden, J. Connerney, J. Halekas, B. M. Jakosky, "The Solar Energetic Particle experiment on MAVEN: First results," in *46th Lunar and Planetary Science Conference* (Lunar and Planetary Institute, Houston, TX, 2015), abstract 2890.
21. D. L. Mitchell, C. Mazelle, J. P. McFadden, D. Larson, J. S. Halekas, J. E. P. Connerney, J. Espley, L. Andersson, J. G. Luhmann, R. J. Lillis, M. Fillingim, T. Hara, D. A. Brain, "MAVEN observations of the martian ionosphere and magneotheath [sic]," in *46th Lunar and Planetary Science Conference* (Lunar and Planetary Institute, Houston, TX, 2015), abstract 3015.
22. D. J. Strickland, J. R. Jasperse, J. A. Whalen, Dependence of auroral FUV emissions on the incidence electron spectrum and neutral atmosphere. *J. Geophys. Res.* **88**, 8051–8062 (1983). doi: 10.1029/JA088iA10p08051
23. B. M. Jakosky *et al*., MAVEN observations of the response of Mars to an interplanetary coronal mass ejection. *Science* **350**, aad0210 (2015).
24. D. J. Strickland, D. L. Book, T. P. Coffey, J. A. Fedder, Transport equation techniques for the deposition of auroral electrons. *J. Geophys. Res.* **81**, 2755–2764 (1976). doi: 10.1029/JA081i016p02755
25. D. J. Strickland, R. R. Meier, J. H. Hecht, A. B. Christensen, Deducing composition and incident electron spectra from ground-based auroral optical measurements: Theory and model results. *J. Geophys. Res.* **94**, 13527–13539 (1989). doi: 10.1029/JA094iA10p13527
26. J. S. Evans *et al*., Ultraviolet plume instrument imaging from the LACE satellite: Analysis of broadband UV auroral limb data. *J. Geophys. Res.* **99**, 17591–17600 (1994). doi: 10.1029/94JA01143
27. D. F. Strobel, R. R. Meier, M. E. Summers, D. J. Strickland, Nitrogen airglow sources: Comparison of Triton, Titan, and Earth. *Geophys. Res. Lett.* **18**, 689–692 (1991). doi: 10.1029/91GL00133
28. D. F. Strobel, M. E. Simmers, F. Herbert, B. R. Sandel, The photochemistry of methane in the atmosphere of Triton. *Geophys. Res. Lett.* **17**, 1729–1732 (1990). doi: 10.1029/GL017i010p01729
29. D. J. Strickland *et al*., Atmospheric Ultraviolet Radiance Integrated Code (AURIC): Theory, software architecture, inputs, and selected results. *J. Quant. Spectrosc. Radiat. Transf.* **62**, 689–742 (1999). doi: 10.1016/S0022-4073(98)00098-3
30. J. S. Evans *et al*., Retrieval of CO2 and N2 in the martian thermosphere using dayglow observations by IUVS on MAVEN. *Geophys. Res. Lett.* 10.1002/2015GL065489 (2015).
31. E. Millour, F. Forget, A. Spiga, T. Navarro, J.-B. Madeleine, L. Montabone, F. Lefevre, J.-Y. Chaufray, M. A. Lopez-Valverde, F. Gonzalez-Galindo, S. R. Lewis, P. L. Read, M.-C. Desjean, J.-P. Huot; the MCD/GCM Development Team, "The Mars Climate Database, MCD version 5.1," in *Eighth International Conference on Mars* (Lunar and Planetary Institute, Houston, TX, 2014), no. 1791, p. 1184.
32. D. A. Brain, R. J. Lillis, D. L. Mitchell, J. S. Halekas, R. P. Lin, Electron pitch angle distributions as indicators of magnetic field topology near Mars. *J. Geophys. Res.* **112**, A09201 (2007). doi: 10.1029/2007JA012435
33. J. L. Phillips, A. I. F. Stewart, J. G. Luhmann, The Venus ultraviolet aurora: Observations at 130.4 nm. *Geophys. Res. Lett.* **13**, 1047–1050 (1986). doi: 10.1029/GL013i010p01047
34. J. Fox, A. I. F. Stewart, The Venus ultraviolet aurora: A soft electron source. *J. Geophys. Res.* **96**, 9821–9828 (1991). doi: 10.1029/91JA00252
35. T. G. Slanger, D. L. Huestis, P. C. Cosby, N. J. Chanover, T. A. Bida, The Venus nightglow: Ground-based observations and chemical mechanisms. *Icarus* **182**, 1–9 (2006). doi: 10.1016/j.icarus.2005.12.007
36. C. L. Gray, thesis, New Mexico State University (2015).
37. M. A. McGrath, E. Lellouch, D. F. Strobel, P. D. Feldman, R. E. Johnson, "Satellite atmospheres," in *Jupiter: The Planet, Satellites and Magnetosphere*, F. Bagenal, T. E. Dowling, W. B. McKinnon, Eds. (Cambridge Planetary Science Series, Cambridge Univ. Press, Cambridge, 2004), pp. 457–484.
38. J.-L. Bertaux *et al*., Nightglow in the upper atmosphere of Mars and implications for atmospheric transport. *Science* **307**, 566–569 (2005). doi: 10.1126/science.1106957; pmid: 15681381
39. A. Stiepen, A. I. F. Stewart, S. K. Jain, N. M. Schneider, J. Deighan, J. S. Evans, M. H. Stevens, F. Montmessin, M. S. Chaffin, W. E. McClintock, J. T. Clarke, G. M. Holsclaw, B. M. Jakosky, "Preliminary analysis of martian nightglow and aurora observed by MAVEN's Imaging Ultraviolet Spectrograph," in *46th Lunar and Planetary Science Conference* (Lunar and Planetary Institute, Houston, TX, 2015), abstract 2937.

ACKNOWLEDGMENTS

The MAVEN mission is supported by NASA through the Mars Exploration Program. A.S. was supported by the Belgian American Educational Foundation and the Rotary District 1630. M.H.S. was supported by the NASA MAVEN Participating Scientist Program. This work was partially supported by the Centre National d'Etudes Spatiales, for the part based on observations with the SWEA instrument. The IUVS data are publicly archived at the Planetary Atmospheres node of the Planetary Data System and can be identified by the file suffix v03_r01.

17 July 2015; accepted 21 September 2015
10.1126/science.aad0313

PLANETARY SCIENCE

Dust observations at orbital altitudes surrounding Mars

L. Andersson,[1] T. D. Weber,[1] D. Malaspina,[1] F. Crary,[1] R. E. Ergun,[1] G. T. Delory,[2] C. M. Fowler,[1] M. W. Morooka,[1] T. McEnulty,[1] A. I. Eriksson,[3] D. J. Andrews,[3] M. Horanyi,[1] A. Collette,[1] R. Yelle,[4] B. M. Jakosky[1]

Dust is common close to the martian surface, but no known process can lift appreciable concentrations of particles to altitudes above ~150 kilometers. We present observations of dust at altitudes ranging from 150 to above 1000 kilometers by the Langmuir Probe and Wave instrument on the Mars Atmosphere and Volatile Evolution spacecraft. Based on its distribution, we interpret this dust to be interplanetary in origin. A comparison with laboratory measurements indicates that the dust grain size ranges from 1 to 12 micrometers, assuming a typical grain velocity of ~18 kilometers per second. These direct observations of dust entering the martian atmosphere improve our understanding of the sources, sinks, and transport of interplanetary dust throughout the inner solar system and the associated impacts on Mars's atmosphere.

Dust in the martian atmosphere arises from several sources. Dust from the surface can be lifted to altitudes of 80 to 100 km by dust devils and during global dust storms (*1*), but aerosols and dust from the lower atmosphere are not expected to reach altitudes of ~200 km. Dust originating from the two moons Phobos and Deimos could reach these altitudes (*2*); such dust would be created by surface erosion and could create a dust ring around Mars. A dust ring would be expected to have a decreasing abundance of dust grains at low altitudes, because individual grains at these altitudes should have elliptical orbits and would be lost as a result of atmospheric friction (*3*). Another possible source of dust at low altitudes is interplanetary dust. These dust particles are known to enter planetary atmospheres with above-Keplerian speeds and, through ablation processes, are the primary contributor to the metallic meteor layer at around 80 km above Earth (*4*, *5*). Thus far, interplanetary dust influx into an atmosphere has been observed only at Earth.

The Mars Atmosphere and Volatile Evolution (MAVEN) mission (*6*) arrived at Mars in the fall of 2014. Dust can be detected by MAVEN's Langmuir Probe and Waves (LPW) instrument owing to its ability to measure high-frequency electric fields (*7*). It can observe the current pulses due to plasma clouds forming when grains hit the spacecraft at orbital speeds (typically a few to a few tens of kilometers per second) and the associated changes in the spacecraft potential. Because the entire spacecraft surface acts as a detector, very low dust fluxes can be recorded. To observe these effects with an electric field instrument, it is best to measure the potential between the sensor and the spacecraft at a high cadence (*8*). LPW takes snapshots of time series called data bursts (*9*), and the signature of a dust impact in the time series can vary (Fig. 1). The dust observed by LPW is small (nano- to micrometer grain radii), and these impacts do not endanger the spacecraft.

Dust detection using electric field instruments has been demonstrated by many previous interplanetary and planetary missions (*10*–*15*). Instrument response to a dust impact depends on many factors, including spacecraft orientation, electrical connection between spacecraft surfaces, and the design of the electric field instrument. Recently, laboratory experiments have verified that dust impacts can create signals from charge recollection on spacecraft surfaces and on the sensor itself (*16*). The combination of currents being collected by the spacecraft body and the antenna gives rise to a bipolar voltage signature (Fig. 1, top). The current collected from the plasma cloud can be positive or negative, depending on the surface potential with respect to the plasma potential. At low altitudes, MAVEN charges negatively and therefore is collecting ion currents from the plasma cloud.

The LPW instrument only intermittently records data bursts that are suitable for dust detection, and therefore only a lower bound on the observed dust fluxes can be estimated. We determined the observed flux level over ~7 months as a function of altitude (Fig. 2C). This flux is derived using the total number of measured dust impacts at each altitude and the total time the satellite spent at each altitude interval. The observed fluxes are approximately constant at high altitudes and then increase below 300 km. However, this increase at lower altitudes is probably an observational artifact, due to increased measurement sensitivity resulting from spacecraft charging (*9*). The fraction of bursts containing a dust signal does not vary as a function of altitude when only low charging events are included (Fig. 3).

The size of the observed dust grains can be estimated using the impact signal amplitude, after making necessary assumptions regarding the impact speed and the spacecraft material that is receiving the impacts. Recent laboratory experiments have demonstrated that many spacecraft materials have similar responses to dust impacts (*17*), with the amplitude of the measured voltage spike scaling predictably based on the impactor's mass and velocity. Using the same laboratory test setup, the primary surface material of the MAVEN spacecraft (a multilayer insulation) was tested, revealing the following relationship

$$Q/m = 0.0230\ v^{3.42} \text{ for } v > \sim 4 \text{ km s}^{-1}$$

where v is the dust impact velocity (km s^{-1}) and Q/m is the ratio of the charge Q, liberated by the impact, to the dust grain's mass m (C kg^{-1}). This empirically determined sensitivity suggests that the MAVEN spacecraft should be able to observe

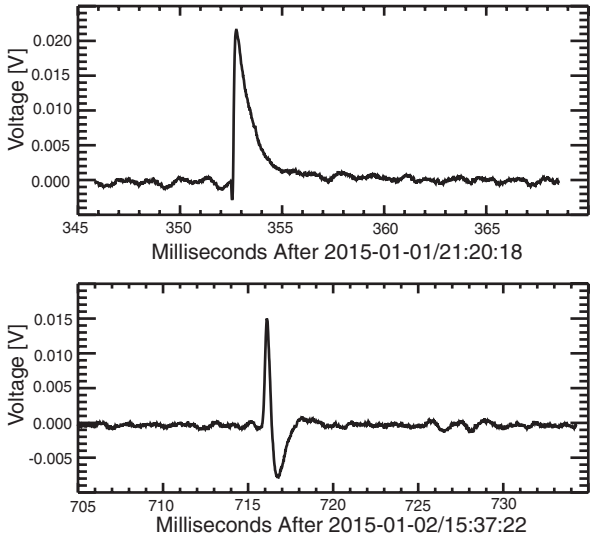

Fig. 1. Two examples of dust impacts recorded by the LPW instrument. The shape of the time series depends on the location of the impact, dust size, dust velocity, and spacecraft-to-sensor potential. (**Top**) An example of current recollection by the LPW sensor. (**Bottom**) A bipolar signal of current recollected by both the LPW sensor and the spacecraft body (*16*).

[1]Laboratory for Atmospheric and Space Physics, University of Colorado–Boulder, Boulder, CO 80303, USA. [2]Space Science Laboratory, University of California–Berkeley, Berkeley, CA 94720, USA. [3]Swedish Institute of Space Physics, Uppsala, Sweden. [4]Lunar and Planetary Laboratory, University of Arizona, Tucson, AZ 85721, USA.
*Corresponding author. E-mail: laila.andersson@lasp.colorado.edu

Downloaded from www.sciencemag.org on November 5, 2015

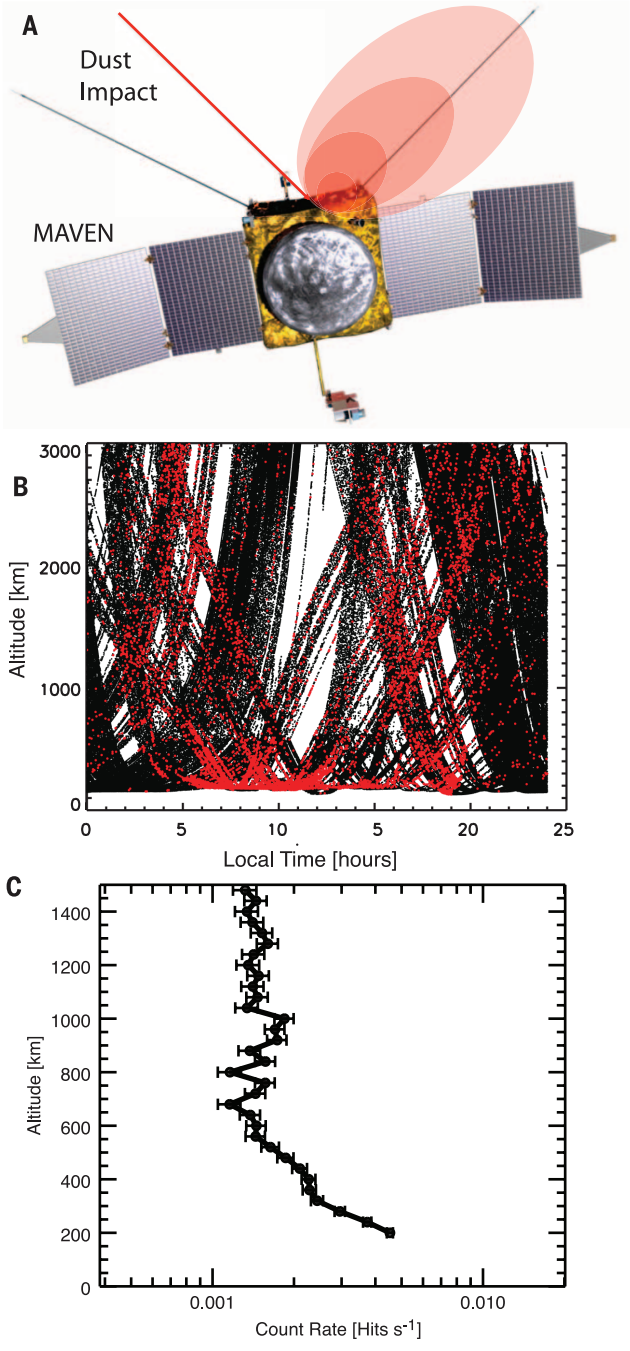

Fig. 2. Dust impacts on the MAVEN spacecraft observed below 1500 km. A dust impact hitting the spacecraft is illustrated in (**A**). The orbit coverage from the first ~7 months of operation is shown by the black dots in (**B**) as function of solar zenith angle and altitude. The red dots indicate where dust impacts were observed. The lower limit on the dust count rate, as function of altitude, is shown in (**C**). The presented uncertainty is the standard deviation.

dust signals more frequently than other missions, such as the Solar Terrestrial Relations Observatory (*17*).

Dust grains are typically assumed to have a mass density of ~2.5 g cm^{-3} (*5*). The size of the dust grains can be estimated using the above relationship, the observed signal amplitude, an assumed mass density and impact velocity, and a body capacitance for the MAVEN spacecraft of ~200 pF (the vacuum capacity of a 2-m sphere to infinity). The observed dust-pulse amplitudes increase with decreasing altitude (Fig. 4). The dust size is derived on the basis of two assumed impact velocities: (i) the spacecraft velocity, which is ~4 km/s, and (ii) the expected average speed of interplanetary dust at Mars, ~18 km/s (*18*). Based on the lower bound, typical dust sizes are ~5 to 25 μm, with a mass of ~10^{-12} to 10^{-10} kg. Using the upper bound suggests slightly smaller grains, with sizes of ~1 to 5 μm and masses of ~10^{-14} to 10^{-12} kg.

Given the observed constant or increased flux with decreasing altitude (Fig. 2C), the most likely source of the dust particles is the atmosphere. Recent imaging of Mars (*19*) suggests that dust may be lofted to high altitudes from the lower atmosphere. However, no currently acting physical processes are thought to be able to lift ~1- to 20-μm particles to altitudes of ~200 km above Mars's surface. Therefore, we conclude that the lower atmosphere is probably not the source of the observed dust.

Based on theoretical studies that model dust from Phobos and Deimos, observable densities of dust grains with masses of ~10^{-12} kg could be possible at altitudes below 600 km. (*3*). The theoretical expectations of dust fluxes at low altitudes for these masses are similar to our observed fluxes (Fig. 2C), suggesting that Phobos and Deimos could be viable sources. However, dust from the moons should be confined mainly to their respective orbital planes, resulting in a doughnut-shaped ring around the equator of Mars (*3*). The dust impacts observed over our ~7-month period of analysisz do not exhibit this shape (fig. S1), indicating that the moons are not the source of the observed dust. The dust flux from the moons is also predicted to decrease with altitude as a result of increasing gas drag and elliptical dust orbits, an effect which is not evident in our observations.

The expected interplanetary dust fluxes at 1 astronomical unit for particles of ~10^{-14} to 10^{-12} kg are ~5×10^{-7} to 5×10^{-5} m^{-2} s^{-1} (*20*). To compare this with the observed MAVEN fluxes, we first needed to identify the detection cross section. We assumed the upper limit of the cross section for detecting the dust to be the spacecraft body, at ~9 m^2. Scaling the interplanetary fluxes to Mars's orbit (*20*), the MAVEN lower-bound dust levels are slightly higher than but close to the expected interplanetary dust fluxes, with fluxes of 10^{-4} to 5×10^{-4} m^{-2} s^{-1}. The atmospheric ablation process was verified by a simple model to begin well below the MAVEN periapsis altitude, and therefore no correction of the dust flux as function of altitude is needed (*5*). Because of the agreement between the observed and predicted fluxes, and the nearly constant flux rate with altitude for low spacecraft potentials (Fig. 3), we conclude that MAVEN probably is observing interplanetary dust at Mars.

There are other indications that the dust observed by MAVEN is of interplanetary origin. During MAVEN's cruise phase, when the booms were stowed, the instrument detected dust particles in the interplanetary medium, although a direct flux comparison cannot be made because of the different instrument configuration. In addition, observations of dust above Mars are fairly constant up to ~3000 km, suggesting a source far from the planet. Finally, interplanetary dust is expected to have a preferred flow direction with respect to the motion of the planet. The dust fluxes observed thus far as MAVEN's orbit precessed show no indication of being equatorially confined, whereas an increased flux on the dayside is observed (Fig. 2). The orbital coverage is currently too limited to conclusively indicate a favored directionality.

The dynamics of interplanetary dust influence atmospheric composition and planetary mass balances. Interplanetary dust contributes 0.6 to 30 kg s^{-1} to Earth's atmosphere (*21*). The surface area of Mars's atmosphere is smaller, and the speed of the dust particles should be ~20%

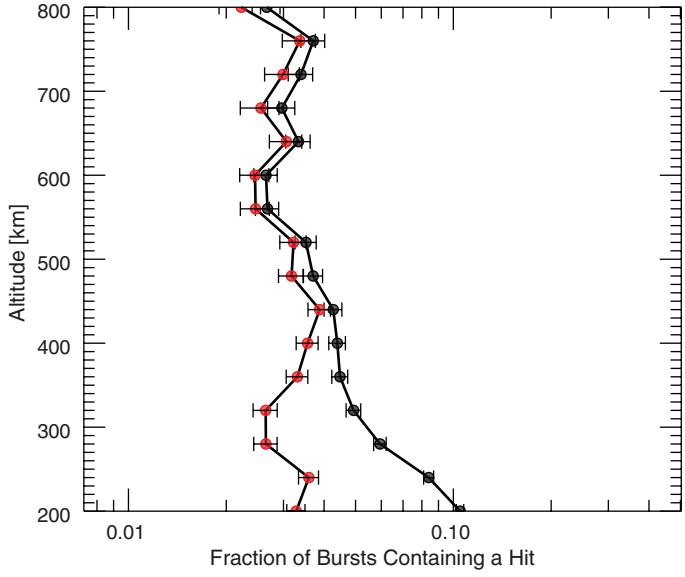

Fig. 3. Fraction of data bursts containing a dust impact (hit), as function of altitude. The black dots encompass the full data set, whereas the red dots only show data bursts where the magnitude of the spacecraft potential was <3 V. The presented uncertainty is the standard deviation.

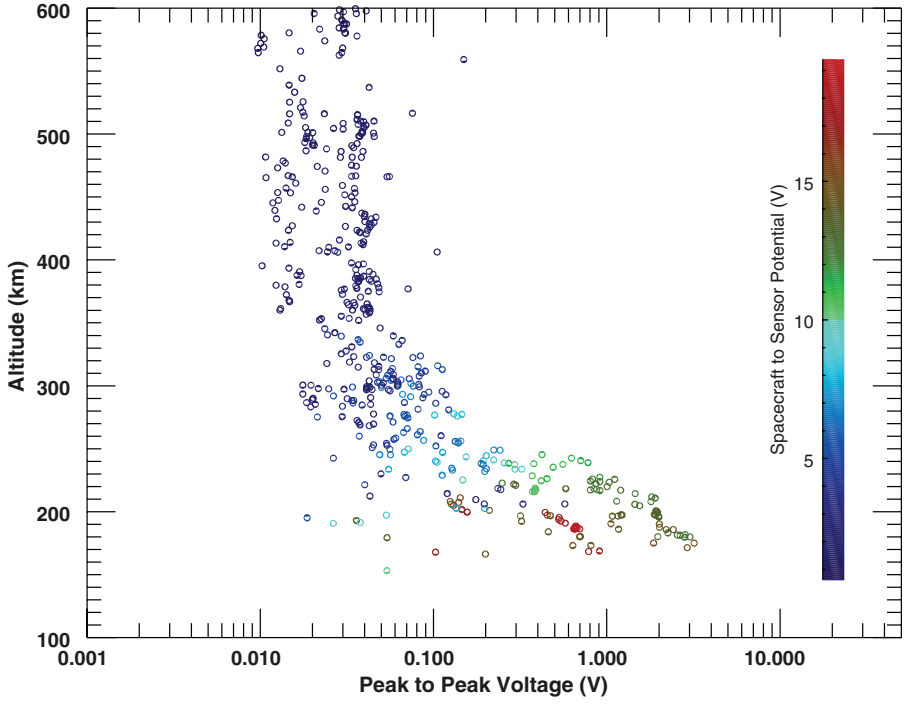

Fig. 4. Peak-to-peak amplitudes of dust impacts, as function of altitude. These observations were obtained when the LPW instrument measured the voltage between the sensor and the spacecraft. The spacecraft potential during the observed dust impact is indicated by the colors.

slower because of the increased distance from the Sun (*21*) and because interplanetary dust fluxes decrease farther out in the solar system (*20*). Based on these considerations, Mars's atmosphere would be expected to receive interplanetary dust at a rate of 0.1 to 3 kg s^{-1}. We estimate that the dust observed by MAVEN contributes only ~0.001 to 0.1 kg s^{-1}, based on observed fluxes (Fig. 2C) and the spacecraft velocity. Thus, we conclude that the observed dust particles represent only a small portion of the likely total influx of interplanetary dust particles.

REFERENCES AND NOTES

1. S. A. Haider, V. Sheel, M. D. Smith, W. C. Maguire, G. J. Molina-Cuberos, Effect of dust storms on the D region of the Martian ionosphere: Atmospheric electricity. *J. Geophys. Res.* **115**, A12336 (2010). doi: 10.1029/2010JA016125
2. W.-H. Ip, M. Banaszkiewicz, On the dust/gas tori of Phobos and Deimos. *Geophys. Res. Lett.* **17**, 857–860 (1990). doi: 10.1029/GL017i006p00857
3. A. Zakharov, M. Horanyi, P. Lee, O. Witasse, F. Cipriani, Dust at the Martian moons and in the circummartian space. *Planet. Space Sci.* **102**, 171–175 (2014). doi: 10.1016/j.pss.2013.12.011
4. V. N. Lebedinets, A. V. Manochina, V. B. Shushkova, Interaction of the lower thermosphere with the solid component of the interplanetary medium. *Planet. Space Sci.* **21**, 1317–1332 (1973). doi: 10.1016/0032-0633(73)90224-9
5. J. G. Molina-Cuberos, J. J. López-Moreno, F. Arnold, Meteoric layers in planetary atmospheres. *Space Sci. Rev.* **137**, 175–191 (2008). doi: 10.1007/s11214-008-9340-5
6. B. M. Jakosky *et al.*, The Mars Atmosphere and Volatile Evolution (MAVEN) mission. *Space Sci. Rev.* 10.1007/s11214-015-0139-x (2015).
7. L. Andersson *et al.*, The Langmuir Probe and Waves (LPW) instrument for MAVEN. *Space Sci. Rev.* (2015). doi: 10.1007/s11214-015-0194-3
8. P. Oberc, Electric antenna as a dust detector. *Adv. Space Res.* **17**, 105–110 (1996). doi: 10.1016/0273-1177(95)00766-8 pmid: 11540354
9. Materials and methods are available as supplementary materials on *Science* Online.
10. D. A. Gurnett, E. Grün, D. Gallagher, W. S. Kurth, F. L. Scarf, Micron-sized particles detected near Saturn by the Voyager plasma wave instrument. *Icarus* **53**, 236–254 (1983). doi: 10.1016/0019-1035(83)90145-8
11. P. Oberc, W. Parzydlo, O. L. Vaisberg, Correlations between the Vega 2 plasma wave (APV-N) and dust (SP-1) observations at Comet Halley. *Icarus* **86**, 314–326 (1990).
12. B. T. Tsurutani *et al.*, Dust impacts at Comet P/Borrelly. *Geophys. Res. Lett.* **30**, 2134 (2003). doi: 10.1029/2003GL017580
13. W. S. Kurth, T. F. Averkamp, D. A. Gurnett, Z. Wang, Cassini RPWS observations of dust in Saturn's E Ring. *Planet. Space Sci.* **54**, 988–998 (2006). doi: 10.1016/j.pss.2006.05.011
14. A. Zaslavsky *et al.*, Interplanetary dust detection by radio antennas: Mass calibration and fluxes measured by STEREO/WAVES. *J. Geophys. Res.* **117**, A05102 (2012). doi: 10.1029/2011JA017480
15. D. M. Malaspina *et al.*, Interplanetary and interstellar dust observed by the Wind/WAVES electric field instrument. *Geophys. Res. Lett.* **41**, 266–272 (2014). doi: 10.1002/2013GL058786
16. A. Collette, G. Meyer, D. Malaspina, Z. Sternovsky, Laboratory investigation of antenna signals from dust impacts on spacecraft. *J. Geophys. Res. Space Phys.* **120**, 5298–5305 (2015). doi: 10.1002/2015JA021198
17. A. Collette, E. Grün, D. Malaspina, Z. Sternovsky, Micrometeoroid impact charge yield for common spacecraft materials. *J. Geophys. Res. Space Physics* **119**, 6019–6026 (2014). doi: 10.1002/2014JA020042
18. G. J. Molina-Ciberos, O. Witasse, J.-P. Lebreton, R. Rodrigo, J. J. López-Moreno, Meteoric ions in the atmosphere of Mars. *Planet. Space Sci.* **51**, 239–249 (2003). doi: 10.1016/S0032-0633(02)00197-6
19. A. Sánchez-Lavega *et al.*, An extremely high-altitude plume seen at Mars' morning terminator. *Nature* **518**, 525–528 (2015). doi: 10.1038/nature14162; pmid: 25686601
20. E. GrüH. A. n, H. Zook, R. H. Fechtig, , Collisional balance of the meteoric complex. *Icarus* **62**, 244–272 (1985). doi: 10.1016/0019-1035(85)90121-6
21. I. Mann *et al.*, Dusty plasma effects in near Earth space and interplanetary medium. *Space Sci. Rev.* **161**, 1–47 (2011). doi: 10.1007/s11214-011-9762-3

ACKNOWLEDGMENTS

The data used in our analyses are available via NASA's Planetary Data System at http://atmos.nmsu.edu/data_and_services/atmospheres_data/MAVEN/maven_main.html. NASA funding for the MAVEN project through the Mars Exploration Program supported this work.

SUPPLEMENTARY MATERIALS

www.sciencemag.org/content/350/6261/aad0398/suppl/DC1
Materials and Methods
Fig. S1

16 July 2015; accepted 17 September 2015
10.1126/science.aad0398

PLANETARY SCIENCE

Early MAVEN Deep Dip campaign reveals thermosphere and ionosphere variability

S. Bougher,[1*] B. Jakosky,[2] J. Halekas,[3] J. Grebowsky,[4] J. Luhmann,[5] P. Mahaffy,[4] J. Connerney,[4] F. Eparvier,[2] R. Ergun,[2] D. Larson,[5] J. McFadden,[5] D. Mitchell,[5] N. Schneider,[2] R. Zurek,[6] C. Mazelle,[7,8] L. Andersson,[2] D. Andrews,[9] D. Baird,[10] D. N. Baker,[2] J. M. Bell,[11] M. Benna,[4] D. Brain,[2] M. Chaffin,[2] P. Chamberlin,[4] J.-Y. Chaufray,[12] J. Clarke,[13] G. Collinson,[4] M. Combi,[1] F. Crary,[2] T. Cravens,[14] M. Crismani,[2] S. Curry,[5] D. Curtis,[5] J. Deighan,[2] G. Delory,[5] R. Dewey,[2] G. DiBraccio,[4] C. Dong,[1] Y. Dong,[2] P. Dunn,[5] M. Elrod,[4] S. England,[5] A. Eriksson,[9] J. Espley,[4] S. Evans,[15] X. Fang,[2] M. Fillingim,[5] K. Fortier,[2] C. M. Fowler,[2] J. Fox,[16] H. Gröller,[17] S. Guzewich,[4] T. Hara,[5] Y. Harada,[5] G. Holsclaw,[2] S. K. Jain,[2] R. Jolitz,[5] F. Leblanc,[12] C. O. Lee,[5] Y. Lee,[1] F. Lefevre,[12] R. Lillis,[5] R. Livi,[5] D. Lo,[17] Y. Ma,[18] M. Mayyasi,[13] W. McClintock,[2] T. McEnulty,[2] R. Modolo,[12] F. Montmessin,[12] M. Morooka,[2] A. Nagy,[1] K. Olsen,[1] W. Peterson,[2] A. Rahmati,[14] S. Ruhunusiri,[3] C. T. Russell,[18] S. Sakai,[14] J.-A. Sauvaud,[7,8] K. Seki,[19] M. Steckiewicz,[7,8] M. Stevens,[20] A. I. F. Stewart,[2] A. Stiepen,[2] S. Stone,[17] V. Tenishev,[1] E. Thiemann,[2] R. Tolson,[11] D. Toublanc,[7,8] M. Vogt,[13] T. Weber,[2] P. Withers,[13] T. Woods,[2] R. Yelle[17]

The Mars Atmosphere and Volatile Evolution (MAVEN) mission, during the second of its Deep Dip campaigns, made comprehensive measurements of martian thermosphere and ionosphere composition, structure, and variability at altitudes down to ~130 kilometers in the subsolar region. This altitude range contains the diffusively separated upper atmosphere just above the well-mixed atmosphere, the layer of peak extreme ultraviolet heating and primary reservoir for atmospheric escape. In situ measurements of the upper atmosphere reveal previously unmeasured populations of neutral and charged particles, the homopause altitude at approximately 130 kilometers, and an unexpected level of variability both on an orbit-to-orbit basis and within individual orbits. These observations help constrain volatile escape processes controlled by thermosphere and ionosphere structure and variability.

The Mars upper atmosphere—the top ~100 to 500 km encompassing the thermosphere, ionosphere, and lower portion of the exosphere—constitutes the reservoir that regulates present-day escape processes from the planet. Understanding the coupling of the lower to upper atmosphere is essential to characterizing energy deposition and upward flow of material that can ultimately result in neutral and ion escape from the planet (*1*). In principle, it is possible to constrain the short-term (current) atmospheric escape rates making use of the Mars Atmosphere and Volatile Evolution (MAVEN) measurements over this reservoir region and at higher altitudes. However, without knowledge of the physics and chemistry operating in this reservoir region and driving its variations (such as solar cycle, seasonal, and diurnal), it is not possible to reliably extrapolate the results over evolutionary history. The characterization of this upper atmosphere reservoir is therefore one of the major science objectives of the MAVEN mission (*2*).

Here, we present measurements of subsolar neutral atmospheric composition and temperature, together with ionospheric charged-particle and magnetic-field structure, extending from near the homopause to above the exobase, as enabled by MAVEN's "Deep Dip" campaigns. During each week-long campaign, periapsis is lowered from a nominal altitude of ~150 to 170 km to ~120 to 135 km in order to reach a peak mass density of ~2 to 3.5 kg/km^3. This strategy allows direct in situ sampling of the entire reservoir region for atmospheric escape, from the exosphere downward to near the homopause (*3*). During each orbit, MAVEN makes in situ measurements along the elliptical orbit track of neutral and thermal ion species, thermal electrons, magnetic fields, and suprathermal electrons and ions, using a suite of science instruments (*4*). Periapsis migrates around the planet during the course of the mission, providing comprehensive coverage of latitude and local time, and deep dips are dispersed in time in order to sample different regions of interest (*5*). We focused on the second campaign (DD2), spanning 17 to 22 April 2015, which provided sampling near the subsolar region (local time = 12 to 13), late in the martian year (L_S ~ 327 to 330), and near the equator (*6*). Measurements of the subsolar region are important for constraining neutral-ion chemistry and dynamics in numerical simulations that estimate both neutral and ion escape rates. In addition, thermosphere-ionosphere structure and neutral temperatures are believed to be controlled in part by the changing solar extreme ultraviolet–ultraviolet (EUV-UV) fluxes; this forcing is greatest at low solar zenith angles (SZAs).

We present two sequential DD2 orbits (O1085 and O1086, on 22 April 2015), the first focusing on charged-particle and field measurements and the second on neutral composition and temperatures (Fig. 1). The thermal ion and neutral measurements were made with NGIMS on alternating orbits, necessitating the emphasis on two sequential orbit passes. Both of these orbits had periapses in a region with moderate crustal magnetic fields and occurred during nominal upstream solar wind conditions. We also examined the full suite of DD2 orbits for orbit-to-orbit neutral density and temperature variability.

Neutral composition and temperature observations

The martian upper atmosphere between the exosphere and the homopause encompasses the region of changing importance of heterogeneous (diffusive separation) and homogeneous (small-scale mixing) processes that control the density structure, the location of the peak solar EUV energy deposition, and the main reservoir for escaping particles (*1*). During nominal orbits, MAVEN does not reach the well-mixed atmosphere, but during the Deep Dip campaigns, MAVEN instruments can sample the column extending from near the homopause upward into the exosphere, where neutral and ion escape can occur.

During the DD2 campaign, MAVEN successfully made measurements of the structure and variability of this critical altitude range in the subsolar region. Previously, the thermospheric neutral composition had only been directly measured in situ with the Upper Atmosphere Mass Spectrometer (UAMS) instruments onboard the descending Viking Landers 1 and 2 (*7*). These two descent profiles provided measurements for

[1]CLaSP Department, University of Michigan, Ann Arbor, MI, USA. [2]Laboratory for Atmospheric and Space Physics, University. of Colorado, Boulder, CO, USA. [3]Department of Physics and Astronomy, University of Iowa, Iowa City, IA, USA. [4]NASA/Goddard Space Flight Center, Greenbelt, MD, USA. [5]Space Sciences Laboratory, University of California at Berkeley, Berkeley, CA, USA. [6]Jet Propulsion Laboratory, California Institute of Technology, Pasadena, CA, USA. [7]CNRS/Institut de Recherche en Astrophysique et Planétologie, Toulouse, France. [8]University Paul Sabatier, Toulouse, France. [9]Swedish Institute of Space Physics, Kiruna, Sweden. [10]NASA/Johnson Space Center, Houston, TX, USA. [11]National Institute of Aerospace, Hampton, VA, USA. [12]Laboratoire Atmosphères, Milieux, Observations Spatiales /CNRS, Verrieres-le-Buisson, France. [13]Department of Astronomy, Boston University, Boston, MA, USA. [14]Department of Physics and Astronomy, University of Kansas, Lawrence, KS, USA. [15]Computational Physics, Springfield, VA, USA. [16]Department of Physics, Wright State University, Fairborn, OH, USA. [17]Lunar and Planetary Laboratory, University of Arizona, Tucson, AZ, USA. [18]Institute of Geophysics and Planetary Physics, University of California, Los Angeles, Los Angeles, CA, USA. [19]Solar-Terrestrial Environment Laboratory, Nagoya University, Nagoya, Aichi, Japan. [20]Naval Research Laboratory, Washington, DC, USA.
*Corresponding author. E-mail: bougher@umich.edu

Downloaded from www.sciencemag.org on November 5, 2015

SZA near 44° at low-to-middle latitude for two afternoon locations during solar minimum and near aphelion conditions. The total mass density of the Mars thermosphere has also been measured by several spacecraft accelerometers (*5*, *8*, *9*).

The MAVEN NGIMS instrument measures the neutral composition of the major gas species (such as He, N, O, CO, N_2, O_2, NO, Ar, and CO_2) and their major isotopes, with a vertical resolution of ~5 km for targeted species and a target accuracy of <25% for most of these species (*10*). Corresponding temperatures can be derived from the neutral-scale heights. These multispecies measurements are obtained along an orbit trajectory that combines both vertical and horizontal variations of the upper atmosphere structure (*1*). These convolved variations cannot be separated without the use of numerical models.

Four key neutral species are presented (CO_2, Ar, N_2, and O) for the inbound leg (Fig. 2). The NGIMS and Mars Global Ionosphere-Thermosphere Model (M-GITM)–simulated CO_2, N_2, and Ar density profiles match reasonably well throughout the altitude range (supplementary text S1) (*9*). For example, in the range of 160 to 220 km, M-GITM diurnal variations of CO_2 encompass NGIMS densities quite well, whereas below 160 km, M-GITM underestimates NGIMS CO_2 densities (up to a factor of ~2 at 130 km). Both models and observations show an exponential variation of density with altitude. The scale heights of these species are different at higher altitudes, with most of them (CO_2, Ar, and N_2) showing a common scale height as 130 km is approached. This is consistent with a homopause near 130 km, but quantitative confirmation of the precise homopause altitude cannot be seen in this figure. Atomic O scale heights do not follow this pattern of transitioning scale heights because local chemical production and loss processes are important (*3*). These multispecies, subsolar, neutral-atmosphere measurements capture near-homopause (~130 km) to exosphere (above ~200 km) structure together on the same orbit.

The atomic O density profiles from NGIMS (Fig. 2) constrain the ion-neutral chemistry, thermal heat budget, and dynamics of the Mars dayside upper atmosphere (*1*). NGIMS-measured O densities have been corrected for (i) open-source neutral beaming (OSNB) retrieval, (ii) contributions from CO_2 at lower altitudes, and (iii) "pile up" RAM direction enhancement of densities when approaching periapsis altitudes, with largest corrections present for the higher densities during Deep Dip orbits. Atomic O densities are determined to be reliable (within the ~25% error) down to ~150 km. Comparison of measured and simulated DD2 atomic O profiles shows reasonable agreement at all altitudes, with densities at ~200 km close to ~5.0×10^7 to 6.0×10^7 cm^{-3}. These NGIMS-measured O densities are nearly a factor of ~5 larger than corresponding Mars Express (MEx)/Spectroscopy for Investigation of Characteristics of the Atmosphere of Mars (SPICAM) estimates derived via remote sensing (*11*). The differences in the seasonal (equinox versus aphelion) and solar cycle (solar moderate versus minimum)

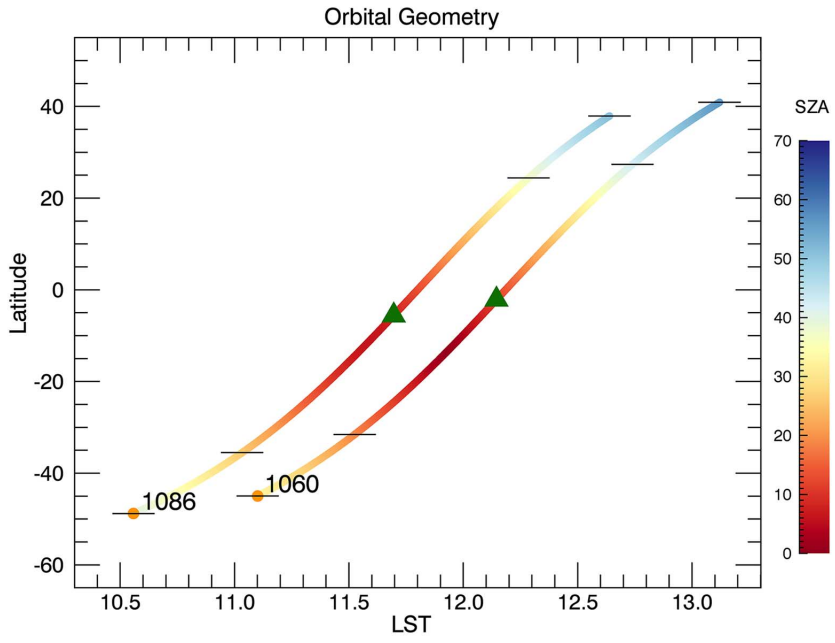

Fig. 1. MAVEN Deep Dip 2 orbital geometry. MAVEN spacecraft "along-track" latitude versus local time coverage of DD2 sampling below 500 km is illustrated (NGIMS measurements are limited to this altitude range). Beginning (O1060) and ending (O1086) orbit information is provided, capturing both inbound and outbound legs, plus the periapsis location (triangles). The 500 and 300 km points on each leg are also delineated by black tick marks. The start of each inbound leg is identified (yellow dots). Specific orbits selected for detailed investigation (O1085 and O1086) fall in between these bounding orbits. SZA is also indicated along these orbit trajectories.

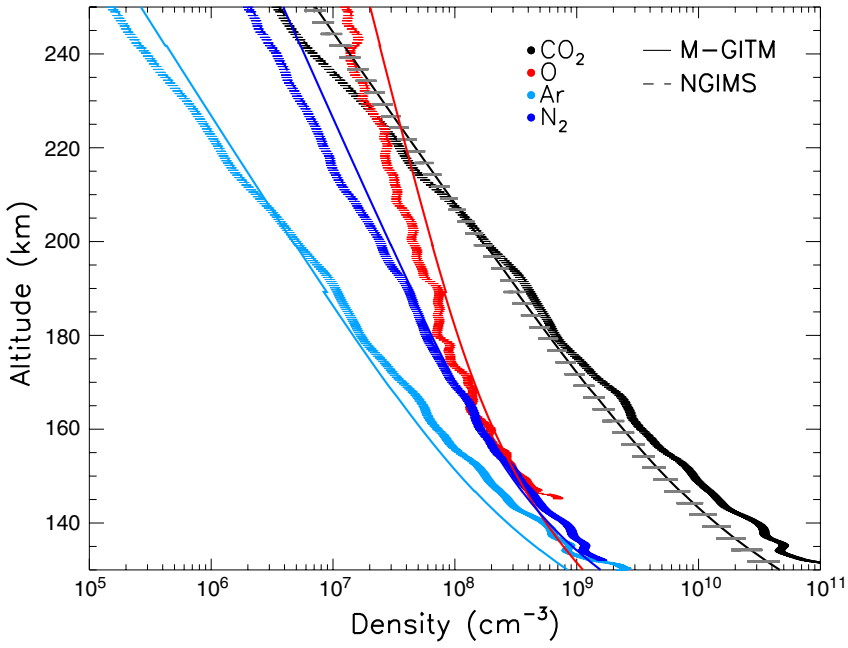

Fig. 2. Neutral density environment near periapsis during the subsolar DD2 campaign. These altitude profiles are provided over ~130 to 250 km specifically for a single orbit (O1086) from 22 April 2015 (supplementary text S2). Four key neutral species are plotted (CO_2, Ar, N_2, and O) for the inbound leg (hashed curves). Simulated subsolar density profiles from the M-GITM, calculated at the location of the spacecraft along its orbit for the solar moderate case (Equinox), are overplotted (solid curves) for comparison (supplementary text S1). The plotted NGIMS densities have been processed by using a 20-s polynomial time-averaging technique so as to remove high-frequency, small-scale variations (supplementary text S3). Calculated NGIMS error bars are included in each profile (supplementary text S4). In addition, 1-[σ] variance bars are added to the 1-SOL averaged M-GITM CO_2 densities in order to illustrate their expected diurnal variation.

sampling between these two data sets may be responsible for this factor of ~5 variation. This substantial variation in atomic O densities at 200 km may have important implications for mass loading of the solar wind because thermospheric and exospheric O densities are simulated to respond similarly to solar cycle and seasonal changes (*12*).

The O/CO_2 ratio is expected to vary with the changing solar EUV-UV fluxes reaching Mars (affecting CO_2 photolysis rates) and the ability of the thermospheric circulation to transport atomic O around the planet (*1*). A data-model comparison shows that the altitude at which this ratio is unity occurs around ~225 km for both NGIMS and M-GITM profiles near the subsolar region (Fig. 3A). This profile determines that the O abundance becomes important above 225 km in the Mars exosphere. This cold O constraint is important for making proper calculations of hot O escape (*1*). Similarly, this O/CO_2 ratio near 150 km (about ~20 km above the expected primary ion peak) is measured to be ~4.0% and is consistent with the NGIMS-measured O_2^+/CO_2^+ ratio of ~6.0 at the same altitude. This occurs because this ion ratio is directly controlled by the atomic O abundance (*13*).

As the measured N_2 and CO_2 profiles approach ~130 km, the N_2/CO_2 ratio converges on the bulk atmosphere value of ~2.0% (Fig. 3B), recently measured by the Mars Science Laboratory (MSL) Sample Analysis at Mars Suite (SAMS) instrument (*14*). The decrease of the ratio with decreasing height is expected because the N_2 scale height is larger than that for CO_2. The convergence of this NGIMS N_2/CO_2 ratio to the constant value of ~2.0% near 130 km indicates that the N_2 homopause altitude during this orbit is located at ~130 km. In fact, all species are subject to the same small-scale mixing, but each has a slightly different homopause altitude owing to small variations in molecular diffusion coefficients (*3*). By this same method, the simulated M-GITM N_2/CO_2 ratio places the N_2 homopause at ~120 km altitude. The difference between these two homopause altitudes implies that some refinement of the small-scale mixing (eddy diffusion) is needed in the M-GITM code (supplementary text S1) (*9*). This model adjustment is expected because the homopause altitude is very sensitive to small-scale mixing, which is itself poorly constrained other than by these new MAVEN measurements. In addition, M-GITM assumes the Viking mixed-atmosphere value of the N_2/CO_2 ratio (~2.7%) (*7*), which is larger than measured by SAMS (*14*). These NGIMS density profiles provide an important initial determination of the dayside homopause altitude, which was previously estimated from Viking modeling studies to be located between ~120 and 130 km (*7*).

Derived NGIMS and simulated M-GITM average temperature profiles (over the entire DD2 campaign) each include averaging over longitude and various wave features (Fig. 4). These averaged NGIMS temperature profiles are constructed by using the Snowden method with hydrostatic integration over the DD2 averaged Ar and N_2 density profiles (*15*). Such averaging serves to smooth out much of the wave structure and determines that the upper-boundary temperature gradients should be close to zero (isothermal).

For M-GITM, simulated temperatures are extracted along each orbit trajectory and subsequently averaged together over all DD2 orbits. The

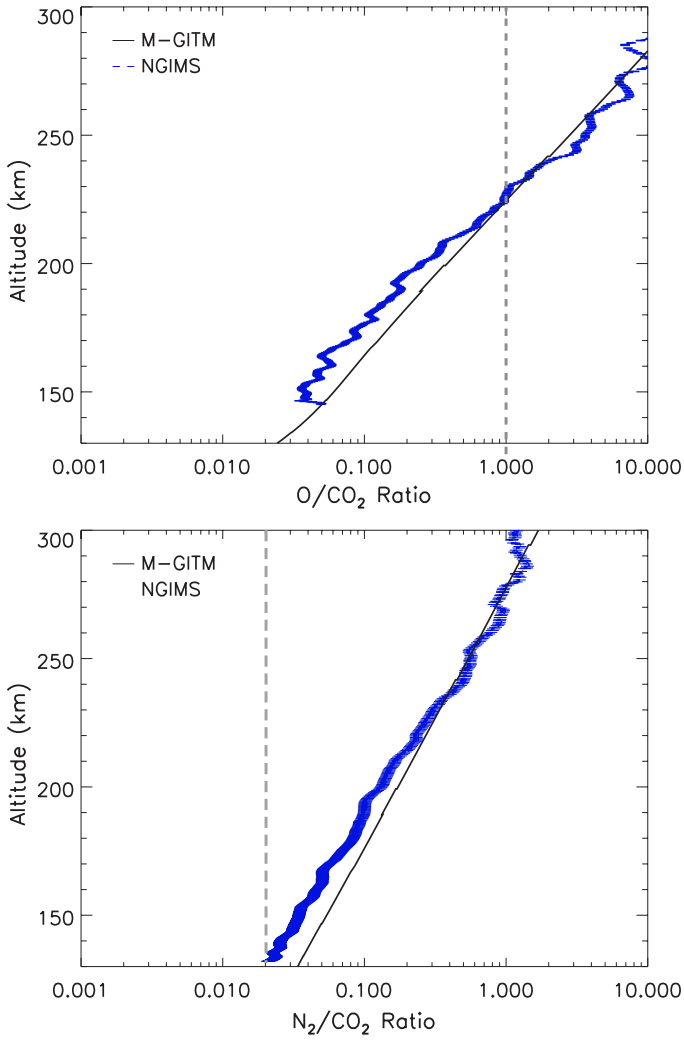

Fig. 3. Altitude plots illustrating key neutral density ratios below 300 km for DD2. These ratios (**Top**) O/CO_2 and (**Bottom**) N_2/CO_2 are composed of the same O1086 NGIMS and M-GITM density profiles illustrated in Fig. 2. The $O/CO_2 = 1$ crossover point near ~225 km (for both NGIMS and M-GITM) is indicated with a vertical dashed line. The measured N_2/CO_2 MSL mixed-atmosphere value of ~2.0% is also indicated with a vertical dashed line (*14*).

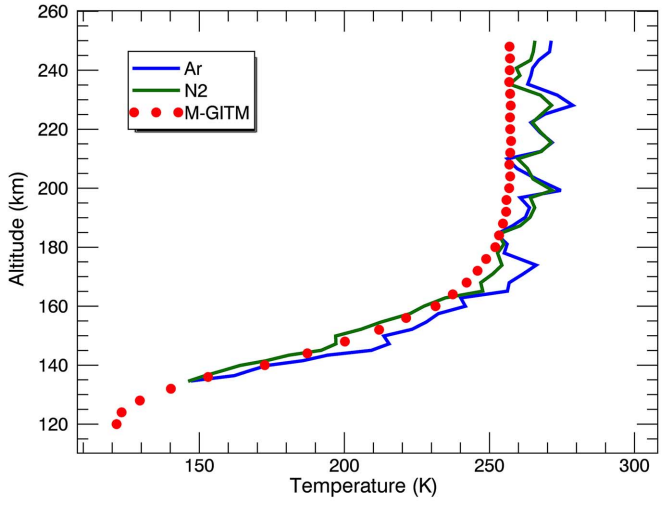

Fig. 4. Profiles of averaged temperature profiles from the entire DD2 campaign. Both NGIMS derived (N_2 and Ar) and M-GITM–simulated temperature profiles are plotted up to 250 km. Mean exospheric temperatures (200 to 250 km) approach ~268 K (NGIMS) and ~257 K (M-GITM).

observed large vertical temperature gradient over ~140 to 170 km coincides with the peak layer of EUV heating, whereas the topside temperatures approach isothermal values above ~200 km. In particular, exospheric temperatures (T_{exo}) are separately extracted from Ar densities by averaging temperatures over ~200 to 250 km for each orbit, then averaging all orbit values together. CO_2 and N_2 densities could also be used, yielding similar temperatures (*16*). The resulting NGIMS extracted mean T_{exo} value of ~268 K is compared with the simulated mean value of ~257 K from M-GITM.

This MAVEN dayside temperature profile is the result of averaging over several DD2 orbits and consequently masks the significant orbit-to-orbit (1σ) variability of NGIMS exospheric temperatures (268 ± 19 K) (*16*). This temporal behavior is similar to that observed from MEx dayside measurements (~270 ± 25 K) extracted from SPICAM dayglow scale heights over 2004–2009 (*17*, *18*). Furthermore, M-GITM simulations (primarily solar-driven) cannot capture this orbit-to-orbit variability, yet M-GITM simulations can reasonably match the DD2 orbit mean T_{exo} value. This large orbit-to-orbit variability implies that dayside thermospheric temperatures are not controlled exclusively by solar EUV forcing, as models might predict (*17*, *18*).

Repeated MAVEN sampling at the 200-km level provides another method for characterization of upper-atmosphere variability near the base of the exosphere. NGIMS neutral densities show a substantial orbit-to-orbit variability throughout the DD2 campaign. Altitude profiles of O and CO_2 densities spanning 14 orbits from O1060 to O1086 show substantial variability on ~4- to 5-hour time scales (Fig. 5). The altitude at which the O/CO_2 ratio crosses through unity varies from ~225 to 238 km for these orbits. The O and CO_2 variations at a constant altitude are also substantial, with measured O densities at 200 km ranging from ~5.0×10^7 to ~1.0×10^8 cm^{-3} (factor of 2), whereas CO_2 densities vary from ~1.3×10^8 to ~3.5×10^8 cm^{-3} (factor of 2.7). These density variations are notable, especially when combined with exospheric temperature variations described above. The implication is that upper-atmosphere structure near 200 km varies substantially from orbit to orbit (on at least ~5-hour time scales), and also as a function of season and solar cycle as illustrated by MEx versus MAVEN results. Orbit-to-orbit variability may be driven from below owing to gravity wave interactions with the global wind structure and small-scale mixing processes (*19*, *20*). This combined density and temperature variability at this exobase altitude (*21*) ultimately has a direct impact upon volatile escape rates (*1*).

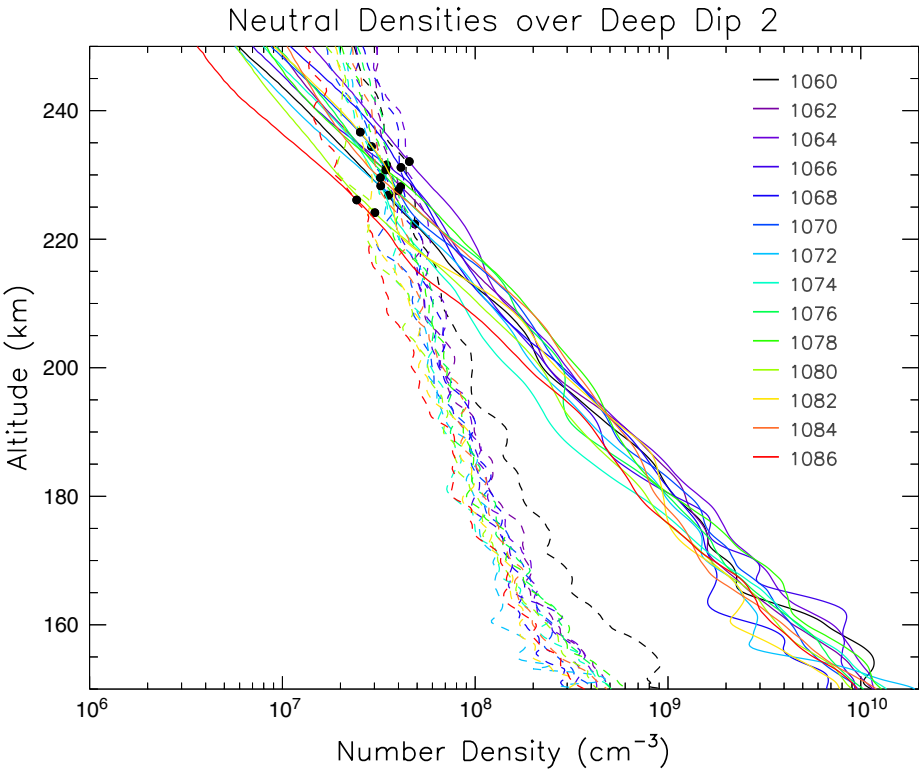

Fig. 5. Altitude plots of O and CO_2 densities over 150 to 250 km. NGIMS O (dashed lines) and CO_2 (solid lines) density profiles are plotted throughout the DD2 campaign, spanning 14 orbits from O1060 to O1086. Separate profiles are color-coded for orbit identification. The black dots for each orbit correspond to the crossing point at which the O/CO_2 ratio is unity. These altitudes range from ~225 to 238 km. The mean height is 230.5 ± 2.5 km.

Charged-particle and magnetic-field observations

Plasma measurements extending from the magnetosphere down to the main peak of the subsolar martian ionosphere have been collected by MAVEN. MGS and MEx previously explored the induced magnetosphere and the transition to the upper ionosphere (*22*, *23*), but neither mission carried a complete complement of plasma instrumentation. Meanwhile, characterization of the lower-altitude collisional ionosphere has primarily used remote sounding techniques (*24*, *25*), revealing variable structure (*26*) and only occasionally a Venus-like ionopause (*27*). Viking provided the only previous direct measurements of lower ionospheric structure and composition (*13*), but only in a narrow range of SZA.

Measurements from MAG (*28*), SWEA (*2*), SWIA (*29*), LPW (*30*), and NGIMS (*10*) reveal the complex morphology of the inner magnetosphere and ionosphere (Figs. 6 and 7). Periapsis for this orbit (O1085) occurred at 48°W, 6°S, in a region with moderate crustal magnetic fields, at an altitude of ~130 km and SZA of ~5°. During this period, the spacecraft remained below the induced magnetospheric boundary until 02:18 UTC, after which MAVEN observed suprathermal particles characteristic of the magnetosheath. Before 02:18 UTC, electron spectra displayed features characteristic of atmospheric photoelectrons throughout. Outside of the main peak of the ionosphere (before 02:02 and after 02:12 UTC), in the transport-dominated regime (above ~200 km, major ion lifetimes are >~600 s), charged-particle populations and magnetic fields show substantial structure, likely consisting of a mix of transient variations and horizontal and/or vertical structure. O^+ and O_2^+ dominate the thermal ion composition, with both varying over orders of magnitude, particularly on the outbound pass. The draped magnetic-field rotations, compositional changes, and electron temperature changes associated with the ion density layers at L3 and L4 and the intervening density depletions suggest that these represent primarily temporal variations, implying rapid ionospheric reconfigurations, indicative of substantial transport and/or strong compressional waves.

At times L1 and L2, the spacecraft passed sharp thermal ion density layers (more pronounced on the inbound segment). At the same locations, MAVEN observed the signatures of localized currents, visible as a discontinuity in the magnetic field [and a rotation toward a more horizontal field below the layers (Fig. 7)]. These features occurred just above a transition to a smoothly varying photoelectron population, which is consistent with the collisional photochemically controlled region of the ionosphere (*31*). This ion layer may represent the topside layer previously seen in radar (*32*) and radio sounding (*33*) by MEx [perhaps also in the Viking-2 descent (*13*)] but appears narrower (~5 to 10 km) than is apparent from remote measurements. The sharpness of the layer in comparison with expected variations in neutral density and EUV energy deposition implies vertical transport and suggests that it could represent a transition between a region dominated by draped and/or induced magnetic fields and one dominated by crustal fields (*33*, *34*). Localized electric fields could also play a role, as previously observed at Earth (*35*). The sharp drop in electron temperature

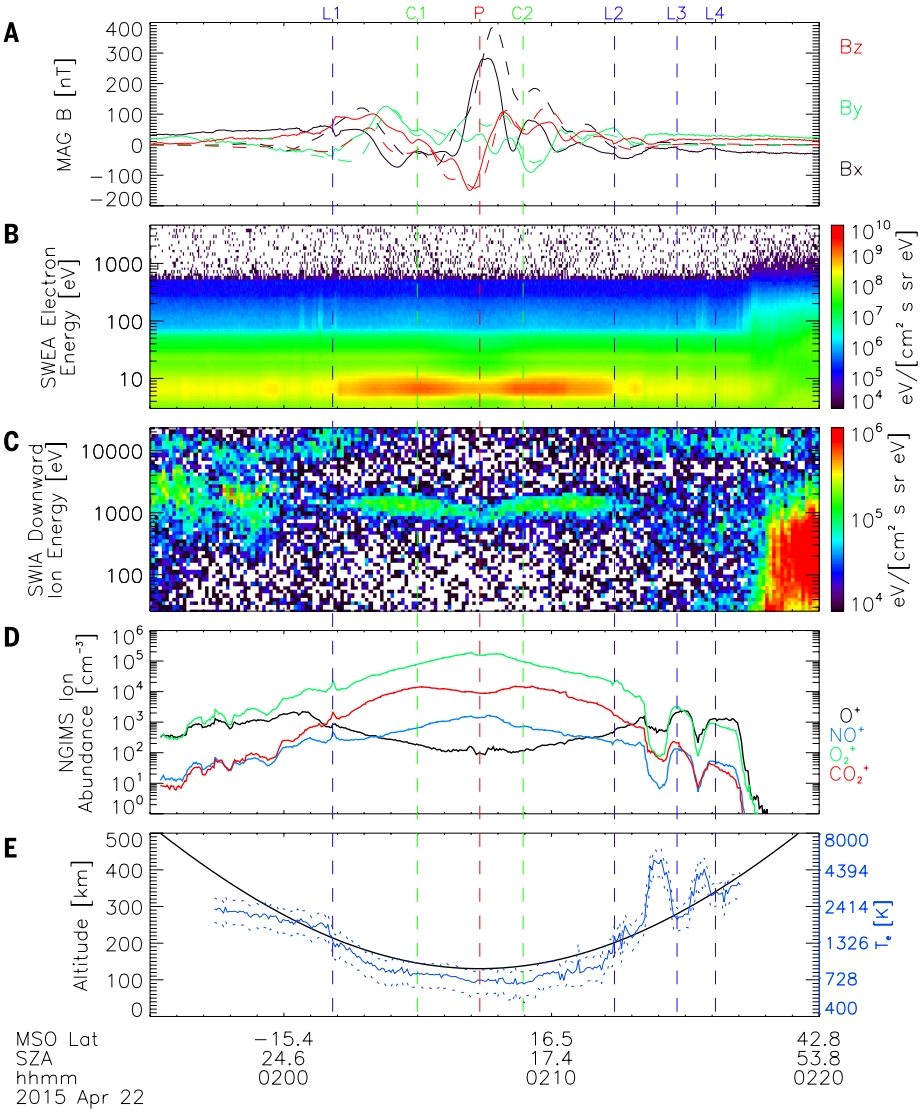

Fig. 6. Plasma environment near periapsis during the subsolar DD2 campaign. These time series plots are provided over 130 to 500 km in a region with moderate crustal fields, during a time period with quiet solar wind conditions, and specifically for 01085 (22 April 2015). (**A**) MAG-measured (solid) and spherical harmonic model (dashed) crustal magnetic-field vector components (Bx, By, and Bz) in Mars-Solar-Orbital coordinates. (**B**) SWEA energy spectra of suprathermal electrons. (**C**) SWIA energy spectra of downward-going suprathermal ions. (**D**) NGIMS abundances of major ion species (O^+, O_2^+, CO_2^+, and NO^+). (**E**) Spacecraft altitude plus LPW electron temperatures (dashed lines indicate upper and lower bounds, with the solid lines showing the best-fit value). Mars-Solar-Orbital latitude (MSO Lat), solar zenith angle (SZA), and universal time coordinated hour and minute (hhmm) are also provided along the time series below 500 km. Labeled vertical dashed lines are provided to highlight features discussed in the text, including localized ion layers (L1 to L4), peaks in CO_2^+ density (C1 and C2), and periapsis (P), which occurs at 02:07 UTC, at a SZA of ~5°.

below this layer also indicates a topological boundary that locally affects photoelectron transport and suggests that photochemical processes play a role (*36*).

At lower altitudes, O^+ densities drop rapidly owing to reactions with neutral molecules, but suprathermal photoelectrons and thermal CO_2^+ ions continue to increase in density (with very similar altitude dependence, commensurate with their production primarily from neutral CO_2). These populations peak at the times marked C1 and C2—at altitudes of ~140 km, below which they decrease—presumably because of recombination and reactions with neutral species. CO_2^+ densities peak at a higher altitude than that of O_2^+ densities, and higher than observed at higher SZA by Viking (*13*). Meanwhile, O_2^+ densities continue to increase until just above periapsis (time P). The slight decrease in density at periapsis may indicate that the spacecraft reached the main M2 peak of the ionosphere, which is consistent with the periapsis altitude.

The different altitude profiles for major ion species and photoelectrons reflect the variations in source and loss processes as a function of altitude, stemming from the varying deposition of EUV and other energy inputs (comprehensively measured by MAVEN), changes in neutral composition, and the steeply increasing neutral density. Multifluid magnetohydrodynamic (MHD) model results capture some, but not all, of the observed variations in ion abundance along the orbit track (supplementary text S5) (*37*, *38*). The model correctly reproduces the structure of the dominant O_2^+ ions at altitudes below ~220 km and also captures the structure of the CO_2^+ ions over most of this altitude range. Above ~220 km, in the transport-dominated region, the time-stationary model results cannot adequately capture the transient dynamics. The model also underestimates O^+ density everywhere except periapsis and does not capture the turnover in the CO_2^+ density at low altitudes.

All the major ion species show substantial wave structure on the outbound segment (but not on the inbound), extending almost down to periapsis. This wave structure correlates closely (although not one-to-one everywhere) with fluctuations seen in the neutral density at the same time, suggesting that many of the observed neutral and ion fluctuations might have a common origin, presumably gravity waves (*19*, *20*).

Suprathermal ion measurements provide another probe of collisional processes in the atmosphere. A downward-going population of ~1 keV ions appears between L1 and L2. These ions represent the products of hydrogen energetic neutral atoms (ENAs) produced through charge exchange between solar wind protons and exospheric atoms in the distant corona outside of the bow shock (*39*, *40*). In neutral form, these particles pass through the magnetosphere unaffected by electromagnetic form, maintaining the same velocity as that of the solar wind. Upon encountering the atmosphere, some of the ENAs undergo charge-stripping reactions and regain their charge, allowing MAVEN to measure them. As the neutral density rises, these particles lose energy through numerous collisions with atmospheric gases. The ratio of electron-stripping to charge-exchange cross sections decreases sharply at lower energies, leading to a decrease in the charged fraction of the precipitating hydrogen between C1 and C2. These penetrating solar wind particles represent an additional source of energy to the upper atmosphere, with a different deposition profile from that of EUV. They also provide a proxy measurement of the solar wind, allowing us to infer an upstream solar wind speed of ~500 km/s and density of ~1.1 cm^{-3} (*40*).

At higher energies of ~10 to 20 keV, SWIA observes an additional population of precipitating ions, which penetrate well into the photochemical region of the atmosphere (below the "exobase"). When this population extends to higher altitudes, at which suprathermal ion composition measurements in this energy range from STATIC (*2*) are available, they indicate predominantly O^+, which is consistent with pickup ions produced by photoionization and charge-transfer reactions in the upstream corona. These precipitating ions

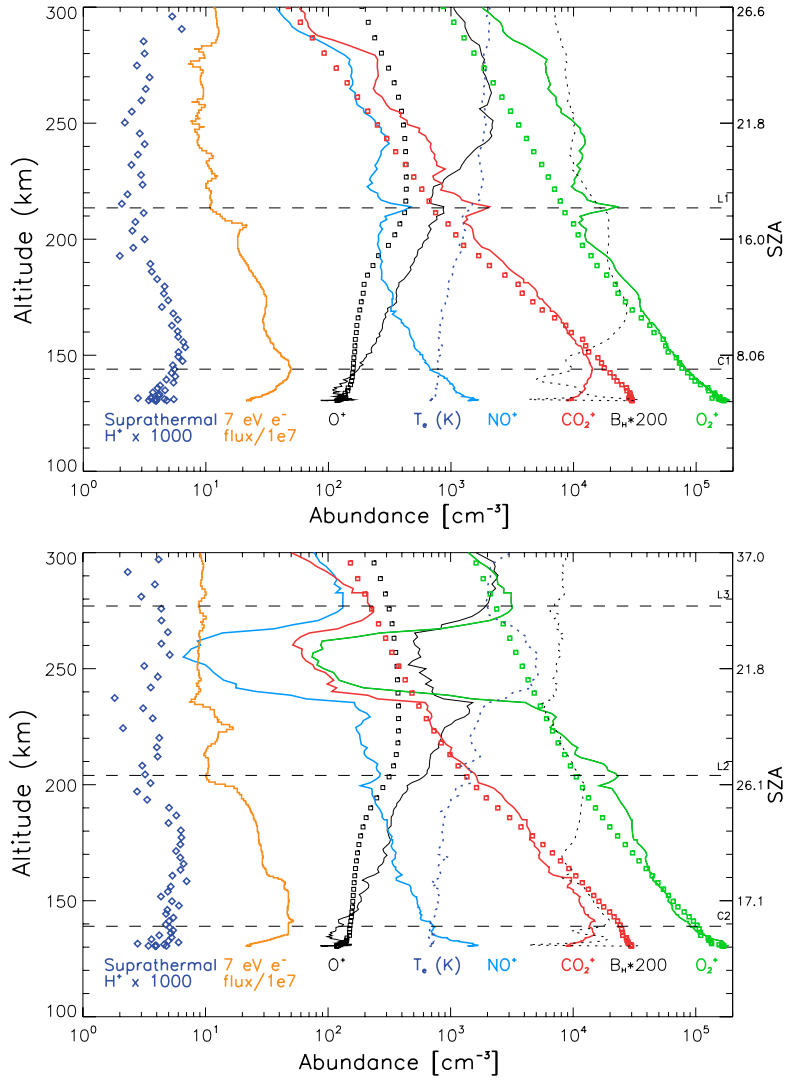

Fig. 7. Altitude plots of ion densities and other plasma fields over 130 to 300 km. NGIMS ion densities are plotted for DD2 orbit 01085, with the corresponding SZA indicated on the right. Four NGIMS key ion species are provided (O^+, O_2^+, CO_2^+, and NO^+) for the (**Top**) inbound and (**Bottom**) outbound legs (solid, color-coded curves). Corresponding simulated ion density profiles along the orbit from the multifluid MHD model are plotted (colored squares) for comparison (O^+, O_2^+, CO_2^+ only) (supplementary text S5) (*37*, *38*, *42*). The measured inbound ratio (O_2^+/CO_2^+) at 150 km is a factor of ~6, whereas that at 220 km is a factor of ~10. These ratios can be compared with corresponding values of 6 and 7 to 9 from Viking Landers 1 and 2, respectively (*13*). Also shown for context are scaled values corresponding to the electron temperature, the horizontal magnetic-field magnitude measured by MAG, the suprathermal electron flux measured at 7 eV (the peak of the suprathermal electron flux) by SWEA, and the suprathermal H^+ density measured by SWIA.

may drive sputtering escape of the neutral atmospheric particles (*41*).

Interpretations and implications

The thermospheric neutral densities and temperatures vary substantially from orbit to orbit, driven in part by tidal and gravity wave forcing. Solar EUV regulation of mean exospheric temperatures (averaged over several orbits) is confirmed for these DD2 measurements, in comparison with solar-driven numerical model simulations. However, this solar forcing does not appear to control interorbital variations of these temperatures. Like the neutral atmosphere to which it is coupled, the ionosphere revealed by MAVEN is highly dynamic, with substantial structure and temporal variations often observed within a single orbit. Crustal fields clearly affect the structure of the ionosphere, and their effects on transport may lead to the formation of the observed narrow current-carrying plasma layers.

REFERENCES AND NOTES

1. S. W. Bougher, T. E. Cravens, J. Grebowsky, J. Luhmann, The aeronomy of Mars: Characterization by MAVEN of the upper atmosphere reservoir that regulates volatile escape. *Space Sci. Rev.* (2014). doi: 10.1007/s11214-014-0053-7
2. B. M. Jakosky *et al.*, The Mars Atmosphere and Volatile Evolution (MAVEN) Mission to Mars. *Space Sci. Rev.* (2015). doi: 10.1007/s11214-015-0139-x
3. The homopause altitude of a given planetary upper atmosphere is commonly estimated as the altitude at which a given species diffusion coefficient matches the specified eddy diffusion coefficient. This altitude represents that level in the atmosphere below which this species is well mixed (homosphere) and above which molecular diffusion serves to separate species according to their individual scale heights (heterosphere). Each species has its particular homopause altitude, owing to the slight variation of molecular diffusion coefficients by species. In reality, the homopause is not a single altitude level, but a transition region across which these molecular and eddy diffusion processes gradually exchange their dominant roles. For Mars, a common mixed-atmosphere scale height is revealed by CO_2, Ar, and N_2 below their homopauses. However, photochemically active species (such as O) do not conform to this mixed-atmosphere scale height.
4. The MAVEN in situ instruments are the Accelerometer (ACC), Langmuir Probe and Waves (LPW), Magnetometer (MAG), Neutral Gas and Ion Mass Spectrometer (NGIMS), Solar Wind Electron Analyzer (SWEA), Solar Wind Ion Analyzer (SWIA), and Supra-thermal and Thermal Ion Composition (STATIC).
5. R. W. Zurek, R. H. Tolson, D. Baird, M. Z. Johnson, S. W. Bougher, M. Z. Johnson, and S. W. Bougher, Application of MAVEN accelerometer and attitude control data to Mars atmospheric characterization. *Space Sci. Rev.* (2014). doi: 10.1007/s11214-014-0095-x
6. Areocentric longitude of the Sun, Ls, is used as an angular measure of the Mars year: Ls = 0, 90, 180, and 270 correspond to the start of the northern spring, summer, fall, and winter, respectively.
7. A. O. Nier, M. B. McElroy, Composition and structure of Mars' upper atmosphere: Results from the neutral mass spectrometers on Viking 1 and 2. *J. Geophys. Res.* **82**, 4341–4349 (1977). doi: 10.1029/JS082i028p04341
8. G. M. Keating *et al.*, The structure of the upper atmosphere of mars: In situ accelerometer measurements from mars global surveyor. *Science* **279**, 1672–1676 (1998). doi: 10.1126/science.279.5357.1672; pmid: 9497278
9. S. W. Bougher *et al.*, Mars Global Ionosphere-Thermosphere Model: Solar cycle, seasonal and diurnal variations of the Mars upper atmosphere. *J. Geophys. Res.* **120**, 311–342 (2015). doi: 10.1002/2014JE004715
10. P. R. Mahaffy *et al.*, The Neutral Gas and Ion Mass Spectrometer on the Mars Atmosphere and Volatile Evolution Mission. *Space Sci. Rev.* **185**, 1–25 (2014). doi: 10.1007/s11214-014-0043-9
11. J.-Y. Chaufray, F. Leblanc, E. Quemerais, J.-L. Bertaux, Martian oxygen density at the exobase deduced from OI 1304.-nm observations by Spectroscopy for the Investigation of the Characteristics of the Atmosphere of Mars on Mars Express. *J. Geophys. Res.* **114** (E2), E02006 (2009). doi: 10.1029/2008JE003130
12. A. Valeille, M. R. Combi, S. W. Bougher, V. Tenishev, A. F. Nagy, Three-dimensional study of Mars upper thermosphere-ionosphere and hot oxygen corona: Solar cycle, seasonal variations and evolution over history. *J. Geophys. Res.* **114**, E11006 (2009). doi: 10.1029/2009JE003389
13. W. B. Hanson, S. Sanatani, D. R. Zuccaro, The Martian ionosphere as observed by the Viking retarding potential analyzers. *J. Geophys. Res.* **82**, 4351–4363 (1977). doi: 10.1029/JS082i028p04351
14. P. R. Mahaffy *et al.*, Abundance and isotopic composition of gases in the martian atmosphere from the Curiosity rover. *Science* **341**, 263–266 (2013). pmid: 23869014
15. D. Snowden *et al.*, The thermal structure of Titan's upper atmosphere, I. Temperature profiles from Cassini INMS observations. *Icarus* **226**, 552–582 (2013). doi: 10.1016/j.icarus.2013.06.006
16. P. R. Mahaffy *et al.*, Structure and composition of the neutral upper atmosphere of Mars from the MAVEN NGIMS investigation. *Geophys. Res. Lett.* **42**, (2015). doi: 10.1002/2015GL065329
17. F. LeBlanc, J. Y. Chaufray, J. Lilenstein, O. Witasse, J.-L. Bertaux, Martian dayglow as seen by the SPICAM UV spectrograph on Mars Express. *J. Geophys. Res.* **111** (E9), E09S11 (2006). doi: 10.1029/2005JE002664
18. A. Stiepen *et al.*, Mars thermospheric scale height: CO Cameron and CO_2^+ dayglow observations from Mars Express. *Icarus* **245**, 295–305 (2015). doi: 10.1016/j.icarus.2014.09.051
19. A. S. Medvedev, E. Yiğit, P. Hartogh, E. Becker, Influence of gravity waves on the Martian atmosphere: General circulation modeling. *J. Geophys. Res.* **116** (E10), E10004 (2011). doi: 10.1029/2011JE003848

20. A. Medvedev, E. Yigit, Thermal effects of internal gravity waves in the Martian upper atmosphere. *Geophys. Res. Lett.* **39**, L05201 (2012). doi: 10.1029/2012GL050852
21. The exobase of a given planetary upper atmosphere is traditionally estimated as the altitude at which, for a single constituent atmosphere, the collision mean free path equals the temperature scale height of this constituent. For Mars, atomic O is the dominant species considered, and calculated global averaged exobase heights vary from ~170 km (Equinox, solar minimum conditions) to ~185 km (Equinox, solar maximum conditions) (*43*). In reality, the exobase is not a fixed altitude that separates collisional (thermosphere) and collisionless (exosphere) regimes. Instead, a full transitional domain must be considered, which extends from the altitude at which a hot O particle produced in this region has a high probability to be thermalized to an altitude at which the collision frequency is very low. Modern hot O exosphere models confirm that this transitional domain extends from ~135 to 300 km altitude (*43*). The ~200 km altitude is commonly used as an approximation for the traditional exobase altitude.
22. A. F. Nagy *et al*., The plasma environment of Mars. *Space Sci. Rev.* **111**, 33–114 (2004). doi: 10.1023/B:SPAC.0000032718.47512.92
23. E. Dubinin *et al*., Plasma morphology at Mars. ASPERA-3 observations. *Space Sci. Rev.* **126**, 209–238 (2006). doi: 10.1007/s11214-006-9039-4
24. M. H. G. Zhang, J. G. Luhmann, A. J. Kliore, J. Kim, A post-Pioneer Venus reassessment of the Martian dayside ionosphere as observed by radio occultation methods. *J. Geophys. Res.* **95** (B9), 14,829–14,839 (1990). doi: 10.1029/JB095iB09p14829
25. D. A. Gurnett *et al*., Large density fluctuations in the Martian ionosphere as observed by the Mars Express radar sounder. *Icarus* **206**, 83–94 (2010). doi: 10.1016/j.icarus.2009.02.019
26. P. Withers, A review of observed variability in the dayside ionosphere of Mars. *Adv. Space Res.* **44**, 277–307 (2009). doi: 10.1016/j.asr.2009.04.027
27. F. Duru *et al*., Steep, transient density gradients in the Martian ionosphere similar to the ionopause at Venus. *J. Geophys. Res.* **114** (A12), A12310 (2009). doi: 10.1029/2009JA014711
28. J. E. P. Connerney *et al*., The MAVEN magnetic field investigation. *Space. Sci. Rev.* 10.1007s11214-015-0169-4 (2015).
29. J. S. Halekas *et al*., The Solar Wind Ion Analyzer for MAVEN. *Space Sci. Rev.* (2013). doi: 10.1007/s11214-013-0029-z
30. R. Ergun *et al*., Dayside electron temperature and density profiles at Mars: First results from the MAVEN Langmuir Probe and Waves instrument. *Geophys. Res. Lett.* **42**, (2015). doi: 10.1002/2015GL065280
31. J. L. Fox, A. Dalgarno, Ionization, luminosity, and heating of the upper atmosphere of Mars. *J. Geophys. Res.* **84** (A12), 7315 (1979). doi: 10.1029/JA084iA12p07315
32. A. J. Kopf, D. A. Gurnett, D. D. Morgan, D. L. Kirchner, Transient layers in the topside ionosphere of Mars. *Geophys. Res. Lett.* **35**, L17102 (2008). doi: 10.1029/2008GL034948
33. P. Withers *et al*., A clear view of the multifaceted dayside ionosphere of Mars. *Geophys. Res. Lett.* **39**, L18202 (2012). doi: 10.1029/2012GL053193
34. H. Shinagawa, T. E. Cravens, The ionospheric effects of a weak intrinsic magnetic field at Mars. *J. Geophys. Res.* **97** (E1), 1027–1035 (1992). doi: 10.1029/91JE02720
35. S. Kirkwood, H. Nilsson; Kirkwood and Nilsson, High-latitude sporadic-E and other thin layers - the role of magnetospheric electric fields. *Space Sci. Rev.* **91**, 579–613 (2000). doi: 10.1023/A:1005241931650
36. J. L. Fox, K. E. Yeager, Morphology of the near-terminator Martian ionosphere: A comparison of models and data. *J. Geophys. Res.* **111** (A10), A10309 (2006). doi: 10.1029/2006JA011697
37. C. Dong *et al*., Solar wind interaction with Mars upper atmosphere: Results from the one-way coupling between the multi-fluid MHD model and the MTGCM model. *Geophys. Res. Lett.* **41**, 2708–2715 (2014). doi: 10.1002/2014GL059515
38. C. Dong *et al*., Solar wind interaction with the Martian upper atmosphere: Crustal field orientation, solar cycle, and seasonal variations. *J. Geophys. Res.* **120**, (2015). doi: 10.1002/2015JA020990
39. E. Kallio, S. Barabash, Atmospheric effects of precipitating energetic hydrogen atoms on the Martian atmosphere. *J. Geophys. Res.* **106** (A1), 165–177 (2001). doi: 10.1029/2000JA002003
40. J. S. Halekas *et al*., MAVEN observations of solar wind hydrogen deposition in the atmosphere of Mars. *Geophys. Res. Lett.* **42**, (2015). doi: 10.1002/2015GL064693
41. J. Luhmann, J. U. Kozyra, Dayside Pickup Oxygen Ion Precipitation at Venus and Mars - Spatial Distributions, Energy Deposition and Consequences. *J. Geophys. Res.* **96** (A4), 5457–5467 (1991). doi: 10.1029/90JA01753
42. D. Najib, A. Nagy, G. Toth, Y. Ma, Three-dimensional, multi-fluid, high spatial resolution MHD model studies of the solar wind interaction with Mars. *J. Geophys. Res.* (2011). doi: 10.1029/2010JA016272
43. Y. Lee, M. Combi, V. Tenishev, S. Bougher, D. Pawlowski, N. Franklin, Impacts of the Martian crustal magnetic fields on the thermosphere, ionosphere, and hot oxygen corona. *Bulletin of the American Astronomical Society*, **46**, abstract 306.01, Div. for Planetary Sciences, 46th Annual Meeting, Tucson, AZ (2014).

ACKNOWLEDGMENTS

The MAVEN Deep Dip 2 data sets reported in the paper are archived on the public version of the MAVEN Science Data Center (SDC) website, at the LASP url (https://lasp.colorado.edu/maven/sdc/public/) and on the Planetary Data System (PDS). Datacubes from three-dimensional model simulations reported in this paper are also available on the public MAVEN SDC website at https://lasp.colorado.edu/maven/sdc/public/pages/models.html. This work was partially supported by the Centre National d'Études Spatiales for the part based on observations with the SWEA instrument embarked on Maven. Part of this research was also carried out at the Jet Propulsion Laboratory, California Institute of Technology, under a contract with the National Aeronautics and Space Administration (NASA). A. Stiepen was supported by the Belgian American Educational Foundation and the Rotary District 1630. G. DiBraccio was supported by a NASA Postdoctoral Program appointment at NASA Goddard Space Flight Center, administered by Oak Ridge Associated Universities through a contract with NASA. The MAVEN project is supported by NASA through the Mars Exploration Program.

SUPPLEMENTARY MATERIALS

www.sciencemag.org/content/350/6261/aad0459/suppl/DC1
Supplementary Text

17 July 2015; accepted 21 September 2015
10.1126/science.aad0459

RESEARCH

Herbertsmithite appears to be a quantum spin liquid

Fu et al., *p. 655*

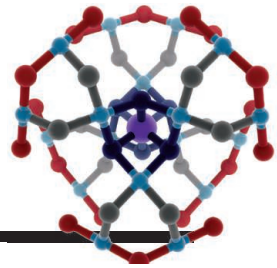

IN *SCIENCE* JOURNALS

Edited by **Stella Hurtley**

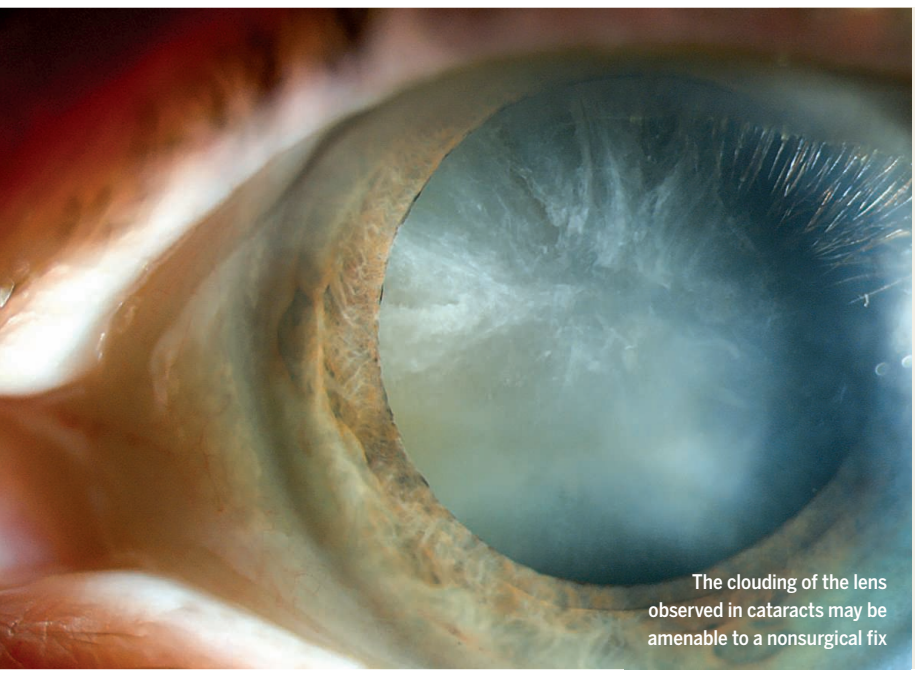

The clouding of the lens observed in cataracts may be amenable to a nonsurgical fix

OPHTHALMOLOGY

A visionary approach to transparency

Cataracts are the most common cause of vision loss, especially in our ever-increasing elderly population. Cataracts arise when crystallin, a major protein component of the eye lens, begins to aggregate, which causes the lens to become cloudy. Makley *et al.* explored whether small molecules that reverse this aggregation might have therapeutic potential for treating cataracts, which normally require surgery (see the Perspective by Quinlan). They used a screening method that monitors the effect of ligands on temperature-dependent protein unfolding and identified several compounds that bind and stabilize the soluble form of crystallin. In proof-of-concept studies, one of these compounds improved lens transparency in mice. — PAK

Science, this issue p. 674; see also p. 636

PLANT SCIENCE

Protecting against too much of a good thing

The slimy pink rot of potatoes is caused by the bacterium *Clostridium puniceum*, which cannot grow in the presence of oxygen. These bacteria produce a polyphenolic metabolite known as clostrubin that functions as an antibiotic. Shabuer *et al*. now show that the bacteria also use clostrubin to protect themselves from the aerobic environment of the potato tuber. — PJH

Science, this issue p. 670

MOVEMENT CONTROL

Generating complex movement patterns

What exactly does neuronal activity in the brain's motor cortex encode? In monkeys, Griffin *et al*. simultaneously recorded from a large number of muscles and from motor cortex cells that project directly to the motor neurons of the spinal cord. Even though the cortical cells had conventional directional tuning curves, different cortical cells were functionally connected to spinal cells with different muscle actions. — PRS

Science, this issue p. 667

ACTINIDE CHEMISTRY

High fives and sixes for Americium ions

You've probably heard of uranium and plutonium. Americium (Am) is less widely discussed outside chemistry circles, but the separation of this heavier radioactive element from nuclear waste streams is a major goal of fuel reprocessing research. The trouble is that trivalent Am ions are hard to tease apart from similarly charged lanthanide ions. Dares *et al*. now show that terpyridyl ligands appended to an electrode can promote the oxidation of trivalent Am ions to the pentavalent and hexavalent states (see the Perspective by Soderquist). These more highly charged ions should be easier to isolate for the subsequent use of the Am in next-generation nuclear reactors. — JSY

Science, this issue p. 652; see also p. 635

CLIMATE CHANGE

Historical perspectives on Old World drought

To understand the significance of climate prediction models of future drought, it is important to establish regional patterns of drought in the past. Cook *et al.* developed a drought atlas for the "Old World" (north Africa, the Mediterranean Basin, and Europe) based on tree-ring reconstructions. The data confirm that the Northern Hemisphere experienced unusually severe and extensive drought before the 20th century for reasons that are, as yet, not clear. — KVH

Sci. Adv. 10.1126. sciadv.15-00561 (2015).

QUANTUM SIMULATION

Filling a molecular lattice of light

Cold atoms in optical lattices normally interact only when two of them occupy the same lattice site. More-complex interactions would expand

PHOTO: PAUL WHITTEN/SCIENCE SOURCE

Downloaded from www.sciencemag.org on November 5, 2015

Published by AAAS

the potential of the system for quantum simulation. A promising approach is to use polar molecules instead of atoms, which interact at much longer length scales. However, "packing" the lattice with molecules is tricky. Moses *et al*. introduced bosonic ^{87}Rb atoms and fermionic ^{40}K atoms into an optical lattice, combined them into molecules, and brought the molecules into their ground state, achieving a considerable lattice filling of 25%. — JS

Science, this issue p. 659

PLANT GENETICS

How flowers separate males and females

Most flowering plant families have bisexual flowers with both male and female function. However, most members of the *Cucurbiticeae* family, which includes melons, cucumbers, and gourds, have unisexual flowers. To understand this difference in sex expression, Boualem *et al*. identified a cucumber gene expressed in the female flowers. Mutations in this gene were associated with solely male flowers. By integrating this finding into a sex determination model, the authors explain how unisexual flowers can coexist in the same plant. — LMZ

Science, this issue p. 688

NONHUMAN GENOMICS

Symbionts are adapted to work with corals

Many corals have formed mutualistic associations with dinoflagellate symbionts, which are thought to provide nutrients and other benefits. To examine the underlying genetics of this association, S. Lin *et al*. sequenced the genome of the endosymbiont dinoflagellate *Symbiodinium kawagutii*. The genome includes gene number expansions and encodes microRNAs that show complementarity to genes within the coral genome. Such microRNAs may be involved in regulating coral genes. Furthermore, coral and *S. kawagutii* appear to share homologs of genes encoding specific nutrient transporters. The findings shed light on how symbiosis is established and maintained between dinoflagellates and corals. — LMZ

Science, this issue p. 691

INFECTIOUS DISEASE

Outflanking RSV

Respiratory syncytial virus (RSV) infection can cause a severe respiratory illness in young children. Researchers are working to fashion a live attenuated vaccine, which would mimic the natural course of infection, but blocking viral replication also stems the immune response. Now Karron *et al.* report on a version of RSV that induced a protective immune response with decreased viral shedding in humans. Children who received the vaccine produced antibodies to RSV without symptoms in the subsequent RSV season. — ACC

Sci. Transl. Med. **7**, 312ra175 (2015).

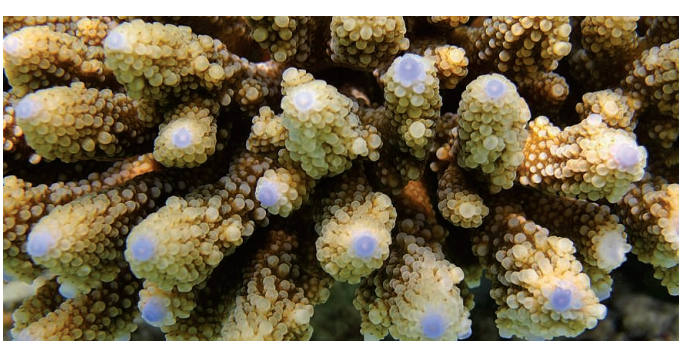

The genome-sequenced coral *Acropora digitifera* harbors the *Symbiodinium kawagutii* endosymbiont

PHOTOS: (FROM LEFT) MDC SEAMARC MALDIVES/WIKICOMMONS; EYE OF SCIENCE/SCIENCE SOURCE

IN OTHER JOURNALS

Edited by **Kristen Mueller** *and* **Jesse Smith**

Ocean-dwelling *Synechococcus* cyanobacteria can produce hydrocarbons

MICROBIOLOGY

Marine hydrocarbon cycling revealed

Up to 4 million tons of crude oil leak into the oceans every year as a result of human activities and natural seepage. But hydrocarbons and hydrocarbon-degrading bacteria abound even in waters minimally polluted by oil. Knowing that cyanobacteria have the capacity to produce long-chain alkanes and are abundant in surface waters, Lea-Smith *et al.* set out to determine whether these bacteria are a significant source of hydrocarbons. It turns out that together, the cyanobacteria *Prochlorococcus* and *Synecoccus* produce up to 700 million tons of hydrocarbons per year via their alkane biosynthetic pathways. These cyanobacteria may help to sustain hydrocarbon-degrading bacteria and thus unwittingly help to mitigate some fraction of anthropogenic pollution in the ocean. — CA

Proc. Natl. Acad. Sci. U.S.A. 10.1073/pnas.1507274112 (2015).

IMMUNOGENETICS

How heritable is autoimmunity?

For many complex diseases, a mix of a person's genes and their environment determines their susceptibility, with genetic influences often playing a greater role in children. Li *et al*. investigated how genes contribute to the development of autoimmune diseases such as type I diabetes and ulcerative colitis in children. By comparing 5000 pediatric autoimmune pediatric cases with over 36,000 healthy controls, the authors determined that genetics contributes substantially to susceptibility to autoimmune diseases. The highest heritability was observed for type 1 diabetes and juvenile idiopathic arthritis, whereas the environment played a greater role in

Published by AAAS

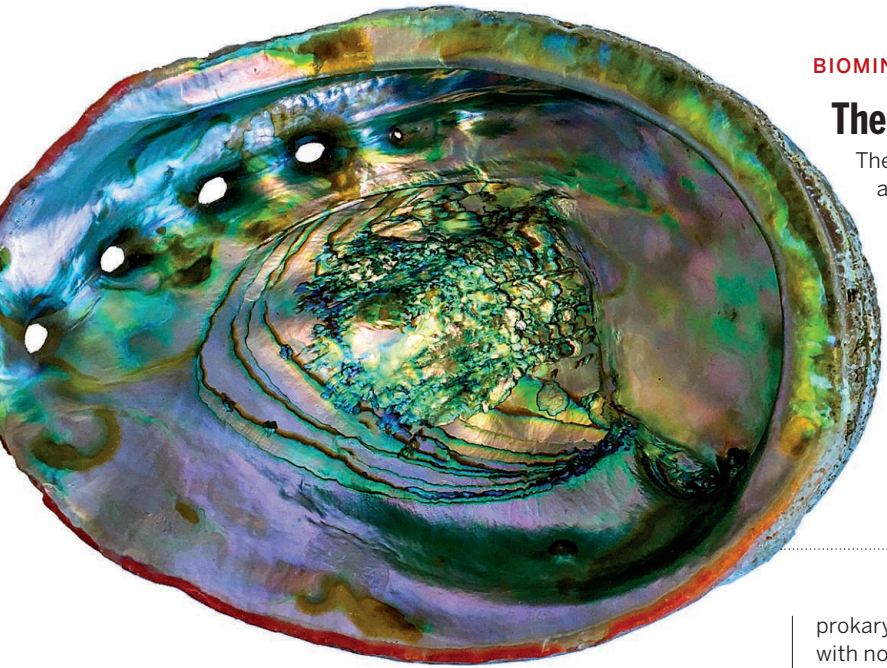

Abalone shells grow from amorphous calcium carbonate precursors

BIOMINERALIZATION

The pathway to mother of pearl

The material inside mollusk shells, nacre, is remarkably tough and also gives the shells their sheen. Nacre is a hybrid of aragonitic calcium carbonate and an organic matrix, but it's unclear how it starts growing. Using synchrotron-based microscopy and spectroscopy, DeVol *et al.* identified amorphous calcium carbonate from nacre growth fronts in sea snails. The amorphous precursors, which had previously been observed in calcitic biominerals such as sea urchin spicules, more closely resembled calcite than aragonite. Yet coral, which is also aragonitic, grows via an aragonite-like precursor. How nacre transforms calcite-like precursors into aragonite crystals remains unresolved. — NW

J. Am. Chem. Soc. 10.1021/jacs.5b07931 (2015).

susceptibility to lupus. Similar to autoimmunity in adults, heritability correlated highly with genetic variation in the major histocompatibility region. — LMZ

Nat. Commun. **6**, 8442 (2015).

DNA REPAIR

A membrane scaffold for repairing DNA

Many cellular processes inadvertently cause DNA damage, so cell survival critically depends on high-fidelity DNA repair. In *Escherichia coli*, the protein RecA plays a central role in repairing damaged DNA. RecA forms filaments on the ends of broken DNA, which allow the DNA repair machinery to search the genome for homologous sequences for accurate repair of the DNA break. Rajendram *et al*. now show that RecA interacts with specific lipids in the inner plasma membrane of *E. coli*. This membrane scaffolding acts to store RecA in the absence of DNA breaks. It also helps to nucleate and stabilize RecA filament bundles when breaks form, promoting DNA repair. — GR

Mol. Cell. 10.1016/j.molcel.2015.09.009 (2015).

STRUCTURAL BIOLOGY

Filling the structural landscape

Despite an ever-increasing number of high-resolution protein structures, as of 2013, about 40% of protein families had no representative structures, hindering understanding of their function. Ovchinnikov *et al*. take a step toward filling in this landscape by predicting structures for 58 of the 121 prokaryotic protein families with no known structures. They combined a recent version of Rosetta, which computes structures on the basis of an energy function, with amino acid residue contacts inferred from coevolution patterns in related protein sequences. The authors validated their methods by accurately predicting the structures of two proteins whose structures had previously been solved experimentally. — VV

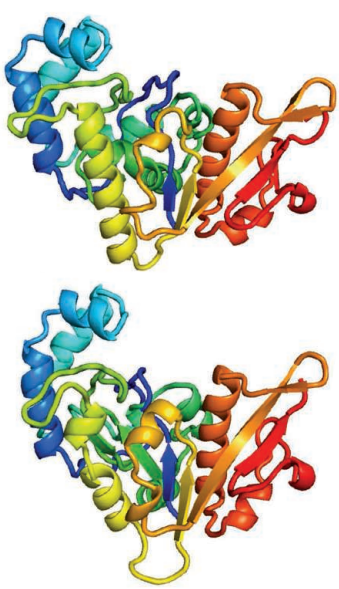

Authors' predicted protein structure (top) compared to the x-ray crystal structure (bottom)

eLife 10.7554/eLife.09248 (2015).

EDUCATION

MOOCs: Retention versus achievement

Massive open online courses (MOOC) open up higher education to citizens across the globe. As MOOCs continue to rapidly expand, the empirical research surrounding them strives to keep pace. Through examination of input characteristics, including learner demographics, prior experience, and self-reported commitment (data points that can be collected before the MOOC begins), Greene *et al*. provide insight into student retention and performance within the same MOOC. Coupled with survivor analysis, results showed that considerations such as intent to earn a certificate predicted retention, whereas the prior level of schooling predicted achievement. Depending on the goals of institutions interested in using MOOCs, data from this study can be used to determine whether any specific interventions should be implemented. — MM

Am. Educ. Res. J. **52**, 925 (2015).

MATERIALS SCIENCE

Grafting olefin polymers for stretchiness

Thermoplastic elastomers (TPEs) are stretchy rubber-like polymers that can be melt-processed, do not require cross-linking, and, unlike rubbers, can be recycled. Ohtaki *et al.* set out to create TPEs based solely on olefin polymers that would not require or be limited by the need for living polymerization processes. They grafted either isotactic or syndiotactic polypropylene segments to a backbone made from ethylene and α-olefins. The polypropylene is crystalline and imparts stiffness and a physical networks structure to the polymer, whereas the noncrystallizing backbone lets the polymer stretch. Samples showed up to 85% elastic recovery when stretched up to 1000%, rivaling the best linear block polyolefin TPEs. — MSL

Macromolecules 10.1021/acs.macromol.5b01975 (2015).

CREDITS: (FROM TOP) P.U.P.A. GILBERT; OVCHINNIKOV *ET AL*., *ELIFE* **4** (3 SEPTEMBER 2015) © ELIFE SCIENCES PUBLICATIONS LTD.

Published by AAAS

ALSO IN *SCIENCE* JOURNALS

Edited by **Stella Hurtley**

MICROBIOME

Function in the tree of life

How does the composition of microbial communities integrate functionally with the wider environment? Martiny *et al*. review how patterns of microbial species abundances in different environments and disease states can have strong evolutionary signals. Some environmental changes select the survival of organisms with conserved metabolisms requiring complex configurations of proteins and cofactors that have long evolutionary histories, such as methane producers. In contrast, surviving antibiotic exposure may only require a single gene that can be traded promiscuously among many unrelated organisms. So, depending on the key ingredient (whether it is temperature, light, nutrient, or a dose of antibiotic) and the evolutionary history of its complementary metabolism, shifting environmental conditions will have predictable effects at different levels within the microbial tree of life. — CA

Science, this issue p. 649

METABOLIC HEALTH

The clockwork of insulin release

In healthy people, blood glucose levels are maintained within a narrow range by several physiological mechanisms. Key among them is the release of the hormone insulin by pancreatic β cells, which occurs when glucose levels rise after a meal. In response to insulin, blood glucose is taken up by tissues that need fuel, such as muscle. β cells can anticipate the body's varying demand for insulin throughout the 24-hour day because they have their own circadian clock. How this clock controls insulin release has been unclear. Perelis *et al*. now show that the activity of transcriptional enhancers specific to β cells regulates the rhythmic expression of genes involved in the assembly and trafficking of insulin secretory vesicles (see the Perspective by Dibner and Schibler). — PAK

Science, this issue p. 650; see also p. 628

EPIGENETICS

Generations affected by histone changes

Parent and even grandparent environmental exposure can transmit adverse health effects to offspring. The mechanism of transmission is unclear, but some studies have implicated variations in DNA methylation. In a mouse model, Siklenka *et al*. found that alterations in histone methylation during sperm formation in one generation leads to reduced survival and developmental abnormalities in three subsequent generations (see the Perspective by McCarrey). Although changes in DNA methylation were not observed, altered sperm RNA content and abnormal gene expression in offspring were measured. Thus, chromatin may act as a mediator of molecular memory in transgenerational inheritance. — BAP

Science, this issue p. 651; see also p. 634

FRUSTRATED MAGNETISM

Peeking into an exotic magnetic structure

Cooling materials that contain magnetic interactions generally leads to an ordered magnetic state. In materials known as quantum spin liquids (QSLs), the geometry of the crystal lattice may prevent this ordered state from forming, even at absolute zero. The material herbertsmithite is thought to be a strong candidate for a QSL, but the nature of its ground state is still a mystery. Fu *et al*. measured shifts in the nuclear magnetic resonance signals of herbertsmithite to conclude that its ground state has a zero spin and is separated from the first excited state by an energy gap (see the Perspective by Furukawa). The results suggest that herbertsmithite is indeed a QSL. — JS

Science, this issue p. 655; see also p. 631

MICROBIOME

What makes the gut microbiome stable?

Classically, we think of our microbiome as stable, benign, and cooperative. Recent experimental work is beginning to unpick essential functions that can be attributed to the stable microbiota of humans. To be able to manipulate the microbiome to improve health, we need to understand community structure and composition and we need models to quantify and predict stability. Coyte *et al*. applied concepts and tools from community ecology to gut microbiome assembly. Independently developed models converged on a surprising answer: A high diversity of species is likely to coexist stably when the system is dominated by competitive, rather than cooperative, interactions. — CA

Science, this issue p. 663

PROTEIN SYNTHESIS

Proximity best for building protein complexes

The synthesis of protein subunits and their assembly into a fully functional complex are generally thought to be two distinct processes. Shieh *et al*. studied the synthesis and assembly of the luciferase complex in *Escherichia coli*. Organization of the luciferase subunits LuxA and LuxB side by side into an operon promotes their colocalized synthesis and assembly into an active enzyme complex. Indeed, the association between the subunits occurs as they are being synthesized on ribosomes, which helps order the sequence of subunit interactions. — GR

Science, this issue p. 678

STRUCTURAL BIOLOGY

Getting rid of carbon dioxide

In mammals, red blood cells deliver oxygen to tissues and remove carbon dioxide. Key to this essential process is a membrane protein called anion exchanger 1 (AE1) which transports bicarbonate (formed from carbon dioxide) out of red blood cells in exchange for chloride. This decreases the pH inside the blood cells, so that oxygen is released from hemoglobin and can diffuse into tissues. Arakawa *et al*. report the crystal structure of the transmembrane anion exchanger domain of AE1, which includes 14 transmembrane helices. The structure provides a basis for understanding the effects of mutations that lead to red blood cell diseases and also gives insight into the mechanism of ion transport. — VV

Science, this issue p. 680

PLANT EVOLUTION

Distant relatives can share gene function

The plants *Arabidopsis thaliana* and *Papaver rhoeas* (poppy) shared a common ancestor approximately 140 million years ago. Because of this evolutionary distance, although many of their genes share function, the mechanisms that allow these

genes to function are expected to have diverged. However, Z. Lin *et al*. found that a pair of genes that prevent self-fertilization in poppy can confer the same trait when expressed in *Arabidopsis*. This incompatibility was much more like that of poppy than that of incompatible close relatives of *Arabidopsis*. Thus, similar long-distance transfer of incompatibility, a trait of interest for plant breeding, may be useful between other distantly related species. — LMZ

Science, this issue p. 684

PUBLIC HEALTH

Hope for dengue control?

Each year, almost 400 million people around the world, many of them children, are infected with dengue virus. Most experience no or mild symptoms, but those that develop severe dengue may die. A recently developed vaccine offers hope but has modest efficacy. In a Perspective, Wilder-Smith and Gubler argue that the use of this vaccine can nevertheless have major public health benefits. The vaccine shows promise for reducing hospitalizations and appears to be safe for children between 9 and 16 years old. Licensing and using the vaccine now is likely to reduce the public health burden from dengue. It would also provide an opportunity to learn from its use while research toward more effective vaccines continues. — JFU

Science, this issue p. 626

GPCR SIGNALING

Agonist control of voltage sensitivity

Some G protein–coupled receptors (GPCRs) are affected by changes in plasma membrane potential. Rinne *et al*. found that depolarization enhanced signaling by the M_3 muscarinic acetylcholine receptor when the agonists choline or pilocarpine were bound. In contrast, depolarization attenuated M_3 receptor signaling when the agonists carbachol or acetylcholine were bound. Mutation of a critical residue in the binding pocket for agonists switched the response of the carbachol-bound receptor so that signaling was enhanced by membrane depolarization. These results may help to explain why drugs that are agonists of the same GPCR can have distinct effects. — JFF

Sci. Signal. **8**, ra110 (2015).

REVIEW SUMMARY

MICROBIOME

Microbiomes in light of traits: A phylogenetic perspective

Jennifer B. H. Martiny,* Stuart E. Jones, Jay T. Lennon, Adam C. Martiny

BACKGROUND: Microbial communities—microbiomes—are intricately linked to human health and critical ecosystem services. New technologies allow the rapid characterization of hundreds of samples at a time and provide a sweeping perspective on microbiome patterns. However, a systematic understanding of what determines microbiome diversity and composition and its implications for system functioning is still lacking. A focus on the phenotypic characteristics of microorganisms—their traits—offers a path for interpreting the growing amount of microbiome data. Indeed, a variety of trait-based approaches have been proposed for plants and animal communities, and this approach has helped to clarify the mechanisms underlying community assembly, diversity-process relationships, and ecosystem responses to environmental change.

Although there is a growing emphasis on microbial traits, the concept has not been fully appreciated in microbiology. However, a trait focus for microorganisms may present an even larger research opportunity than for macroorganisms. Not only do microorganisms play a central role in nutrient and energy cycling in most systems, but the techniques used to characterize microbiomes usually provide extensive molecular and phylogenetic information.

ADVANCES: One major difference between macro- and microorganisms is the potential for horizontal gene transfer (HGT) in microbes. Higher rates of HGT mean that many microbial traits might be unrelated to the history of the vertically descended parts of the genome. If true, then the taxonomic composition of a microbiome might reveal little about the health or functioning of a system. We first review key aspects of microbial traits and then recent studies that document the distribution of microbial traits onto the tree of life. A synthesis of these studies reveals that, despite the promiscuity of HGT, microbial traits appear to be phylogenetically conserved, or not distributed randomly across the tree of life. Further, microbial traits appear to be conserved in a hierarchical fashion, possibly linked to their biochemical and genetic complexity. For instance, traits such as pH and salinity preference are relatively deeply conserved, such that taxa within deep clades tend to share the trait. In contrast, other traits like the ability to use simple carbon substrates or to take up organic phosphorus are shallowly conserved, and taxa share these traits only within small, shallow clades.

ON OUR WEB SITE

Read the full article at http://dx.doi.org/10.1126/science.aac9323

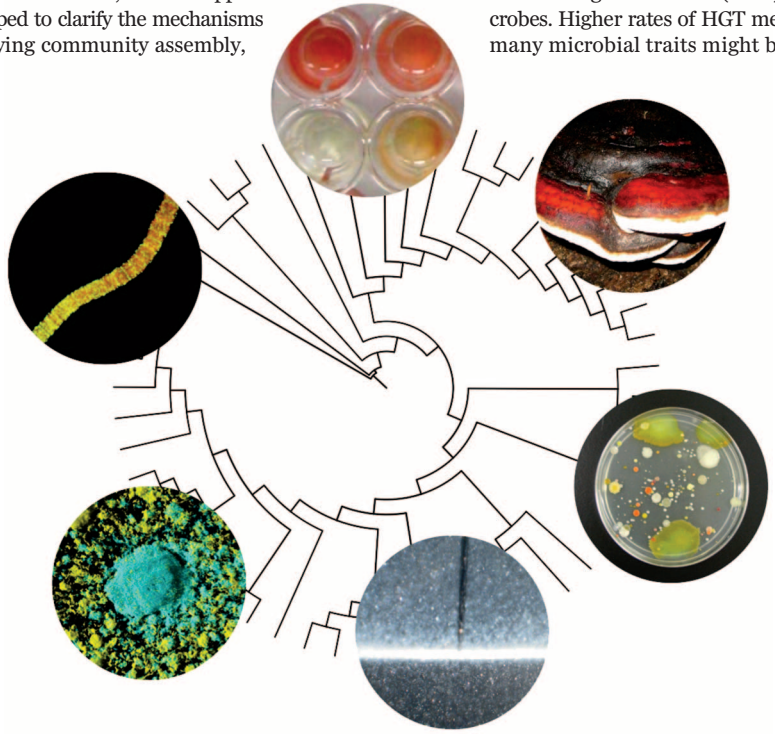

Measuring and mapping the phylogenetic distribution of microbial traits. Microbial traits encompass a range of phenotypic characteristics that vary in complexity, including (clockwise from top) virus resistance, cellulose degradation, salinity preference, nitrogen fixation, biofilm formation, and the production of alkaline phosphatase. Each trait can be measured in innumerable ways. For instance, it can be described by discrete or continuous metrics (e.g., the presence of a gene versus the number of gene copies) of potential or realized phenotypes (e.g., those assayed by functional metagenomics versus in situ activity). [Credits: C. Wiehe; M. Maltz; J. Martiny; L. Riemann; J. Haagensen; K. Frischkorn]

OUTLOOK: The phylogenetic, trait-based framework that emerges offers a path to interpret microbiome variation and its connection to the health and functioning of environmental, engineered, and human systems. In particular, the taxonomic resolution of biogeographic patterns provides information about the traits under selection, even across entirely different systems. Parallels observed among human and free-living communities support this idea. For instance, microbial traits related to growth on different substrates (e.g., proteins, fats, and carbohydrates) in the human gut appear to be conserved at approximately the genus level, a resolution associated with the level of conservation of glycoside hydrolase genes in bacteria generally. A focus on two particular types of traits—response and effect traits—may also aid in microbiome management, whether that means maintaining human health or mitigating climate change impacts. Future work on microbial traits must consider three challenges: the influence of different trait measurements on cross-study comparisons; correlations between traits within and among microorganisms; and interactions among microbial traits, the environment, and other organisms. Our conclusions also have implications for the growing field of community phylogenetics beyond applications to microorganisms. ■

The list of author affiliations is available in the full article online.
*Corresponding author. E-mail: jmartiny@uci.edu
Cite this article as J. B. H. Martiny *et al.*, *Science* 350, aac9323 (2015). DOI: 10.1126/science.aac9323

Downloaded from www.sciencemag.org on November 5, 2015

REVIEW

MICROBIOME

Microbiomes in light of traits: A phylogenetic perspective

Jennifer B. H. Martiny,[1]* Stuart E. Jones,[2] Jay T. Lennon,[3] Adam C. Martiny[1,4]

A focus on the phenotypic characteristics of microorganisms—their traits—offers a path for interpreting the growing amount of microbiome data. We review key aspects of microbial traits, as well as approaches used to assay their phylogenetic distribution. Recent studies reveal that microbial traits are differentially conserved across the tree of life and appear to be conserved in a hierarchical fashion, possibly linked to their biochemical complexity. These results suggest a predictive framework whereby the genetic (or taxonomic) resolution of microbiome variation among samples provides information about the traits under selection. The organizational parallels seen among human and free-living microbiomes seem to support this idea. Developments in this framework may offer predictions not only for how microbial composition responds to changing environmental conditions, but also for how these changes may alter the health or functioning in human, engineered, and environmental systems.

Microbial communities—microbiomes—are intricately linked to human health (*1*) and critical ecosystem services (*2*). New genetic technologies allow for the rapid characterization of hundreds of microbiome samples at a time (*3*, *4*). Although these data provide a sweeping perspective on microbiome patterns, we still lack a systematic understanding of what determines microbiome diversity and composition and its implications for system functioning.

A focus on microbial traits could help address this challenge. All of biology deals with traits, the phenotypic characteristics of organisms. Natural selection operates on traits within a species, altering or maintaining trait frequencies and the genes underlying them. An organism's traits govern its physiology and its interactions with other species and the environment. Ultimately, the collective traits of a community interact with the environment to regulate ecosystem functioning—the biological, chemical, and physical processes that transform nutrients and energy within an ecosystem.

Driven by an effort to be more quantitative and predictive, community ecology has renewed its focus on organismal traits. This approach has helped to reveal mechanisms underlying community assembly (*5*), the relationship between biodiversity and ecosystem functioning (*6*), and an ecosystem's response to environmental change (*7*). Much of current microbiome research—whether in human, natural, or engineered systems—aims to understand similar phenomena. Therefore, a trait-based approach could be useful for microorganisms as well.

Although there is a growing emphasis on microbial traits (*8*–*13*), the concept has not been fully appreciated in microbiology. On the one hand, characterizing microbial traits presents unique challenges. While plant traits, such as leaf thickness and biomass, can easily be measured on individuals from many species in a community context, similar in situ trait quantification of microbial individuals is technically difficult. Grappling with the breadth of evolutionary history of microorganisms also adds enormous complexity.

On the other hand, there are several reasons why a trait focus for microorganisms presents an even larger opportunity than for macroorganisms. First, a primary motivation for a trait-based approach is that particular traits should be closely linked to ecosystem functioning (*14*, *15*). Generally, traits that affect ecosystem functioning are termed "effect traits" (*7*). Most metabolic traits of microorganisms might be considered effect traits as they directly influence processes such as nutrient cycling (e.g., carbohydrate degradation and phosphate acquisition) and trace gas emissions (e.g., methanogenesis and methanotrophy). Thus, the number of gut microbes with the trait to degrade cellulose likely influences the digestion efficiency of plant material, just as the prevalence of microbes that can metabolize or produce methane likely influence the rate of methane emissions from soil.

Second, new approaches allow microbiologists to target the molecular underpinnings of traits from many individuals in a community (*16*), whereas plant traits are either measured on a handful of individuals in a community or inferred from trait databases (*17*). For microbiomes, metagenomics may offer a way to scale from the traits of individual organisms to community processes based on a random sample of individuals from a community (*16*), although not without some limitations (*18*).

Third, genomic techniques available to microbiologists provide phylogenetic information of the traits being characterized and give simultaneous insight into their evolutionary constraints. This phylogenetic context can be applied across different levels of genetic resolution to provide a path to compare results across systems and taxa. The same trait can be studied over short time scales within a population or across the entire tree of life, allowing both strain-level differences and macroevolutionary patterns to be considered. Such a flexible framework is imperative for microorganisms where the time scales of evolutionary and ecological processes overlap (*19*, *20*), but may also be useful for larger organisms (*21*).

Here, we summarize key aspects of microbial traits and recent approaches used to map their phylogenetic distribution onto the microbial tree of life. We place special emphasis on how traits vary in their degree of phylogenetic conservation and discuss the implications of this variation for interpreting microbiome variation. Finally, we present a phylogenetic framework for understanding how traits determine microbial composition and biogeographic patterns across diverse environments, including the human body, oceans, and soils.

Classifying and measuring microbial traits

We define traits broadly to encompass the physiological, morphological, or behavioral characteristics of a microorganism, without regard to whether they can be deconstructed into simpler traits (*22*, *23*). The flexible nature of the trait concept means that it is crucial to consider how traits are classified and measured when making cross-study comparisons (*15*).

One way to classify microbial traits is by their complexity (Fig. 1). The simplest traits are encoded by just one genetic locus, such that an organism's genotype matches a particular phenotype. But most traits are much more complex. Complex traits involve the interactions of many parts of the genome (i.e., epistasis), and their phenotypic manifestations are altered by interactions with the environment (*24*). An example of a simple trait is the ability to produce alkaline phosphatase (encoded by the presence of one gene) and therefore hydrolyze phosphorus from organic compounds (*25*) (Fig. 1A). A bacteriophage's host range might also be considered a relatively simple trait (Fig. 1B), as the ability to infect a particular host can be determined by a point mutation at a single locus (*26*). Like any classification system, however, this one is imperfect. When viewed at a broader scale, different constraints operate on host range. Coliphages are restricted to infecting coliform bacteria, whereas cyanophages are restricted to infecting cyanobacteria. Thus, host range probably involves most of a phage's genome and, in this way, is quite complex.

[1]Department of Ecology and Evolutionary Biology, University of California, Irvine, CA, USA. [2]Department of Biological Sciences, University of Notre Dame, Notre Dame, IN, USA. [3]Department of Biology, Indiana University, Bloomington, IN, USA. [4]Department of Earth System Science, University of California, Irvine, CA, USA.
*Corresponding author. E-mail: jmartiny@uci.edu

Examples of traits		Trait	Type of measurement: Discrete – Potential	Discrete – Realized	Continuous – Potential	Continuous – Realized
Simple	A	Organic phosphate utilization	Alkaline phosphatase activity in culture	Presence of strain in high/low P regions	Enzyme kinetics	Correlation of abundance with organic P gradient
	B	Bacteriophage host range	Infection of a particular host culture	Co-occurrence patterns with bacterial hosts	Rate of adsorption to susceptible hosts	Fraction of bacteria that a phage can infect in a community
	C	Cellulose degradation	Presence of cellulases or cellulosome complex in genome	In situ cellulose degradation	Number of cellulases in a genome	In situ rate of cellulose degradation
	D	Biofilm formation	Ability to form a biofilm in culture	In situ biofilm formation	Biofilm thickness in culture	Relative abundance in biofilm versus nonbiofilm samples
	E	Nitrogen fixation	Ability to fix nitrogen in culture	In situ expression of *nif* genes	Kinetics of nitrogen fixation	Correlation of *nif* genes with N fixation rates
	F	Methanogenesis	Presence of genetic pathway in genome	Ability to produce methane in situ	Methane production kinetics	In situ rate of methane production
Complex	G	Salinity preference	Preference for marine or freshwater media	Found in marine versus terrestrial habitats	Salinity optimum in lab assay	Salinity corresponding with peak abundance

Fig. 1. Examples of microbial traits and their measurement. The traits are ordered vertically from simple to complex and consider not only how many genes are directly involved in encoding the trait, but also how integrated the trait is with the rest of the organism's cellular machinery. While each trait can be measured in a variety of ways, the matrix contrasts discrete versus continuous and potential versus realized measurements (see text). Photos: (**A**) *Trichodesmium* trichome from the Sargasso Sea incubated with the ELF 97 phosphatase substrate. Green labeling indicates sites of alkaline phosphatase activity; orange is autofluorescence of the phycoerythrin pigment. (**B**) Infection of a bacteriophage on the marine cyanobacterium *Synechococcus*. The pink wells are *Synechococcus* without phage; the bottom wells include phage, which lyses the cells and clears the culture's pigments. (**C**) Brown rot fungi like *Antrodia juniperina* degrade cellulose. (**D**) Biofilm of two green fluorescent protein–labeled *Vibrio cholerae* strains imaged by confocal microscopy. (**E**) Growth of a heterotrophic diazotroph in N-free medium with a vertical oxygen gradient. An oxygen microelectrode points to the band of growth. (**F**) Methanogens produce large amounts of methane in the rumens of cattle. (**G**) Diversity of salt marsh heterotrophs growing on high-saline agar. [Photo credits: K. Frischkorn, Dyhrman Lab, Columbia University; C. Wiehe; M. Maltz; J. Haagensen; L. Riemann, University of Copenhagen; K. Dill-McFarland, University of Wisconsin-Madison; J. Martiny]

To further complicate matters, the same trait can be measured in innumerable ways. For instance, all traits can be described discretely or continuously (Fig. 1). The ability of a fungus to degrade cellulose is a discrete metric (Fig. 1C), but the kinetic parameters of a particular cellulase enzyme are continuous, as they describe activity as a function of substrate concentration. The salinity preference of bacteria can be classified into freshwater or marine-occurring species (Fig. 1G), much as plants are traditionally classified into shade-tolerant and sun-loving species. Alternatively, its preference could be defined quantitatively by the salinity of optimal growth.

Another key axis of trait measurement is whether the metric assesses potential or realized phenotypes. Analogous to the fundamental versus realized niche concept used in classical ecology (*27*), the range of an organism's potential phenotypes is likely broader than the range of realized phenotypes that occur in its natural habitat. Thus, the presence or absence of particular genes or pathways in a microbial genome is a discrete assessment of its potential phenotype (*28*, *29*). For instance, codon usage bias and ribosomal RNA (rRNA) operon copy number provide continuous estimates of potential growth strategies (*30*, *31*).

Laboratory assays also measure potential traits, although more directly than genomic information. In particular, physiological performance curves provide detailed predictions about the potential range (niche width) and optimal conditions for a microbe's growth across an environmental gradient [e.g., temperature (*32*) or soil moisture (*23*)]. Laboratory cultures can also be used to test predicted phenotypes on the basis of genome sequences—for instance, whether the number of extracellular enzyme genes reflects an organism's potential to degrade carbohydrates (Fig. 1C). A laboratory study supports this idea for some genes; the number of polyphenol oxidase

genes in fungal genomes was correlated with the enzyme's activity in cultures (*33*).

Nonetheless, an organism's realized phenotype in situ may differ from measures of its potential phenotype. Traits can be modified by interactions with the environment (i.e., trait plasticity) and interactions with other organisms. As a result, a microbe's optimal temperature for growth in the laboratory might differ from the temperature of its maximum abundance in the field (*34*), or the sequence-based inference of gene function may be incorrect (*35*). For plants, realized phenotypes are often quantified in the field (e.g., leaf area or photosynthetic rate). In microbial systems, direct quantification of trait phenotypes "in the wild" is challenging, although technologies such as microautoradiography and fluorescence in situ hybridization (MAR-FISH), nanoscale secondary ion mass spectrometry (NanoSIMS), and cell sorting show great promise (*36*–*38*). Mostly, however, realized phenotypes are inferred from the biogeographic patterns of microorganisms (*39*), which we will return to below.

Phylogenetic conservatism of traits

The collection of traits that defines an organism depends on its evolutionary history. However, the potential for horizontal gene transfer (HGT) among microorganisms means that many traits might be unrelated to the history of the vertically descended parts of the genome (*40*). Gene loss and rapid evolution can further obscure a trait's phylogenetic signal. Yet, recent work indicates that most traits are at least somewhat conserved across Bacteria and Archaea (*11*, *41*), as well as microbial eukaryotes like Fungi (*42*). Specifically, despite the promiscuity of HGT, closely related microbial taxa share more similar traits than expected if the traits were distributed randomly across a phylogenetic tree. [This test of trait conservatism differs from that of phylogenetic niche conservatism, which only considers changes by vertical descent (*43*).]

Not only are microbial traits phylogenetically conserved, but the depth of their conservation differs among traits. This result holds true when using at least three different approaches. The first approach links phenotypic traits of isolates to their evolutionary relatedness. In such studies, microbial traits are quantified by using laboratory isolates and a genetic estimation of phylogenetic relatedness among the isolates. For example, a variety of continuous trait metrics, ranging from maximum respiration rate to optimal soil moisture, were quantified for a collection of heterotrophic bacteria and fungi isolated from soil communities (*23*). Subsequently, the variation of each trait among taxonomic levels was partitioned. For traits associated with soil moisture preference, much of the variation among strains was deeply conserved; more than half of the variation in moisture niche breadth (the tolerance of a strain to variation in soil moisture) could be assigned at the phylum level. In contrast, only one-third of the variability in motility could be accounted for at the class level (Fig. 2A).

Another example comes from a study that probed hundreds of bacterial isolates to determine their ability to grow on a diverse array of carbon substrates (*41*). Here, the depth of phylogenetic conservatism of a trait was estimated from the average sequence distance to the root node of clades, where at least 90% of taxa share the trait. In general, the ability to use each substrate was nonrandomly distributed across the phylogeny; however, the level of conservation of these traits was shallow. Thus, closely related strains of >98% similarity in 16*S* rRNA sequence may still have distinct substrate use profiles.

A second approach quantifies trait conservation by extracting information from the wealth of microbial genome sequences that are available (presently ~30,000). For simple traits, one can quantify the presence or absence of individual genes in a genome. For instance, the potential ability to degrade various carbohydrates can be assayed by the presence of various families of glycoside hydrolase genes (*44*). For more complex traits, one can target particular genomic subsystems or whole-cell metabolic networks (*45*). For example, in an analysis of 19 subsystems across 26 prokaryotic phyla, oxygenic photosynthesis, a trait found only in the phylum Cyanobacteria, was the most deeply conserved subsystem (*41*). In contrast, metabolic capabilities like sulfur oxidation and nitrogen fixation were less conserved, albeit more so than carbon substrate usage (Fig. 2B).

A third way to estimate phylogenetic conservation of traits relies on compositional variation among sampled communities. These patterns can provide correlative evidence about the taxonomic and genetic level at which microbial groups share response traits, or traits that influence how a species' abundance or biomass is altered by an environmental change (*7*, *46*). Thus, the ability to enter dormancy is a trait that may influence a microorganism's response to environmental stresses, such as fire and drought (*47*). Often, however, it is useful to consider a taxon's response to the environment as a trait itself (*22*, *48*), rather than the conglomerate of traits underlying the response (*49*). For instance, the abundance of some bacterial phyla (e.g., Verrucomicrobia, Bacteriodetes, and Acidobacteria) showed significant correlations with soil properties like pH and inorganic nutrient concentrations within a pasture, suggesting that taxa within these phyla share similar traits (*39*). In a larger-scale study of soils collected throughout the United States, bacteria within the class β-Proteobacteria and phylum Bacteroidetes tended to be more abundant in soils with higher organic carbon availability (as measured by carbon mineralization rate), whereas those within the phylum Acidobacteria were more abundant in soils with lower carbon availability (*50*). This pattern indicates that the traits underlying an oligotrophic (low nutrient) or copiotrophic (high nutrient) strategy may be deeply conserved among soil bacteria.

Experiments can also provide evidence about the conservation of response traits. For example, the responses of soil microbes to added water were quantified by rRNA abundances in dry California grasslands (*51*) (Fig. 2C). The response strategies to sudden water availability were highly conserved. Taxa within a phyla responded in a consistent manner; representatives from Verrucomicrobia and Actinobacteria responded quickly, whereas Proteobacteria tended to show more delayed responses. In a longer-term experiment, the responses of grassland leaf litter microbes to 3 years of drought (reduced by temporary rain shelters) and added nitrogen were also significantly conserved (*52*). Here, the depth of response was quantified by correlating the genetic distance between all taxon pairs and the similarity of their response. The responses of fungal taxa to drought and nitrogen were both positively correlated at the finer taxonomic levels (<5% shared 28*S* rDNA sequence similarity; Fig. 2D). However, drought responses were also signficantly correlated at broader levels of taxonomic resolution (up to 7.6% sequence similarity) than were nitrogen responses, indicating that drought responses are more deeply conserved than nitrogen responses.

A hierarchy of trait conservation

To quantify patterns of microbial trait conservatism, we searched for published studies that estimated (or allowed us to estimate) the depth of clades where prokaryotic taxa consistently shared trait values. For instance, clades of the marine cyanobacterium *Synechococcus* show distinct temperature profiles (a continuous, realized metric) on the basis of their biogeographic patterns (*53*). We then estimated the median depth of these different clades using a 16*S* rRNA phylogeny in another study (*54*). In another example, the estimate of the depth of methanogenesis was based on a discrete, potential metric—the presence of this subsystem across all sequenced bacterial genomes (*41*). Such cross-study differences in trait classes and measurement could bias the estimates of phylogenetic depth in some unknown way. At the same time, phylogenetic depth was assayed with the same phylogenetic marker (the 16*S* rRNA gene) in all but one study (table S1), and in this way, the estimates are comparable.

Despite these complications, the synthesis reveals a hierarchy of phylogenetic conservatism among traits. The response traits of pH and salinity preference appear to be relatively deeply conserved (Fig. 3), in agreement with past studies showing that pH and salinity affect the biogeographic distribution of deep phylogenetic clades (*55*, *56*). In contrast, long-term drought response and temperature optimum are more finely conserved, or only shared consistently by taxa within smaller clades of bacteria. A similar hierarchy appears to apply to effect traits involving the use of alternative electron acceptors; methanogenesis is the most deeply conserved trait noted in Fig. 3, whereas dissimilative sulfate reduction and denitrification are notably less so. The effect traits of simple carbon use and organic P uptake seem to be much shallower than those modifying the electron transport chain. Finally, resistance to specific bacteriophage varies depending on particular point mutations and thus, one might argue that this trait is not conserved at all.

Our findings are consistent with the view that traits encoded by more complex subsystems

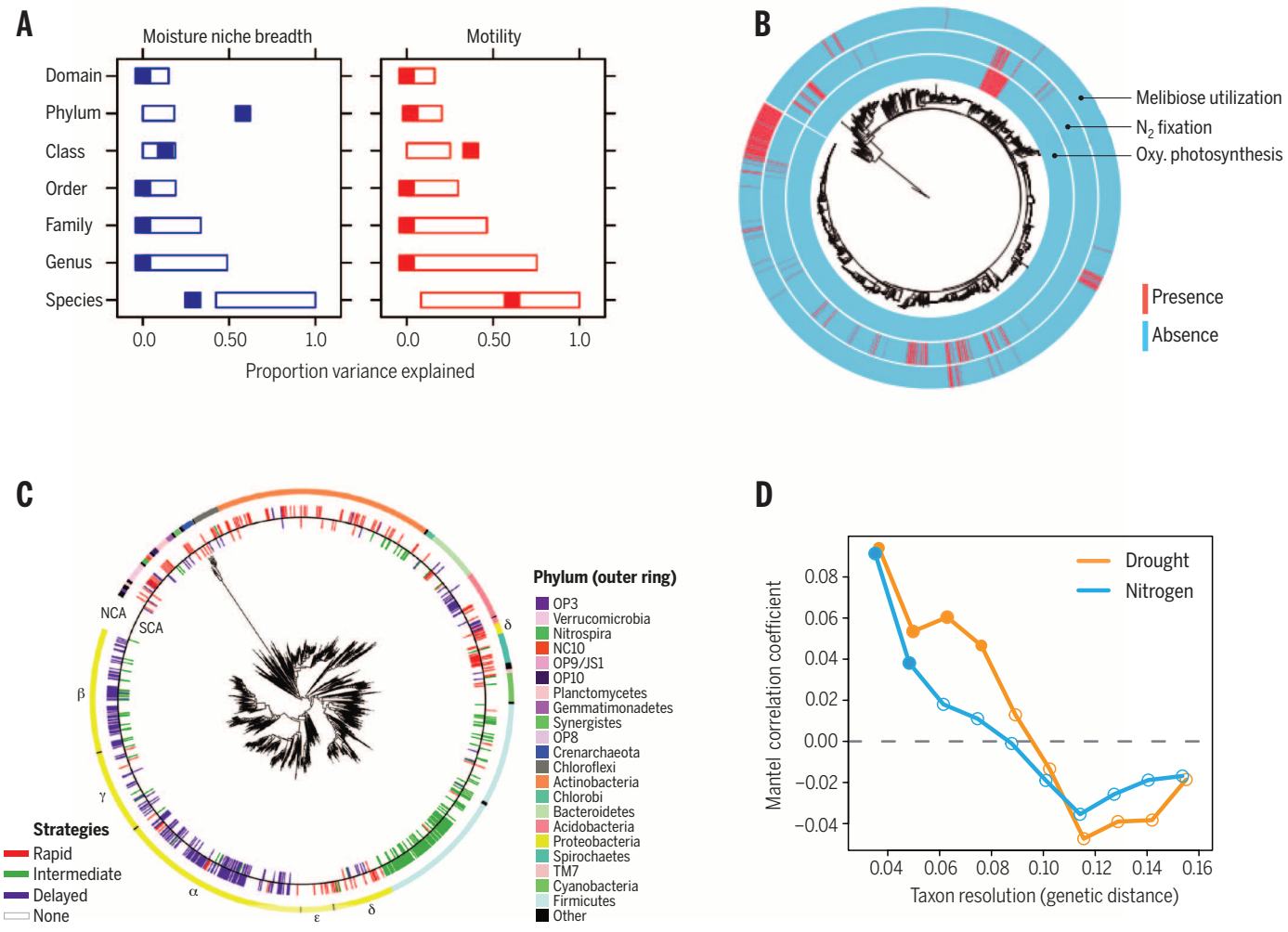

Fig. 2. Evidence for the phylogenetic conservatism of microbial traits. (**A**) By measuring phenotypic traits among a collection of bacterial and fungal soil isolates, variation in moisture niche breadth and motility can be attributed to different taxonomic levels (*23*). (**B**) With the use of data from fully sequenced prokaryotes, the presence (red lines) or absence (blue lines) of genes encoding three traits (the three concentric rings) can be determined. The phylogenetic depth of each lineage sharing this trait can then be quantified and compared against a random model. [Reprinted with permission from (*41*)]. (**C**) An experiment provides information on the phylogenetic distribution of a prokaryote's response to increased water availability. The response strategy (rapid, intermediate, or delayed) of each soil taxon to added water is shown by the red, green, and purple lines in the inner two circles (one for each of two field locations labeled NCA and SCA) around the phylogenetic tree. The outermost ring indicates the phylum designation of the taxa. [Reprinted with permission from (*51*)]. (**D**) A global change experiment suggests that the response of leaf litter fungi to drought (orange) is more deeply conserved than that to nitrogen addition (blue). The significance of the correlation relating the genetic distance between two fungal taxa and the similarity of their response to the treatment (drought or nitrogen addition) depends on the genetic resolution of the taxon definition (filled circles denote a significant correlation and open circles, a nonsignificant correlation). The drought response shows significant correlations at broader resolutions (the genetic distance of the taxon definition) than the nitrogen response. [Redrawn with permission from (*52*)]

involving many interacting proteins are less likely to be subject to horizontal transfer (*41*, *57*). Methanogenesis, the most deeply conserved trait examined, involves a large subsystem of genes for conversion of CO_2 (or acetate) to methane, as well as for synthesizing unique cofactors. In comparison to methanogenesis, dissimilative sulfate reduction requires fewer additional proteins, but does use a unique membrane-bound cytochrome complex and an atypical mechanism for translocation of protons (*58*). Although denitrification uses several unique membrane proteins, it is widely distributed among prokaryotes (*59*) and biochemically quite similar to aerobic metabolism. Thus, it is perhaps relatively easy for denitrification proteins to transfer into an aerobic ancestor (or evolve convergently). At the same time, it seems somewhat surprising that conservation of temperature preference is so shallow, when this phenotype could potentially involve a variety of underlying traits throughout a cell's machinery. However, while this reasoning may apply to extreme temperature adaptation (*60*), a shallow level of conservation suggests that adaptation to minor temperature differences involves simpler traits that evolve on shorter time scales (*61*).

Trait conservatism and biogeography

The idea that traits are hierarchically conserved is directly applicable to the interpretation of microbial biogeography, broadly defined as the spatial and temporal variability in microbial composition among free-living and host environments. To illustrate this point, we first consider the case study of the Cyanobacterium *Prochlorococcus*, for which we know a great deal about both the phylogenetic distribution of its traits and its biogeographic patterns. This phototroph is found throughout the world's oceans, spanning multiple environmental gradients. At the deepest phylogenetic level, *Prochlorococcus* is broadly divided into two groups: high- and low-light adapted clades (Fig. 4A), first defined by physiological measurements of cultured isolates (*62*). At the next-deepest level, metagenomic sequencing suggests that the

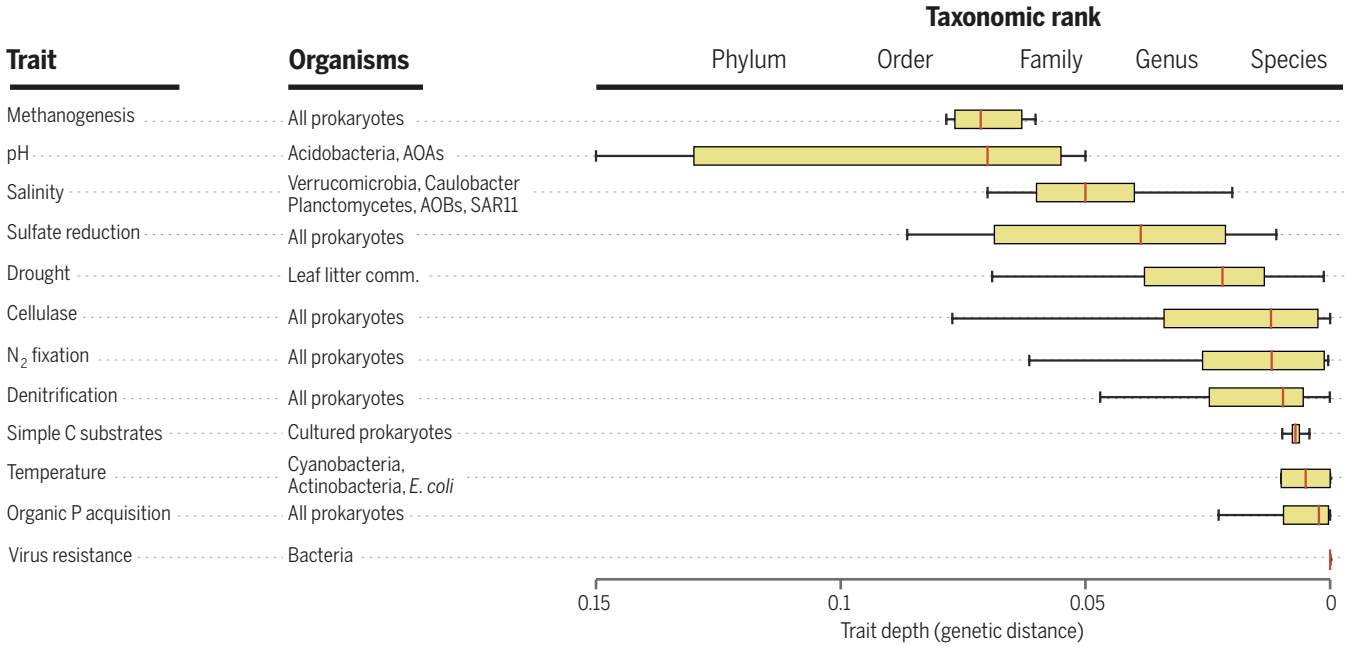

Fig. 3. Prokaryotic traits are conserved at different phylogenetic depths. A box plot of the depth of clades within which taxa consistently share a trait measured as the genetic distance to the root node of a clade (bottom axis; usually of the 16S rRNA gene). For some traits, the distribution is based on several studies, each with one estimate. For other traits, we report the distribution calculated by a single study. For comparison, we show rough taxonomic levels on the top axis. Details of studies are reported in table S1.

high-light clade can be divided into high- and low-iron adapted clades (*63*). The high-iron clade can be further divided into subclades that differ in their temperature preferences (Fig. 4A) (*64*), and at the finest phylogenetic scale, genomic and physiological analyses demonstrate variability in nitrogen and phosphorus acquisition traits (*65*–*67*).

The macroevolutionary picture of *Prochlorococcus* traits that emerges is consistent with how its biogeographic patterns depend on phylogenetic resolution. Depending on the sequence similarity used to define a taxon, the ability of specific environmental variables to explain *Prochlorococcus* composition varies in agreement with the relevant traits (Fig. 4B) (*68*). Hence, light level explains a significant amount of compositional variation across samples from the Pacific and Atlantic oceans when *Prochlorococcus* is grouped into broad taxa, whereas nutrient concentrations only explain variation at the finest taxonomic levels.

Although our detailed understanding of the *Prochlorococcus* lineage is exceptional, the idea of differentially conserved traits may generally help to predict compositional variation in any microbial system. Specifically, changes in the environment that select on deep traits should alter microbiome composition at broad taxonomic levels (orange versus blue symbols in Fig. 5). In contrast, selection on shallow traits should result in compositional shifts at finer taxonomic levels (solid versus hatched symbols in Fig. 5). Thus, the resolution at which microbiome composition varies among samples may give information about the phylogenetic conservation of the traits under selection.

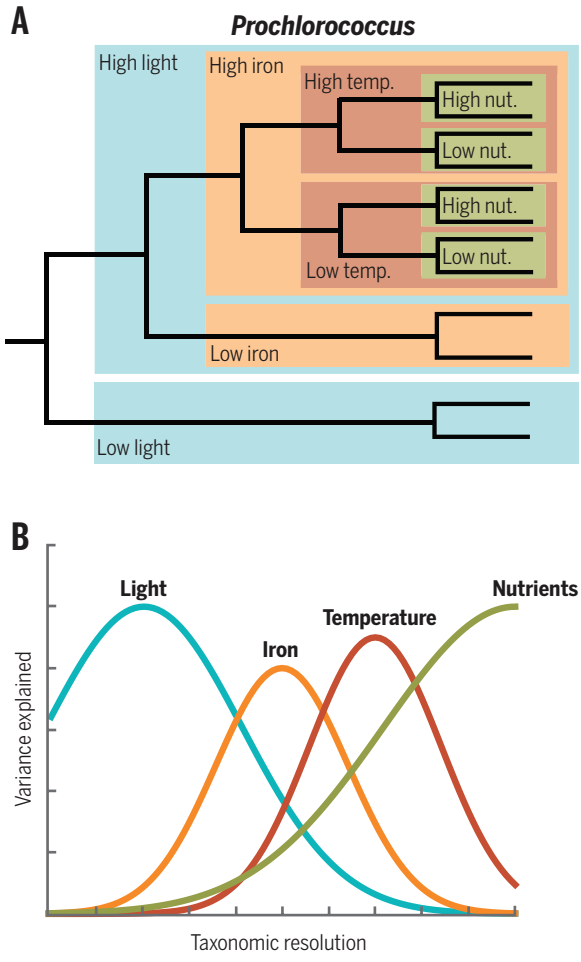

Fig. 4. Trait conservation in *Prochlorococcus* is related to its biogeographic patterns. (**A**) Traits involving adaptations to light, iron concentration, temperature, and nutrient acquisition levels map onto the *Prochlorococcus* phylogeny in a hierarchical manner. (**B**) A schematic of the relationship between taxonomic resolution (usually defined by sequence similarity of a marker gene) and the ability of various environmental variables to explain variation in *Prochlorococcus*. The resolution at which the environmental variables best explain composition (the peak of the curves) corresponds to the phylogenetic depth of distinct trait divisions shown in (A). [Adapted from (*68*)]

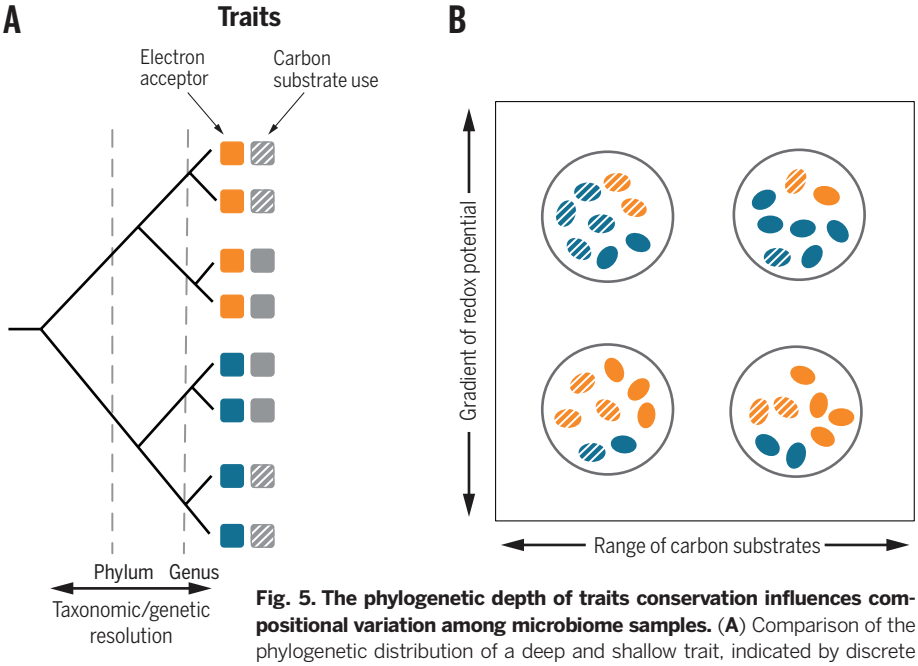

Fig. 5. The phylogenetic depth of traits conservation influences compositional variation among microbiome samples. (**A**) Comparison of the phylogenetic distribution of a deep and shallow trait, indicated by discrete categories for each taxon at the tips of the tree. A deeply conserved trait, such as the ability to use some alternative electron acceptors, is denoted by the orange and blue symbols. A shallower trait, like the ability to use a particular carbon substrate, is denoted by the solid and striped gray symbols. (**B**) How microbial composition shifts among samples will depend on the depth of conservation of the traits under selection. In this cartoon landscape, the large circles represent a sample; the cells within that sample carry traits designated by the colors and patterns in (A). In this example, a change in redox potential across a landscape (*y* axis) alters microbial composition at the phylum level, such that the relative abundance of blue and orange cells is altered. A change in carbon substrate availability (*x* axis) alters composition at the genus level, so that the relative abundance of striped and solid cells shifts, but not that of orange and blue cells.

Both host-associated and free-living systems provide examples of this connection between trait conservation and microbiome variation. The human skin microbiome differs in composition among three habitat types: dry, moist, and sebaceous skin (*69*). Further analysis reveals that these habitat preferences are only consistent [or "coherent" sensu (*39*)] among taxa within the genus or sharing at least 97% 16*S* rRNA sequence similarity (*70*). Exactly which traits are driving this distribution remain to be determined. A common species in moist skin sites, *Staphylococcus epidermidis*, grows aerobically and uses urea as a nitrogen source, whereas the most common species in sebaceous sites, *Propionibacterium acnes*, is a facultative anaerobe and hydrolyzes the triglycerides in skin lipids (*71*).

In contrast, virulence traits of skin microorganisms appear to be even more finely conserved than habitat preference. For example, the genetic differences among strains of *P. acnes* associated with acne versus healthy skin are relatively minor (*72*). Similarly, virulent strains of *S. epidermidis* differ from nonvirulent strains by a four-gene operon involved in biofilm formation and an insertion sequence element, genetic changes that may be associated with horizontal gene transfer (HGT) events (*73*). In general, virulence potential may be a shallow trait, as it often appears to evolve independently via HGT—for instance, among microbes such as *Escherichia coli* (*74*) and *Pseudomonas aeruginosa* (*75*).

Microbial traits related to growth on different substrates (e.g., proteins, fats, and carbohydrates) in the human gut appear to be conserved at approximately the genus level, a resolution also associated with gut enterotypes (*76*). In response to both short- and long-term dietary patterns, gut taxa within a genus seem to respond similarly, whereas the responses of genera within phyla are not consistent (*77*, *78*). Specifically, within the phylum Bacteroidetes, *Bacteroides* species are generally enriched in diets high in protein and fat, whereas *Prevotella* species are enriched in diets high in carbohydrates. These compositional shifts may be due to selection for traits, such as the ability to degrade particular carbohydrates (*79*) and bile tolerance (*77*). Echoing the taxonomic level of these diet responses, an analysis of bacterial genome sequences finds that bacterial glycoside hydrolase (GH) genes are generally conserved at the genus or species level (*44*). Supporting this pattern, family level is not predictive of the abundance of carbohydrate-active enzymes (GHs and polysaccharide lyases) encoded by human-associated bacterial genomes (*80*).

Finally, chronic gut syndromes in humans appear to differ from those of healthy microbiomes at even broader taxonomic levels. Thus, the composition of gut microbiomes from inflammatory bowel disease (IBD, including ulcerative colitis and Crohn's disease) patients differs from that of healthy microbiomes at the class and phylum levels (*81*). The relative abundance of taxa within the class Clostridia and phylum Bacteroidetes decreased in IBD patients, whereas taxa within the Proteobacteria and Bacilli increased. Similar community patterns were observed in patients with *Clostridium difficile* infections relative to that of healthy volunteers also receiving antibiotic treatment (*82*). These broad-scale shifts suggest that inflammatory conditions impose selection for deep microbial traits, perhaps related to oxygen and redox potential preference. Likewise, the phylum-level shifts found along redox gradients in ocean oxygen minimum zones or sediment profiles (*83*, *84*) are parallel to the broad changes found in chronic gut syndromes.

Challenges and implications

Microbial traits appear to vary consistently in the degree to which they are conserved. Further, the parallels among host-associated and free-living communities suggest that this hierarchy of trait conservation may underlie similar community shifts across entirely different systems. Specifically, we propose that selection on shallow traits in a microbiome will lead to fine-scale taxonomic shifts, whereas selection on deeper traits will lead to broader-scale shifts. Thus, viewing microbiome patterns in light of traits in one system can provide an initial hypothesis for the distribution of traits in other systems. Such hypotheses may further shed light on unexplained microbiome variation by narrowing down the traits that might be under selective pressure.

It is worth highlighting several obstacles to inferring the level of trait conservation from distributional patterns. First, interpretations about trait conservation will be sensitive to the particular taxa present in a study. If a phylum is only represented by a handful of narrow lineages, then these lineages may not be representative of the phylum in other systems. A similar issue arises when interpreting variation in the abundance of broad taxonomic groups, without regard to whether individual lineages within those groups vary consistently (*70*). In both cases, the trait of interest might be conserved at a finer phylogenetic level than suggested by the samples at hand.

Second, we have primarily discussed traits in isolation to one another, but for a variety of reasons, traits within and among taxa are often correlated (*85*), presenting challenges and opportunities for studying microbial traits. For example, within an organism, the use of methods such as metagenomics and metatranscriptomics to characterize some traits might be misleading, because interactions with other traits might be essential to their realized phenotype (*18*). Across taxa, if many traits are correlated, then one may be able to reduce the multidimensionality of microbial traits. This idea is demonstrated well by the leaf economic spectrum in plants; the combination of leaf traits in a plant species appears constrained by physiological trade-offs (correlations) between these traits (*86*). Correlations between response

and effect traits may also present an opportunity for predicting how changes in environmental conditions lead to changes in microbial functioning (*46*, *48*). For example, a model based on the response and effect traits of phytoplankton performed well in predicting gross primary production in lakes across a variety of environmental conditions (*87*).

Last, the extent to which gene-by-environment interactions (trait plasticity) and biotic interactions (such as microbe with microbe or host with microbe) influence microbial composition is unclear. Such interactions might hinder inferences across systems, but with so little comparative data on these issues [but see (*88*)], it is difficult to speculate about the importance of this complication.

Our conclusions also have implications for the growing field of community phylogenetics (*89*–*91*) beyond applications to microorganisms. For instance, one question of broad interest is whether phylogenetic diversity (the amount of phylogenetic distance between all species in a community) influences ecosystem functioning (*92*, *93*). A hierarchy of trait conservation would imply that the strength of this relationship should depend on the traits involved. Variation in traits that are generally finely conserved (such as simple carbon usage or nutrient uptake for microbes) may not be captured by phylogenetic relatedness metrics that emphasize deep relationships between species. This might explain why some studies find a phylogenetic diversity-functioning relationship (*94*) and others do not (*95*).

Likewise, differences in trait conservation may help to explain the mixed support for the hypothesis that evolutionary relatedness can help predict the outcome of species interactions (*96*). For example, if the outcome of competition depends on a microbe's ability to acquire organic phosphate, a trait that seems to be finely conserved, then the large phylogenetic distance between most species in the community may not be correlated with their competitive outcome. In contrast, if the outcome depends on niche partitioning of a moisture axis, which seems to be more deeply conserved, then phylogenetic distance might better capture this trait variation.

There is growing evidence that microbial composition can directly affect functioning in human and environmental systems (*97*, *98*). This fact has practical implications for human health, engineering, and natural environments (*99*–*101*). However, it remains unclear when and where microbial composition will be functionally relevant. For microorganisms specifically, a phylogenetic trait framework offers a path toward a predictive understanding of this role. Pinpointing the effect and response traits responsible—and their degree of phylogenetic conservation—may aid in microbiome management, whether that means maintaining human health or mitigating climate change impacts.

REFERENCES AND NOTES

1. A. L. Kau, P. P. Ahern, N. W. Griffin, A. L. Goodman, J. I. Gordon, Human nutrition, the gut microbiome and the immune system. *Nature* **474**, 327–336 (2011). doi: 10.1038/nature10213; pmid: 21677749
2. A. L. Peralta, D. Stuart, A. D. Kent, J. T. Lennon, A social–ecological framework for "micromanaging" microbial services. *Front. Ecol. Environ* **12**, 524–531 (2014). doi: 10.1890/130308
3. J. Peterson *et al*., The NIH Human Microbiome Project. *Genome Res.* **19**, 2317–2323 (2009). doi: 10.1101/gr.096651.109; pmid: 19819907
4. J. A. Gilbert, J. K. Jansson, R. Knight, The Earth Microbiome Project: Successes and aspirations. *BMC Biol.* **12**, 69 (2014). doi: 10.1186/s12915-014-0069-1; pmid: 25184604
5. J. D. Olden, N. L. Poff, K. R. Bestgen, Life-history strategies predict fish invasions and extirpations in the Colorado River basin. *Ecol. Monogr.* **76**, 25–40 (2006). doi: 10.1890/05-0330
6. W. K. Cornwell *et al*., Plant species traits are the predominant control on litter decomposition rates within biomes worldwide. *Ecol. Lett.* **11**, 1065–1071 (2008). doi: 10.1111/j.1461-0248.2008.01219.x; pmid: 18627410
7. S. Lavorel, E. Garnier, Predicting changes in community composition and ecosystem functioning from plant traits: Revisiting the Holy Grail. *Funct. Ecol.* **16**, 545–556 (2002). doi: 10.1046/j.1365-2435.2002.00664.x
8. J. L. Green, B. J. M. Bohannan, R. J. Whitaker, Microbial biogeography: From taxonomy to traits. *Science* **320**, 1039–1043 (2008). doi: 10.1126/science.1153475; pmid: 18497288
9. E. Litchman, C. A. Klausmeier, Trait-based community ecology of phytoplankton. *Annu. Rev. Ecol. Evol. Syst.* **39**, 615–639 (2008). doi: 10.1146/annurev.ecolsys.39.110707.173549
10. P. L. Chagnon, R. L. Bradley, H. Maherali, J. N. Klironomos, A trait-based framework to understand life history of mycorrhizal fungi. *Trends Plant Sci.* **18**, 484–491 (2013). doi: 10.1016/j.tplants.2013.05.001; pmid: 23756036
11. L. Philippot *et al*., The ecological coherence of high bacterial taxonomic ranks. *Nat. Rev. Microbiol.* **8**, 523–529 (2010). doi: 10.1038/nrmicro2367; pmid: 20531276
12. M. D. Wallenstein, E. K. Hall, A trait-based framework for predicting when and where microbial adaptation to climate change will affect ecosystem functioning. *Biogeochemistry* **109**, 35–47 (2012). doi: 10.1007/s10533-011-9641-8
13. S. Krause *et al*., Trait-based approaches for understanding microbial biodiversity and ecosystem functioning. *Frontiers in Microbiology* **5**, 251 (2014). doi: 10.3389/fmicb.2014.00251; pmid: 24904563
14. S. Díaz *et al*., Incorporating plant functional diversity effects in ecosystem service assessments. *Proc. Natl. Acad. Sci. U.S.A.* **104**, 20684–20689 (2007). doi: 10.1073/pnas.0704716104; pmid: 18093933
15. C. Violle *et al*., Let the concept of trait be functional! *Oikos* **116**, 882–892 (2007). doi: 10.1111/j.0030-1299.2007.15559.x
16. N. Fierer, A. Barberán, D. C. Laughlin, Seeing the forest for the genes: Using metagenomics to infer the aggregated traits of microbial communities. *Front. Microbiol.* **5**, 614 (2014). doi: 10.3389/fmicb.2014.00614; pmid: 25429288
17. J. Kattge *et al*., TRY - a global database of plant traits. *Glob. Change Biol.* **17**, 2905–2935 (2011). doi: 10.1111/j.1365-2486.2011.02451.x
18. J. I. Prosser, Dispersing misconceptions and identifying opportunities for the use of 'omics' in soil microbial ecology. *Nat. Rev. Microbiol.* **13**, 439–446 (2015). doi: 10.1038/nrmicro3468; pmid: 26052662
19. C. A. Hanson, J. A. Fuhrman, M. C. Horner-Devine, J. B. H. Martiny, Beyond biogeographic patterns: Processes shaping the microbial landscape. *Nat. Rev. Microbiol.* **10**, 497–506 (2012). pmid: 22580365
20. O. X. Cordero, M. F. Polz, Explaining microbial genomic diversity in light of evolutionary ecology. *Nat. Rev. Microbiol.* **12**, 263–273 (2014). doi: 10.1038/nrmicro3218; pmid: 24590245
21. N. L. Poff *et al*., Functional trait niches of North American lotic insects: Traits-based ecological applications in light of phylogenetic relationships. *J. N. Am. Benthol. Soc.* **25**, 730–755 (2006). doi: 10.1899/0887-3593(2006)025[0730:FTNONA]2.0.CO;2
22. S. Díaz *et al*., Functional traits, the phylogeny of function, and ecosystem service vulnerability. *Ecol Evol* **3**, 2958–2975 (2013). doi: 10.1002/ece3.601; pmid: 24101986
23. J. T. Lennon, Z. T. Aanderud, B. K. Lehmkuhl, D. R. Schoolmaster Jr., Mapping the niche space of soil microorganisms using taxonomy and traits. *Ecology* **93**, 1867–1879 (2012). doi: 10.1890/11-1745.1; pmid: 22928415
24. D. S. Falconer, T. F. C. Mackay, *Introduction to Quantitative Genetics* (Pearson, Essex, UK, ed. 4, 1996).
25. A. Torriani-Gorini, E. Yagil, S. Silver, Eds., *Phosphate in Microorganisms: Cellular and Molecular Biology* (American Society of Microbiology, Washington, DC, 1994).
26. F. Tétart, F. Repoila, C. Monod, H. M. Krisch, Bacteriophage T4 host range is expanded by duplications of a small domain of the tail fiber adhesin. *J. Mol. Biol.* **258**, 726–731 (1996). doi: 10.1006/jmbi.1996.0281; pmid: 8637004
27. G. E. Hutchinson, Concluding remarks. *Cold Spring Harb. Symp. Quant. Biol.* **22**, 415–427 (1957). doi: 10.1101/SQB.1957.022.01.039
28. R. Caspi *et al*., The MetaCyc database of metabolic pathways and enzymes and the BioCyc collection of Pathway/Genome Databases. *Nucleic Acids Res.* **42**, D459–D471 (2014). doi: 10.1093/nar/gkt1103; pmid: 24225315
29. W. Zhang, E. Zeng, D. Liu, S. E. Jones, S. Emrich, Mapping genomic features to functional traits through microbial whole genome sequences. *Int. J. Bioinform. Res. Appl.* **10**, 461–478 (2014). doi: 10.1504/IJBRA.2014.062995; pmid: 24989863
30. J. A. Klappenbach, J. M. Dunbar, T. M. Schmidt, rRNA operon copy number reflects ecological strategies of bacteria. *Appl. Environ. Microbiol.* **66**, 1328–1333 (2000). doi: 10.1128/AEM.66.4.1328-1333.2000; pmid: 10742207
31. S. Vieira-Silva, E. P. C. Rocha, The systemic imprint of growth and its uses in ecological (meta)genomics. *PLOS Genet.* **6**, e1000808 (2010). pmid: 20090831
32. D. A. Ratkowsky, J. Olley, T. A. McMeekin, A. Ball, Relationship between temperature and growth rate of bacterial cultures. *J. Bacteriol.* **149**, 1–5 (1982). pmid: 7054139
33. J. Talbot, F. Martin, A. Kohler, B. Henrissat, K. Peay, Functional guild classification predicts the enzymatic role of fungi in litter and soil biogeochemistry. *Soil Biol. Biochem.* **88**, 441–456 (2015).
34. E. R. Zinser *et al*., Influence of light and temperature on *Prochlorococcus* ecotype distributions in the Atlantic Ocean. *Limnol. Oceanogr.* **52**, 2205–2220 (2007). doi: 10.4319/lo.2007.52.5.2205
35. V. Sabarly *et al*., The decoupling between genetic structure and metabolic phenotypes in *Escherichia coli* leads to continuous phenotypic diversity. *J. Evol. Biol.* **24**, 1559–1571 (2011). doi: 10.1111/j.1420-9101.2011.02287.x; pmid: 21569155
36. T. Li *et al*., Simultaneous analysis of microbial identity and function using NanoSIMS. *Environ. Microbiol.* **10**, 580–588 (2008). doi: 10.1111/j.1462-2920.2007.01478.x; pmid: 18028417
37. D. A. Fike, C. L. Gammon, W. Ziebis, V. J. Orphan, Micron-scale mapping of sulfur cycling across the oxycline of a cyanobacterial mat: A paired nanoSIMS and CARD-FISH approach. *ISME J.* **2**, 749–759 (2008). doi: 10.1038/ismej.2008.39; pmid: 18528418
38. M. W. Lomas, J. A. Bonachela, S. A. Levin, A. C. Martiny, Impact of ocean phytoplankton diversity on phosphate uptake. *Proc. Natl. Acad. Sci. U.S.A.* **111**, 17540–17545 (2014). doi: 10.1073/pnas.1420760111; pmid: 25422472
39. L. Philippot *et al*., Spatial patterns of bacterial taxa in nature reflect ecological traits of deep branches of the 16S rRNA bacterial tree. *Environ. Microbiol.* **11**, 3096–3104 (2009). doi: 10.1111/j.1462-2920.2009.02014.x; pmid: 19638171
40. W. F. Doolittle, Phylogenetic classification and the universal tree. *Science* **284**, 2124–2128 (1999). doi: 10.1126/science.284.5423.2124; pmid: 10381871
41. A. C. Martiny, K. Treseder, G. Pusch, Phylogenetic conservatism of functional traits in microorganisms. *ISME J.* **7**, 830–838 (2013). doi: 10.1038/ismej.2012.160; pmid: 23235290
42. K. K. Treseder *et al*., Evolutionary histories of soil fungi are reflected in their large-scale biogeography. *Ecol. Lett.* **17**, 1086–1093 (2014). pmid: 24912000
43. J. B. Losos, Phylogenetic niche conservatism, phylogenetic signal and the relationship between phylogenetic relatedness and ecological similarity among species. *Ecol. Lett.* **11**, 995–1003 (2008). doi: 10.1111/j.1461-0248.2008.01229.x; pmid: 18673385
44. R. Berlemont, A. C. Martiny, Genomic potential for polysaccharide deconstruction in bacteria. *Appl. Environ. Microbiol.* **81**, 1513–1519 (2015). doi: 10.1128/AEM.03718-14; pmid: 25527556
45. C. Pál, B. Papp, M. J. Lercher, Adaptive evolution of bacterial metabolic networks by horizontal gene transfer. *Nat. Genet.* **37**, 1372–1375 (2005). doi: 10.1038/ng1686; pmid: 16311593
46. K. N. Suding *et al*., Scaling environmental change through the community-level: A trait-based response-and-effect framework for plants. *Glob. Change Biol.* **14**, 1125–1140 (2008). doi: 10.1111/j.1365-2486.2008.01557.x
47. J. T. Lennon, S. E. Jones, Microbial seed banks: The ecological and evolutionary implications of dormancy. *Nat. Rev. Microbiol.* **9**, 119–130 (2011). doi: 10.1038/nrmicro2504; pmid: 21233850

48. S. D. Allison, J. B. H. Martiny, Colloquium paper: Resistance, resilience, and redundancy in microbial communities. *Proc. Natl. Acad. Sci. U.S.A.* **105** (Suppl 1), 11512–11519 (2008). doi: 10.1073/pnas.0801925105; pmid: 18695234
49. K. F. Edwards, E. Litchman, C. A. Klausmeier, Functional traits explain phytoplankton responses to environmental gradients across lakes of the United States. *Ecology* **94**, 1626–1635 (2013). doi: 10.1890/12-1459.1; pmid: 23951722
50. N. Fierer, M. A. Bradford, R. B. Jackson, Toward an ecological classification of soil bacteria. *Ecology* **88**, 1354–1364 (2007). doi: 10.1890/05-1839; pmid: 17601128
51. S. A. Placella, E. L. Brodie, M. K. Firestone, Rainfall-induced carbon dioxide pulses result from sequential resuscitation of phylogenetically clustered microbial groups. *Proc. Natl. Acad. Sci. U.S.A.* **109**, 10931–10936 (2012). doi: 10.1073/pnas.1204306109; pmid: 22715291
52. A. S. Amend *et al*., Microbial response to simulated global change is phylogenetically conserved and linked with functional potential. *ISME J.* (2015). doi: 10.1038/ismej.2015.96; pmid: 26046258
53. K. Zwirglmaier *et al*., Global phylogeography of marine *Synechococcus* and *Prochlorococcus* reveals a distinct partitioning of lineages among oceanic biomes. *Environ. Microbiol.* **10**, 147–161 (2008). pmid: 17900271
54. S. Mazard, M. Ostrowski, F. Partensky, D. J. Scanlan, Multi-locus sequence analysis, taxonomic resolution and biogeography of marine *Synechococcus*. *Environ. Microbiol.* **14**, 372–386 (2012). doi: 10.1111/j.1462-2920.2011.02514.x; pmid: 21651684
55. C. L. Lauber, M. Hamady, R. Knight, N. Fierer, Pyrosequencing-based assessment of soil pH as a predictor of soil bacterial community structure at the continental scale. *Appl. Environ. Microbiol.* **75**, 5111–5120 (2009). doi: 10.1128/AEM.00335-09; pmid: 19502440
56. A. Eiler *et al*., Productivity and salinity structuring of the microplankton revealed by comparative freshwater metagenomics. *Environ. Microbiol.* **16**, 2682–2698 (2014). pmid: 24118837
57. R. Jain, M. C. Rivera, J. A. Lake, Horizontal gene transfer among genomes: The complexity hypothesis. *Proc. Natl. Acad. Sci. U.S.A.* **96**, 3801–3806 (1999). doi: 10.1073/pnas.96.7.3801; pmid: 10097118
58. H. D. Peck Jr., J. Van Beeumen, J. LeGall, Biochemistry of dissimilatory sulphate reduction. *Philos Trans. R. Soc. Lond. B Biol. Sci.* **298**, 443–466 (1982). doi: 10.1098/rstb.1982.0091; pmid: 6127735
59. W. G. Zumft, Cell biology and molecular basis of denitrification. *Microbiol. Mol. Biol. Rev.* **61**, 533–616 (1997). pmid: 9409151
60. K. O. Stetter, Extremophiles and their adaptation to hot environments. *FEBS Lett.* **452**, 22–25 (1999). doi: 10.1016/S0014-5793(99)00663-8; pmid: 10376671
61. A. F. Bennett, R. E. Lenski, J. E. Mittler, Evolutionary adaptation to temperature. 1. Fitness responses of *Escherichia coli* to changes in its thermal environment. *Evolution* **46**, 16–30 (1992). doi: 10.2307/2409801
62. L. R. Moore, G. Rocap, S. W. Chisholm, Physiology and molecular phylogeny of coexisting *Prochlorococcus* ecotypes. *Nature* **393**, 464–467 (1998). doi: 10.1038/30965; pmid: 9624000
63. D. B. Rusch, A. C. Martiny, C. L. Dupont, A. L. Halpern, J. C. Venter, Characterization of *Prochlorococcus* clades from iron-depleted oceanic regions. *Proc. Natl. Acad. Sci. U.S.A.* **107**, 16184–16189 (2010). doi: 10.1073/pnas.1009513107; pmid: 20733077
64. Z. I. Johnson *et al*., Niche partitioning among *Prochlorococcus* ecotypes along ocean-scale environmental gradients. *Science* **311**, 1737–1740 (2006). doi: 10.1126/science.1118052; pmid: 16556835
65. M. L. Coleman, S. W. Chisholm, Ecosystem-specific selection pressures revealed through comparative population genomics. *Proc. Natl. Acad. Sci. U.S.A.* **107**, 18634–18639 (2010). doi: 10.1073/pnas.1009480107; pmid: 20937887
66. A. C. Martiny, M. L. Coleman, S. W. Chisholm, Phosphate acquisition genes in *Prochlorococcus* ecotypes: Evidence for genome-wide adaptation. *Proc. Natl. Acad. Sci. U.S.A.* **103**, 12552–12557 (2006). doi: 10.1073/pnas.0601301103; pmid: 16895994
67. A. C. Martiny, Y. Huang, W. Li, Occurrence of phosphate acquisition genes in Prochlorococcus cells from different ocean regions. *Environ. Microbiol.* **11**, 1340–1347 (2009). doi: 10.1111/j.1462-2920.2009.01860.x; pmid: 19187282
68. A. C. Martiny, A. P. K. Tai, D. Veneziano, F. Primeau, S. W. Chisholm, Taxonomic resolution, ecotypes and the biogeography of *Prochlorococcus*. *Environ. Microbiol.* **11**, 823–832 (2009). doi: 10.1111/j.1462-2920.2008.01803.x; pmid: 19021692
69. E. A. Grice *et al*.NISC Comparative Sequencing Program, Topographical and temporal diversity of the human skin microbiome. *Science* **324**, 1190–1192 (2009). doi: 10.1126/science.1171700; pmid: 19478181
70. A. F. Koeppel, M. Wu, Lineage-dependent ecological coherence in bacteria. *FEMS Microbiol. Ecol.* **81**, 574–582 (2012). doi: 10.1111/j.1574-6941.2012.01387.x; pmid: 22486161
71. E. A. Grice, J. A. Segre, The skin microbiome. *Nat. Rev. Microbiol.* **9**, 244–253 (2011). doi: 10.1038/nrmicro2537; pmid: 21407241
72. S. Fitz-Gibbon *et al*., *Propionibacterium acnes* strain populations in the human skin microbiome associated with acne. *J. Invest. Dermatol.* **133**, 2152–2160 (2013). pmid: 23337890
73. G. J. M. Christensen, H. Brüggemann, Bacterial skin commensals and their role as host guardians. *Benef. Microbes* **5**, 201–215 (2014). doi: 10.3920/BM2012.0062; pmid: 24322878
74. R. A. Welch *et al*., Extensive mosaic structure revealed by the complete genome sequence of uropathogenic *Escherichia coli*. *Proc. Natl. Acad. Sci. U.S.A.* **99**, 17020–17024 (2002). doi: 10.1073/pnas.252529799; pmid: 12471157
75. J. P. Allen, E. A. Ozer, A. R. Hauser, Different paths to pathogenesis. *Trends Microbiol.* **22**, 168–169 (2014). doi: 10.1016/j.tim.2014.02.013; pmid: 24629347
76. O. Koren *et al*., A guide to enterotypes across the human body: Meta-analysis of microbial community structures in human microbiome datasets. *PLOS Comput. Biol.* **9**, e1002863 (2013). doi: 10.1371/journal.pcbi.1002863; pmid: 23326225
77. L. A. David *et al*., Diet rapidly and reproducibly alters the human gut microbiome. *Nature* **505**, 559–563 (2014). doi: 10.1038/nature12820; pmid: 24336217
78. G. D. Wu *et al*., Linking long-term dietary patterns with gut microbial enterotypes. *Science* **334**, 105–108 (2011). doi: 10.1126/science.1208344; pmid: 21885731
79. A. El Kaoutari, F. Armougom, J. I. Gordon, D. Raoult, B. Henrissat, The abundance and variety of carbohydrate-active enzymes in the human gut microbiota. *Nat. Rev. Microbiol.* **11**, 497–504 (2013). doi: 10.1038/nrmicro3050; pmid: 23748339
80. B. L. Cantarel, V. Lombard, B. Henrissat, Complex carbohydrate utilization by the healthy human microbiome. *PLOS ONE* **7**, e28742 (2012). doi: 10.1371/journal.pone.0028742; pmid: 22719820
81. D. N. Frank *et al*., Molecular-phylogenetic characterization of microbial community imbalances in human inflammatory bowel diseases. *Proc. Natl. Acad. Sci. U.S.A.* **104**, 13780–13785 (2007). doi: 10.1073/pnas.0706625104; pmid: 17699621
82. S. Fuentes *et al*., Reset of a critically disturbed microbial ecosystem: Faecal transplant in recurrent *Clostridium difficile* infection. *ISME J.* **8**, 1621–1633 (2014). doi: 10.1038/ismej.2014.13; pmid: 24577353
83. J. J. Wright, K. M. Konwar, S. J. Hallam, Microbial ecology of expanding oxygen minimum zones. *Nat. Rev. Microbiol.* **10**, 381–394 (2012). pmid: 22580367
84. F. Inagaki *et al*., Microbial community in a sediment-hosted CO2 lake of the southern Okinawa Trough hydrothermal system. *Proc. Natl. Acad. Sci. U.S.A.* **103**, 14164–14169 (2006). pmid: 16959888
85. A. A. Agrawal, J. K. Conner, S. Rasmann, in *Evolution Since Darwin: The First 150 Years*, M. A. Bell, D. J. Futuyma, W. F. Eanes, J. S. Levinton, Eds. (Sinauer Associates, Sunderland, MA, 2010), pp. 243-268.
86. I. J. Wright *et al*., The worldwide leaf economics spectrum. *Nature* **428**, 821–827 (2004). doi: 10.1038/nature02403; pmid: 15103368
87. J. A. Zwart, C. T. Solomon, S. E. Jones, Phytoplankton traits predict ecosystem function in a global set of lakes. *Ecology* **96**, 2257–2264 (2015). doi: 10.1890/14-2102.1; pmid: 26405750
88. J. K. Goodrich *et al*., Human genetics shape the gut microbiome. *Cell* **159**, 789–799 (2014). doi: 10.1016/j.cell.2014.09.053; pmid: 25417156
89. C. O. Webb, D. D. Ackerly, M. A. McPeek, M. J. Donoghue, Phylogenies and community ecology. *Annu. Rev. Ecol. Syst.* **33**, 475–505 (2002). doi: 10.1146/annurev.ecolsys.33.010802.150448
90. J. Cavender-Bares, K. H. Kozak, P. V. A. Fine, S. W. Kembel, The merging of community ecology and phylogenetic biology. *Ecol. Lett.* **12**, 693–715 (2009). doi: 10.1111/j.1461-0248.2009.01314.x; pmid: 19473217
91. J. J. Wiens *et al*., Niche conservatism as an emerging principle in ecology and conservation biology. *Ecol. Lett.* **13**, 1310–1324 (2010). doi: 10.1111/j.1461-0248.2010.01515.x; pmid: 20649638
92. M. W. Cadotte, B. J. Cardinale, T. H. Oakley, Evolutionary history and the effect of biodiversity on plant productivity. *Proc. Natl. Acad. Sci. U.S.A.* **105**, 17012–17017 (2008). doi: 10.1073/pnas.0805962105; pmid: 18971334
93. D. S. Srivastava, M. W. Cadotte, A. A. M. MacDonald, R. G. Marushia, N. Mirotchnick, Phylogenetic diversity and the functioning of ecosystems. *Ecol. Lett.* **15**, 637–648 (2012). doi: 10.1111/j.1461-0248.2012.01795.x; pmid: 22583836
94. P. A. Venail, M. J. Vives, Positive effects of bacterial diversity on ecosystem functioning driven by complementarity effects in a bioremediation context. *PLOS ONE* **8**, e72561 (2013). doi: 10.1371/journal.pone.0072561; pmid: 24023751
95. A. S. Amend, K. L. Matulich, J. B. H. Martiny, Nitrogen addition, not initial phylogenetic diversity, increases litter decomposition by fungal communities. *Front. Microbiol.* **6**, 109 (2015). doi: 10.3389/fmicb.2015.00109; pmid: 25741330
96. P. A. Venail *et al*., The influence of phylogenetic relatedness on species interactions among freshwater green algae in a mesocosm experiment. *J. Ecol.* **102**, 1288–1299 (2014). doi: 10.1111/1365-2745.12271
97. P. J. Turnbaugh *et al*., An obesity-associated gut microbiome with increased capacity for energy harvest. *Nature* **444**, 1027–1031 (2006). doi: 10.1038/nature05414; pmid: 17183312
98. H. E. Reed, J. B. H. Martiny, Microbial composition affects the functioning of estuarine sediments. *ISME J.* **7**, 868–879 (2013). doi: 10.1038/ismej.2012.154; pmid: 23235294
99. T. Curtis *et al*., Crystal ball – 2013. *Microb. Biotechnol.* **6**, 3–16 (2013). doi: 10.1111/1751-7915.12014
100. E. K. Costello, K. Stagaman, L. Dethlefsen, B. J. M. Bohannan, D. A. Relman, The application of ecological theory toward an understanding of the human microbiome. *Science* **336**, 1255–1262 (2012). doi: 10.1126/science.1224203; pmid: 22674335
101. B. K. Singh, R. D. Bardgett, P. Smith, D. S. Reay, Microorganisms and climate change: Terrestrial feedbacks and mitigation options. *Nat. Rev. Microbiol.* **8**, 779–790 (2010). doi: 10.1038/nrmicro2439; pmid: 20948551

ACKNOWLEDGMENTS

We thank S. Allison and K. Whiteson for helpful discussions and comments. This work was supported by the National Science Foundation (DEB-1442230, DEB-144246, OCE-1332740, OCE-1046297); the U.S. Department of Energy, Office of Science, Office of Biological and Environmental Research (BER), under Award no. DE-PS02-09ER09-25; and the U.S. Army Research Office (W911NF-14-1-0411).

SUPPLEMENTARY MATERIALS

www.sciencemag.org/content/350/6261/aac9323/suppl/DC1
Table S1
References (*102*–*118*)

10.1126/science.aac9323

RESEARCH ARTICLE SUMMARY

METABOLIC HEALTH

Pancreatic β cell enhancers regulate rhythmic transcription of genes controlling insulin secretion

Mark Perelis,* Biliana Marcheva,* Kathryn Moynihan Ramsey, Matthew J. Schipma, Alan L. Hutchison, Akihiko Taguchi, Clara Bien Peek, Heekyung Hong, Wenyu Huang, Chiaki Omura, Amanda L. Allred, Christopher A. Bradfield, Aaron R. Dinner, Grant D. Barish, Joseph Bass†

INTRODUCTION: The circadian clock is a molecular oscillator that coordinates behavior and physiology in anticipation of the daily light cycle. Desynchrony of circadian cycles, through genetic or environmental perturbation, contributes to metabolic disorders such as cardiovascular disease, obesity, and type 2 diabetes. We previously showed that disruption of the clock transcription factors CLOCK and BMAL1 in the pancreas causes hypoinsulinemic diabetes in mice. The mechanism(s) linking clock dysfunction to pancreatic β cell failure and the means by which CLOCK and BMAL1 affect glucose metabolism in the whole organism are not well understood.

RATIONALE: The circadian system helps to maintain glucose homeostasis across the sleep-wake cycle. This system requires cross-talk between the master clock in the central nervous system, which coordinates feeding and sleep, and peripheral tissue clocks, which synchronize behavior with the storage, mobilization, and synthesis of glucose. Although it is clear that clocks within distinct organs participate in glucose turnover, the molecular basis for time-of-day variation in organismal glucose responsiveness is still not understood. Here, we combined genome-wide analyses with gene targeting in mice to study the impact of the cell-autonomous clock on β cell function.

RESULTS: We found that cell-autonomous expression of CLOCK and BMAL1 in pancreatic islets isolated from wild-type mice generates robust 24-hour rhythms of glucose- and potassium chloride–stimulated insulin secretion ex vivo. About 27% of the β cell transcriptome exhibited circadian oscillation. Many of these transcripts correspond to genes coding for proteins that are involved in the assembly, trafficking, and membrane fusion of vesicles that participate in insulin secretion. Chromatin immunoprecipitation sequencing revealed that CLOCK and BMAL1 regulate cycling genes in β cells by binding at distal regulatory elements distinct from those controlling the circadian transcription of metabolic gene networks within the liver. The regulatory sites of cycling genes in the β cell resided primarily within transcriptionally active enhancers that were also bound by the pancreatic transcription factor PDX1. Finally, we found that in islets from adult mice, *Bmal1* ablation either in vivo or ex vivo abrogates nutrient-responsive insulin secretion, demonstrating clock control of pancreatic β cell function throughout adult life.

ON OUR WEB SITE

Read the full article at http://dx.doi.org/10.1126/science.aac4250

CONCLUSION: Our results show that local clock-driven genomic rhythms program cell function across the light-dark cycle, including the priming of insulin secretion within limited time windows each day. Cell type–specific transcriptional regulation by the clock localizes to rhythmic enhancers that are unique to the β cell. Thus, our findings uncover a transcriptional process through which the core clock aligns physiology with the light cycle, revealing pathways that are important in both health and disease states such as type 2 diabetes. ■

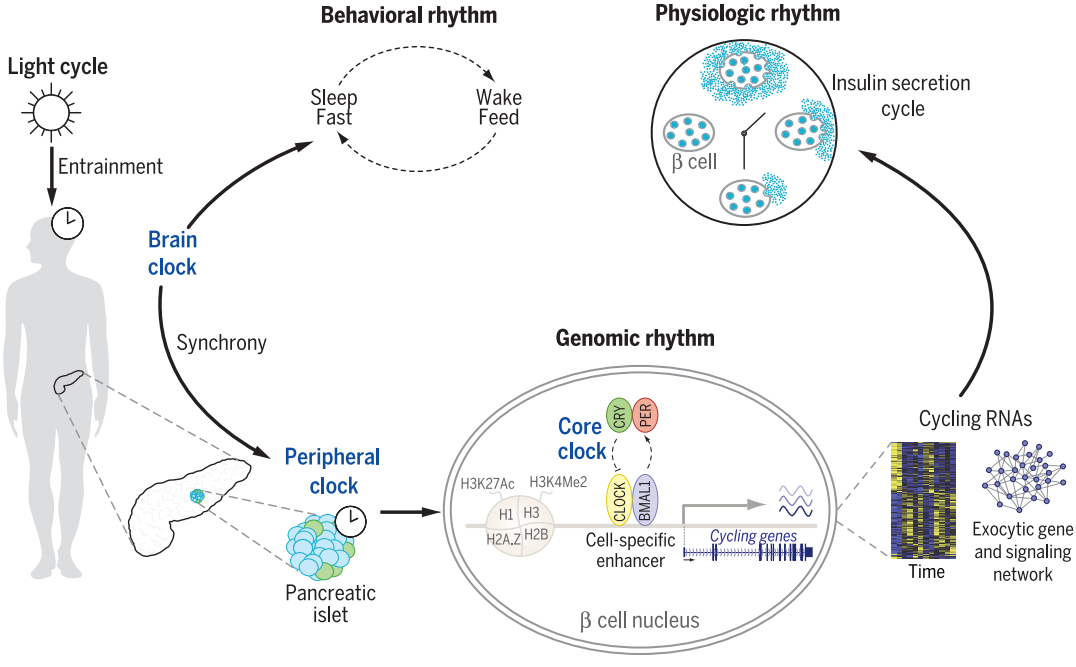

β cell–specific enhancers control the rhythmic transcription of genes linked to insulin secretion. Peripheral clocks maintain glucose homeostasis across the sleep-wake cycle by gating β cell insulin secretion through genome-wide transcriptional control of the assembly and trafficking of insulin secretory vesicles. Clock transcription factors bind within cell type–specific enhancer neighborhoods of cycling genes, revealing the mechanisms that synchronize rhythmic metabolism at transcriptional and physiologic levels across the light-dark cycle.

The list of affiliations is available in the full article online.
*These authors contributed equally to this work. †Corresponding author.
E-mail: j-bass@northwestern.edu
Cite this article as M. Perelis *et al.*, *Science* **350**, aac4250 (2015).
DOI: 10.1126/science.aac4250

Downloaded from www.sciencemag.org on November 5, 2015

RESEARCH ARTICLE

METABOLIC HEALTH

Pancreatic β cell enhancers regulate rhythmic transcription of genes controlling insulin secretion

Mark Perelis,[1]* Biliana Marcheva,[1]* Kathryn Moynihan Ramsey,[1] Matthew J. Schipma,[2] Alan L. Hutchison,[3,4,5] Akihiko Taguchi,[1] Clara Bien Peek,[1] Heekyung Hong,[1] Wenyu Huang,[1] Chiaki Omura,[1] Amanda L. Allred,[1] Christopher A. Bradfield,[6] Aaron R. Dinner,[4,5,7] Grant D. Barish,[1] Joseph Bass[1]†

The mammalian transcription factors CLOCK and BMAL1 are essential components of the molecular clock that coordinate behavior and metabolism with the solar cycle. Genetic or environmental perturbation of circadian cycles contributes to metabolic disorders including type 2 diabetes. To study the impact of the cell-autonomous clock on pancreatic β cell function, we examined pancreatic islets from mice with either intact or disrupted BMAL1 expression both throughout life and limited to adulthood. We found pronounced oscillation of insulin secretion that was synchronized with the expression of genes encoding secretory machinery and signaling factors that regulate insulin release. CLOCK/BMAL1 colocalized with the pancreatic transcription factor PDX1 within active enhancers distinct from those controlling rhythmic metabolic gene networks in liver. We also found that β cell clock ablation in adult mice caused severe glucose intolerance. Thus, cell type–specific enhancers underlie the circadian control of peripheral metabolism throughout life and may help to explain its dysregulation in diabetes.

The mammalian circadian system is organized hierarchically and is driven by cellular transcriptional oscillators that coordinate behavior and metabolism with the light-dark cycle. Specifically, CLOCK/BMAL1 within the forward limb of the clock induces the expression of repressors (PERs/CRYs) in the negative limb and stabilizing factors (ROR/REV-ERB) in a cycle that repeats itself every 24 hours (*1*, *2*). A transformation in our understanding of clock function emerged from the discovery of autonomous circadian oscillation within individual tissues, and even in fibroblasts, ex vivo (*3*). Molecular rhythms play a critical role in systemic health, as indicated by observations that disruption of central and peripheral clocks can alter body weight and glucose homeostasis. However, there has been a major gap in our understanding of how the molecular clock synchronizes transcription in distinct peripheral tissues to maintain overall physiological homeostasis (*4*–*8*).

[1]Department of Medicine, Division of Endocrinology, Metabolism and Molecular Medicine, Northwestern University Feinberg School of Medicine, Chicago, IL 60611, USA. [2]Center for Genetic Medicine, Northwestern University, Chicago, IL 60611, USA. [3]Medical Scientist Training Program, University of Chicago, Chicago, IL 60637, USA. [4]Graduate Program in the Biophysical Sciences, University of Chicago, Chicago, IL 60637, USA. [5]James Franck Institute, University of Chicago, Chicago, IL 60637, USA. [6]McArdle Laboratory for Cancer Research, University of Wisconsin, Madison, WI 52705, USA. [7]Department of Chemistry, University of Chicago, Chicago, IL 60637, USA.
*These authors contributed equally to this work. †Corresponding author. E-mail: j-bass@northwestern.edu

Genome-wide analyses in liver indicate extensive rhythmicity of processed RNAs and noncoding enhancer RNAs (eRNAs) that are dependent on temporal binding of circadian transcription factors to both promoters and enhancers (*9*–*11*). Yet the circadian clock exerts different effects on glucose metabolism within liver and other peripheral tissues. Thus, we sought to examine the genomic mechanism of clock control of pancreatic β cell insulin secretion (*5*, *6*). Here, we define the targets of clock transcriptional regulation within the β cell and investigate the impact of clock disruption on the temporal control of insulin secretion and glucose homeostasis.

The β cell clock produces rhythmic insulin secretion and secretory gene transcription

First, to determine whether transcriptional oscillations in pancreatic islets give rise to rhythmic islet physiology, we examined the phase dependence of pancreatic islet function by analyzing nutrient-induced insulin secretion in parallel with live-cell clock oscillation in islets from *Per2*^{Luc} reporter mice (*12*). After synchronization with forskolin (*6*, *13*), we assessed insulin secretion every 4 hours in individual groups of five islets at each time point over the ensuing 72-hour window (fig. S1A; materials and methods) and observed a striking self-sustained, time of day–dependent variation in the magnitude of response to stimulatory concentrations of both glucose and KCl, which triggers insulin exocytosis through direct depolarization of the β cell (Fig. 1A). Intracellular insulin content did not cycle (fig. S1B) despite rhythmic glucose-stimulated insulin secretion (GSIS) (Fig. 1A), consistent with circadian regulation at a step after translation of insulin. We further confirmed that GSIS rhythms were autonomous by monitoring insulin secretion after forskolin synchronization at times corresponding to the nadir (36 hours after forskolin shock) and zenith (48 hours after forskolin shock) of the wild-type GSIS rhythm in islets isolated from *PdxCreER;Bmal1*$^{flx/flx}$ mice (Fig. 1B and fig. S1C), which when treated with tamoxifen ex vivo displayed >60% reduction in *Bmal1* expression (fig. S1D). Vehicle-treated islets displayed significantly higher GSIS at the zenith than at the nadir, whereas tamoxifen-treated islets exhibited constitutively low levels of insulin secretion (Fig. 1B). Together, these data suggest that the islet molecular clock gates the rhythmic secretory response downstream of membrane depolarization.

We next sought to examine the genome-wide effect of rhythmic transcription on insulin secretory dynamics by performing RNA sequencing (RNA-seq) over two circadian cycles in RNA isolated from wild-type islets synchronized ex vivo (fig. S1A; materials and methods). We analyzed polyadenylated RNAs using eJTK_CYCLE (*14*), a modified nonparametric algorithm with increased sensitivity for detecting cycling transcripts. We detected a total of 3905 cycling transcripts (Bonferroni-corrected $P < 0.05$), which accounted for ~27% of all expressed transcripts within the islet that met a minimum mean expression threshold of 10 normalized counts (Fig. 1C). As expected, we observed high-amplitude rhythms for the core clock transcription factors, including *Bmal1*, *Clock*, *Npas2*, *Per2*, *Cry1*, *Rev-Erbα*, and *Rorα*, with *Bmal1* and its repressor *Rev-Erbα* displaying antiphasic expression (Fig. 1C) (*15*).

To determine the identity of functional circadian gene networks in the islet, we tested for overrepresentation of defined KEGG (Kyoto Encyclopedia of Genes and Genomes) pathways among rhythmic RNAs. We observed enrichment of factors mediating vesicle exocytosis, which suggests that daily variation in insulin secretory capacity arises from genomic regulation of the transport and release of peptidergic hormone (Fig. 1C and table S1). Overrepresented pathways in the circadian transcriptome included factors involved in (i) vesicle budding, including genes encoding the COPII coat proteins (*Sec24a* and *Sec31a*), which mediate vesicle budding from the endoplasmic reticulum (*16*, *17*); (ii) cargo trafficking, specifically the motor proteins (*Kif1b*, *Myo9a*, and *Dync2h1*) that enable vesicle transport along cytoskeletal filaments (*18*); and (iii) vesicle tethering and fusion to the plasma membrane, including v- and t-SNAREs such as *Vamp1*, *Vamp5*, *Vamp8*, *Stx1a*, *Stx4a*, and *Stx8* (*19*, *20*). In addition to the cycling of RNAs that encode factors involved in insulin exocytosis, we also identified rhythmic RNA expression of insulinotropic signals involved in vesicle movement and membrane fusion, including (i) targets of cAMP/

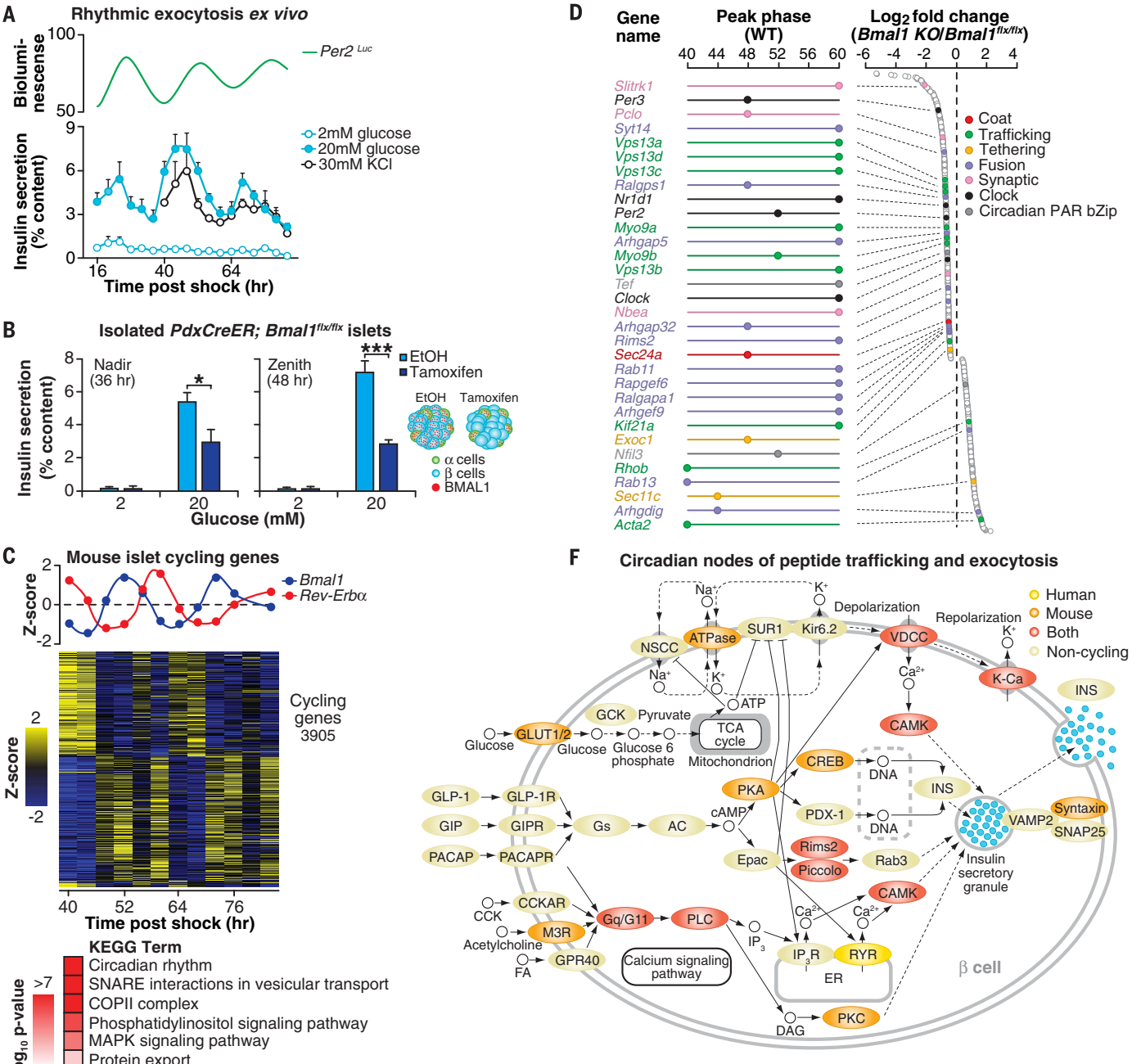

Fig. 1. Isolated pancreatic islets display rhythmic insulin secretion and transcription of secretory genes in mice and humans. (**A**) Bottom: Glucose- and KCl-stimulated insulin secretion in synchronized wild-type mouse islets across 3 or 2 consecutive days, respectively (n = 3 replicate sets of islets pooled from 6 to 9 mice each). Top: Bioluminescence monitoring (counts/s) in islets from *Per2*^{Luc} reporter mice was performed in parallel. (**B**) Glucose-stimulated insulin secretion in ethanol- or tamoxifen-treated islets from *PdxCreER;Bmal1*$^{flx/flx}$ mice at the nadir (36 hours after forskolin shock) and zenith (48 hours after forskolin shock) of cyclic insulin secretion in wild-type islets from Fig. 1A (n = 4 islet pools per time point, three replicates per islet pool). Ethanol-treated islets displayed significant difference in GSIS comparing 36 to 48 hours (P = 0.038), whereas tamoxifen-treated islets did not (P = 0.974). (**C**) Top: *Bmal1* and *Rev-erbα* RNA expression. Middle: Heat map of all cycling genes identified by eJTK_CYCLE analysis. Bottom: Significantly enriched KEGG ontology pathways shown within the cycling gene set. (**D**) Left: Peak phase expression (hours after forskolin shock) of cycling genes in synchronized wild-type islets that were also altered in *PdxCre;Bmal1*$^{flx/flx}$ islets at ZT2. Right: Log_2 change in expression in *PdxCre;Bmal1*$^{flx/flx}$ (KO) islets relative to *Bmal1*$^{flx/flx}$ (control) at ZT2 for subset of genes relevant to insulin secretion. (**E**) Heat map showing expression patterns of cycling trafficking and exocytosis genes in synchronized human islets. (**F**) Mapping of cycling RNAs in both human and mouse islets onto the "Insulin Secretion" KEGG pathway. All values in (A) and (B) represent mean ± SEM; $^*P < 0.05$, $^{***}P < 0.001$.

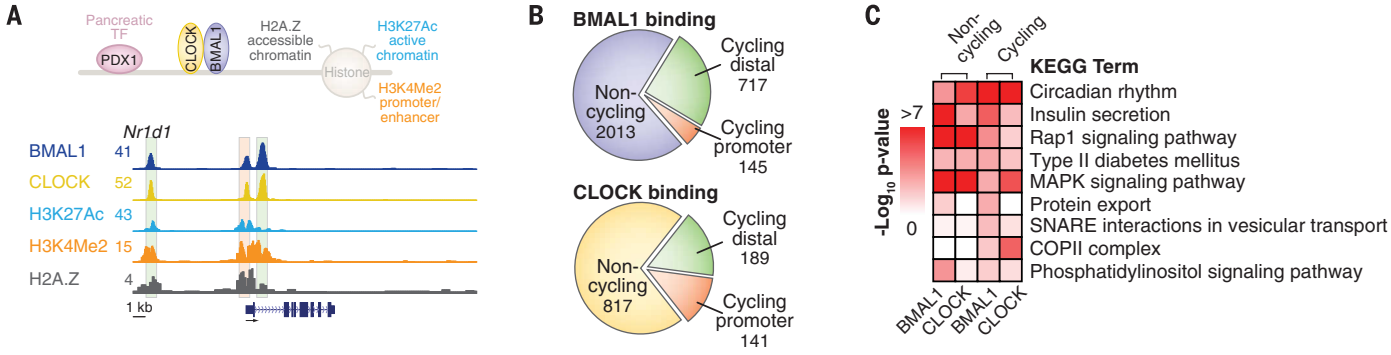

Fig. 2. BMAL1 and CLOCK bind to cycling genes at distal regulatory sites. (**A**) Top: Model of transcriptional targets and chromatin modifications for ChIP-seq experiments. Bottom: UCSC Genome Browser tracks at *Nr1d1* (*Rev-erbα*) locus in β cells. Maximum track heights within viewable window are indicated to the right of each factor. Shaded columns are described in text. (**B**) Distribution of BMAL1 and CLOCK peaks at cycling and noncycling gene targets expressed in islets. Binding sites at cycling genes are separated into promoter proximal and distal sites (<2 kb and >2 kb from TSS of nearest gene, respectively). (**C**) KEGG ontology terms enriched in cycling and noncycling BMAL1 and CLOCK target genes.

EPAC (cyclic adenosine monophosphate/exchange protein activated by cAMP) signaling (*Pclo*, *Rims2*, *Rab3b*, *Rap1a*, *Rap1b*, *Rapgef2*, *Rapgef6*), which mediate vesicle docking and fusion to the plasma membrane (*21*, *22*); (ii) Ca^{2+}-sensing synaptotagmins (*Syt11*, *Syt14*, *Syt16*), which stimulate membrane fusion of synaptic vesicles (*23*, *24*); and (iii) calmodulin-dependent protein kinases (*Camk1*, *Camk4*, *Camkk2*, *Camk2g*), which regulate vesicle exocytosis and recycling (*25*). Lastly, we detected significant oscillation in targets of phosphoinositide signaling, including protein kinase C (*Prkca*, *Prkcb*) (*26*), exocyst actin-interacting factors such as *Exoc1/Sec3* (*27*), and the cytoskeletal filament–remodeling Rho guanosine triphosphatases (GTPases) *Rho*, *RhoA*, *RhoB*, and *RhoC* (*18*). Collectively, cycling of RNAs that encode factors involved in insulin exocytosis and signaling components reveals a genomic basis for circadian variation in insulin secretion.

To further understand the physiologic function of tissue-specific rhythmic gene transcription, we compared genome-wide rhythms of RNA expression in wild-type islets to those in pancreas-specific clock mutant mice (*PdxCre;Bmal1*$^{flx/flx}$), which exhibit severe hypoinsulinemic diabetes due to defects downstream of glucose metabolism and mitochondrial respiration (fig. S2) (*6*). We performed RNA-seq using RNA isolated from *PdxCre;Bmal1*$^{flx/flx}$ and control littermate islets at the start of the light phase [zeitgeber time 2 (ZT2), the time of maximal GSIS impairment] (fig. S3A) (*6*). We identified changes in the expression of 1757 genes in islets isolated from clock mutant animals relative to littermate controls (*Bmal1*$^{flx/flx}$), including transcripts that were both decreased (1074) and increased (683) in expression, consistent with actions of the clock as both an activator and repressor of gene expression [false discovery rate (FDR)–adjusted $P < 0.05$] (fig. S3, B and C).

Many of the RNAs that were altered in islet clock knockout mice were identified as cycling RNAs in wild-type islets; overall, a total of 720 oscillating genes exhibited altered expression in animals with disrupted pancreatic clock function (fig. S3C), indicating an autonomous role of the islet clock in the rhythmic transcriptional regulation of insulin secretion. Among the most significantly changed RNAs were factors in the negative limb of the core clock containing the canonical E-box transcription motif, in addition to circadian PAR bZip transcription factors including *Per2*, *Rev-Erbα* (*Nr1d1*), *Tef*, and *E4bp4* (*Nfil3*) (Fig. 1D). We also found a broad range of alterations in cycling genes that are circadian outputs and grouped by KEGG annotation into exocytosis networks similar to those described for the wild-type islets, including genes encoding factors involved in trafficking, such as the vacuolar protein sorting factors *Vps13b* and *Vps13c*; *Myo9*, the motor protein involved in vesicular transport; the kinesin transport factor *Kif21*; and the small GTPase *Rab11*, a factor in trans-Golgi vesicular biogenesis (*28*) (Fig. 1D, fig. S3, E and F, and table S1). Ontology analysis also identified genes related to vesicle tethering and fusion as altered in clock-deficient islets, including the conserved exocyst component *Exoc1/Sec3*, cAMP/EPAC-controlled *Rims2* and *Pclo*, and the synaptotagmin *Syt14* (Fig. 1D); islet genes involved in glucose sensing were unchanged (table S2). Whereas the complete set of cycling RNAs displayed broadly distributed peak phases (fig. S3D), the majority of exocytosis-related RNAs that were differentially expressed in clock mutants exhibited peak expression at two distinct phases (48 and 60 hours after forskolin shock) (Fig. 1D). Although this suggests that these genes may represent direct targets of CLOCK/BMAL1 and/or a clock repressor (REVERBα/β or E4BP4), nascent RNA-seq studies indicate that peak circadian mRNA phases are not directly correlated with nascent transcription (*11*). Collectively, sequencing results indicate that secretory pathway genes represent a major output of the islet clock.

To determine whether the rhythmic islet transcriptome is conserved from mouse to humans, we performed RNA-seq in RNA isolated from synchronized human islets (fig. S4A). Human islets displayed characteristic circadian patterns in the expression of core clock components *BMAL1* and *REV-ERBα* (fig. S4B) (*29*) and genome-wide rhythmic patterns in the transcriptome with 1800 cycling RNAs (Bonferroni-corrected $P < 0.05$) (fig. S4B). Although striking differences have been described between mouse and human islet cell composition and cytoarchitecture (*30*), the expression of key genes involved in insulin release is conserved between species (*30*). Remarkably, 481 of the rhythmic human islet genes were orthologous to those in mouse islets (fig. S4C), including factors involved in exocytosis, trafficking, and fusion (Fig. 1, E and F, and fig. S4C). Mapping cycling human islet RNAs onto KEGG-curated human insulin secretion pathways revealed regulation of heterotrimeric G protein–coupled receptor (GPCR), cAMP, Ca^{2+}, and phosphoinositide-responsive signaling molecules important in nutrient response and hormone release (Fig. 1, E and F). Specifically, these included *GNAQ* (G_q protein), *RIMS2* and *PCLO* (insulin vesicle–associated), *CAMK2G* (calmodulin-activated protein kinase), and *PLCB4* (phospholipase C), all of which were also rhythmic in mouse islets (Fig. 1, E and F, and fig. S4D). Circadian gene regulation in the endocrine pancreas of both mice and humans thus converges on the late secretory pathway, demonstrating conservation of clock control of rhythmic tissue function across species.

BMAL1 and CLOCK bind near cell type–specific enhancers in pancreatic β cells

Because our genome-wide RNA sequencing studies indicate that genomic regulation by the clock gives rise to rhythmic insulin secretion, we next sought to analyze how core circadian transcription factors regulate this process by analyzing the extent of binding by BMAL1 and CLOCK to rhythmically expressed genes. In this context, cistrome studies have recently characterized β cell transcriptional hubs encoding genes that program both development and function (*31*), revealing colocalization within regions of accessible chromatin (H2A.Z) and active enhancers [monomethylated histone 3 Lys^4 (H3K4Me1) colocalized with acetylated histone 3 Lys^{27} (H3K27Ac)] containing binding sites for lineage-determining transcription factors (PDX1, MAFB, FOXA2, NKX6-2, and NKX2-2) (*31*–*33*). To determine the intersection

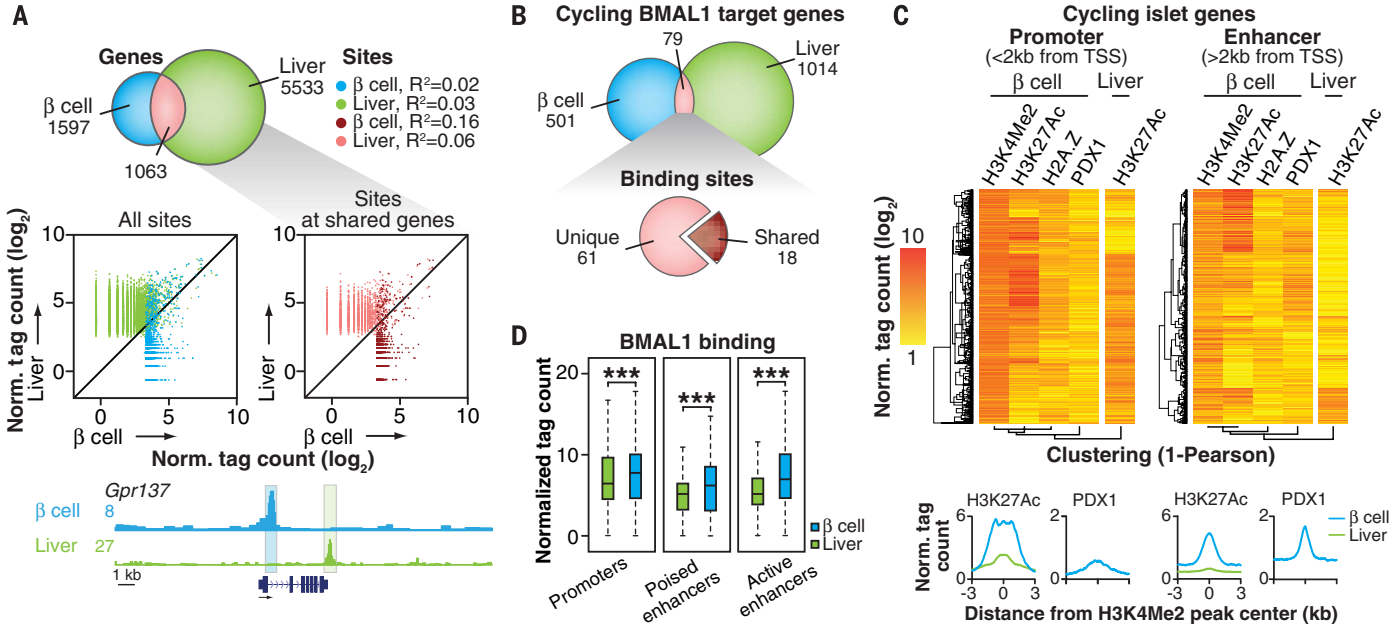

Fig. 3. β cell circadian cistrome is determined by tissue-specific enhancer repertoire. (**A**) Top: Overlap of genes identified at BMAL1 binding sites in β cells and liver. Middle: Scatterplots show BMAL1 binding in liver (*y* axis) versus β cells (*x* axis) within 500-bp windows surrounding peaks identified in each tissue. Bottom: Browser track view of BMAL1 binding in β cells and liver at the *Gpr137* locus. (**B**) Top: Overlap of cycling and direct BMAL1 target genes in β cells that have been reported to cycle in liver. Bottom: Cycling BMAL1 direct target genes containing shared or unique binding sites in β cells and liver. (**C**) Top: Heat maps comparing binding of indicated factors within 1-kb windows surrounding promoter (3492) and enhancer (5771) localized H3K4Me2 peaks annotating to genes containing cycling RNAs in wild-type islets. Bottom: Histograms summarizing normalized tag counts for H3K27Ac (in β cells and liver) and PDX1 (in β cells) across 6-kb span centered at all β cell H3K4Me2 peaks. (**D**) Box-and-whisker plots (whiskers represent interquartile range 1.5) comparing BMAL1 binding in β cells and liver at loci corresponding to H3K4Me2 peaks defined in heat maps. Poised enhancers refer to H3K4Me2 sites that do not colocalize with H3K27Ac, whereas active enhancers are defined as H3K4Me2 sites colocalized with H3K27Ac. ***$P < 0.0001$ by Mann-Whitney nonparametric unpaired *t* test. All reported ChIP-seq tag counts were normalized per 10^7 reads.

between circadian transcription factor regulation and genomic binding at regulatory loci, we performed chromatin immunoprecipitation sequencing (ChIP-seq) in the mouse β cell line Beta-TC6 (Fig. 2A). As expected, we found that both BMAL1 and CLOCK physically bound to sites at core clock and other gene targets in β cells that were enriched for the canonical CACGTG E-box motif, often occurring in tandem, as previously reported at BMAL1 binding sites in liver (fig. S5A) ($P = 10^{-38}$ and $P = 10^{-91}$, respectively) (*9*, *34*). Moreover, we also observed a correlation between the genome-wide binding of BMAL1 and CLOCK (fig. S5B). A representative UCSC Genome Browser track at the *Rev-erbα* (*Nr1d1*) locus is shown in Fig. 2A, revealing colocalization of BMAL1 and CLOCK binding sites at three distinct regulatory regions at the *Nr1d1* locus, including within the promoter region [shaded light orange and defined as within 2 kb of the transcription start site (TSS)] and within intragenic and intergenic distal enhancer regions (shaded light green and defined as binding regions greater than 2 kb from the TSS). Histone markers representing active and accessible chromatin (H3K27Ac and H2A.Z, respectively) localized to the same promoter and enhancer regions within the *Nr1d1* locus, indicating active transcriptional regulation by BMAL1 and CLOCK (Fig. 2A).

To determine whether BMAL1 and CLOCK directly regulate the oscillating transcripts identified in the synchronized wild-type islets (Fig. 1C), we evaluated the overlap between the BMAL1 and CLOCK cistromes with genes oscillating in the wild-type islets. Among binding sites localized to expressed RNAs, 30% (862 binding sites) and 29% (330 binding sites) of the BMAL1 and CLOCK targets, respectively, exhibited rhythmic transcription in synchronized wild-type islets (Fig. 2B), which collectively accounted for 742 cycling direct target genes, of which 165 were differentially expressed in *Bmal1* knockouts (fig. S5C). These findings suggest direct BMAL1 and CLOCK regulation. Moreover, KEGG analysis of the direct gene targets in mouse islets that were present in BMAL1 and CLOCK cistromes revealed enrichment in pathways related to protein export, COPII-mediated vesicle budding from the endoplasmic reticulum, and SNARE vesicular transport and membrane fusion, in the cycling set relative to the noncycling set of BMAL1- and CLOCK-controlled transcripts (KEGG pathways listed in order of descending $-\log_{10} P$ values in Fig. 2C and table S1). Together, these findings identify direct transcriptional targets of CLOCK/BMAL1 that mediate rhythmic islet physiology.

BMAL1 binds to distinct enhancers in liver and pancreatic β cells

Given evidence for tissue-specific regulation at enhancers as a predominant mode of circadian regulation in liver (*10*), we next analyzed the binding position of BMAL1 and CLOCK in relation to the TSS of rhythmic genes in β cells. Because genome-wide promoter activity studies and epigenetic characterization of mammalian regulatory regions have indicated that the majority of core promoter activity is localized within 2 kb of the TSS (*35*–*37*), we classified binding events occurring within 2 kb of the nearest annotated gene TSS as promoter-proximal. Surprisingly, we found that BMAL1 and CLOCK bind predominantly at distal sites (defined as greater than 2 kb from the TSS) rather than at proximal promoter sites (defined as less than 2 kb from the TSS) of rhythmically regulated genes (Fig. 2B and fig. S5D). This finding suggests that the islet clock transcription factors affect rhythmic physiology through binding to distal regulatory sites, an observation concordant with the general finding that transcription factors exert physiologic effects through regulation within tissue-specific enhancers (*31*).

Although clock factors have been shown to exert distinct physiologic functions across tissues, a major gap remains in understanding the underlying genomic mechanisms accounting for these tissue-specific functions. To determine whether BMAL1 regulates rhythmic genes through unique sites in the β cell compared to liver, the tissue in which the circadian cistrome has been best characterized (*9*–*11*, *34*, *38*), we compared sites of BMAL1 occupancy in the β cells to a published set of liver BMAL1 peaks (*9*). Unexpectedly, although there

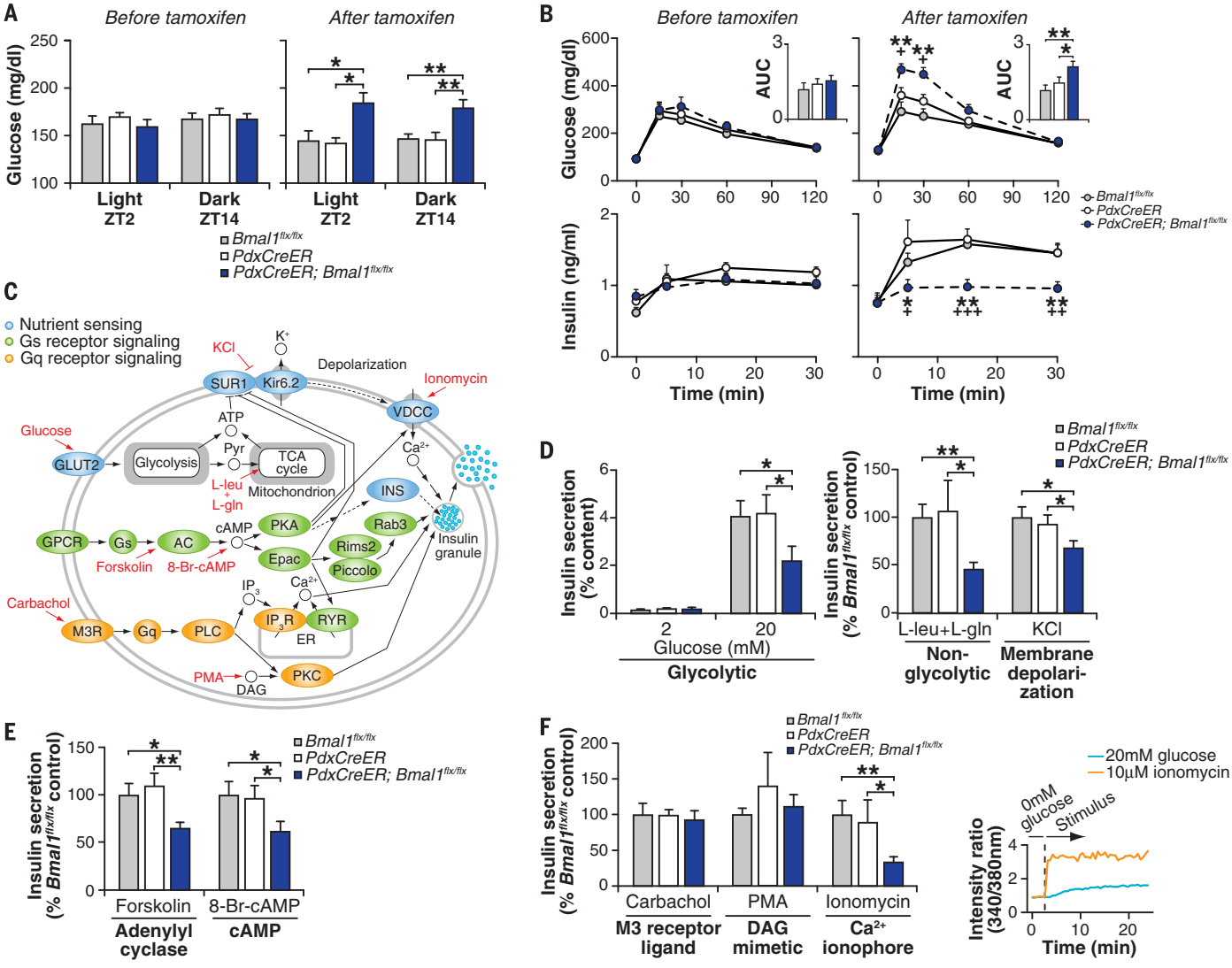

Fig. 4. Clock disruption in β cells during adulthood causes acute hypoinsulinemic diabetes in mice. (**A**) Blood glucose levels in ad libitum–fed *PdxCreER;Bmal1*$^{flx/flx}$ mice and littermate controls before and after tamoxifen administration (n = 6 to 12 mice per genotype). (**B**) Glucose tolerance and insulin secretion at ZT2 after intraperitoneal glucose administration in *PdxCreER;Bmal1*$^{flx/flx}$ mice and littermate controls before and after tamoxifen treatment (n = 4 to 11 mice per genotype). Inset represents area under the curve for glucose (10^4 mg/dl per 120 min). (**C**) Model of intersecting pathways driving insulin exocytosis. Nutrient, G_s, and G_q receptor signaling that are used to stimulate insulin secretion in (D) to (F) are highlighted. (**D** to **F**) Glucose- and nutrient-stimulated (D), cyclase pathway–stimulated (E), and catecholamine-stimulated (F) insulin secretion in islets isolated from tamoxifen-treated *PdxCreER;Bmal1*$^{flx/flx}$ and control mice (n = 3 to 8 mice per genotype, three repeats per mouse). Inset of (F) shows ratiometric determination of intracellular Ca^{2+} using Fura2-AM dye in Beta-TC6 cells in response to insulin secretagogs (n = 3 replicates per condition). All values represent mean ± SEM. For (B), asterisks denote significance between *Bmal1*$^{flx/flx}$ and *PdxCreER;Bmal1*$^{flx/flx}$; plus symbols denote significance between *PdxCreER* and *PdxCreER;Bmal1*$^{flx/flx}$. */+P < 0.05, **/++P < 0.01, +++P < 0.001.

was a considerable overlap of genes identified as direct BMAL1 binding targets in β cells and liver (40%, 1063 genes out of 2660 total β cell target genes) (Fig. 3A), BMAL1 binding at the regulatory regions of those shared gene sets localized to distinct sites (Fig. 3A). Remarkably, in comparing genome-wide binding patterns, we observed common locations of binding in only 4% of these instances; thus, BMAL1 binding at all β cell–defined sites is uncorrelated with BMAL1 binding at all liver-defined sites (Fig. 3A and fig. S5E) (R^2 = 0.01874 and 0.03286 for BMAL1 binding at β cell and liver sites, respectively), whereas binding at canonical E-box sites in *Per2*, *Cry1*, and *Dbp* was similar between tissues (fig. S5F). Furthermore, when we compared the shared set of BMAL1 target genes that were rhythmic in islets and also reported to be rhythmic at the mRNA level in liver, BMAL1 likewise bound to unique sites (*9*) (Fig. 3B). These data suggest convergent regulation of BMAL1 targets in β cell and liver sites through divergent regulatory elements.

Because BMAL1 predominantly bound at distal regulatory regions in islets that were divergent from liver, we next sought to examine the chromatin regulatory context at all cycling genes in β cells. To do so, we defined all regulatory regions at cycling loci using dimethylated histone 3 Lys^4 (H3K4Me2) peaks within 2 kb of the TSS (promoter) and more than 2 kb from the TSS (enhancer) (Fig. 3C). The binding patterns of the histone marks H3K4Me2, H2A.Z, and H3K27Ac (which represent promoter/enhancer regulatory regions, chromatin accessibility, and enhancer activity, respectively), as well as binding of the lineage-determining transcription factor for β cells PDX1 (*39*) at promoters and enhancer regions, are displayed in heat maps in Fig. 3C. Hierarchical clustering revealed that all epigenetic and PDX1 signals at promoter and distal enhancer regions at cycling genes more frequently displayed correlated binding than did H3K27Ac at these loci in liver, as indicated by the clustering dendrogram (Fig. 3C). Accordingly, the genomic coordinates in liver corresponding to enhancers defined in β cells displayed markedly

reduced H3K27Ac, indicating that these enhancers defined specific loci of β cell regulation (Fig. 3C). Frequent binding of PDX1 at distal enhancer loci suggested that tissue specificity arose from early events in islet cell development (Fig. 3C) (*40*). Consistent with tissue-specific clock transcription factor regulation at β cell regulatory regions, BMAL1 displayed a greater degree of binding to promoter and enhancer regions at cycling genes in β cells than in liver, particularly at active enhancers containing both H3K4Me2 and H3K27Ac (Fig. 3D). These results indicate that clock transcription factors generate unique patterns of rhythmic RNA expression across tissues according to the pattern of cell-specific enhancer repertoires and provide a molecular basis for the distinct and opposing effects of the clock in pancreas and liver, which primarily affect postprandial and fasting glucose metabolism, respectively (*5*, *6*).

β cell clock disruption during adulthood impairs insulin secretion and causes diabetes

To test the hypothesis that clock genes modulate genome-wide transcription on a daily basis throughout adult life, we examined the impact of acute clock inhibition on glucose metabolism in *PdxCreER;Bmal1*$^{flx/flx}$ mice at 2 to 3 months of age after administration of tamoxifen, which abrogates BMAL1 expression exclusively within the β cell (fig. S6) (*41*). Although these mice displayed normal wheel-running rhythms, period length, food intake, and body weight (fig. S7) relative to littermate tamoxifen-treated *PdxCreER* and *Bmal1*$^{flx/flx}$ animals, they developed significant hyperglycemia, impaired glucose tolerance, and hypoinsulinemia within 10 to 14 days after tamoxifen administration during both the day (ZT2) and night (ZT14) (Fig. 4, A and B, and fig. S8), despite no differences in islet mass (fig. S9A). These results establish that circadian disruption in fully differentiated cells is sufficient to induce metabolic disease, independent of effects on early development.

We further found that islets isolated from tamoxifen-treated *PdxCreER;Bmal1*$^{flx/flx}$ mice secreted significantly less insulin relative to littermate controls when exposed to (i) 20 mM glucose; (ii) 10 mM leucine combined with 2 mM glutamine, which bypasses glycolysis to trigger mitochondrial adenosine triphosphate (ATP) production; or (iii) 30 mM KCl, which chemically closes the K_{ATP} channel, thus inducing membrane depolarization distal to glucose metabolism and an increase in cytosolic calcium (Fig. 4, C and D); glucose-stimulated calcium influx was unchanged between the two groups (fig. S9B). Remarkably, these data are consistent with our observation that circadian oscillation in insulin secretory capacity is regulated downstream of K_{ATP} channel closure. Consistent with impaired G_s-coupled GPCR signaling, *PdxCreER;Bmal1*$^{flx/flx}$ islets also secreted significantly less insulin than controls in response to glucose together with the cyclase agonist forskolin and the nonhydrolyzable cAMP analog 8-br-cAMP (Fig. 4, C and E).

Finally, we tested the response to G_q-type GPCR signaling by stimulating islets with the muscarinic agonist carbachol, the diacylglycerol (DAG) mimetic phorbol 12-myristate 13-acetate (PMA), and the Ca^{2+} ionophore ionomycin. Surprisingly, carbachol and PMA restored insulin secretion in *PdxCreER;Bmal1*$^{flx/flx}$ islets (Fig. 4, C and F), whereas the response to ionomycin, which raised intracellular Ca^{2+} in β cells (Fig. 4F), was significantly reduced in mutants, indicating that the DAG arm of the G_q pathway restored second messenger signaling. DAG regulates exocytosis in β cells and other neurosecretory cells by acting as a ligand for the vesicle priming protein Munc13-1 (*42*) and protein kinase C (PKC), which phosphorylates and activates SNAP25 and MUNC18-1 to initiate vesicle fusion (*43*). We observed rhythmic RNA expression of the PKC-activating Rho and Rap GTPases *Rho*, *Rhoa*, *Rhob*, and *Rap1a* in wild-type islets, which raises the intriguing possibility that elevated DAG concentrations in carbachol- or PMA-treated islets pharmacologically bypass a deficiency in Rho- and Rap-mediated signaling. Together, these results demonstrate that pharmacologic G_q agonism reverses the insulin secretory blockade induced by clock disruption, indicating convergence of cholinergic and phosphoinositol signaling within the β cell in temporal homeostasis.

Discussion

We have established the genome-wide basis of coordinated cross-tissue circadian oscillation through integrated studies of β cell physiology and cistrome regulation. We focused on pancreatic β cells as a paradigm of peripheral clock regulation of metabolism because clock disruption in the islet leads to severe hypoinsulinemic diabetes and has direct application to understanding human tissue rhythms and disease. Although the circadian system functions as a hierarchy in the intact animal, our results reveal organ-autonomous cycles of nutrient-coupled insulin secretion in isolated islets ex vivo that result in a high amplitude in maximal glucose responsiveness, suggesting that the clock primes insulin secretion within limited windows each day. We further find that circadian-driven transcriptional oscillation within pancreas drives daily waves of expression of genes involved in the biogenesis, transport, and signal-induced activation of peptide exocytosis, indicating that genomic rhythmicity gives rise to tissue-specific function of the clock. Our observations suggest that autonomous transcription cycles enable islet cells to anticipate diurnal changes in the demand for insulin.

Cistromic profiling within the β cell provides further insight into the regulation of tissue-specific genome oscillation. We found that CLOCK and BMAL1 bind predominantly within distal tissue-specific enhancers rather than the promoters of cycling genes in proximity to H3K4Me2-, H2A.Z-, and H3K27Ac-modified nucleosomes that are co-occupied by PDX1. Consistent with tissue specificity in enhancer selection across cell types, BMAL1 binding in islet cells was highly divergent from liver, even within shared cycling target genes across the two tissues. These findings suggest that the establishment of accessible chromatin domains during development is a critical determinant of the available regulatory sites for clock-mediated transcription across distinct cell types. Further studies will be needed to define the underlying mechanisms through which divergent tissue-specific regulation gives rise to convergent oscillation of rhythmic genes.

Finally, our studies using chemically inducible genetic clock inactivation demonstrate that inhibition of circadian signaling in differentiated β cells acutely blocks peptide exocytosis and leads to hypoinsulinemic diabetes, providing evidence that clock function throughout adult life is necessary for glucose constancy. An intriguing possibility is that cell-autonomous genomic rhythms may regulate peptidergic secretion across diverse secretory and neuronal cell types, coordinating the availability of signaling molecules with the sleep/wake cycle each day. Furthermore, given the association between circadian and sleep disruption with human metabolic disease in both clinical (*44*, *45*) and genetic (*46*) studies, the finding that circadian transcription is conserved in human islets suggests that clock dysregulation in β cells may contribute to the pathogenesis of human diabetes. The demonstration of coordinated circadian genomic and physiologic rhythms in pancreatic β cell insulin exocytosis and its control by enhancers provides a new window to understanding how geophysical and physiologic time are transcriptionally coupled, and how errors in this process may contribute to diabetes and other metabolic disorders.

Materials and methods

Animals

Male wild-type C57BL/6J mice were purchased from the Jackson Laboratory. *Per2*^{Luc} (*12*) and *PdxCre;Bmal1*$^{flx/flx}$ (*6*) mice were produced and maintained on a C57BL/6J background at the Northwestern University Center for Comparative Medicine. *Bmal1*$^{flx/flx}$ mice (*47*) were crossed with *PdxCreER* transgenic mice (kindly provided by D. Melton, Harvard University) (*48*) to generate *PdxCreER;Bmal1*$^{flx/flx}$ mice, as well as *Bmal1*$^{flx/flx}$ and *PdxCreER* littermate controls. Unless otherwise stated, mice were maintained on a 12:12 light:dark (LD) cycle with free access to regular chow and water. All animal care and use procedures were conducted in accordance with regulations of the Institutional Animal Care and Use Committee at Northwestern University.

Islet isolation, insulin secretion assays, and in vitro islet synchronization

Mouse pancreatic islets were isolated via bile duct collagenase digestion (Collagenase P, Sigma) and Ficoll gradient separation and left to recover overnight (16 hours) at 37°C in RPMI 1640 with 10% fetal bovine serum (FBS), 1% L-glutamine, and 1% penicillin/streptomycin. For standard insulin release assays, five islets were statically incubated in Krebs-Ringer buffer (KRB) and stimulated for 1 hour at 37°C with various glucose

concentrations, 30 mM KCl, 2.5 μM forskolin, 1 mM 8-Br-cAMP, 10 mM L-leucine + 2 mM L-glutamine, 1 mM carbachol, 10 μM PMA, or 10 μM ionomycin. Supernatant was collected and assayed for insulin content by enzyme-linked immunosorbent assay (ELISA; Crystal Chem Inc.). Islets were then sonicated in acid-ethanol solution and solubilized overnight at 4°C before assaying total insulin content by ELISA. For rhythmic insulin release assays, islets were first synchronized with 10 μM forskolin (Sigma) for 1 hour and allowed to recover for 16 hours. Insulin secretion assays were then performed as above in individual groups of five islets every 4 hours for 72 hours (fig. S1A). Human islets (obtained from IIDP) were cultured in RPMI 1640 with 10% human AB serum, 1% L-glutamine, and 1% penicillin/streptomycin (see table in fig. S4A for details of sex, age, BMI, and IIDP ID numbers of the three donors). For the rhythmic analysis of RNAs in murine and human islets, RNA was isolated (described below) in groups of 200 islets every 4 hours for 48 or 24 hours, respectively, starting 40 hours after forskolin synchronization (fig. S1A).

LumiCycle analysis

Approximately 2 hours before the start of the dark period (i.e., lights off), ~100 to 150 pancreatic islets were isolated from *Per2*^{Luc} mice as described above. Islets were cultured on tissue culture membranes (Millipore) in Dulbecco's modified Eagle's medium (DMEM; Gibco, 1.2 ml) containing sodium bicarbonate (352.5 μg/ml), 10 mM HEPES (Gibco), 2 mM L-glutamine, 2% B-27 serum-free supplement (Invitrogen), penicillin (25 U/ml), streptomycin (Gibco, 20 μg/ml), and 0.1 mM luciferin sodium salt (Biosynth AG). Sealed cultures were placed at 37°C in a LumiCycle luminometer (Actimetrics) and bioluminescence from tissues was recorded continuously. After several days in culture, islets were synchronized by 10 μM forskolin (Sigma) treatment for 1 hour followed by incubation in fresh media. Period was calculated via a modified best-fit sine wave analysis using LumiCycle analysis software (Actimetrics).

Measurement of islet oxygen consumption

After bile duct collagenase digestion, 40 purified pancreatic islets were plated in wells of a 96-well respirometry plate (Seahorse Bioscience) and cultured overnight in complete medium. The next day, culture medium was replaced with assay buffer containing 3 mM glucose, 0.8 mM Mg^{2+}, 1.8 mM Ca^{2+}, 143 mM NaCl, 5.4 mM KCl, 0.91 mM NaH_2PO_4, and phenol red (Seahorse Bioscience; 15 mg/ml) and allowed to equilibrate at 37°C in a CO_2-free incubator for 1 to 2 hours. The plate was then loaded into a Seahorse XF96 instrument, and the oxygen consumption rate (OCR) was measured for four sequential 3-min intervals at basal conditions and after injection of glucose (20 mM final concentration), oligomycin (F1FO ATP synthase inhibitor) (5 μM final concentration), and antimycin A (complex III inhibitor) (5 μM final concentration). OCR values given represent the average of four sequential measurements. Mitochondrial oxygen consumption was calculated by subtracting OCR values after antimycin A treatment (representing non-mitochondrial oxygen consumption).

RNA isolation and qPCR mRNA quantification

Islets were added to microfuge tubes containing Tri Reagent (Molecular Research Center Inc.) and frozen at −80°C. RNA was isolated according to the manufacturer's protocol and purified using RNeasy columns (Qiagen). cDNAs were then synthesized using the High Capacity cDNA Reverse Transcription Kit (Applied Biosystems). Real-time quantitative polymerase chain reaction (qPCR) analysis was performed with SYBR Green Master Mix (Applied Biosystems) and analyzed using an Applied Biosystems 7900 Fast Real-Time PCR System. Relative expression levels were determined using the comparative C_T method to normalize target gene mRNA to *Gapdh*. Exon-specific primer sequences for qPCR were as follows: *Bmal1* exons 5 to 7, forward, 5′-ATCGCAAGAGGAAAGGCAGT-3′; reverse, 5′-ATCCTTCCTTGGTGTTCTGCAT-3′. *Bmal1* exons 7 to 9, forward, 5′- AGGCCCACAGTCAGATTGAA-3′; reverse, 5′-TGGTACCAAAGAAGCCAATTCAT-3′. *Bmal1* exon 8, forward, 5′-GGCGTCGGGACA-AAATGAAC-3′; reverse, 5′-TCTAACTTCCTGG-ACATTGCAT-3′. *Bmal1* exons 8 and 9, forward, 5′-TGCAATGTCCAGGAAGTTAGAT-3′; reverse, 5′-TGGTGGCACCTCTCAAAGTT-3′. *Bmal1* exons 10 to 12, forward, 5′-TAGGATGTGACCGAGGGAAG-3′; reverse, 5′- AGCTCTGGCCAATAAGGTCA-3′.

RNA sequencing and analysis

After RNA isolation (described above), RNA quality was assessed using a Bioanalyzer (Agilent), and sequencing libraries were constructed using an Illumina TruSeq Stranded mRNA sample prep kit LT (Illumina, RS-122-2101) according to the manufacturer's instructions. Libraries were quantified using both a Bioanalyzer (Agilent) and qPCR-based quantification (Kapa Biosystems) and sequenced on either an Illumina HiSEq 2000 or NextSEq 500 instrument to a depth of at least 30 million reads using 100–base pair (bp) or 75-bp paired-end reads, respectively.

For differential expression comparison between *PdxCre;Bmal1*$^{flx/flx}$ and *Bmal1*$^{flx/flx}$ islets, RNA raw sequence reads were aligned to the reference genome (mm10) using STAR version 2.3.1s_r366 (*49*). Differentially expressed RNAs were identified using DESEq 2 version 1.6.3 (*50*) (FDR-adjusted $P < 0.05$).

For cycling RNAs, raw sequence reads were similarly aligned using STAR (mm10 index for mouse and hg19 for human), and uniquely mapped reads (tags) were normalized using the algorithm used in DESEq 2 (*50*). The geometric mean of the raw read counts was calculated for each gene. A normalization factor was calculated for each sample using the median of the raw read counts of each gene divided by the geometric mean of the gene. The normalized read counts were computed by dividing the raw read counts by the normalization factor. The normalized tags for the mouse and human time series were separately concatenated and z-scored within each gene (*14*). Rhythm detection of the z-scored and normalized counts was performed with empirical JTK_CYCLE with asymmetry search, which increases sensitivity of detecting cycling transcripts by extending comparisons to reference waveforms beyond cosines, including arbitrary asymmetric waveforms that better represent expression patterns seen in biological data. Rhythmic time series were examined with reference waveforms with a period of 24 hours; a phase of 0, 4, 8, 12, 16, or 20; and an asymmetry of 4, 12, or 20. Because of the small number of waveforms compared, the Bonferroni correction was used instead of the empirical P values. Genes with a Bonferroni-adjusted P value below 0.05 were considered to be rhythmic.

For KEGG ontology term enrichment (*51*, *52*), Ensembl gene IDs were supplied and analyzed using Homer (version 4.7.2) command "findGO" (*53*).

Genes exhibiting rhythmic mRNA accumulation in vivo in liver were derived from reported "exon cycling" transcripts (*9*).

β cell culture

Beta-TC6 cells were purchased from ATCC (CRL-11506) and cultured in DMEM supplemented with 15% FBS, 1% L-glutamine, and 1% penicillin/streptomycin. All cells used in experiments were at fewer than 15 passages.

Mouse BMAL1 and CLOCK polyclonal antibody generation

Guinea pig anti-mouse BMAL1 and CLOCK polyclonal antibodies were generated using a 37– and 39–amino acid peptide fragment of the mouse BMAL1 and CLOCK proteins, respectively (RS synthesis). Guinea pigs were immunized with KLH-conjugated peptides (Pocono Farms), and BMAL1- and CLOCK-specific antibodies were affinity-purified from whole serum using resin cross-linked with antigen peptides (Pierce).

Chromatin immunoprecipitation (ChIP)

Beta-TC6 cells (~40 to 160 million) were fixed for 30 min in 2 mM disuccinimidyl glutarate and for 10 min in 1% formaldehyde and then either frozen at −80°C or processed immediately. Nuclei were isolated in buffer containing 1% SDS, 10 mM EDTA, 50 mM Tris-HCl (pH 8.0), and protease inhibitors and sonicated using a Diagenode Bioruptor to shear chromatin into 200- to 1000-bp fragments. Protein-DNA complexes were incubated with antibodies against BMAL1 and CLOCK (affinity-purified guinea pig IgGs as described above), H3K4Me2 (Abcam), H3K27Ac (Active Motif), H2AZ (Active Motif), or PDX1 (Novus Biologicals) and immunoprecipitated with IgG paramagnetic beads (Invitrogen). Eluted chromatin was isolated using MinElute PCR purification columns (Qiagen).

ChIP sequencing and analysis

Sequencing libraries were generated using KAPA DNA Library Preparation kits (Kapa Biosystems,

KK8504) according to manufacturer's instructions. Library concentrations were assessed by both a Bioanalyzer (Agilent) and qPCR-based quantification (Kapa Biosystems). Libraries were sequenced using 75-bp single-end reads on an Illumina Next-SEq 500 instrument to a depth of >10 million mapped reads.

Raw sequence reads were aligned to the mm10 reference genome and displayed using UCSC annotated genes using bowtie version 1.1.1 (*54*) with parameters "-best" and "-m 1" to ensure reporting of uniquely mapped reads (tags). ChIP-seq peaks were designated as regions with a factor of 4 enrichment over both the input sample and the local background and were normalized to 10 million reads using default parameters for the Homer "findPeaks" command (*53*) and specifying "-style factor" for BMAL1, CLOCK, and PDX1 and "-style histone" for H2A.Z, H3K4Me2, and H3K27Ac. For BMAL1 and CLOCK peaks, promoter binding was defined as peaks occurring within 2 kb of the nearest gene TSS, and distal binding was defined as those occurring greater than 2 kb from a nearest TSS.

To identify consensus motifs for BMAL1 and CLOCK, we scanned 50-bp windows surrounding transcription factor peaks using "findMotifsGenome.pl" with standard background (random genomic sequences sampled according to GC content of peak sequences). We determined the occurrence of tandem E-boxes with variable-length spacing by generating synthetic canonical E-box motifs separated by the indicated number of random spacers (i.e., CACGTGNNNCACGTG = 3 spacers) using "seq2profile.pl" allowing for two mismatches and testing for their occurrence at BMAL1 and CLOCK peaks using "annotatePeaks.pl".

Fastq files for all BMAL1 and H3K27Ac ChIP-seq were downloaded from the ENA server (study accession number SRP014752) and raw sequence reads for 12 sequential time points were concatenated into a single file. Alignments and peak calling were performed using bowtie and Homer as described above. Shared BMAL1 binding sites were identified by comparing binding locations between β cells and liver using the Homer command "mergePeaks" and specifying "-d 200," which identified peaks occurring within 200 bp as shared across tissues.

Tamoxifen treatment

For in vivo delivery of tamoxifen (Sigma, dissolved in corn oil), mice received three intraperitoneal (i.p.) injections of 200 μg tamoxifen/g body weight, administered every other day. Subsequent experiments were conducted 10 to 14 days after tamoxifen treatment. For in vitro administration of tamoxifen, isolated islets were incubated for 24 hours with 1 mM tamoxifen (dissolved in ethanol) prior to transfer to complete media for 24 hours to recover. Islets were then synchronized with forskolin prior to insulin secretion assays as described above.

Immunohistochemical analysis

Mice were anesthetized with i.p. injection of phenobarbital (Nembutal, 50 mg/ml) and perfused with heparinized saline, followed by 4% paraformaldehyde (PFA) (Sigma) in PBS. Brain and pancreas were removed and post-fixed with 4% PFA overnight at 4°C. Brain tissues were then cryoprotected in 30% sucrose (Sigma), frozen in O.T.C. (Tissue Tek), and 30-μm brain sections collected for antibody staining. Pancreata were embedded in paraffin, and blocks of 6-μm sections were mounted on slides. The following primary antibodies were used for staining: guinea pig anti-insulin (1:500, DAKO), mouse anti-glucagon (1:500, Sigma), and rabbit anti-BMAL1 (1:500, Novus Biological). Triple staining was visualized with the following secondary antibodies: AMCA goat anti–guinea pig (1:400, Jackson ImmunoResearch), Alexa Fluor 488–conjugated goat anti-mouse (1:400, Invitrogen), and Alexa Fluor 546–conjugated goat anti-rabbit (1:400, Life Technologies). Nuclei were counterstained with 4′,6-diamidino-2-phenylindole (DAPI) as indicated. Images were acquired with PictureFrame 1.0 using a Zeiss Axioskop 50. β cell mass was assessed by morphometric analysis of insulin immunostained pancreatic sections (DAKO; Histomouse Plus kit, Life Technologies). Four pancreatic sections, spaced 50 μm apart, were stained for each animal, and endocrine versus total pancreas area was calculated using Image-Pro Premier software (Media Cybernetics) using the smart segmentation feature.

Glucose and insulin measurements and glucose tolerance tests

Blood glucose and plasma insulin levels in ad libitum–fed mice were assessed at ZT2 and ZT14 from tail vein bleeds. Glucose tolerance tests were performed in mice after a 14-hour fast, and blood glucose and plasma insulin levels were measured at the indicated times after i.p. glucose injection of either 2 or 3 g/kg body weight, respectively. Plasma insulin levels were measured by ELISA.

Behavioral analysis

Locomotor activity was analyzed in 2- to 4-month-old pancreas-specific *Bmal1* knockout mice and their respective littermate controls after tamoxifen treatment. All animals were individually housed in standard mouse cages equipped with running wheels and allowed free access to food and water. Mice were placed in a 12:12 LD cycle for 14 days, followed by 14 days in constant darkness (DD). Total activity data was recorded and analyzed in 6-min bouts using ClockLab software (Actimetrics). The free-running period was determined as the duration of time between the major activity periods on consecutive days in DD. Period was calculated using a χ^2 periodogram for days 7 to 14 in DD. Food consumption was analyzed in pancreas-specific *Bmal1* knockout mice and their littermate controls before and after tamoxifen treatment. All animals were individually housed with free access to water and regular chow. Daytime and nighttime food consumption was determined by manual measurement of food at both ZT0 and ZT12 for three consecutive days.

Intracellular calcium determination

BetaTC-6 cells were plated at a density of 100,000 cells per well in black 96-well plates with clear bottoms and cultured overnight at 37°C and 5% CO_2. Islets were dispersed to single cells by incubating in 0.05% Trypsin-EDTA at 37°C for 3 min and plated at a density of 100 islets per well in laminin-treated black 96-well plates with clear bottoms and cultured in complete media for 48 hours at 37°C and 5% CO_2. Cells were then washed with BSA-free KRB buffer with no glucose and loaded with 5 μM Fura-2 (Invitrogen) and 0.04% Pluronic F-127 (Invitrogen) for 30 min at 37°C. Following a wash with BSA-free KRB, Fura-2 intensity was measured after injection of either glucose or ionomycin (Sigma) to final concentrations of 20 mM or 10 μM, respectively. Cells were alternately excited with 340- and 380-nm light, and the emitted light was detected at 510 nm using a Cytation 3 Cell Imaging Multi-Mode Reader (Bio Tek) at sequential 30-s intervals. Raw fluorescence data were exported to Microsoft Excel and expressed as the 340/380 ratio for each well.

REFERENCES AND NOTES

1. N. Preitner *et al*., The orphan nuclear receptor REV-ERBα controls circadian transcription within the positive limb of the mammalian circadian oscillator. *Cell* **110**, 251–260 (2002). doi: 10.1016/S0092-8674(02)00825-5; pmid: 12150932
2. I. Zamir *et al*., A nuclear hormone receptor corepressor mediates transcriptional silencing by receptors with distinct repression domains. *Mol. Cell. Biol.* **16**, 5458–5465 (1996). doi: 10.1128/MCB.16.10.5458; pmid: 8816459
3. A. Balsalobre, F. Damiola, U. Schibler, A serum shock induces circadian gene expression in mammalian tissue culture cells. *Cell* **93**, 929–937 (1998). doi: 10.1016/S0092-8674(00)81199-X; pmid: 9635423
4. F. W. Turek *et al*., Obesity and metabolic syndrome in circadian Clock mutant mice. *Science* **308**, 1043–1045 (2005). doi: 10.1126/science.1108750; pmid: 15845877
5. K. A. Lamia, K. F. Storch, C. J. Weitz, Physiological significance of a peripheral tissue circadian clock. *Proc. Natl. Acad. Sci. U.S.A.* **105**, 15172–15177 (2008). doi: 10.1073/pnas.0806717105 pmid: 18779586
6. B. Marcheva *et al*., Disruption of the clock components CLOCK and BMAL1 leads to hypoinsulinaemia and diabetes. *Nature* **466**, 627–631 (2010). doi: 10.1038/nature09253 pmid: 20562852
7. L. A. Sadacca, K. A. Lamia, A. S. deLemos, B. Blum, C. J. Weitz, An intrinsic circadian clock of the pancreas is required for normal insulin release and glucose homeostasis in mice. *Diabetologia* **54**, 120–124 (2011). doi: 10.1007/s00125-010-1920-8 pmid: 20890745
8. C. B. Peek *et al*., Circadian clock NAD^+ cycle drives mitochondrial oxidative metabolism in mice. *Science* **342**, 1243417 (2013). doi: 10.1126/science.1243417; pmid: 24051248
9. N. Koike *et al*., Transcriptional architecture and chromatin landscape of the core circadian clock in mammals. *Science* **338**, 349–354 (2012). doi: 10.1126/science.1226339 pmid: 22936566
10. B. Fang *et al*., Circadian enhancers coordinate multiple phases of rhythmic gene transcription in vivo. *Cell* **159**, 1140–1152 (2014). doi: 10.1016/j.cell.2014.10.022; pmid: 25416951
11. J. S. Menet, J. Rodriguez, K. C. Abruzzi, M. Rosbash, Nascent-Seq reveals novel features of mouse circadian transcriptional regulation. *eLife* **1**, e00011 (2012). pmid: 23150795
12. S. H. Yoo *et al*., PERIOD2:LUCIFERASE real-time reporting of circadian dynamics reveals persistent circadian oscillations in mouse peripheral tissues. *Proc. Natl. Acad. Sci. U.S.A.* **101**, 5339–5346 (2004). pmid: 14963227
13. J. S. O'Neill, E. S. Maywood, J. E. Chesham, J. S. Takahashi, M. H. Hastings, cAMP-dependent signaling as a core component of the mammalian circadian pacemaker. *Science* **320**, 949–953 (2008). doi: 10.1126/science.1152506 pmid: 18487196
14. A. L. Hutchison *et al*., Improved statistical methods enable greater sensitivity in rhythm detection for genome-wide data. *PLOS Comput. Biol.* **11**, e1004094 (2015). doi: 10.1371/journal.pcbi.1004094; pmid: 25793520
15. H. R. Ueda *et al*., System-level identification of transcriptional circuits underlying mammalian circadian

clocks. *Nat. Genet.* **37**, 187–192 (2005). doi: 10.1038/ng1504; pmid: 15665827
16. X. W. Chen *et al.*, SEC24A deficiency lowers plasma cholesterol through reduced PCSK9 secretion. *eLife* **2**, e00444 (2013). doi: 10.7554/eLife.00444; pmid: 23580231
17. A. J. Noble *et al.*, A pseudoatomic model of the COPII cage obtained from cryo-electron microscopy and mass spectrometry. *Nat. Struct. Mol. Biol.* **20**, 167–173 (2013). doi: 10.1038/nsmb.2467; pmid: 23262493
18. Z. Wang, D. C. Thurmond, Mechanisms of biphasic insulin-granule exocytosis - roles of the cytoskeleton, small GTPases and SNARE proteins. *J. Cell Sci.* **122**, 893–903 (2009). doi: 10.1242/jcs.034355; pmid: 19295123
19. Y. Liu, Y. Sugiura, W. Lin, The role of synaptobrevin1/VAMP1 in Ca^{2+}-triggered neurotransmitter release at the mouse neuromuscular junction. *J. Physiol.* **589**, 1603–1618 (2011). doi: 10.1113/jphysiol.2010.201939; pmid: 21282288
20. M. Ohara-Imaizumi *et al.*, Correlation of syntaxin-1 and SNAP-25 clusters with docking and fusion of insulin granules analysed by total internal reflection fluorescence microscopy. *Diabetologia* **47**, 2200–2207 (2004). doi: 10.1007/s00125-004-1579-0; pmid: 15647897
21. K. Fujimoto *et al.*, Piccolo, a Ca^{2+} sensor in pancreatic beta-cells. Involvement of cAMP-GEFII.Rim2. Piccolo complex in cAMP-dependent exocytosis. *J. Biol. Chem.* **277**, 50497–50502 (2002). doi: 10.1074/jbc.M210146200; pmid: 12401793
22. H. Takahashi *et al.*, Role of Epac2A/Rap1 signaling in interplay between incretin and sulfonylurea in insulin secretion. *Diabetes* **64**, 1262–1272 (2015). pmid: 25315008
23. M. Fukuda, Molecular cloning, expression, and characterization of a novel class of synaptotagmin (Syt XIV) conserved from *Drosophila* to humans. *J. Biochem.* **133**, 641–649 (2003). doi: 10.1093/jb/mvg082; pmid: 12801916
24. A. Milochau *et al.*, Synaptotagmin 11 interacts with components of the RNA-induced silencing complex RISC in clonal pancreatic β-cells. *FEBS Lett.* **588**, 2217–2222 (2014). pmid: 24882364
25. R. A. Easom, CaM kinase II: A protein kinase with extraordinary talents germane to insulin exocytosis. *Diabetes* **48**, 675–684 (1999). doi: 10.2337/diabetes.48.4.675; pmid: 10102681
26. T. J. Biden *et al.*, The diverse roles of protein kinase C in pancreatic beta-cell function. *Biochem. Soc. Trans.* **36**, 916–919 (2008). doi: 10.1042/BST0360916; pmid: 18793161
27. X. Zhang *et al.*, Membrane association and functional regulation of Sec3 by phospholipids and Cdc42. *J. Cell Biol.* **180**, 145–158 (2008). doi: 10.1083/jcb.200704128 pmid: 18195105
28. G. Jedd, J. Mulholland, N. Segev, Two new Ypt GTPases are required for exit from the yeast trans-Golgi compartment. *J. Cell Biol.* **137**, 563–580 (1997). doi: 10.1083/jcb.137.3.563; pmid: 9151665
29. P. Pulimeno *et al.*, Autonomous and self-sustained circadian oscillators displayed in human islet cells. *Diabetologia* **56**, 497–507 (2013). doi: 10.1007/s00125-012-2779-7; pmid: 23242133
30. C. Benner *et al.*, The transcriptional landscape of mouse beta cells compared to human beta cells reveals notable species differences in long non-coding RNA and protein-coding gene expression. *BMC Genomics* **15**, 620 (2014). doi: 10.1186/1471-2164-15-620; pmid: 25051960
31. L. Pasquali *et al.*, Pancreatic islet enhancer clusters enriched in type 2 diabetes risk-associated variants. *Nat. Genet.* **46**, 136–143 (2014). doi: 10.1038/ng.2870; pmid: 24413736
32. M. P. Creyghton *et al.*, Histone H3K27ac separates active from poised enhancers and predicts developmental state. *Proc. Natl. Acad. Sci. U.S.A.* **107**, 21931–21936 (2010). doi: 10.1073/pnas.1016071107; pmid: 21106759
33. H. H. He *et al.*, Nucleosome dynamics define transcriptional enhancers. *Nat. Genet.* **42**, 343–347 (2010). doi: 10.1038/ng.545; pmid: 20208536
34. G. Rey *et al.*, Genome-wide and phase-specific DNA-binding rhythms of BMAL1 control circadian output functions in mouse liver. *PLOS Biol.* **9**, e1000595 (2011). doi: 10.1371/journal.pbio.1000595; pmid: 21364973
35. N. D. Heintzman *et al.*, Distinct and predictive chromatin signatures of transcriptional promoters and enhancers in the human genome. *Nat. Genet.* **39**, 311–318 (2007). doi: 10.1038/ng1966; pmid: 17277777
36. S. J. Cooper, N. D. Trinklein, E. D. Anton, L. Nguyen, R. M. Myers, Comprehensive analysis of transcriptional promoter structure and function in 1% of the human genome. *Genome Res.* **16**, 1–10 (2006). doi: 10.1101/gr.4222606 pmid: 16344566
37. P. Carninci *et al.*, Genome-wide analysis of mammalian promoter architecture and evolution. *Nat. Genet.* **38**, 626–635 (2006). doi: 10.1038/ng1789; pmid: 16645617
38. C. Vollmers *et al.*, Circadian oscillations of protein-coding and regulatory RNAs in a highly dynamic mammalian liver epigenome. *Cell Metab.* **16**, 833–845 (2012). doi: 10.1016/j.cmet.2012.11.004; pmid: 23217262
39. D. A. Stoffers, N. T. Zinkin, V. Stanojevic, W. L. Clarke, J. F. Habener, Pancreatic agenesis attributable to a single nucleotide deletion in the human IPF1 gene coding sequence. *Nat. Genet.* **15**, 106–110 (1997). doi: 10.1038/ng0197-106; pmid: 8988180
40. B. G. Hoffman *et al.*, Locus co-occupancy, nucleosome positioning, and H3K4me1 regulate the functionality of FOXA2-, HNF4A-, and PDX1-bound loci in islets and liver. *Genome Res.* **20**, 1037–1051 (2010). doi: 10.1101/gr.104356.109 pmid: 20551221
41. C. Gu *et al.*, Pancreatic beta cells require NeuroD to achieve and maintain functional maturity. *Cell Metab.* **11**, 298–310 (2010). doi: 10.1016/j.cmet.2010.03.006; pmid: 20374962
42. L. Kang *et al.*, Munc13-1 is required for the sustained release of insulin from pancreatic beta cells. *Cell Metab.* **3**, 463–468 (2006). doi: 10.1016/j.cmet.2006.04.012; pmid: 16697276
43. O. Genç O. Kochubey, R. F. Toonen, M. Verhage, R. Schneggenburger, Munc18-1 is a dynamically regulated PKC target during short-term enhancement of transmitter release. *eLife* **3**, e01715 (2014). doi: 10.7554/eLife.01715 pmid: 24520164
44. C. J. Morris *et al.*, Endogenous circadian system and circadian misalignment impact glucose tolerance via separate mechanisms in humans. *Proc. Natl. Acad. Sci. U.S.A.* **112**, E2225–E2234 (2015). doi: 10.1073/pnas.1418955112 pmid: 25870289
45. O. M. Buxton *et al.*, Adverse metabolic consequences in humans of prolonged sleep restriction combined with circadian disruption. *Sci. Transl. Med.* **4**, 129ra43 (2012). pmid: 22496545
46. A. Bonnefond *et al.*, Rare MTNR1B variants impairing melatonin receptor 1B function contribute to type 2 diabetes. *Nat. Genet.* **44**, 297–301 (2012). doi: 10.1038/ng.1053; pmid: 22286214
47. B. P. Johnson *et al.*, The hepatocyte circadian clock controls acetaminophen bioactivation through NADPH-cytochrome P450 oxidoreductase. *Proc. Natl. Acad. Sci. U.S.A.* **111**, 18757–18762 (2014). doi: 10.1073/pnas.1421708111; pmid: 25512522
48. G. Gu, J. Dubauskaite, D. A. Melton, Direct evidence for the pancreatic lineage: $NGN3^+$ cells are islet progenitors and are distinct from duct progenitors. *Development* **129**, 2447–2457 (2002). pmid: 11973276
49. A. Dobin *et al.*, STAR: Ultrafast universal RNA-seq aligner. *Bioinformatics* **29**, 15–21 (2013). doi: 10.1093/bioinformatics/bts635; pmid: 23104886
50. M. I. Love, W. Huber, S. Anders, Moderated estimation of fold change and dispersion for RNA-seq data with DESeq2. *Genome Biol.* **15**, 550 (2014). doi: 10.1186/s13059-014-0550-8 pmid: 25516281
51. M. Kanehisa *et al.*, Data, information, knowledge and principle: Back to metabolism in KEGG. *Nucleic Acids Res.* **42**, D199–D205 (2014). doi: 10.1093/nar/gkt1076; pmid: 24214961
52. H. Ogata *et al.*, KEGG: Kyoto Encyclopedia of Genes and Genomes. *Nucleic Acids Res.* **27**, 29–34 (1999). doi: 10.1093/nar/27.1.29; pmid: 9847135
53. S. Heinz *et al.*, Simple combinations of lineage-determining transcription factors prime cis-regulatory elements required for macrophage and B cell identities. *Mol. Cell* **38**, 576–589 (2010). doi: 10.1016/j.molcel.2010.05.004; pmid: 20513432
54. B. Langmead, C. Trapnell, M. Pop, S. L. Salzberg, Ultrafast and memory-efficient alignment of short DNA sequences to the human genome. *Genome Biol.* **10**, R25 (2009). doi: 10.1186/gb-2009-10-3-r25; pmid: 19261174

ACKNOWLEDGMENTS

Supported by National Institute of Diabetes and Digestive and Kidney Diseases (NIDDK) grant R01DK090625, National Institute on Aging grant P01AG011412, Chicago Biomedical Consortium S-007, Juvenile Diabetes Research Foundation grants17-2013-511, 1-INO-2014-178-A-V, and 1-INO-2015-23-A-V, and University of Chicago Diabetes Research and Training Center grant P60DK020595 (J.B.); NIDDK T32 grant DK007169 (B.M.); National Heart, Lung, and Blood Institute T32 grant HL007909 (M.P.); Defense Advanced Research Projects Agency grant D12AP00023 (A.R.D.); and National Institute of Environmental Health Science grant ES05703 (C.A.B.). A.L.H. is a trainee of the NIH Medical Scientist Training program at the University of Chicago (National Institute of General Medical Sciences grant T32GM07281). We thank E. Rosenzweig and The Next Generation Sequencing Core Facility at Northwestern University for assistance with library generation, sequencing, and analysis, as well as all members of the Bass and Barish laboratories for helpful discussions. J.B. has financial interest in and serves as an advisor to Reset Therapeutics. RNA-seq data sets, including lists of cycling genes in mouse and human islets, have been deposited in the NCBI's Gene Expression Omnibus accession GSE69889, and ChIP-seq data sets have been deposited in accession GSE70960.

SUPPLEMENTARY MATERIALS

www.sciencemag.org/content/350/6261/aac4250/suppl/DC1
Figs. S1 to S9
Tables S1 and S2

24 April 2015; accepted 25 September 2015
10.1126/science.aac4250

RESEARCH ARTICLE SUMMARY

EPIGENETICS

Disruption of histone methylation in developing sperm impairs offspring health transgenerationally

Keith Siklenka, Serap Erkek, Maren Godmann, Romain Lambrot, Serge McGraw, Christine Lafleur, Tamara Cohen, Jianguo Xia, Matthew Suderman, Michael Hallett, Jacquetta Trasler, Antoine H. F. M. Peters,* Sarah Kimmins*

INTRODUCTION: Despite the father transmitting half of the heritable information to the embryo, the focus of preconception health has been the mother. Paternal effects have been linked to complex diseases such as cancer, diabetes, and obesity. These diseases are increasing in prevalence at rates that cannot be explained by genetics alone and highlight the potential for disease transmission via nongenetic inheritance, through epigenetic mechanisms. Epigenetic mechanisms include DNA methylation, posttranslational modifications of histones, and noncoding RNA. Studies in humans and animals suggest that epigenetic mechanisms may serve in the transmission of environmentally induced phenotypic traits from the father to the offspring. Such traits have been associated with altered gene expression and tissue function in first and second offspring generations, a phenomenon known as intergenerational or transgenerational inheritance, respectively. The mechanisms underlying such paternal epigenetic transmission are unclear.

RATIONALE: Sperm formation involves rapid cell division and distinctive transcription programs, resulting in a motile cell with highly condensed chromatin. Within the highly compacted sperm nucleus, few histones are retained in a manner that suggests an influential role in development. Despite being the major focus of studies in epigenetic inheritance, the role of DNA methylation in paternal epigenetic inheritance is unresolved, as only minor changes in DNA methylation in sperm at CpG-enriched regions have been associated with transmission of environmentally induced traits. Instead, there may be a combination of molecular mechanisms underlying paternal transgenerational epigenetic inheritance involving changes in histone states and/or RNA in sperm. The function of sperm histones and their modifications in embryonic development, offspring health, and epigenetic inheritance is unknown. By overexpressing the human KDM1A histone lysine 4 demethylase during mouse spermatogenesis, we generated a mouse model producing spermatozoa with reduced H3K4me2 within the CpG islands of genes implicated in development, and we studied the development and fitness of the offspring.

RESULTS: Male transgenic offspring were bred with C57BL/6 females, generating the experimental heterozygous transgenic (TG) and nontransgenic (nonTG) brothers. Each generation from TG and nonTG animals (F_1 to F_3 in our transgenerational studies) was bred with C57BL/6 females, and the offspring (pups from generations F_1 to F_4) were analyzed for intergenerational and transgenerational effects. We found that KDM1A overexpression in one generation severely impaired development and survivability of offspring. These defects lasted for two subsequent generations in the absence of KDM1A germline expression. We characterized histone and DNA methylation states in the sperm of TG and nonTG sires. Overexpression of *KDM1A* was associated with a specific loss of H3K4me2 at more than 2300 genes, including many developmental regulatory genes. Unlike in other examples of paternal transgenerational inheritance, we observed no changes in sperm DNA methylation associated with primarily CpG-enriched regions. Instead, we measured robust and analogous changes in sperm RNA content of TG and nonTG descendants, as well as in their offspring, at the two-cell stage. These changes in expression and the phenotypic abnormalities observed in offspring correlated with altered histone methylation levels at genes in sperm. This study demonstrates that KDM1A activity during sperm development has major developmental consequences for offspring and implicates histone methylation and sperm RNA as potential mediators of transgenerational inheritance. Our data emphasize the complexity of transgenerational epigenetic inheritance likely involving multiple molecular factors, including the establishment of chromatin states in spermatogenesis and sperm-borne RNA.

ON OUR WEB SITE

Read the full article at http://dx.doi.org/10.1126/science.aab2006

CONCLUSION: Correct histone methylation during spermatogenesis is critical for offspring development and survival over multiple generations. These findings demonstrate the potential of histone methylation as a molecular mechanism underlying paternal epigenetic inheritance. Its modification by environmental influences may alter embryo development and complex disease transmission across generations. An essential next step is to establish functional links between environmental exposures, the composition of the sperm epigenome, and consequent altered gene expression and metabolic processes in offspring. Considering the mounting evidence, it may soon be reasonable to suggest that future fathers protect their sperm epigenome. ■

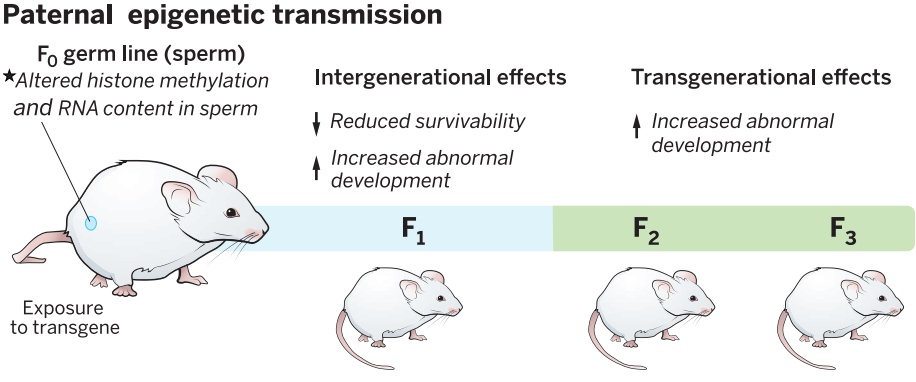

Disruption of histone methylation in developing sperm by exposure to the KDM1A transgene in one generation severely impaired development and survivability of offspring. These defects were transgenerational and occurred in nonTG descendants in the absence of KDM1A germline expression. Developmental defects in offspring and embryos were associated with altered RNA expression in sperm and embryos.

The list of author affiliations is available in the full article online.
*Corresponding author. E-mail: sarah.kimmins@mcgill.ca (S.K.); antoine.peters@fmi.ch (A.H.F.M.P.)
Cite this article as K. Siklenka *et al.*, *Science* **350**, aab2006 (2015). DOI: 10.1126/science.aab2006

Downloaded from www.sciencemag.org on November 5, 2015

RESEARCH ARTICLE

EPIGENETICS

Disruption of histone methylation in developing sperm impairs offspring health transgenerationally

Keith Siklenka,[1]* Serap Erkek,[2,3]*†‡ Maren Godmann,[4]§ Romain Lambrot,[4] Serge McGraw,[5]|| Christine Lafleur,[4] Tamara Cohen,[4] Jianguo Xia,[4,6] Matthew Suderman,[7] Michael Hallett,[8] Jacquetta Trasler,[5,9] Antoine H. F. M. Peters,[2,3]*¶ Sarah Kimmins[1,4]*¶

A father's lifetime experiences can be transmitted to his offspring to affect health and development. However, the mechanisms underlying paternal epigenetic transmission are unclear. Unlike in somatic cells, there are few nucleosomes in sperm, and their function in epigenetic inheritance is unknown. We generated transgenic mice in which overexpression of the histone H3 lysine 4 (H3K4) demethylase KDM1A (also known as LSD1) during spermatogenesis reduced H3K4 dimethylation in sperm. KDM1A overexpression in one generation severely impaired development and survivability of offspring. These defects persisted transgenerationally in the absence of KDM1A germline expression and were associated with altered RNA profiles in sperm and offspring. We show that epigenetic inheritance of aberrant development can be initiated by histone demethylase activity in developing sperm, without changes to DNA methylation at CpG-rich regions.

Birth defects occur in 3% of human babies and can be caused by genetic factors or environmental exposures, although 50% of birth defects are idiopathic (*1*, *2*). The focus on prevention has largely been geared toward the mother, despite the father contributing half of the genetic information and possibly some epigenetic information to the embryo.

[1]Department of Pharmacology and Therapeutics, Faculty of Medicine, McGill University, Montreal, Quebec, Canada. [2]Friedrich Miescher Institute for Biomedical Research (FMI), CH-4058 Basel, Switzerland. [3]Faculty of Sciences, University of Basel, Basel, Switzerland. [4]Department of Animal Science, Faculty of Agricultural and Environmental Sciences, McGill University, Montreal, Quebec, Canada. [5]Department of Pediatrics, Faculty of Medicine, McGill University, Montreal, Quebec, Canada. [6]Institute of Parasitology, Faculty of Agricultural and Environmental Sciences, McGill University, Montreal, Quebec, Canada. [7]MRC Integrative Epidemiology Unity, School of Social and Community Medicine, University of Bristol, Bristol, UK. [8]McGill Centre for Bioinformatics, School of Computer Science, Faculty of Science, McGill University, Montreal, Quebec, Canada. [9]Department of Human Genetics and Department of Pharmacology and Therapeutics, Research Institute of the McGill University Health Centre at the Montreal Children's Hospital, Montreal, Quebec, Canada.

*These authors contributed equally to this work. †Present address: European Molecular Biology Laboratory, Meyerhofstrasse 1, 69117 Heidelberg, Germany. ‡Present address: German Cancer Research Center (DKFZ), Im Neuenheimer Feld 280, 69120 Heidelberg, Germany. §Present address: Department of Cell Biology, Institute of Biochemistry and Biophysics, Center for Molecular Biomedicine (CMB), Friedrich Schiller University Jena, Jena, Germany. ||Present address: Department of Obstetrics and Gynecology, Faculty of Medicine, Sainte-Justine Hospital Research Centre, Université de Montréal, Montreal, Quebec, Canada. ¶**Corresponding author. E-mail: sarah.kimmins@mcgill.ca (S.K.); antoine.peters@fmi.ch (A.H.F.M.P.)**

Studies in humans and animals suggest that epigenetic mechanisms may serve in the transmission of environmentally induced phenotypic traits from parents to offspring (*3*–*8*). Such traits have been associated with altered gene expression and tissue function in first, second, and/or third offspring generations (*3*–*8*). Depending on the number of generations and parental origin, this phenomenon is referred to as intergenerational or transgenerational epigenetic inheritance (Fig. 1). Maternal and paternal transmission of such effects has been related to alterations of DNA methylation in germ cells (*7*, *9*–*11*). DNA methylation occurs at the 5 position of cytosine residues and is associated with heritable gene silencing when promoter sequences containing multiple CpG dinucleotides [CpG islands (CGIs)] are methylated. Likewise, DNA methylation suppresses transcription of endogenous retrotransposable elements (*12*). In sperm, DNA methylation at gene promoters is uncommon, whereas repetitive elements are frequently methylated (*13*–*15*). Despite being the major focus of studies in epigenetic inheritance, the importance of DNA methylation in paternal epigenetic inheritance is unresolved. Most studies reported only minor changes in DNA methylation in sperm at CpG-enriched regions that have been associated with the transmission of environmentally induced traits (*5*, *7*, *8*, *10*, *11*). Paternal transgenerational epigenetic inheritance may therefore involve changes in histone states (*16*–*18*), RNA (*19*), and/or other sperm components.

During the final stages of sperm formation, chromatin undergoes extensive remodeling in which most histones are replaced by sperm-specific protamine proteins enabling extensive compaction of DNA in sperm nuclei (*20*). Nonetheless, a small percentage of histones (about 1% in mice and 15% in humans) are retained in mature sperm (*16*, *18*). Several recent studies characterized the genome-wide distribution of nucleosomes in mature sperm of mice and humans, with partially discordant results (*17*, *18*, *21*), as reviewed by Saitou and Kurimoto (*22*). Using a protocol that enables efficient opening of the extremely compact mouse sperm nucleus, followed by micrococcal nuclease digestion and deep sequencing, we observed an approximately 10-fold overrepresentation of sequences localizing to promoters enriched in CpG dinucleotides in nucleosome-associated DNA (*17*). Histone retention in mouse sperm is predictable, occurring mainly at regions of high CpG density and low DNA methylation—for instance, at promoters of housekeeping and development-regulating genes (*17*). Retention at nonmethylated CGIs is conserved between mice and humans (*16*–*18*, *23*). In sperm, promoter regions of housekeeping genes contain the histone variant H3.3 and are marked by histone H3 lysine 4 (H3K4) di- and trimethylation. In contrast, developmental regulatory genes in sperm contain both H3.3 and canonical H3.1/H3.2 histones and are marked by trimethylation of H3K27 (H3K27me3) at their promoters (*16*, *17*). The function of sperm histones and their modifications in embryonic development, offspring health, and epigenetic inheritance is largely unknown.

In *Caenorhabditis elegans*, loss of the H3K4me2 demethylase *spr-5* is associated with a transgenerational phenotype appearing as progressive sterility due to stable accumulation of H3K4me2 in primordial germ cells (*24*). The mouse homolog, lysine demethylase 1A (Kdm1a), controls gene expression and development by catalyzing mainly the removal of mono- and dimethylation of H3K4 (*25*). To study the role of retained histones in sperm for embryo development and transgenerational epigenetic inheritance, we targeted H3K4 methylation, an epigenetic mark associated with developmental genes in sperm (*17*). We aimed to generate a mouse model for producing spermatozoa with reduced H3K4me2 within the CGIs of genes implicated in development. Toward this goal, we overexpressed the human KDM1A histone lysine 4 demethylase during spermatogenesis in mice and studied the development and fitness of offspring.

Offspring sired by heterozygous transgenic (TG) fathers and nontransgenic (nonTG) descendants had increased rates of birth defects, neonatal mortality, and altered gene expression. We characterized histone and DNA methylation states in the sperm of TG and nonTG sires. Overexpression of *KDM1A* was associated with specific losses of H3K4me2 in more than 2300 genes, including many developmental regulatory genes. Unlike in other examples of paternal transgenerational inheritance (*11*, *26*, *27*), we observed no changes in sperm DNA methylation at CpG-enriched regions. Instead, we measured robust and analogous changes in sperm RNA content

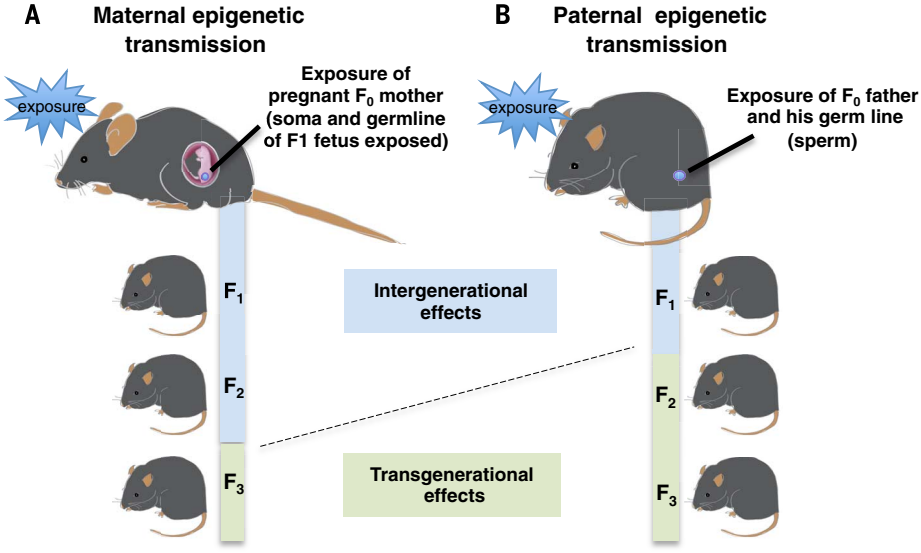

Fig. 1. Transgenerational and intergenerational definitions in maternal and paternal epigenetic inheritance. (**A**) In the pregnant female mouse (F_0), exposure to environmental factors (toxicants, nutrients, stress) can alter the soma and the germ line of the F_1 generation. These are considered intergenerational effects. When the F_1 offspring are bred, any phenotypic effects in F_2 animals are also considered to be intergenerational, as the F_2 generation originates from the F_1 germ cell that was exposed in utero. In maternal epigenetic inheritance, the F_3 animals are the first generation with no direct connection to the exposure and are considered to have a transgenerational phenotype, should abnormalities be detected. (**B**) In males, exposure of the F_0 mouse includes his sperm that fertilizes the oocyte to produce the F_1 generation. Thus, phenotypic effects in the F_1 animals are considered to be intergenerational. Breeding F_1 mice to generate F_2 animals results in the first unexposed generation. In contrast to females, F_2 males and males of subsequent generations can be subject to transgenerational phenotypes [based on (*64*)].

of TG and nonTG descendants, as well as in their offspring at the two-cell stage. These changes in expression and the phenotypic abnormalities observed in offspring correlate with altered histone methylation levels for genes in sperm. This study demonstrates that KDM1A activity and related reduced histone methylation during sperm development have catastrophic consequences for offspring. Additionally, our study implicates histone methylation and sperm RNA as potential mediators of transgenerational inheritance.

Results

The KDM1A transgene is specifically overexpressed in the mouse male germ line

We generated two lines of transgenic mice that express human *KDM1A* histone lysine 4 demethylase under the control of the gonad-specific, truncated form of the human polypeptide chain elongation factor 1 α (EF-1α) promoter (*28*) (Fig. 2A and fig. S1, A and B). This promoter is active in testicular germ cells but not somatic tissue (Fig. 2B and fig. S1, C and D). Transgenic *KDM1A* mRNA localized to spermatogonia and spermatocytes and weakly in round spermatids (Fig. 2C). A similar distribution was observed for the transgene marker green fluorescent protein (GFP) (fig. S1C). Histopathological evaluation of testes revealed normal spermatogenesis at all ages examined, from the first wave of spermatogenesis and throughout adulthood, in the offspring of both lines. Likewise, testis and epididymal weights, as well as sperm counts, were largely unaffected (fig. S2). To assess DNA integrity, we monitored phosphorylation of γH2AX and used terminal deoxynucleotidyl transferase–mediated deoxyuridine triphosphate nick end labeling (TUNEL) to detect DNA damage. The cellular distribution of H2AX phosphorylation in spermatogonia, spermatocytes, and spermatids was invariant between transgenic and control animals (fig. S3A). Likewise, we did not observe an increased number of TUNEL-positive cells in the testes of transgenic males (fig. S3, C and D). Finally, expression of the retrotransposon LINE-1 did not differ between TG, nonTG, and control testes (fig. S3B). Together, these data indicate that *KDM1A* expression does not induce DNA damage or genome instability (*29*).

Transgenerational paternal effects in TG- and nonTG-sired descendants

We conducted breedings from TG sires and nonTG sires to determine possible inter- and transgenerational paternal effects of *KDM1A* overexpression on offspring fitness. Pedigrees and generations are shown in Fig. 2. Male transgenic offspring were bred with C57BL/6 females, generating the experimental heterozygous TG and nonTG brothers. Males from TG^2-to-TG^4 ($TG^{2\text{-}4}$) and $nonTG^3$-to-$nonTG^5$ ($nonTG^{3\text{-}5}$) generations (representing F_0 to F_3 in our transgenerational studies) were bred with C57BL/6 females, and offspring (pups from generations F_1 to F_4) were analyzed for intergenerational and transgenerational effects (Fig. 2, D and E). First, we analyzed the pups of TG and nonTG sires over multiple generations for development and survival (Fig. 2, F to I). We determined the litter size at birth and weighed, sexed, and examined the pups 36 and 48 hours after birth and on postnatal days (PND) 6 and 21 (table S1). Neonatal survival rates of offspring sired by $TG^{2\text{-}4}$ and $nonTG^3$ males were reduced compared with survival rates of C57BL/6 controls ($P < 0.05$) (Fig. 2, F and G). We observed cumulative effects of transgene expression on survivability: With each successive generation of exposure of developing sperm to the transgene ($TG^{2\text{-}4}$), survivability of transgenic offspring (encompassing generations F_1 to F_3) decreased in both lines ($P < 0.05$) (Fig. 2, F and G). We also observed pups that were abnormal and runted (<75% of average body weight of the litter), with apparent abnormalities in the limbs, skeleton (table S1), and skin (flaky as pups, gray-and-white flecked as adults) (Fig. 2, H and I). Analysis of offspring sired by individual males showed that the described phenomenon is not driven by transmission of abnormalities by a few males to many offspring but by many males transmitting epigenetic alterations to a variable number of offspring (fig. S4). Moreover, frequencies of pup survival and abnormalities were not related to whether or not the offspring inherited the transgene from a transgenic father ($P < 0.05$). The presence of possible alterations in the epigenome of haploid spermatozoa that do not carry the actual transgene is probably due to the fact that in TG heterozygous sires, KDM1A is active in germ cells at various stages of spermatogenesis, such as spermatogonia and spermatocytes, which are diploid cells. Moreover, even after the two meiotic divisions, haploid spermatids share mRNAs via cellular bridges resulting from incomplete mitotic and meiotic divisions. Consequently, although the transgene is transcribed in only 50% of spermatids, all haploid spermatids within the cellular syncytium will be affected (*30*, *31*). Because transgene expression is restricted to the developing germ line (Fig. 2, B and C, and fig. S1, C and D) and nonTG sires do not express the transgene in their developing sperm, these data indicate that the aberrant phenotypes observed in nonTG pups (F_1 to F_3) are related to transgenerational epigenetic phenomena.

C57BL/6 mothers likely culled pups that were perceived as abnormal. As a consequence, we may have underestimated the phenotypic abnormalities assessed in the pups (table S1). To address this possibility and to further characterize the developmental defects across generations, we performed detailed phenotypic analysis at embryonic day 18.5 (E18.5). Each $TG^{2\text{-}4}$ (F_0 to F_2) and $nonTG^{3\text{-}5}$ (F_1 to F_3) sire was mated with at least two females, and pregnancies were assessed for litter size, pre- and postimplantation loss (combined to give total pregnancy loss), and abnormal fetuses (Figs. 3 and 4). In TG-sired offspring, abnormalities were varied and affected multiple systems. Examples of developmental errors included skeletal anomalies observed as malformed digits,

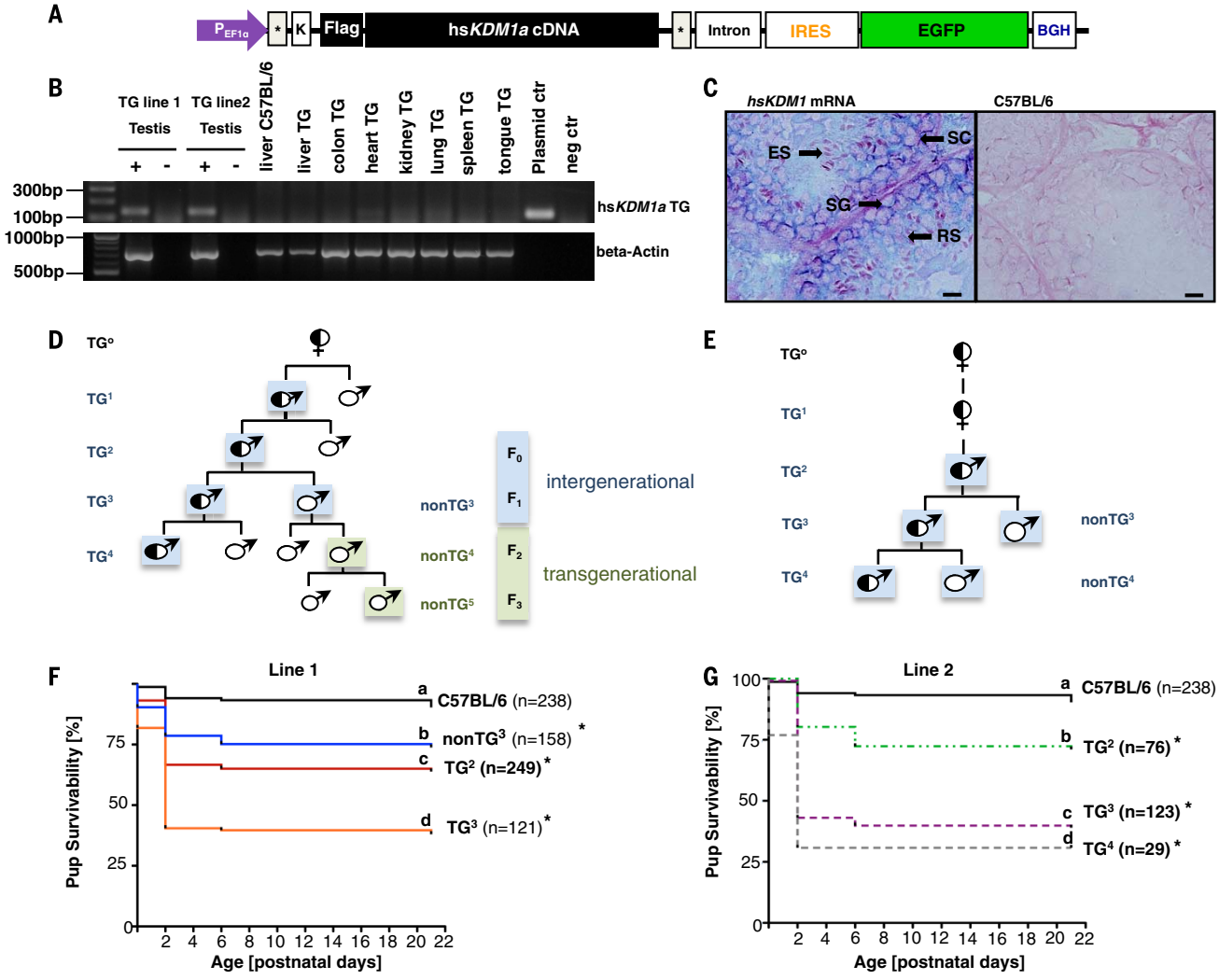

Fig. 2. Transgenic *KDM1A* expression in developing male germ cells impairs the development and survival of offspring. (**A**) Human (hs) *KDM1A* is expressed under the control of the human elongation factor 1 alpha promoter (EF1α), which has a truncated regulatory region that drives transcription in germ cells. Kozak (K) sequence, internal ribosomal entry site (IRES), EGFP, and bovine growth hormone (BGH) are present in the polyadenylation signal. (**B**) Reverse transcriptase PCR analysis shows that *KDM1A* transgene expression is restricted to the testis. (**C**) In situ hybridization reveals *KDM1A* mRNA (blue) in spermatogonia (SG), spermatocytes (SC), and round spermatids (RS). Elongated spermatids (ES) were negative. Scale bars, 10 μm. (**D** and **E**) Pedigrees. (D) In line 1, the female heterozygous transgenic founder (TG^0) was bred with a C57BL/6 male to generate TG^1 male pups and their nontransgenic brothers ($nonTG^1$). We subsequently bred heterozygous transgenic males (TG^{1-4}) with C57BL/6 females. We assayed the effects of paternal transgenic exposure on nonTG descendants over multiple generations ($nonTG^{3-5}$). (E) In line 2, a female heterozygous transgenic founder (TG^0) was bred with a WT C57BL/6 male to generate TG^1 offspring. The first breeding of the founder resulted in only viable female transgenic offspring. Therefore, from the TG^2 generation onward, the transgene was passed through the father. For both lines, we bred TG^{2-4} and $nonTG^{3-5}$ males with WT C57BL/6 females. After E18.5 embryonic analysis from line 1 TG^3 sires and their $nonTG^3$ brothers, we sacrificed the males and used their sperm for epigenomic analysis. (**F** and **G**) Reduced survival of offspring sired by TG^{2-3} and $nonTG^3$ males in line 1 (G) and TG^{2-4} males in line 2 (H), in comparison with C57BL/6-sired offspring. Survivor curves with different letters are significantly different (log rank statistical test). *n* indicates the number of offspring at $P < 0.05$, as marked by asterisks. (**H** and **I**) PND 6 TG-sired pups with abnormal skin are shown in comparison to a normal pup sired by a control mating (asterisk).

spinal defects, abnormal craniofacial structures, and failures in the development of limbs and body segments (Figs. 3 and 4). Likewise, in pups sired by $nonTG^3$ (F_1) and $nonTG^4$ (F_2) animals, we observed F_2 and F_3 offspring with visible abnormalities and skeletal defects occurring with significantly greater frequency than in control offspring ($P < 0.05$) (Fig. 3 and table S2). Abnormalities in F_3 offspring (sired by a $nonTG^4$ father) represent transgenerational effects (Figs. 3 and 4). Rates of pregnancy loss increased in several TG and nonTG generations (Fig. 3). No gross visible abnormalities were observed in E18.5 F_4 offspring sired by $nonTG^5$ males (Fig. 3). To further identify the specific nature of the skeletal defects and to confirm observations in nonTG offspring, a subset of pups was analyzed specifically for skeletal abnormalities. These

A

Sire / filial generation (n sires/n litters)	Line 1 TG^2 (F_o) (8 /15)	Line 1 TG^3 (F_1) (12/24)	Line 1 $nonTG^3$(F_1) (10/18)	Line 1 $nonTG^4$(F_2) (16/30)	Line 1 $nonTG^5$(F_3) (14/20)	Line 2 TG^3 (F_1) (2/4)	Line 2 TG^4 (F_2) (9/16)	Line 2 $nonTG^3$(F_1) (9/17)	Control C57BL/6 (21/32)
Fetuses (n)	134	197	142	249	186	30	144	139	298
Litter size ± stdev	8.93 ± 1.49	8.20 ± 1.66	7.88 ± 1.94	8.3 ± 2.12	9.3±1.89	7.5 ± 4.65	9.0 ± 1.37	8.18 ± 2.10	9.31 ± 1.42
Total preg. loss/group [%]	15.2	19.6**	20.2**	20.7***	12.9	25.0*	22.2***	22.8***	10.8
Abnormal fetuses [%]	25.3***	7.61**	11.3***	6.42**	3.23	10.0*	13.9***	10.1***	1.68
[Abnormal/total]	[34/134]	[15/197]	[16/142]	[16/249]	[6/186]	[3/30]	[20/144]	[14/139]	[5/298]
[Major abnormal/total]	30/134 (22.4%)	12/197 (6.09%)	14/142 (9.86)	12/249 (4.82%)	5/186 (2.69%)	3/30 (10.0%)	17/144 (11.8%)	12/139 (8.63%)	5/298 (1.68%)
[Minor abnormal/total]	4/134 (2.99%)	3/197 (1.52%)	2/142 (1.41%)	4/249 (1.61%)	1/186 (0.54%)	0 /30 (0.00%)	3/144 (2.08%)	2/139 (1.44%)	0/298 (0.00%)

Fig. 3. E18.5 fetuses sired by TG and nonTG descendants show a range of abnormalities. (**A**) Phenotypic frequencies observed in embryonic day E18.5. Total pregnancy loss per group [%] = (no. of CL – no. of total embryos) per group/no. of CL per group × 100; no. of abnormal fetuses per group [%] = (sum of abnormal fetuses per group/no. of embryos per group) × 100. Major abnormalities included craniofacial and skeletal defects, edema, hemorrhagic gut, extra digits, and missing eyes. Minor abnormalities included pale skin, color disfigurement, and growth retardation. (**B**) Normal E18.5 fetus sired by a C57BL/6 control father. (**C**) Runt with limb abnormality (arrow) and hemorrhagic foci. (**D**) Extra digit on left hindpaw. (**E**) Blunted snout, underdeveloped forearms and digits (thin arrow), and multiple hemorrhagic foci (wide arrow). (**F**) Craniofacial abnormalities and edema. (**G**) Hemorrhagic gut and underdeveloped limbs with failure in ossification. (**H** to **J**) Severely malformed fetuses. (**K**) Umbilical hernia. (**L**) Line 1 and (**M**) line 2 total pregnancy loss per group. (**N**) Line 1 and (**O**) line 2 total abnormalities per group (line 1: C57BL/6, n = 298 abnormalities; TG^2, n = 134; TG^3, n = 197; $nonTG^3$, n = 142; $nonTG^4$, n = 249; $nonTG^5$, n = 186; line 2: C57BL/6, n = 298; TG^3, n = 30; TG^4, n = 144; $nonTG^4$, n = 139). Total pregnancy loss per group [%] = (no. of CL – no. of total embryos) per group/no. of CL per group × 100; abnormal fetuses per group [%] = (sum of abnormal fetuses per group/no. of embryos per group) × 100. Statistical test for litter size: Student's t test; statistical test for total pregnancy loss and abnormalities per group: Fisher's exact test. *P < 0.05; **P < 0.01; ***P < 0.001.

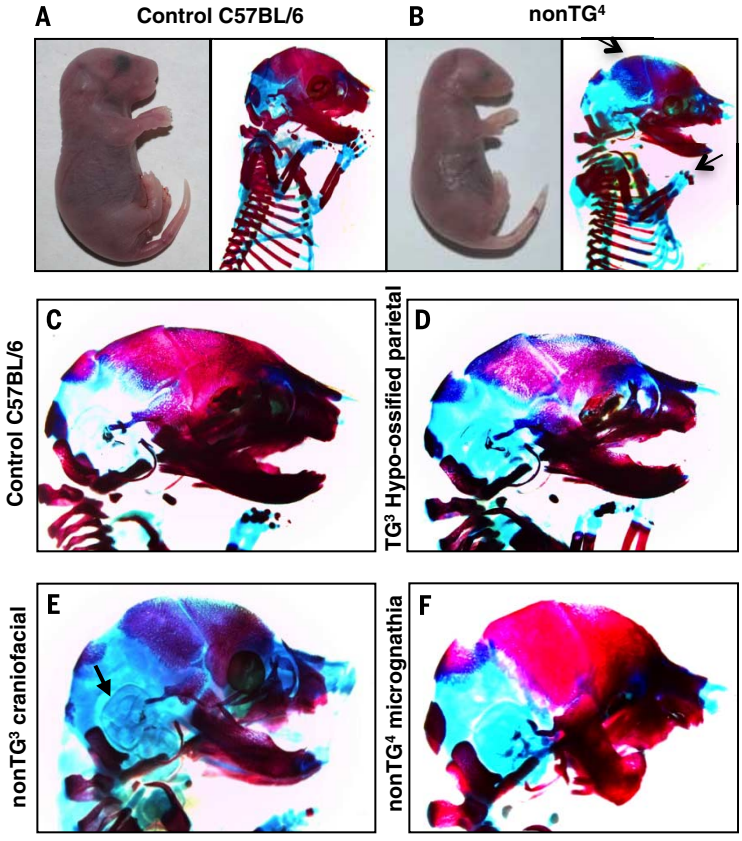

Fig. 4. Common skeletal abnormalities in pups sired by TG and nonTG$^{3\text{-}4}$ descendants. (**A**) Control-sired C56BL/6 pup at E18.5 and the corresponding skeletal stain. Red, bone; blue, cartilage. (**B**) nonTG^4-sired fetus at E18.5 and the corresponding skeletal stain. The nonTG^4-sired fetus had an abnormal craniofacial structure with reduced parietal ossification (arrow) and an extended cartilage deposit in the snout. Front limb digits were also underdeveloped (arrow). (**C**) Control C57BL/6-sired fetus. (**D**) TG^3-sired fetus with hypo-ossified parietal, frontal, and supraoccipital bones and abnormal eye socket. (**E**) Lack of temporal bones (arrow), hypo-ossified skull, and abnormal snout. (**F**) nonTG^4-sired fetus micrognathia. (Refer to Fig. 2D for origin or generation and nomenclature and fig. S5 for a reference for normal skeletal anatomy and staining.)

analyses revealed abnormalities such as errors in ossification, spinal defects, and missing or abnormal craniofacial structures in both TG and nonTG offspring (Fig. 4 and table S2). The dilution of the gross abnormalities in F_4 offspring sired by nonTG^5 males was confirmed by our skeletal analysis (table S2). Thus, by three generations after transgene exposure, we observed a normalization of offspring phenotypes in terms of birth defects at the levels detectable in our analysis (gross morphological and skeletal). Nonetheless, we have probably underestimated offspring abnormalities, as in-depth pathology analysis was not performed, and abnormalities were limited to those detected by observation of pups or skeletal analysis.

Transgenic KDM1A expression alters H3K4 dimethylation in sperm

To relate the developmental defects in offspring to possible changes in chromatin states in parental spermatozoa, we profiled the KDM1A target H3K4me2 in a genome-wide manner in sperm from TG^3 males (n = 11 animals), their nontransgenic littermates (nonTG^3, n = 9), and age-matched C57BL/6 controls (n = 11), using the previously mentioned method that was specifically developed for analyzing chromatin states in highly condensed sperm (*32*). We prepared nucleosomes by micrococcal nuclease digestion and performed chromatin immunoprecipitation (ChIP) with H3K4me2-specific antibodies, followed by next-generation sequencing (ChIP-seq) (fig. S6). In read-count–normalized libraries, we observed a reduction in H3K4me2 enrichments at CpG-rich sequences within transcription start site (TSS) regions of different genes in TG^3 sperm compared with that of controls (Fig. 5A). To identify TSS regions with altered H3K4me2 profiles in a genome-wide manner, we calculated the enrichment of H3K4me2 for genomic regions encompassing 250 base pairs (bp) upstream and downstream (+/−) of TSS for the different sperm samples. Because we previously showed that nucleosomes are retained in mouse spermatozoa at CpG-rich sequences [e.g., close to TSS (*17*)], the selected windows thus correspond to regions with the highest nucleosome occupancy in sperm and are most likely to transmit any histone-encoded information to the offspring. Reduced H3K4me2 levels occurred at 28.7% of the 8171 TSS regions marked by H3K4me2 in TG^3 samples, whereas 3.4% of the TSS regions displayed modest elevated levels of H3K4me2 (Fig. 5, B and C). The predominant down-regulation of H3K4me2 levels is consistent with the reported H3K4me2 demethylase activity of KDM1A.

Direct sequencing of nucleosome-associated DNA did not reveal differences in nucleosome occupancies between TSS regions with differential H3K4me2 levels in TG^3 sperm, nor were differences observed between TG^3 mice, nonTG^3 littermates, and control samples (fig. S7). These results exclude impairment of nucleosome retention as a putative cause underlying the reduction of H3K4me2 at certain loci in TG^3 sperm. To assess the reasoning underlying reduced H3K4me2 occupancy levels at certain TSSs, we categorized the regions according to CpG density and various chromatin attributes, such as the occupancy of the histone variant H3.3 and levels of H3K4me3 and H3K27me3, as measured in the sperm of control animals (*17*); these attributes are associated with specific gene functions (Fig. 5, B and C) (*17*). We found that regions with reduced H3K4me2 levels are CpG-rich (Fig. 5D), which suggests that targeting of human KDM1A is related to CpG density. Endogenous murine Kdm1a is particularly localized at CpG-dense TSS regions in mouse spermatocytes that are characterized by H3K4 methylation in sperm (*17*, *33*) (Fig. 5, A to C). Moreover, regions with reduced H3K4me2 levels in TG^3 sperm have higher occupancy levels of murine Kdm1a as compared with regions that have unchanged H3K4me2 levels (Fig. 5E). This finding points to specificity in human KDM1a activity at target sites of endogenous murine Kdm1a. Together, these data suggest that transgenic human KDM1A is targeted to selected regions that are extensively bound by endogenous murine Kdm1a during spermatogenesis.

As measured in control sperm, TSS regions with reduced H3K4me2 levels are strongly enriched for H3.3 (Fig. 5F) (*17*). Because high levels of H3.3 at strong CGIs in sperm correspond to high nucleosome turnover at CGIs in spermatids (*17*), locally reduced H3K4me2 levels at strong CGI promoters in TG^3 sperm may reflect the inability of H3K4 histone methyltransferases to counteract local TG-conferred KDM1A activity and may thereby fail to reestablish the H3K4me2 state during nucleosome turnover in spermatids of TG^3 males.

The results of our gene ontology analysis suggest that transgenic KDM1A regulates specific classes of genes (tables S3 and S4). Genes of the H3K4me3 high- and intermediate-chromatin classes with reduced H3K4me2 levels in TG^3 males serve functions in various cellular metabolic protein processes. For example, in TG^3 sperm, reduced levels of H3K4me2 were observed for *Pdpk1* (3-phosphoinositide dependent protein kinase 1) and *E2F6* (Fig. 5A). Conditional ablation of Pdpk1 in the pancreas leads to diabetes (*34*), and knockout mice have impaired embryogenesis, growth, and

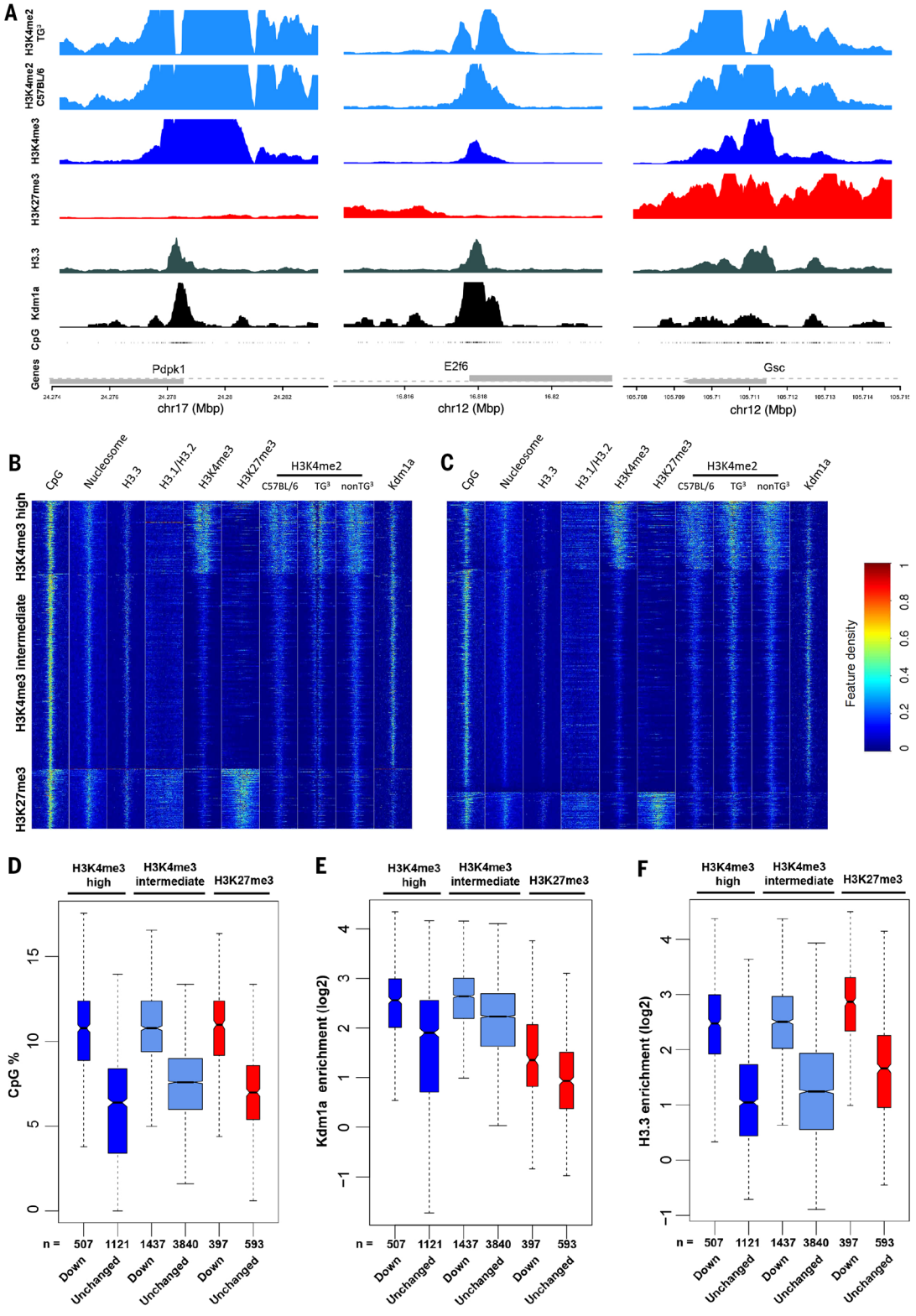

Fig. 5. H3K4me2 occupancy is severely reduced at nucleosome-containing TSS regions of CGI genes in TG^3 sperm only. (**A**) Snapshots of H3K4me2 occupancy at different loci in sperm of TG^3 and WT sires (this study). Occupancies of H3K4me3, H3K27me3, and H3.3 in sperm and of Kdm1a in spermatocytes of WT animals were taken from (*17*, *33*). *Pdpk1* and *E2F6* represent loci marked by high and intermediate H3K4me3 occupancy, respectively, whereas *Gsc* represents H3K27me3-marked genes, as observed in WT sperm. All three genes show reduced H3K4me2 levels at TSS sequences strongly enriched for H3.3-containing nucleosomes in WT sperm. We interpret the high histone modification occupancies at flanking sequences with low H3.3 nucleosome occupancy as the result of high ChIP efficiencies even at sites with low histone retention levels in the majority of sperm. (**B** and **C**) Heatmaps showing reduced (B) or unchanged (C) H3K4me2 occupancy at TSSs in TG^3 sperm for three groups of genes classified according to the H3K4me3 and H3K27me3 states in WT sperm. The plots show CpG density; nucleosomes; and H3.3, H3.1/H3.2, H3K4me3, and H3K27me3 coverages in WT mice (*17*) and H3K4me2 coverages around TSSs (±3 kilobases) in sperm of C57BL/6 WT, KDM1A TG^3, and nonTG^3 littermates and Kdm1a coverage in a WT spermatocyte (*33*). (**D** to **F**) Boxplots for the distributions of CpG percentage (D), Kdm1a occupancy around TSSs (±500 bp) (E), and H3.3 enrichment around TSSs (±250 bp) (F) for different groups of genes. "Down" and "unchanged" refer to genes with reduced or unchanged levels, respectively, of H3K4me2 in sperm of KDM1A TG^3 males. Number of genes per group is as follows (from left to right): 507, 1121, 1437, 3840, 397, and 593.

nervous system development (*35*, *36*). The loss of *E2F6* results in skeletal defects (*37*). H3K27me3-marked genes with reduced levels of H3K4me2 serve various functions during embryonic development. For instance, *Gsc* (Goosecoid homeobox) has a reduced amount of H3K4me2 in TG^3 sperm at a region overlapping H3K27me3, H3K4me3, and Kdm1a binding (Fig. 5, B and C). A targeted mutation of *Gsc* gave rise to mice with craniofacial

abnormalities and skeletal defects (*38*). These phenotypes reported in gene ablation models are highly reminiscent of those observed in TG^{1-4} and $nonTG^{3-4}$ offspring, yet the connection to altered histone methylation in developing sperm remains unclear. Our gene ontology analysis of embryonically expressed genes indicates that genes with a loss of H3K4me2 are involved in morphogenesis, patterning, vasculature development, cartilage development, and catabolic and metabolic processes (table S4). In contrast, H3K4me3 high- and intermediate-chromatin genes with unchanged H3K4me2 levels in TG^3 males execute functions in spermatogenesis and various nuclear processes, respectively. These results emphasize the targeting of hKDM1A to specific subsets of genes that may preferentially alter offspring development. Moreover, the gene subsets are directly in line with our phenotypes, where defects were not observed on spermatogenesis in transgenic sires but were seen in the TG-sired offspring.

Changes to histone H3K4me2 are independent of DNA methylation state

In contrast to TG^3 spermatozoa, our ChIP-seq analysis of sperm from $nonTG^3$ males (littermates of TG^3 animals) did not reveal any differences in H3K4me2 occupancy in comparison to sperm from TG^3 or control males (Fig. 5, B and C). These data suggest that the phenotypic aberrations seen in the offspring of $nonTG^3$ sires are not directly related to reduced H3K4me2 levels, as observed in mature sperm of TG^3 sires. Previously, KDM1A was reported to mediate the removal of H3K9 mono- and dimethylation in some cases (*39*, *40*). In various somatic cells, H3K9me2 is an abundant heterochromatic modification that is localized in large domains throughout the genome (*41*). H3K9me2 generally does not localize to and is mutually exclusive with regions marked by H3K4me2 and/or H3K27me3, which are prevalent at CGI regions containing nucleosomes in sperm (*41*). Such anticorrelation minimizes a possible contribution of H3K9me2 to paternal transmission of the embryonic impairment traits observed in TG and nonTG offspring.

Altered DNA methylation has been associated with phenotypes induced by paternal environmental exposures and has been suggested as a mechanism underlying epigenetic inheritance (*42*). To address whether reduced H3K4me2 may cause heritable changes in DNA methylation levels, we first used a targeted approach to assess DNA methylation in sperm from TG^3 (F_1) and $nonTG^3$ (F_1) littermates. Target selection was based on enrichment for CpGs and identification of regions as being differentially methylated in TG^3 sperm for H3K4me2 in comparison to C57BL/6 controls (three overlapping windows of 250 bp each). Selected targets were analyzed for altered DNA methylation by quantitative Sequenom MassARRAY, a technique based on bisulfite conversion followed by mass spectrometry (MS) analysis with a resolution at the CpG level. In all 24 targeted genes, we failed to observe any significant differences in DNA methylation in TG^3 and $nonTG^3$ sperm in comparison to controls (fig. S8).

Next, we used reduced representation bisulfite sequencing (RRBS) for a genome-wide comparison of DNA methylation levels, predominantly at CpG islands in control, TG^3, and $nonTG^3$ sperm. Analysis based on methylation percentages of single CpG sites found across the genome showed a high degree of similarity between samples of all three genotypes (R = 0.98 to 0.99) with no apparent group clustering (fig. S9A). When testing individual CpG sites for significant association with genotype, we found only a few more than expected by chance (fig. S9, B and C). In summary, using targeted Sequenom analysis and RRBS, we did not observe an overrepresentation of changes in CpG methylation levels in spermatozoa of TG^3 and $nonTG^3$ transgenic mice versus control samples. These findings indicate that DNA methylation at CpG islands is not implicated in the molecular processes leading to the observed transgenerational phenotypes.

Overexpression of KDM1A is associated with altered sperm RNA content

RNA analysis of sperm from TG^3 and $nonTG^3$ mice revealed a common nongenetic molecular change (Fig. 6). Sperm is a rich source of diverse RNAs that may function as potential mediators of paternally transmitted effects (*43*). We used the Affymetrix GeneChip ST2.0 Array to compare the RNA content of sperm from TG^3 and $nonTG^3$ mice to that of controls. This method enables the detection of 28,000 coding transcripts and more than 7000 noncoding RNAs, including ~2000 long intervening/intergenic noncoding RNAs (lincRNAs). TG^3 and $nonTG^3$ spermatozoa displayed a comparable molecular change in RNA content relative to controls, with 564 RNAs commonly misregulated among 650 RNAs altered in TG^3 sperm and 619 in $nonTG^3$ sperm [$\log_2$ fold change > 1.0; false discovery rate (FDR) < 0.05]. Among the shared misregulated RNAs in nonTG and TG sperm, 67 were noncoding RNAs and 471 were protein-coding transcripts (table S5). As would be predicted with reduction of a gene-activating histone modification, 99% of differential RNAs were reduced in TG^3 and $nonTG^3$ sperm compared to controls (643 of 650 and 613 of 619, respectively). More than 60% of RNA-associated promoters were marked by H3K4me3 in wild-type (WT) sperm, potentially reflecting transcriptional activity at preceding stages of male germ cell development (*17*) (Fig. 6B). Only ~3% of RNAs (15 of 564) were marked by H3K27me3 in WT sperm. Finally, 41 commonly deregulated transcripts were associated with genes with reduced H3K4me2 levels at their TSS in TG^3 sperm (Fig. 6B). These findings present the possibility that transcripts and regulatory RNAs are transmitted via TG^3 and $nonTG^3$ sperm to the embryo and may be implicated in transmission of the phenotype to the offspring.

TG and nonTG sperm alter gene expression in early embryos

To understand whether there was a link between genes bearing altered histone methylation in the TG^3 sperm to embryo gene expression and offspring phenotypes, we performed array expression analysis from TG^8, $nonTG^8$, and control-sired two-cell embryos. We chose to examine two-cell embryos because, in terms of developmental timing, they are close to sperm in which we observed H3K4me2 changes. We hypothesized that potential changes in paternal chromatin states would be the least diluted in two-cell embryos compared with later stages of development. We identified 874 RNAs in embryos sired by TG^8 and 123 RNAs in $nonTG^8$ embryos (F_2 generation) that were differentially expressed (table S6) (FDR < 0.3). Most deregulated genes in TG^8-sired embryos were up-regulated (80%; 703 of 874 RNAs), whereas about half of the genes were up-regulated in $nonTG^8$-sired embryos (46%; 56 of 123 RNAs). Notably, 71 genes were commonly misexpressed in two-cell embryos sired by TG^8 and $nonTG^8$ littermates (Fig. 6, D and E, and table S6) (FDR < 0.3). Moreover, 110 genes deregulated in two-cell embryos had reduced H3K4me2 at TSSs in TG^3 sperm. A subset of these genes is also marked by H3K27me3 and H3K4me3 (Fig. 6, C to E). Some of the differentially expressed genes in the embryos that overlap with reduced H3K4me2 in TG^3 sperm, or regions in sperm enriched in H3K27me or H3K4me3, can be linked to the developmental abnormalities observed in TG- and nonTG-sired pups (Fig. 6E). These data establish that the triggering event leading to altered H3K4me2 in developing sperm has consequences for gene expression in embryos.

Discussion

Here we show that increased expression of the chromatin modifier KDM1A during spermatogenesis induces major developmental defects, which were transmitted paternally for three generations, even in the absence of transgene expression in the germ line of nontransgenic offspring. Our data suggest that the critical initiating event in our model is the alteration in histone methylation in developing male germ cells, leading to offspring abnormalities. We show that changes to histone methylation in the hKDM1A model occurred in the absence of changes to DNA methylation at CGIs in sperm. We also observed altered RNA profiles in sperm of TG and nonTG males (F_1 generation) and their two-cell embryonic offspring (F_2 generation) (Fig. 6). Our data emphasize that the mechanisms of transgenerational epigenetic inheritance are complex and probably involve several molecular factors, such as the establishment of chromatin states in spermatogenesis, DNA methylation, and sperm-borne RNA.

We observed a large diversity in aberrant phenotypes, including abnormalities in bone and skin, reduced survivability, and retarded growth. These aberrations were present in many offspring sired by many fathers, rather than many offspring from a few fathers. Together with the high penetrance of phenotypes that was resolved by the fourth generation of nontransgenic offspring, these observations point to an epigenetic mechanism driving impaired

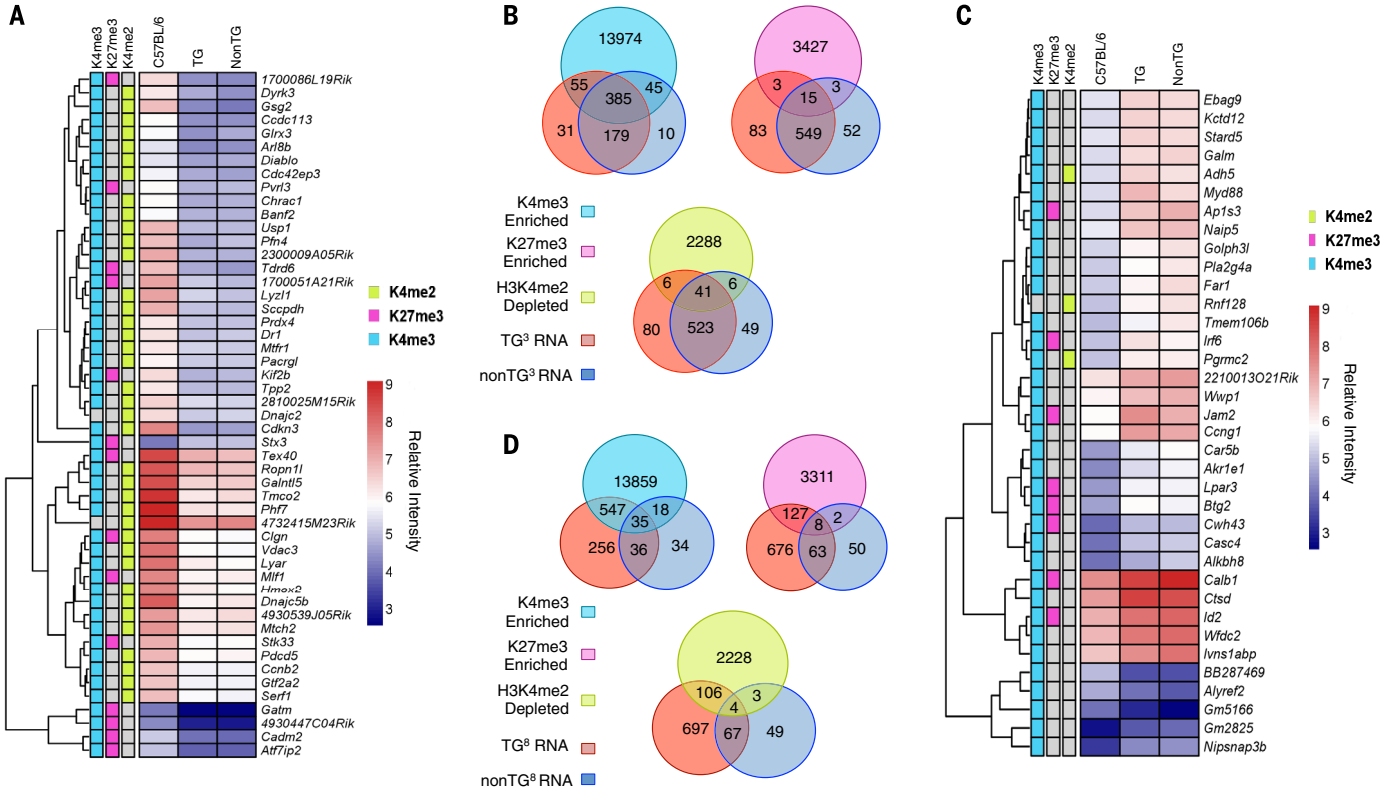

E

Symbol	Genotype		Histone modification in Sperm			Log2 FoldChange		Associated Phenotype in mutants
	TG	nonTG	H3K4me2	H3K4me3	H3K27me3	TG	nonTG	
Btg2	yes	yes	no	yes	yes	1.54	1.22	cervical and thoracic vertebrae abnormalities
Irf6	yes	yes	no	yes	yes	1.48	1.22	abnormal skin, limb and craniofacial development
Jam2	yes	yes	no	yes	yes	1.96	1.42	abnormal bone marrow cell morphology and development
Id2	yes	yes	no	yes	yes	1.16	1.45	abnormal bone marrow cell morphology and development
Lpar3	yes	yes	no	yes	yes	1.40	1.34	Impaired and delayed embryo implantation
Ets2	yes	no	yes	yes	yes	1.38	N/A	decreased embryo size, partial embryonic lethality during organogenesis
Wdr1	yes	no	yes	yes	No	1.09	N/A	abnormal osteoclast physiology, embryonic lethality during organogenesis
Dock1	yes	no	yes	yes	yes	0.97	N/A	lethality during fetal development, abnormal development, edema
Crim1	yes	no	yes	yes	yes	0.97	N/A	kidney cortex cysts, decreased survivor rate, edema

Fig. 6. Differential gene expression in two-cell embryos as related to sperm chromatin content. (**A**) RNA content in TG^3 and $nonTG^3$ sperm is depicted by a heatmap of selected genes, as related to identified regions of H3K4me2 loss in TG^3 sperm or regions enriched for H3K4me3 or H3K27me3 in C57BL/6 sperm. (**B**) Venn diagrams comparing the number of RNA transcripts with significantly different levels of abundance in the sperm of TG^3 and $nonTG^3$ males with respect to controls. (**C**) Heatmap depicting selected RNAs that differed from control-sired embryos and those sired by TG^8 or $nonTG^8$ males (F_2 generation embryos), as related to identified regions of H3K4me2 loss in TG^3 sperm or sperm-enriched regions for H3K4me3 or H3K27me3. (**D**) Venn diagrams depicting differential gene expression in two-cell embryos sired by TG^8, $nonTG^8$, or control animals, as related to identified regions of H3K4me2 loss in TG^3 sperm or sperm-enriched regions for H3K4me3 or H3K27me3. (**E**) The phenotypes observed in TG and nonTG offspring resemble those of mouse mutants for differentially expressed genes.

development. It is unlikely that hKDM1A expression during spermatogenesis behaves comparably to a chemical mutagen or induces a mutator phenotype in germ cells or offspring, given the very high frequency of abnormalities observed (*44*–*46*). Consistent with that notion, our assessments using multiple approaches revealed no DNA damage or chromatin instability. Additionally, the normal sperm-head morphology lends further support to the stability of sperm chromatin. Human and mouse mutants with altered sperm histone content have misshapen sperm heads that lack compaction (*47*, *48*). Unlike prior studies of transgenerational inheritance, however, we used several methods—including genome-wide DNA methylation analysis by RRBS and targeted analysis with Epityper—to confirm that DNA methylation occurring mainly at CGIs was not altered in TG or nonTG sperm.

Transgenic KDM1A expression induces a major local reduction in H3K4me2 occupancy at many CGI-containing promoters in sperm from TG sires. Reductions in sperm H3K4me2 levels are observed at sites of high Kdm1a occupancy in spermatocytes, supporting the notion that transgenic KDM1A functions preferentially at sites of endogenous Kdm1a proteins. Because $nonTG^3$ animals sire offspring with developmental defects, as do TG^3 males, reduction in H3K4me2 as observed in TG^3 sperm probably does not directly mediate epigenetic inheritance of developmental defects across generations. Instead, our data point to the idea that disruptions in H3K4me2 have a cascading effect, altering transcription at genes in spermatogenesis and the RNA content of sperm. Correspondingly, H3K4me2 changes in sperm were correlated with changes in expression from genes bearing H3K4me3, and those bearing H3K27me3, that are normally already present in sperm at CGIs of subsets of genes known to control embryonic development (*17*). Correspondingly, genes with altered expression in two-cell embryos sired by either TG or nonTG males were associated with genes in sperm enriched in histone methylation (H3K4me2, H3K4me3, and H3K27me3).

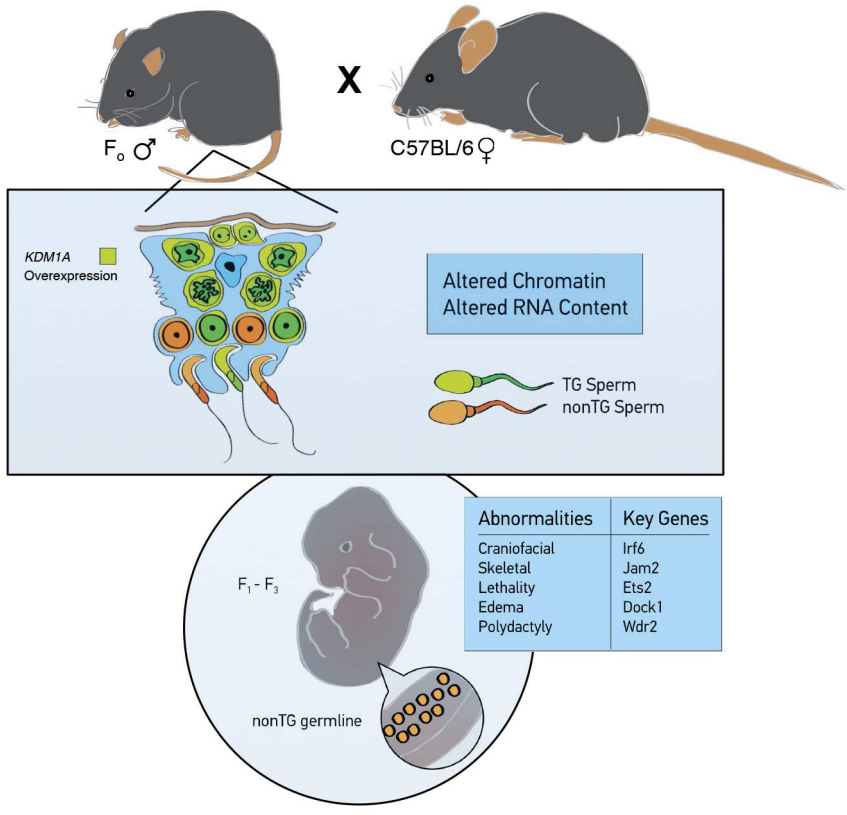

Fig. 7. Disruption of histone methylation in developing sperm by KDM1A transgene overexpression from one generation severely impaired embryo development and survivability of offspring. These defects were transgenerational and occurred in nonTG descendants in the absence of KDM1A germline expression, which suggests that regions in the nonTG germline escape epigenetic reprogramming. Developmental defects in offspring were associated with altered RNA content in sperm and gene expression in embryos.

This suggests that altered histone methylation in sperm can influence early embryo gene expression. Similarly, mutation of the *Smarca5*^{MommeD4} allele of the Snf2h chromatin remodeler during spermatogenesis has been associated with changes in expression of the epigenetic-sensitive *agouti viable yellow* (*A*^{vy}) gene. As in our study, WT offspring of heterozygous *Smarca5*^{MommeD4} sires had variable phenotypes (*49*), which indicates that proper chromatin regulation during spermatogenesis plays an important role in offspring fitness and gene expression.

Our data also offer the possibility of sperm RNA content as a contributing factor to the offspring phenotypes. We observed substantial overlap in the RNA content of TG and nonTG sperm, with ~85% similarity in RNAs that were different from control sperm RNAs. An example of paternal effects via RNA was demonstrated in *C. elegans*, where induced viral expression led to paternal transmission of small viral RNA (viRNA) across multiple generations. As in our model, the WT offspring worm descendants inherited the viRNA molecules and the phenotype of viral protection. This transgenerational effect was extinguished by the third generation beyond exposure to the transgene, thus indicating a gradual loss of the phenotype, consistent with our observations (*50*).

However, the likelihood that a diffusible agent such as RNA could drive the observed transgenerational phenotype is low, because germ cell fate in mammals is specified during gastrulation, which occurs many cell divisions after fertilization. In the absence of a means to amplify a diffusible RNA signal, this signal will be lost over the many cell divisions until germline specification. Therefore, we propose a model for mammals in which altered chromatin in developing sperm is associated with abnormal sperm-borne RNAs. These RNAs could then signal to chromatin to regulate gene expression during development (Fig. 7). Regulatory RNAs made up a significant portion of the differential RNA content in sperm from TG and nonTG males compared with controls. Functions of regulatory RNA include control of pluripotency, differentiation, and guidance in the setting of the epigenome (*51*–*53*). Sperm is known to transmit long noncoding RNAs (lncRNAs) to the embryo; these RNAs have been postulated to affect the postfertilization genome (*19*). If lncRNAs are not correctly transcribed in developing germ cells, altered lncRNA levels could then be transported to the embryo, where gene expression could be modified. LncRNAs interact with chromatin regulatory machinery and serve in guiding chromatin changes. Moreover, lincRNA knockouts (*Fendrr*, *Peril*, and *Mdgt*) display peri- and postnatal lethality before PND 20 (*54*), a common observation in our transgenic descendants.

Conclusion

Our data show that, independent of DNA methylation at CGIs, abnormalities in histone methylation during spermatogenesis are associated with altered embryo gene expression and development. Our findings of transgenerational epigenetic inheritance indicate genetic lesions in chromatin modifiers and environmentally induced alterations in histone methylation during spermatogenesis as underlying causes of birth defects and disease that may be traceable to the father. Individual responses to environment and inheritance of sensitivities and/or predisposition to disease may be shaped by factors such as gene copy number of chromatin modifiers.

Materials and methods

Generation of KDM1 transgenic mice

For the generation of KDM1 TG mice, full-length human KDM1 cDNA [National Center for Biotechnology Information (NCBI) Nucleotide Database and Consensus CDS Database accession numbers NM_015013 and CCDS30627, respectively] was subcloned into a modified IRES-EGFP (internal ribosomal entry site–enhanced green fluorescent protein) vector (Clontech). We replaced the cytomegalovirus promoter of the expression vector by an isoform of the human EF-1α promoter driving germ cell–specific expression of the KDM1 transgene (*28*). We microinjected the transgenic construct into C57BL/6 zygotes and obtained two female transgenic founders. We crossed founders with C57BL/6 males to create the two transgenic lines. We subsequently transmitted the transgene by heterozygous males bred to C57BL/6 females. The two transgenic lines showed similar developmental phenotypes in offspring and served as a control for transgene integration site effects. We extracted genomic DNA from tail biopsies and performed Southern blot analysis to determine the transgene copy number. All C57BL/6 control mice were obtained from Charles River Laboratories International (Wilmington, MA). Mice were provided with water and standard mouse chow ad libitum and housed under conditions of controlled light (12-hour light, 12-hour dark cycle) at 21°C and 50% humidity. All animal procedures were approved by the Animal Care and Use Committee of McGill University, Montreal, Canada.

In situ hybridization

In situ hybridizations were performed as previously described (*55*), using digoxigenin-labeled RNA probes (Roche).

Genotyping by PCR on genomic DNA

Genotyping was performed on tail-tip DNA as previously described (*56*). Oligonucleotide primers used for genotyping by polymerase chain reaction (PCR) were: hsEF1alpha-fw1 (TTC TCA AGC CTC AGA CAG TGG), Flag-re1 (TCG TCA TCG TCC

TTG TAG TCC), hsLSD1-ex19-fw1 (TAC GAT CCG TAA CTA CCC AGC), and pIRES-EGFP-re2 (TCT TAG CGC AGA AGT CAT GCC).

RNA isolation and reverse transcriptase PCR

Total RNA was extracted using Purezol (BioRad, Hercules, CA) according to the manufacturer's instructions and was treated with DnaseI (RNeasy Mini Kit, Qiagen). Isolated RNA was reverse transcribed with random primers using the High-Capacity cDNA Reverse Transcription Kit (Applied Biosystems, Foster City, CA). cDNAs were subjected to PCR using the following oligonucleotide primers: *beta-Act1*-fw [5′ ACC TTC AAC ACC CCM GCC ATG TAC G 3′ (M = A/C)], *beta-Act2*-re [5′ CTR ATC CAC ATC TGC TGG AAG GTG G 3′ (R = A/G)], *hKDM1A*-ex2-fw1 (5′ TGG ATG AAA GCT TGG CCA ACC 3′), hsLSD1-ex3-re1 (5′ AGA AGT CAT CCG GTC ATG AGG 3′), and *hsKDM1A*-ex11-fw1 (5′ GCC ACC CAG AGA TAT TAC 3′). For embryo transgene expression analysis, major organs from three transgenic embryos at E18.5 were homogenized via mortar and pestle and then extruded through a 25-gauge needle. RNA was extracted using the Qiagen RNeasy RNA purification kit (product no. 1050349, lot no. 145015691). RNA (1 μg) from each sample was converted to cDNA using the High-Capacity cDNA Reverse Transcriptase Kit (Applied Biosystems; product no. 4368814, lot no. 1108153). To determine expression of *hsKDM1A*, hsKDM1A-ex2-fw1 and hsLSD1-ex3-re1 primers were used as above. Primers for *Gapdh* were used as a loading control (forward: 5′ ACT TTG GCA TTG AAG GGC TG 3′; reverse: 5′ TGG AAG AGT GGG AGT TGC TGT TG 3′).

The PCR protocol was as follows: predenaturation of one cycle at 94°C for 4 min, followed by PCR amplification repeated for 40 cycles of denaturation at 94°C for 40 s, annealing at 60°C for 25 s, and elongation at 72°C for 60 s. The final elongation was performed at 72°C for 10 min. PCR reactions were visualized on the Qiaxcel Advanced System using the QiAxcel DNA Screening Kit (Product 74104; Lot 145019088)

Sperm isolation, count, and morphology

For sperm counts, spermatozoa were recovered from paired cauda epididymides of sexually mature mice as follows: Cauda epididymides were placed into phosphate-buffered saline (PBS), cut, and gently agitated at 37°C to allow sperm to swim out. After 5 min of incubation, a 10-μl aliquot of the sperm solution was removed and subjected to hemacytometric counts following standard procedures. For isolation of sperm for ChIP-seq, a swim-up procedure was used to ensure pure cell population (*32*).

Analysis of pups

We bred C57BL/6 (n = 18 animals), line 1 TG^{2-3} (n = 10 and 14) and $nonTG^{3-5}$ (n = 8, 7, and 4), and line 2 TG^{2-4} (n = 4, 6, and 5) males with C57BL/6 females. Shortly after copulation, as determined by the presence of a vaginal plug, males were removed from females. Litter size was determined at birth, and pups were sexed, weighed, and examined at 36 and 48 hours after birth, as well as on PND 6 and 21. TG and nonTG pups with and without external malformations and C57BL/6 controls were subjected to skeletal staining. Abnormal pups were identified by the appearance of gross morphological defects, such as the presence of a skin abnormality, underdeveloped limb, or runting. Frequency of morphologically abnormal pups was calculated based on the total number of offspring per generation.

Analysis of E18.5 fetuses and assessment of pregnancy loss

We bred C57BL/6 (n = 21 animals), line 1 (L1) TG^{2-3} (n = 8 and 12) and $nonTG^{3-5}$ (n = 10, 16, and 14), and line 2 (L2) TG^{3-4} (n = 2 and 9) and $nonTG^{4}$ (n = 9) males with C57BL/6 females. Control matings were age-matched so that statistical comparisons were always between matings in which the sires were the same age. Copulation was determined by the presence of a vaginal plug. The day of the plug was established as E0.5. Fetuses were collected from the uteri of the female mice at E18.5 after mating. Each fetus was carefully examined, and sex, weight, and crown-to-rump length were determined. Moreover, placental gross morphology, weight, and diameter were ascertained. Fetuses with external malformations and the corresponding controls were subjected to skeletal staining or were fixed in Bouin's fixative solution and subsequently subjected to histopathological analysis. We determined the number of ovulations by counting the number of corpora lutea (CL) in E18.5 pregnant females from the above matings (C57BL/6, n = 32; L1 TG^{2-3}, n = 15 and 24; L1 $nonTG^{3-5}$, n = 18, 30, and 20; L2 TG^{3-4}, n = 4 and 16; L2 $nonTG^{4}$, n = 17; n = number of females per group). Ovaries were placed into PBS in separate drops, and CL were counted blindly with respect to the number of embryos actually recovered using a dissecting microscope with top lighting. The sum of pre- and postimplantation losses was used as a measure of total pregnancy loss. This was done by comparing the number of CL produced with the number of total embryos per group: total pregnancy loss per group [%] = (no. of CL − no. of total embryos) per group/no. of CL per group × 100.

Skeletal staining and histopathology

Alcian blue and Alizarin red staining of cleared skeletal preparations was performed according to Hogan *et al.* (*57*). Skin and viscera were removed, and carcasses were fixed overnight in 95% ethanol (EtOH). Afterward, carcasses were stained overnight in Alcian blue 8GS (80 ml of 95% EtOH/20 ml of acetic acid/15 mg of Alcian blue 8GS), fixed in 95% EtOH for 2 to 5 hours, and transferred to 2% KOH for 24 hours. Skin and muscles were then removed, and carcasses were stained overnight in 1% KOH/0.015% Alizarin red S. Next, skeletons were cleared in 1% KOH/20% glycerol for ~48 hours. Skeletons were stored in 20% glycerol for analysis.

ChIP sequencing

As described previously (*17*, *32*), ChIP sequencing experiments were performed using an antibody against H3K4me2 (Millipore 07-030). ChIP-seq libraries were prepared using the Illumina ChIP-seq DNA Sample Prep Kit (catalog no. IP-102-1001) and sequenced on Illumina GA II. Processing and alignment of the ChIP-seq data were performed as described previously (*17*) and were based on mouse mm9 assembly (July 2007 Build 37 assembly by NCBI and Mouse Genome Sequencing Consortium).

Classification of H3K4me2 signal around TSS in KDM1A transgenic mice

Enrichment values for regions surrounding TSSs (±250 bp) were calculated in a similar way as described in (*17*). Enrichments refer to the ratio of H3K4me2 signal in sperm from KDM1A TG^{3} males over the H3K4me2 signal from sperm of C57BL/6 WT mice. Genes with ≥5 reads ($\log_2$ scale) in the regions analyzed in both replicates of WT H3K4me2 were referred to as H3K4me2-positive (fig. S6A). We used the averages of two H3K4me2 data sets as the WT H3K4me2 measurements. To identify genes with altered H3K4me2 levels in KDM1A TG^{3} sperm, we determined the ratio of H3K4me2 occupancy around TSSs (±250 bp) in TG^{3} over WT sperm (fig. S6B). Because the H3K4me2 ratios were not normally distributed for down-regulated TSS regions, we performed k-means clustering analysis coupled to heatmap visualization to set the cut-off for genes with down-regulated H3K4me2 levels (see Fig. 4, B and C, and fig. S6). To increase sensitivity, k-means clustering accounted for the occupancies of nucleosomes, H3K4me3, H3K27me3, H3.3, and H3.1/H3.2 histones in WT sperm. For clusters with more than 1000 genes, we randomly chose 1000 genes for heatmap visualization purposes. For setting the right cut-off, we arbitrarily identified the upper 10% of TSS regions with elevated H3K4me2 levels in TG^{3} over WT sperm. Chromatin snapshots (Fig. 4A) were generated as described by Erkek *et al.* (*17*). Chromatin images represent the read counts per base averaged over a moving 300-bp interval. Averaged read counts were normalized for total read counts across samples.

Sequenom MassARRAY methylation analysis

DNA (1 μg) from TG (n = 5 animals), nonTG (n = 5), and control C57/BL6 (n = 5) sperm was bisulfite-treated with the EZ DNA Methylation Gold Kit (Zymoresearch, D5007). We used the Sequenom EpiDesigner application to design primers for the amplification of different amplicons of selected targets. Targeted regions encompassed a 250-bp window showing a large reduction of H3K4me2 (ratio of TG versus WT control <−2.5) and high CpG density and H3.3 occupancy (*17*). Sequenom MassARRAY methylation analysis was then performed using the MassARRAY Compact System (Sequenom, San Diego, CA). This system is based on MS analysis for qualitative and quantitative detection of DNA methylation using homogeneous MassCLEAVE base-specific cleavage and matrix-assisted laser desorption/ionization–time-of-flight MS. Spectra were elaborated by the Epityper software v1.2.0 (Sequenom), which provides

methylation values of each CpG unit, expressed as percentages. Such values result from the calculation of the ratio of mass signals between methylated and nonmethylated DNA.

RRBS analysis

Reduced representation bisulfite sequencing libraries were generated according to previously published protocols using the gel-free technique (*58*). Briefly, 500 ng of DNA from each of the 15 samples (TG^3, $n = 5$; $nonTG^3$, $n = 5$; and control, $n = 5$) was used in the RRBS experiments. Multiplexed samples were used in paired-end sequencing (HiSeq sequencer, Illumina). BSMAP version 2.6 was used to trim reads (phred quality >30 and Illumina adapters), align reads to mm10, and obtain CpG methylation calls (*59*).

RNA analysis from sperm

Sperm (~7×10^6) were isolated by swim-out from each TG^3, $nonTG^3$, or C57BL/6 male. To increase sperm RNA yield for analysis, sperm were pooled from four or five males to give a total of ~20×10^6 sperm per replicate (C57BL/6, one replicate, $n = 5$ per replicate; TG, three replicates, $n = 4$ per replicate; nonTG, three replicates, $n = 4$ per replicate). RNA was extracted from pooled sperm. Somatic cell contamination was avoided by washing with somatic cell lysis buffer (0.1% SDS and 0.5% Triton-X) (*60*). After two washes with PBS, spermatozoa were homogenized by vortexing in buffer RLT (Qiagen RNeasy), supplemented with β-mercaptoethanol (50 mM) and steel beads (100 mg, 0.2 mm). RNA was extracted through Qiazol (Qiagen), followed by chloroform. The aqueous layer containing RNA was processed with the RNeasy RNA extraction kit (Qiagen).

RNA analysis from two-cell embryos

Two-cell embryos were collected from multiple C57BL/6 pregnancies sired by a C57BL/6 ($n = 8$ animals), TG ($n = 4$), or nonTG ($n = 5$) male. The number of embryos collected per pregnancy ranged from 1 to 23, and therefore, pooling of embryos from multiple sires within each genotype was necessary. On average, 26 embryos were pooled for total RNA extraction. Plug-positive females were sacrificed and oviducts flushed with PBS + 0.01% bovine serum albumin to collect embryos. Cells were stored at −80°C until embryos from two to six breedings were collected. For each genotype analyzed, the following technical replicates were used: C57BL/6 (three replicates), TG (three), and nonTG (two). Experimental details are summarized in table S7.

Microarray data analysis

RNA from sperm and embryos was converted to double-stranded cDNA using the SensationPlus WT kit and hybridized to GeneChip Mouse Exon 2.0 ST arrays (Affymetrix). CEL files for sperm and embryo data were separately read into R (version 3.1.0), where the Bioconductor package *oligo* was used to calculate transcript-cluster-level expression values with the RMA (robust multi-array average) algorithm. Differential expression analysis between the experimental groups was conducted using the limma package (*61*). The expected FDR was estimated using the Benjamini-and-Hochberg method, and statistical significance for differential expression of sperm RNA was set to FDR < 5%, coupled with a minimal difference of 1 on the $\log_2$ scale (|fold change| > 2). Statistical significance for differential expression of embryo RNA was set to FDR < 30%, due to $n = 2$ replicates in nonTG-sired embryos. Genes reaching statistical significance were submitted to DAVID (*62*) and Mouse Genome Informatics (www.informatics.jax.org) for functional analysis.

Functional analysis of ChIP-seq data

Functional analysis was performed using the R package topGO (*63*). Genes depleted in H3K4me2, which were also enriched in high levels of H3K4me3 or in H3K27me3, were selected (see table S3). Enrichment analysis was performed using Fisher's exact test, and significance was called at $P < 0.01$.

Statistical analyses

The level of significance for all statistical tests used was set at $P < 0.05$, and all tests were two-tailed. The assessment of abnormalities in TG- and nonTG-sired pups and E18.5 embryos was conducted on a per-generation basis. Litter size was depicted as mean ± SEM and analyzed with a Student's t test. The survivability of pups was estimated by applying a Kaplan-Meier analysis, followed by a log-rank test using GraphPad Prism 5 software (GraphPad Software, La Jolla, CA). Total abnormalities and frequency of live pups, total pregnancy loss, and total abnormal E18.5 embryos were tested for a significant difference from control offspring, using Fisher's exact test, uncorrected for multiple comparisons. DNA methylation data were analyzed using an unpaired Student's t test, and all data were analyzed with the aid of Systat 13 and the R statistical computing environment.

REFERENCES AND NOTES

1. I. Lobo, K. Zhaurova, Birth defects: causes and statistics. *Nat. Educ.* **1**, 18 (2008).
2. T. J. Mathews, M. F. MacDorman, "Infant mortality statistics from the 2005 period linked birth/infant death data set" (National Vital Statistics Reports, National Center for Health Statistics, Hyattsville, MD, 2008), vol. 57.
3. M. D. Anway, A. S. Cupp, M. Uzumcu, M. K. Skinner, Epigenetic transgenerational actions of endocrine disruptors and male fertility. *Science* **308**, 1466–1469 (2005). doi: 10.1126/science.1108190; pmid: 15933200
4. M. E. Pembrey *et al.*ALSPAC Study Team, Sex-specific, male-line transgenerational responses in humans. *Eur. J. Hum. Genet.* **14**, 159–166 (2006). doi: 10.1038/sj.ejhg.5201538; pmid: 16391557
5. B. R. Carone *et al.*, Paternally induced transgenerational environmental reprogramming of metabolic gene expression in mammals. *Cell* **143**, 1084–1096 (2010). doi: 10.1016/j.cell.2010.12.008; pmid: 21183072
6. S. F. Ng *et al.*, Chronic high-fat diet in fathers programs β-cell dysfunction in female rat offspring. *Nature* **467**, 963–966 (2010). doi: 10.1038/nature09491; pmid: 20962845
7. R. Lambrot *et al.*, Low paternal dietary folate alters the mouse sperm epigenome and is associated with negative pregnancy outcomes. *Nat. Commun.* **4**, 2889 (2013). doi: 10.1038/ncomms3889; pmid: 24326934
8. B. G. Dias, K. J. Ressler, Parental olfactory experience influences behavior and neural structure in subsequent generations. *Nat. Neurosci.* **17**, 89–96 (2014). doi: 10.1038/nn.3594; pmid: 24292232
9. M. K. Skinner, C. Guerrero-Bosagna, Role of CpG deserts in the epigenetic transgenerational inheritance of differential DNA methylation regions. *BMC Genomics* **15**, 692 (2014). doi: 10.1186/1471-2164-15-692; pmid: 25142051
10. M. Zeybel *et al.*, Multigenerational epigenetic adaptation of the hepatic wound-healing response. *Nat. Med.* **18**, 1369–1377 (2012). doi: 10.1038/nm.2893; pmid: 22941276
11. E. J. Radford *et al.*, In utero undernourishment perturbs the adult sperm methylome and intergenerational metabolism. *Science* **345**, 1255903 (2014). pmid: 25011554
12. T. H. Bestor, D. Bourc'his, Transposon silencing and imprint establishment in mammalian germ cells. *Cold Spring Harb. Symp. Quant. Biol.* **69**, 381–387 (2004). doi: 10.1101/sqb.2004.69.381; pmid: 16117671
13. S. A. Smallwood *et al.*, Dynamic CpG island methylation landscape in oocytes and preimplantation embryos. *Nat. Genet.* **43**, 811–814 (2011). doi: 10.1038/ng.864; pmid: 21706000
14. H. Kobayashi *et al.*, Contribution of intragenic DNA methylation in mouse gametic DNA methylomes to establish oocyte-specific heritable marks. *PLOS Genet.* **8**, e1002440 (2012). doi: 10.1371/journal.pgen.1002440; pmid: 22242016
15. Z. D. Smith *et al.*, A unique regulatory phase of DNA methylation in the early mammalian embryo. *Nature* **484**, 339–344 (2012). doi: 10.1038/nature10960; pmid: 22456710
16. U. Brykczynska *et al.*, Repressive and active histone methylation mark distinct promoters in human and mouse spermatozoa. *Nat. Struct. Mol. Biol.* **17**, 679–687 (2010). doi: 10.1038/nsmb.1821; pmid: 20473313
17. S. Erkek *et al.*, Molecular determinants of nucleosome retention at CpG-rich sequences in mouse spermatozoa. *Nat. Struct. Mol. Biol.* **20**, 868–875 (2013). doi: 10.1038/nsmb.2599; pmid: 23770822
18. S. S. Hammoud *et al.*, Distinctive chromatin in human sperm packages genes for embryo development. *Nature* **460**, 473–478 (2009). pmid: 19525931
19. E. Sendler *et al.*, Stability, delivery and functions of human sperm RNAs at fertilization. *Nucleic Acids Res.* **41**, 4104–4117 (2013). doi: 10.1093/nar/gkt132; pmid: 23471003
20. R. Balhorn, The protamine family of sperm nuclear proteins. *Genome Biol.* **8**, 227 (2007). doi: 10.1186/gb-2007-8-9-227; pmid: 17903313
21. B. R. Carone *et al.*, High-resolution mapping of chromatin packaging in mouse embryonic stem cells and sperm. *Dev. Cell* **30**, 11–22 (2014). doi: 10.1016/j.devcel.2014.05.024; pmid: 24998598
22. M. Saitou, K. Kurimoto, Paternal nucleosomes: Are they retained in developmental promoters or gene deserts? *Dev. Cell* **30**, 6–8 (2014). doi: 10.1016/j.devcel.2014.06.025; pmid: 25026032
23. T. Vavouri, B. Lehner, Chromatin organization in sperm may be the major functional consequence of base composition variation in the human genome. *PLOS Genet.* **7**, e1002036 (2011). doi: 10.1371/journal.pgen.1002036; pmid: 21490963
24. D. J. Katz, T. M. Edwards, V. Reinke, W. G. Kelly, A C. elegans LSD1 demethylase contributes to germline immortality by reprogramming epigenetic memory. *Cell* **137**, 308–320 (2009). doi: 10.1016/j.cell.2009.02.015; pmid: 19379696
25. Y. Shi *et al.*, Histone demethylation mediated by the nuclear amine oxidase homolog LSD1. *Cell* **119**, 941–953 (2004). doi: 10.1016/j.cell.2004.12.012; pmid: 15620353
26. C. Guerrero-Bosagna *et al.*, Epigenetic transgenerational inheritance of vinclozolin induced mouse adult onset disease and associated sperm epigenome biomarkers. *Reprod. Toxicol.* **34**, 694–707 (2012). doi: 10.1016/j.reprotox.2012.09.005; pmid: 23041264
27. Y. Wei *et al.*, Paternally induced transgenerational inheritance of susceptibility to diabetes in mammals. *Proc. Natl. Acad. Sci. U.S.A.* **111**, 1873–1878 (2014). doi: 10.1073/pnas.1321195111; pmid: 24449870
28. T. Furuchi, K. Masuko, Y. Nishimune, M. Obinata, Y. Matsui, Inhibition of testicular germ cell apoptosis and differentiation in mice misexpressing Bcl-2 in spermatogonia. *Development* **122**, 1703–1709 (1996). pmid: 8674410
29. J. Blanco-Rodríguez, γH2AX marks the main events of the spermatogenic process. *Microsc. Res. Tech.* **72**, 823–832 (2009). doi: 10.1002/jemt.20730; pmid: 19405149
30. C. Cho *et al.*, Haploinsufficiency of protamine-1 or -2 causes infertility in mice. *Nat. Genet.* **28**, 82–86 (2001). doi: 10.1038/ng0501-82; pmid: 11326282
31. R. E. Braun, R. R. Behringer, J. J. Peschon, R. L. Brinster, R. D. Palmiter, Genetically haploid spermatids are

phenotypically diploid. *Nature* **337**, 373–376 (1989). doi: 10.1038/337373a0; pmid: 2911388
32. M. Hisano *et al*., Genome-wide chromatin analysis in mature mouse and human spermatozoa. *Nat. Protoc.* **8**, 2449–2470 (2013). doi: 10.1038/nprot.2013.145; pmid: 24232248
33. J. Zhang *et al*., SFMBT1 functions with LSD1 to regulate expression of canonical histone genes and chromatin-related factors. *Genes Dev.* **27**, 749–766 (2013). doi: 10.1101/gad.210963.112; pmid: 23592795
34. N. Hashimoto *et al*., Ablation of PDK1 in pancreatic β cells induces diabetes as a result of loss of β cell mass. *Nat. Genet.* **38**, 589–593 (2006). doi: 10.1038/ng1774; pmid: 16642023
35. B. J. Collins, M. Deak, V. Murray-Tait, K. G. Storey, D. R. Alessi, In vivo role of the phosphate groove of PDK1 defined by knockin mutation. *J. Cell Sci.* **118**, 5023–5034 (2005). doi: 10.1242/jcs.02617; pmid: 16219676
36. M. A. Lawlor *et al*., Essential role of PDK1 in regulating cell size and development in mice. *EMBO J.* **21**, 3728–3738 (2002). doi: 10.1093/emboj/cdf387; pmid: 12110585
37. M. Courel, L. Friesenhahn, J. A. Lees, E2f6 and Bmi1 cooperate in axial skeletal development. *Dev. Dyn.* **237**, 1232–1242 (2008). doi: 10.1002/dvdy.21516; pmid: 18366140
38. M. Blum *et al*., Gastrulation in the mouse: The role of the homeobox gene goosecoid. *Cell* **69**, 1097–1106 (1992). doi: 10.1016/0092-8674(92)90632-M; pmid: 1352187
39. E. Metzger *et al*., LSD1 demethylates repressive histone marks to promote androgen-receptor-dependent transcription. *Nature* **437**, 436–439 (2005). pmid: 16079795
40. M. Wissmann *et al*., Cooperative demethylation by JMJD2C and LSD1 promotes androgen receptor-dependent gene expression. *Nat. Cell Biol.* **9**, 347–353 (2007). doi: 10.1038/ncb1546; pmid: 17277772
41. F. Lienert *et al*., Genomic prevalence of heterochromatic H3K9me2 and transcription do not discriminate pluripotent from terminally differentiated cells. *PLOS Genet.* **7**, e1002090 (2011). doi: 10.1371/journal.pgen.1002090; pmid: 21655081
42. N. A. Youngson, E. Whitelaw, Transgenerational epigenetic effects. *Annu. Rev. Genomics Hum. Genet.* **9**, 233–257 (2008). doi: 10.1146/annurev.genom.9.081307.164445; pmid: 18767965
43. C. Lalancette, D. Miller, Y. Li, S. A. Krawetz, Paternal contributions: New functional insights for spermatozoal RNA. *J. Cell. Biochem.* **104**, 1570–1579 (2008). doi: 10.1002/jcb.21756; pmid: 18393352
44. L. B. Russell, P. R. Hunsicker, W. L. Russell, Comparison of the genetic effects of equimolar doses of ENU and MNU: While the chemicals differ dramatically in their mutagenicity in stem-cell spermatogonia, both elicit very high mutation rates in differentiating spermatogonia. *Mutat. Res.* **616**, 181–195 (2007). doi: 10.1016/j.mrfmmm.2006.11.003; pmid: 17174358
45. K. L. Burr *et al*., The effects of MSH2 deficiency on spontaneous and radiation-induced mutation rates in the mouse germline. *Mutat. Res.* **617**, 147–151 (2007). doi: 10.1016/j.mrfmmm.2007.01.010; pmid: 17331550
46. R. C. Barber *et al*., The effects of in utero irradiation on mutation induction and transgenerational instability in mice. *Mutat. Res.* **664**, 6–12 (2009). doi: 10.1016/j.mrfmmm.2009.01.011; pmid: 19428375
47. M. Ihara *et al*., Paternal poly (ADP-ribose) metabolism modulates retention of inheritable sperm histones and early embryonic gene expression. *PLOS Genet.* **10**, e1004317 (2014). pmid: 24810616
48. D. T. Carrell, Elucidating the genetics of male infertility: Understanding transcriptional and translational regulatory networks involved in spermatogenesis. *Int. J. Androl.* **31**, 455–456 (2008). doi: 10.1111/j.1365-2605.2008.00913.x; pmid: 18710407
49. S. Chong *et al*., Modifiers of epigenetic reprogramming show paternal effects in the mouse. *Nat. Genet.* **39**, 614–622 (2007). doi: 10.1038/ng2031; pmid: 17450140
50. O. Rechavi, G. Minevich, O. Hobert, Transgenerational inheritance of an acquired small RNA-based antiviral response in *C. elegans*. *Cell* **147**, 1248–1256 (2011). doi: 10.1016/j.cell.2011.10.042; pmid: 22119442
51. L. R. Sabin, M. J. Delás, G. J. Hannon, Dogma derailed: The many influences of RNA on the genome. *Mol. Cell* **49**, 783–794 (2013). doi: 10.1016/j.molcel.2013.02.010; pmid: 23473599
52. I. Ulitsky, D. P. Bartel, lincRNAs: Genomics, evolution, and mechanisms. *Cell* **154**, 26–46 (2013). doi: 10.1016/j.cell.2013.06.020; pmid: 23827673
53. F. Borges, R. A. Martienssen, Establishing epigenetic variation during genome reprogramming. *RNA Biol.* **10**, 490–494 (2013). doi: 10.4161/rna.24085; pmid: 23774895
54. M. Sauvageau *et al*., Multiple knockout mouse models reveal lincRNAs are required for life and brain development. *eLife* **2**, e01749 (2013). doi: 10.7554/eLife.01749; pmid: 24381249
55. V. Delmas, F. van der Hoorn, B. Mellström, B. Jégou, P. Sassone-Corsi, Induction of CREM activator proteins in spermatids: Down-stream targets and implications for haploid germ cell differentiation. *Mol. Endocrinol.* **7**, 1502–1514 (1993). pmid: 8114765
56. M. Godmann *et al*., Krüppel-like factor 4 is involved in functional differentiation of testicular Sertoli cells. *Dev. Biol.* **315**, 552–566 (2008). doi: 10.1016/j.ydbio.2007.12.018; pmid: 18243172
57. B. Hogan, R. Beddington, F. Costantini, E. Lacy, *Manipulating the Mouse Embryo: A Laboratory Manual* (Cold Spring Harbor Laboratory Press, New York, ed. 2, 1994).
58. S. McGraw *et al*., Transient DNMT1 suppression reveals hidden heritable marks in the genome. *Nucleic Acids Res.* **43**, 1485–1497 (2015). doi: 10.1093/nar/gku1386; pmid: 25578964
59. Y. Xi, W. Li, BSMAP: Whole genome bisulfite sequence MAPping program. *BMC Bioinformatics* **10**, 232 (2009). doi: 10.1186/1471-2105-10-232; pmid: 19635165
60. R. Goodrich, G. Johnson, S. A. Krawetz, The preparation of human spermatozoal RNA for clinical analysis. *Arch. Androl.* **53**, 161–167 (2007). doi: 10.1080/01485010701216526; pmid: 17612875
61. M. E. Ritchie *et al*., limma powers differential expression analyses for RNA-sequencing and microarray studies. *Nucleic Acids Res.* **43**, e47 (2015). doi: 10.1093/nar/gkv007; pmid: 25605792
62. W. Huang, B. T. Sherman, R. A. Lempicki, Systematic and integrative analysis of large gene lists using DAVID bioinformatics resources. *Nat. Protoc.* **4**, 44–57 (2009). doi: 10.1038/nprot.2008.211; pmid: 19131956
63. A. Alexa, J. Rahnenfuhrer, topGO: Enrichment analysis for Gene Ontology. R package version 2.10.0 (2010).
64. E. Heard, R. A. Martienssen, Transgenerational epigenetic inheritance: Myths and mechanisms. *Cell* **157**, 95–109 (2014). doi: 10.1016/j.cell.2014.02.045; pmid: 24679529

ACKNOWLEDGMENTS

We thank M. Stadler, H. Royo, and D. Gaidatzis (FMI) for advice on computational data analysis; B. K. Hall (Dalhousie University) and J. Tanny and D. Bernard (McGill University) for advice; X. Giner for technical expertise; the Laboratoire de Transgénèse Center de Recherché, Centre Hospitalier de l'Université de Montréal, Canada, for microinjection and generation of the transgenic *hKDM1A* founders; Y. Shi (Harvard University) for providing full-length human KDM1 cDNA; T. Pastinen, G. Bourque, M. Caron, and platform personnel of the McGill Epigenomics Mapping and Data Coordinating Centers in the McGill University, as well as Génome Québec Innovation Centre, for setting up the RRBS sequencing data analysis pipeline; and F. Lefebvre for support with microarray analysis. This research was funded by the Canadian Institute of Health Research (S.K. and J.T.), Genome Quebec (S.K. and J.T.), the Reseau de Reproduction Quebecois, Fonds de Recherche du Québec – Nature et Technologies (FRQNT) (S.K. and J.T), Boehringer Ingelheim Fond (S.E.), Swiss National Science Foundation (grant 31003A_125386) (A.H.F.M.P.), and the Novartis Research Foundation (A.H.F.M.P.). The data reported in this paper are available at Gene Expression Omnibus: Microarray data, including both the CEL files and the transcript-level expression values, are under accession number GSE66052; ChIP-seq and nucleosome data are under accession number GSE55471. K.S., S.E., M.G., R.L., S.M., J.T., A.H.F.M.P., and S.K. conceived and designed the experiments. K.S., S.E., M.G., R.L., C.L., T.C., S.M., J.X., J.T., M.S., A.H.F. M.P., and S.K. performed the experiments and analyzed the data. M.H. provided advice on the data analysis and the manuscript. K.S., J.T., A.H.F.M.P., and S.K. wrote the manuscript. We declare no conflicts of interest that would prejudice the impartiality of this work.

SUPPLEMENTARY MATERIALS

www.sciencemag.org/content/350/6261/aab2006/suppl/DC1
Figs. S1 to S9
Tables S1 to S7
Reference (*65*)

26 March 2015; accepted 18 September 2015
Published online 8 October 2015
10.1126/science.aab2006

REPORTS

ACTINIDE CHEMISTRY

Electrochemical oxidation of ^{243}Am(III) in nitric acid by a terpyridyl-derivatized electrode

Christopher J. Dares,[1] Alexander M. Lapides,[1] Bruce J. Mincher,[2] Thomas J. Meyer[1]*

Selective oxidation of trivalent americium (Am) could facilitate its separation from lanthanides in nuclear waste streams. Here, we report the application of a high-surface-area, tin-doped indium oxide electrode surface-derivatized with a terpyridine ligand to the oxidation of Am(III) to Am(V) and Am(VI) in nitric acid. Potentials as low as 1.8 volts (V) versus the saturated calomel electrode were applied, 0.7 V lower than the 2.6 V potential for one-electron oxidation of Am(III) to Am(IV) in 1 molar acid. This simple electrochemical procedure provides a method to access the higher oxidation states of Am in noncomplexing media for the study of the associated coordination chemistry and, more important, for more efficient separation protocols.

Nuclear energy continues to be an attractive large-scale energy source due to its high power density and lack of carbon emissions (*1*). However, there are drawbacks to its expanded use, including the management of used fuel and high-level waste (HLW) (*2*, *3*). The presence of the minor actinide americium in the nuclear waste stream greatly limits the storage capacity of geologic repositories due to heat production, especially from ^{241}Am, which is a major contributor to the long-term radiotoxicity of HLW. Closed nuclear fuel recycling schemes that improve uranium efficiency and minimize the volume of HLW are under development in nuclear energy programs worldwide. In these schemes, Am must be separated from the lanthanides before transmutation because their high-neutron cross sections would otherwise disrupt the fission efficiency of the recycled fuel. Some schemes also separate Am from curium to facilitate radiologically safe fuel fabrication (*4*).

Partitioning of Am from the lanthanides is arguably the most difficult separation in radiochemistry. The stable oxidation state of Am in aqueous, acidic solutions is Am(III). With its ionic radius comparable to the radii of the trivalent lanthanide ions, its coordination chemistry is similar, leaving few options for separation. One approach is the use of soft donor ligands that exploit the slightly more diffuse nature of the actinide 5f-orbitals over the harder lanthanide 4f-orbitals. This provides a stronger, more covalent bond between actinides and N-donor ligands. Notable progress has been made in complexation-based strategies, but considerable challenges have been encountered when attempting to adapt their narrow pH range requirements for process scale-up, stimulating efforts to find alternatives. Another approach is oxidation and separation using the higher oxidation states of Am (*5*, *6*). Unlike the lanthanides, with the exception of the ceric cation, Am(III) can be oxidized and forms $[Am^{V}O_2]^+$ and $[Am^{VI}O_2]^{2+}$ complex ions in acidic media. The high oxidation state ions could be separated from the lanthanides by virtue of their distinct charge densities using well-developed solvent extraction methods (*4*).

Penneman and Asprey first reported the generation of Am(V) and Am(VI) in the 1950s (*7*). Determination of the formal reduction potentials has relied on both direct electrochemical measurements and indirect calorimetry. Formal potentials for the Am(IV/III) couple were evaluated in the 1960s and 1970s in concentrated phosphoric acid solutions (≈2 to 15 M) with Am(IV) stabilized and Am(V) destabilized by phosphate coordination, decreasing the driving force for disproportionation (*8*–*12*). Am(IV) is also stabilized in mildly acidic, concentrated fluoride solutions (*13*). Reported values for the Am(IV/III) potential have varied from as low as 2.2 V to as high as 2.9 V, with the standard value of 2.62 V versus the saturated calomel electrode (SCE) in 1 M perchloric acid derived from enthalpy of formation measurements by Morss and Fuger (*14*, *15*). The generally accepted $[AmO_2]^{2+}/[AmO_2]^+$ reduction potential of 1.6 V versus SCE in 1 M acid is based on direct electrochemical measurements by Penneman and Asprey (*7*). No electrochemical data are available for the $[AmO_2]^+$/Am(III) couple; a value of 1.72 V versus SCE in 1 M perchloric acid has been obtained based on calorimetric measurements.

Oxidizing Am(III) in noncomplexing media is hampered by the high potential for the intermediate Am(IV/III) couple (Fig. 1) (*15*). Only a limited number of chemical oxidants, including persulfate and bismuthate, have been explored for this purpose (*16*). Oxidation by persulfate gives sulfate as a by-product, which complicates subsequent vitrification of the waste (*17*). Bismuthate suffers from very low solubility, necessitating a filtration step that complicates its removal (*16*). Adnet and co-workers have patented a method for the electrochemical generation of high-oxidation-state Am in nitric acid solutions (*18*), based on earlier results by Milyukova *et al.* (*19*, *20*), who demonstrated Am(III) oxidation to Am(VI) in acidic persulfate solutions with Ag(I) added as an electron transfer mediator with $E^{o}[Ag(II/I)] = 1.98$ V versus SCE. In both measurements, phosphotungstate was added to coordinate Am with formation of a heteropolyanion complex facilitating electron transfer. However, separation schemes involving phosphotungstate (PW) failed due to coordination of Am(IV) by PW inhibiting further oxidation (*21*). Electrochemical generation of Am(VI) in the absence of chemical additives would open separations options using relatively simple and inexpensive process systems while greatly minimizing secondary waste production and treatment.

The coordination chemistry of Am(VI) is almost unknown because of its instability and the challenges inherent in its generation, including interferences caused by chemical oxidants or their by-products. Thus, information about selective ligand affinities for Am(VI) is lacking. Typically, assumptions about Am(VI) coordination chemistry are based on analogy to the behavior of U(VI), which also forms the dioxocation $[UO_2]^{2+}$ (*22*). An electrochemical method for generating the higher oxidation states of Am in noncomplexing media without interferences from chemical oxidants and their reduction products could greatly facilitate advances in Am(VI) coordination chemistry.

Generation of Am(V) in the absence of additives could also enable distinct separation strategies. The $[AmO_2]^+$ ion has lower charge density than the trivalent lanthanides, which can therefore be selectively coordinated by ligands that facilitate their extraction, leaving Am(V) in the raffinate. This approach has been investigated in tandem with bismuthate oxidation but ultimately failed because the reduced Bi(III) product interfered with lanthanide extraction (*16*).

We have sought to overcome these oxidation challenges by application of surface-modified electrodes. Our group previously pioneered the development and fabrication of high-surface-area porous

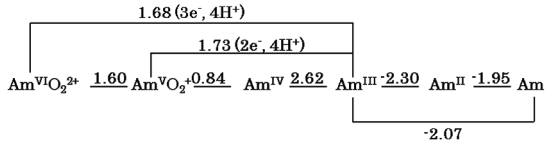

Fig. 1. Latimer diagram for Am in 1 M perchloric acid. Potentials listed are V versus the SCE.

[1]Department of Chemistry, The University of North Carolina at Chapel Hill, Chapel Hill, NC 27599, USA. [2]Idaho National Laboratory, Aqueous Separations and Radiochemistry Department, Idaho Falls, ID, USA.
*Corresponding author. E-mail: tjmeyer@unc.edu

Downloaded from www.sciencemag.org on November 5, 2015

oxide electrodes adapted for electrochemistry. These include planar fluoride-doped tin oxide (FTO) glass and reticulated vitreous carbon (RVC) coated with thin layers of conducting nanoparticle oxides, typically tin-doped indium oxide (ITO), antimony-doped tin oxide (ATO), and FTO (*23*, *24*). These electrodes have multiple advantages, including high conductivities, high surface areas, and well-developed chemistry for surface modification and derivatization (*23*–*25*).

Surface modification by covalent attachment of molecules can dramatically alter electrode behavior by imparting the reactivity and interfacial properties of the molecules to the surface. Examples from our previous work have included electrocatalysis with surface-bound Ru(II) polypyridyl-based electrocatalysts anchored through phosphonic acid–derivatized ligands, as well as assemblies of catalysts covalently bound through electropolymerization (*26*–*28*). The resulting modified electrodes catalyze a variety of reactions, including water oxidation and C-H functionalization (*27*, *29*). In this extension to Am oxidation, we derivatized mesoscopic metal oxide nanoparticle electrodes with covalently attached 4′-phosphonyl-(4-phenyl)-2,2′:6′,2″-terpyridine (p-tpy) as a surface-bound ligand. As shown in Fig. 2, this ligand binds to the metal oxide through the phosphonic acid group, creating a tpy-based surface binding site with an extensive and well-established d-block transition metal coordination chemistry and the ability to coordinate Am(III) (*30*). N-donor ligands were chosen because they have often been used for Am(III) separation in liquid-liquid extraction (*31*, *32*). They are oxidatively robust in acidic solutions and have sufficient affinity for Am(III) to be useful in surface electrochemical oxidation (*31*–*33*). By using a p-tpy–modified, high-surface-area oxide electrode, we demonstrate here the electrochemical oxidation of Am(III) to Am(V) and Am(VI) in nitric acid solutions without any additional ligands.

Cyclic voltammograms showed noticeably higher capacitive backgrounds and lower anodic currents for the derivatized electrodes than for nonderivatized controls at potentials beyond the thermodynamic potential for water oxidation (1.17 V versus NHE at pH 1) (fig. S1). Based on these results, derivatization of nanoITO with p-tpy increases the overpotential for water oxidation, in turn likely increasing the faradic efficiency for Am oxidation.

The surface coverage of p-tpy on nanoITO was estimated to be 4.1×10^{-9} mol·cm^{-2} by placing a 0.6 cm^2 electrode in a 1 mM solution of $Fe(ClO_4)_2$ for 20 min and then measuring the charge passed through the $[Fe(p\text{-}tpy)]^{3+/2+}$ surface wave at 0.93 V versus SCE in 0.1 M nitric acid by cyclic voltammetry (fig. S2). This value is a lower limit because it is based on surface formation of a $[Fe(p\text{-}tpy)_2]^{2+}$ couple and coordination of two p-tpy ligands. Surface analysis by monitoring the p-tpy–based ligand reduction wave for nanoITO-$[Fe(p\text{-}tpy)_2]^{2+}$ at ≈ −1 V was not possible because of interference due to reduction of Sn(II) sites on the electrode surface before ligand reduction.

All experiments involving Am were carried out using ^{243}Am in a radiologically designated fume hood with high-efficiency particulate-absorbing (HEPA) filtered exhaust. Low americium concentrations were used to ensure that whole-body radiation dose rates were below 10 mrem/hour. To satisfy these conditions, the upper handling limit for Am solutions for experiments in this study was approximately 2 mM. Two experimental protocols were employed for spectrophotometric monitoring of Am-containing solutions during the course of the electrochemical oxidations: discrete sampling and continual flow (fig. S4). In both, a two-compartment cell with compartments separated by a fine glass frit was used for electrochemistry. Proper equipment and instrument operation was ensured before the introduction of any americium-containing species. Speciation of Am was evaluated during electrolysis by spectroscopic monitoring of the f-f transitions of Am(III) (504 nm, $\epsilon \approx 300$ L·mol^{-1}·cm^{-1}), Am(V) (718 nm, $\epsilon \approx 60$ L·mol^{-1}·cm^{-1}), and Am(VI) (666 nm, $\epsilon \approx 27$ L·mol^{-1}·cm^{-1}).

Controlled potential electrolyses were carried out at 1.8 V, 2.25 V, and 2.7 V in 0.1 M nitric acid, with 0.9 M added sodium nitrate to retard migration of Am across the frit to the counter electrode. Complexation between nitrate and Am(III) is not extensive even with 8 M nitrate (*34*). Electrolyses at each applied potential were performed at least twice to ensure consistent spectroscopic quantification of each Am species. In each case, the maximum deviation in the highest proportion of Am(VI) and Am(V) formed was no more than 20%, with variations attributed to different setups (constant flow versus discrete measurements). Am concentrations varied based on availability of stock solutions and handling limits but were checked by γ-spectroscopy using 5-min count times. Samples of the counter-electrode compartments at the end of the electrolysis periods were counted by γ-spectroscopy, with the results confirming that Am migration across the frit had not occurred. No Am(III) oxidation was observed using underivatized electrodes at potentials between 1.8 and 2.7 V versus SCE. Noticeable electrode decomposition was evident at potentials above 2 V for electrolysis periods as short as 1 hour. Possible Am adsorption on both derivatized and underivatized ITO electrodes was investigated by mixing varying amounts of ITO powder into solutions of Am(III) at 1 μM. The ITO was filtered off, digested in 6.5 M nitric acid, and the resulting solution counted by γ-spectroscopy. No appreciable Am intercalation or adsorption into the ITO was observed in either case.

Visible absorption spectra of a solution containing 0.43 mM ^{243}Am(III) were acquired every 3 min during an electrolysis at 1.8 V to ascertain oxidation state speciation. At this potential and initial concentration, a decrease in Am(III) with time was observed with concurrent ingrowth of Am(V) (Fig. 3). The low molar extinction coefficients for the f-f transitions necessitated modeling the acquired spectra by a Gaussian peak analysis (fig. S5). No Am(VI) was detected at this applied potential; mass balance was reached by accounting for Am(III) and Am(V) in the solution. No changes in speciation were observed beyond 60 min, with about half of the Am(III) oxidized to Am(V) (0.19 mM Am(V), 0.25 mM Am(III)). At this potential, Am(VI) is thermodynamically accessible (Fig. 1), and its absence is attributed to the slow electrochemical oxidation of Am(V) with competing autoreduction of Am(VI) as it is formed. Increasing the initial Am(V) concentration to 0.55 mM, with 0.40 mM Am(III) (fig. S6), resulted in rapid conversion of Am(V) to Am(VI) at 1.8 V, whereas oxidation of Am(III) was slow. At pH 1, the potentials for the two couples are comparable (Fig. 1): 1.60 V for Am(VI/V) and 1.61 V for Am(V/III). This assumes a 0.236 V cathodic shift (0.059 V shift per proton) in the Am(V/IV) couple at pH 1 instead of pH 0. Rapid oxidation of Am(V) to Am(VI) is consistent with simple electron transfer oxidation of $[AmO_2]^+$ to $[AmO_2]^{2+}$, whereas oxidation of aquated Am(III) to $[AmO_2]^+$ is more complex, involving a change in coordination number as well as oxo formation.

We thus observe formation of high-oxidation-state Am—in this case, below the potential for the intermediate one-electron Am(IV/III) couple at 2.6 V in noncomplexing media. The surface-bound p-tpy ligand is key to this underpotential oxidation. Coordination of p-tpy to Am(III) at the

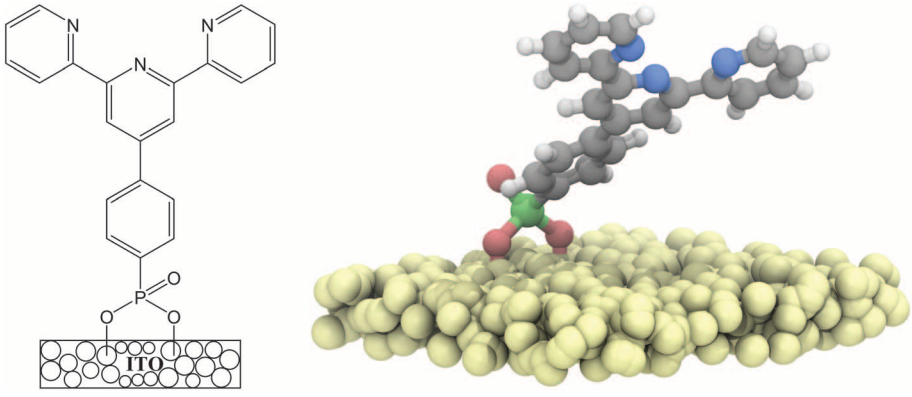

Fig. 2. Molecular structure of p-tpy on the surface of an ITO particle with the protonation state depicted as expected in neutral pH. (Left) A simple molecular illustration. (Right) A density functional theory–optimized p-tpy structure with pyridine rings oriented to show the potential tridentate bonding motif, ideally placed on a surface.

electrode surface presumably decreases the thermodynamic barrier for the one-electron oxidation to Am(IV). Coordination effects are known to play an important role for Am(III). For example, formation of the 1:1 complex between Am(III) and 2-amino-4,6-di-(pyridine-2-yl)-1,3,5-triazine in a methanol-water mixture occurs with a ΔG° = –32.9 kJ/mol (*31*, *32*). By contrast, coordination effects for $[AmO_2]^+$ are expected to be negligible due to the lower charge density of a monovalent dioxocation. Due to its instability, no information on the coordination preferences of Am(IV) exists; however, based on the better-known chemistry of Pu(IV), Am(IV) is expected to remain bound and undergo electrochemical oxidation to Am (V) before diffusing from the electrode surface (Fig. 3).

Reducing agents, including those generated radiolytically, such as hydrogen peroxide, are the culprits for the instability of Am(VI) and inhibit complete oxidation of Am(III). To demonstrate this, we varied the applied potential and total Am concentration under spectroscopic monitoring.

Electrolysis of an 84 μM solution of Am(III) at 2.25 V, 130 mV below the Am(IV/III) couple, gives Am(V) and Am(VI), both of which grow linearly in concentration with time (Fig. 4). After 1 hour, the increase in Am(VI) remains linear but with a noticeable decrease in rate. The growth in Am(V) also slows after 1 hour, eventually leveling off to reach a steady-state concentration of 30 μM. After 13 hours of electrolysis, the composition of the solution was 9 μM (11%) Am(III), 45 μM (54%) Am(V), and 30 μM (36%) Am(VI).

A further increase in applied potential to 2.7 V, this time with 1.84 mM Am(III), was sufficient to generate Am(IV) by direct oxidation at the electrode, resulting in an increase in the rate of appearance of Am(VI) relative to Am(V) without Am(V) reaching a steady state (fig. S7). After a 7-hour electrolysis period, the solution composition was 0.14 mM (8%) Am(III), 0.73 mM (40%) Am(V), and 0.97 mM (53%) Am(VI), which represents the highest final proportion of Am(VI) generated electrochemically in these studies (fig. S9).

Autoreduction by radiolytic intermediates provides an explanation for only partial oxidation of Am(III) to Am(V) and Am(VI) at the electrolysis steady state, as observed here. Quantitating the extent of autoreduction and its role in defining the electrolysis steady state are important elements in possible electrochemical/separation schemes for Am. Compared with chemical oxidation, the electrochemical procedure offers the advantage of avoiding complications from oxidizing agents and their reduced forms (*16*).

Radiolysis of water by Am generates one-electron reducing agents such as H atoms and two-electron reducing agents such as hydrogen peroxide, as well as other redox transients (*35*). The concentration of radiolysis products varies linearly with total Am concentration, with zero-order reduction kinetics observed for the appearance or disappearance of Am species. Under these conditions, rate constants for these Am species during autoreduction can therefore be derived from the slopes of concentration-time plots (*36*, *37*).

Radiolytically produced one-electron and two-electron reductants provide independent pathways for Am(VI) reduction, with an overall rate constant for Am(VI) loss of 23.4×10^{-6} s^{-1} (fig. S10). The Am(IV) produced from the two-electron reduction of Am(VI) by radiolytic intermediate or intermediates, presumably H_2O_2, rapidly disproportionates to Am(V) and Am(III). The reduction of Am(V) to Am(IV) or Am(III) is slow on this time scale (fig. S10). Therefore, the rate of appearance of Am(III) is due entirely to the disproportionation of Am(IV). The measured rate of Am(III) appearance is 7.3×10^{-6} s^{-1}, which implies that the rate of autoreduction of Am(VI) to Am(IV) is 14.6×10^{-6} s^{-1}. The rate constant for the appearance of Am(V) was measured to be 16.4×10^{-6} s^{-1} and is due both to the one-electron reduction of Am(VI) and to the disproportionation of Am(IV). Subtracting the contribution from Am(IV) disproportionation (7.3×10^{-6} s^{-1}) gives a one-electron reduction rate to produce Am(V) from Am(VI) of 9.1×10^{-6} s^{-1} (fig. S10).

Our results demonstrate low-potential oxidation of Am(III) to Am(VI) in noncoordinating solutions at high-surface-area metal oxide electrodes derivatized with a surface-bound terpyridine ligand. The mechanism appears to involve surface binding of Am(III) and oxidation to Am (IV) followed by further oxidation to Am(V) with release as $[AmO_2]^+$. Electrochemical oxidation is

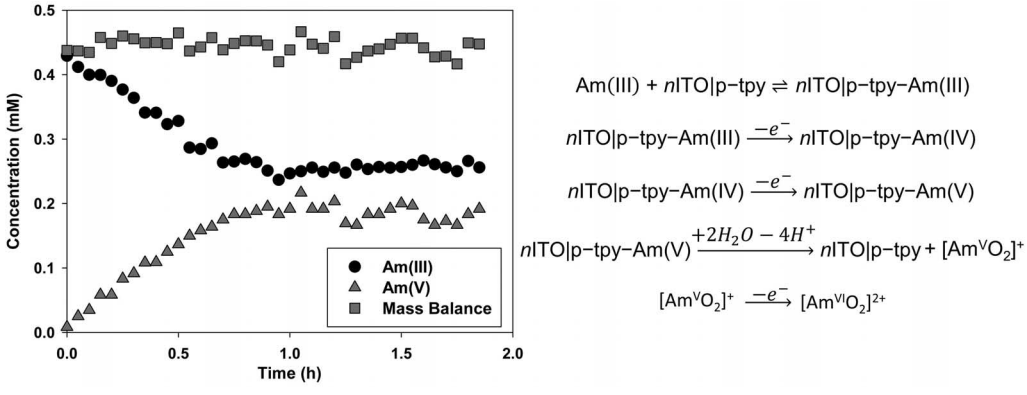

Fig. 3. Electrochemical oxidation of 0.43 mM Am(III) in 0.1 M nitric acid with 0.9 M sodium nitrate using a p-tpy–derivatized ITO electrode. (Left) Am speciation measured by visible spectroscopy in a 1-cm cuvette at an applied potential of 1.8 V versus SCE. The appearance of Am(V), concurrent loss of Am(III), and overall mass balance are plotted. (Right) Electrochemical Am oxidation scheme involving a p-tpy–derivatized electrode.

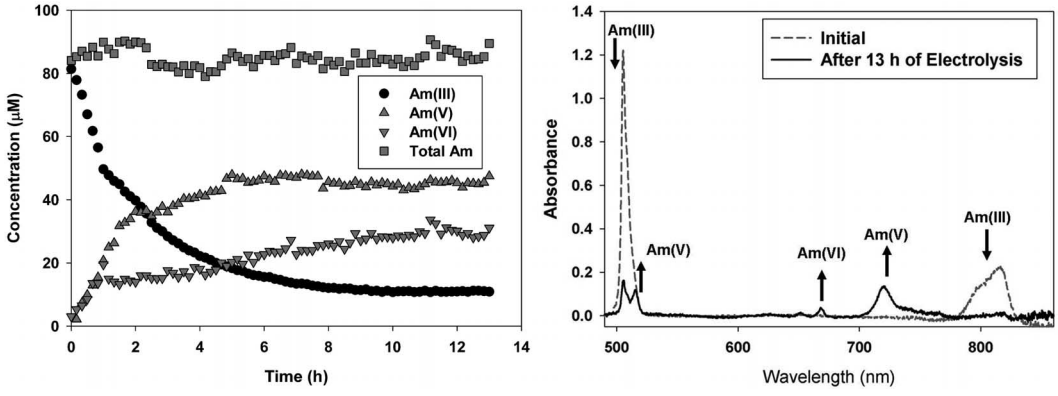

Fig. 4. Electrochemical oxidation of 84 μM Am(III) in 0.1 M nitric acid with 0.9 M sodium nitrate using a p-tpy–derivatized ITO electrode at an applied potential of 2.25 V versus SCE. (**Left**) Am speciation as measured by visible spectroscopy in a 50-cm waveguide. (**Right**) Visible spectra of species before controlled potential electrolysis and after 13 hours of electrolysis with highlighted speciation changes.

in competition with autoreduction by radiolysis intermediates, with Am(VI) more susceptible to reduction than Am(V).

REFERENCES AND NOTES

1. D. J. Rose, *Science* **184**, 351–359 (1974).
2. A. S. Kubo, D. J. Rose, *Science* **182**, 1205–1211 (1973).
3. E. E. Angino, *Science* **198**, 885–890 (1977).
4. B. J. Mincher, L. R. Martin, N. C. Schmitt, *Solv. Extract. Ion Exch.* **30**, 445–456 (2012).
5. W. H. Runde, B. J. Mincher, *Chem. Rev.* **111**, 5723–5741 (2011).
6. B. J. Mincher *et al.*, *Solv. Extract. Ion Exch.* **32**, 153–166 (2014).
7. R. A. Penneman, L. B. Asprey, *Rep. AECU-936* (U.S. Atomic Energy Commission, 1950).
8. Y. M. Kulyako, I. A. Lebedev, V. Y Frenkel, T. I. Trofimov, B .F. Myasoedov, *Radiokhimiya* **23**, 837–843 (1981).
9. I. A. Lebedev, *Radiokhimiya* **20**, 653–655 (1978).
10. I. A. Lebedev *et al.*, *Radiokhimiya* **18**, 652–658 (1976).
11. B. F. Myasoedov *et al.*, *Radiochem. Radioanal. Lett.* **14**, 17–24 (1973).
12. E. Yanir, M. Givon, Y. Marcus, *Inorg. Nucl. Chem. Lett.* **6**, 415–419 (1970).
13. E. Yanir, M. Givon, Y. Marcus, *Inorg. Nucl. Chem. Lett.* **5**, 369–372 (1969).
14. L. R. Morss, J. Fuger, *J. Inorg. Nucl. Chem.* **43**, 2059–2064 (1981).
15. A. J. Bard, R. Parsons, J. Jordan, *Standard Potentials in Aqueous Solution* (Marcel Dekker, Inc., 1983).
16. B. J. Mincher, L. R. Martin, N. C. Schmitt, *Inorg. Chem.* **47**, 6984–6989 (2008).
17. B. A. Moyer *et al.*, *Inorg. Chem.* **52**, 3473–3490 (2013).
18. J. M. Adnet, L. Donnet, P. Brossard, J. Bourges, U.S. Patent Office (1997), no. 5609745.
19. M. N. Litvina, M. S. Milyukova, B. F. Myasoedov, *J. Radioanal. Nucl. Chem.* **121**, 355–363 (1988).
20. M. S. Milyukova, M. N. Litvina, B. F. Myasoedov, *Radiokhimiya* **25**, 706 (1983).
21. S. Picart, D. Chartier, L. Donnet, J. M. Adnet, *Scientific Report* (Marcoule, 1999).
22. T. S. Franczyk, K. R. Czerwinski, K. N. Raymond, *J. Am. Chem. Soc.* **114**, 8138–8146 (1992).
23. M. A. Mendéz, C. J. Dares, L. Alibabaei, J. J. Concepcion, T. J. Meyer,, U. S. Patent Application (2014), App. No. 14/224,606.
24. M. A. Méndez, L. Alibabaei, J. J. Concepcion, T. J. Meyer, *ACS Cat.* **3**, 1850–1854 (2013).
25. Y. Tamaki, A. K. Vannucci, C. J. Dares, R. A. Binstead, T. J. Meyer, *J. Am. Chem. Soc.* **136**, 6854–6857 (2014).
26. P. Kang, Z. Chen, A. Nayak, S. Zhang, T. J. Meyer, *Environ. Sci.* **7**, 4007–4012 (2014).
27. W. Song *et al.*, *J. Am. Chem. Soc.* **136**, 9773–9779 (2014).
28. K. Hanson *et al.*, *Chem. Mater.* **25**, 3–5 (2013).
29. M. K. Coggins, M. A. Méndez, J. J. Concepcion, R. A. Periana, T. J. Meyer, *J. Am. Chem. Soc.* **136**, 15845–15848 (2014).
30. M. G. B. Drew *et al.*, *Dalton Trans.* **2000** (5): 821–830 (2000).
31. M. Miguirditchian *et al.*, *Inorg. Chem.* **44**, 1404–1412 (2005).
32. P. Panak, A. Geist, *Chem. Rev.* **113**, 1199–1236 (2013).
33. A. Afsar, L. M. Harwood, M. J. Hudson, P. Distler, J. John, *Chem. Commun.* **50**, 15082–15085 (2014).
34. W. W. Schulz, *The Chemistry of Americium* (Technical Information Center, Energy Research and Development Administration, 1976).
35. G. Choppin, J.-O. Liljienzin, J. Rydberg, C. Ekberg, *Radiochemistry and Nuclear Chemistry* (Academic Press, ed. 4, 2013).
36. A. A. Zaitsev, V. N. Kosyakov, A. G. Rykov, *Radiokhimiya* **2**, 348–350 (1960).
37. S. M. Woods, A. Cain, J. C. Sullivan, *J. Inorg. Nucl. Chem.* **36**, 2605–2607 (1974).

ACKNOWLEDGMENTS

This research was supported by the U.S. Department of Energy (DOE) Office of Nuclear Energy, Fuel Cycle Research and Development Program, under DOE Idaho Operations Office contract DE-AC07-99ID13727. This research made use of equipment for electrode fabrication including homogenizer, spin-coater, and annealing furnaces funded by the University of North Carolina Energy Frontier Research Center: Center for Solar Fuels, supported by the U.S. DOE Office of Science, Office of Basic Energy Sciences, under award number DE-SC0001011. A.M.L. thanks the U.S. Department of Defense, Air Force Office of Scientific Research, for funding through National Defense Science and Engineering Graduate Fellowship award FA9550-11-C-0028. Authors C.J.D., A.M.L., and T.J.M. at University of North Carolina at Chapel Hill and B.J.M. at Idaho National Laboratory have filed for a provisional patent application with the U.S. Patent and Trademark Office under application no. 62/202,428 on the electrochemical oxidation of americium at derivatized metal oxide electrodes. The authors also thank B. A. Moyer for encouragement and helpful technical discussions. Correspondence and requests for materials should be addressed to T.J.M. Author Contributions: C.J.D., T.J.M., and B.J.M. conceived experiments; A.M.L. synthesized the ligand p-tpy; C.J.D. prepared electrodes, designed and fabricated custom equipment, and conducted all experiments; C.J.D., T.J.M, and B.J.M. analyzed and interpreted data; C.J.D., A.M.L, B.J.M., and T.J.M. wrote the manuscript.

SUPPLEMENTARY MATERIALS

www.sciencemag.org/content/350/6261/652/suppl/DC1
Materials and Methods
Figs. S1 to S11
Reference (*38*)

29 June 2015; accepted 6 October 2015
10.1126/science.aac9217

FRUSTRATED MAGNETISM

Evidence for a gapped spin-liquid ground state in a kagome Heisenberg antiferromagnet

Mingxuan Fu,[1] Takashi Imai,[1,2]* Tian-Heng Han,[3,4] Young S. Lee[5,6]

The kagome Heisenberg antiferromagnet is a leading candidate in the search for a spin system with a quantum spin-liquid ground state. The nature of its ground state remains a matter of active debate. We conducted oxygen-17 single-crystal nuclear magnetic resonance (NMR) measurements of the spin-1/2 kagome lattice in herbertsmithite [$ZnCu_3(OH)_6Cl_2$], which is known to exhibit a spinon continuum in the spin excitation spectrum. We demonstrated that the intrinsic local spin susceptibility χ_{kagome}, deduced from the oxygen-17 NMR frequency shift, asymptotes to zero below temperatures of 0.03*J*, where *J* ~ 200 kelvin is the copper-copper superexchange interaction. Combined with the magnetic field dependence of χ_{kagome} that we observed at low temperatures, these results imply that the kagome Heisenberg antiferromagnet has a spin-liquid ground state with a finite gap.

The realization and characterization of a kagome Heisenberg antiferromagnet (KHA) with a corner-shared triangle structure (Fig. 1A) is crucial to the search for a quantum spin-liquid ground state (*1*, *2*). Spin liquids consist of entangled pairs of spin singlets and do not undergo a magnetic phase transition. The successful synthesis of the structurally ideal kagome lattice of Cu^{2+} ions (spin $S = 1/2$) in herbertsmithite [$ZnCu_3(OH)_6Cl_2$; Fig. 1, B to E] (*3*) was a major milestone (*4*). $ZnCu_3(OH)_6Cl_2$ remains paramagnetic at least down to ~50 mK (*5*, *6*). Moreover, inelastic neutron scattering measurements (*7*) on single crystals (*8*) have demonstrated that the spin excitation spectrum does not exhibit conventional magnons, but rather a spinon continuum. Despite the recent progress, fundamental issues regarding the nature of the ground state of the KHA are not yet understood. For example, the central question of the existence of a gap in the spin excitation spectrum has not been settled. This information is critical for comparatively evaluating the leading theories on the ground state of the $S = 1/2$ KHA: a gapped spin liquid, gapless spin liquid, or valence-bond solid (*1*, *2*, *9*–*14*)

In $ZnCu_3(OH)_6Cl_2$, weakly interacting Cu^{2+} defects occupy the nonmagnetic Zn^{2+} sites between the kagome layers with ~15% probability (*15*). Their contributions dominate bulk-averaged thermodynamic properties at low temperatures (*3*, *5*, *8*, *16*, *17*), making it difficult to measure the intrinsic low-energy properties of this material. Similarly, the Cu^{2+} impurity moments can contribute to the inelastic neutron scattering, obscuring the response of the intrinsic kagome spins at low energies (<2 meV) (*7*). Nuclear magnetic resonance (NMR) is an ideal local probe with which to investigate the intrinsic magnetic behavior under the presence of magnetic defects, as demonstrated by successful investigations of Kondo oscillations and analogous phenomena in metals (*18*), high-temperature superconductors (*19*), and low-dimensional spin systems (*20*). Our primary goal was to uncover the intrinsic behavior of the spin susceptibility, χ_{kagome}, separately from the defect-induced local spin susceptibility, χ_{defect},

[1]Department of Physics and Astronomy, McMaster University, Hamilton, Ontario L8S4M1, Canada. [2]Canadian Institute for Advanced Research, Toronto, Ontario M5G1Z8, Canada. [3]James Franck Institute and Department of Physics, University of Chicago, Chicago, IL 60637, USA. [4]Materials Science Division, Argonne National Laboratory, Argonne, IL 60439, USA. [5]Department of Physics, Massachusetts Institute of Technology, Cambridge, MA 02139, USA. [6]Department of Applied Physics and Department of Photon Science, Stanford University and SLAC National Accelerator Laboratory, Stanford, CA 94305, USA.
***Corresponding author. E-mail: imai@mcmaster.ca**

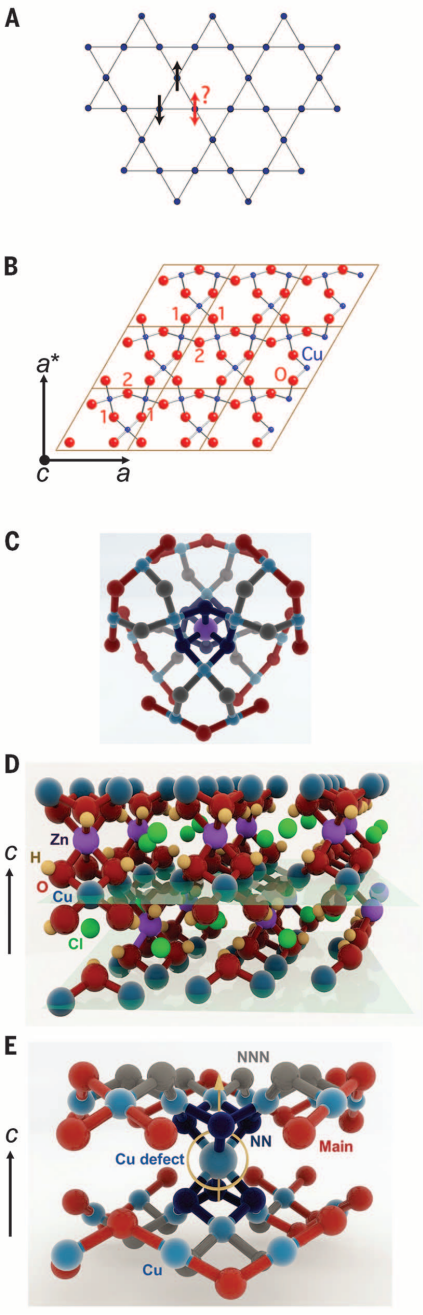

Fig. 1. Kagome lattice and the structure of $ZnCu_3(OH)_6Cl_2$. (**A**) A kagome lattice formed by corner-shared triangles. The antiferromagnetic interactions between NN sites frustrate the spin system (black arrows indicate two spins forming a singlet pair; the red double-headed arrow with the question mark represents a frustrated spin). (**B**) Top view of the Cu_3O_3 kagome layer in $ZnCu_3(OH)_6Cl_2$. The local geometries of the main1 and main2 ^{17}O sites (marked as 1 and 2, respectively) are not equivalent under the presence of B_{ext} || a^*. (**C**) Zn^{2+} sites (purple) are located either above or below the center of the Cu_3O_3 triangles (blue and red) and have 6 NN (navy blue) and 12 NNN (gray) ^{17}O sites in the adjacent kagome planes. (**D**) Oblique view of $ZnCu_3(OH)_6Cl_2$. (**E**) Cu^{2+} defect moment at a Zn^{2+} site polarized by B_{ext} || c (gold arrow), and its local environment.

using ^{17}O NMR measurements of an isotope-enriched single crystal of $ZnCu_3(OH)_6Cl_2$. We demonstrated that the spin excitation spectrum exhibits a finite gap $\Delta = 0.03J$ to $0.07J$ between a $S = 0$ spin-liquid ground state and the excited states, where $J \sim 200$ K represents the Cu-Cu superexchange interaction (*5*, *21*).

A major advantage of using a single crystal for NMR is that we can achieve high resolution by applying an external magnetic field B_{ext} along specific crystallographic directions. In Fig. 2A, we present the ^{17}O (nuclear spin $I = 5/2$; gyromagnetic ratio $\gamma_n/2\pi = 5.772$ MHz/T) NMR line shape measured at 295 K in $B_{ext} = 9$ T, applied along the c axis; the temperature dependence of the line shape is presented in Fig. 2C. Unlike previously measured powder-averaged ^{35}Cl and ^{17}O NMR line shapes (*22*, *23*), we can resolve the five $I_z = m$ to $m + 1$ transitions (I_z, z component of the nuclear spin angular momentum; magnetic quantum number $m = -5/2, -3/2, -1/2, +1/2, +3/2$), which are separated by a nuclear quadrupole frequency $\nu_Q^{(c)}$. In addition, the central peak frequency f for the $I_z = -1/2$ to $+1/2$ transition is shifted from the bare resonance frequency $f_o = (\gamma_n/2\pi)B_{ext}$ by the effects of the hyperfine magnetic fields from nearby Cu^{2+} sites, and the shift of the peak (marked "main" in Fig. 2A) is proportional to χ_{kagome}. Such an NMR frequency shift may be expressed in terms of the Knight shift, $^{17}K^{(c)} = f/f_o - 1 = A_{hf}\,\chi_{kagome}$, where A_{hf} is the hyperfine coupling constant between the ^{17}O nuclear spin and the Cu^{2+} electron spins. We can fit the line shape in Fig. 2A with three sets of five peaks with three distinct values of $^{17}K^{(c)}$ and $\nu_Q^{(c)}$. That is, the presence of the Cu^{2+} defects at the Zn^{2+} sites results in three distinct ^{17}O sites in $ZnCu_3(OH)_6Cl_2$. Taking into account the difference in the transverse relaxation that affects the apparent signal intensities (fig. S1), we estimated the population of the three sites as 13 ± 4%, 28 ± 5%, and 59 ± 8%, in agreement with earlier ^2D NMR observations of three corresponding sites in a deuterated single crystal of $ZnCu_3(OD)_6Cl_2$ (*24*).

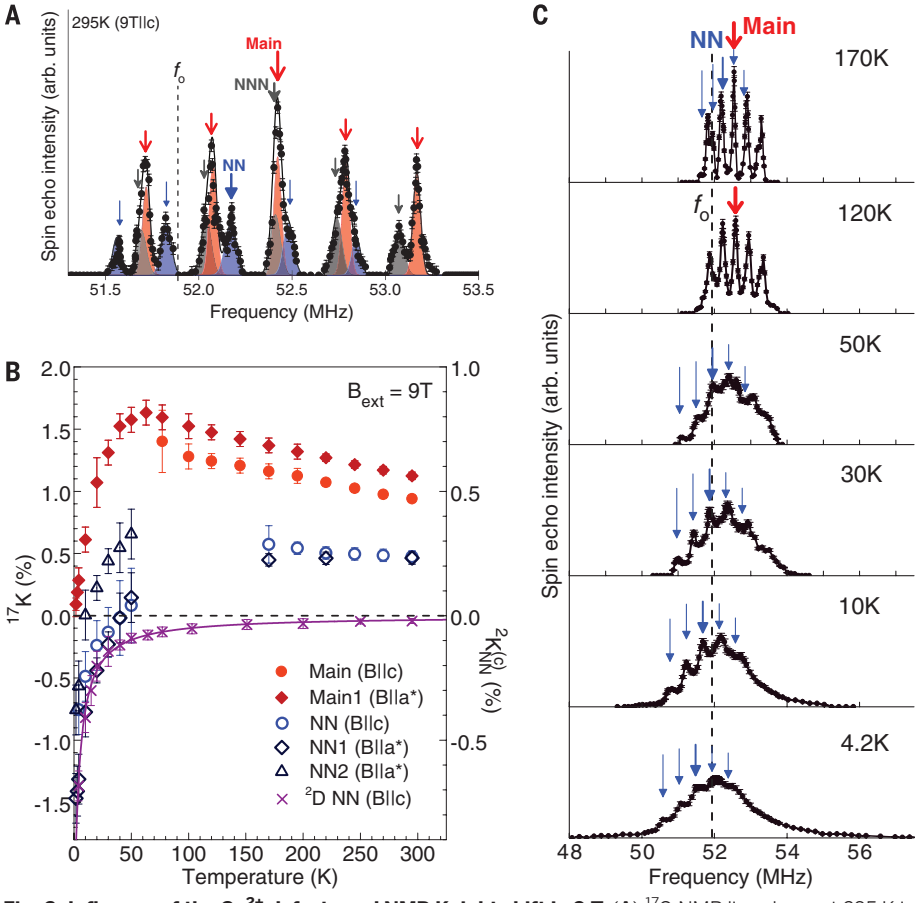

Fig. 2. Influence of the Cu^{2+} defects and NMR Knight shift in 9 T. (**A**) ^{17}O NMR line shape at 295 K in $B_{ext} = 9$ T || c, fitted with three sets of five peaks arising from the main ($\nu_Q^{(c)} \sim 360$ kHz), NN ($\nu_Q^{(c)} \sim 310$ kHz), and NNN ($\nu_Q^{(c)} \sim 350$ kHz) sites. The vertical dashed line represents the zero-shift frequency $f_o = (\gamma_n/2\pi)B_{ext} \sim 51.9$ MHz, where $^{17}K^{(c)} = 0$. (**B**) A summary of $^{17}K^{(a^*)}$ and $^{17}K^{(c)}$ measured in 9 T. Solid and open symbols represent the data for the main and NN sites, respectively. Also plotted is the ^2D NMR frequency shift $^2K^{(c)}_{NN}$ at the NN ^2D sites, measured in 8.4 T, that is dominated entirely by χ_{defect}; the solid curve is a Curie-Weiss fit, $^2K^{(c)}_{NN} \sim -(T - \theta)^{-1}$, with $\theta \sim -1.2$ K (*24*). (**C**) Representative ^{17}O NMR line shapes measured in $B_{ext} = 9$ T || c below 295 K. Red arrows show the central peak of the main sites, whereas blue arrows mark the five transitions of the NN sites. Error bars represent uncertainties in the NMR signal intensity in (A) and (C) and experimental errors of the Knight shifts in (B).

It is straightforward to assign these three ^{17}O signals to the nearest neighbor (NN) of the Cu^{2+} defects, the next-NN (NNN) of the Cu^{2+} defects, and the intrinsic main sites located far from defects, respectively, for the following reasons. First, the Cu^{2+} defects occupying the Zn^{2+} sites with ~15% probability (*15*) are the cause of a large Curie-Weiss contribution, χ_{defect}, in the bulk magnetic susceptibility data at low temperatures (*24*). This means that ~15% of ^{17}O (and ^{2}D) at the NN sites experiences an additional, transferred hyperfine coupling A_{hf}^{defect} with these Cu^{2+} defect spins polarized by B_{ext}. As shown in Fig. 2B, the large Curie-Weiss contribution $A_{hf}^{defect}\chi_{defect}$ to $^{17}K^{(c)}$ at the NN ^{17}O sites overwhelms the intrinsic contribution $A_{hf}\,\chi_{kagome}$ at low temperatures, similar to the defect-induced Curie-Weiss behavior of $^{2}K_{NN}^{(c)}$ at the NN ^{2}D sites reported previously (*24*). Both $^{17}K^{(c)}$ and $^{2}K_{NN}^{(c)}$ are negative at low temperatures because $A_{hf}^{defect} < 0$. Second, because the abundance of the NNN ^{17}O sites should be twice that of the NN sites, as shown in Fig. 1, C and E, we can assign the 28 ± 5% signal to the NNN. The remaining 59 ± 8% arises from the intrinsic main sites.

Our high-resolution single-crystal NMR data show no evidence for the presence of Zn^{2+} antisite defects occupying the Cu^{2+} sites within the kagome plane, in disagreement with earlier powder-averaged ^{17}O NMR data, which were obtained from lower-resolution measurements (*23*). The previous powder work (*23*) misidentified the NN peaks as arising from singlet "D-sites" induced by antisite defects in the kagome plane, as explained in detail in (*25*).

The NMR properties at the NNN and main sites are very similar, and we could distinguish them only near 295 K, where the NMR lines are narrow. Their similarity suggests that the spin polarization induced by the Cu^{2+} defects decays very quickly within the kagome plane, unlike the long-range nature of the Kondo oscillations in metals (*18*). Our observation is consistent with the expectation that the spin-spin correlation length is comparable to the Cu-Cu distance in the KHA (*7*, *26*, *27*). The primary effect of the quenched randomness of the Cu^{2+} defects on the main peaks is therefore the broadening of the individual NMR line in proportion to χ_{defect} (fig. S2). The broad high-frequency tail of the main peak observed below 4.2 K in 9 T (Fig. 2C and figs. S3 to S4), however, may also indicate that the Cu^{2+} defects induce a short-range spin density oscillation within the kagome plane and that some NNN sites have a large positive ^{17}K (fig. S4).

In the field geometry of $B_{ext} \parallel c$, accidental superposition of the NN peaks prevented us from resolving the central part of the main peak below ~70 K (Fig. 2C). Instead, we found that $B_{ext} \parallel a^*$ is the ideal geometry for investigating χ_{kagome} at low temperatures. For the $B_{ext} \parallel a^*$ geometry (Fig. 1B), the direction of B_{ext} is at a 60º angle to the Cu-O-Cu bond of two ^{17}O sites ("main1") within each triangle, and it is orthogonal to the bond of the remaining ^{17}O site ("main2"). As a consequence (Fig. 3A), the ^{17}O NMR signals from the main1 and main2 sites appear separately, with the integrated intensity ratio of 2:1 and different magnitudes of $^{17}K^{(a^*)}$ and the quadrupole splitting [$\nu_Q^{(a^*)}$ ~ 8 kHz for main1 and $\nu_Q^{(a^*)}$ ~ 520 kHz for main2]. Normally, the partitioning of the ^{17}O NMR lines into main1 and main2 would merely complicate the overall spectrum. In this case, owing to the small value of $\nu_Q^{(a^*)}$ ~ 8 kHz, all five of the $I_z = m$ to $m + 1$ transitions of main1 are bundled into a large peak, which we were able to resolve down to 1.8 K (~0.01*J*). Moreover, we were able to selectively measure the main1 line shape (Fig. 3B) by exciting all five transitions at once with longer radio-frequency pulses (*25*); the isolated main1 peak frequency in Fig. 3B closely matched that of Fig. 3A, providing additional confidence in our line assignment.

In Fig. 4A, we summarize the temperature dependence of $^{17}K^{(a^*)}$ for the main1 sites measured in B_{ext} = 3.2 T || a^*. The results for $^{17}K^{(a^*)}$ measured in B_{ext} = 9 T || a^* (Fig. 2B) are nearly identical, except below ~10 K, as discussed below. The superposition of the large main1 peak made it difficult to accurately measure $^{17}K^{(a^*)}$ at the central transition of main2, but the frequency shift of the isolated uppermost satellite peak of main2 shows a similar trend with temperature (Fig. 3A and fig. S5). Unlike the bulk-averaged magnetic susceptibility data (*3*, *5*, *8*), $^{17}K^{(a^*)}$ decreases below ~60 K. Moreover, $^{17}K^{(a^*)}$, and hence χ_{kagome}, asymptotes to zero below ~5 K (~0.03*J*), implying the absence of thermally accessible excited states. The results of the ^{17}O nuclear spin-lattice relaxation rate $1/T_1$ are also consistent with diminishing intrinsic spin excitations toward $T = 0$ (fig. S6). Combined with the fact that the structural analysis at low temperatures (based on Rietveld refinement) revealed no evidence of the formation of the large unit cell expected for valence-bond solids (*15*), we conclude that $ZnCu_3(OH)_6Cl_2$ has a quantum spin-liquid ground state with the total spin $S = 0$, and its excitation spectrum has a finite gap.

To estimate the magnitude of the gap Δ, we fitted $^{17}K^{(a^*)}$ below 4.2 K to an exponential function with a pre-factor T (where T represents temperature), $^{17}K^{(a^*)} \sim T \cdot \exp(-\Delta/T)$, as shown in Fig. 4B; we obtained Δ ~ 6.8 K for B_{ext} = 3.2 T. The constant background term $^{17}K_{chem}$, arising from the chemical shift, is generally negligibly small (~±0.02%) at the ^{17}O sites in copper oxides (*28*) and does not affect our estimation of Δ in a meaningful way. We included the pre-actor T to phenomenologically account for the effects

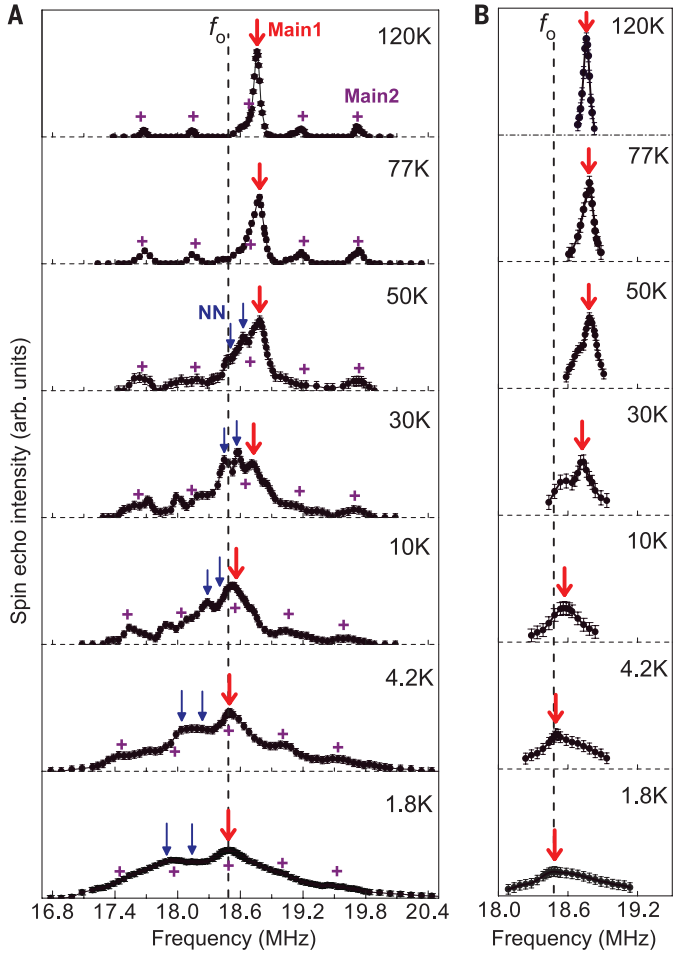

Fig. 3. ^{17}O NMR line shapes measured in B_{ext} = 3.2 T || a^*. (**A**) ^{17}O NMR line shapes measured with radio-frequency pulse conditions optimized for individual $I_z = m$ to $m + 1$ transitions. Red arrows mark a bundle of all five transitions of main1. Purple crosses indicate approximate frequencies of the five individual transitions of main2; blue arrows indicate approximate frequencies of the central transitions of the NN1 (left arrows) and NN2 (right arrows) sites (fig.S3). (**B**) ^{17}O NMR line shapes measured with longer radio-frequency pulses optimized to excite the five $I_z = m$ to $m+1$ transitions of main1 simultaneously. Over-pulsing suppresses other peaks. Red arrows in (B) mark the same main1 peak frequencies shown in the corresponding panels of (A). The dashed vertical line in both panels represents the zero-shift frequency $f_o = (\gamma_n/2\pi)B_{ext}$ ~ 18.5 MHz. Error bars represent uncertainties in the NMR signal intensity.

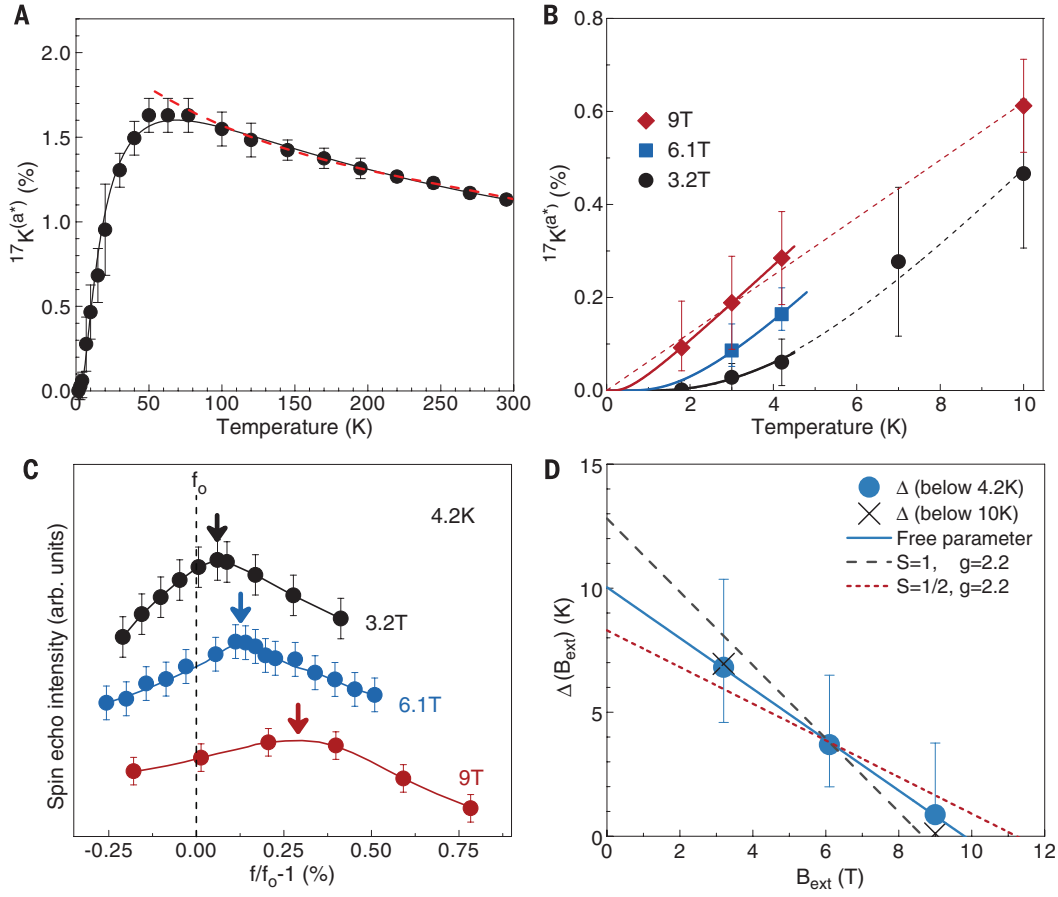

Fig. 4. Intrinsic spin susceptibility χ_{kagome} and spin excitation gap Δ. (**A**) Temperature dependence of χ_{kagome}, deduced from $^{17}K^{(a^*)}$, observed at main1 in B_{ext} = 3.2 T || a^*. The red dashed curve represents a theoretical prediction based on high-temperature series expansion (*21*) with J = 180 K, matched at 295 K; the solid curve is a guide to the eye. (**B**) Temperature and field dependences of $^{17}K^{(a^*)}$ at low temperatures, with a fit to $^{17}K^{(a^*)} \sim T \cdot \exp(-\Delta/T)$ in the temperature range up to 4.2 K (solid curves) and 10 K (dashed curves). (**C**) Main1 line shapes at 4.2 K in B_{ext} = 3.2, 6.1, and 9 T || a^*, plotted as a function of the normalized frequency $f/f_o - 1$ (= $^{17}K^{(a^*)}$). (**D**) The spin excitation gap, $\Delta(B_{ext})$, deduced from (B) for the fitting range up to 4.2 K (solid circles) and 10 K (crosses). Dashed and dotted lines are the best fits under the constraint of S = 1 and S = 1/2 , respectively, whereas the solid line represents the best free-parameter fit. Error bars represent uncertainties in the magnitude of $^{17}K^{(a^*)}$ in (A) and (B), the NMR signal intensity in (C), and the magnitude of the gap in (D).

of antiferromagnetic spin correlations that tend to suppress the spin susceptibility, even without a gap. The same pre-factor T also arises for the uniform Pauli spin susceptibility of spinon excitations in the gapped Dirac fermion model (*11*). It is important to realize that the magnetic Zeeman energy $g\mu_B SB_{ext}$ of the Cu^{2+} electron spins (g, g factor; μ_B, Bohr magneton) is comparable to Δ; hence, the magnetic field reduces the energy gap as $\Delta(B_{ext}) = \Delta(0) - g\mu_B SB_{ext}$ (*29*), where the g factor of the Cu^{2+} is ~2.2 (*30*). We expect S = 1/2 for spinons, whereas S = 1 for spin triplets or two bound spinons. As shown in Fig. 4C, the peak frequency of the NMR line shape, plotted as a function of the normalized frequency $f/f_o - 1$ (= $^{17}K^{(a^*)}$), shows a systematic dependence on B_{ext} at low temperatures, implying that Δ, and hence $^{17}K^{(a^*)}$, depend on B_{ext}. Values of $^{17}K^{(a^*)}$ observed for various B_{ext} are compared in Fig. 4B and the resulting fitted values of $\Delta(B_{ext})$ are summarized in Fig. 4D. From the linear fits in Fig. 4D, we estimate the zero-field gap as $\Delta(0) \sim 10 \pm 3$ K. Large uncertainties in the slope of the linear fits prevented us from discerning the total spin of the excited state, S = 1/2 or S = 1. Our estimation of $\Delta(0)/J$ = 0.03 to 0.07 is comparable to the theoretical prediction based on density-matrix renormalization group calculations, $\Delta(0)/J$ = 0.07 to 0.12 (*9*). Our results also imply that the Dzyaloshinskii-Moriya interaction is not strong enough to induce appreciable nonzero susceptibility at the lowest measured temperatures. Thus, NMR on the single crystal provides strong quantitative evidence for a spin gap in $ZnCu_3(OH)_6Cl_2$. In addition, the ability to distinguish the behavior among different sites far from and near to Cu^{2+} defects allows us to conclude that the gapped behavior is intrinsic to the kagome lattice.

REFERENCES AND NOTES

1. P. A. Lee, *Science* **321**, 1306–1307 (2008).
2. L. Balents, *Nature* **464**, 199–208 (2010).
3. M. P. Shores, E. A. Nytko, B. M. Bartlett, D. G. Nocera, *J. Am. Chem. Soc.* **127**, 13462–13463 (2005).
4. B. G. Levi, *Phys. Today* **60**, 16–19 (2007).
5. J. S. Helton *et al.*, *Phys. Rev. Lett.* **98**, 107204 (2007).
6. P. Mendels *et al.*, *Phys. Rev. Lett.* **98**, 077204 (2007).
7. T.-H. Han *et al.*, *Nature* **492**, 406–410 (2012).
8. T.-H. Han *et al.*, *Phys. Rev. B* **83**, 100402(R) (2011).
9. S. Yan, D. A. Huse, S. R. White, *Science* **332**, 1173–1176 (2011).
10. Y. Ran, M. Hermele, P. A. Lee, X.-G. Wen, *Phys. Rev. Lett.* **98**, 117205 (2007).
11. Y. M. Lu, Y. Ran, P. A. Lee, *Phys. Rev. B* **83**, 224413 (2011).
12. S. Sachdev, *Phys. Rev. B* **45**, 12377–12396 (1992).
13. Z. Hao, O. Tchernyshyov, *Phys. Rev. B* **87**, 214404 (2013).
14. R. R. P. Singh, D. A. Huse, *Phys. Rev. B* **77**, 144415 (2008).
15. D. E. Freedman *et al.*, *J. Am. Chem. Soc.* **132**, 16185–16190 (2010).
16. T. Asaba *et al.*, *Phys. Rev. B* **90**, 064417 (2014).
17. T.-H. Han *et al.*, (2014); http://arxiv.org/abs/1402.2693.
18. D. V. Lang, D. C. Lo, J. B. Boyce, C. P. Slichter, *Phys. Rev. B* **9**, 3077–3085 (1974).
19. J. Bobroff *et al.*, *Phys. Rev. Lett.* **86**, 4116–4119 (2001).
20. F. Tedoldi, R. Santachiara, M. Horvatic, *Phys. Rev. Lett.* **83**, 412–415 (1999).
21. M. Rigol, R. R. P. Singh, *Phys. Rev. Lett.* **98**, 207204 (2007).
22. T. Imai, E. A. Nytko, B. M. Bartlett, M. P. Shores, D. G. Nocera, *Phys. Rev. Lett.* **100**, 077203 (2008).
23. A. Olariu *et al.*, *Phys. Rev. Lett.* **100**, 087202 (2008).
24. T. Imai, M. Fu, T.-H. Han, Y. S. Lee, *Phys. Rev. B* **84**, 020411(R) (2011).
25. Materials and methods are available as supplementary materials on *Science* Online.
26. S. Depenbrock, I. P. McCulloch, U. Schollwöck, *Phys. Rev. Lett.* **109**, 067201 (2012).
27. M. A. de Vries *et al.*, *Phys. Rev. Lett.* **103**, 237201 (2009).
28. T. Imai, K. R. Thurber, K. M. Shen, A. W. Hunt, F. C. Chou, *Phys. Rev. Lett.* **81**, 220 (1998).
29. K. Matan *et al.*, *Nat. Phys.* **6**, 865 (2010).
30. T. Han, S. Chu, Y. S. Lee, *Phys. Rev. Lett.* **108**, 157202 (2012).

ACKNOWLEDGMENTS

We thank P. A. Lee and T. Sakai for helpful discussions and P. Dube, J. Britten, and V. Jarvis of the Brockhouse Institute for technical assistance. The work at McMaster University was supported by the Natural Sciences and Engineering Research Council of Canada and the Canadian Institute for Advanced Research. The work at the Massachusetts Institute of Technology was supported by the U.S. Department of Energy, Office of Science, Office of Basic Energy Sciences, under grant no. DE-FG02-07ER46134. T.-H.H. acknowledges support from a Grainger Fellowship, provided by the Department of Physics at the University of Chicago.

SUPPLEMENTARY MATERIALS

www.sciencemag.org/content/350/6261/655/suppl/DC1
Materials and Methods
Supplementary Text
Figs. S1 to S8

26 March 2015; accepted 8 September 2015
10.1126/science.aab2120

QUANTUM SIMULATION

Creation of a low-entropy quantum gas of polar molecules in an optical lattice

Steven A. Moses, Jacob P. Covey, Matthew T. Miecnikowski, Bo Yan,* Bryce Gadway,† Jun Ye,‡ Deborah S. Jin‡

Ultracold polar molecules, with their long-range electric dipolar interactions, offer a unique platform for studying correlated quantum many-body phenomena. However, realizing a highly degenerate quantum gas of molecules with a low entropy per particle is challenging. We report the synthesis of a low-entropy quantum gas of potassium-rubidium molecules (KRb) in a three-dimensional optical lattice. We simultaneously load into the optical lattice a Mott insulator of bosonic Rb atoms and a single-band insulator of fermionic K atoms. Then, using magnetoassociation and optical state transfer, we efficiently produce ground-state molecules in the lattice at those sites that contain one Rb and one K atom. The achieved filling fraction of 25% should enable future studies of transport and entanglement propagation in a many-body system with long-range dipolar interactions.

Polar molecules are an ideal candidate system for studying spin physics and emulating quantum magnetism (*1*–*3*). However, low temperatures and long lifetimes are required. Ultracold fermionic KRb molecules have been created at a temperature T close to the Fermi temperature T_F (*4*), but cooling a trapped molecular gas deeply into quantum degeneracy has yet to be demonstrated (*5*–*7*). For KRb, the biggest problem is that two molecules can chemically react, which limits the lifetime of the trapped gas (*8*). Furthermore, the chemical reaction rate increases in an applied electric field because of the attractive part of the dipole-dipole interactions (*8*). A solution to this problem is to confine the molecules in a deep optical lattice in order to restrict collisions (*9*–*11*). In particular, the lifetime of ground-state molecules in a deep three-dimensional (3D) lattice was demonstrated to be longer than 20 s and limited by off-resonant scattering of the lattice light (*11*). With the chemical reactions mitigated, the remaining challenge is to create a low-entropy system, which in the lattice corresponds to increasing the filling fraction. Here, we report the realization of a high-filling, low-entropy quantum gas of ground-state molecules in a deep 3D lattice using a quantum synthesis approach.

Simulating quantum many-body physics with lattice-confined atoms requires a filling near unity and correspondingly low entropy (*12*). This condition can be substantially relaxed with polar molecules thanks to their long-range dipolar interactions, which allow for a decoupling of spin and motion so that only the spin entropy, which can be prepared to be near zero, is relevant (*3*). This was recently demonstrated in (*13*, *14*), where a spin-½ system was realized by encoding spin in the rotational degree of freedom of the KRb molecules. At dilute lattice fillings, spin exchange via dipolar interactions was observed in the density-dependent decay of, and oscillations in, the spin coherence. To go beyond this observation and explore problems such as the spin-½ Hamiltonian for quantum magnetism (*15*–*21*), the propagation of excitations and the growth of entanglement and correlations (*22*, *23*), many-body localization (*24*), exotic quantum phases (*25*–*29*), and spin-orbit coupling with molecules (*30*), higher lattice fillings will be essential. Determining what constitutes high lattice filling depends on the specific experiment in question; one benchmark is the percolation threshold, which for an infinite simple cubic lattice with nearest-neighbor interactions corresponds to a filling of ~0.3 (*31*). Because of the molecules' long-range interactions and the finite system size, a filling near this percolation threshold is sufficient for exploring dynamics such as the propagation of excitations.

Our strategy for realizing higher lattice fillings for polar molecules is to take advantage of the precise experimental control available for manipulating the initial atomic quantum gas mixture in a 3D lattice (*32*, *33*). Specifically, one needs to prepare a low-entropy state of two atomic species in the lattice and combine this with efficient molecule production. We use magnetoassociation to first create very weakly bound Feshbach molecules followed by optical transfer to the molecular ro-vibrational ground state. Previously, we showed that the conversion efficiency from atoms to Feshbach molecules is high (87 ± 13%) for lattice sites containing exactly one Rb atom and one K atom (*11*). In addition, previous measurements of inelastic collisional loss rates for Feshbach molecules with K or Rb atoms (*8*, *34*) suggest that having an extra atom on a lattice site will be detrimental to molecule production at that site.

The basic scheme is illustrated in Fig. 1. By loading a nearly pure Bose-Einstein condensate (BEC) of Rb atoms into a 3D optical lattice, we achieve a Mott insulator (MI) state, where repulsive interactions between the Rb atoms drive a transition to a state that has an integer number of particles per site (*35*). The lattice depth is subsequently increased to pin the Rb atoms. The initial BEC density should be low enough to avoid having multiply occupied sites. For spin-polarized fermionic K atoms, Pauli blocking will prevent any site from having more than one K atom if the atoms are all prepared in the lowest band. The optimum case is a K band insulator (*36*, *37*) of one atom per site, which requires starting with a relatively large initial K density. Creating both insulators simultaneously is very challenging. The densities of both species should be ~$(\lambda/2)^{-3}$

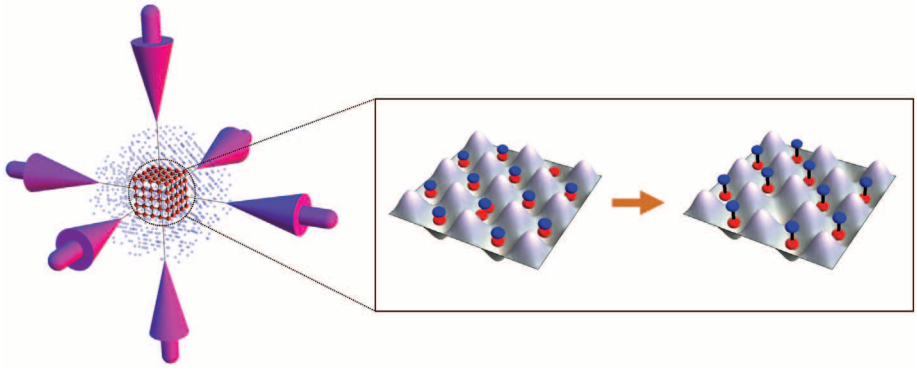

Fig. 1. Quantum synthesis for creating polar molecules. Left: We load K (blue) and Rb (red) atoms into a 3D optical lattice, with many more K atoms than Rb atoms. In the center of the lattice where the two atom clouds overlap, we realize a Rb Mott insulator and a K single-band insulator, each with near-unity filling. Right: Sites with one Rb and one K have a high probability of producing molecules, whereas sites with multiple Rb or with only a single atomic species do not yield molecules.

JILA, National Institute of Standards and Technology and University of Colorado, and Department of Physics, University of Colorado, Boulder, CO 80309, USA. *Present address: Department of Physics, Zhejiang University, Hangzhou 310027, China. †Present address: Department of Physics, University of Illinois at Urbana-Champaign, Urbana, IL 61801, USA. ‡Corresponding author. E-mail: ye@jila.colorado.edu (J.Y.); jin@jilau1.colorado.edu (D.S.J.)

Downloaded from www.sciencemag.org on November 5, 2015

prior to loading the lattice, where $\lambda/2$ is the lattice spacing. When loading both species into a common optical lattice, we thus need to work with a Rb BEC with small atom number and a degenerate Fermi gas with large atom number. The Rb MI must be well spatially overlapped with the center of the much larger K distribution. We also need to preserve the high filling of each atomic species in the presence of the other. Finally, any excess atoms should be removed quickly from the lattice after the molecule production.

To prepare the atomic quantum gases, we evaporate Rb in the $|1,1\rangle$ state and sympathetically cool K in the $|^9/_2, -^9/_2\rangle$ state in a crossed-beam optical dipole trap with a wavelength $\lambda = 1064$ nm. Here, the atomic hyperfine states are denoted by $|F, m_F\rangle$, where F is the total atomic spin and m_F is its projection. The evaporation is performed at a magnetic field B of 540 G, where the interspecies scattering length a_{KRb} is $-100a_0$, with a_0 the Bohr radius. This field provides for modest interspecies interactions while being close to an interspecies Feshbach resonance (*38*) at $B_0 = 546.6$ G that is used for tuning interactions as well as for molecule creation. The final optical trap is cylindrically symmetric with a typical axial trap frequency of $\omega_z = 2\pi \times 180$ Hz (along gravity) and a radial trap frequency of $\omega_r = 2\pi \times 25$ Hz for Rb. The measured trap frequencies for K are $2\pi \times 260$ Hz and $2\pi \times 30$ Hz. The larger vertical trap frequency helps prevent separation of the Rb and K clouds due to gravitational sag. Immediately after the evaporation, we turn off the interspecies interactions by ramping B to 543.6 G where $a_{KRb} = 0$. At this point, we have a Fermi gas of 1×10^5 to 2×10^5 K atoms and a nearly pure Rb BEC with 10^3 to 10^4 atoms. Once Rb condenses, it no longer thermalizes efficiently with K, and as a result the temperature of the K gas does not reach below $T/T_F \approx 0.3$. We then smoothly turn on, in 150 ms, three retro-reflected beams with $\lambda = 1064$ nm that form a cubic optical lattice. Two of the lattice beams are in the horizontal plane; the third beam is at an angle of 6° from vertical. The final lattice depth is between 20 and 25 E_R^{Rb}, where $E_R^{Rb} = \hbar^2k^2/2m$ is the recoil energy for Rb, $k = 2\pi/\lambda$, $\hbar$ is the Planck constant divided by 2π, and m is the mass of the Rb atom.

We image the atom clouds, either in situ in the lattice or after a time-of-flight (TOF) expansion, using resonant absorption imaging with a probe beam that propagates along the vertical direction. As the lattice depth is increased beyond the superfluid-MI transition of the Rb gas, coherent matter wave interference disappears (Fig. 2A). Figure 2B shows a TOF image of 1.8×10^5 K atoms, where the lattice was turned off more slowly for band mapping (*39*). A trace through this image along the direction of one of the horizontal lattice beams, which is rotated by roughly 45° with

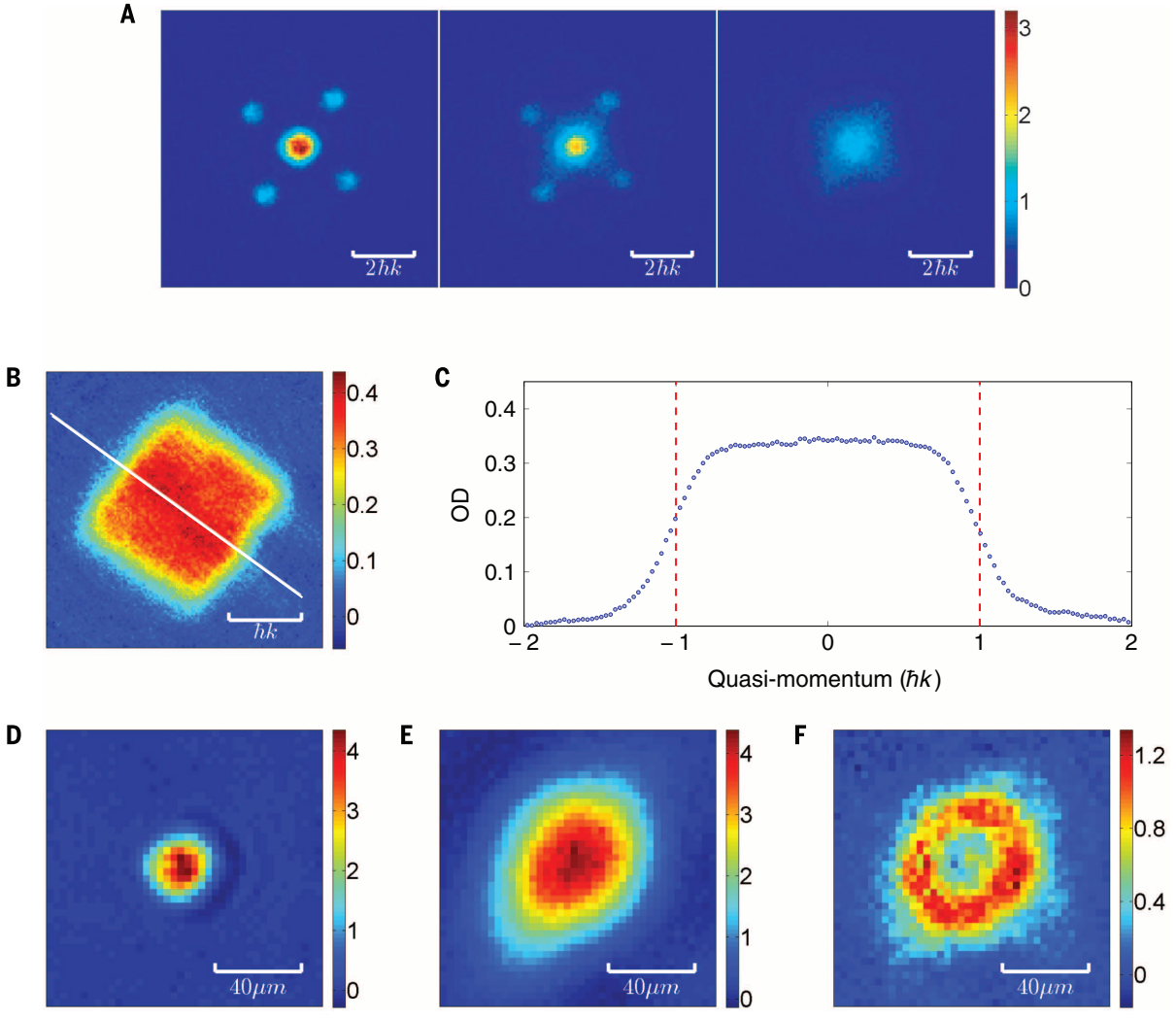

Fig. 2. Imaging of Rb and K clouds. (**A**) The superfluid–Mott insulator transition for Rb, with ~8×10^4 atoms. The images were taken with TOF = 8 ms; the final lattice depth is 12, 17, or 22 E_R^{Rb} from left to right. The optical depth (OD) for each image is indicated by the color bar to the right of the image; scale bar units refer to momentum. (**B**) Band mapping of K, imaged after 11.5 ms of expansion. The white line shows the direction of the cut shown in (C). (**C**) Cut through the K band-mapping image, showing OD versus quasi-momentum. (**D**) In situ image of 2×10^4 Rb atoms. (**E**) In situ image of 1.8×10^5 K atoms. (**F**) In situ image of the K cloud after initiating loss due to K-Rb inelastic collisions. The resulting hole in the K cloud demonstrates good initial spatial overlap with the Rb cloud in all three directions.

respect to the camera axes (and averaged along the other direction), shows that most of the atoms are in the lowest band (Fig. 2C). In situ images of Rb (Fig. 2D) and K (Fig. 2E) reveal that the Rb cloud is much smaller than the K cloud. To verify that the clouds are spatially overlapped, we used a radio-frequency (RF) pulse to transfer the Rb atoms to the $|2,2\rangle$ state in order to induce spin-changing collisions that result in loss of K and Rb atoms on the same lattice site. The resultant hole in the K distribution (Fig. 2F) clearly demonstrates that the clouds are overlapped in the trap.

We determine the peak filling fraction from fits to the measured atomic distributions. We fit the K Fermi gas with a Gaussian. In this case, the peak filling is

$$f_K = \frac{N(\lambda/2)^3}{(2\pi)^{3/2}\sigma_x\sigma_y\sigma_z} \quad (1)$$

where N is the number of atoms and σ_x, σ_y, and σ_z are the Gaussian root mean square widths. The Rb MI is better described by a Thomas-Fermi (TF) distribution (*40*), and the peak filling is

$$f_{Rb} = \frac{15N(\lambda/2)^3}{8\pi R_x R_y R_z} \quad (2)$$

where R_x, R_y, and R_z are the TF radii. We image the gas along z, so we determine the radial size. The vertical size is smaller by a factor of $A = 6.4 \pm 0.1$, which is measured for a thermal gas of Rb in the combined potential of the optical trap and lattice.

Figure 3A shows f_{Rb} versus Rb number. For a comparison to the data, we calculate the $T = 0$ MI distribution for our trap, convolve this distribution with a Gaussian filter to account for the finite imaging resolution, bin the data into pixels, and then fit with a TF distribution (*41*). For very small samples, the size of the cloud is about twice the imaging resolution. The data correspond well to the $T = 0$ calculation, and from this comparison, we infer that the $N = 1$ Rb MI occurs for fewer than 5000 atoms in our trap.

Figure 3B shows f_K versus K number in a 23 E_R^{Rb} lattice. Given the different mass and ac polarizability for K, this is equivalent to only 9 E_R^K, where E_R^K is the recoil energy for K atoms. We find that f_K rises with increasing K atom number (blue points) and saturates around 80% for K numbers ≥1 × 10^5. For these data, T/T_F decreases with increasing K number (red points). The saturation of f_K is consistent with the onset of a band insulator in the center of the lattice.

The data in Fig. 3, A and B, show that to achieve optimal molecule production, the initial BEC should have fewer than 5000 atoms for a MI with mostly one atom per site, whereas the Fermi gas should have more than 10^5 atoms to reach the band insulating limit. When loading both atom species at very low temperatures, one might expect attractive interactions to enhance the overlap between the two species (*33*, *42*). For the temperatures achieved in our experiment, the hotter K gas affects the filling of Rb, and we find empirically that turning off interactions by going to $a_{KRb} = 0$ is optimum (*41*). To illustrate this effect, fig. S1 shows how f_{Rb} and the initial BEC fraction depend on a_{KRb}.

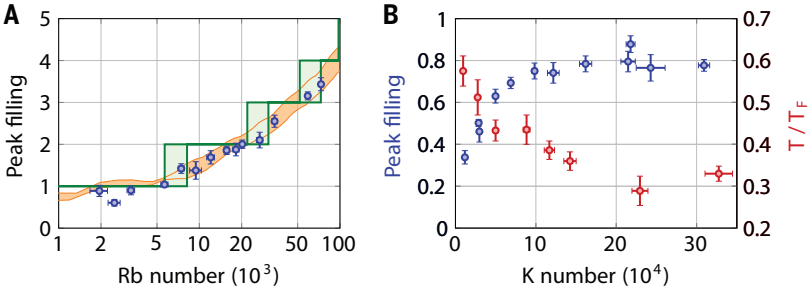

Fig. 3. Peak filling for Rb and K clouds. (**A**) f_{Rb} (blue points) versus Rb number. The cloud size was extracted from a TF fit to the in situ image; the Rb number was extracted from the in situ image or from a Gaussian fit to the cloud after a few milliseconds of free expansion. The filling was computed according to Eq. 2. The green staircase displays the calculated peak occupancy for a $T = 0$ distribution (*41*). The total harmonic confinement (including the lattice light) is represented by $\omega_r = 2\pi \times (38 \pm 2)$ Hz and $\omega_z = (6.4 \pm 0.1)\omega_r$. The orange band shows a fit to the calculated density distribution, accounting for finite imaging resolution and pixelation present in the experiment. (**B**) Peak filling f_K versus K number for a lattice depth of 9 E_R^K (blue points), indicating the onset of a K band insulator for $N_K > 10^5$. The red points show the measured T/T_F of the initial K gas before loading the lattice.

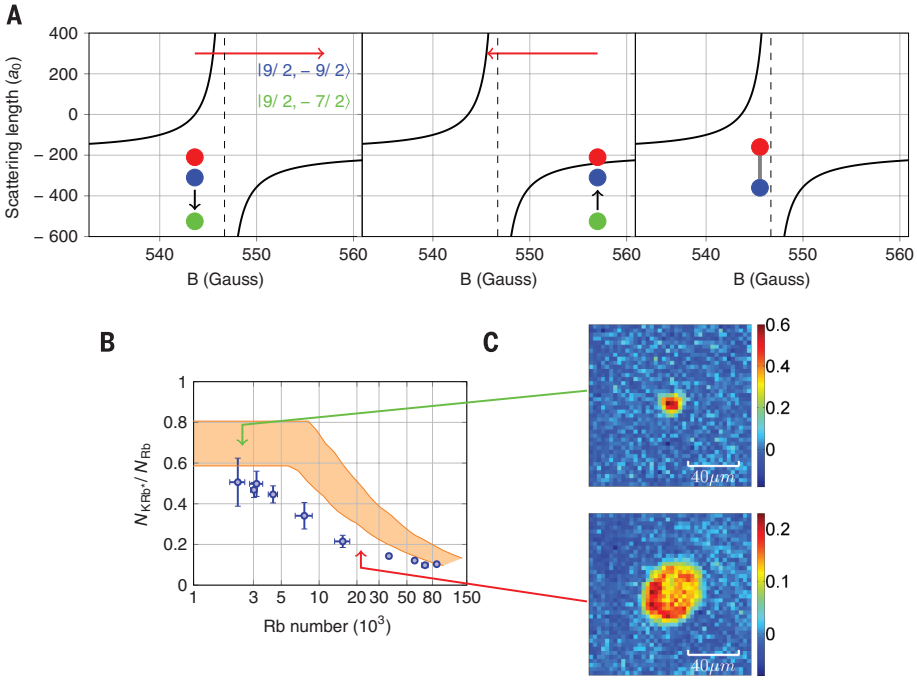

Fig. 4. Molecule formation. (**A**) The interspecies Feshbach resonance. The atoms are loaded into the lattice at $a_{KRb} = 0$. The K atoms are then transferred to a hyperfine state ($|9/2, -7/2\rangle$) that does not participate in the resonance, and B is swept above the resonance. After transferring K back to the $|9/2, -9/2\rangle$ state, magnetoassociation proceeds by sweeping B from above to below the resonance (center and right panels). The Feshbach molecules are then transferred to the absolute ground state via STIRAP. (**B**) Fraction of Rb atoms converted to Feshbach molecules. The orange-shaded region shows the expected fraction of Rb atoms that are on a site with exactly one Rb atom and one K atom. (**C**) In situ images of ground-state KRb molecules after a 40-ms hold in the lattice. For low initial Rb number (top image, average of three repeated experiments), we find a filling fraction of 25 ± 4%. For higher Rb number (bottom image, average of seven shots), we observe a hole in the center of the molecular distribution, and the filling is much lower.

The first step in creating ground-state molecules is magnetoassociation, which consists of adiabatically sweeping B across the K-Rb Feshbach resonance from high to low field (Fig. 4A). However, starting from $a_{KRb} = 0$, which occurs for $B < B_0$, we first need to jump B to the high-field side of the resonance. This jump should be diabatic in order to avoid promoting atoms to higher lattice bands (*39*); however, the high local atom densities in the lattice make it difficult to sweep the field fast enough. To overcome this problem, we use an RF pulse to transfer the K atoms to a spin state, $|^9/_2, -^7/_2\rangle$, that does not experience the 546.6 G resonance. After ramping B above B_0, we transfer the K atoms back to the $|^9/_2, -^9/_2\rangle$ state and then proceed with magnetoassociation. We find that applying these RF transitions improves the final filling of ground-state molecules by 60% relative to the case of not doing these RF transitions.

Figure 4B shows the measured fraction of the Rb number, N_{Rb}, that is converted to Feshbach molecules (blue points). Because we operate with many more K atoms than Rb atoms, a large background of K atoms remains after making molecules. To determine the number of Feshbach molecules N_{KRb^*}, we use RF to transfer the background K atoms to another spin state before dissociating the molecules and imaging the resulting K (*41*). For comparison with the data, the shaded band in Fig. 4B shows the product of the measured $f_K = 0.80 \pm 0.05$, the calculated fraction of Rb atoms of a $T = 0$ MI that are on singly occupied sites, and the conversion efficiency of preformed pairs reported in (*11*). We find that the trend of the calculation matches the data, with the conversion efficiency decreasing for higher Rb number. This is consistent with the expectation that molecules are not produced on sites that have more than one Rb atom. The data lie slightly below the calculation; possible explanations for this include finite temperature effects on the MI, leading to fewer singly occupied sites, or reduced conversion efficiency for sites with one Rb and one K atom. For small Rb numbers, we find that N_{KRb^*}/N_{Rb} exceeds 50%.

As a last step, we use stimulated Raman adiabatic passage (STIRAP) to transfer the Feshbach molecules to their ro-vibrational ground state (*4*). The typical efficiency of this transfer is 89 ± 4%. After STIRAP, we apply resonant light pulses to remove all unpaired atoms from the lattice; without this step, the molecule lifetime in the lattice is only a few milliseconds, which we attribute to K tunneling followed by molecule-atom chemical reactions (*8*). After holding the ground-state molecules in the lattice for 40 ms, we take in situ images of the molecule distribution by reversing the STIRAP process, dissociating the Feshbach molecules, and then imaging the K atoms. Figure 4C shows images of the ground-state molecules in the lattice for cases of high (top) and low conversion (bottom), corresponding to starting with roughly 2500 and 25,000 Rb atoms, respectively. The bottom image exhibits a central hole in the molecule distribution, which is consistent with the central lattice sites containing multiple Rb atoms and therefore not producing molecules.

For the higher-conversion case, we perform a TF fit to the ground-state molecular distribution. From the fit we find 7.9 (±0.5) × 10^2 molecules with a TF radius of 12.0 (±0.2) μm. This gives $f_{mol} = 0.27 \pm 0.02$. As an alternative approach, we can determine the filling by comparing the width of the molecular cloud to that of our simulated $T = 0$ Rb distribution and assuming a uniform conversion efficiency of Rb into molecules. The molecules are best described by a distribution that corresponds to an initial Rb number of 3.2 (±0.4) × 10^3. Taking the ratio of the measured number of molecules to this Rb number, we find $f_{mol} = 0.25 \pm 0.04$, which is consistent with the other method. From the product of the previous measurements, namely f_{Rb}, N_{KRb^*}/N_{Rb}, and the STIRAP efficiency, one might expect $f_{mol} \approx 0.35$. We attribute the lower measured filling to molecular loss caused by the atom removals.

Given the ac polarizability (*43*) and mass of the ground-state molecules, a 25 E_R^{Rb} lattice corresponds to 62 E_R^{KRb}, where E_R^{KRb} is the recoil energy for a KRb molecule. The tunneling rate for molecules is therefore negligible, and the lifetime is long and limited by single-photon scattering (*11*). In this case, the entropy per molecule can be estimated from the filling in the lattice, with some assumption about the shape of the distribution. Our approach likely leads to a molecular distribution that is much more homogeneous than the alternative approach of adiabatically loading a Fermi gas of molecules into the lattice. The K Fermi gas is homogeneous within the confines of the Rb MI, and the entropy per particle in this region is roughly that of a lattice system with a uniform filling of 80%, which is about 0.6 k_B. For an average filling of f in a uniform lattice, the entropy per particle is $(-k_B/f)[f \ln(f) + (1-f)\ln(1-f)]$ (*44*). Similarly, for $f_{mol} = 25\%$, the entropy per molecule is 2.2 k_B. For comparison, the lowest entropy we have achieved in a harmonic trap is about 6 k_B per molecule, corresponding to $T/T_F \approx 1$.

The system realized here is appropriately sized for imaging with quantum gas microscopy (*45*–*47*), where dynamics associated with percolation can be investigated. More generally, this work elucidates the many challenges in, and extends the experimental toolbox for, synthesizing ultracold molecule systems that can realize novel quantum many-body behavior.

REFERENCES AND NOTES

1. A. Micheli, G. K. Brennen, P. Zoller, *Nat. Phys.* **2**, 341–347 (2006).
2. R. Barnett, D. Petrov, M. Lukin, E. Demler, *Phys. Rev. Lett.* **96**, 190401 (2006).
3. K. R. A. Hazzard, S. R. Manmana, M. Foss-Feig, A. M. Rey, *Phys. Rev. Lett.* **110**, 075301 (2013).
4. K.-K. Ni *et al.*, *Science* **322**, 231–235 (2008).
5. T. Takekoshi *et al.*, *Phys. Rev. Lett.* **113**, 205301 (2014).
6. P. K. Molony *et al.*, *Phys. Rev. Lett.* **113**, 255301 (2014).
7. J. W. Park, S. A. Will, M. W. Zwierlein, *Phys. Rev. Lett.* **114**, 205302 (2015).
8. S. Ospelkaus *et al.*, *Science* **327**, 853–857 (2010).
9. H. P. Büchler *et al.*, *Phys. Rev. Lett.* **98**, 060404 (2007).
10. M. H. G. de Miranda *et al.*, *Nat. Phys.* **7**, 502–507 (2011).
11. A. Chotia *et al.*, *Phys. Rev. Lett.* **108**, 080405 (2012).
12. I. Bloch, J. Dalibard, S. Nascimbene, *Nat. Phys.* **8**, 267–276 (2012).
13. B. Yan *et al.*, *Nature* **501**, 521–525 (2013).
14. K. R. A. Hazzard *et al.*, *Phys. Rev. Lett.* **113**, 195302 (2014).
15. A. V. Gorshkov *et al.*, *Phys. Rev. Lett.* **107**, 115301 (2011).
16. A. de Paz *et al.*, *Phys. Rev. Lett.* **111**, 185305 (2013).
17. T. Fukuhara *et al.*, *Nat. Phys.* **9**, 235–241 (2013).
18. P. Richerme *et al.*, *Nature* **511**, 198–201 (2014).
19. P. Jurcevic *et al.*, *Nature* **511**, 202–205 (2014).
20. J. Cai, A. Retzker, F. Jelezko, M. B. Plenio, *Nat. Phys.* **9**, 168–173 (2013).
21. S. Ravets *et al.*, *Nat. Phys.* **10**, 914–917 (2014).
22. K. R. A. Hazzard *et al.*, *Phys. Rev. A* **90**, 063622 (2014).
23. J. Schachenmayer, B. P. Lanyon, C. F. Roos, A. J. Daley, *Phys. Rev. X* **3**, 031015 (2013).
24. N. Y. Yao *et al.*, *Phys. Rev. Lett.* **113**, 243002 (2014).
25. K. A. Kuns, A. M. Rey, A. V. Gorshkov, *Phys. Rev. A* **84**, 063639 (2011).
26. M. Knap, E. Berg, M. Ganahl, E. Demler, *Phys. Rev. B* **86**, 064501 (2012).
27. S. R. Manmana, E. M. Stoudenmire, K. R. A. Hazzard, A. M. Rey, A. V. Gorshkov, *Phys. Rev. B* **87**, 081106 (2013).
28. L. He, W. Hofstetter, *Phys. Rev. A* **83**, 053629 (2011).
29. N. Y. Yao *et al.*, *Phys. Rev. Lett.* **110**, 185302 (2013).
30. S. V. Syzranov, M. L. Wall, V. Gurarie, A. M. Rey, *Nat. Commun.* **5**, 5391 (2014).
31. D. Stauffer, A. Aharon, *Introduction to Percolation Theory* (Taylor and Francis, London, revised ed. 2, 1994).
32. B. Damski *et al.*, *Phys. Rev. Lett.* **90**, 110401 (2003).
33. J. K. Freericks *et al.*, *Phys. Rev. A* **81**, 011605 (2010).
34. J. J. Zirbel *et al.*, *Phys. Rev. Lett.* **100**, 143201 (2008).
35. I. Bloch, J. Dalibard, W. Zwerger, *Rev. Mod. Phys.* **80**, 885–964 (2008).
36. U. Schneider *et al.*, *Science* **322**, 1520–1525 (2008).
37. R. Jördens, N. Strohmaier, K. Günter, H. Moritz, T. Esslinger, *Nature* **455**, 204–207 (2008).
38. C. Klempt *et al.*, *Phys. Rev. A* **78**, 061602 (2008).
39. M. Köhl, H. Moritz, T. Stöferle, K. Günter, T. Esslinger, *Phys. Rev. Lett.* **94**, 080403 (2005).
40. B. DeMarco, C. Lannert, S. Vishveshwara, T.-C. Wei, *Phys. Rev. A* **71**, 063601 (2005).
41. See supplementary materials on *Science* Online.
42. S. Sugawa *et al.*, *Nat. Phys.* **7**, 642–648 (2011).
43. B. Neyenhuis *et al.*, *Phys. Rev. Lett.* **109**, 230403 (2012).
44. D. Budker, D. Kimball, D. Demille, *Atomic Physics: An Exploration Through Problems and Solutions* (Oxford Univ. Press, Oxford, ed. 2, 2008).
45. W. S. Bakr, J. I. Gillen, A. Peng, S. Fölling, M. Greiner, *Nature* **462**, 74–77 (2009).
46. J. F. Sherson *et al.*, *Nature* **467**, 68–72 (2010).
47. N. Gemelke, X. Zhang, C.-L. Hung, C. Chin, *Nature* **460**, 995–998 (2009).

ACKNOWLEDGMENTS

We thank Z. Fu for experimental assistance and M. Wall, A. Safavi, K. Hazzard, and A. M. Rey for many useful discussions. Supported by a National Defense Science and Engineering graduate fellowship (J.P.C.), the National Institute of Standards and Technology, the Air Force Office of Scientific Research Multidisciplinary University Research Initiative (MURI), the Army Research Office MURI, and NSF grant 1125844.

SUPPLEMENTARY MATERIALS

www.sciencemag.org/content/350/6261/659/suppl/DC1
Materials and Methods
Fig. S1

24 May 2015; accepted 30 September 2015
10.1126/science.aac6400

MICROBIOME

The ecology of the microbiome: Networks, competition, and stability

Katharine Z. Coyte,[1,2]* Jonas Schluter,[1,2,3]*† Kevin R. Foster[1,2]†

The human gut harbors a large and complex community of beneficial microbes that remain stable over long periods. This stability is considered critical for good health but is poorly understood. Here we develop a body of ecological theory to help us understand microbiome stability. Although cooperating networks of microbes can be efficient, we find that they are often unstable. Counterintuitively, this finding indicates that hosts can benefit from microbial competition when this competition dampens cooperative networks and increases stability. More generally, stability is promoted by limiting positive feedbacks and weakening ecological interactions. We have analyzed host mechanisms for maintaining stability—including immune suppression, spatial structuring, and feeding of community members—and support our key predictions with recent data.

The human microbiome contains hundreds of species and trillions of cells that reside predominantly in the gastrointestinal tract (*1*, *2*). These microbes provide many health benefits, including the breakdown of complex molecules in food, protection from pathogens, and healthy immune development (*3*–*6*). The gut microbiome is often noted for its ecological stability. Different people may carry different microbial species, but any one individual tends to carry the same key set of species for long periods (*6*–*8*). This stability is considered critical for host health and well-being, because it ensures that beneficial symbionts and their associated functions are maintained over time (*9*–*12*). Correspondingly, major shifts in microbial community composition are often associated with ill health (*4*, *13*).

Research into gut communities has been characterized by a large volume of empirical work. Nevertheless, we are far from a clear understanding of microbiome communities and, in particular, what promotes or disrupts their stability. There is a pressing need for complementary theory to identify overarching principles and patterns for the microbiome. Some progress has been made through the use of individual-based models (*14*) and other analyses of two-species communities (*15*). However, the microbiome contains many diverse species interacting with one another (*16*), which makes the full system complex and challenging to understand. The field of theoretical ecology has a long history of using network models that are specifically intended to deal with large and complex communities (*17*, *18*). Here we develop ecological network theory to identify the general principles underlying microbiome stability. We then use these principles to identify and analyze candidate mechanisms that a host can use to promote stability in its microbiome. Finally, we show that our key predictions are supported by recent data from the mammalian microbiome.

Seminal work by May suggests that species diversity can be problematic for community stability (*17*, *19*). However, May's work focused on networks where the types of interactions between species are randomly distributed, meaning that +/+ (cooperation) and –/– (competition) interactions occur with half the probability of +/– (exploitation) interactions. Also, whereas ecological competition is thought to be prevalent in natural microbial communities (*20*), it is commonly assumed that the functioning of microbiome communities rests upon species that engage in cooperative metabolism (+/+) and provide health benefits for the host (*3*, *21*–*24*). There is a clear rationale for this assumption. Competition between microbes—captured by the number and magnitude of mutually negative interactions in our models—is associated with both antibiotic warfare (*25*, *26*) and a reduction in the cooperative secretions that promote community productivity (*27*). Both have the potential to severely reduce the efficiency of any cooperative metabolism that benefits the host (*3*, *21*–*24*, *28*). However, although intuitive, this argument neglects the potential effects of cooperation or competition on the ecological stability of microbiome communities.

To understand ecological stability in the microbiome, therefore, we must consider the specific effects of cooperation and how cooperation interacts with other community characteristics, such as microbiome diversity, to influence community dynamics. To do this, we have developed a dedicated body of theory based on Wigner's semicircle law and subsequent analyses (*18*, *29*, *30*). First, we derive a general analytic stability criterion that captures all potential community types, covering the full range of possible interactions and species diversities [Fig. 1 and supplementary method 1 (*31*)]. We develop our theory for unstructured ecological networks because, unlike in plant-pollinator communities or food webs (*32*, *33*), there is no evidence of strong structuring within microbial communities (*16*). However, although no single structure type dominates in these communities, our mathematics

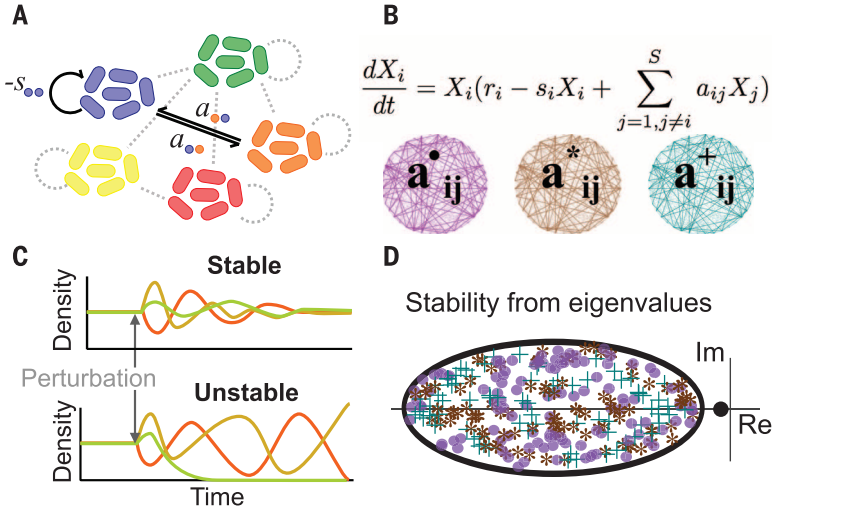

Fig. 1. Ecological theory and microbiota stability. (**A**) Ecological network theory captures networks of microbial species that interact with themselves (–*s*) and other genotypes (a_{ij}). (**B**) Coupled ordinary differential equations capture all possible combinations of connectivity, interaction types (e.g., cooperation, competition, exploitation), and species numbers (*S*) covering any biologically feasible equilibrium microbiota. X_i, density of species *i*; r_i, growth rate of species *i*; *t*, time. Three sample networks are shown. (**C**) Communities that return to their previous densities after perturbation are classified as stable, those that return to their equilibrium faster are categorized as more stable, and those that continue to diverge from the equilibrium are considered unstable (*17*, *18*). (**D**) Linear stability analysis uses the eigenvalues' real (Re) and imaginary (Im) parts, shown plotted here. The largest real part of the eigenvalues underlying a community determines whether, and how fast, the community will return after perturbation. If this quantity is negative, the community is stable; more negative values indicate that the community returns to stability more quickly. The imaginary parts of the eigenvalues predict the extent of oscillations in species densities during a return to equilibrium: Larger imaginary components predict more frequent oscillations. Eigenvalues are shown for the three sample communities from (B) (purple, brown, green), and our analytic bound for their localization (black ellipse). Our analysis also derives one special eigenvalue location that, for some parameters, will lie outside of the ellipse (black dot).

[1]Department of Zoology, University of Oxford, Oxford, UK. [2]Oxford Centre for Integrative Systems Biology, University of Oxford, Oxford, UK. [3]The Graduate University for Advanced Studies, Hayama, Kanagawa 240-0193, Japan.
*These authors contributed equally to this work. †Corresponding author. E-mail: jonas.schluter+sokendai@gmail.com (J.S.); kevin.foster@zoo.ox.ac.uk (K.R.F.)

Downloaded from www.sciencemag.org on November 5, 2015

concurrently analyzes all network arrangements and therefore naturally capture biologically critical network motifs, including chains of cross-feeding metabolic exchanges between species (*34*). Furthermore, unstructured networks are amenable to comprehensive mathematical analysis, which means we can simultaneously analyze the ecological stability of all possible network permutations as a function of our focal parameters. Specifically, we can account for any variation in the proportion of cooperation (+/+), competition (–/–), exploitation (+/–), commensalism (+/0), and amensalism (–/0) in networks with any combination of connectivity, C, and species number, S [method 1 (*31*)]. Stability is assessed from the network's eigenvalues, which give three measures of stability: (i) the probability that the community will return to its previous state after a small perturbation, (ii) the population dynamics during this return, and (iii) how long the return will take, which is a form of resilience (*35*) (Fig. 1).

We first show that May's (*17*) destabilizing effect of species diversity still holds in communities with any mixture of interaction types. From purely cooperative networks to mixed-interaction networks to purely competitive networks (fig. S1), our model predicts that high species diversity leads to unstable microbiome communities. How though does altering the level of cooperation between species affect microbiome stability? We find that gradually increasing only the proportion of cooperative interactions within communities nearly always decreases the overall return rate and the likelihood of stability [Fig. 2 and method 1b (*31*)]. We confirm our analytic results with numerical analyses [Fig. 2B, figs. S3 to S6, and method 1f (*31*)]. These results contrast with a recent analysis of macroscopic communities, which predicts that ecological stability can be maximized for an intermediate frequency of cooperative interactions (*32*). In the supplementary materials, we show that our analytical model recapitulates these numerical simulations and that the predictions rest on assumptions that suit macroscopic communities but not the microbiome [method 1g (*31*) and figs. S4 to S9] (*32*, *36*).

This method, known as local stability analysis, has the benefits of being both extremely general and able to analyze communities with large numbers of species. However, this approach is only able to analyze whether viable communities are stable when they are close to their equilibrium (*37*); it provides no information on how communities behave away from this equilibrium. We therefore also develop a second new analysis, based on a different method known as permanence analysis (*38*) [method 2 (*31*)]. Permanence analysis is considered one of the most rigorous methods of community analysis, but the numerical analysis of permanence was, until now, limited solely to purely competitive or exploitative communities. Therefore, we expand traditional permanence methods here to study the effects of cooperation. Although this method is very different from local stability analysis, we find the same prediction that cooperation is destabilizing. However, as discussed in the supplementary materials, positive feedbacks arising from cooperative interactions can still constrain this analysis such that it may underestimate the number of permanent communities. Consequently, we also develop a third method—an individual-based model—to evaluate the relationship between cooperation and ecological stability in a microbial community [method 3 (*31*)]. Although it is less general than the other methods, our individual-based model is more explicit. It allows us to follow the dynamics of each species over time and to examine additional factors, including explicit spatial structure that puts an upper limit on the community size. This third method again confirms our finding that cooperation is destabilizing for the community (Fig. 2E).

The reason for the destabilizing effect of cooperation in our models is that cooperation causes coupling between species and positive feedbacks. This means that if, for example, one species decreases in abundance, it will tend to pull others down with it and destabilize the system. It has been hypothesized that cooperative and productive microbial communities are the reason for the marked stability of the microbiome (*23*). However, even though cooperation means that one species is helping another to survive and replicate, and thus might facilitate colonization, this does not equate to stability, because cooperation can create dependency and the potential for mutual downfall. Under these circumstances, therefore, our analyses suggest that the host faces a trade-off: Though increased cooperation within communities is expected to promote overall metabolic efficiency (*3*, *24*, *25*, *27*), it comes at the cost of decreasing ecological stability.

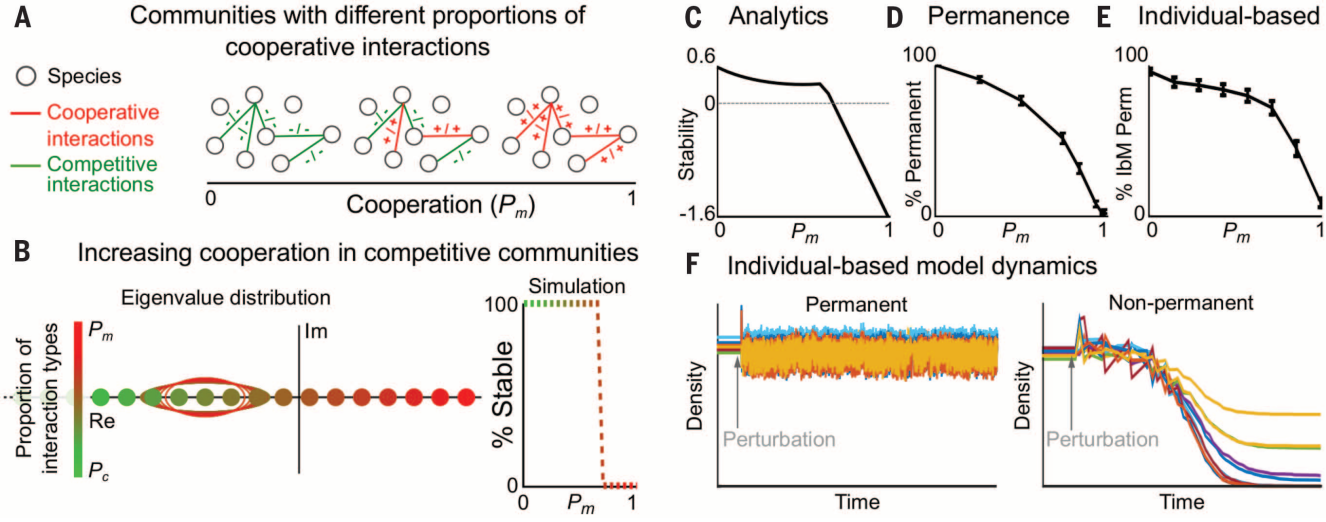

Fig. 2. Cooperation reduces community stability. (**A**) Illustration of changing the proportion of cooperative links in networks. P_m, proportion of cooperative interactions. (**B**) Linear stability analysis (also see fig. S2). The plot at left shows solutions for eigenvalue locations as a function of increasing cooperation (shown as increasing redness). The largest value of the real components (x axis) determines whether, and how fast, a return to equilibrium occurs (stability), whereas the imaginary components (y axis) determine the frequency of oscillations in population densities after perturbations (see Fig. 1). The solutions give the position of all eigenvalues in the form of an ellipse, with the exception of a single eigenvalue that corresponds to the average row sum of the interaction matrix (represented by a dot that may lie outside of the ellipse). Increasing cooperation increases the largest eigenvalues; therefore, stability decreases. Solutions hold for any permutation of a community network with a given parameter set [here S = 100, C = 0.7, $-s$ = –1, standard deviation σ = 0.05; see method 1b (*31*) for parameter sweeps showing that cooperation is nearly always destabilizing]. P_c, proportion of competitive interactions. Simulation results are plotted at right. This graph shows the proportion of communities that are stable and confirms our analytic results. (**C** to **E**) The effect of cooperation on community stability, shown with linear stability analysis [(C), also shown in (B)], permanence analysis (D), and individual-based modeling (E). The latter two methods are computationally expensive, which requires us to analyze smaller networks than those studied with linear stability analysis (*31*). Parameters shown here: S = 10, C = 0.7, $-s$ = –0.2, σ = 0.05 for 100 samples. Error bars indicate SEM. (**F**) Dynamics of the individual-based model. Permanent communities maintain all of their original species after a perturbation, even if species densities do not return to their initial values. In nonpermanent communities, perturbations to species densities will lead to the extinction of some or all species.

Our model predicts that ecological competition improves microbiome stability. However, a notable feature of the mammalian microbiome is species diversity, and we have seen that high species numbers tend to be destabilizing (fig. S1). Therefore, we investigated how the stabilizing effects of ecological competition interact with the destabilizing effects of increasing diversity. Specifically, we explored whether a diverse and competitive community leads to a stable microbiome. We again turned to local stability analysis, as this method can deal with communities containing many species [Fig. 3A and method 1 (*31*)]. Although increasing species numbers is a destabilizing process (fig. S1), the concurrent increase in competition introduces negative-feedback loops that have a stabilizing effect. We find a wide range of diversities for which this stabilizing effect dominates the destabilizing effect of increased species numbers (Fig. 3, B and C, and fig. S10). Even though competition may drive inefficiencies, it dampens the destabilizing effects of cooperation that can lead to the loss of community members (Fig. 2F). The key is that the new interactions from the introduction of additional species are competitive (or exploitative) (fig. S11). The additional species need not be other bacteria; phages in microbial communities (*39*) have the potential for effects comparable to those of the exploitative species in our model (fig. S11) (*40*).

Our analyses allow us to identify key principles (*41*) that are important for a stable microbiome community. In particular, the stabilizing effect of competition reflects the more general principle that dampening of positive-feedback loops promotes stability. Can we use such principles to better understand host biology and, more specifically, how a host should interact with its symbionts? To answer this, we develop a further set of analyses dedicated to clarifying how key features of host biology influence ecological stability. A clear candidate for promoting stability in the gut is the immune system. During dysbiosis and infection, adaptive immunity is thought to help reestablish a healthy microbiome by suppressing species whose abundance is causing harm (*3*–*5*, *23*). We can add such density-dependent regulation to our model and find that it is indeed stabilizing. Moreover, the reason this occurs is because immune regulation, like competition, will prevent run-away positive-feedback loops [method 1d (*31*)].

Dampening positive feedbacks is an important route to stability. A second key principle affecting stability in our models is the strength of interactions between species. Processes that weaken interactions between species will generally promote stability, as these processes reduce the coupling that drives instability. Redundancy can promote stability when a few strong cooperative interactions are replaced by several weaker ones [method 1e (*31*) and fig. S13]. But a key candidate mechanism by which a host can actively weaken ecological interactions is through the introduction of spatial structure (*27*, *42*). In particular, introducing spatial structure (e.g., patchy growth with limited mixing) (fig. S14) between species is known to reduce the strength of between-species interactions without reducing interactions within a species (*42*). Implementing this effect in our models greatly improves the potential for community stability (Fig. 4). We predict, therefore, that a host can benefit from compartmentalizing species within gut communities to control interactions and limit the risk of extinctions.

Another candidate mechanism to influence microbial interactions is host epithelial feeding. Nutrients are provided for symbionts from the epithelial surface, especially during starvation periods, when lumen nutrient concentrations are less abundant (*43*). Recent work has shown that knockout mice lacking the ability to feed the microbiota with fucose show a significantly decreased community diversity (*44*). There is also the potential for some specificity in host feeding that occurs through fucose residues whose digestion relies on specific enzymes (*43*, *45*, *46*). In the context of our models, feeding is expected to promote the stability of communities, provided that such feeding can preferentially weaken interactions between cooperating species by, for example, providing an alternative carbon source to that involved in microbial cross-feeding (Fig. 4B and fig. S12).

So far we have studied communities that are intrinsically limited by their own interactions. Feeding has the potential to alter this by causing populations to grow until they are extrinsically limited by the capacity of the host. Though high symbiont population sizes might harm a host for reasons unrelated to stability (*47*), we can nevertheless use our individual-based model to examine the effect of this scenario on ecological stability. Specifically, we ask what happens if feeding, or any process that drives high intrinsic growth rates, causes communities to expand until they become extrinsically limited by the capacity of the host environment. We find that such communities are stable to further perturbations (Fig. 4C), even those that start with many cooperative interactions. Therefore, the possession of strongly growing communities that are extrinsically regulated by the host is another potential route to ecological stability. However, after expansion, these communities are much less cooperative, because the increase in population densities means that species are now competing for the limited capacity of the host (Fig. 4C). Once again, we find that ecological stability is associated with competition.

Although the stability and composition of gut microbial communities are considered central to the benefits they provide to a host (*9*–*12*), we lack a clear understanding of what underlies the stability of microbiome communities. Here we have developed a body of theory to identify key principles underlying microbiome stability. We have also shown how these principles allow us to reinterpret and predict key features of host biology, including immune suppression, the potential for spatial structuring, and host feeding of microbes. Can we use existing data to test whether the principles we have identified are indeed at work in real communities? Currently, few data are available on

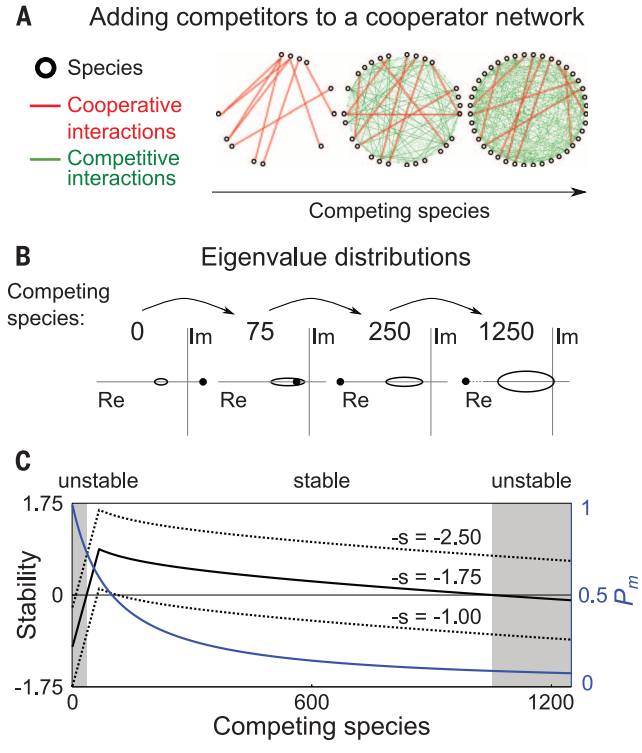

Fig. 3. Introduction of species can stabilize a network of cooperators. (**A**) Illustration of increasing species number and competition (green) in a network that originally contained only cooperating species (red). (**B**) Eigenvalue distribution changes after the addition of competitor species to 100 cooperating species ($C = 0.7$, $-s = -1.75$, $\sigma = 0.05$). As in Figs. 1 and 2, the eigenvalues are contained within ellipses, except for one eigenvalue that may lie outside of the ellipse. Crucially, this latter eigenvalue is reduced when we add competitive species (i.e., the dot moves left), which results in a stabilizing effect. However, the ellipse containing all other eigenvalues becomes wider with additional species, leading to a reduction in stability once the ellipse contains the rightmost eigenvalue (i.e., once the dot moves inside the ellipse). (**C**) Ecological stability as a function of the number of added competing species (solid black line). Competitors are initially stabilizing because they reduce the proportion of cooperative interactions (P_m, blue line). Eventually, however, adding competitors begins to have a destabilizing effect, which corresponds to the widening of the ellipse in (B). This behavior holds for a wide range of self-regulation strengths ($-s$, dotted black lines). Note that we do not apply permanence analysis or the individual-based model here, as these analyses are limited to low species diversities (*31*).

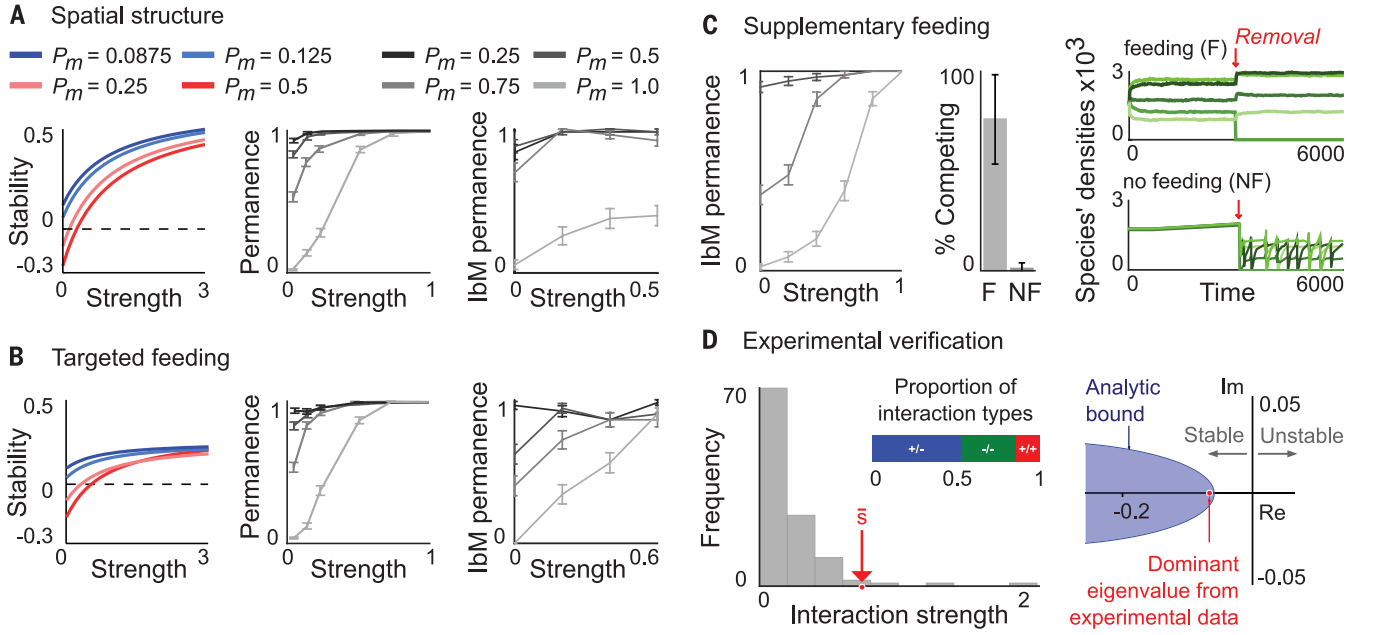

Fig. 4. Host strategies to promote ecological stability. (**A**) Spatial structure promotes ecological stability in linear stability analysis (LAS) (left), permanence analysis (PA) (middle), and an individual-based model (IbM) (right). (**B**) Targeted feeding. Host-supplied nutrients that weaken cooperative interactions promote ecological stability. We observed an exception for which targeted feeding may destabilize more competitive communities in the IbM (P_m = 0.25), but the effect is weak. (**C**) Nontargeted feeding may stabilize communities when it increases the growth rates of all species such that they become limited by the host's capacity (left). However, limited space means that most previously cooperative species become competitors. Competition is demonstrated by removing one species from a community and observing increased densities for most remaining species (middle) (P_m = 0.9). F, feeding; NF, no feeding. IbM time-series plots show that feeding can stabilize communities upon species removal (right). (**D**) (Left) Empirical interaction parameters (mouse microbiome communities) (*16*) confirm our predictions: Most interactions are weak (less than self-interaction, s) and predominantly competitive or exploitative, with a small set of cooperative interactions [experimental validation in (*31*)]. (Right) Our general analytical model predicts stability in a real community, using community parameters from the mouse data set (S, C, P_m, P_c, σ, s). In (A) to (C), LAS: S = 300, C = 0.7, $-s$ = –1, σ = 0.05; PA and IbM: S = 10, $-s$ = –0.2; error bars indicate SEM. PA and IbM are computationally expensive and require smaller communities.

ecological interactions within the microbiome. Nevertheless, we can validate our approach and test our key predictions with recently published data on interactions in the mouse gut microbiome (*16*). Stein *et al.* used time-resolved metagenomics and machine learning to infer the interactions within communities. In Fig. 4D, we use these data to parameterize our general model and show that it correctly predicts stability within a real community. In addition, we plot the distribution of ecological interactions within the mouse microbiome. As we predicted, ecological interactions tend to be both noncooperative and weak [Fig. 4D and method 4 (*31*)].

In conclusion, microbiome communities consist of many interacting species, making it difficult for a host to exercise control over each species individually. However, our work emphasizes that hosts can act as ecosystem engineers that manipulate general, system-wide properties of their microbial communities to their benefit. Identifying when and how hosts alter their symbionts' ecology will be important if we are to comprehend the dynamics of microbiome communities. More generally, although there is a vast and rapidly growing body of data on the mammalian microbiome, little attention has been paid to the strength or sign of ecological interactions. To understand and manipulate the microbiome, we will need to dissect and engineer the interactions within these critical communities.

REFERENCES AND NOTES

1. C. Lozupone *et al.*, *Genome Res.* **22**, 1974–1984 (2012).
2. S. R. Gill *et al.*, *Science* **312**, 1355–1359 (2006).
3. F. Bäckhed, R. E. Ley, J. L. Sonnenburg, D. A. Peterson, J. I. Gordon, *Science* **307**, 1915–1920 (2005).
4. S. K. Mazmanian, J. L. Round, D. L. Kasper, *Nature* **453**, 620–625 (2008).
5. Y. K. Lee, S. K. Mazmanian, *Science* **330**, 1768–1773 (2010).
6. L. Dethlefsen, D. A. Relman, *Proc. Natl. Acad. Sci. U.S.A.* **108** (suppl. 1), 4554–4561 (2011).
7. T. Vanhoutte, G. Huys, E. Brandt, J. Swings, *FEMS Microbiol. Ecol.* **48**, 437–446 (2004).
8. J. J. Faith *et al.*, *Science* **341**, 1237439 (2013).
9. D. A. Relman, *Nutr. Rev.* **70** (suppl. 1), S2–S9 (2012).
10. A. Giongo *et al.*, *ISME J.* **5**, 82–91 (2011).
11. C. A. Lozupone, J. I. Stombaugh, J. I. Gordon, J. K. Jansson, R. Knight, *Nature* **489**, 220–230 (2012).
12. P. De Cruz *et al.*, *Inflamm. Bowel Dis.* **18**, 372–390 (2012).
13. E. Y. Hsiao *et al.*, *Cell* **155**, 1451–1463 (2013).
14. J. Schluter, K. R. Foster, *PLOS Biol.* **10**, e1001424 (2012).
15. V. Bucci, S. Bradde, G. Biroli, J. B. Xavier, *PLOS Comput. Biol.* **8**, e1002497 (2012).
16. R. R. Stein *et al.*, *PLOS Comput. Biol.* **9**, e1003388 (2013).
17. R. M. May, *Nature* **238**, 413–414 (1972).
18. S. Allesina, S. Tang, *Nature* **483**, 205–208 (2012).
19. K. S. McCann, *Nature* **405**, 228–233 (2000).
20. K. R. Foster, T. Bell, *Curr. Biol.* **22**, 1845–1850 (2012).
21. G. Eberl, *Mucosal Immunol.* **3**, 450–460 (2010).
22. R. D. Sleator, *Med. Hypotheses* **74**, 214–215 (2010).
23. P. Van den Abbeele, T. Van de Wiele, W. Verstraete, S. Possemiers, *FEMS Microbiol. Rev.* **35**, 681–704 (2011).
24. R. Di Cagno *et al.*, *BMC Microbiol.* **11**, 219 (2011).
25. F. Fiegna, G. J. Velicer, *PLOS Biol.* **3**, e370 (2005).
26. J. C. Clemente *et al.*, *Sci. Adv.* **1**, e1500183 (2015).
27. N. M. Oliveira, R. Niehus, K. R. Foster, *Proc. Natl. Acad. Sci. U.S.A.* **111**, 17941–17946 (2014).
28. B. S. Samuel, J. I. Gordon, *Proc. Natl. Acad. Sci. U.S.A.* **103**, 10011–10016 (2006).
29. E. P. Wigner, *Ann. Math.* **67**, 325–327 (1958).
30. H. J. Sommers, A. Crisanti, H. Sompolinsky, Y. Stein, *Phys. Rev. Lett.* **60**, 1895–1898 (1988).
31. See the supplementary materials on *Science* Online.
32. A. Mougi, M. Kondoh, *Science* **337**, 349–351 (2012).
33. R. P. Rohr, S. Saavedra, J. Bascompte, *Science* **345**, 1253497 (2014).
34. P. Louis, G. L. Hold, H. J. Flint, *Nat. Rev. Microbiol.* **12**, 661–672 (2014).
35. C. S. Holling, *Annu. Rev. Ecol. Syst.* **4**, 1–23 (1973).
36. M. Kondoh, A. Mougi, *Popul. Ecol.* **57**, 21–27 (2015).
37. X. Chen, J. E. Cohen, *J. Theor. Biol.* **212**, 223–235 (2001).
38. W. Jansen, *J. Math. Biol.* **25**, 411–422 (1987).
39. A. S. Waller *et al.*, *ISME J.* **8**, 1391–1402 (2014).
40. J. Hofbauer, K. Sigmund, *J. Math. Biol.* **27**, 537–548 (1989).
41. J. K. Fredrickson, *Science* **348**, 1425–1427 (2015).
42. H. J. Kim, J. Q. Boedicker, J. W. Choi, R. F. Ismagilov, *Proc. Natl. Acad. Sci. U.S.A.* **105**, 18188–18193 (2008).
43. L. V. Hooper, J. Xu, P. G. Falk, T. Midtvedt, J. I. Gordon, *Proc. Natl. Acad. Sci. U.S.A.* **96**, 9833–9838 (1999).
44. P. C. Kashyap *et al.*, *Proc. Natl. Acad. Sci. U.S.A.* **110**, 17059–17064 (2013).
45. J. L. Sonnenburg *et al.*, *Science* **307**, 1955–1959 (2005).
46. V. Tremaroli, F. Bäckhed, *Nature* **489**, 242–249 (2012).
47. F. H. Login *et al.*, *Science* **334**, 362–365 (2011).

ACKNOWLEDGMENTS

We thank V. Bucci, S. Knowles, S. Rakoff-Nahoum, L. MacNally, S. Mitri, H. Ohtsuki, A. Sasaki, S. Murray, D. Palmer, B. Grenfell, D. Berry, K. Yashima, and J. Xavier for valuable comments and discussion. K.R.F. is supported by European Research Council grant 242670, K.Z.C. is supported by the Engineering and Physical Sciences Research Council, and J.S. is supported by Japan Society for the Promotion of Science and the Goldschmidt family.

SUPPLEMENTARY MATERIALS

www.sciencemag.org/content/350/6261/663/suppl/DC1
Materials and Methods
Figs. S1 to S14
References (*48*–*54*)

17 August 2015; accepted 30 September 2015
10.1126/science.aad2602

MOVEMENT CONTROL

Corticomotoneuronal cells are "functionally tuned"

Darcy M. Griffin,[1,2] Donna S. Hoffman,[1,2,3] Peter L. Strick[1,2,3]*

Corticomotoneuronal (CM) cells in the primary motor cortex (M1) have monosynaptic connections with motoneurons. They are one of the few sources of descending commands that directly influence motor output. We examined the contribution of CM cells to the generation of activity in their target muscles. The preferred direction of many CM cells differed from that of their target muscles. Some CM cells were selectively active when a muscle was used as an agonist. Others were selectively active when the same muscle was used as a synergist, fixator, or antagonist. These observations suggest that the different functional uses of a muscle are generated by separate populations of CM cells. We propose that muscle function is one of the dimensions represented in the output of M1.

Even simple movements are produced by complex patterns of muscle activity. For example, during wrist flexion, some muscles function as agonists to generate force in the direction of flexion. Other muscles function as fixators to prevent joint motion in the radial and ulnar direction, and still others serve as antagonists to brake movement and assist in speed control (*1*). Movement dexterity depends on the central control over the precise timing and amplitude not only of agonist muscle activity but also of the activity of muscles performing other functions.

We examined the contribution of corticomotoneuronal (CM) cells in the primary motor cortex (M1) to the generation and control of different patterns of muscle activity. CM cells are output neurons in M1 that have monosynaptic connections with motoneurons in the spinal cord. CM cells are located in a distinct caudal portion of M1 that is both phylogenetically and ontogenetically new (*2*, *3*). We identified 41 CM cells and their target muscles using spike-triggered averaging (SpTA) of electromyographic (EMG) activity from 12 to 13 forearm muscles (*4*). We examined the directional tuning of CM cells and their target muscles while a monkey performed wrist movements in eight directions with the limb in three different postures (*5*). Twenty CM cells (~49%)

[1]University of Pittsburgh Brain Institute, Center for the Neural Basis of Cognition and Systems Neuroscience Institute, Pittsburgh, PA, USA. [2]Department of Neurobiology, University of Pittsburgh School of Medicine, Pittsburgh, PA, USA. [3]Research Service, Department of Veterans Affairs Medical Center, Pittsburgh, PA, USA.
*Corresponding author. E-mail: strickp@pitt.edu

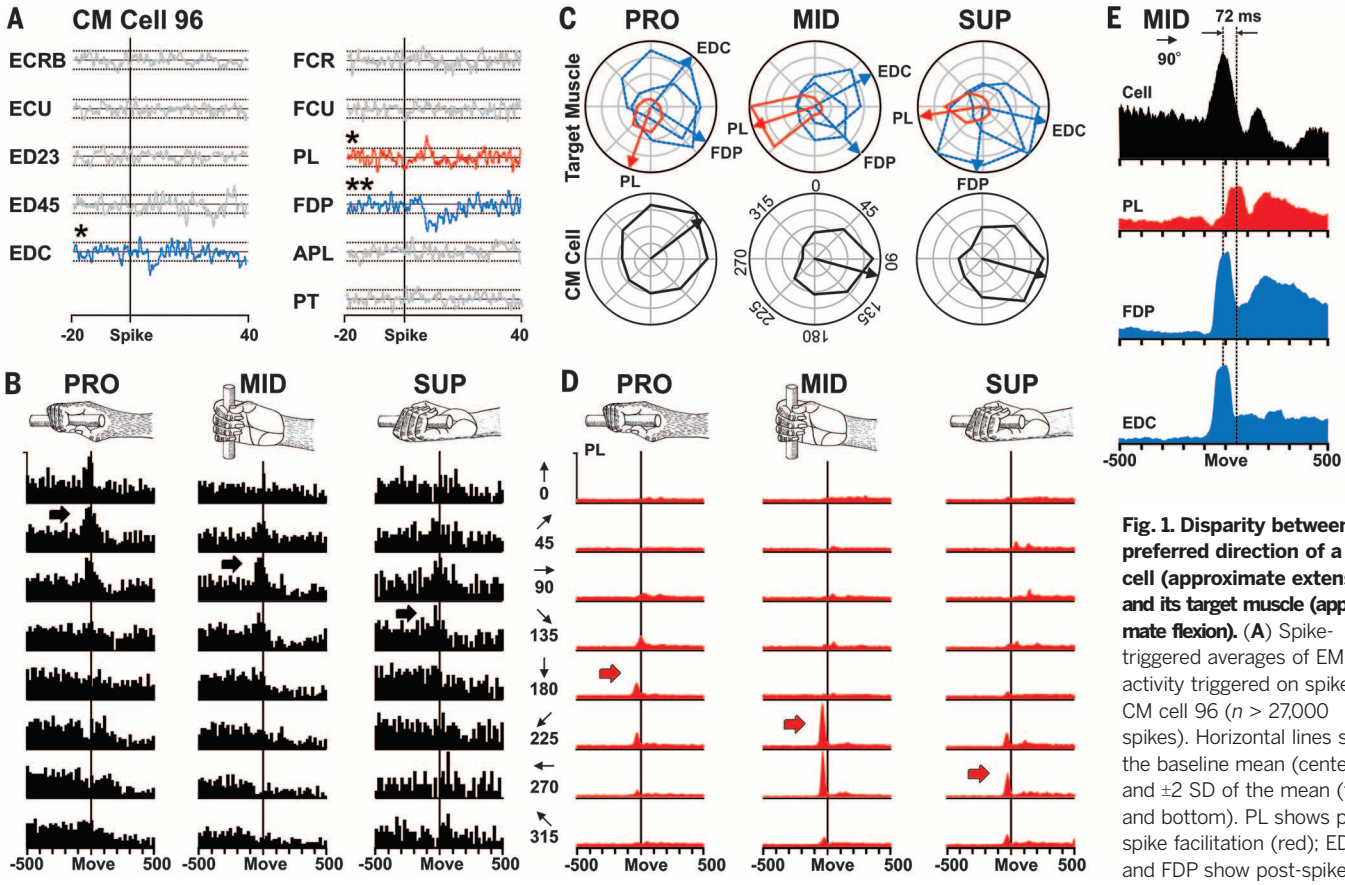

Fig. 1. Disparity between the preferred direction of a CM cell (approximate extension) and its target muscle (approximate flexion). (**A**) Spike-triggered averages of EMG activity triggered on spikes of CM cell 96 (n > 27,000 spikes). Horizontal lines show the baseline mean (center) and ±2 SD of the mean (top and bottom). PL shows post-spike facilitation (red); EDC and FDP show post-spike suppression (blue). Asterisks indicate size of effect: *, 2 to 3.9 SD; **, 4 to 5.9 SD. (**B**) CM cell activity aligned on movement onset (n ≥ 13 trials). Large black arrows indicate the target close to the neuron's preferred direction. Small black arrows and numbers to the right indicate the movement direction. (**C**) Preferred directions of the CM cell (black) and its target muscles. (**D**) Activity of PL during movement (n ≥ 13 trials). Large red arrows indicate the target close to PL's preferred direction. (**E**) Activity of the CM cell and its target muscles in the MID posture aligned on movement onset for movements to the 90° target (n = 37 trials). Left dotted line is aligned with the peak of CM cell activity. Right dotted line is aligned with the peak of PL's activity.

Downloaded from www.sciencemag.org on November 5, 2015

were directionally tuned for all three wrist postures. Nearly all of these CM cells (19 of 20) were considered to be "muscle-like," and none were considered to be "extrinsic-like" [see the supplementary materials (fig. S1)]. We compared the preferred direction of these CM cells (i.e., the direction of cell's maximal activity) with that of their target muscles.

We found a marked disparity between the preferred directions of many CM cells and the preferred directions of their target muscles. Only 6 of 20 (30%) directionally tuned CM cells had preferred directions that matched or were within ±45° of their target muscles. An equal number of directionally tuned CM cells (6 of 20, 30%) had preferred directions that were opposite to or differed by ≥ ±135° from the preferred direction of their target muscles. The preferred directions of the remaining 8 CM cells were intermediate (i.e., differed by ±46° to ±134° from the preferred direction of their target muscles). Overall, the majority of the directionally tuned CM cells (14 of 20) had preferred directions that were distinctly different (≥±46°) from the average preferred direction of their target muscles.

One example of a disparity between the preferred direction of a CM cell and that of the single wrist muscle it facilitated [palmaris longus (PL)] is illustrated in Fig. 1 (CM cell 96). This CM cell also suppressed two digit muscles [flexor digitorum profundus (FDP) and extensor digitorum communis (EDC)] (Fig. 1A). When the limb was pronated (Pro), this CM cell was most active for movements to the 45° target, whereas the wrist muscle (PL) facilitated by this CM cell was most active for movements to the 180° target (compare Fig. 1B-Pro with Fig. 1D-Pro; also compare Fig. 1C-Pro, top, with Fig. 1C-Pro, bottom).

CM cell 96 displayed orderly shifts in its maximal activity to the 90° and 135° targets as the limb posture was rotated to Mid (midway between pronation and supination) and Sup (supination) (Fig. 1B-Mid and Fig. 1B-Sup; see also Fig. 1C-Mid, bottom, and Fig. 1C-Sup, bottom). The same rotation in limb posture also resulted in orderly shifts in the maximal activity of its target muscle (PL), but to the 225° and 270° targets (Fig. 1D-Mid and Fig. 1D-Sup; see also Fig. 1C-Mid, top, and Fig. 1C-Sup, top). Thus, the disparity between the preferred direction of CM cell 96 and that of the target muscle it facilitated was maintained across shifts in limb posture.

These observations make it unlikely that the activity of CM cell 96 contributed to the generation of the initial agonist bursts of activity in the muscle it facilitated. Instead, the activity of this CM cell was consistent with it contributing to the generation of antagonist bursts of activity in the muscle it facilitated (PL) (Fig. 1E). The cell's activity also was consistent with its contributing to the prompt termination of activity in the muscles it inhibited (FCU and EDC) (Fig. 1E).

Another example of an extreme disparity between the preferred direction of a CM cell and that of its target muscles is shown in Fig. 2 (CM cell 200). This CM cell facilitated eight muscles: one wrist extensor [extensor carpi ulnaris (ECU)], three digit extensors [extensor digiti secondi et tertii proprius (ED23), extensor digiti quinti proprius (ED45), and EDC], one wrist flexor [flexor carpi ulnaris (FCU)], one digit flexor (FDP), one thumb abductor [abductor policis longus (APL)], and one elbow flexor [brachioradialis (BR)] (Fig. 2A). When the limb was in Pro, CM cell 200 was most active for movements to the 180° target (Fig. 2B-Pro and Fig. 2C-Pro, bottom). Under the same conditions, the most strongly facilitated target muscle (ECU) was most active for movements to the 90° target (Fig. 2D-Pro and Fig. 2C-Pro, top). The other four directionally tuned muscles that were facilitated by CM cell 200 also had preferred directions that differed from the CM cell by more than 45° (Fig. 2C-Pro, top, and fig. S2).

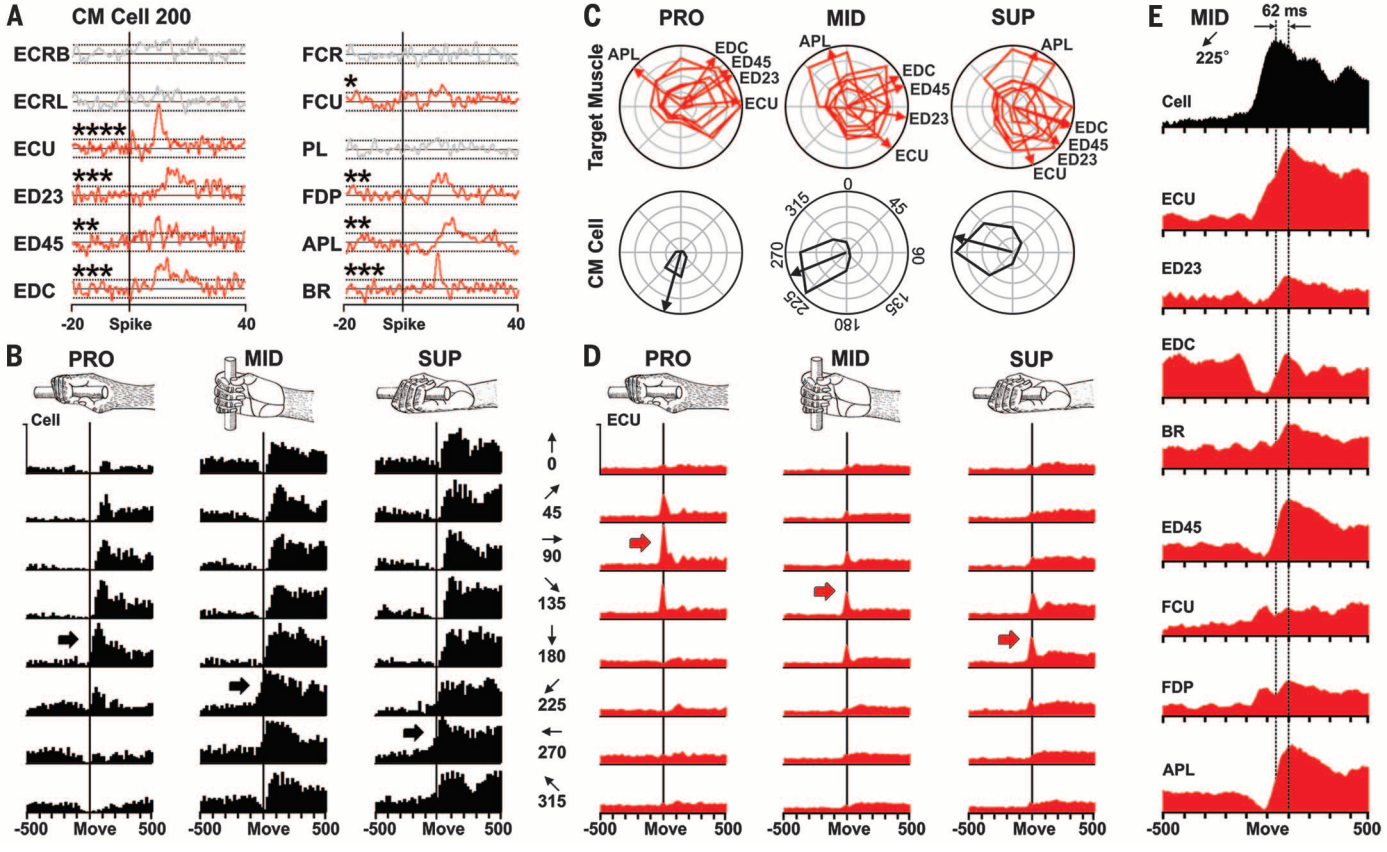

Fig. 2. Disparity between the preferred direction of a CM cell (approximate flexion) and its target muscles (approximate extension). See Fig. 1 legend for description. (**A**) Spike-triggered averages of EMG activity triggered on spikes of CM cell 200 (n > 33,000 spikes). ***, 6 to 8.9 SD; ****, ≥9 SD. (**B**) CM cell activity aligned on movement onset (n ≥ 8 trials). (**C**) Preferred directions of the CM cell (black) and its target muscles. (**D**) Activity of ECU during movement (n ≥ 8 trials). (**E**) Activity of the CM cell and its target muscles in the MID posture aligned on movement onset (n = 26 trials). Movements were to the 225° target. Left dotted line is aligned with the peak of CM cell activity. Right dotted line is aligned with the peak of ECU's activity.

CM cell 200 displayed orderly shifts in its maximal activity when the limb posture was rotated to Mid and Sup (Fig. 2B-Mid and Fig. 2B-Sup; see also Fig. 2C, bottom). The same rotations in the limb position also resulted in orderly shifts in ECU's maximal activity, but to different targets (Fig. 2D-Mid and Fig. 2D-Sup; see also Fig. 2C, top). CM cell 200 was most active for movements to the 225° target in Mid and to the 270° target in Sup. In contrast, ECU was most active for movements to the 135° target in Mid and to the 180° target in Sup. The other target muscles of CM cell 200 displayed similar shifts in their maximal activity associated with changes in limb position (Fig. 2C, top, and fig. S2). Thus, the disparity between the CM cell's preferred direction and the preferred directions of its target muscles was maintained across shifts in limb posture. Here again, our observations make it unlikely that the activity of CM cell 200 contributed to the generation of the initial agonist bursts of activity in the muscles it facilitated. Instead, the activity of this CM cell was consistent with its contributing to the generation of increases in activity that occurred when its target muscles were used as fixators or antagonists (Fig. 2E)

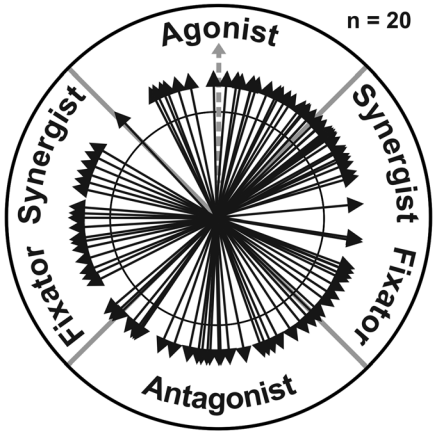

Fig. 3. Spatial relationship between CM cells and their target muscles. Preferred directions of 20 directional CM cells (black lines with arrows) in three postures. We normalized the preferred direction of each facilitated muscle to the 0° target (dashed vertical gray line with arrow). We plotted the preferred directions of each CM cell for the three postures (black lines with arrows) in relation to their target muscle.

We examined the angular relationship between the preferred directions of individual CM cells and the preferred directions of their target muscles. We normalized the preferred direction of each facilitated muscle to 0° (Fig. 3, dashed gray line). Then, we plotted the preferred direction of each CM cell in relation to the normalized preferred direction of the muscle (Fig. 3, black lines). Because we examined neuron and muscle activity in three postures, this analysis resulted in three vectors for each CM cell-target muscle combination. The broad distribution of the vectors (Fig. 3) suggests that the agonist, synergist, fixator and antagonist functions of target muscles are each well-represented by the activity of individual CM cells.

This conclusion is supported by an examination of the angular relationships between individual CM cells and the specific target muscles they facilitated (Fig. 4). Nine muscles were the target of facilitation for more than one of the 20 directionally tuned CM cells in our sample. For eight of these muscles, the multiple CM cells facilitating the same muscle displayed different functional relationships. For example, FCR was facilitated by two different CM cells (Fig. 4I). The preferred direction of cell 115 was consistent with its contributing to the agonist function of the muscle, whereas the preferred direction of cell 103 was consistent with its contributing to the antagonist function of the muscle. Another compelling example is EDC, which was facilitated by five different CM cells in our sample (Fig. 4B). Agonist, synergist, fixator, and antagonist functions of EDC were represented by the preferred direction of at least one of the five CM cells in our sample that facilitated it. These results support the concept that the different functional uses of muscles are represented by separate populations of CM cells. This concept is further supported by the timing differences between CM cells that contribute to the agonist function of the muscles they facilitated versus those that contribute to the antagonist function of the muscles they facilitated (fig. S3). CM cells that facilitated agonists were active before CM cells that facilitated antagonists. The greater delay between the onset of CM cell facilitation and the onset of antagonist activity may be due the arrival of the facilitation at a time when the antagonist motoneuron pool is relatively inactive and perhaps suppressed.

The key result of the present study is that for many CM cells there is a major disparity between

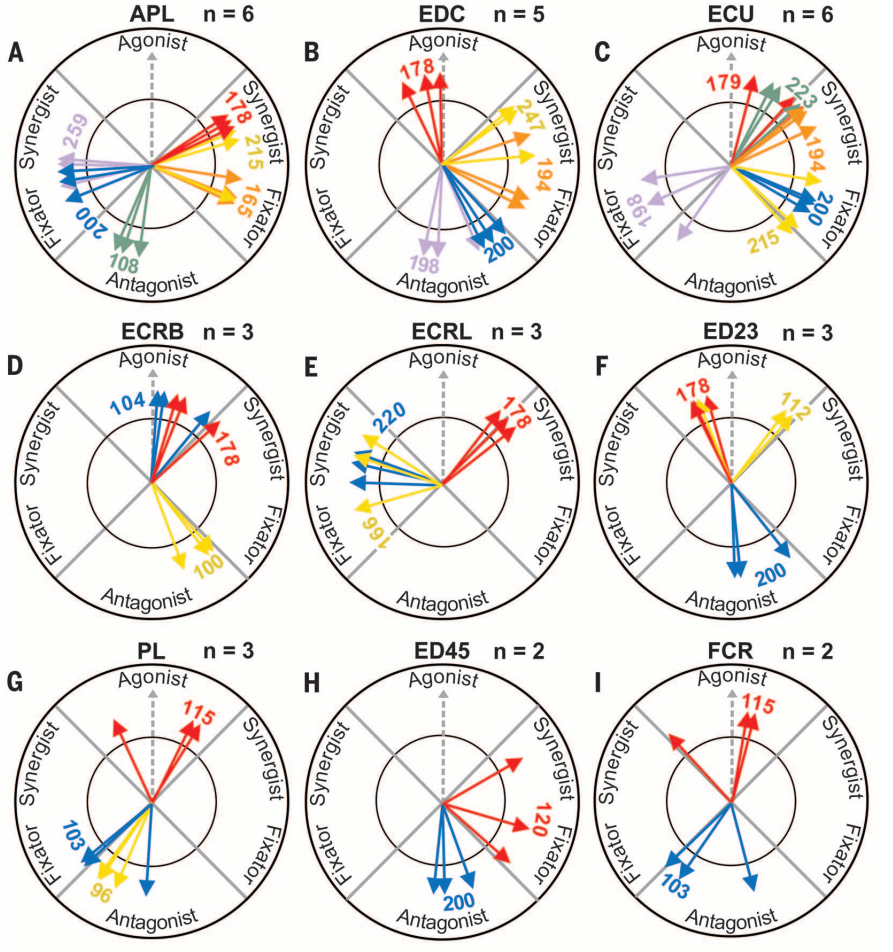

Fig. 4. Preferred directions of different CM cells (colored arrows) that facilitated the same target muscle. Each numbered arrow is the average of three different postures for a single CM cell. The target muscles are (**A**) APL, *n* = 6 CM cells; (**B**) EDC, *n* = 5 CM cells; (**C**) ECU, *n* = 6 CM cells; (**D**) extensor carpi radialis brevis (ECRb), *n* = 3 CM cells; (**E**) extensor carpi radialis longus (ECRl), *n* = 3 CM cells; (**F**) ED23, *n* = 3 CM cells; (**G**) PL, *n* = 3 CM cells; (**H**) ED45, *n* = 2 CM cells; (**I**) flexor carpi radialis (FCR), *n* = 2 CM cells.

the cell's preferred direction and the preferred directions of its target muscles. We interpret this result as indicating that individual CM cells are functionally tuned. Indeed, we provide evidence that some CM cells specifically contribute to the agonist function of a muscle, whereas other CM cells specifically contribute to the synergist, fixator, or antagonist function of the same muscle. From this perspective, the multiple functions of a target muscle are represented by the activity of separate populations of CM cells. The concept of functional tuning is supported by Muir and Lemon's (*6*) observation that some CM cells were more active during a precision grip, whereas others were more active during a power grip, even though both types of CM cells facilitated the same target muscles. In their case, like ours, CM cell activity was linked to the functional use rather than the magnitude of muscle activity.

A major question raised by our results concerns the origin of the functional tuning that we observed. It is possible that the functional tuning reflects an explicit representation of different motor functions in New M1, just as orientation and ocular dominance are explicitly represented in primary visual cortex. In this sense, the different motor functions of CM cells would be either categorically (e.g., agonist, fixator, and antagonist) or continuously represented. The results shown in Fig. 3 support a continuous representation. However, the broad directional tuning of CM cells and their target muscles could obscure a categorical representation if it exists.

It is also possible that functional tuning is an emergent property of New M1. The wrist movements and patterns of muscle activity required by our task are not part of the animal's natural repertoire. Thus, skilled performance of the task requires an animal to generate new patterns of muscle activity that are acquired through extensive practice. We have previously argued that "the direct access to motoneurons afforded by CM cells enables New M1 to bypass spinal cord mechanisms and sculpt novel patterns of motor output that are essential for highly skilled movements" (*3*). Thus, functional tuning of CM cells may emerge as part of the sculpting process during extended practice on the task. In any event, functional tuning, whether explicitly represented or an emergent property, reflects a clear expansion of the known motor dimensions that M1 generates and controls.

REFERENCES AND NOTES

1. D. S. Hoffman, P. L. Strick, *Brain Res.* **367**, 287–291 (1986).
2. J. A. Rathelot, P. L. Strick, *Proc. Natl. Acad. Sci. U.S.A.* **103**, 8257–8262 (2006).
3. J. A. Rathelot, P. L. Strick, *Proc. Natl. Acad. Sci. U.S.A.* **106**, 918–923 (2009).
4. E. E. Fetz, P. D. Cheney, *J. Neurophysiol.* **44**, 751–772 (1980).
5. S. Kakei, D. S. Hoffman, P. L. Strick, *Science* **285**, 2136–2139 (1999).
6. R. B. Muir, R. N. Lemon, *Brain Res.* **261**, 312–316 (1983).

ACKNOWLEDGMENTS

We thank R. Dum for surgical assistance; M. Watach and K. Thiel for technical assistance; K. Reinert for statistical assistance; and M. Page (Great Island Software, Chatham, MA) and S. Hoffman (Reflective Computing, Olympia, WA) for development of custom computer programs. This work was supported by funds from the Department of Veterans Affairs, Medical Research Service (P.L.S.) and NIH grants R01NS24328 (P.L.S.), P30NS076405 (P.L.S.), and FNS070366A (D.M.G.). The contents do not represent the views of the Department of Veterans Affairs or the United States Government. The supplementary materials contain additional data. All other data are available upon request from the corresponding author.

SUPPLEMENTARY MATERIALS

www.sciencemag.org/content/350/6261/667/suppl/DC1
Materials and Methods
Figs. S1 to S3
References (*7*–*16*)

9 February 2015; accepted 25 September 2015
10.1126/science.aaa8035

PLANT SCIENCE

Plant pathogenic anaerobic bacteria use aromatic polyketides to access aerobic territory

Gulimila Shabuer,[1]* Keishi Ishida,[1]* Sacha J. Pidot,[1,2]* Martin Roth,[3] Hans-Martin Dahse,[4] Christian Hertweck[1,5]†

Around 25% of vegetable food is lost worldwide because of infectious plant diseases, including microbe-induced decay of harvested crops. In wet seasons and under humid storage conditions, potato tubers are readily infected and decomposed by anaerobic bacteria (*Clostridium puniceum*). We found that these anaerobic plant pathogens harbor a gene locus (type II polyketide synthase) to produce unusual polyketide metabolites (clostrubins) with dual functions. The clostrubins, which act as antibiotics against other microbial plant pathogens, enable the anaerobic bacteria to survive an oxygen-rich plant environment.

The global food supply is weakened by infectious plant diseases and microbe-mediated decay during crop storage and transportation (*1*). Infections of potato (*Solanum tuberosum*), one of the top four food crops cultivated worldwide, result in losses amounting to 65 billion kg of food and $16 billion annually, of which 30 to 50% are caused by pectolytic bacteria (*2*, *3*). In wet seasons and humid storage conditions, potato tubers are infected and decomposed by *Clostridium puniceum* that grow in the absence of oxygen (*4*). The potato tuber is, however, an oxygen-rich environment.

Of the many known plant pathogenic bacteria, *C. puniceum* is the only characterized representative of the diverse genus *Clostridium* (*5*). These obligate anaerobes are typically killed by normal atmospheric oxygen concentrations, yet they are frequently isolated from oxic plant matter (*6*). It has been argued that mixed bacterial infections could account for an anaerobic microenvironment in diseased tubers (*7*, *8*). However, pure cultures of *C. puniceum* also cause potato slimy rot, manifested by formation of pink pigments by the bacterium (*4*).

To study the pathogenesis of this anaerobe, we reproduced potato slimy rot by stab-inoculating *C. puniceum* into potato tubers. Over 4 days, potato decomposition accompanied accumulation of pink pigment and slime (Fig. 1A). High-performance liquid chromatography (HPLC) analysis of the ethyl acetate extract showed two main peaks with ultraviolet (UV)/visible maxima at 530 nm (Fig. 1B). The HPLC profile resembled that derived from the soil anaerobe *C. beijerinckii* (*9*). By HPLC-HRMS (high-resolution mass spectroscopy) correlation using clostrubin A (**1**) as an authentic reference, we identified one of the main products of *C. puniceum* as **1**, an aromatic polyketide (*9*). Obtaining the second main product, clostrubin B (**2**) as a pure compound was an arduous task because of its strong adhesive properties, low solubility, and propensity to appear in various mesomeric forms. We isolated pure **2** (4.0 mg) from 8.0 liters of cultured *C. beijerinckii*. Analyses including HRMS, UV spectroscopy, and nuclear magnetic resonance (NMR) spectroscopy (figs. S1 to S3, including ^{13}C labeling experiments) revealed that **1** and **2** share the same aromatic polyketide backbone (Fig. 1C). However, extensive one- and two-dimensional NMR studies revealed that **2** features a sugar-like linear side chain connected to position C-2 (supplementary text and table S1).

To investigate how clostrubins A and B affect plant disease, we tested for phytotoxic activity. Applied clostrubins had no effect and thus did not act as virulence factors. Because clostrubin A

[1]Department of Biomolecular Chemistry, Leibniz Institute for Natural Product Research and Infection Biology (HKI), Jena, Germany. [2]Department of Microbiology and Immunology, University of Melbourne at the Peter Doherty Institute for Infection and Immunity, VIC 3010, Australia. [3]Bio Pilot Plant, Leibniz Institute for Natural Product Research and Infection Biology (HKI), Jena, Germany. [4]Department of Infection Biology, Leibniz Institute for Natural Product Research and Infection Biology (HKI), Jena, Germany. [5]Department of Natural Product Chemistry, Friedrich Schiller University, Jena, Germany.
*These authors contributed equally to this work. **†Corresponding author. E-mail: christian.hertweck@leibniz-hki.de**

Downloaded from www.sciencemag.org on November 5, 2015

(**1**) showed strong antibacterial activities against the human pathogens MRSA (methicillin-resistant *Staphylococcus aureus*) and VRE (vancomycin-resistant enterococci) (*9*), we reasoned that the clostrubins might be produced by the plant pathogen to battle microbial competitors. We therefore tested the effect of clostrubins on some of the more common microbial pathogens of potato: soft rot (*Bacillus pumilus*), ring rot (*Clavibacter michiganensis* subsp. *sepedonicus*), and common scab (*Streptomyces scabies*) (*10*, *11*). Both *C. puniceum* metabolites showed antibacterial activity against all tested potato pathogens, with minimal inhibition concentration (MIC) values in the nanomolar range (Fig. 1D and table S2). Thus, clostrubins are effective at removing competitors in a resource-limited niche (*12*). The microbial competitors tested were aerobic plant pathogens, whereas *C. puniceum* was described as a strictly anaerobic bacterium (*4*). We found, however, that *C. puniceum* is capable of growing in tubers in an aerobic environment. To unveil the genetic inventory for tolerance of reactive oxygen species (ROS) by the plant pathogen, we sequenced the genome of *C. puniceum* using Illumina MiSeq technology. By bioinformatic genome analysis, we found orthologs of typical superoxide dismutase, catalase, peroxidase, rubredoxin, and rubrerythrin genes (table S4), which have been described for various other anaerobes (*13*–*17*).

C. puniceum produced stronger pigmentation when grown in the presence of oxygen. To study this relationship, we needed a clostrubin-negative mutant of *C. puniceum*. On the basis of the clostrubin structure, we reasoned that the most likely biosynthetic route would be via a type II polyketide synthase (PKS) (*18*). However, type II PKSs are characteristic of actinomycetes; only two compounds derived from type II PKSs have been identified in bacteria outside the actinomycetes (*19*, *20*). Moreover, we were unable to find any type II PKS genes in more than 210 sequenced anaerobe genomes (*21*). In contrast, BLAST (*22*) and antiSMASH (*23*) analyses revealed that the *C. puniceum* genome harbors a gene locus (*clr*) coding for a putative type II PKS, including the minimal PKS [*clr*A, KSα (ketosynthase); *clr*B, CLF (chain length factor); *clr*C, ACP (acyl carrier protein)], cyclases, and modifying enzymes (Fig. 1E and table S3). The predicted PKS shows the highest homology to the resistomycin (*rem*) PKS, which produces a polycyclic ring system in the aerobe *Streptomyces resistomycificus* (*24*). For comparison, we also sequenced and analyzed the clostrubin biosynthesis gene clusters in two pigmented *C. beijerinckii* strains and found a nearly identical gene locus architecture (Fig. 1E). Phylogenetic analysis using the maximum likelihood algorithm showed that the ClrA and ClrB variants cluster most closely with KSα and CLF proteins, yet form a distinct clade (Fig. 1F and fig. S12).

To confirm that the *clr* locus is responsible for the production of clostrubins, we generated knockout mutants deficient in an essential PKS gene. We constructed two individual *clr*A-inactivated mutants of *C. puniceum* and a Δ*clr*A mutant of *C. beijerinckii* using the Clostron gene inactivation system (*25*), which uses a retro-homing bacterial group II intron to insert within a specific DNA sequence in the genome. Introduction of the knockout plasmid by conjugation from an *Escherichia coli* donor strain resulted in positive colonies on antibiotic-selective agar plates. Insertion of the introns was confirmed by polymerase chain reaction (Fig. 1G and figs. S6 and S9). The Δ*clr*A mutants lost pigmentation and were also incapable of producing clostrubins (Fig. 1H and figs. S5 and S7). Thus, the aromatic polyketide clostrubin is indeed the product of a type II PKS.

We compared the physiology and pathogenicity of the clostrubin-negative *C. puniceum* Δ*clr*A mutant to that of the wild type. We infected potato slices under anaerobic conditions with the same number of wild-type or Δ*clr*A mutant bacteria (2×10^8), then measured the amount of degraded plant matter. After 4 days, wild-type and mutant bacteria caused similar amounts of degradation (74% reduction in the weight of rinsed slices) (Fig. 2A, top). However, the situation changed under aerobic conditions (Fig. 2A, bottom). Growth of the Δ*clr*A mutant was radically impaired in the presence of air. In contrast, the wild-type strain grew well and produced pink pigments. Quantification of the pectinolytic activity in four independent experiments revealed that the Δ*clr*A mutant caused little tissue rot (less than 5% degradation) (Fig. 2B). Addition of clostrubins **1** and **2** (1 μl, 1 mg ml^{-1} in dimethyl sulfoxide) to tuber slices inoculated with the Δ*clr*A mutant restored the wild-type phenotype (Fig. 2, A and B).

Because the absence of clostrubins had no effect on the action of the plant pathogen under anaerobic conditions, we concluded that clostrubins are not needed for plant infection and tissue degradation. However, our findings imply that the clostrubins permit survival of the plant pathogen in an oxygen-rich atmosphere. To test this hypothesis, we investigated the fate of the *C. puniceum* strains under anaerobic and aerobic conditions. In liquid culture, growth curves of the wild type and the clostrubin-negative mutant were identical under anaerobic conditions but different in oxygenated (pO_2 40%) liquid medium. Whereas the Δ*clr*A mutant cells died immediately, the clostrubin producer survived and only showed a delayed log phase relative to anaerobic conditions (Fig. 3A). The experiment was repeated at a smaller scale for chemical complementation of

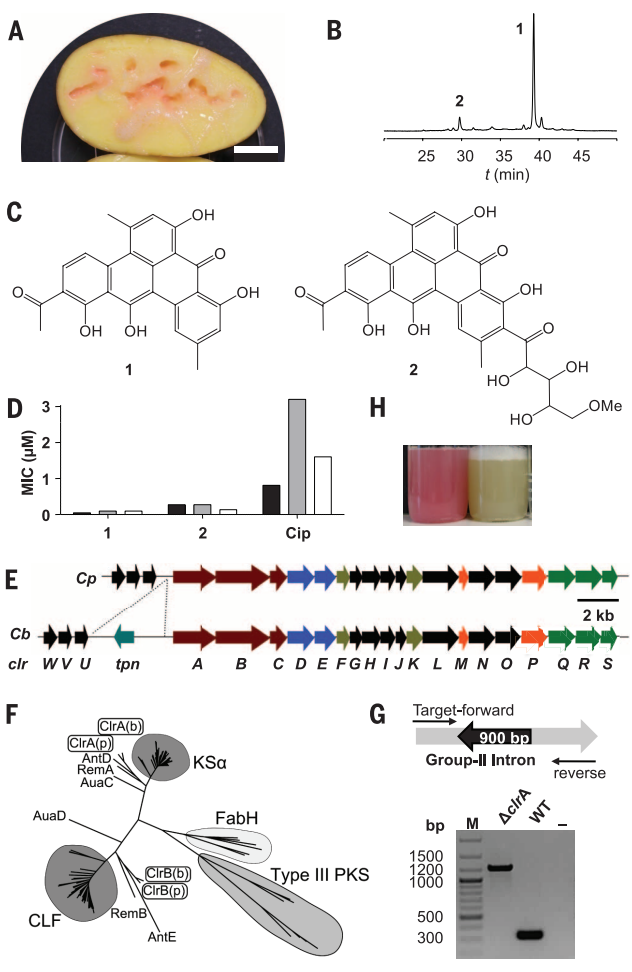

Fig. 1. Structure, genetic basis, and antibiotic activity of pigments (clostrubins) formed during *C. puniceum* infection. (**A**) Typical appearance of potato tubers stab-inoculated with pectinolytic clostridia. Scale bar, 1 cm. (**B**) HPLC profile of extract of diseased tubers showing clostrubin A (**1**) and clostrubin B (**2**) as main metabolites. (**C**) Structures of **1** and **2**. (**D**) Minimum inhibitory concentrations (MICs) of **1**, **2**, and Cip (ciprofloxacin) against selected potato pathogenic bacteria (black, *B. pumilus*; gray, *C. michiganensis*; white, *S. scabies*). (**E**) Organization of the clostrubin biosynthesis gene clusters in *C. puniceum* (*Cp*) and *C. beijerinckii* (*Cb*). (**F**) Phylogeny of the principal polyketide synthase components (maximum likelihood algorithm). ClrA(p) and ClrB(p), ClrA and ClrB from *C. puniceum*; ClrA(b) and ClrB(b), ClrA and ClrB from *C. beijerinckii*. (**G**) Genetic evidence for successful gene disruption; WT, wild type. (**H**) Photograph showing appearance of wild-type (left) and Δ*clr*A mutant (right) cultures.

the mutant. The mutant culture supplemented with clostrubin grew even faster than the wild type, likely because clostrubin was already present at the point of inoculation (fig. S11). The same phenotypes were observed for the wild type and Δ*clr*A mutant of *C. beijerinckii* (fig. S8). These findings show that oxygen tolerance is conferred by the presence of clostrubin.

To investigate the impact of the polyphenols in the context of infection, we quantified live and dead cells in the potato infection assay using the plant pathogen. We recovered the bacterial lawns of the wild type, mutant, and chemically complemented mutant of *C. puniceum* from the infected potato slices and subjected them to live/dead staining followed by fluorescence-activated cell sorter (FACS) analysis (Fig. 3B and fig. S10). In the absence of oxygen, similar ratios of living cells were detected in wild-type (97% live) and mutant (90.4% live) cultures. In the presence of oxygen, the situation was markedly different. Whereas 57% of the wild-type cells survived, no living cells of the Δ*clr*A mutant could be detected. Indeed, it was not even possible to recover the

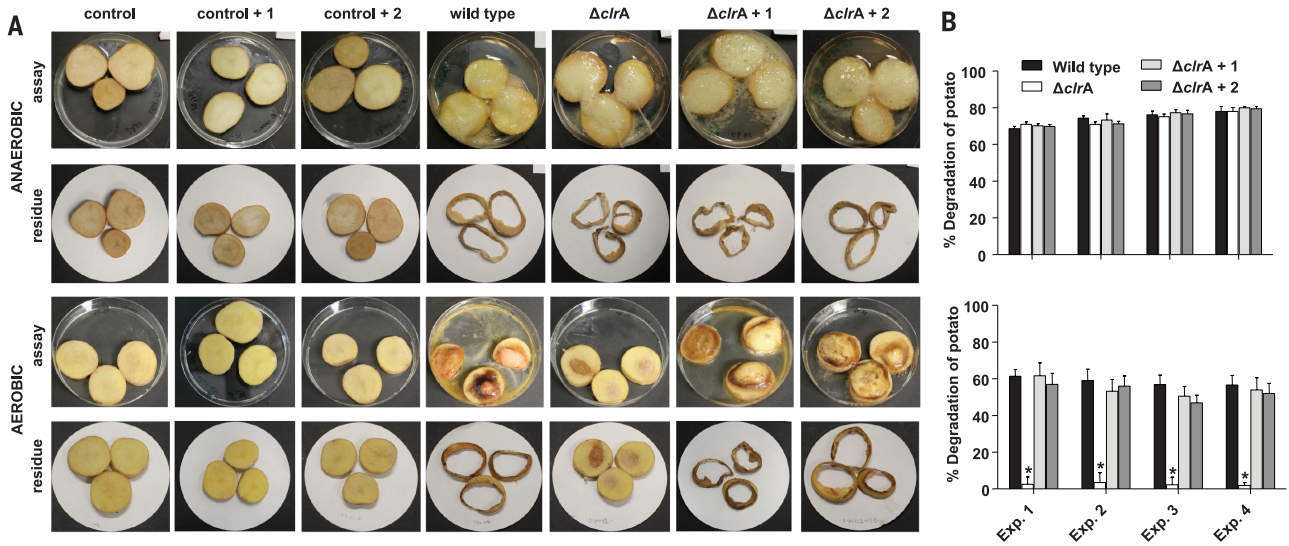

Fig. 2. Impact of clostrubins on slimy rot disease. Potato tuber infection assay was performed by measuring the degradation level of potato slices under anaerobic or aerobic conditions. (**A**) Potato slices were inoculated with 2 × 10^8 cells of wild-type, mutant, or mutant *C. puniceum* supplemented with solutions of **1** or **2**. (**B**) Summary and statistical evaluation of experiments. Under anaerobic conditions, bars were not significantly different ($P > 0.05$). Under aerobic conditions, the absence of clostrubin reduced potato degradation to <5%. *$P < 0.001$ [Bonferroni's means comparison test, two-way analysis of variance (ANOVA)]. Data (means ± SD) are representative of four independent experiments; each experiment was performed in six biological replicates with three tuber slices each.

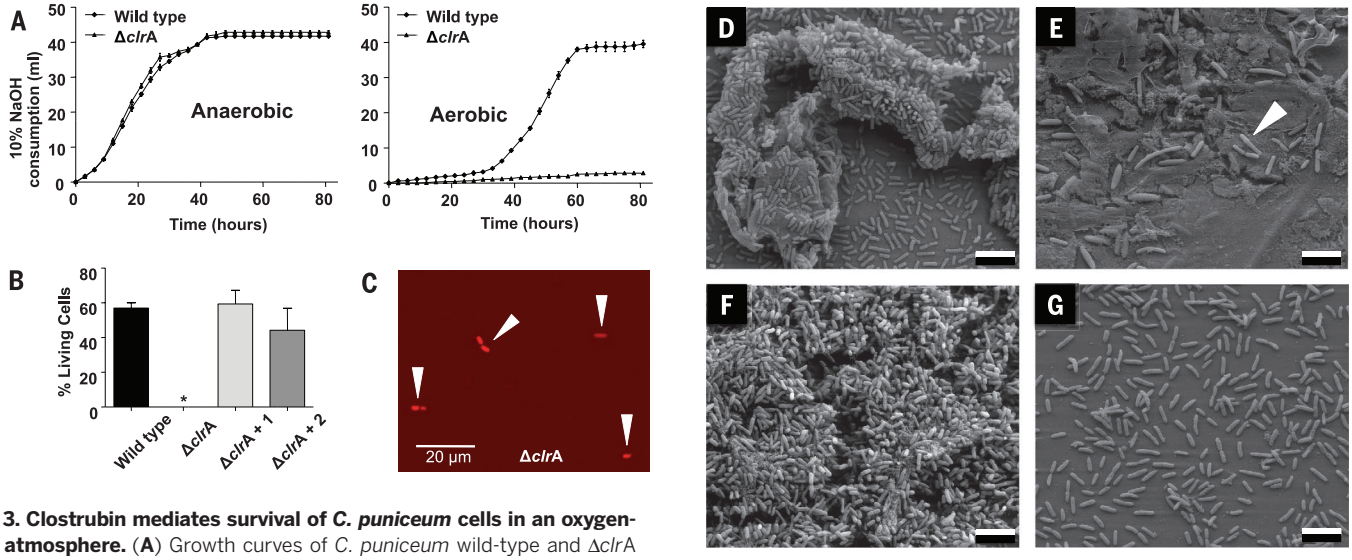

Fig. 3. Clostrubin mediates survival of *C. puniceum* cells in an oxygen-rich atmosphere. (**A**) Growth curves of *C. puniceum* wild-type and Δ*clr*A strains in P2 media (fermenter) under anaerobic and aerobic (pO_2 40%) conditions. Data are means ± SD. (**B**) Summarized results from live/dead flow cytometric assays [BacLight stain (ThermoFisher), FACS plots, and gating strategy for live/dead cell stain] of *C. puniceum* strains after 4 days of incubation on potato slices under aerobic conditions. Potato slices were inoculated with 2 × 10^8 cells of wild type, mutant, or chemically complemented mutant (solutions of **1** or **2**). Five independent FACS experiments consisted of five biological replicates. *$P < 0.001$ (Bonferroni's means comparison test, one-way ANOVA). Data are means ± SD. (**C**) Confocal fluorescence microscope image of dead Δ*clr*A cells (red, live/dead BacLight stain) recovered after 4 days of incubation on potato slices under aerobic conditions. (**D** to **G**) SEM images of *C. puniceum* cells from inoculated tubers after 2 days of incubation under aerobic conditions. (D) Wild type. (E) Δ*clr*A mutant; arrowhead highlights sporulating cell. (F) and (G) Chemically complemented mutant (with **1** and **2**, respectively). Scale bars, 2 µm.

appropriate number of mutant cells required for FACS analysis (1×10^6 cells ml^{-1}). Live/dead staining followed by fluorescence imaging revealed that all Δ*clr*A mutant cells were dead (Fig. 3C). However, chemical complementation of the mutant with clostrubins restored the viability (44 to 59% living cells). The impact of clostrubin on survival was evident within 2 days of inoculation under aerobic conditions. Scanning electron microscopy (SEM) showed differences between the wild type and the Δ*clr*A mutant cells, most of which were distinct from vegetative cells (Fig. 3, D to G). Again, chemically complemented mutants were similar to the wild type.

It would be conceivable that clostrubins interfere with the plant wound response, which involves the generation of hydrogen peroxide. Under anoxic conditions, H_2O_2 would not be generated, thus explaining why clostrubins are expendable under this condition. However, this scenario is unlikely because clostrubin is essential for bacterial survival in synthetic liquid medium (Fig. 3A) and on autoclaved potato infusion agar (Fig. 4A). We also tested whether hydrogen peroxide affects the growth of the wild type and/or mutant, but no significant difference in growth between the wild type and mutant was observed (Fig. 4B). Thus, the effect of clostrubin cannot be attributed to inactivating ROS formed in the context of plant defense mechanisms. Furthermore, an established assay [2,2-diphenyl-1-picrylhydrazyl (DPPH)] for testing radical scavengers was negative for clostrubin. Other standardized ROS assays were infeasible for clostrubin because of the interference of the absorption spectrum with the colorimetric assay methods. As an alternative, we performed functional profiling using a range of antioxidants that cover diverse ROS-scavenging activities (Fig. 4C). All compounds were tested for their ability to complement the effect of clostrubin. We supplemented antioxidants to potato tubers inoculated with the Δ*clr*A mutant; cell growth was determined by the bacterial pectolytic activity. We found that vitamin C and cysteine complementation were most similar to the effect of clostrubin. In contrast, uric acid and tocopherol proved to be less potent. At present, it is unclear exactly how clostrubin functions in its antioxidant capacity, and the next challenge for this work is to solve the mechanism of clostrubin action.

During the past decade, analyses of the enzymatic repertoire that confers oxygen tolerance upon obligate anaerobes have implicated enzymes that scavenge ROS (*26*). The comparison of clostrubin-positive and -negative clostridia shows that *C. puniceum* uses a different strategy to cope with an oxygen-rich environment, because the typical repertoire of ROS-inactivating genes is not sufficient for this plant pathogen to grow in the aerobic conditions of a potato tuber. Our data demonstrate that clostrubins promote survival of *C. puniceum* and *C. beijerinckii* under aerobic conditions. Thus, these clostridia are not obligate anaerobes but rather facultative anaerobes when producing clostrubins. By tolerating oxygen, the anaerobe gains access to an oxygen-rich plant environment.

Analysis of more than 210 published genome sequences of anaerobes did not reveal any *clr*-like gene loci. Thus, the involvement of aromatic polyketides in the aerobic growth of anaerobes is not a general phenomenon but a particular trait of individual clostrubin-positive strains. However, the presence of transposons (*tnp*) in vicinity of the *clr* locus indicates that the gene cluster is transferable to other bacteria.

In this context, it should also be highlighted that many bacteria use redox-active pigments, such as phenazines, as antibiotics to inhibit competitors (*27*) and which may also function as regulators that can even control community behavior (*28*). Notably, phenazine redox cycling may also enhance the anaerobic survival of pseudomonads (*29*), which is the reversal of the effect of clostrubins under aerobic conditions.

We have shown that clostrubin is essential for a pathogenic anaerobe to enter an oxygen-rich world. The clostrubins thus have a dual function in securing the niche of the plant pathogen, as they represent highly potent antibiotics against potential competitors in the aerobic environment. Clostrubin synthase may be a useful target for development of antibacterial therapeutics and plant-protective agents.

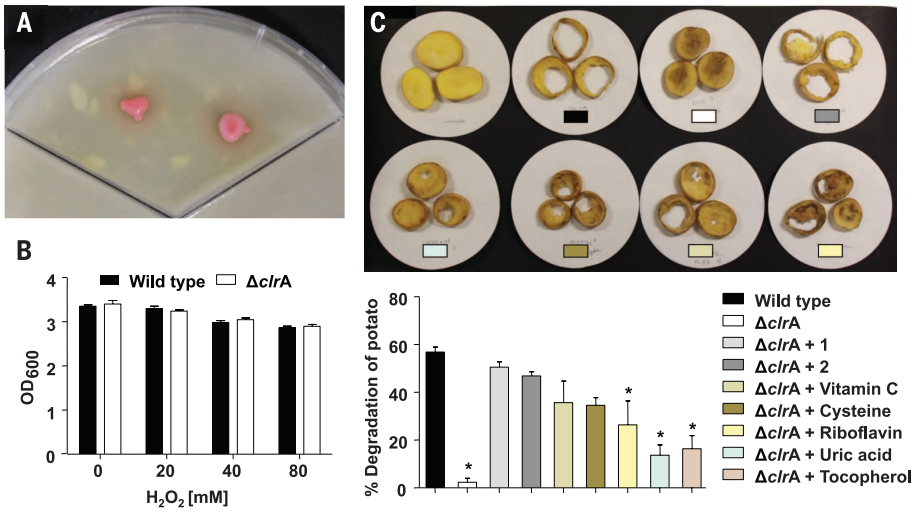

Fig. 4. Evaluation of the antioxidative effect of clostrubin. (**A**) Clostrubin production of *C. puniceum* wild-type strain on potato infusion agar after 4 days of incubation under aerobic conditions. (**B**) Survival of *C. puniceum* wild-type and Δ*clr*A mutant strains after exposure to H_2O_2, as assessed by optical density at 600 nm. Exponentially growing cells were incubated with different concentrations of H_2O_2 for 2 days; experiments were performed in three biological replicates. Data are means ± SD. Bars were not significantly different ($P > 0.05$). (**C**) Comparison of clostrubins with typical ROS-inactivating compounds. Potato tuber infection assay was performed by measuring degradation level of potato slices under aerobic conditions. Inoculation of potato slices was assessed with 2×10^8 cells of wild type, mutant, or mutant supplemented with 1 mM vitamin C, cysteine, riboflavin, uric acid, or tocopherol. Experiments were performed in six biological replicates with three tuber slices each; data are means ± SD. *$P < 0.001$, Bonferroni's means comparison test (one-way ANOVA). The photos show representative degraded potato tubers and the negative control (upper left).

REFERENCES AND NOTES

1. R. N. Strange, P. R. Scott, *Annu. Rev. Phytopathol.* **43**, 83–116 (2005).
2. E. C. Oerke, *J. Agric. Sci.* **144**, 31 (2006).
3. R. Czajkowski, M. C. Perombelon, J. A. van Veen, J. M. van der Wolf, *Plant Pathol.* **60**, 999–1013 (2011).
4. B. Lund, T. Brocklehurst, G. Wyatt, *J. Gen. Microbiol.* **122**, 17–26 (1981).
5. C. T. Bull *et al.*, *J. Plant Pathol.* **92**, 551–592 (2010).
6. B. M. Lund, *J. Appl. Bacteriol.* **35**, 609–614 (1972).
7. E. Campos, E. A. Maher, A. Kelman, *Plant Dis.* **66**, 543 (1982).
8. B. M. Lund, in *Phytopathogenic Prokaryotes*, M. S. Mount, G. H. Lacy, Eds. (Academic Press, New York, 1982), vol. 1, pp. 263–283.
9. S. Pidot, K. Ishida, M. Cyrulies, C. Hertweck, *Angew. Chem. Int. Ed.* **53**, 7856–7859 (2014).
10. A. H. Babana *et al.*, *Br. Microbiol. Res. J.* **1**, 41–48 (2011).
11. J. M. van der Wolf, S. H. De Boer, in *Potato Biology and Biotechnology, Advances and Perspectives*, D. Vreugdenhil *et al.*, Eds. (Elsevier, Oxford, 2007), pp. 595–617.
12. J. M. Raaijmakers, M. Mazzola, *Annu. Rev. Phytopathol.* **50**, 403–424 (2012).
13. F. E. J. Jenney Jr., M. F. Verhagen, X. Cui, M. W. Adams, *Science* **286**, 306–309 (1999).
14. M. Lombard, M. Fontecave, D. Touati, V. Nivière, *J. Biol. Chem.* **275**, 115–121 (2000).
15. L. B. Poole, *Arch. Biochem. Biophys.* **433**, 240–254 (2005).
16. F. Hillmann, R. J. Fischer, F. Saint-Prix, L. Girbal, H. Bahl, *Mol. Microbiol.* **68**, 848–860 (2008).
17. O. Riebe, R.-J. Fischer, D. A. Wampler Jr., H. Bahl, *Microbiology* **155**, 16–24 (2009).
18. C. Hertweck, A. Luzhetskyy, Y. Rebets, A. Bechthold, *Nat. Prod. Rep.* **24**, 162–190 (2007).
19. A. Sandmann *et al.*, *Angew. Chem. Int. Ed.* **46**, 2712–2716 (2007).
20. A. O. Brachmann *et al.*, *ChemBioChem* **8**, 1721–1728 (2007).
21. A.-C. Letzel, S. J. Pidot, C. Hertweck, *Nat. Prod. Rep.* **30**, 392–428 (2013).
22. S. F. Altschul *et al.*, *Nucleic Acids Res.* **25**, 3389–3402 (1997).

23. M. H. Medema *et al.*, *Nucleic Acids Res.* **39**, W339–W346 (2011).
24. K. Jakobi, C. Hertweck, *J. Am. Chem. Soc.* **126**, 2298–2299 (2004).
25. J. T. Heap, O. J. Pennington, S. T. Cartman, G. P. Carter, N. P. Minton, *J. Microbiol. Methods* **70**, 452–464 (2007).
26. J. A. Imlay, *Mol. Microbiol.* **68**, 801–804 (2008).
27. A. Price-Whelan, L. E. P. Dietrich, D. K. Newman, *Nat. Chem. Biol.* **2**, 71–78 (2006).
28. L. E. Dietrich, T. K. Teal, A. Price-Whelan, D. K. Newman, *Science* **321**, 1203–1206 (2008).
29. N. R. Glasser, S. E. Kern, D. K. Newman, *Mol. Microbiol.* **92**, 399–412 (2014).

ACKNOWLEDGMENTS

We thank A. Perner for MS measurements, H. Heinecke for NMR measurements, U. Knüpfer and M. Cyrulies for anaerobic fermentation support, K. Martin for assistance in sample preparation, S. Linde for recording micrographs, L. D. Halder for recording confocal fluorescence microscope images, and T. Stinear and T. Seemann for assistance with DNA sequencing and bioinformatic analyses. Supported by an Alexander von Humboldt Foundation fellowship (S.J.P.) and Deutsche Forschungsgemeinschaft grant SFB 1127 ChemBioSys. G.S., K.I., S.J.P., C.H., and the Leibniz Institute for Natural Product Research and Infection Biology (Hans Knoell Institute) have filed a patent application (WO 2015/113761 A1) that relates to the structures of clostrubins A and B and their biological activities. Author contributions: G.S., K.I., and C.H. designed the research; G.S., K.I., S.J.P., and C.H. prepared the manuscript; G.S. performed anaerobic/aerobic bacterial culture experiments, potato tuber infection experiments, and antibacterial assays and constructed the Δ*clrA* mutant; K.I. and S.J.P. isolated clostrubins; K.I. elucidated structures; S.J.P. performed full genome sequencing and bioinformatic analyses and constructed the *C. beijerinckii* Δ*clrA* mutant; H.-M.D. performed FACS analyses; and M.R. designed and supervised anaerobic cultivation in fermenters. Supplement contains additional data.

SUPPLEMENTARY MATERIALS

www.sciencemag.org/content/350/6261/670/suppl/DC1
Materials and Methods
Supplementary Text
Figs. S1 to S13
Tables S1 to S4
References (*30*–*42*)

10 July 2015; accepted 23 September 2015
10.1126/science.aac9990

OPHTHALMOLOGY

Pharmacological chaperone for α-crystallin partially restores transparency in cataract models

Leah N. Makley,[1]* Kathryn A. McMenimen,[1]* Brian T. DeVree,[3] Joshua W. Goldman,[2] Brittney N. McGlasson,[2] Ponni Rajagopal,[4] Bryan M. Dunyak,[1] Thomas J. McQuade,[5] Andrea D. Thompson,[1] Roger Sunahara,[3] Rachel E. Klevit,[4] Usha P. Andley,[2]† Jason E. Gestwicki[1,5]†

Cataracts reduce vision in 50% of individuals over 70 years of age and are a common form of blindness worldwide. Cataracts are caused when damage to the major lens crystallin proteins causes their misfolding and aggregation into insoluble amyloids. Using a thermal stability assay, we identified a class of molecules that bind α-crystallins (cryAA and cryAB) and reversed their aggregation in vitro. The most promising compound improved lens transparency in the R49C cryAA and R120G cryAB mouse models of hereditary cataract. It also partially restored protein solubility in the lenses of aged mice in vivo and in human lenses ex vivo. These findings suggest an approach to treating cataracts by stabilizing α-crystallins.

The mammalian lens grows by terminal differentiation of epithelial cells into elongated fiber cells. Protein synthesis and turnover in the mature fiber cell are halted, so that the proteins of the lens can remain soluble and transparent throughout life. This remarkable feat is accomplished, in part, by αA-crystallin (cryAA) and αB-crystallin (cryAB), which are molecular chaperones that belong to a family of small heat shock proteins (sHSPs) (*1*, *2*). Together, cryAA and cryAB constitute 30% of the protein content of the lens, where they help maintain the solubility of the other lens proteins, such as β- and γ-crystallins (*2*). Accumulated damage to these proteins over an individual's lifetime can lead to age-related nuclear cataracts, which are composed of aggregated crystallin proteins (*3*) (*2*, *4*–*6*). Clues to the mechanism(s) of age-associated cataracts come from hereditary forms of the disease, which are caused by mutations, such as R120G cryAB, that destabilize the lens proteins (*7*). For example, the R120G mutation disrupts ionic interactions that normally stabilize the cryAB dimer (fig. S1A). It is thought that the unstable protein then assembles into amyloid-like fibers, forming a physical barrier to light and also, in the case of cryAA or cryAB, reducing the available chaperone activity in the lens. Thus, one potential way to treat cataracts may be to identify molecules that bind and stabilize crystallins, favoring the soluble native forms (*8*).

Pharmacological chaperones (PCs) are small molecules that bind and stabilize a native state of a protein (*9*). A PC has been approved for clinical use in the treatment of transthyretin amyloidosis (*10*), and other PCs are being explored in late-stage clinical trials for use in treating a number of other misfolding diseases, such as Gaucher disease (*11*) and Anderson-Fabry disease (*12*). In the current work, we wanted to identify PCs that stabilize the soluble forms of cryAB to suppress its aggregation. Unlike previous targets for PC discovery (*11*), cryAB lacks natural substrates that are suitable as a starting point for drug design (*13*). Moreover, cryAB has no enzymatic activity, making it more difficult to envision a convenient high-throughput screen (HTS) strategy (*10*). These features place cryAB in a family of disease-associated proteins, including tau, myocilin, α-synuclein, and huntingtin, that are often considered to be "undruggable" (*14*, *15*).

We wondered whether differential scanning fluorimetry (DSF) might provide a way to circumvent some of these challenges. In a typical DSF experiment, an apparent melting transition (T_m) of the protein target is measured in the presence of potential ligands (*16*). Binding of a ligand usually adds free energy to the state that it binds, shifting the apparent T_m. DSF has been used for decades in biochemical studies but has only recently been adapted for high throughput (*15*, *17*–*19*). To see if high-throughput DSF might be applicable to the discovery of PCs for cryAB, we first purified recombinant human R120G cryAB and wild-type cryAB and confirmed that both proteins were soluble and nonaggregated in solution (fig. S1B) (*20*). Upon gentle heating, R120G cryAB formed amyloids more readily than did wild-type cryAB, as measured by light scattering and electron microscopy (EM) (fig. S1, Aa and Ab). Because amyloids are relatively heat-resistant structures, we suspected that samples of R120G cryAB might be more difficult to melt. To investigate this possibility, R120G cryAB and wild-type cryAB were heated in the ThermoFluor DSF platform. Consistent with the model, the apparent T_m of wild-type cryAB was 64.1° ± 0.5°C, whereas the T_m of the R120G cryAB mutant was 68.3° ± 0.2°C (fig. S1Ac). Based on these observations, we hypothesized that molecules able to reduce the apparent T_m of R120G cryAB might be good candidates.

For the pilot screens, we turned to the model protein Hsp27. Hsp27 was used because, although it retains the highly conserved crystallin domain found in cryAA and cryAB (fig. S1C), we found

[1]Departments of Pathology, Biological Chemistry, and Medicinal Chemistry and the Life Sciences Institute, University of Michigan, Ann Arbor, MI, USA. [2]Department of Ophthalmology and Visual Sciences, Washington University School of Medicine, St. Louis, MO, USA. [3]Department of Pharmacology, University of Michigan, Ann Arbor, MI, USA. [4]Department of Biochemistry, University of Washington, Seattle, WA, USA. [5]Center for Chemical Genomics, University of Michigan, Ann Arbor, MI, USA.
*These authors contributed equally to this work. **†Corresponding author. E-mail: jason.gestwicki@ucsf.edu (J.E.G.); andley@vision.wustl.edu (U.P.A.)**

Downloaded from www.sciencemag.org on November 5, 2015

that it had a relatively high melting transition (T_m = 72°C by three independent biophysical methods; fig. S1D). This feature provided a superior signal:noise ratio in the high-throughput DSF platform, with Z′ factor values, a measure of assay robustness, between 0.5 and 0.8 and an average coefficient of variation of 8% at a final volume of only 7 μl in 384-well plates. Accordingly, we screened ~2450 compounds from the MS2000 and NCC collections at a screening concentration between 20 and 40 μM. These compound collections include both natural and synthetic molecules that are known to have activity in a wide variety of assays. The primary screen identified 45 compounds (1.8%) that decreased the apparent T_m by at least three standard deviations (±0.6°C) (Fig. 1B). All 45 of these "actives" were explored in dose-dependence experiments, revealing 32 (71%; 1.3% overall) that decreased the T_m at half-maximal concentrations less than 20 μM. Twelve of the 32 confirmed actives belonged to a single class of related sterols, so we selected this scaffold for further investigation. One of the weakly active sterols was lanosterol. While this manuscript was under review, Zhao *et al.* reported that lanosterol has anti-cataract activity (*21*). However, this compound has limited solubility, and it was only weakly active by HT-DSF, which inspired us to collect 32 additional sterols similar to compound 1 and screen them against R120G cryAB using the DSF procedure. Two compounds (28, 5α-cholestan-3b-ol-6-one; and 29, 5-cholesten-3b,25-diol) were at least two to three times more potent than sterol 1 (Fig. 1C), reducing the apparent T_m by at least 2°C (Fig. 1D and fig. S2, A and E). Many of the other sterols were inactive, suggesting a specific interaction. For example, compound 16 is structurally related to compounds 28 and 29 (fig. S2B), yet it was inactive (Fig. 1D). To confirm the direct interaction of compound 29 with R120G cryAB, we used biolayer interferometry. Immobilized R120G cryAB bound to compound 29 with a dissociation constant (K_d) of 10.1 ± 4.4 μM (Fig. 1D and fig. S2, C and D), whereas compound 16 did not bind (K_d > 50 μM). To examine where on R120G cryAB this interaction takes place, we used ^{15}N–heteronuclear single quantum coherence nuclear magnetic resonance (NMR) experiments to show that compound 29, but not compound 16, bound to the crystallin domain at the dimer interface (fig. S3, A to C). Based on the chemical shift perturbations, we docked compound 29 to cryAB, revealing that this compound fits into a groove that lies between the two protomers (Fig. 2B). In this configuration, compound 29 is predicted to make contacts with both cryAB subunits, suggesting that it might stabilize the native state.

To test whether compound 29 might block amyloid formation, we treated R120G cryAB (15 μM) with compounds 29 or 16 (100 μM), and the extent of aggregation was examined by EM. These studies confirmed that compound 29, but not 16 or the vehicle control, partially suppressed amyloid formation when added before the initiation of aggregation (Fig. 2A). To test whether 29 might also have an effect on pre-formed aggregates, we pre-generated R120G cryAB amyloids and then treated them with compound 29 or 16. Again, compound 29, but not 16, was able to partially reverse amyloid formation (Fig. 2A). The reversal took approximately 2 days, suggesting a slow equilibrium between the amyloid and the soluble forms of cryAB. To quantify these activities, we again treated R120G cryAB with 29 or 16, then

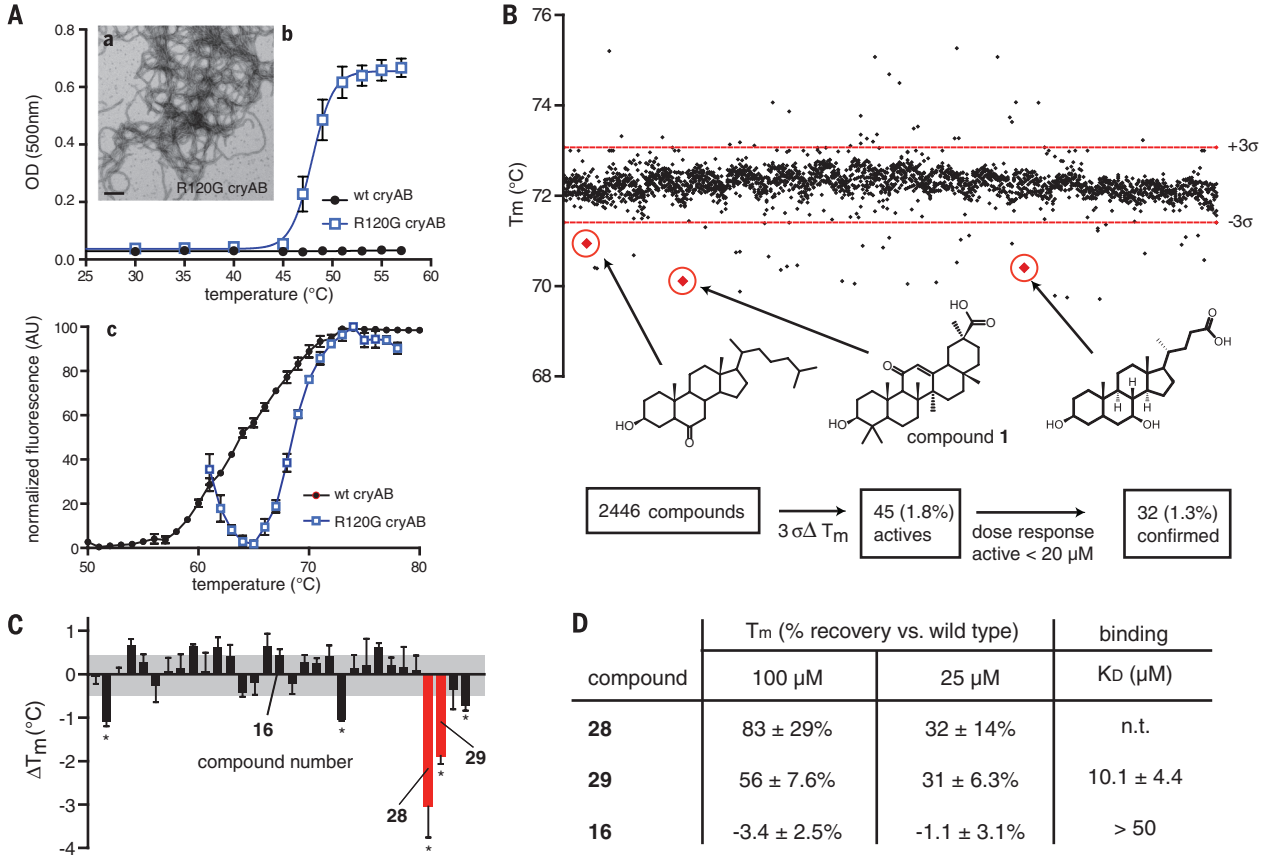

compound	Tm (% recovery vs. wild type) 100 μM	Tm (% recovery vs. wild type) 25 μM	binding KD (μM)
28	83 ± 29%	32 ± 14%	n.t.
29	56 ± 7.6%	31 ± 6.3%	10.1 ± 4.4
16	-3.4 ± 2.5%	-1.1 ± 3.1%	> 50

Fig. 1. A HT-DSF screen identifies pharmacological chaperones for a small HSP. (**A**) The R120G mutant of cryAB (blue) forms heat-resistant amyloids, as judged by EM (a), light scattering (b), and DSF (c). Wild-type (wt) cryAB (black) is more resistant to misfolding and has a lower melting transition by DSF, but will form amyloids under harsher conditions (fig. S1). Results are the average of triplicates, and error bars represent SEM. Microscopy results are representative of studies on at least three independent samples. Scale bar, 0.25 μm. (**B**) Summary of DSF screen against Hsp27. The structures of three active sterols are shown. (**C**) A collection of 32 sterols, based on compound 1, were screened at 20 μM for the ability to restore the T_m of R120G cryAB. Compounds 28 and 29 were two to three times more potent than the initial active molecule. (**D**) Compounds 28 and 29, but not the control compound 16, partially restored the T_m of R120G cryAB and bound to the protein. Results are the average of at least triplicates, and error is SEM.

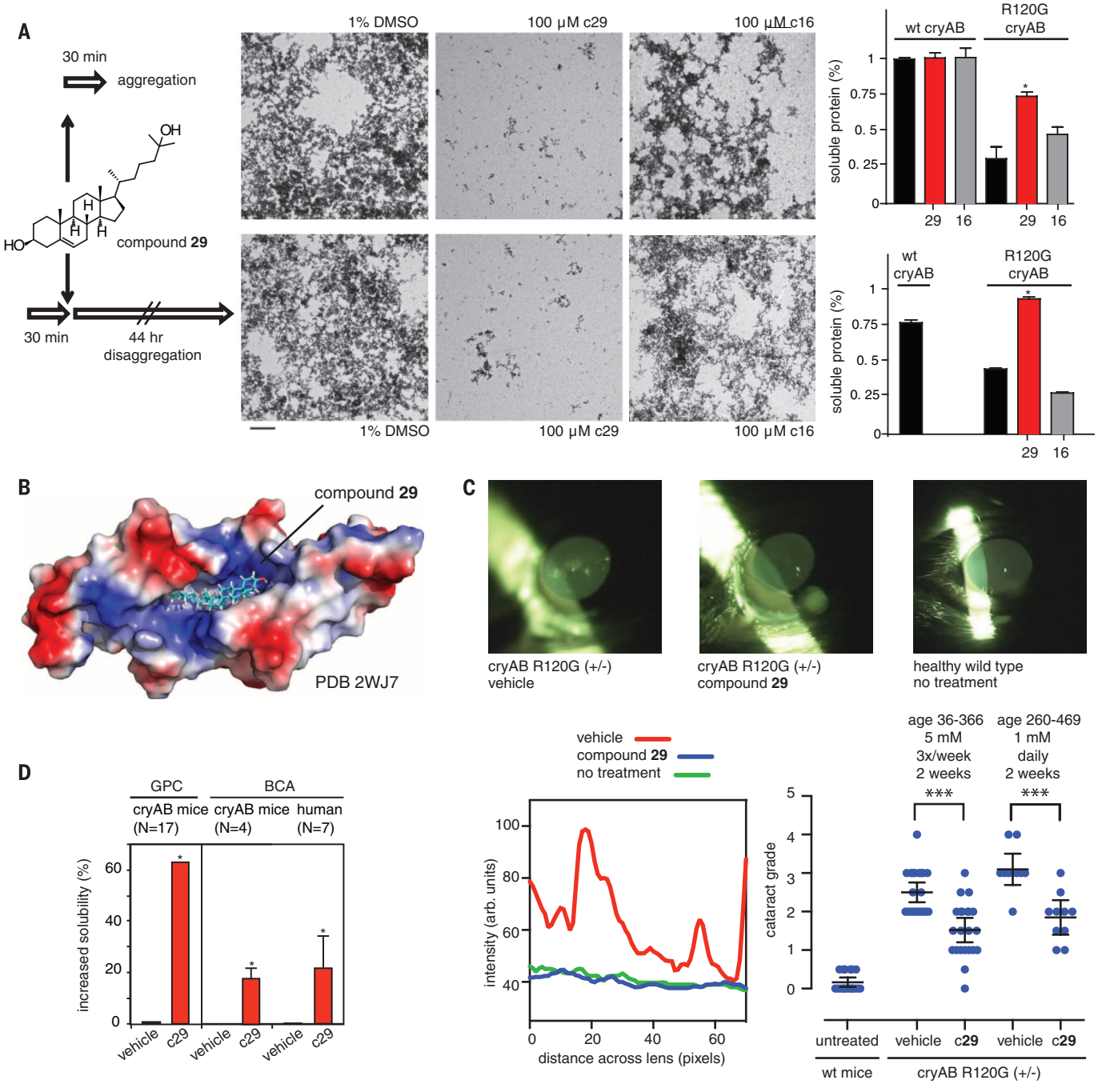

Fig. 2. Compound 29 reverses cataract formation in vitro and in the R120G cryAB knockin mouse. (**A**) Purified R120G cryAB (20 µM) was treated with compound 29 (100 µM), 16 (100 µM,) or a DMSO control (1%) and then aggregated at ambient temperature with shaking for 30 min for the aggregation study. For the disaggregation study, amyloid fibrils were formed using the conditions above (40 µM), and then the samples were treated with 100 µM compound. Aliquots were visualized at 44 hours after treatment. Samples were visualized by EM and then centrifuged to remove insoluble material. The levels of soluble and insoluble R120G cryAB were assessed by absorbance at 280 nm. Results are the average of independent triplicates, and the error bars represent SEM. Electron micrographs are representative of independent triplicates. Scale bar, 1 µm. (**B**) Docking of compound 29 to the crystallin domain of cryAB, based on NMR titrations and chemical shift perturbations (see the supplementary materials for details). (**C**) Summary of the treatment of R120G cryAB knockin mice with compound 29. Slit lamp images and corresponding densitometry plots are shown for wild-type mice aged 60 to 240 days; cryAB R120G heterozygotes aged 66 to 366 days, treated with vehicle control or 29 (5 mM) every other day for 2 weeks; and cryAB R120G heterozygotes aged 260 to 469 days treated with vehicle or compound 29 (1 mM) daily for 2 weeks. The transparency of the treated mice was measured using a LOCS III scoring system on masked images. In both dosing schedules, compound 29 significantly improved transparency ($P < 0.001$). (**D**) Treatment with compound 29 improved the solubility of mouse and human lens proteins, as measured by BCA assays.

separated the insoluble and soluble material by centrifugation and measured the amount of protein in these fractions using bicinchininic acid (BCA) assays. Consistent with the EM results, compound 29, but not 16 or the vehicle control, shifted cryAB into the soluble fraction when added either before or after aggregation (Fig. 2A). Together, these results show that compound 29 can block aggregation and partially reverse R120G cryAB insolubility in vitro. To test whether this activity was restricted to the R120G model, we next used the DSF platform to test whether compound 29 could restore the solubility of other cataract-associated proteins. We found that compound 29 could improve the T_m of three mutants in cryAA (R49C, F71L, and R116C) by at least 2°C (fig. S4). This effect might be expected, because cryAA and cryAB are highly conserved, especially in the region that binds compound 29 (fig. S1C). However, compound 29 had no effect on two mutants of the structurally unrelated lens protein γ-crystallin (P23T or W42R cryGD) (fig. S4), which lacks the α-crystallin domain. Thus, compound 29 appears to bind a specific region of cryAA and cryAB to restore solubility and partially reverse aggregation.

The R120G cryAB knockin mouse develops severe age-associated cataracts, with 100% showing lens opacities by 20 weeks of age (*22*). To test whether compound 29 can reverse this process, a single drop of compound 29 or vehicle (cyclodextrin) was delivered to the right eye of aged R120G cryAB knockin mice three times per week for 2 weeks. These mice had already developed severe cataracts before the treatments. Lens opacity was then assessed with a video slit lamp and scored using a five-grade scale adapted from the Lens Opacities Classification System III (LOCS III) cataract scoring system. In heterozygous R120G cryAB mice (age 36 to 366 days), we observed a substantial improvement in lens opacity grade (lens opacity grade 0.98 ± 0.46; n = 22; P < 0.001) (Fig. 2C). Compound 16 was inactive (lens opacity grade 2 ± 0; n = 3; P > 0.2). The effect of compound 29 was striking by visual inspection (Fig. 2C), quantification of the pixel intensities (Fig. 2C), or quantitative reconstructions of the slit lamp videos (fig. S5). To examine the durability of this effect, we examined the mice 4 weeks after ending treatment with compound 29. In these mice, the LOCS III cataract score was indistinguishable from the values taken immediately after treatment (lens opacity grade ~1.0). The cataracts in R120G cryAB mice become more dramatic with age. To test whether compound 29 could act on these cataracts, a second group of older heterozygotes was treated with a 1 mM solution three times per week for 2 weeks, revealing that lens opacity was significantly improved (lens opacity grade 1.25 ± 0.46; n = 10; P < 0.001) (Fig. 2C). Thus, compound 29 could even partially restore the transparency of older cryAB R120G heterozygous mice.

The R49C cryAA heterozygous knockin mouse also develops cataracts. To investigate the effect of compound 29 on this second model of hereditary cataract, we treated mice with 5 mM compound 29 or vehicle control three times per week for 4 weeks. We found that the lens transparency was significantly increased (lens opacity grade 1.11 ± 0.72; n = 14; P < 0.001) (fig. S6A). Similarly, a second group of R49C cryAA heterozygotes was treated with a lower dose (1 mM solution of compound 29) three times per week for 2 weeks, showing similar efficacy (lens opacity grade 1.3 ± 0.51; n = 5; P = 0.006) (fig.. S6A). Thus, compound 29 could partially restore transparency to two distinct models of hereditary cataract.

Although cataracts and the amount of total insoluble lens protein are only indirectly related (*1*), an improvement in overall protein solubility might be expected for compounds that have substantial anti-aggregation activity. To test whether compound 29 could restore protein solubility, we separated the soluble and insoluble fractions of treated lenses by centrifugation and measured the amount of crystallins (α, β, and γ) by gel permeation chromatography (GPC). We found that compound 29 improved the solubility of the α-crystallins (including cryAA and cryAB) by 63% (S6B). Moreover, the shape of this curve was similar to that of the untreated α-crystallins, suggesting that compound 29 favors a normal structure of the proteins. To verify this finding using a different method, we measured the total amount of soluble and insoluble protein in a subset of the treated lenses by BCA assays. Consistent with this model, compound 29 increased the ratio of soluble:insoluble protein by 16 ± 5% (Fig. 2D). Again, older heterozygous mice showed a more robust response (fig. S6C).

Hereditary cataracts are relatively rare in humans, so we next explored whether compound 29 might have an effect on the more prevalent, age-related cataracts. The exact mechanisms of age-associated cataracts are not clear, but are likely to involve oxidative and other damage to crystallin proteins, resulting in aggregation. Five C57BL/6J wild-type mice (aged 118 to 263 days) with spontaneous age-associated opacities were treated with compound 29 for 2 weeks and then examined by slit lamp biomicroscopy. We found that compound 29, but not vehicle control, improved transparency by at least one grade on the LOCS III scoring system in four of the five mice. Finally, we collected lens material from human patients (aged 63 to 80 years) with grade 1 to 4 cataracts and treated them with either vehicle or compound 29 for 6 days ex vivo. Compound 29, but not the vehicle, increased the amount of soluble protein by 18%, as assessed by BCA assays (Fig. 2D and fig. S6D). Thus, compound 29 may be a promising lead toward the nonsurgical treatment of both hereditary and age-associated cataracts. This molecule partially reversed protein aggregation by binding and stabilizing the more soluble forms of cryAA and cryAB, suggesting that it is a PC for these crystallins. Based on the in vitro, in vivo, and ex vivo studies, we suggest that compound 29 stabilizes the native forms of cryAB, which are in slow equilibrium with the amyloid forms. Once stabilized, the bound cryAB is less likely to misfold, a key feature of a PC. The GPC results also suggest that the treated cryAB is now partly capable of keeping other lens crystallin proteins soluble, suggesting that its chaperone activity is at least partially intact. Finally, and more broadly, these findings suggest that DSF-based HTS campaigns might be ideally suited for identifying PCs with activity against other "undruggable" targets.

REFERENCES AND NOTES

1. H. Bloemendal *et al.*, *Prog. Biophys. Mol. Biol.* **86**, 407–485 (2004).
2. M. Haslbeck, T. Franzmann, D. Weinfurtner, J. Buchner, *Nat. Struct. Mol. Biol.* **12**, 842–846 (2005).
3. H. M. Leibowitz *et al.*, *Surv. Ophthalmol.* **24**, 335–610 (1980).
4. S. Meehan *et al.*, *J. Biol. Chem.* **279**, 3413–3419 (2004).
5. S. Meehan *et al.*, *J. Mol. Biol.* **372**, 470–484 (2007).
6. A. Pande *et al.*, *Proc. Natl. Acad. Sci. U.S.A.* **98**, 6116–6120 (2001).
7. P. Vicart *et al.*, *Nat. Genet.* **20**, 92–95 (1998).
8. K. L. Moreau, J. A. King, *Trends Mol. Med.* **18**, 273–282 (2012).
9. F. E. Cohen, J. W. Kelly, *Nature* **426**, 905–909 (2003).
10. P. Hammarström, R. L. Wiseman, E. T. Powers, J. W. Kelly, *Science* **299**, 713–716 (2003).
11. A. R. Sawkar, W. D'Haeze, J. W. Kelly, *Cell. Mol. Life Sci.* **63**, 1179–1192 (2006).
12. J. Q. Fan, S. Ishii, *FEBS J.* **274**, 4962–4971 (2007).
13. A. Biswas, K. P. Das, *J. Biol. Chem.* **279**, 42648–42657 (2004).
14. L. N. Makley, J. E. Gestwicki, *Chem. Biol. Drug Des.* **81**, 22–32 (2013).
15. J. N. Burns *et al.*, *ACS Chem. Biol.* **5**, 477–487 (2010).
16. M. D. Cummings, M. A. Farnum, M. I. Nelen, *J. Biomol. Screen.* **11**, 854–863 (2006).
17. O. Fedorov, F. H. Niesen, S. Knapp, *Methods Mol. Biol.* **795**, 109–118 (2012).
18. L. L. Major, T. K. Smith, *Mol. Biol. Int.* **2011**, 389364 (2011).
19. J. J. Lavinder, S. B. Hari, B. J. Sullivan, T. J. Magliery, *J. Am. Chem. Soc.* **131**, 3794–3795 (2009).
20. Materials and methods are available as supplementary materials on *Science* Online
21. L. Zhao *et al.*, *Nature* **523**, 607–611 (2015).
22. U. P. Andley, P. D. Hamilton, N. Ravi, C. C. Weihl, *PLOS ONE* **6**, e17671 (2011).

ACKNOWLEDGMENTS

We thank J.–M. Fontaine for wild-type cryAB. This work was supported by NIH grants EY017370, EY05681, EY02687, UL1RR024986, and GM007767 and a predoctoral fellowship from the American Foundation for Pharmaceutical Education (L.N.M.). This work was also supported by a grant from Research to Prevent Blindness. J.E.G. is a co-founder of, and is on the Scientific Advisory Board of, Viewpoint Therapeutics, a biotechnology company developing treatments for cataract. L.N.M. is a co-founder and Chief Scientific Officer of Viewpoint Therapeutics. U.P.A. is on the Scientific Advisory Board of, and has stock options in, Viewpoint Therapeutics. The Regents of the University of Michigan hold U.S. Patent 13/944477 covering the method of using oxysterols to treat eye diseases. In addition, Viewpoint Therapeutics has filed provisional patent applications covering unrelated small molecules predicted to bind cryAB.

SUPPLEMENTARY MATERIALS

www.sciencemag.org/content/350/6261/674/suppl/DC1
Materials and Methods
Figs. S1 to S6
References (*23–30*)

10.1126/science.aac9145

PROTEIN SYNTHESIS

Operon structure and cotranslational subunit association direct protein assembly in bacteria

Yu-Wei Shieh,[1] Pablo Minguez,[2] Peer Bork,[2,3] Josef J. Auburger,[1] D. Lys Guilbride,[1,4] Günter Kramer,[1]* Bernd Bukau[1]*

Assembly of protein complexes is considered a posttranslational process involving random collision of subunits. We show that within the *Escherichia coli* cytosol, bacterial luciferase subunits LuxA and LuxB assemble into complexes close to the site of subunit synthesis. Assembly efficiency decreases markedly if subunits are synthesized on separate messenger RNAs from genes integrated at distant chromosomal sites. Subunit assembly initiates cotranslationally on nascent LuxB in vivo. The ribosome-associated chaperone trigger factor delays the onset of cotranslational interactions until the LuxB dimer interface is fully exposed. Protein assembly is thus directly coupled to the translation process and involves spatially confined, actively chaperoned cotranslational subunit interactions. Bacterial gene organization into operons therefore reflects a fundamental cotranslational mechanism for spatial and temporal regulation that is vital to effective assembly of protein complexes.

Oligomeric protein complexes are thought to assemble by diffusion and random collision of subunits within the cytosol (*1*) ["trans-assembly" (fig. S1)]. However, this mechanism does not explain how unassembled subunits avoid nonspecific interactions, aggregation, and quality control sequestration to proteases and chaperones or how subunits navigate crowded and occluded cellular environments. We postulated that for complex subunits translated from polycistronic mRNAs, local confinement of assembly around the translation sites ["cis-assembly" (fig. S1)] would promote efficient, nonstochastic assembly.

To test our hypothesis, we used the bacterial *Vibrio harveyi* heterodimeric luciferase complex, which contains the subunits LuxA (α) and LuxB (β) (*2*), encoded by the *luxCDABE* operon (*3*). To express *luxA* and *luxB* from the same or distinct operons, we integrated plasmids harboring artificial *lux* operons (fig. S2B) into the *Escherichia coli* chromosome at distinct sites (fig. S2A). We fused genes encoding monomeric variant forms of enhanced yellow fluorescent protein (YFP) or cyan fluorescent protein (CFP) to the 5′ end of each *lux* gene (fig. S2B). We created four different strains (1 through 4 in Fig. 1A), each with two artificial operons carrying different tag configurations of the *yfp/cfp-luxA* and *yfp/cfp-luxB* fusion genes integrated into the chromosome (see supplementary materials and methods).

To assess luciferase assembly in the vicinity of synthesis, we assayed specific luciferase activities and fluorescence resonance energy transfer (FRET) efficiencies in strains 1 and 2 (Fig. 1A). Both strains encode *luxA* followed by *luxB* in each operon. The FRET pair (YFP and CFP) in strain 1 tags LuxA and LuxB within each operon, whereas in strain 2, YFP tags both LuxA and LuxB subunits in one operon and CFP tags both subunits in the other. The strains exhibit similar specific luciferase activities (Fig. 1B, left, and fig. S3A), consistent with the identical genetic order of *luxA* and *luxB* within the operons. However, strain 2, which encodes each partner of the FRET

[1]Center for Molecular Biology of the University of Heidelberg (ZMBH) and German Cancer Research Center (DKFZ), DKFZ-ZMBH Alliance, Im Neuenheimer Feld 282, Heidelberg D-69120, Germany. [2]European Molecular Biology Laboratory (EMBL), Meyerhofstrasse 1, 69117 Heidelberg, Germany. [3]Max-Delbrück-Centre for Molecular Medicine, Robert-Rössle-Strasse 10, 13125 Berlin, Germany. [4]Malaria Research Foundation, Post Office Box 10420, Aspen, CO 81612, USA.
*Corresponding author. E-mail: bukau@zmbh.uni-heidelberg.de (B.B.); g.kramer@zmbh.uni-heidelberg.de (G.K.)

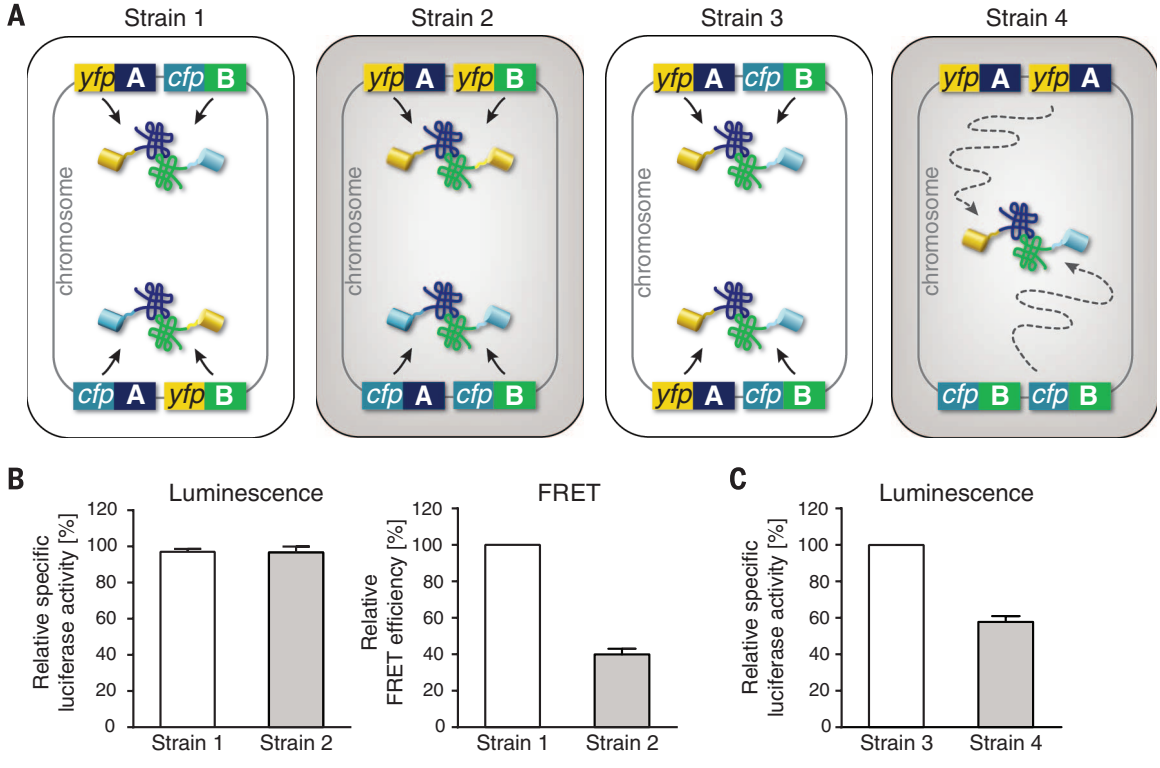

Fig. 1. Assembly of bacterial luciferase. (**A**) *E. coli* strains 1 to 4 with two bicistronic operons integrated into the chromosome. Operons encode fluorescently tagged *luxA* or *luxB* genes under control of isopropyl-β-D-thiogalactopyranoside–inducible promoters and strong Shine-Dalgarno sequences. (**B**) Relative specific luciferase activities (mean ± SEM, $n = 3$ replicates, unpaired t test, $P = 0.9207$) (fig. S3A) and relative FRET efficiencies (mean ± SEM, $n = 3$, unpaired t test, $P < 0.0001$) of strains 1 and 2 determined in vivo. (**C**) Relative specific luciferase activities of strains 3 and 4 determined in vivo (mean ± SEM, $n = 19$, unpaired t test, $P < 0.0001$) (fig. S3B, right). We used GraphPad Prism 6 software for the significance tests.

Downloaded from www.sciencemag.org on November 5, 2015

pair in separate operons, displays only 40 ± 3% of the FRET efficiency of strain 1, which encodes the FRET pair within each operon (Fig. 1B, right). This observation demonstrates that bacterial luciferase heterodimers are predominantly assembled in a cis configuration from subunits synthesized from the same bicistronic mRNA molecule.

To establish whether operon organization promoting cis-assembly confers any advantage to the assembly process, we compared specific luciferase activities in cells where *luxA* and *luxB* are expressed from the same (strain 3) or separate (strain 4) operons (Fig. 1A). Expression levels for the fusion proteins are comparable between the two strains (fig. S3B). Expression from separate mRNAs (strain 4), however, shows only 60 ± 3% of the specific luciferase activity measured in strain 3 (Fig. 1C). This difference was not caused by subunit aggregation (fig. S3C). Synthesis of complex subunits from one bicistronic mRNA encoded by an operon therefore strongly increases the efficiency of cis-assembly compared with trans-assembly.

We postulated that complexes might be assembled cotranslationally, effectively preempting pre-assembly diffusion. We used selective ribosome profiling (SeRP) to uncover any nascent subunit interactions during luciferase complex assembly in vivo (*4*). This method (*4*, *5*) allowed us to compare the distribution profile of nuclease-protected mRNA fragments (ribosome footprints) isolated from all translating ribosomes to the profile of ribosomes selected by immunopurification (IP) of YFP-tagged luciferase subunits (fig. S4A, IP ribosomes). We constructed two strains of *E. coli* (strains 5 and 6), each containing a single luciferase operon where either *luxA* (strain 6) or *luxB* (strain 5), but not both, is fused at the 5′ end with *yfp* (fig. S4B). Genetic fusion of YFP to LuxA or LuxB N termini allows enrichment of potentially two classes of translating ribosomes: those directly translating the YFP-Lux protein (fig. S4A, IP part) versus those translating the untagged partner subunit, if and when cotranslational engagement of the YFP-Lux protein occurs (fig. S4A, co-IP part). The N-terminal YFP tagging allows IP of the first class of ribosomes engaged with the YFP-tagged subunit. Independent selection of *yfp-luxB* (strain 5) and *yfp-luxA* (strain 6) gene products generates a profile for each that shows strong ribosome footprint enrichment once the YFP part (248 residues) of the nascent YFP-LuxB and YFP-LuxA chains has emerged (fig. S5, upper panel), confirming that IP is highly selective.

We then compared the density of ribosome footprints across *lux* genes of both data sets, the immunopurified ribosomes and the total pool of all ribosomes. We find strong evidence for the second class of translating ribosomes: IP of YFP-LuxA copurifies ribosomes synthesizing LuxB, which directly demonstrates that nascent LuxB cotranslationally interacts with YFP-LuxA [Fig. 2A, right, without trigger factor (TF)]. This interaction is unlikely to occur after cell lysis because the crowded cytoplasm becomes highly diluted, which greatly reduces the possibility of nascent subunit interactions (supplementary text). As translation of *luxB* starts, footprint enrichment (reflecting interaction with YFP-LuxA) fluctuates around background levels but rises with increasing length of nascent LuxB. We defined a stable twofold enrichment threshold to reliably indicate initiation of cotranslational subunit interactions. According to this threshold, interaction of YFP-LuxA with nascent LuxB starts after ~120 residues of LuxB are synthesized and becomes more robust with increasing length until a 20-fold enrichment, reflecting strongly interacting subunits, is reached near the termination of *luxB* translation. Assuming the ribosomal exit tunnel protects 30 C-terminal residues, emergence of the 90 N-terminal residues of LuxB is evidently sufficient to initiate the assembly interactions. We also detected interactions of YFP-LuxB with nascent LuxA, at much lower enrichment (maximally sixfold), reflecting less robust interactions (Fig. 2A, left, without TF). We conclude that both nascent luciferase subunits can initiate complex assembly, but cotranslational assembly initiates predominantly on nascent LuxB.

For these experiments, we used a Δ*tig* mutant background lacking the ribosome-associated TF

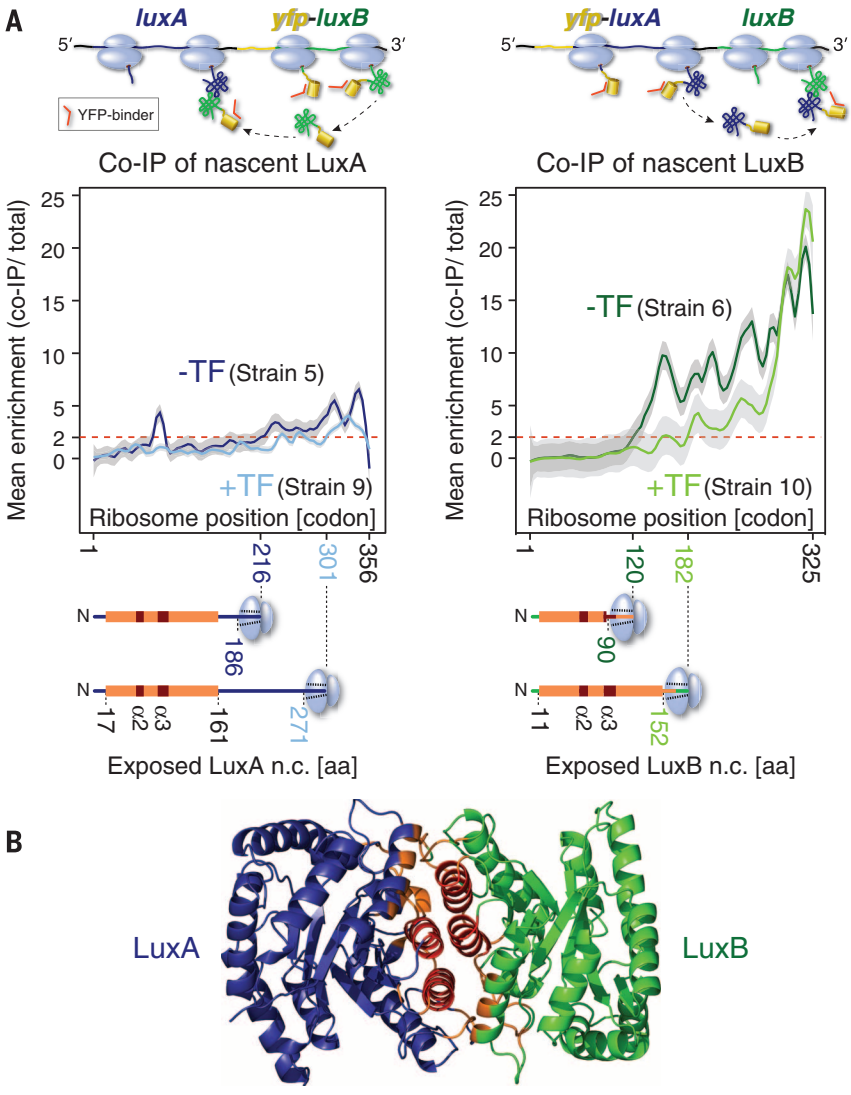

Fig. 2. Assembly of bacterial luciferase occurs cotranslationally. (**A**) Engagement of (left) nascent LuxA by YFP-LuxB and (right) nascent LuxB by YFP-LuxA without TF (strains 5 and 6, –TF) or with TF (strains 9 and 10, +TF). (Top) Cartoons illustrate *luxA* and *luxB* operons and the principle of SeRP analysis (fig. S4A). (Middle) Mean enrichments were corrected for nonspecific background binding analyzed with strains 11 and 12 (fig. S7A and table S2). Gray zones denote local regression curves (span parameter = 0.1) with a 95% confidence interval. Colored numbers indicate ribosome positions when the mean enrichments stably cross the twofold threshold. (Bottom) Cartoons show exposed nascent chain (n.c.) lengths. Orange, dimer interface; red, helices α2 and α3. aa, amino acids. (**B**) Crystal structure of the heterodimer of LuxA (blue) and LuxB (green) (Protein Data Bank accession code 1LUC). Orange, dimer interface; red, helices α2 and α3. LuxA and LuxB subunit residues involved in subunit interaction are listed in table S1.

chaperone. TF interacts transiently with most nascent cytosolic proteins a nascent chain with minimal average length of ~110 residues is synthesized (*4*). To test the effect of TF, we expressed wild-type levels of TF in strains 3 and 4 (making strains 7 and 8, respectively) and strains 5 and 6 (making strains 9 and 10). In vivo luciferase activity measurements of strains 7 and 8 indicate no effect of TF on the enhanced efficiency of cis-assembly (fig. S6). However, SeRP experiments of strains 9 (*yfp-luxB* in bicistronic organization with unlabeled *luxA*) and 10 (*yfp-luxA* in bicistronic organization with unlabeled *luxB*) reveal that TF does affect cotranslational interactions of the nascent luciferase subunits (Fig. 2A). Comparison of the cotranslational interaction of YFP-LuxB with nascent LuxA in the absence (strain 5) and presence (strain 9) of TF shows that TF efficiently suppresses interactions of YFP-LuxB with nascent LuxA (Fig. 2A, left). In contrast, TF delays but does not block the interaction of YFP-LuxA with nascent LuxB, shifting the minimal length of nascent LuxB that is required for cotranslational interaction from 90 to 152 residues (Fig. 2A, right), without affecting the ~20-fold enrichment of ribosome footprints near the end of *luxB* translation. We infer that TF chaperone activity shields nascent LuxB from premature interactions with LuxA but allows the exposure of the dimerization fold for timely interactions with LuxA molecules in the vicinity of the ribosome.

The luciferase heterodimer interface is large (residues 17 to 161 in LuxA and 11 to 163 in LuxB). Extensive contacts occur via a parallel four-helix bundle formed by helices α2 and α3 from either subunit (residues 55 to 65 and 83 to 97 in LuxB) (Fig. 2B and table S1) (*2*). Given the length of the ribosomal tunnel, α2 and α3 of nascent LuxB will be fully exposed after translation of the first 127 codons; the complete subunit interface of LuxB will be exposed after translation of codon 193. In the absence of TF, initial contacts of nascent LuxB with LuxA are established upon emergence of helix α3 (translation of the first 120 codons). With TF present, we detected initial interactions of nascent LuxB with LuxA only upon exposure of ~152 N-terminal LuxB residues (translation of the first 182 codons), constituting nearly the complete subunit interface (Fig. 2A, right).

We conclude that association of fully synthesized LuxA with nascent LuxB requires ribosome-associated exposure of critical structural elements of the dimerization interface on LuxB. TF further increases the specificity of subunit interactions by preventing association of LuxB with nascent LuxA and premature association of LuxA with short nascent chains of LuxB, but it selectively allows LuxA association with long nascent chains of LuxB, exposing the complete dimer interface. We propose that TF engagement with nascent LuxA prevents premature interactions of the latter with LuxB and effectively promotes timely delivery of full-length LuxA to nascent LuxB. Likewise, during the early stages of translation, interaction of TF with nascent LuxB may protect the nascent subunit from incorrect and premature folding and interactions, until the assembly-competent part of LuxB is sufficiently exposed at the ribosomal surface for productive interaction with LuxA. Our results provide proof of principle for organized and regulated protein assembly in bacteria and validate previous observations that suggested translational coupling affects protein complex assembly (*6*). The SeRP data provided for bacterial luciferase are consistent with the concept that a fully synthesized subunit encoded by an upstream gene interacts with the nascent subunit encoded by the downstream gene of an operon. Assembly, which is considered a final, posttranslational step in the generation of oligomeric proteins, emerges as a process that is physically and kinetically coupled to the fundamental processes of protein biogenesis, folding, and translation. Our findings add a further dimension to the concept of the operon, originally defined by Jacob and Monod as a genetic unit for coordinated regulation of transcription (*7*). The genetic organization into operons of genes for products destined for assembly into protein complexes determines local concentration of subunits and crucial timing of assembly.

REFERENCES AND NOTES

1. Y. Phillip, G. Schreiber, *FEBS Lett.* **587**, 1046–1052 (2013).
2. T. O. Baldwin *et al.*, *Curr. Opin. Struct. Biol.* **5**, 798–809 (1995).
3. C. M. Miyamoto *et al.*, *J. Bacteriol.* **161**, 995–1001 (1985).
4. E. Oh *et al.*, *Cell* **147**, 1295–1308 (2011).
5. A. H. Becker, E. Oh, J. S. Weissman, G. Kramer, B. Bukau, *Nat. Protoc.* **8**, 2212–2239 (2013).
6. P. Pradhan, W. Li, P. Kaur, *J. Mol. Biol.* **385**, 831–842 (2009).
7. F. Jacob, J. Monod, *J. Mol. Biol.* **3**, 318–356 (1961).

ACKNOWLEDGMENTS

We thank A. Becker, V. van Noort, and C. Andréasson for valuable contributions; V. Sourjik and co-workers for help with in vivo FRET analysis; M. Langlotz and the fluorescence-activated cell sorting facility of the ZMBH for support; D. Ibberson for optimizing DNA sample preparation protocols; Y. Vainshtein for support with data analysis; and B. Zachmann-Brand for technical support. Sequencing was carried out at Genomics and Proteomics Core (DKFZ) and Genomics Core (EMBL) facilities. This work was supported by research grants from the German Science Foundation (DFG SFB638 and FOR1805) to G.K. and B.B.

SUPPLEMENTARY MATERIALS

www.sciencemag.org/content/350/6261/678/suppl/DC1
Materials and Methods
Supplementary Text
Figs. S1 to S8
Tables S1 to S3
References (*8–20*)
Notes S1 and S2

17 June 2015; accepted 15 September 2015
Published online 24 September 2015;
10.1126/science.aac8171

STRUCTURAL BIOLOGY

Crystal structure of the anion exchanger domain of human erythrocyte band 3

Takatoshi Arakawa,[1,2,3]* Takami Kobayashi-Yurugi,[1,3]* Yilmaz Alguel,[4,5,6]* Hiroko Iwanari,[7]* Hinako Hatae,[8] Momi Iwata,[4,5] Yoshito Abe,[9] Tomoya Hino,[1,3] Chiyo Ikeda-Suno,[1,2,3] Hiroyuki Kuma,[8] Dongchon Kang,[10] Takeshi Murata,[1,3,11] Takao Hamakubo,[7] Alexander D. Cameron,[1,4,5,6,12]† Takuya Kobayashi,[1,2,3,13]† Naotaka Hamasaki,[8]† So Iwata[1,2,3,4,5,6,13]†

Anion exchanger 1 (AE1), also known as band 3 or SLC4A1, plays a key role in the removal of carbon dioxide from tissues by facilitating the exchange of chloride and bicarbonate across the plasma membrane of erythrocytes. An isoform of AE1 is also present in the kidney. Specific mutations in human AE1 cause several types of hereditary hemolytic anemias and/or distal renal tubular acidosis. Here we report the crystal structure of the band 3 anion exchanger domain ($AE1_{CTD}$) at 3.5 angstroms. The structure is locked in an outward-facing open conformation by an inhibitor. Comparing this structure with a substrate-bound structure of the uracil transporter UraA in an inward-facing conformation allowed us to identify the anion-binding position in the $AE1_{CTD}$, and to propose a possible transport mechanism that could explain why selected mutations lead to disease.

Efficient delivery of oxygen to tissues and the removal of carbon dioxide from the blood are fundamental for respiration. This is principally achieved via the red blood cells or erythrocytes. Anion exchanger 1 (AE1), also known as band 3 or SLC4A1, predominates in the erythrocyte ghost membrane and constitutes 30% of its protein (*1*). It plays a major role in gas transport. Carbon dioxide generated by metabolic processes in the tissues diffuses into the red blood cells. There it reacts with water in a reversible process catalyzed by carbonic anhydrase II to form HCO_3^- and protons (*2*). As the bicarbonate concentration in the erythrocyte increases, the anions are transported by AE1 out into the blood plasma in an electroneutral exchange for chloride ions. With ~10^6 AE1 molecules per cell (*1*) and each single protein transporting 4×10^4 to

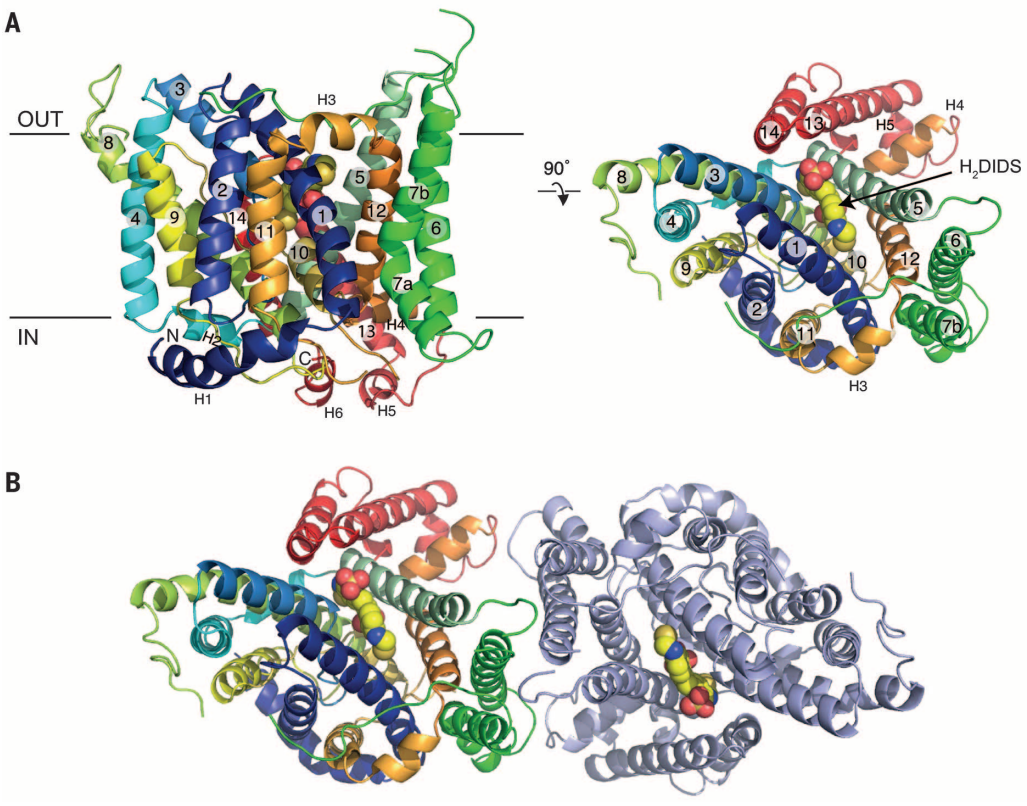

Fig. 1. Structure of $AE1_{CTD}$ in an outward-facing conformation. (**A**) View of the structure in the plane of the membrane (left) and from the extracellular side of the membrane (right). The cartoon representation of the structure has been colored in rainbow order from blue at the N terminus to red at the C terminus. The H_2DIDS is shown as spheres (C, yellow; S, dark yellow; O, red; N, blue). Numbers indicate TMs. Six short helices on the membrane surface are shown as H1 to H6. OUT, extracellular side IN, intracellular side. (**B**) Structure of the dimer, viewed from the extracellular side. The color coding of the left monomer is the same as in (A). The right monomer is shown in gray.

5×10^4 ions per second (*3*, *4*), transport is extremely fast, and ~90% of the CO_2 is taken from the tissues to the lungs as the more soluble form of bicarbonate. Within the erythrocyte, the net result is the accumulation of protons from the hydration of CO_2. As a result of the Bohr effect, the low pH causes hemoglobin to release oxygen, which can then diffuse into the tissues. When the blood reaches the lungs, the process is reversed and CO_2 is exhaled.

Erythrocyte AE1 is the most abundant and widely studied anion exchanger, but AE1 and its close homologs AE2 and AE3 are found in diverse tissues (*5*, *6*), playing important roles in the regulation of intracellular pH, cell volume, and membrane potential through the exchange of HCO_3^- and Cl^-. AE1 is highly expressed as an N-terminally truncated form in the kidney, where it is instrumental in the reabsorption of bicarbonate (*7*). Many morphological and anemic disorders in the erythrocytes, as well as distal renal tubular acidosis in the kidney, are caused by inherited mutations in AE1 (*8*).

Human erythrocyte AE1 is a 110-kD glycoprotein. It is built from two domains (*9*), a cytosolic N-terminal domain (residues 1 to 360) and an integral membrane domain (residues 361 to 911). Anion exchange is catalyzed by the C-terminal domain (*10*–*12*). However, only the crystal structure of the cytosolic N-terminal domain (*13*)—which is important as an anchoring point for other proteins, including the scaffolding protein ankyrin (*14*, *15*) and deoxyhemoglobin—has been determined (*16*, *17*). A wealth of biochemical experiments, including cysteine scanning mutagenesis (*18*–*23*) and N-glycan insertion mutagenesis (*24*, *25*), have been used to derive topology models of AE1. The only three-dimensional structural information available to date for the transmembrane domain is from electron microscopy (*26*, *27*), with the best maps at a resolution of 7.5 Å, calculated from two-dimensional crystals (*28*). As such, the membrane topology, substrate recognition, and anion-transport mechanism of this fundamental protein remain unclear, and diverse models have been proposed (*28*–*31*). Here we report the crystal structure at 3.5 Å resolution of the membrane domain of human AE1, locked in an outward-facing open conformation by a covalently bound inhibitor, in complex with a Fab fragment from a monoclonal antibody.

The C-terminal anion exchanger domain of AE1 ($AE1_{CTD}$), with the N terminus cleaved by trypsin, was purified directly from white ghost membranes of human erythrocytes and treated with H_2DIDS (4,4-diisothiocyanatodihydro-stilbene-2,2-disulfonic acid), a disulfonic stilbene derivative that irreversibly inhibits anion exchangers by covalently binding to the protein and blocking the transport cycle (*32*, *33*). Two steps were required to obtain well-diffracting crystals. First, the transporter was deglycosylated with N-glycosidase F. Second, the protein was cocrystallized with a monoclonal antibody Fab fragment that binds tightly to a conformational epitope of $AE1_{CTD}$. This antibody was selected from a panel of antibodies raised by the inoculation of mice with $AE1_{CTD}$-displaying baculovirus (*34*). The structure was solved using MIRAS (multiple isomorphous replacement with anomalous scattering), in combination with noncrystallographic symmetry averaging, and refined at a resolution of 3.5 Å to an *R* factor of 27.4% and a free *R* factor of 29.0% (tables S1 and S2) (*32*). The final model contains all residues

[1]Japan Science and Technology Agency (JST), Exploratory Research for Advanced Technology (ERATO) Human Receptor Crystallography Project, Konoe-cho, Yoshida, Sakyo-ku, Kyoto 606-8501, Japan. [2]JST, Research Acceleration Program, Membrane Protein Crystallography Project, Konoe-cho, Yoshida, Sakyo-ku, Kyoto 606-8501, Japan. [3]Department of Cell Biology, Kyoto University Faculty of Medicine, Konoe-cho, Yoshida, Sakyo-ku, Kyoto 606-8501, Japan. [4]Division of Molecular Biosciences, Membrane Protein Crystallography group, Imperial College London, London SW7 2AZ, UK. [5]Membrane Protein Laboratory, Diamond Light Source, Harwell Science and Innovation Campus, Didcot, Chilton, Oxfordshire OX11 0DE, UK. [6]Research Complex at Harwell Rutherford, Appleton Laboratory, Harwell Oxford, Didcot, Oxfordshire OX11 0FA, UK. [7]Department of Quantitative Biology and Medicine, Research Center for Advanced Science and Technology, The University of Tokyo, 4-6-1 Komaba, Meguro-ku, Tokyo 153-8904, Japan. [8]Faculty of Pharmaceutical Sciences, Nagasaki International University, 2825-7 Huis Ten Bosch-cho, Sasebo, Nagasaki 859-3298, Japan. [9]Department of Protein Structure, Function and Design, Graduate School of Pharmaceutical Sciences, Kyushu University, 3-1-1 Maidashi, Higashi-ku, Fukuoka 812-8582, Japan. [10]Department of Clinical Chemistry and Laboratory Medicine, Graduate School of Medical Sciences, Kyushu University, Fukuoka 812-8582, Japan. [11]Department of Chemistry, Graduate School of Science, Chiba University, 1-33 Yayoi-cho, Inage, Chiba 263-8522, Japan. [12]School of Life Sciences, University of Warwick, Gibbet Hill Road, Coventry CV4 7AL, UK. [13]Platform for Drug Discovery, Informatics, and Structural Life Science, Konoe-cho, Yoshida, Sakyo-ku, Kyoto 606-8501, Japan.
*These authors contributed equally to this work.
†Corresponding author. E-mail: a.cameron@warwick.ac.uk (A.D.C.); t-coba@mfour.med.kyoto-u.ac.jp (T.K.); naotaka.hamasaki@city.sasebo.lg.jp (N.H.); s.iwata@mfour.med.kyoto-u.ac.jp (S.I.)

from 381 to 887, apart from three loop regions (553 to 567, 640 to 649, and 742 to 753). The asymmetric unit of the crystal contains two dimers of $AE1_{CTD}$, with one Fab fragment bound on the outer side of each protomer (figs. S1 and S2).

Each protomer comprises 14 transmembrane segments (TMs) (Fig. 1) and has dimensions of about 60 × 60 × 50 Å. The lengths of the individual TMs vary from 18 to 42 Å. Like many other secondary transporters, the structure is built from two repeats inverted in the plane of the membrane (fig. S3). In $AE1_{CTD}$, the repeat is made of seven TMs, with the third TM of each repeat only partially spanning the membrane before the helical structure unravels. Although it is difficult to superpose all TMs from the inverted repeat as a unit, if the repeat is treated as a two-component module, TMs 1 to 4 can be superposed on TMs 8 to 11 [root mean square deviation (RMSD) of 2.1 Å for 62 out of 103 Cα atoms (supplementary materials)] and TMs 5 to 7 onto TMs 12 to 14 (RMSD of 2.1 Å for 53 out of 100 Cα atoms) (fig. S3B).

The inverted repeat units intertwine to form two structural domains separated by a cleft on the extracellular side of the protein (Fig. 1A). We define these structural domains as the core (TMs 1 to 4 and 8 to 11) and the gate (TMs 5 to 7 and 12 to 14), following the convention of the uracil transporter UraA (*35*, *36*). Within the core domain, the N termini of the two half-helices (TMs 3 and 10) face one another at a distance of ~10 Å, creating the appearance of a continuous helix (Fig. 2 and fig. S2B).

The overall fold of AE1 is very similar to the structure of UraA (*35*), although they have only 12% sequence identity, as aligned using the structures (fig. S4). This structural similarity has been previously suggested on the basis of threading combined with mutagenesis experiments (*29*). UraA is also made of two seven-TM repeat units that form two domains. As shown in Fig. 2, the core domains of $AE1_{CTD}$ and UraA are similar and can be superposed with a RMSD of 1.8 Å for 145 of 268 Cα atoms (1.9 Å for 131 out of 190 Cα atoms when only the TM segments are considered; fig. S5). The gate domains of the two proteins also have the same topology, but it is more difficult to superpose these domains (RMSD of 2.0 Å for only 55 out of 166 Cα atoms) (Fig. 2, C and D, and fig. S5). This is in part because the relative positions of the three pairs of helices (TMs 5 and 12, TMs 6 and 7, and TMs 13 and 14) are different between AE1 and UraA. Given that the gate domains are directly involved in substrate binding, as discussed below, the structural variation could reflect the different substrates of the two proteins.

$AE1_{CTD}$ is a physiological dimer (*37*), but dimerization is not necessary for transport (*38*, *39*). The dimer in the crystal consists of two $AE1_{CTD}$ monomers with 1092 $Å^2$ of surface area buried at the interface (*32*). The monomers are related by a twofold axis parallel to the membrane normal, consistent with dimer formation in the erythrocyte membrane (Fig. 1B). There is no obvious difference between the two dimers as observed in the crystal at the current resolution. The interaction between subunits is formed exclusively through residues on the gate domains, including TMs 5, 6, and 7 (Fig. 1B).

The Fab fragments bind solely to the core domain of each $AE1_{CTD}$ (figs. S1 and S2). The interactions between $AE1_{CTD}$ and the Fab are identical for the four molecules of the asymmetric unit. The predominant interactions are between the heavy chain of the Fab and the C-terminal end of TM 3, the following loop, and the loop before TM 8 (fig. S1). The light chain of the Fab interacts with the end of TM 1 and the following loop.

H_2DIDS covalently crosslinks Lys^{539} and Lys^{851} (*40*); a nonprotein density between them, consistent with the inhibitor, is evident in the electron density maps (fig. S6). However, part of the H_2DIDS density is poorly defined, and it is possible either that the link may have been damaged by radiation or that the crosslinking may not have been carried out to completion (fig. S6, A and B). The H_2DIDS molecule spans TMs 5 and 13 of the gate domain (Fig. 2A) at the entrance of a large cavity 15 Å wide, 7 Å long, and 11 Å deep, on the extracellular side of the protein between the core and gate domains (Fig. 3A and figs. S6 to S8). The cavity is formed by TMs 1, 3, 5, 13, and 14 and has predominantly hydrophobic walls, with polar residues near the entrance and at the bottom.

Mutagenesis studies of mouse AE1 demonstrate that the protein is still capable of Cl^- self-exchange when the lysine residues interacting with H_2DIDS are mutated (*41*), suggesting that the inhibitor does not bind in the same place as the substrate does. Under the H_2DIDS molecule, the cavity opens out slightly (18 Å) where the N termini of TMs 3 and 10 meet (Fig. 3). This region has been suggested as a cation selectivity filter (*23*). In UraA, uracil binds in the space between the positive dipoles TMs 3 and 10. The uracil interacts with two glutamate residues, one on TM 8 (Glu^{241}) and the other on TM 10 (Glu^{290}) (Fig. 3B) (*35*). In $AE1_{CTD}$, Glu^{681} and the positively charged Arg^{730} take the positions of these two glutamates on TMs 8 and 10, respectively (Fig. 3B). Both of these residues are conserved in AE1, and anion exchange is lost if either is mutated (*19*, *42*–*44*). Although there is no apparent density indicating a substrate, and substrate binding could be blocked by bound H_2DIDS, a bicarbonate ion can be placed between the positive dipoles of TMs 3 and 10. The negatively charged bicarbonate could interact with the positively charged Arg^{730} and could hydrogen-bond to Glu^{681}. The anions may also interact directly with the amide protons at the N termini of TMs 3 and 10 (Fig. 3B). Consistent with anion binding in this space, mutagenesis studies indicate that only a conservative mutation to a threonine (*30*) or cysteine (*29*) is tolerated at Ser^{465} at the N terminus of TM 3. Mutation to the larger isoleucine (*29*), asparagine, or aspartic acid (*30*) abolishes transport. The arrangement of an anion between the positively charged dipoles of half-helices (TMs 3 and 10 in AE1), with a negatively charged residue nearby (Glu^{681} in AE1), is similar to the selectivity filter of the CLC chloride transporter, although the topology of the two proteins is completely different (fig. S9) (*45*).

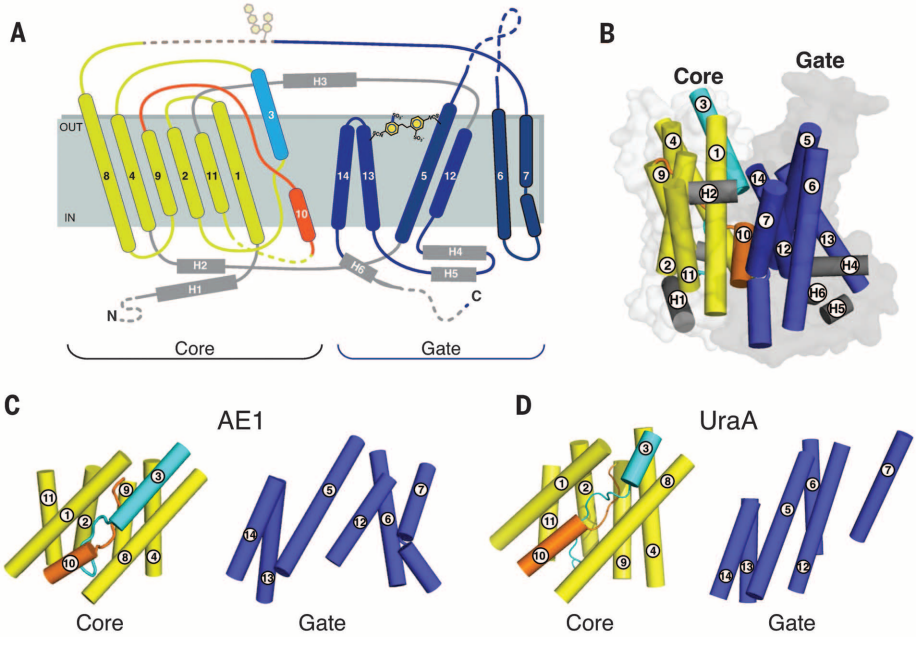

Fig. 2. Structural framework of $AE1_{CTD}$ and comparison with UraA. (**A**) Topology and (**B**) overall structure of $AE1_{CTD}$, viewed in the plane of the membrane. TM 3 is shown in cyan and TM 10 is shown in orange. The other transmembrane helices of the core domain are colored yellow, and those of the gate domain are blue. (**C**) The core and gate domains of AE1. The left panel shows the core domain viewed from the gate domain; the right panel shows the gate domain viewed from the core domain. Coloring is as in (A). (**D**) As in (C), but for UraA (Protein Data Bank accession code 3QE7). The two proteins were aligned on their respective core domains.

AE1 exhibits modes of transport other than the physiological 1:1 exchange of bicarbonate and chloride ions. It can also conduct anions (*46*) or cotransport protons to drive the uptake of divalent sulfate (*47*) or chloride ions (*48*). These ions can easily be accommodated in the basic cavity (figs. S7 and S8). Glu^{681} on the translocation pathway is a potential proton acceptor during cotransport of H^+ and SO_4^{2-}, because modification to an alcohol (Glu681OH) or mutation to a glutamine leads to a highly proton-independent SO_4^{2-}/Cl^- exchange (*42*, *49*, *50*).

Specific mutations in the $AE1_{CTD}$ domain (fig. S10) are related to red cell diseases such as spherocytosis (*51*), stomatocytosis (*52*), and Southeast Asian ovalocytosis (SAO) (*53*). Some of these mutations, particularly those leading to spherocytosis, cause misfolding of the protein, whereas others exhibit abnormal transport kinetics. Some of the mutations in the transport domain are listed in table S3 and shown in Fig. 4 and figs. S11 and S12. An increase in membrane permeability to monovalent cations, caused by mutations in AE1, has been observed in a number of human pedigrees with dominantly inherited hemolytic anemia (*22*, *44*, *52*). These mutations mostly occur on the cytoplasmic half of the core domain (Fig. 4). They include mutation of Arg^{730}, the putative bicarbonate-binding residue, to Cys, as well as two other mutations on the half-helix TM 10 (Ser^{731} to Pro and His^{734} to Arg). The deletion of residues 400 to 408, which leads to SAO, also causes a cation leak in intact red cells (*54*). These residues reside at the TM 1 N terminus at the interface with TM 7 of the gate domain (Fig. 4 and fig. S12), and the mutations in the residues would presumably alter the structure of the core domain, as well as the interaction between $AE1_{CTD}$ and the N-terminal cytoplasmic domain. It is interesting that this deletion may confer protection against cerebral malaria (*54*). Fewer mutations have been reported in the gate domain.

The structure of $AE1_{CTD}$ reported here is in an outward-facing conformation (Figs. 1 and 3). $AE1_{CTD}$ is reported to undergo large conformational changes during transport, in line with the alternating access mechanism (*55*, *56*). By comparing the outward-facing $AE1_{CTD}$ structure with a substrate-bound, inward-facing UraA structure (*35*), we can gain some insight into the transport mechanism (Fig. 3A and fig. S13).

The core domains of these two proteins, including the uracil binding site in UraA, are very similar (Fig. 3B and fig. S5). The primary difference between the two structures is in the relative positions of the gate and core domains (Fig. 2, C and D, and fig. S5). The rotation of one domain against another as the transporter moves from outward- to inward-facing, as shown in fig. S5, is similar to the predominant movements observed for other families of transporters, including the LeuT family transporters, to which there is also some structural similarity (fig. S14) (*36*, *57*–*61*). Figure S13 shows a possible transport mechanism for AE1. Starting from an outward-facing open conformation of the protein, chloride at a high concentration in plasma binds to the anion-binding site. This causes some local conformational changes of the core domain, enabling it to rotate against the gate domain to form the inward-facing structure. At this point, chloride diffuses out and is replaced by bicarbonate to reverse the process. This is consistent with various results from kinetic studies that indicate that chloride and bicarbonate ions share the same binding site (*4*). The structure of the human $AE1_{CTD}$ and the proposed transport mechanism

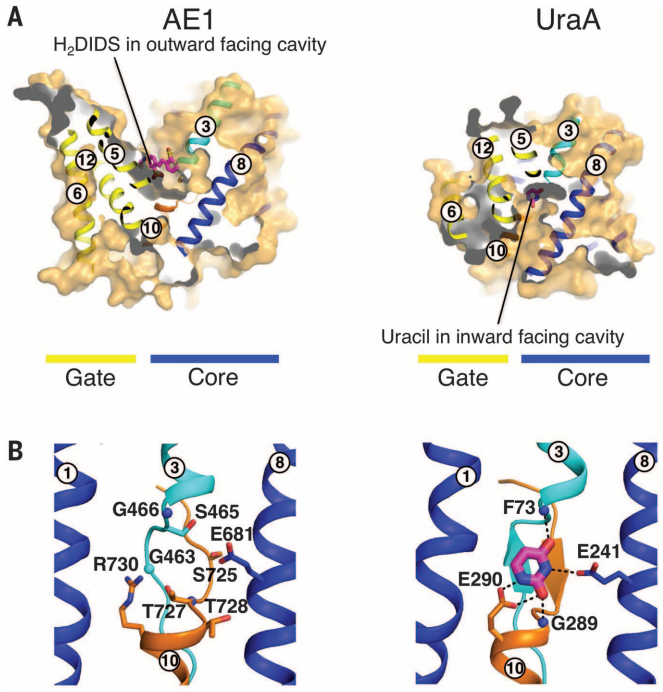

Fig. 3. Outward- and inward-facing cavities and substrate binding sites in AE1 and UraA. (**A**) Surface representations of the outward-facing structure of the substrate-free $AE1_{CTD}$ complex with H_2DIDS (left) and the inward-facing structure of UraA with uracil (right). These views are in the plane of the membrane. The surfaces are semi-transparent and slabbed to show the positions of the transmembrane helices, which are colored as in Fig. 2. H_2DIDS and uracil are shown in magenta in the left and right panels, respectively. (**B**) Comparison of the putative anion binding site in AE1 (left) with the uracil binding site in UraA (right). The coloring is as in (A). Glu^{241} and Glu^{290} of uracil correspond to Glu^{681} and Arg^{730} of AE1, respectively. The dark blue spheres represent the amide nitrogens of the depicted residues, and the cyan sphere represents the Cα atom of Gly^{463}.

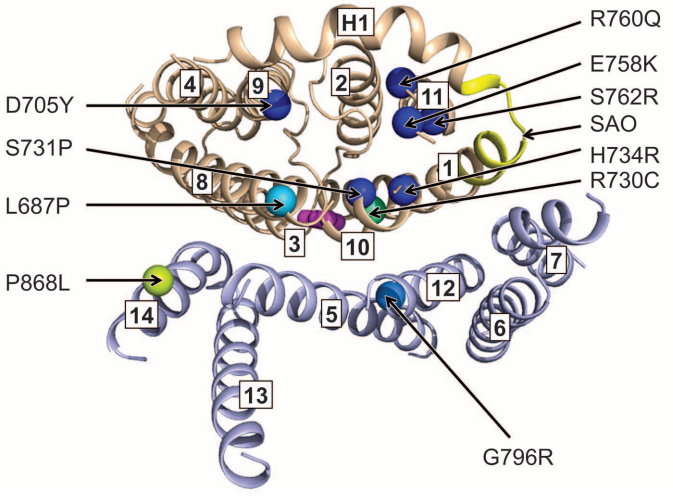

Fig. 4. Some mutations that are reported to cause diseases, plotted on the structure of $AE1_{CTD}$. The core domain is shown in tan and the gate domain is shown in gray. The view is from the cytoplasmic side of the membrane. The deletion mutation of residues 400 to 408, which causes SAO, is shown in yellow. Point mutations are shown by spheres, with coloring according to conservation among human SLC4 family transporters. The level of conservation was analyzed with the assistance of the ConSurf server (http://consurf.tau.ac.il/) (*62*) using seven homologs, including AE1 to -4, electrogenic sodium bicarbonate cotransporters 1 and 2 (NBCe1 and -2), electroneutral sodium bicarbonate cotransporter (NBCn1), sodium-driven chloride bicarbonate exchanger (NDCBE), sodium-dependent bicarbonate transporter (NCBE), and sodium bicarbonate transporter–like protein 11 (BTR1). Colors (in rainbow order) represent degree of conservation, with blue indicating the most highly conserved and red indicating the most poorly conserved residues among these homologues. R^{730} is only conserved among the electrogenic family members. The details of mutations are described in table S3 and figs. S11 and S12. The position of uracil in the UraA structure, corresponding to the possible anion binding site in AE1, is shown with magenta spheres.

provide a framework with which to understand the many mutations in the protein that lead to diseases.

REFERENCES AND NOTES

1. G. Fairbanks, T. L. Steck, D. F. Wallach, *Biochemistry* **10**, 2606–2617 (1971).
2. J. W. Vince, R. A. Reithmeier, *Biochemistry* **39**, 5527–5533 (2000).
3. J. Brahm, *J. Gen. Physiol.* **70**, 283–306 (1977).
4. H. Passow, *Rev. Physiol. Biochem. Pharmacol.* **103**, 61–203 (1986).
5. S. L. Alper, R. R. Kopito, S. M. Libresco, H. F. Lodish, *J. Biol. Chem.* **263**, 17092–17099 (1988).
6. R. R. Kopito *et al.*, *Cell* **59**, 927–937 (1989).
7. F. C. Brosius 3rd, S. L. Alper, A. M. Garcia, H. F. Lodish, *J. Biol. Chem.* **264**, 7784–7787 (1989).
8. S. L. Alper, *J. Exp. Biol.* **212**, 1672–1683 (2009).
9. R. R. Kopito, H. F. Lodish, *Nature* **316**, 234–238 (1985).
10. S. Lepke, H. Passow, *Biochim. Biophys. Acta* **455**, 353–370 (1976).
11. S. Grinstein, S. Ship, A. Rothstein, *Biochim. Biophys. Acta* **507**, 294–304 (1978).
12. S. Lepke, A. Becker, H. Pascow, *Biochim. Biophys. Acta* **1106**, 13–16 (1992).
13. D. Zhang, A. Kiyatkin, J. T. Bolin, P. S. Low, *Blood* **96**, 2925–2933 (2000).
14. J. L. Grey, G. C. Kodippili, K. Simon, P. S. Low, *Biochemistry* **51**, 6838–6846 (2012).
15. L. Davis, S. E. Lux, V. Bennett, *J. Biol. Chem.* **264**, 9665–9672 (1989).
16. M. J. Tanner, *Curr. Opin. Hematol.* **9**, 133–139 (2002).
17. J. A. Walder *et al.*, *J. Biol. Chem.* **259**, 10238–10246 (1984).
18. J. Fujinaga, X. B. Tang, J. R. Casey, *J. Biol. Chem.* **274**, 6626–6633 (1999).
19. X. B. Tang, J. Fujinaga, R. Kopito, J. R. Casey, *J. Biol. Chem.* **273**, 22545–22553 (1998).
20. A. M. Taylor, Q. Zhu, J. R. Casey, *Biochem. J.* **359**, 661–668 (2001).
21. Q. Zhu, D. W. Lee, J. R. Casey, *J. Biol. Chem.* **278**, 3112–3120 (2003).
22. D. Barneaud-Rocca, B. Pellissier, F. Borgese, H. Guizouarn, *Int. J. Cell Biol.* **2011**, 136802 (2011).
23. Q. Zhu, J. R. Casey, *J. Biol. Chem.* **279**, 23565–23573 (2004).
24. J. C. Cheung, R. A. Reithmeier, *Mol. Membr. Biol.* **22**, 203–214 (2005).
25. M. Popov, J. Li, R. A. Reithmeier, *Biochem. J.* **339**, 269–279 (1999).
26. D. N. Wang, W. Kühlbrandt, V. E. Sarabia, R. A. Reithmeier, *EMBO J.* **12**, 2233–2239 (1993).
27. D. N. Wang, V. E. Sarabia, R. A. Reithmeier, W. Kühlbrandt, *EMBO J.* **13**, 3230–3235 (1994).
28. T. Yamaguchi *et al.*, *J. Mol. Biol.* **397**, 179–189 (2010).
29. D. Barneaud-Rocca, C. Etchebest, H. Guizouarn, *J. Biol. Chem.* **288**, 26372–26384 (2013).
30. P. Bonar, H. P. Schneider, H. M. Becker, J. W. Deitmer, J. R. Casey, *J. Mol. Biol.* **425**, 2591–2608 (2013).
31. T. Hirai, N. Hamasaki, T. Yamaguchi, Y. Ikeda, *Biochem. Cell Biol.* **89**, 148–156 (2011).
32. Materials and methods are available as supplementary materials on *Science* Online.
33. Y. Shami, A. Rothstein, P. A. Knauf, *Biochim. Biophys. Acta* **508**, 357–363 (1978).
34. R. Saitoh *et al.*, *J. Immunol. Methods* **322**, 104–117 (2007).
35. F. Lu *et al.*, *Nature* **472**, 243–246 (2011).
36. Å. Västermark, M. H. Saier Jr., *Proteins* **82**, 336–346 (2014).
37. J. R. Casey, R. A. Reithmeier, *J. Biol. Chem.* **266**, 15726–15737 (1991).
38. N. K. Dahl *et al.*, *J. Biol. Chem.* **278**, 44949–44958 (2003).
39. S. Lindenthal, D. Schubert, *Proc. Natl. Acad. Sci. U.S.A.* **88**, 6540–6544 (1991).
40. K. Okubo, D. Kang, N. Hamasaki, M. L. Jennings, *J. Biol. Chem.* **269**, 1918–1926 (1994).
41. P. G. Wood, H. Müller, M. Sovak, H. Passow, *J. Membr. Biol.* **127**, 139–148 (1992).
42. M. N. Chernova *et al.*, *J. Gen. Physiol.* **109**, 345–360 (1997).
43. D. Karbach, M. Staub, P. G. Wood, H. Passow, *Biochim. Biophys. Acta* **1371**, 114–122 (1998).
44. A. K. Stewart *et al.*, *Am. J. Physiol. Cell Physiol.* **300**, C1034–C1046 (2011).
45. R. Dutzler, E. B. Campbell, M. Cadene, B. T. Chait, R. MacKinnon, *Nature* **415**, 287–294 (2002).
46. P. A. Knauf, G. F. Fuhrmann, S. Rothstein, A. Rothstein, *J. Gen. Physiol.* **69**, 363–386 (1977).
47. M. L. Jennings, *J. Membr. Biol.* **28**, 187–205 (1976).
48. M. L. Jennings, *J. Membr. Biol.* **40**, 365–391 (1978).
49. M. L. Jennings, J. S. Smith, *J. Biol. Chem.* **267**, 13964–13971 (1992).
50. X. B. Tang, M. Kovacs, D. Sterling, J. R. Casey, *J. Biol. Chem.* **274**, 3557–3564 (1999).
51. P. Jarolim *et al.*, *Blood* **85**, 634–640 (1995).
52. L. J. Bruce *et al.*, *Nat. Genet.* **37**, 1258–1263 (2005).
53. P. Jarolim *et al.*, *Proc. Natl. Acad. Sci. U.S.A.* **88**, 11022–11026 (1991).
54. L. J. Bruce *et al.*, *Biochim. Biophys. Acta* **1416**, 258–270 (1999).
55. O. Jardetzky, *Nature* **211**, 969–970 (1966).
56. W. Furuya, T. Tarshis, F. Y. Law, P. A. Knauf, *J. Gen. Physiol.* **83**, 657–681 (1984).
57. C. Lee *et al.*, *Nature* **501**, 573–577 (2013).
58. E. M. Quistgaard, C. Löw, P. Moberg, L. Trésaugues, P. Nordlund, *Nat. Struct. Mol. Biol.* **20**, 766–768 (2013).
59. N. Reyes, C. Ginter, O. Boudker, *Nature* **462**, 880–885 (2009).
60. T. Shimamura *et al.*, *Science* **328**, 470–473 (2010).
61. X. Zhou *et al.*, *Nature* **505**, 569–573 (2014).
62. F. Glaser *et al.*, *Bioinformatics* **19**, 163–164 (2003).

ACKNOWLEDGMENTS

We thank the beamline scientists at Diamond Light Source, European Synchrotron Radiation Facility and SPring-8 for help with data collection; L. Bruce at the Bristol Institute for Transfusion Sciences; National Health Service Blood and Transplant; and A. Toye at the University of Bristol for useful discussion. S. Weyand contributed to the refinement of the Fab fragment, and R. Suno at Kyoto University contributed to the preparation of the figures. The project was funded by the Biotechnology and Biological Sciences Research Council (grants BB/G023425/1 and BB/D019516/1 to S.I.); the ERATO Human Receptor Crystallography Project of JST (to S.I.); the Targeted Proteins Research Program of the Ministry of Education, Culture, Sports, Science, and Technology, Japan (MEXT) (to S.I.); a Grant-in-Aid for Scientific Research (B) (grants 20370035 and 23370049 to T.K.); MEXT's Platform for Drug Discovery, Informatics, and Structural Life Science (to T.K. and S.I.); and the European Union's European Drug Initiative for Channels and Transporters (grant 201924 to S.I. and A.C.). The authors are grateful for the use of the Membrane Protein Laboratory, funded by the Wellcome Trust (grant WT089809) at the Diamond Light Source. The authors declare no competing interests. The project was conceived by S.I., D.K., and N.H. H.H., H.K., and N.H. purified the $AE1_{CTD}$ protein. H.I. and T.Ha. raised the antibody using the $AE1_{CTD}$-expressing baculovirus as an antigen. T.A., T.Hi., C.I.-S., and T.M. screened the antibody. T.K.-Y., T.K., T.A., Y.Ab., and M.I. crystallized the $AE1_{CTD}$ protein. T.K., Y.Al., A.D.C., and S.I. collected diffraction data. The structure was solved and refined by T.A., Y.Al. and A.D.C. The manuscript was written by T.K., A.D.C., Y.Al., and S.I. The coordinates and structure factors have been deposited with the Protein Data Bank (4YZF, band 3 with Fab4201; 5a16, Fab4201). T.A., T.K., T.K.-Y., T.Hi., T.M., N.N., S.I., T.Ha., H.I., Y.M., and N.H. are authors on a patent filed by JST Agency (JP 2013-103881 A) that covers the monoclonal antibody to human band 3.

SUPPLEMENTARY MATERIALS

www.sciencemag.org/content/350/6261/680/suppl/DC1
Materials and Methods
Figs. S1 to S15
Tables S1 to S3
References (*63–84*)

10 December 2014; accepted 25 September 2015
10.1126/science.aaa4335

PLANT EVOLUTION

The *Papaver rhoeas S* determinants confer self-incompatibility to *Arabidopsis thaliana* in planta

Zongcheng Lin,* Deborah J. Eaves, Eugenio Sanchez-Moran, F. Christopher H. Franklin, Vernonica E. Franklin-Tong†

Self-incompatibility (SI) is a major genetically controlled system used to prevent inbreeding in higher plants. *S* determinants regulate allele-specific rejection of "self" pollen by the pistil. SI is an important model system for cell-to-cell recognition and signaling and could be potentially useful for first-generation (F_1) hybrid breeding. To date, the transfer of *S* determinants has used the complementation of orthologs to "restore" SI in close relatives. We expressed the *Papaver rhoeas S* determinants *PrsS* and *PrpS* in *Arabidopsis thaliana*. This enabled pistils to reject pollen expressing cognate *PrpS*. Moreover, plants coexpressing cognate *PrpS* and *PrsS* exhibit robust SI. This demonstrates that PrsS and PrpS are sufficient for a functional synthetic *S* locus in vivo. This transfer of novel *S* determinants into a highly divergent species (>140 million years apart) with no orthologs suggests their potential utility in crop production.

Many plants are hermaphrodites, with male and female organs in close proximity. Because this risks self-fertilization and undesirable inbreeding depression, many plants use self-incompatibility (SI) as a mechanism to prevent selfing. SI is controlled by an *S* locus allowing self/nonself recognition between pistil and pollen (*1*, *2*). SI in *Papaver rhoeas* is gametophytically controlled and specified by a pistil *S* determinant, *PrsS* [*P. rhoeas stigma S* (*3*)], and a pollen *S* determinant, *PrpS* [*P. rhoeas pollen S* (*4*)]. PrsS and PrpS interact to trigger a signaling network in incompatible pollen, resulting in programmed cell death (PCD) (*5*–*8*). *Arabidopsis thaliana* is a self-fertile member of the Brassicaceae. Self-compatibility in *Arabidopsis* originated

School of Biosciences, University of Birmingham, Edgbaston, Birmingham B15 2TT, UK.
*Present address: Department of Plant Systems Biology, Vlaams Instituut voor Biotechnologie, 9052 Gent, Belgium.
†Corresponding author. E-mail: v.e.franklin-tong@bham.ac.uk

recently (<0.5 million years ago) (*9*), through loss or inactivation of their *S* determinants SRK (*10*) and SCR (*11*). We recently demonstrated that pollen from *A. thaliana* expressing *PrpS-GFP* (GFP, green fluorescent protein) was inhibited by cognate recombinant PrsS proteins and displayed hallmark features of *Papaver* SI (*8*). We have expressed PrsS in *A. thaliana* pistils and shown that they reject cognate pollen. Moreover, *A. thaliana* coexpressing *PrsS* and *PrpS* set no self-seed. This demonstrates that *PrsS* and *PrpS* function as *S* determinants and are the sole additional requirement to elicit SI. Intergeneric transfer of *S* determinants has only been achieved between closely related species with orthologs of the *Brassica S* determinants, effectively involving complementation using *SRK* and *SCR* pairs to "restore" SI (*12*–*14*). Because the Papaveraceae diverged from the Brassicaceae ~140 million years ago (*8*, *15*) and *Arabidopsis* lacks *PrsS* and *PrpS* orthologs, finding that they function in planta in *A. thaliana* is important because previously only transfer of orthologous *S* determinants between close relatives had been achieved.

PrsS encodes a small secreted protein, specifically and developmentally expressed in *P. rhoeas* stigmas (*3*). The promoter of the *S Locus-Related 1 (SLR1)* gene from *Brassica oleracea* directs stigma-specific, developmentally regulated gene expression (*16*, *17*) and exhibits maximal expression at flower maturity (*16*). Here we show that the expression of *SLR1p* in *Arabidopsis* (Fig. 1A and fig. S1) is spatiotemporally indistinguishable from that of SRK in *B. oleracea* (*16*). Therefore, we used *SLR1p* to drive expression of $PrsS_1$ in *Arabidopsis* by transforming a *SLR1p::*$PrsS_1$ construct into *Col-0* (*At-*$PrsS_1$ lines). Reverse transcription polymerase chain reaction (RT-PCR) analysis of pistil mRNA from 10 independent lines revealed differing $PrsS_1$ transcript levels (Fig. 1B). Western analysis of pistil extracts confirmed the presence of $PrsS_1$ (Fig. 1C). We also transformed *Col-0* with a *SLR1p::*$PrsS_3$ construct to make *At-*$PrsS_3$ lines. RT-PCR analysis compared transgene expression to the highest-expressing *At-*$PrsS_1$ line (Fig. 1D).

To test the functionality of the *At-*$PrsS_1$ lines, we performed semi-vivo pollination assays (fig. S2) on excised pistils from the *At-*$PrsS_1$ lines, using pollen from an *A. thaliana* line expressing $PrpS_1$*-GFP* (*8*), referred to as *At-*$PrpS_1$ hereafter, examining the ability of *At-*$PrsS_1$ stigmas to inhibit *At-*$PrpS_1$ ("incompatible") pollen tube growth.

At-$PrsS_1$ line 9 pistils inhibited *At-*$PrpS_1$ pollen tubes more strongly than did line 4, whereas *Col-0* pollen was not inhibited (Fig. 2A). Quantitation revealed that in *At-*$PrsS_1$ pistils, *At-*$PrpS_1$ pollen tubes were significantly shorter than *Col-0* pollen tubes ($P < 0.001$, *t* test, $n = 40$ pollinations; Fig. 2B). After 70 min on *At-*$PrsS_1$ pistils, *At-*$PrpS_1$ pollen tubes from 8 out of 10 lines were <300 μm; *Col-0* controls were >300 μm (Fig. 2B). Thus, *At-*$PrsS_1$ pistils support pollen tube growth but reject *At-*$PrpS_1$ pollen. At 110 min, *At-*$PrpS_1$ pollen tubes in *At-*$PrsS_1$ pistils remained shorter than controls (fig. S3). The level of inhibition of *At-*$PrpS_1$ pollen tubes in *At-*$PrsS_1$ pistils correlated with $PrsS_1$ expression levels (fig. S4). This provides strong evidence that $PrsS_1$ functions in *A. thaliana* pistils to inhibit *At-*$PrpS_1$ pollen.

A key feature of SI is *S* allele–specific inhibition of pollen. To test this, we pollinated excised *At-*$PrsS_1$ or *At-*$PrsS_3$ pistils with *At-*$PrpS_1$ pollen or pollen from a line expressing $PrpS_3$*-GFP* (*8*), referred to as *At-*$PrpS_3$ hereafter (Fig. 2C). Strong pollen tube inhibition was observed only with cognate combinations of *At-PrsS* with *At-PrpS* (Fig. 2C, i and v). Pollinations using noncognate combinations of *At-PrsS* with *At-PrpS* resulted in normal pollen tube growth (Fig. 2C, ii and iv). Controls (Fig. 2C, iii, vi, vii, viii, and ix) had long pollen tubes. In vivo pollinations of *At-PrsS* pistils also revealed differential inhibition of pollen tubes after 18 hours (fig. S5). This demonstrates *S*-specific pollen tube inhibition by *A. thaliana* expressing PrsS.

With SI, pollination between cognate pollen and pistil *S* alleles results in no seed production. In planta pollinations on *At-*$PrsS_1$ and *At-*$PrsS_3$ stigmas using cognate (incompatible) *At-*$PrpS_1$ and *At-*$PrpS_3$ pollen gave dramatically reduced silique lengths (6.2 ±1.4 and 6.3 ±1.7 mm, respectively) as compared to *Col-0* controls ($P < 0.001$***, *t* test, $n = 10$ siliques; Fig. 2, D and E, fig. S6, and Table 1). In contrast, *At-*$PrsS_1$ and *At-*$PrsS_3$ pistils pollinated with noncognate (compatible) pollen resulted in normal silique lengths, like *At-*$PrsS_1$ and *At-*$PrsS_3$ pistils pollinated with *Col-0* pollen ($P = 0.397$, *ANOVA*, $n = 10$ siliques), and pollination of *Col-0* stigmas with *At-*$PrpS_1$ or *At-*$PrpS_3$ pollen ($P = 0.871$, *ANOVA*, $n = 10$ siliques; Table 1) resulted in normal siliques, similar to selfed *Col-0* siliques, demonstrating that *At-PrsS* stigmas and *At-PrpS* pollen are functional.

Analyzing self-seed set, many siliques were completely empty (7 out of 10 for *At-*$PrsS_1$ pollinated with *At-*$PrpS_1$ and 6 out of 10 for *At-*$PrsS_3$ pollinated with *At-*$PrpS_3$); seed-set for cognate pollinations was between 0.5 ±1.0 and 1.2 ±1.8 seeds per silique ($n = 10$ siliques; Table 1). Pollinations between noncognate combinations resulted

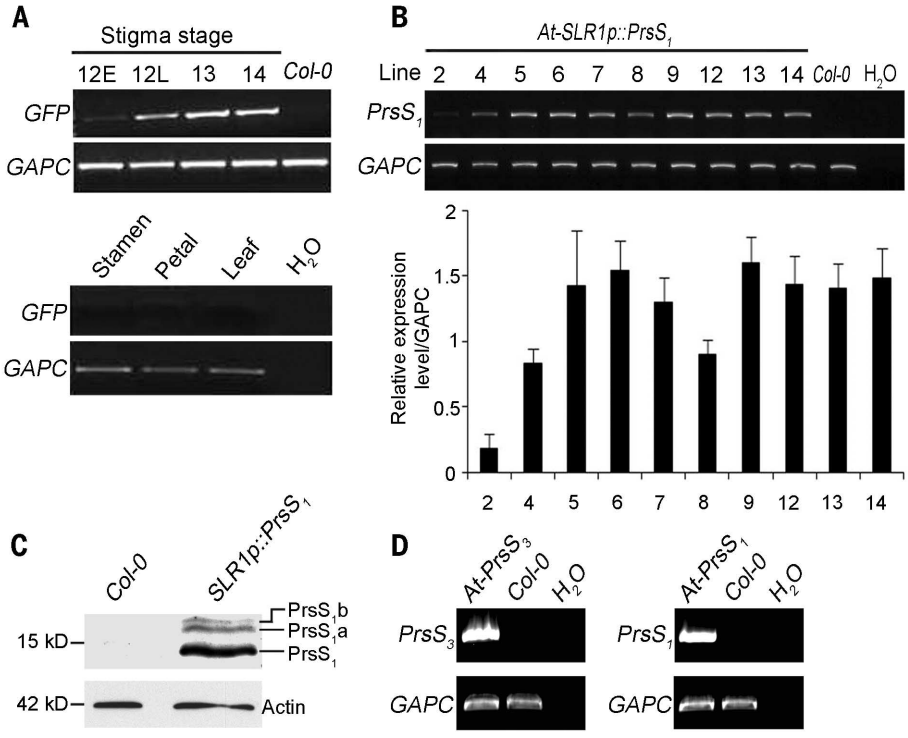

Fig. 1. Expression of the *SLR1* promoter is developmental- and tissue-specific and drives expression of $PrsS_1$ in *A. thaliana*. (**A**) RT-PCR (top) shows *SLR1p::GFP* developmentally expressed in pistils and not expressed in stamen, petal, or leaf tissue. *GAPC* shows equal loading. (**B**) RT-PCR of pistils from *At-*$PrsS_1$ lines shows expression of $PrsS_1$ (top) and quantitation of $PrsS_1$ expression relative to *GAPC* ($n = 3$ RT-PCR experiments, ± SD, *below*). (**C**) Western blot (α-$PrsS_1$ antisera) shows expression of $PrsS_1$ in *At-*$PrsS_1$. (**D**) RT-PCR comparing expression of $PrsS_3$ in *At-*$PrsS_3$ line 8 with that of *At-*$PrsS_1$ line 9.

in normal seed-set (50.6 ± 5, 50.0 ± 3.9, n = 10 siliques), which is significantly different from those with cognate combinations (P < 0.001***, t test). Pollinations between *Col-0* pistils and *At-PrpS$_1$* or *At-PrpS$_3$* pollen gave normal seed-set (49.9 ± 3.7 and 47.6 ± 3.7, n = 10 siliques), so transgenic stigmas and pollen are fully functional. Thus, the *Papaver S* determinants function in vivo in an *S*-specific manner, resulting in failure of fertilization with cognate, but not noncognate, pollen expressing *PrpS*.

We generated *Col-0* lines coexpressing *PrsS$_1$* and *PrpS$_1$* (*SI$_1$* lines) by transforming homozygous *At-PrpS$_1$–GFP* plants with *SLR1p::PrsS$_1$*. Lines coexpressing *PrsS$_3$* and *PrpS$_1$* (*SC* lines) were also generated. Expression of *PrsS$_1$* and *PrpS$_1$* was examined in three *SI$_1$* lines (Fig. 3A). Fluorescence microscopy of pollen from these *SI$_1$* lines confirmed the expression of PrpS$_1$-GFP (Fig. 3B). The *SI$_1$* and *SC* lines had a similar vegetative phenotype to *Col-0*, *At-PrpS$_1$*, and *At-PrsS$_1$* plants (fig. S7). However, when left to set self-seed naturally, the *SI$_1$*-line plants had small siliques (Fig. 3C and fig. S7F), between 3 ± 0.5 and 7 ± 1.4 mm long (n = 470 siliques; fig. S8A), significantly shorter than siliques of control plants (Fig. 3C and fig. S7F) *Col-0* (15.5 ± 0.6 mm), *At-PrpS$_1$* (16.3 ± 1.0), *At-PrsS$_1$* (15.9 ± 0.5), and *SC* plants (15.3 ± 0.5 mm; P < 0.001***, t test; n = 10 siliques per plant). Twelve of the *SI$_1$* lines set no seed; the remaining 35 plants had between 0.1 ± 0.3 and 7.0 ± 1.4 seeds per silique (n = 10 siliques per plant; fig. S8B). This was significantly less (P < 0.001***) than the 58 ± 1.6 seeds per silique in *Col-0* plants, *At-PrpS$_1$* plants (57.7 ± 2.8), *At-PrsS$_1$* plants (58.3 ± 1.6), and *SC* lines (57.1 ± 1.7; n = 10). Total self seed-set from these *SI$_1$* lines gave between 0 and 680 seeds; ~60% had <100 seeds per plant (fig. S8C). Self seed-set of control plants was >8500 seeds per plant (n = 12). This SI response is stronger than previously obtained using the *S* determinants from *A. lyrata* (*12*, *18*) and similar to that achieved by (*19*). Lines coexpressing *PrsS$_3$* and *PrpS$_3$* (*SI$_3$* lines) had a similar vegetative phenotype to *Col-0* plants, except for short siliques (fig. S9). Self–seed-set analysis revealed small siliques (fig. S10, A and B) and no or very low seed-set (fig. S10, B and C), which were similar to those for the *SI$_1$* lines. Analysis of naturally self-pollinated pistils from *SI* lines revealed that pollen tubes were inhibited in the upper pistil, whereas comparable self-pollinated *Col-0* pistils had pollen tubes extending through the pistil (Fig. 3, E and F, and figs. S11 and S12). Together, these data provide compelling evidence that the *SI* lines are self-incompatible.

To confirm that *SI* lines were fully functional, pistils from representative *SI$_1$* lines (*SI$_1$9*, *SI$_1$18*, and *SI$_1$32*) were pollinated with *At-PrpS$_3$* or *Col-0* pollen (Fig. 3D, n = 9 pollinations per line). Siliques obtained were not significantly different from those pollinated using *Col-0* stigmas (P = 0.246, P = 0.703, ANOVA; n = 3 pollinations per line). Pollen from *SI$_1$* lines was also pollinated onto *At-PrpS$_1$* stigmas. They produced siliques and seed-set not significantly different from *At-PrpS$_1$* stigmas pollinated with *Col-0* pollen (P = 0.931, P = 0.803, ANOVA; n = 3 pollinations per line; fig. S13, A and B). Because pollen and pistils from these *SI* lines are functional, the reason why these *SI* lines set no self-seed is not because they have a fertility defect, but because they are self-incompatible.

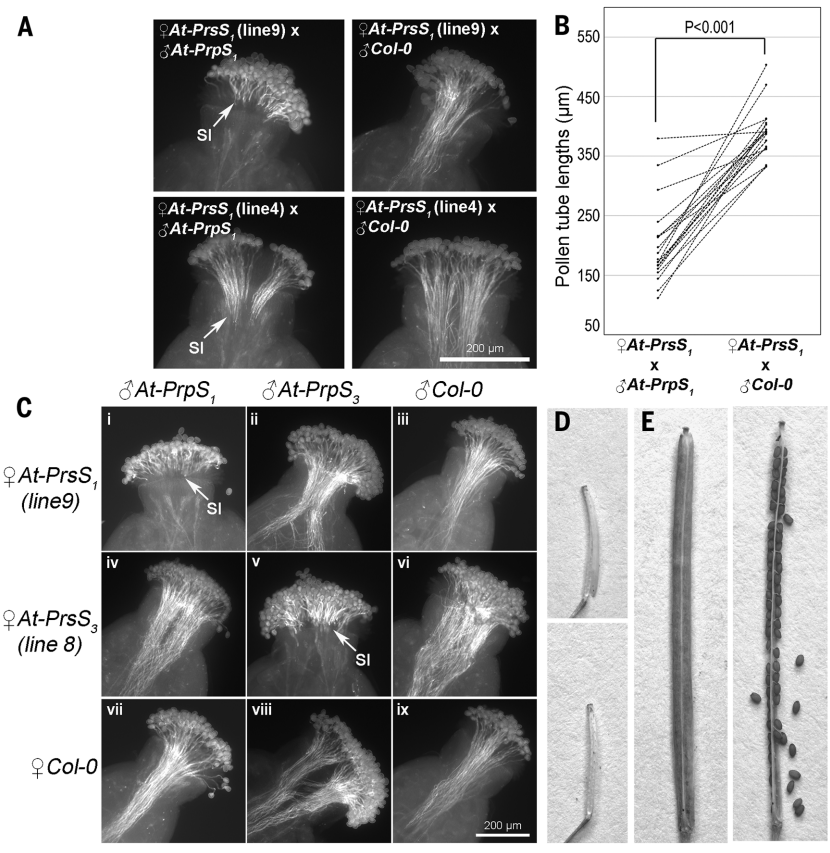

Fig. 2. *At-PrpS* pollen is inhibited on cognate *At-PrsS* pistils, demonstrating *S*-specificity. (**A**) Aniline blue staining of representative semi–in vivo pollinations of *At-PrsS$_1$* pistils with *At-PrpS$_1$* or *Col-0* pollen. (**B**) Quantitation of pollen tube lengths on *At-PrsS$_1$* pistils using *At-PrpS$_1$* pollen (left) or *Col-0* pollen (right); n = 4 stigmas per *At-PrsS$_1$* line. (**C**) *At-PrsS$_1$* and *At-PrsS$_3$* pistils pollinated semi–in vivo with *At-PrpS$_3$* or *At-PrpS$_1$* pollen. *At-PrpS* pollen tubes were inhibited on cognate *At-PrsS* pistils (i and v), whereas controls were not. (**D**) Representative in vivo pollination of an *At-PrsS$_1$* stigma with *At-PrpS$_1$* pollen resulted in a small empty silique. (**E**) *Col-0* pollinated with *Col-0* pollen had a normal-length silique and many seeds.

Table 1. In vivo pollination of *At-PrsS* stigmas with cognate *At-PrpS* pollen resulted in shorter siliques and no seed set. Pollination of emasculated *At-PrsS$_1$* stigmas with *At-PrpS$_1$* pollen resulted in short siliques and reduced seed number, as did pollination of *At-PrsS$_3$* with *At-PrpS$_3$* pollen. Other control pollinations: Noncognate pollination of *At-PrsS$_1$* stigmas with *At-PrpS$_3$* pollen; *At-PrsS$_3$* stigmas with *At-PrpS$_1$* or *Col-0* pollen; and *Col-0* stigmas with *Col-0*, *At-PrpS$_1$*, or *At-PrpS$_3$* pollen gave normal silique length and seed number (mean ± SD, n = 10 siliques pollinated per cross). Numbers in bold indicate incompatible combinations.

♀/♂		*At-PrpS$_1$*	*At-PrpS$_3$*	*Col-0*
At-PrsS$_1$ (line 9)	Silique lengths (mm)	**6.2 ± 1.4**	16.1 ± 0.8	16.4 ± 0.7
	Seeds per silique	**0.5 ± 1.0**	50.6 ± 5.1	49.3 ± 5.3
At-PrsS$_3$ (line 8)	Silique lengths (mm)	16.4 ± 0.8	**6.3 ± 1.7**	16.5 ± 0.5
	Seeds per silique	50.0 ± 3.9	**1.2 ± 1.8**	50.0 ± 3.2
Col-0	Silique lengths (mm)	16.6 ± 1.0	16.6 ± 0.8	16.4 ± 0.7
	Seeds per silique	49.9 ± 3.7	47.6 ± 3.7	47.7 ± 3.6

Our data provide compelling evidence that the *Papaver S* determinants coexpressed in *A. thaliana* make plants self-incompatible and are the sole additional requirement to establish SI in this highly diverged self-compatible species.

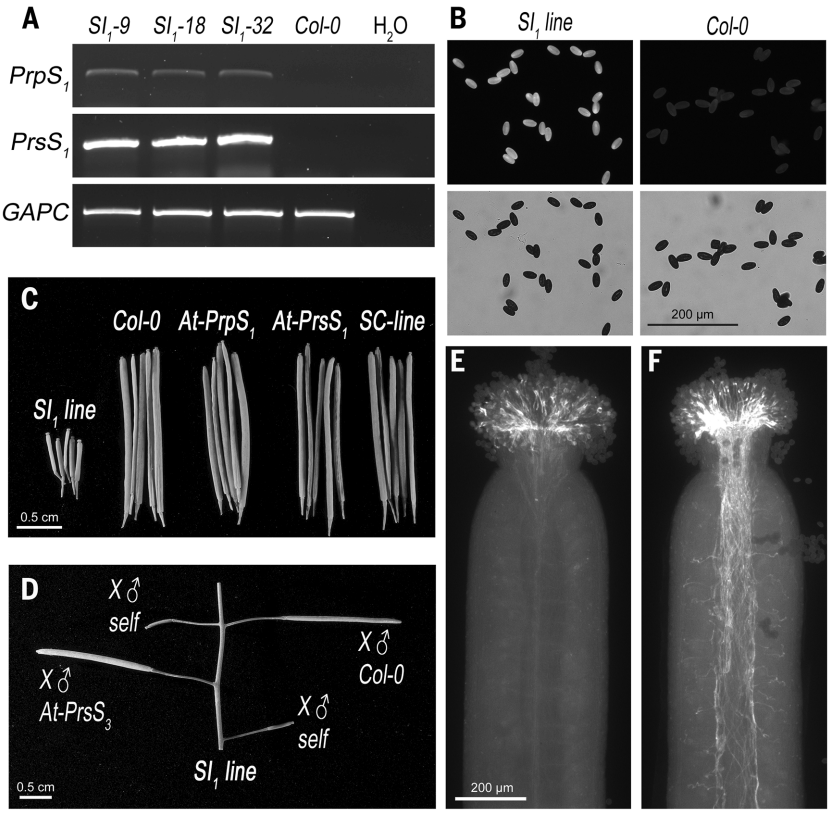

Fig. 3. *A. thaliana* coexpressing $PrsS_1$ and $PrpS_1$ are self-incompatible and set no seed. (**A**) RT-PCR of three *A. thaliana* SI_1 lines coexpressing $PrsS_1$ and $PrpS_1$. (**B**) Pollen from SI_1 lines exhibits GFP fluorescence (top); *Col-0* pollen has weak autofluorescence. (**C**) Self-seed set: SI_1 lines formed short siliques; controls, including an *SC* line coexpressing $PrsS_3$ and $PrpS_1$-*GFP*, set normal siliques. (**D**) A selfed SI_1 plant gave small siliques; pollinations with *Col-0* or *At-PrpS*$_3$ pollen gave normal siliques. (**E**) Aniline blue staining of a self-pollinated SI_1-line pistil; pollen tubes are inhibited in the stigma and style. (**F**) A self-pollinated *Col-0* pistil had long pollen tubes.

This is a milestone, because the successful transfer of *S* determinants to date has been between close relatives sharing an ancestral SI system, using complementation to "restore" SI (*12*, *13*). Because the Papaveraceae and Brassicaceae are evolutionarily separated by ~140 million years (*8*, *15*), our finding that they function in planta in *Col-0* to display a robust SI rejection response is of considerable interest. We are not "restoring" a SI system, because SI in *Brassica* and *Arabidopsis* has genetically and functionally distinct *S* determinants. Because we previously showed that recombinant PrsS can trigger SI-PCD in *Arabidopsis* pollen expressing PrpS (*8*), and there is no evidence that *Brassica* and *Arabidopsis* SI involves PCD, the most economical explanation is that the *Papaver S* determinants can interface with, and activate, a network of common signaling components that mediate PCD to induce a "*Papaver*-like" SI response in *Arabidopsis* pollen. *Papaver* SI uses Ca^{2+}, reactive oxygen species, and pH (*7*, *20*), which have all been described in *Arabidopsis* signaling networks achieving various physiological responses, including PCD (*21*). We hypothesize that these common signaling components are co-opted downstream of PrsS-PrpS interaction to mediate SI. Our findings reinforce proposals that SI may recruit preexisting signaling networks from other biological processes (*8*, *22*). This raises questions about how SI systems evolved, as well as about recruitment and functional diversification of preexisting components (*23*).

Wide transgenera functionality of the *Papaver* SI system opens up the possibility that the transfer of these *S* determinants may, in the longer term, provide a tractable SI system for crop plants. Use of the *SLR1* promoter from *Brassica* (*16*, *17*) allows *PrsS* to be expressed in mature *Col-0* pistils, unlike older *Col-0* pistils expressing *SCRb-SRKb* (*12*, *18*). The production of F_1 hybrid plants in normally self-compatible species typically uses laborious, expensive manual emasculation to prevent self-fertilization. Because it is desirable to be able to control plant fertility for food security, this demonstration of the transfer of a SI system into a self-compatible species suggests an alternative method for the production of F_1 hybrids, a long-term goal of SI research.

REFERENCES AND NOTES

1. V. E. Franklin-Tong, Ed., *Self-Incompatibility in Flowering Plants: Evolution, Diversity, and Mechanisms* (Springer-Verlag, Berlin, 2008).
2. T. Dresselhaus, N. Franklin-Tong, *Mol. Plant* **6**, 1018–1036 (2013).
3. H. C. C. Foote *et al.*, *Proc. Natl. Acad. Sci. U.S.A.* **91**, 2265–2269 (1994).
4. M. J. Wheeler *et al.*, *Nature* **459**, 992–995 (2009).
5. S. G. Thomas, V. E. Franklin-Tong, *Nature* **429**, 305–309 (2004).
6. M. Bosch, V. E. Franklin-Tong, *Proc. Natl. Acad. Sci. U.S.A.* **104**, 18327–18332 (2007).
7. K. A. Wilkins, N. S. Poulter, V. E. Franklin-Tong, *J. Exp. Bot.* **65**, 1331–1342 (2014).
8. B. H. de Graaf *et al.*, *Curr. Biol.* **22**, 154–159 (2012).
9. J. S. Bechsgaard, V. Castric, D. Charlesworth, X. Vekemans, M. H. Schierup, *Mol. Biol. Evol.* **23**, 1741–1750 (2006).
10. J. C. Stein, B. Howlett, D. C. Boyes, M. E. Nasrallah, J. B. Nasrallah, *Proc. Natl. Acad. Sci. U.S.A.* **88**, 8816–8820 (1991).
11. C. R. Schopfer, M. E. Nasrallah, J. B. Nasrallah, *Science* **286**, 1697–1700 (1999).
12. M. E. Nasrallah, P. Liu, J. B. Nasrallah, *Science* **297**, 247–249 (2002).
13. N. A. Boggs *et al.*, *Genetics* **182**, 1313–1321 (2009).
14. M. Yamamoto, T. Nishio, *Horticulture Res.* **1**, 14054 (2014).
15. C. D. Bell, D. E. Soltis, P. S. Soltis, *Am. J. Bot.* **97**, 1296–1303 (2010).
16. B. A. Lalonde *et al.*, *Plant Cell* **1**, 249–258 (1989).
17. R. M. Hackett, M. J. Lawrence, F. C. H. Franklin, *Plant J.* **2**, 613–617 (1992).
18. N. A. Boggs, J. B. Nasrallah, M. E. Nasrallah, S. Independent, *PLOS Genet.* **5**, e1000426 (2009).
19. D. R. Goring, E. Indriolo, M. A. Samuel, *Plant Cell* **26**, 3842–3846 (2014).
20. K. A. Wilkins *et al.*, *Plant Physiol.* **167**, 766–779 (2015).
21. T. Van Hautegem, A. J. Waters, J. Goodrich, M. K. Nowack, *Trends Plant Sci.* **20**, 102–113 (2015).
22. T. Tantikanjana, M. E. Nasrallah, J. B. Nasrallah, *Curr. Opin. Plant Biol.* **13**, 520–526 (2010).
23. F. M. Ausubel, *Nat. Immunol.* **6**, 973–979 (2005).

ACKNOWLEDGMENTS

We thank D. Goring for the Binary Ti vector pORE O3 containing the *SLR1* promoter and S. Price for technical assistance. Z.L. held a Ph.D. studentship from the China Scholarship Council (CSC). D.J.E. was funded by the Biotechnology and Biological Sciences Research Council (BBSRC). V.E.F-T. and F.C.H.F. are co-inventors on a patent application (2691/KOLNP/2011) filed by the University of Birmingham relating to PrsS and PrpS, to engineer plants (ornamental or crop) to exhibit SI by using a *PrsS* and *PrpS S*-allele pair, comprising a functional *S* locus with appropriate tissue-specific promoters. Materials will be freely available upon request for research purposes. The authors declare that they do not have other competing financial interests. The data reported here are available in the supplementary materials.

SUPPLEMENTARY MATERIALS

www.sciencemag.org/content/350/6261/684/suppl/DC1
Materials and Methods
Figs. S1 to S14
Table S1
References (*24*–*27*)

24 August 2015; accepted 18 September 2015
10.1126/science.aad2983

PLANT GENETICS

A cucurbit androecy gene reveals how unisexual flowers develop and dioecy emerges

Adnane Boualem,[1] Christelle Troadec,[1] Céline Camps,[1] Afef Lemhemdi,[1] Halima Morin,[1] Marie-Agnes Sari,[2] Rina Fraenkel-Zagouri,[3] Irina Kovalski,[3] Catherine Dogimont,[4] Rafael Perl-Treves,[3] Abdelhafid Bendahmane[1]*

Understanding the evolution of sex determination in plants requires identifying the mechanisms underlying the transition from monoecious plants, where male and female flowers coexist, to unisexual individuals found in dioecious species. We show that in melon and cucumber, the *androecy* gene controls female flower development and encodes a limiting enzyme of ethylene biosynthesis, ACS11. *ACS11* is expressed in phloem cells connected to flowers programmed to become female, and *ACS11* loss-of-function mutants lead to male plants (androecy). *CmACS11* represses the expression of the male promoting gene *CmWIP1* to control the development and the coexistence of male and female flowers in monoecious species. Because monoecy can lead to dioecy, we show how a combination of alleles of *CmACS11* and *CmWIP1* can create artificial dioecy.

Most angiosperms are hermaphroditic, producing exclusively bisexual flowers. Sex determination is a developmental process that leads to unisexual flowers in ~10% of angiosperm species (*1*). About half of these are monoecious species, with male and female flowers on the same plant, and half are dioecious species, with separate male and female individuals (*1*). The evolutionary pathways from hermaphroditism have been modeled, but empirical evidence is scanty (*2*–*4*). Dioecy appears to have evolved most frequently via monoecy through a series of mutations that alter the ratio of male and female flowers. Dioecy may have also evolved through emergence of unisexual individuals that coexist with hermaphrodites, creating gynodioecy or androdioecy populations (*3*–*6*).

Cucurbitaceae is a large plant family of species that display mostly unisexual flowers. Out of some 800 species investigated, 460 are monoecious and 340 are dioecious, and there have been numerous shifts between monoecy and dioecy (*7*). Several *Cucurbitaceae* species, including cucumber and melon, show different sexual morphs (fig. S1). In monoecious melon (*Cucumis melo*), most of the flowers are male, and female flowers develop at the youngest lateral branches of the growing vines. Cloning of naturally occurring mutations leading to transition from monoecy to different sexual morphs has brought insight to the sex-determination pathway (*8*, *9*). The *andromonoecious* gene *CmACS-7* controls stamina development in female flowers (*9*). The *gynoecious* gene *CmWIP1* controls male flower development, and its loss of function leads to purely female plants (*8*). However, it is not known how male and female flowers coexist on the same plant, in monoecious species, and how purely male plants can emerge from monoecious or hermaphrodite populations.

Because solely male plants have not been described in melon, we investigated natural polymorphisms in the related species cucumber (*Cucumis sativus*) (*10*). Cucumber is also monoecious, and its sex determination system is conserved with melon (*11*). Cucumber plants homozygous for the *androecious* allele (*a*) bear only male flowers (*12*).

We cloned the *androecious* gene (*a*) in cucumber using a positional cloning strategy (fig. S2) that involves a cross between the monoecious line

[1]Institut National de la Recherche Agronomique (INRA), Institute of Plant Sciences Paris-Saclay, CNRS, Université Paris-Sud, Université d'Evry, Université Paris-Diderot, Bâtiment 630, 91405, Orsay, France. [2]Laboratoire de Chimie et Biochimie Pharmacologiques et Toxicologiques, CNRS, UMR 8601, Université René Descartes, Paris, France. [3]The Mina and Everard Goodman Faculty of Life Sciences, Bar-Ilan University, Ramat Gan, Israel. [4]INRA, UR 1052, Unité de Génétique et d'Amélioration des Fruits et Légumes, BP 94, F-84143 Montfavet, France.
*Corresponding author. E-mail: bendahm@evry.inra.fr

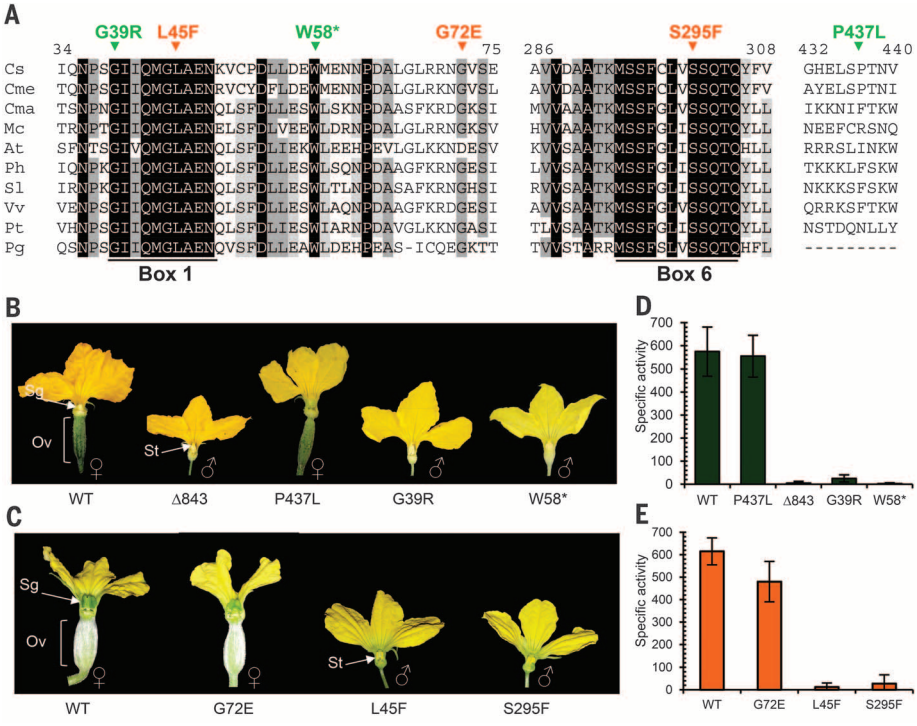

Fig. 1. Molecular characterization of alleles of ACS11. (**A**) Alignments of CsACS11 with homologous proteins from Cme (*Cucumis melo*), Cma (*Cucurbita maxima*), Mc (*Momordica charantia*), At (*Arabidopsis thaliana*), Ph (*Petunia hybrida*), Sl (*Solanum lycopersicum*), Vv (*Vitis vinifera*), Pt (*Populus trichocarpa*), and Pg (*Picea glauca*). Boxes 1 and 6 indicate conserved domains in ACS proteins. TILLING mutations in CsACS11 and CmACS11 are shown above the alignment in green and orange, respectively. (**B**) Cucumber flower types from monoecious plant (WT), androecious (Δ843), and mutants G39R, W58*, and P437L. (**C**) Melon flower types from monoecious plant (WT) and mutants G72E, L45F, and S295F. Ov, ovary; Sg, stigma; St, stamen. (**D** and **E**) ACS enzymatic activity of WT and mutants (D) CsACS11 and (E) CmACS11 isoforms.

Downloaded from www.sciencemag.org on November 5, 2015

Oman and the androecious line Erez. Sequence analysis of the (*a*) locus revealed a single nonsynonymous nucleotide deletion, Δ843, within exon 3 of *Csa2G353460*. This 1–base pair (bp) deletion leads to a premature stop codon, suggesting that Erez is null for *Csa2G353460* (fig. S2, C and D). *Csa2G353460* encodes a 1-aminocyclopropane-1-carboxylic acid synthase (ACS), hereafter CsACS11 (fig. S3). ACS catalyzes the rate-limiting step in ethylene biosynthesis, the production of 1-aminocyclopropane-1-carboxylic acid (ACC) from *S*-adenosylmethionine (SAM). Ethylene is then made from ACC by the ACC oxidase (*13*). To investigate whether this 1-bp deletion is associated with androecy, we resequenced *CsACS11* in a panel of 50 cucumber accessions of different sexual morphs. In contrast to the 1-bp deletion, none of the observed polymorphisms was associated with androecy, supporting that the 1-bp deletion underlies androecy in cucumber (figs. S4 and S5).

Because there is no efficient cucumber transformation protocol, we produced a TILLING (Targeting Induced Local Lesions in Genomes) collection from a monoecious cucumber line and screened for mutations in *CsACS11*. We identified 10 induced mutations with seven silent, one nonsense (W58*), and two missense mutations (G39R and P437L) (table S1) (*14*). G39R occurs in a highly conserved amino acid position and is predicted to affect the function of the protein, whereas the P437L modification affects a nonconserved amino acid (Fig. 1A and fig. S5). Crosses support that the P437L and silent mutations have no impact on the sex of the plant, whereas plants homozygous for the G39R or W58* mutations were androecious, with no female flowers (Fig. 1B and table S1). On the basis of these data, we concluded that *CsACS11* is the *androecious* gene (*A*).

To test whether the genetic determinant controlling female flower development is conserved in *Cucumis*, we screened for mutations in the melon ortholog of *CsACS11*, *MELO3C010779*, hereafter *CmACS11* (fig. S3). CmACS11 and CsACS11 share 92% amino acid sequence identity and are syntenic (figs. S5 and S6). We isolated 10 silent or intronic changes and three missense mutations—L45F, G72E, and S295F—in *CmACS11* (Fig. 1A and table S1). L45F and S295F mutations are in highly conserved amino acid positions and are predicted to affect the function of the protein, unlike the G72E mutation, which is in a nonconserved amino acid position (table S1 and fig. S5). We back-crossed *CmACS11* missense mutant lines to the wild type and observed no effect on the sex of the plant correlated with the G72E mutation, nor for silent and intronic mutations (Fig. 1C and table S1). In contrast, plants homozygous for L45F or S295F mutations were androecious (Fig. 1C). We therefore conclude that CmACS11 controls female flower development in melon and that *ACS11* function evolved before the divergence of *Cucumis melo* and *Cucumis sativus*, ~10 million years ago (*10*).

In the parental line Erez, the *androecy* allele encodes a truncated form of ACS11. In the TILLING screens, all induced mutations leading to androecy are predicted to be loss-of-function (Fig. 1 and figs. S5 and S7). We expressed the ACS11 mutant proteins and assayed their activity in vitro (*11*). As expected, the mutations that lead to androecy—W58*, Δ843, L45F, G39R, and S295F—all display low to undetectable ACS activities, whereas mutations not affecting the sex of the plant, G72E and P437L, have activities comparable with those of the wild type (Fig. 1, D and E). We conclude that *ACS11*-mediated ethylene production is necessary for the development of female flowers in monoecious *Cucumis* species, whereas loss of ACS activity leads to female-to-male transition. Consistent with this, *ACS11* loss-of-function mutants treated with the ethylene-releasing agent Ethephon developed female flowers (fig. S8).

ACS11 mRNA can only be detected in female flower buds from monoecious cucumber and melon plants at stage 4 (Fig. 2, A to C and G) (*15*), in which the bud sex is not morphologically distinguishable, with expression at later stages (Fig. 2, D and I). No *ACS11* expression was detected in vegetative tissues or male flowers (Fig. 2, E and H, and fig. S9). *ACS11* mRNA was strongly localized in vascular bundles of female flowers in both internal and external fascicular phloems (Fig. 2F and fig. S10) but not in the extrafascicular phloem (*16*). This strong signal corresponds to the companion cell sieve element complex in the phloem connected to flower buds with a developing carpel (fig. S10, C and E). In the andromonoecious plants—developing male and hermaphrodite flowers—*ACS11* is highly expressed in the phloem of hermaphrodite flower buds but not in male buds (fig. S11). This supports that *ACS11*-mediated ethylene production is required for the development of the carpel in monoecious and andromonoecious *Cucumis* species.

Expression of *CmWIP1* inhibits carpel development, and the nonexpression or loss-of-function of *CmWIP1* releases this inhibition (*8*). Hence, *CmACS11* function is antagonistic to *CmWIP1* function in flowers programmed to develop carpels. To test the hypothesis that *CmACS11* may be the repressor of *CmWIP1*, we analyzed

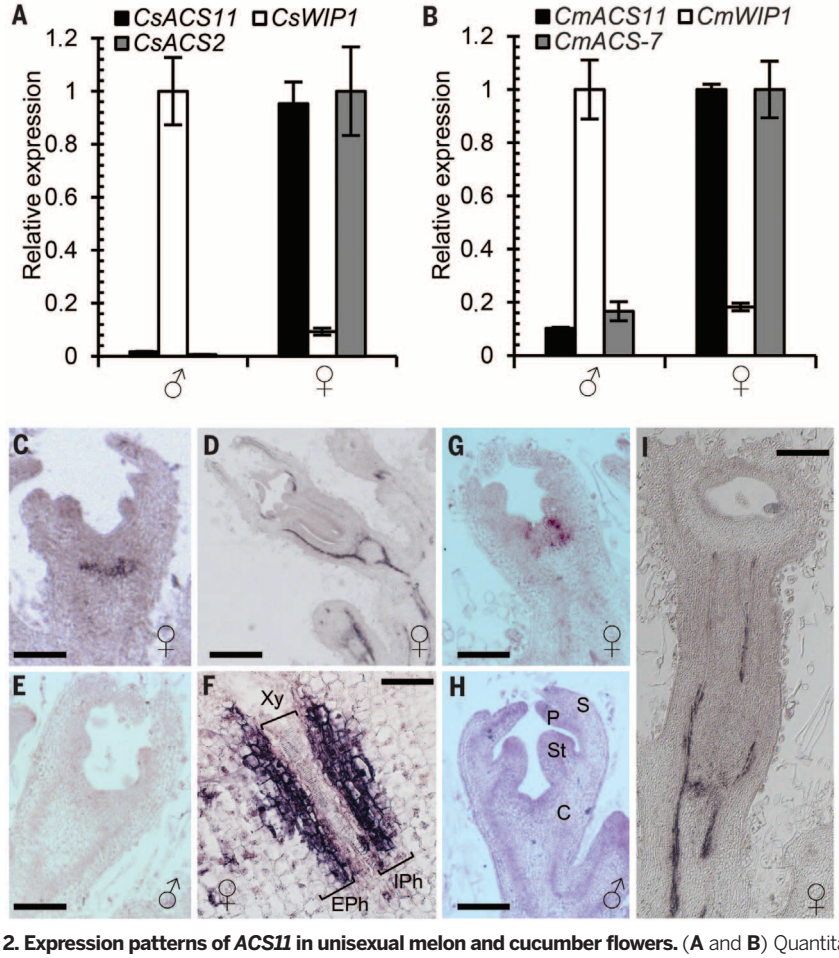

Fig. 2. Expression patterns of *ACS11* in unisexual melon and cucumber flowers. (**A** and **B**) Quantitative reverse transcription polymerase chain reaction (RT-PCR) of *ACS11*, *ACS7*, and *WIP1* in male or female flower buds, collected at stage 4, of (A) cucumber and (B) melon. Shown are the mean ± SD of three biological replicates. (**C** to **E** and **G** to **I**) *ACS11* in situ expression in flower buds at [(C), (E), (G), and (H)] stage 4 and [(D) and (I)] stage 8 of [(C) to (E)] cucumber and [(G) to (I)] melon. (**F**) Longitudinal section of a vascular bundle of a cucumber female flower. C, carpel; St, stamen; P, petal; S, sepal. Xy, xylem; EPh, external phloem; IPh, internal phloem. Scale bars, (F) 15 μm; (C) to (E), (G), and (H) 200 μm ; (I) 500 μm.

the expression of *CmWIP1* in flowers that do or do not express *CmACS11* and in flowers impaired in *CmACS11* function. *CmWIP1* and *CmACS11* expression was diametrically opposite, with *CmWIP1* highly expressed in male buds but not in female buds that express *CmACS11* (Fig. 2B). Expression of *CmWIP1* is reactivated in *CmACS11* loss-of-function mutants (Fig. 3A). We also generated and phenotyped *Cmwip1Cmacs11* double mutants, which were gynoecious like the *Cmwip1* single mutant (Fig. 3B), indicating that *CmWIP1* is epistatic to *CmACS11*. These data also imply that *CmACS11* acts upstream of *CmWIP1* in the sex-determination pathway. We thus generated and characterized double and triple *CmACS11*, *CmWIP1*, and *CmACS-7* mutants (Fig. 3B). The results support a model in which expression of the carpel inhibitor, *CmWIP1*, is dependent on nonexpression of *CmACS11*, and expression of the stamina inhibitor, *CmACS-7*, is dependent on nonexpression of *CmWIP1* (Figs. 2B and 3C). In monoecious and andromonoecious plants, male flowers result from nonexpression of *CmACS11*, which permits *CmWIP1* expression (Figs. 2H and 3C and fig. S11). Female flowers develop on the branches because of expression of *CmACS11* that represses the expression of *CmWIP1*. Consequently, the nonexpression of *CmWIP1* releases the expression of *CmACS-7* that inhibits the stamina development (Fig. 3C). If nonfunctional *CmACS-7* is expressed, hermaphroditic, instead of female, flowers develop (Fig. 3C). Androecious plants result from a loss of function of *CmACS11*, leading to expression of *CmWIP1* in all flowers on a plant. Gynoecious plants are obtained by inactivation of *CmWIP1* function, and hermaphrodite plants are obtained by inactivation of *CmWIP1* and *CmACS-7* (Fig. 3C).

In angiosperms, dioecy is believed to arise most frequently via monoecy and less frequently from other sexual systems, such as gynodioecy (*1*, *3*). Dioecy is theorized to arise from a minimum of two mutations, in which one results in female plants and the other in male individuals (*2*). *CmWIP1* and *CmACS11* fit a single sex-determination model and can explain the development of unisexual flowers (Fig. 3C). We produced a 1:1 sex ratio segregating dioecious population (*G* test) (*17*) by crossing female plants homozygous for the recessive alleles *Cmwip1* and *Cmacs11* and male plants of *Cmwip1*/*CmWIP1* and *Cmacs11*/*Cmacs11* genotype (Fig. 4A). Thus, a combination of alleles of genes controlling monoecy theoretically can result in dioecy (Fig. 4B).

The cloning of the androecy gene and its integration into a genetic model of sex determination indicate the molecular underpinnings of how unisexual flowers coexist and how their relative numbers could be modulated on the same plant in monoecious species, and provide a possible route toward dioecy. The expression of *CsACS11* in the phloem shows that ethylene is a likely signal to be controlling the sex of flowers on the branches. Nevertheless, it still unknown whether *ACS11* mRNA, protein, ACC, or ethylene is the signal. Ethylene signaling controls inhibition of stamina development, through expression

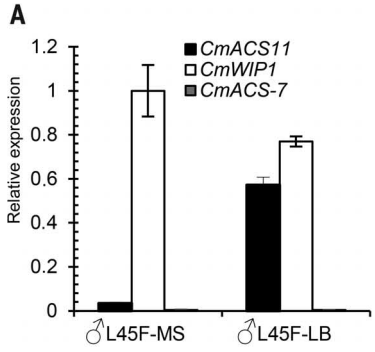

B

Sexual phenotype	Genotype		
	G locus	*M* locus	*A* locus
Gynoecious	*wip1/wip1*	*ACS7/-*	*-/-*
Androecious	*WIP1/-*	*-/-*	*acs11/acs11*
Hermaphrodite	*wip1/wip1*	*acs7/acs7*	*-/-*
Monoecious	*WIP1/-*	*ACS7/-*	*ACS11/-*
Andromonoecious	*WIP1/-*	*acs7/acs7*	*ACS11/-*

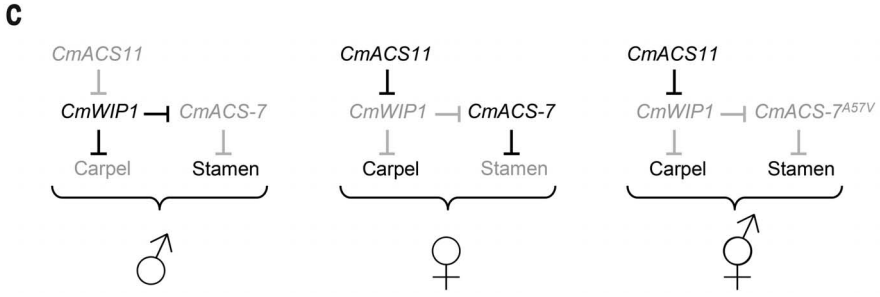

Fig. 3. Expression and function of *CmACS11*, *CmWIP1*, and *CmACS-7* correlates with sex. (**A**) Quantitative RT-PCR of *ACS11*, *ACS-7*, and *WIP1* in stage 4 male flower buds, collected from the main stem (M45F-MS) or the first three nodes of the lateral branches (L45F-LB), of an androecious (male) *Cmacs11*-L45F plant. Shown are the mean ± SD of three biological replicates. (**B**) Sexual morphs of melon plants across a combination of alleles at *G*, *M*, and *A* sex loci. Minus symbol indicates any allele at the locus. (**C**) Model of the sex-determination pathway in melon integrating *CmACS11*, *CmWIP1*, and *CmACS-7* genetic and functional information.

A

Segregation	Total siblings	Female plants	Male plants	Sex ratio	G test
Offspring 1	86	46	40	0.53	0.42 ns
Offspring 2	90	43	47	0.48	0.18 ns

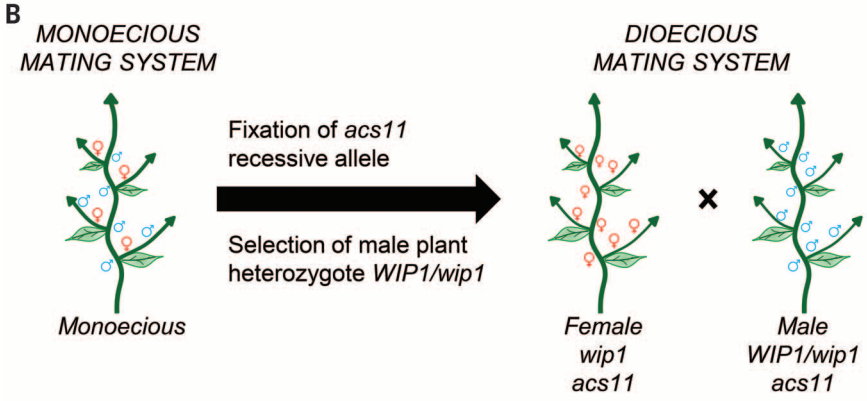

Fig. 4. Engineering dioecy from monoecious melon. (**A**) Fixation of *Cmacs11* loss-of-function alleles at the population level and the maintenance of the dominant allele of *CmWIP1* at the heterozygous level in male plants lead to a dioecious mating system. (**B**) Segregation analysis of two consecutive crosses between male plant of *WIP1/wip1 acs11/acs11* genotype and female plant of *wip1/wip1 acs11/acs11* genotype shows dioecy. Sex ratio was calculated as females/(females + males). *G* statistical test (*G*) is indicated with the level of significance [not significant (ns), $P > 0.05$].

of *CmACS-7* as well as the development of the carpel through expression of *CmACS11*. This is likely due to a tight control of the kinetics of the production of this hormone during sex determination. Because ethylene seems to be a major hormone in sex determination in angiosperms (*18*), it is likely that our model of sex determination in a monoecious plant can be used as a framework for investigations of sex determination in other plant families. Furthermore, this work may allow easier breeding and optimization of the synchronization of male and female flower development on the same plant so as to improve fruit yields in nonmodel, cultivated *Cucurbitaceae* species.

REFERENCES AND NOTES

1. S. S. Renner, *Am. J. Bot.* **101**, 1588–1596 (2014).
2. B. Charlesworth, D. Charlesworth, *Am. Nat.* **112**, 975 (1978).
3. S. S. Renner, R. E. Ricklefs, *Am. J. Bot.* **82**, 596 (1995).
4. S. C. Barrett, *Nat. Rev. Genet.* **3**, 274–284 (2002).
5. D. Lewis, *Biol. Rev. Camb. Philos. Soc.* **17**, 46–67 (1942).
6. D. Charlesworth, B. Charlesworth, *Heredity* **41**, 137–153 (1978).
7. A. Kocyan, L. B. Zhang, H. Schaefer, S. S. Renner, *Mol. Phylogenet. Evol.* **44**, 553–577 (2007).
8. A. Martin *et al*., *Nature* **461**, 1135–1138 (2009).
9. A. Boualem *et al*., *Science* **321**, 836–838 (2008).
10. P. Sebastian, H. Schaefer, I. R. Telford, S. S. Renner, *Proc. Natl. Acad. Sci. U.S.A.* **107**, 14269–14273 (2010).
11. Supplementary text and materials and methods are available as supplementary materials on *Science* Online
12. B. Kubicki, *Genet. Pol.* **10**, 101–122 (1969).
13. P. W. Oeller, M. W. Lu, L. P. Taylor, D. A. Pike, A. Theologis, *Science* **254**, 437–439 (1991).
14. Single-letter abbreviations for the amino acid residues are as follows: A, Ala; C, Cys; D, Asp; E, Glu; F, Phe; G, Gly; H, His; I, Ile; K, Lys; L, Leu; M, Met; N, Asn; P, Pro; Q, Gln; R, Arg; S, Ser; T, Thr; V, Val; W, Trp; and Y, Tyr. In the mutants, other amino acids were substituted at certain locations; for example, G39R describes a mutant in which glycine at position 39 is replaced by arginine.
15. S. L. Bai *et al*., *Planta* **220**, 230–240 (2004).
16. R. Turgeon, K. Oparka, *Proc. Natl. Acad. Sci. U.S.A.* **107**, 13201–13202 (2010).
17. M. L. Tang, Y. B. Pei, W. K. Wong, J. L. Li, *Stat. Methods Med. Res.* **21**, 331–345 (2012).
18. T. F. Law, S. Lebel-Hardenack, S. R. Grant, *Am. J. Bot.* **89**, 1014–1020 (2002).

ACKNOWLEDGMENTS

We thank P. Audigier, F. Vion, N. Giovinazzo, and V. Sarnette for plant care; S. Renner, S. Grant, and G. Marais for critical comments on the manuscript; and V. Gomez-Roldan and C. Clepet for helpful discussions on the manuscript. This work was supported by the Plant Biology and Breeding department in INRA, the grants Program Saclay Plant Sciences (SPS, ANR-10-LABX-40), Initiative d'Excellence Paris-Saclay (Lidex-3P, ANR-11-IDEX-0003-02), L'Agence Nationale de la Recherche MELODY (ANR-11-BSV7-0024), and the European Research Council (ERC-SEXYPARTH). We declare no financial conflicts of interest in relation to this work. Gene sequences of CsACS11 and CmACS11 have been deposited into GenBank (accession nos. KT715743 and KT715744). A provisional patent (WO/2013/107632) has been deposited by A.Be., A.Bo., and C.T. that covers the use of the androecy gene for cucurbit breeding. The described material can be obtained from A.Be. under a materials transfer agreement with INRA. The supplementary materials contain additional data.

SUPPLEMENTARY MATERIALS

www.sciencemag.org/content/350/6261/688/suppl/DC1
Materials and Methods
Supplementary Text
Figs. S1 to S13
Tables S1 to S3
References (*19*–*28*)

20 June 2015; accepted 22 September 2015
10.1126/science.aac8370

NONHUMAN GENOMICS

The *Symbiodinium kawagutii* genome illuminates dinoflagellate gene expression and coral symbiosis

Senjie Lin,[1,2]*† Shifeng Cheng,[3,4,5]† Bo Song,[3]† Xiao Zhong,[3]† Xin Lin,[1]† Wujiao Li,[3] Ling Li,[1] Yaqun Zhang,[1] Huan Zhang,[2] Zhiliang Ji,[6] Meichun Cai,[6] Yunyun Zhuang,[2]‡ Xinguo Shi,[1] Lingxiao Lin,[1] Lu Wang,[1] Zhaobao Wang,[3] Xin Liu,[3] Sheng Yu,[3] Peng Zeng,[3] Han Hao,[7] Quan Zou,[6] Chengxuan Chen,[3] Yanjun Li,[3] Ying Wang,[3] Chunyan Xu,[3] Shanshan Meng,[1] Xun Xu,[3] Jun Wang,[3,8,9] Huanming Yang,[3,9,10] David A. Campbell,[11] Nancy R. Sturm,[11] Steve Dagenais-Bellefeuille,[12] David Morse[12]

Dinoflagellates are important components of marine ecosystems and essential coral symbionts, yet little is known about their genomes. We report here on the analysis of a high-quality assembly from the 1180-megabase genome of *Symbiodinium kawagutii*. We annotated protein-coding genes and identified *Symbiodinium*-specific gene families. No whole-genome duplication was observed, but instead we found active (retro) transposition and gene family expansion, especially in processes important for successful symbiosis with corals. We also documented genes potentially governing sexual reproduction and cyst formation, novel promoter elements, and a microRNA system potentially regulating gene expression in both symbiont and coral. We found biochemical complementarity between genomes of *S. kawagutii* and the anthozoan *Acropora,* indicative of host-symbiont coevolution, providing a resource for studying the molecular basis and evolution of coral symbiosis.

Dinoflagellates are alveolates, with the mostly parasitic apicomplexans as their closest relatives (fig. S1A). Members of the genus *Symbiodinium* are essential photosynthetic endosymbionts in coral reefs (*1*). Dinoflagellates show enigmatic genetic and cytological characteristics, including permanently condensed chromosomes and a high proportion of diverse methylated nucleotides, and often feature large nuclear genomes (up to 250 Gb) (*2*). We report a 0.935-Gbp assembly of the 1.18-Gbp genome of *Symbiodinium kawagutii* (figs. S1B and S2), a Clade F strain originally isolated from a Hawaiian reef ecosystem (*3*). A high-quality *S. kawagutii* genome assembly corresponding to ~80% of the genome was achieved from ~151-Gbp Illumina genome shotgun sequence (~130x genome coverage) (tables S1 to S4 and fig. S3). Genome annotation revealed 36,850 nuclear genes, with 68% occurring in families (1.69 genes per family) (table S5). Only ~9% (3280) of *S. kawagutii* genes were in tandem arrays (1279 clusters) (table S6), with 2 to 10 repeats (76% being ≤4 repeats) per array. The genome encodes the common metabolic pathways expected for typical photosynthetic eukaryotes (fig. S4 and table S7), and we found genes involved in sexual reproduction, cyst formation and germination, and telomere synthesis (table S8). The telomeric motif (TTTAGGG)n was identified at the ends of scaffolds and was also detected by fluorescence in situ hybridization (fig. S1B).

Globally, our analysis revealed extensive genomic innovation in dinoflagellates. A total of 25,112 gene families were clustered from the genomes of *S. kawagutii* and eight other species representing higher plants, chlorophytes, rhodophytes, diatoms, phaeophytes, alveolates, and cnidarians. *S. kawagutii* has 12,516 gene families, of which 7663 were gained in the ancestor of *Symbiodinium* (Fig. 1A and table S9). These genes were enriched in 62 metabolic gene ontologies (table S10). When the gene families were normalized to *z* scores to balance the effect of different total gene numbers, 96 gene families had shrunk (table S11) and 265 gene families had expanded in *Symbiodinium* (table S12). The LINE-1 reverse transcriptase (a retroelement) is the most highly expanded family.

[1]State Key Laboratory of Marine Environmental Science and Marine Biodiversity and Global Change Research Center, Xiamen University, Xiamen 361101, China. [2]Department of Marine Sciences, University of Connecticut, Groton, CT 06340, USA. [3]Beijing Genomics Institute (BGI)–Shenzhen, Shenzhen, 518083, China. [4]Hong Kong University (HKU)–BGI Bioinformatics Algorithms and Core Technology Research Laboratory, The Computer Science Department, The University of Hong Kong, Hong Kong, China. [5]School of Biological Sciences, The University of Hong Kong, Pokfulam, Hong Kong, China. [6]State Key Laboratory of Stress Cell Biology, School of Life Sciences, Xiamen University, Xiamen 361101, China. [7]Bioinformatics Institute, Agency for Science, Technology and Research, Singapore. [8]Department of Biology, University of Copenhagen, DK-2200 Copenhagen, Denmark. [9]Princess Al Jawhara Center of Excellence in the Research of Hereditary Disorders, King Abdulaziz University, Jeddah, Saudi Arabia. [10]James D. Watson Institute of Genome Science, Hangzhou, China. [11]Department of Microbiology, Immunology, and Molecular Genetics, David Geffen School of Medicine, University of California at Los Angeles, Los Angeles, CA 90095, USA. [12]Institut de Recherche en Biologie Végétale, Département de Sciences Biologiques, Université de Montréal, Montréal, Canada.
***Corresponding author. E-mail: senjie.lin@uconn.edu.** †These authors contributed equally to this work. ‡Present address: College of Environmental Science and Engineering, Ocean University of China, Qingdao, Shandong 266100, China.

Our synteny and homology analysis showed no evidence of whole-genome duplication, because little collinearity within *S. kawagutii* genome was observed (table S13). Instead, the *S. kawagutii* genome shows evidence of transposon propagation, in particular long terminal repeat (LTR) retrotransposons and DNA transposons (table S14), which contributes to differences between *S. kawagutii* and *S. minutum* (Fig. 1B). Furthermore, protein domains linked to transposons (table S15) may lead to proliferation of these protein domains in the genome; in the case of cytosine methyltransferase, the resulting expansion of the gene family may help explain the extensive DNA methylation seen in dinoflagellates; in the case of retroelements such as reverse transcriptase and integrase, the expanded families may increase the frequency of transcript retrotranspostion into the genome. In keeping with this latter, we found numerous genes with a full (62 genes) or partial (5506 genes) dinoflagellate spliced leader (DinoSL) (*4*) in their 5′ untranslated region (table S16). The 22-nucleotide (nt) dinoSL is *trans*-spliced to the 5′ end of all mRNAs, and its presence in the genome is a signature of retrotranscript insertion (*5*); this thus represents an efficient mechanism for gene family expansion. Last, horizontal gene transfer (HGT) may also contribute to *S. kawagutii* genome innovation. Conservatively, we found 56 potential HGT genes, 41 of which had best Basic Local Alignment Search Tool (BLAST) hits to marine bacteria (table S17 and fig. S5).

The partial genome (~41%) of *S. minutum* (*6*) allowed some comparative genomic studies. *S. minutum* and *S. kawagutii* have similar genome sizes and gene numbers (table S5) and show some genomic collinearity (Fig. 1B and table S18) and gene ontology profiles (table S19 and fig. S6A). MUMmer (Maximal Unique Matches) alignment data showed that 2.17% (20.4 Mb) of the *S. kawagutii* genome matched to *S. minutum*, and only 5.92% (36.5 Mb) of the *S. minutum* genome matched to *S. kawagutii*. This divergence was confirmed by the reciprocal mapping of their raw reads (fig. S6B and tables S5 and S20), implying that these two species are more diverged than usually assumed. Yet both genomes showed expansion of gene families involving cargo transport and stress responses (fig. S6C and tables S21 and S22), which may reflect the shared symbiotic lifestyles.

The transcriptional machinery of dinoflagellates does not contain the typical eukaryotic TATA box promoter element (*2*). Instead of a TATA-box binding protein (TBP), dinoflagellates express a TBP-like factor that has a stronger affinity to TTTT than to TATA (*7*). A global search of the *S. kawagutii* genome 1000-bp (base pair) region upstream of putative start codons revealed 564 conserved motifs, which were grouped into 108 clusters on the basis of sequence similarities (table S23). About 92% of these were located within 100 bp upstream of the start codon. The motifs with the most conserved positions are remnants of SL (Fig. 1C). Motifs TTTT and TTTG were found in the upstream regions of 34,524 and 35,348 genes, respectively (94% and 96% of the gene repertoire). Curiously, although both are part of the SL, the TTTG motif has a position consistent with that of the SL, whereas TTTT tends to be further upstream (Fig. 1D). This suggests that the TTTT may serve as a core promoter motif replacing the TATA box used by other eukaryotes. The TTTT is typically 30 bp upstream from a potential transcriptional start site (fig. S7). The next most highly enriched motif, (TATG)2, was associated with only 257 promoters and is thus more likely to be a binding target of specific regulators.

Sequences from the genome and purified small RNAs predicted 367 and 354 mature microRNAs (miRNAs), respectively (*3*), with 102 of the latter (table S24) retained after stringent filtering and structural analysis (fig. S8A). We matched 255 of the genome-predicted miRNAs to 99 of the small RNA-based miRNAs. The mature miRNA candidates varied in length from 21 to 24 nt, with most (91.5%) containing 22 nt. Northern blot analysis revealed a decreased expression level for some miRNA in cultures grown at 35°C instead of 25°C (Fig. 2A); of these, scaffold270_6017 is predicted to target heat shock proteins 90 and 70 (table S25), consistent with an expected up-regulation in translation of these thermal stress proteins. A bias toward uridine (U) (47.9%) and against guanine (G) (5.0%) was observed at the 5′-end ultimate nucleotide, as was in *Arabidopsis thaliana* (*8*). Interestingly, of the 102 mature miRNA sequences, 49 were similar to animal miRNAs, 11 to plant miRNAs, and 1 to viral miRNAs (*3*). *S. kawagutii* thus has a miRNA reservoir dominated by miRNAs with considerable sequence identity to those found in animals (fig. S8B).

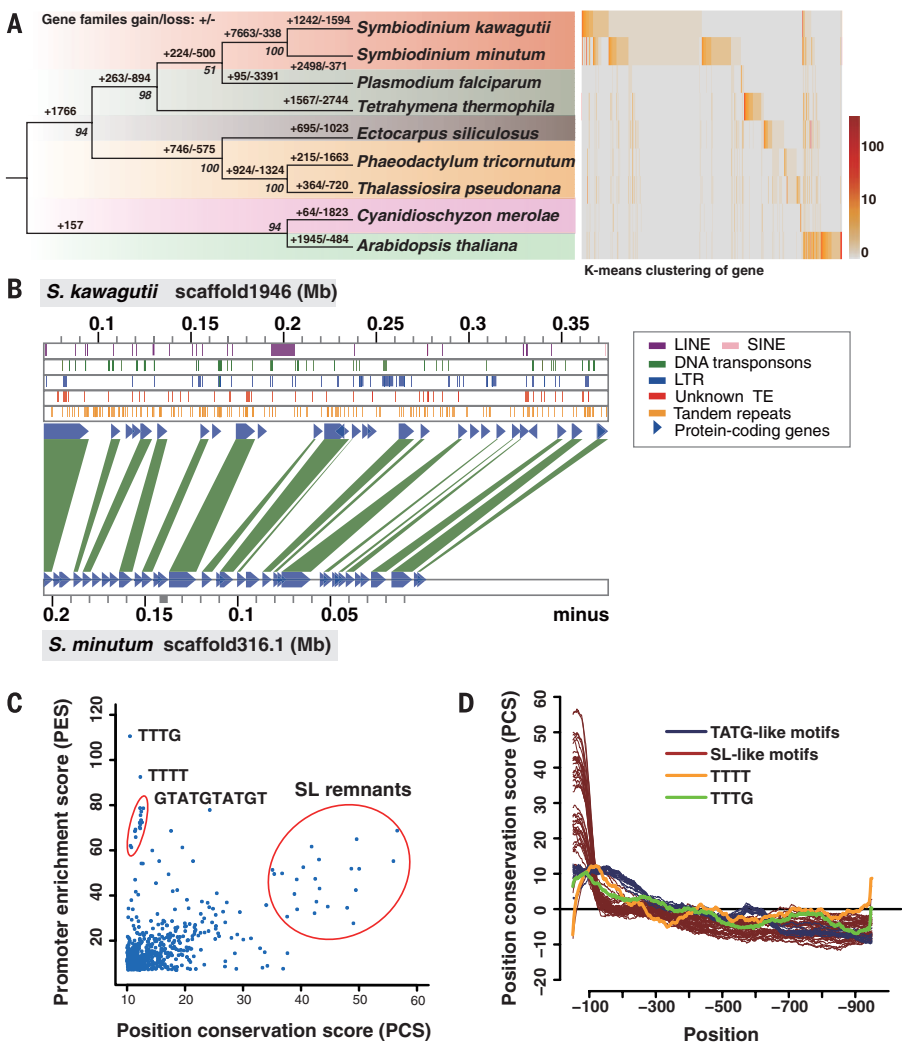

Fig. 1. Comparative genomic analysis between *S. kawagutii* and other eukaryotes. (**A**) (Left) Predicted pattern of gain or loss of gene families across eukaryotes shown on a phylogenetic tree inferred from genome data. Numbers on branches indicate the number of gene families gained (+) or lost (−); those at the left of the nodes are bootstrap values supporting the tree topology. (Right) *K*-means clustering of gene families based on number of members. Columns represent gene families, and rows are species of eukaryote. (**B**) Synteny between regions of the genomes of *S. kawagutii* and *S. minutum*. (**C**) TTTG, TTTT, and (TATG)2 are the top three motifs enriched in the *S. kawagutii* upstream regions and are potential novel promoter elements. (**D**) Promoter enrichment scores for selected motifs as a function of distance upstream from the start codon.

We identified 1 perfect (plant-type) and 6026 partial (animal-type) complementarity miRNA targets in the *S. kawagutii* genome. Among the genes with partial complementarity, 381 were potentially targets of miRNAs with higher expression levels (read counts > 1000), suggesting that these genes are more likely to be regulated by miRNAs. In total, 2557 of all the potential target genes were annotated with known functions (table S25) with enrichments in biological processes of carbohydrate metabolism, transcription regulation, and biosynthesis of amino acids and antibiotics (tables S26 and S27). miRNA targets are often clustered in networks of interacting proteins (*3*), in which some genes are targeted by many miRNAs and some miRNAs target multiple genes (Fig. 2B, fig. S9, and table S28). In addition, the *S. kawagutii* genome harbors small RNA-degrading nucleases 1 and 3, one of which is itself a miRNA target (table S25). Thus, the evidence for miRNA-based gene regulatory machinery is robust and extensive, complementary to the limited transcriptional regulation documented in dinoflagellates (*2*).

We identified a double-stranded RNA (dsRNA)–gated channel protein Systemic RNA Interference Deficiency–1 (SID-1) (*9*) required for systemic RNA interference in animals (*10*). SID-1 sequences in *Symbiodinium* and Cnidaria are similar, suggestive of horizontal gene transfer (fig. S10) (*3*). Pathogen-to-host miRNA transfer has been shown to silence host immunity genes in plants (*11*). We identified 1514 coral genes (table S29) (6.4% of the total number) as potential targets of *S. kawagutii* miRNAs; these had similar molecular functions [Gene Ontology (GO) slim category] as targets in *S. kawagutii* (Fig. 2C), which were enriched in GO categories related to protein modification and regulation of transcription and cell growth (table S30). This suggests that transferred miRNAs might regulate similar processes in symbiont and host.

Recognition of *Symbiodinium* by the host cells is mediated primarily through binding of *Symbiodinium* high-mannose glycans by lectins on the coral cell surface (*12*, *13*) (Fig. 3). We found a glycan biosynthesis pathway in *S. kawagutii* lacking several enzymes catalyzing the final steps of the common glycan biosynthesis pathway (fig. S11). This altered pathway is predicted to produce a (GlcNAc)5(Man)5(Asn)1 glycan that carries abundant free mannose branches and terminal mannose-mannose units available for lectin binding, consistent with previous findings (*14*). However, the enzymes involved in mannose-rich glycan biosynthesis differ between *S. kawagutii* and *S. minutum* (table S31), suggesting that variations in the glycoprotein structure may tune the host recognition specificity.

Other *Symbiodinium* genes may also be related to symbiosis (table S32). These include homologs of nodulation factors involved in establishing the symbiosis between legume and the nitrogen-fixing bacteria rhizobia, as well as cell surface proteins with a role in pathogen infection or host recognition. Furthermore, some *S. kawagutii* and *S. minutum* proteins share homology with *Plasmodium falciparum* proteins involved in the interaction between the parasite and its host (*15*).

To assess their role in symbiosis, we compared genes encoding transporters in *S. kawagutii* with those in *Acropora digitifera,* the only sequenced coral species (*16*) (Fig. 3 and table S33). Remarkably, nearly half of the numerous transporters (>300) in *S. kawagutii* are shared by this coral (table S34). Both dinoflagellate and coral genomes encode transporters of C (bicarbonate), N, P, and trace metals, as well as carbon-concentrating mechanism enzymes, and many of these are lacking in the two nonsymbiotic cnidarians *Hydra magnipapillata* and *Nematostella vectensis* (table S35). Most of the 49 carbonic anhydrases (CA) genes in the *S. kawagutii* genome are cytoplasmic, suggesting that cytoplasmic CA is critical for CO_2 acquisition; only two δ-CAs are predicted to be localized at the plasma membrane and one ß-CA in the thylakoids.

The *S. kawagutii* genome also contains the complete biosynthesis pathways of all the standard amino acids except lysine and histidine and could potentially supply nine of the amino acids that *A. digitifera* cannot produce (fig. S12 and table S35). Interestingly, the majority of the *S. kawagutii* transporters, as well as some of their coral cognates, are potential miRNA targets (red circles, Fig. 3).

Symbiodinium-to-coral translocation of photosynthates is critical for reef growth, with either glycerol (*17*) or glucose (*18*) translocated. The *S. kawagutii* genome contains 12 genes encoding glycerol-3-phosphate dehydrogenase, an enzyme essential for glycerol production in yeast (*19*), as well as a plasma membrane aquaporin with glycerol transport ability and low- and high-affinity glucose transporters (Fig. 3 and table S35). However, the *A. digitifera* genome (*16*) contains only the transporter for glucose and not for glycerol.

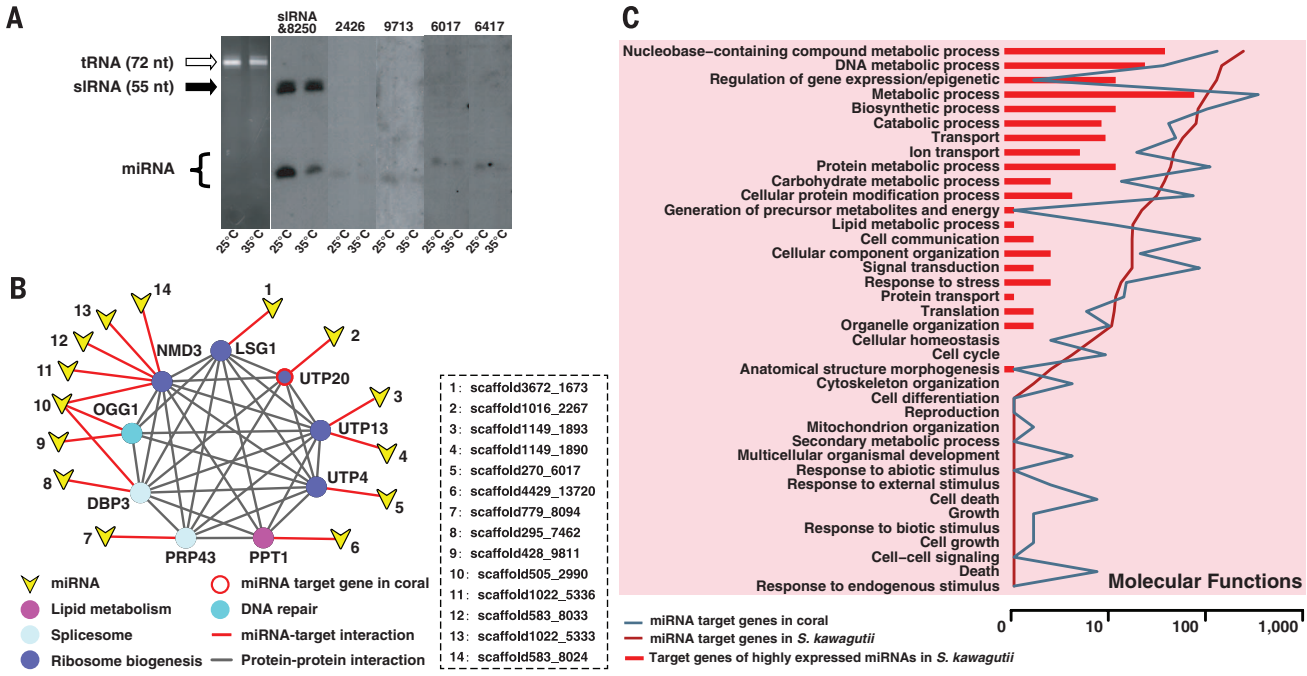

Fig. 2. miRNA in *S. kawagutii* and potential target genes in *S. kawagutii* and coral. (**A**) Northern blot analysis of *Symbiodinium* miRNAs. Most miRNAs are 22 nucleotides as assessed by the migration of DNA oligonucleotides. (**B**) A putative protein-protein interaction network of miRNA target genes. The network is a cluster of highly connected nodes (genes) showing miRNA-target interactions (red lines) and protein-protein interactions (gray lines). Node colors represent different KEGG (Kyoto Encyclopedia of Genes and Genomes) and GO functional annotations (see table S28). (**C**) GO categorization of predicted miRNA target genes in both *S. kawagutii* and coral.

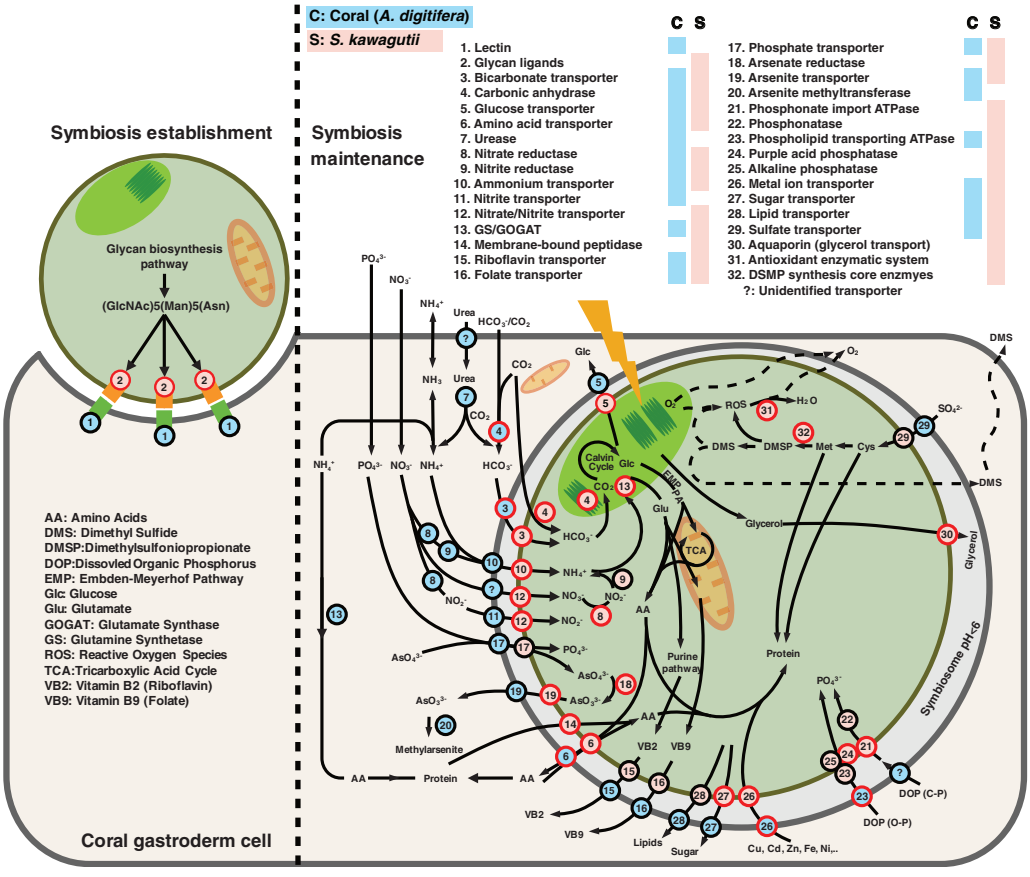

Fig. 3. Schematic summary of host recognition mechanisms and cargo transport. Small circles represent the genes from coral (sky blue fill) and from *S. kawagutii* (pale pink fill), with predicted miRNA target genes marked with red outlines. Only genes considered directly related to symbiosis are shown. All the *S. kawagutii* transporter families shown have members that are computationally predicted to be plasma membrane proteins (see table S35).

This suggests that glucose can be exported to the coral cells, whereas glycerol is exported only to the symbiosome, possibly as an osmolyte (*20*).

S. kawagutii possesses a large ensemble of genes potentially conferring tolerance to thermal stress and ultraviolet irradiation, including expanded gene families encoding heat shock proteins and DNA repair/recombination proteins (table S22). There is also a large set of antioxidant genes, including the large thioredoxin gene family, a diverse set of genes for (Cu/Zn-, Mn/Fe-, Ni-dependent) superoxide dismutases (SOD), and ascorbate peroxidases (APx). We found a Ni-dependent SOD, rarely reported for marine algae, consistent with the abundant high-affinity nickel transporter genes in this species (fig. S6C), as well as six genes encoding xanthine dehydrogenase/oxidase, which catalyzes the oxidation of xanthine to uric acid in purine metabolism (table S35). Uric acid forms crystalline deposits in *Symbiodinium* that function as an N reserve (*21*), and it is a potent antioxidant.

Unexpectedly, the *S. kawagutii* genome lacks the genes of the four major photoprotector mycosporine-like amino acids (MAA) biosynthesis enzymes: dehydroquinate synthase (DHQS), *O*-methyltransferase (*O*-MT), ATP-grasp, and nonribosomal peptide synthetase (NRPS). Their loss may thus represent a coevolution of *S. kawagutii* with its host, because all four genes are found in *A. digitifera*, one of which shows a close relationship with that in other dinoflagellates (fig. S13).

This study provides a portrait of a symbiotic dinoflagellate genome, with insights into genome evolution and regulation of gene expression in dinoflagellates and the molecular basis of coral-*Symbiodinium* symbiosis. Our results are a stepping-stone to understanding how the genetic complementarity between anthozoans and *Symbiodinium* can explain host specificity (*1*, *22*) and to determining the molecular mechanisms responsible for coral bleaching.

REFERENCES AND NOTES

1. A. C. Baker, *Annu. Rev. Ecol. Evol. Syst.* **34**, 661–689 (2003).
2. S. Lin, *Res. Microbiol.* **162**, 551–569 (2011).
3. Materials and methods are available as supplementary materials on *Science* Online.
4. H. Zhang *et al.*, *Proc. Natl. Acad. Sci. U.S.A.* **104**, 4618–4623 (2007).
5. C. H. Slamovits, P. J. Keeling, *Curr. Biol.* **18**, R550–R552 (2008).
6. E. Shoguchi *et al.*, *Curr. Biol.* **23**, 1399–1408 (2013).
7. D. Guillebault *et al.*, *J. Biol. Chem.* **277**, 40881–40886 (2002).
8. S. Mi *et al.*, *Cell* **133**, 116–127 (2008).
9. J. D. Shih, C. P. Hunter, *RNA* **17**, 1057–1065 (2011).
10. W. M. Winston, C. Molodowitch, C. P. Hunter, *Science* **295**, 2456–2459 (2002).
11. A. Weiberg *et al.*, *Science* **342**, 118–123 (2013).
12. L. K. Bay *et al.*, *Diversity* **3**, 356–374 (2011).
13. E. M. Wood-Charlson, L. L. Hollingsworth, D. A. Krupp, V. M. Weis, *Cell. Microbiol.* **8**, 1985–1993 (2006).
14. K.-L. Lin, J.-T. Wang, L.-S. Fang, *Zool. Stud.* **39**, 172–178 (2000).
15. V. K. Goel *et al.*, *Proc. Natl. Acad. Sci. U.S.A.* **100**, 5164–5169 (2003).
16. C. Shinzato *et al.*, *Nature* **476**, 320–323 (2011).
17. L. Muscatine, *Science* **156**, 516–519 (1967).
18. M. S. Burriesci, T. K. Raab, J. R. Pringle, *J. Exp. Biol.* **215**, 3467–3477 (2012).
19. J. Albertyn, S. Hohmann, B. A. Prior, *Curr. Genet.* **25**, 12–18 (1994).
20. A. B. Mayfield, R. D. Gates, *Comparative Biochem. Physiol. A: Mol. Integr. Physiol.* **147**, 1–10 (2007).
21. P. L. Clode, M. Saunders, G. Maker, M. Ludwig, C. A. Atkins, *Plant Cell Environ.* **32**, 170–177 (2009).
22. S. K. Davy, D. Allemand, V. M. Weis, *Microbiol. Mol. Biol. Rev.* **76**, 229–261 (2012).

ACKNOWLEDGMENTS

This work was supported by Natural Science Foundation of China grants K16110 and K16044 (to S.L.), U.S. National Science Foundation grant OCE-0854719 (to S.L. and H.Z.), U.S. NIH awards AI056034 and AI073806 (to D.A.C. and N.R.S.), National Science and Engineering Research Council of Canada grant 171382-03 (to D.M.), and various funds to BGI-Shenzhen, Shenzhen [State Key Laboratory of Agricultural Genomics, Guangdong Provincial Key Laboratory of core collection of crop genetic resources research and application (2011A091000047), Shenzhen Engineering Laboratory of Crop Molecular design breeding, and China National GeneBank-Shenzhen]. The genomic sequences and the annotated genes of *S. kawagutii*, as well as RNA sequencing data (unigenes), are available in our Symka Genome Database in Xiamen University: http://bioinf.xmu.edu.cn/symka_new; these data have also been deposited into the National Center for Biotechnology Information Short Read Archive (SRA) under accession number SRA148697.

SUPPLEMENTARY MATERIALS

www.sciencemag.org/content/350/6261/691/suppl/DC1
Materials and Methods
Figs. S1 to S13
Tables S1 to S35
References (*23*–*56*)

17 July 2015; accepted 25 September 2015
10.1126/science.aad0408

Single Cell Gene Expression

FLOWSCRIPT® HPV Detection Assay

Flow cytometry-based platform for the detection of mRNA

Our new FLOWSCRIPT® HPV E6/E7 assay employs a novel *in situ* hybridization technique utilizing a cocktail of probes specific to multiple sites within the E6 and E7 genes to ensure the detection of mRNA transcripts associated with the most prevalent high risk HPV genotypes. A simple protocol eliminates post-hybridization wash steps, minimizing leakage and signal degradation.

- Results in less than 3 hours with mix-and-read assay
- Compatible with high-throughput testing platforms
- Low input volume saves precious samples for additional analyses

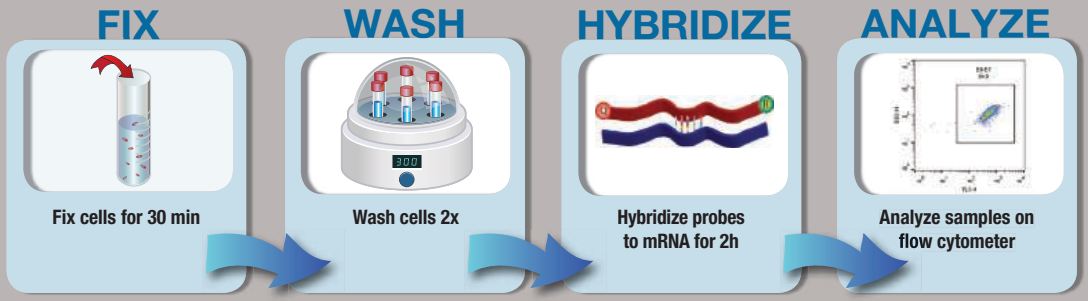

scientists ***enabling*** scientists.™

www.enzolifesciences.com

© 2015 Enzo Life Sciences

EMD MILLIPORE

Take Control
with dynamic cell culture.

Biology is so much more than DMEM/FBS, 37 °C, 5% CO_2.
It's easy to program automated changes to culture media, gas and temperature, while tracking cell responses, with the flexible, intuitive CellASIC® ONIX Microfluidic Platform. By taking control of this truly *in vivo*-like environment, you'll be able to perform dynamic, time-lapse experiments never before possible.

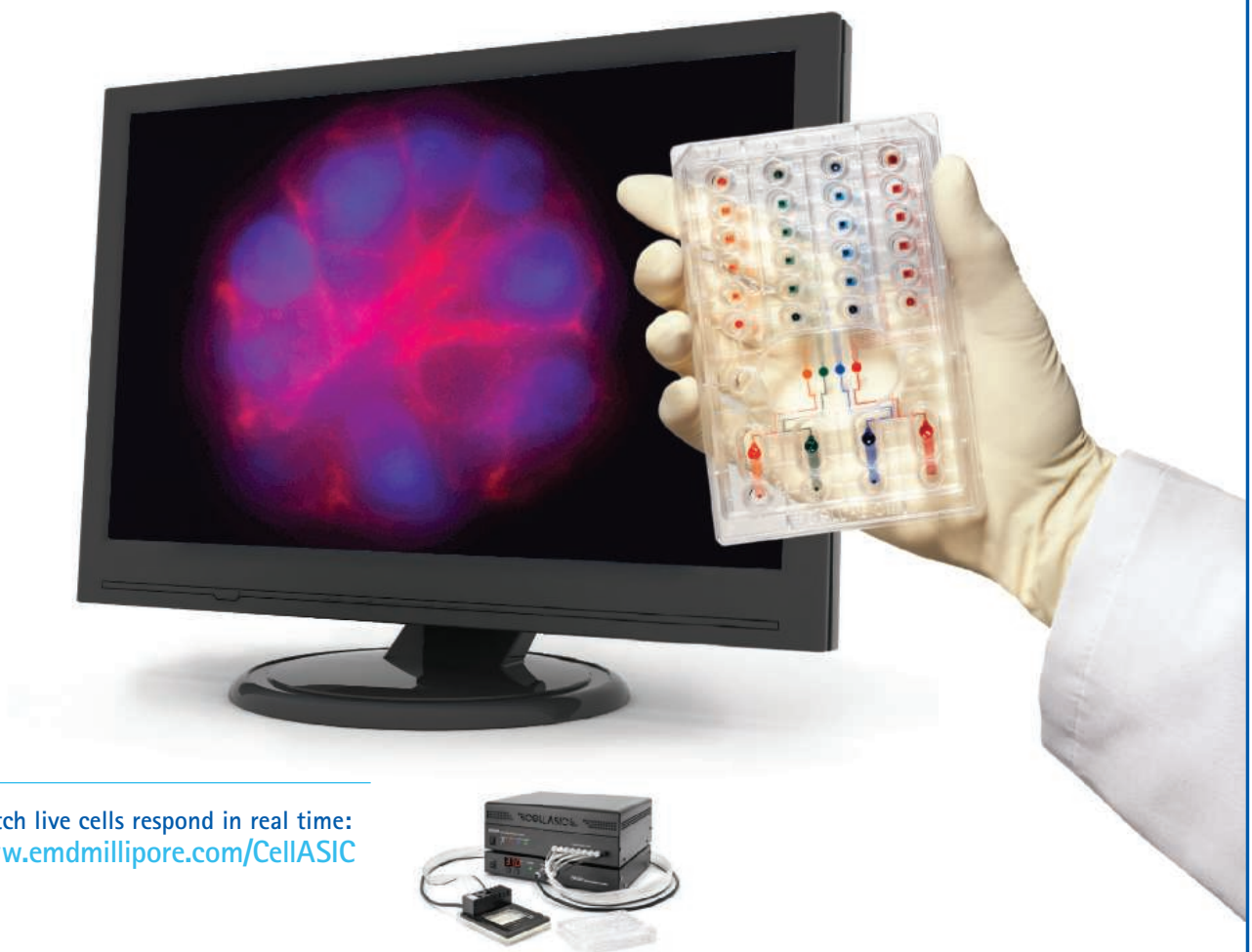

Watch live cells respond in real time:
www.emdmillipore.com/CellASIC

EMD Millipore is a division of Merck KGaA, Darmstadt, Germany

EMD Millipore and the M logo are trademarks and CellASIC is a registered trademark of Merck KGaA, Darmstadt, Germany.
© 2014 EMD Millipore Corporation, Billerica, MA, USA. All rights reserved. BS GEN-14-09917 03/2014

THE TOUGHEST CHALLENGES.
THE WORLD'S SMARTEST SCIENTISTS.
£20 MILLION AWARDS.
Grand Challenge is an ambitious international research funding scheme offering a series of £20 million awards to solve cancer's toughest questions. We're looking for big, innovative ideas from interdisciplinary teams across the world. If you think you have what it takes to tackle one of the grand challenges, we want to hear from you.
For more detail on the challenges, visit...
CRUK.ORG/GRANDCHALLENGE
Call closes 12th February 2016.
Cancer Research UK is a registered charity in England and Wales (1089464), Scotland (SC041666) and the Isle of Man (1103).
© 2015 Cancer Research UK. The Cancer Research UK name and logo are registered trademarks of Cancer Research UK.

THE CHALLENGES

1 **Develop vaccines to prevent non-viral cancers**

The power of the immune system is already being used to treat cancer; now we want to see it harnessed to prevent cancer. Advances in immunotherapy mean there has never been a better time to take on this challenge.

2 **Eradicate EBV-induced cancers from the world**

Every year, 200,000 cancers are caused by Epstein–Barr Virus (EBV). We want to reduce that figure to zero. If you can put together a team with an innovative way of doing this, we want to hear from you.

3 **Discover how unusual patterns of mutation are induced by different cancer-causing events**

To prevent cancer, we need to better understand different mutational signatures in our DNA – the ones we already know about, and the ones we haven't yet discovered.

4 **Distinguish between lethal cancers that need treating, and non-lethal cancers that don't**

Our methods for diagnosing cancer simply aren't good enough. We need to detect the disease at an early stage, but the diagnosis needs to be more accurate too.

5 **Find a way of mapping tumours at the molecular and cellular level**

We won't understand how tumours function until we understand why all the cells are there, how they got there, and what they are doing.

6 **Develop innovative approaches to target the cancer super-controller MYC**

It's one of the most promising therapeutic targets in cancer, but it defies conventional drug discovery. Can innovation and the world's smartest minds unlock its potential?

7 **Deliver biologically active macromolecules to any and all cells in the body**

We don't yet have a good way of getting macromolecules, potentially the most powerful anti-cancer drugs we have, into the body. We're challenging physical scientists, engineers and others to team up with cancer biologists to tackle this challenge.

GRAND CHALLENGE | CANCER RESEARCH UK

Europe's largest platform for single cell analyses

Photo: SciLifeLab/Johan Spinnell

Analyzing single cells. PhD student Gioele La Manno operates the Fluidigm C1 Single-Cell Auto Prep System, one of the high throughput instruments available at the Eukaryotic Single Cell Genomics facility.

The research center Science for Life Laboratory, SciLifeLab, in Sweden comprises four facilities for single cell biology. Together, these form the largest platform for advanced molecular single cell analyses in Europe, rendering technological advances widely available to the scientific community.

Advances in cell sorting and molecular analyses now enable researchers to comprehensively describe properties and functions of individual cells. This is in contrast to conventional biochemistry and molecular biology, which focuses on analyses of whole tissue samples and whole microbial populations or communities.

"Single cell analyses can be applied to understand the heterogeneity of tumors, to explain how genetically identical cells may show distinct behavior, and to explore the vast, uncharacterized microbial landscape. Therefore, these technologies have the potential to revolutionize biology and medicine." says Sten Linnarsson, Professor of Molecular Systems Biology at Karolinska Institutet, Sweden, and head of one of the facilities. The single cell facilities at SciLifeLab are focused on eukaryotic genomics, microbial genomics and proteomics respectively. The aim is to provide new insights into heterogeneity within tissues or communities of cells from all domains of life using high-throughput technologies.

Unique expertise

One of the researchers that have employed these technologies is Marc Friedländer, Assistant Professor at Stockholm University, Sweden. His group is investigating the impact of miRNAs on the transcriptomes of individual cells and the single-cell facilities have sequenced more than a thousand cells for him.

"Since our project is of a highly quantitative nature, it is important for us that technical noise is kept to a minimum. It would therefore have been difficult to produce useful data without the extensive expertise of the facility. Knowing that our cells were handled by the people who originally developed the Smart-Seq2 method gave us confidence in the implementation from the beginning." says Marc Friedländer.

SciLifeLab

www.scilifelab.se

ZymoPURE™

Pushing the limits

of midi, maxi, and giga plasmid purification

Transfection-ready plasmid DNA in 18 minutes

bind
rapid loading onto a spin-column
via vacuum or centrifuge

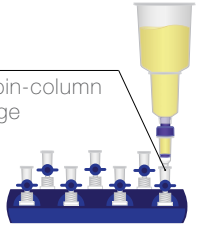

wash
for ultra-pure endotoxin free
plasmid DNA

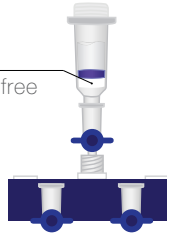

elute
transfection ready
plasmid DNA

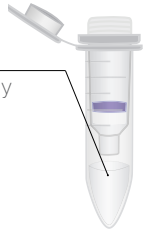

	Learn more: www.zymoresearch.com/zymopure		
	Max. Recovery	Processing Time	Size (Cat. No.)
Midiprep	300 µg	18 min.	25 Preps (D4200) 50 Preps (D4201)
Maxiprep	1200 µg	18 min.	10 Preps (D4202) 20 Preps (D4203)
Gigaprep	10 mg	40-50 min.	5 Preps (D4204)

Plasmid DNA concentration and yield from the ZymoPURE™ Maxiprep kit compared to two separate kits from supplier Q. Plasmid DNA (pGL3®) was isolated from 150 ml of JM109 *E. coli* culture grown overnight following the manufacturer's suggested protocol (in duplicate). One (1) µl of eluted plasmid DNA was visualized post agarose gel electrophoresis. M, ZR 1 kb DNA Marker (Zymo Research).

Patent Pending

Tel: (949) 679-1190

ZYMO RESEARCH
The Beauty of Science is to Make Things Simple®

DNA Purification Made Simple™

www.zymoresearch.com

appliedbiosystems

Connect—
the world is your lab

When your data are always within reach, answers are never far away. Remotely monitor your runs, access results, and collaborate with colleagues—anywhere, anytime using the Thermo Fisher Cloud—with the new Applied Biosystems™ QuantStudio™ 3 and 5 Real-Time PCR Systems.

Get connected at
thermofisher.com/quantstudio3-5

ThermoFisher SCIENTIFIC

For Research Use Only. Not for use in diagnostic procedures. © 2015 Thermo Fisher Scientific Inc. All rights reserved.
All trademarks are the property of Thermo Fisher Scientific and its subsidiaries unless otherwise specified. **CO121866 0815**

invitrogen

One conductor, a symphony of enzymes

Finally, a complete, one-buffer system–for beautifully simple cloning

Introducing the Invitrogen™ Anza™ Restriction Enzyme Cloning System:

- One buffer for all restriction enzymes
- One digestion protocol for all DNA types
- Complete digestion in 15 minutes
- Overnight digestion without star activity

Choose simplicity at **thermofisher.com/Anza**

ThermoFisher SCIENTIFIC

For Research Use Only. Not for use in diagnostic procedures. © 2015 Thermo Fisher Scientific Inc. All rights reserved. All trademarks are the property of Thermo Fisher Scientific and its subsidiaries unless otherwise specified. **CO126010 0815**

Join AAAS. Get instant access to *Science*. Support all of the sciences.

When you subscribe to *Science*, you become part of the American Association for the Advancement of Science (AAAS), a nonprofit community of more than 100,000 members worldwide who believe in the power of science to make the world a better place. AAAS is hard at work promoting science in government, schools, and in the public commons around the globe.

AAAS's award-winning journal *Science* offers the top peer-reviewed research across multiple disciplines. With your subscription, you'll get:

- 51 weeks of home delivery of *Science*
- Instant online retrieval of every *Science* article ever published, dating back to 1880
- Full access to the *Science* mobile site and apps
- Career advice, webinars, blogs and fascinating features exclusively for AAAS members
- Members-only newsletters, and much more

With increasing public skepticism about science–and public funding for research more uncertain than ever–our work has never been more important. Join hands with us today!

Visit promo.aaas.org/joinaaas. Together, we can make a difference.

Science
AAAS

Detection this specific. Even in unpurified samples.

High throughput protein quantification and quality assessment

The Octet platform lets you screen bioprocess samples quickly and accurately, with little to no prep.

- **Antibody and protein concentration.** Measure 96 titers in 2 minutes directly from supernatants or lysates.
- **Host cell protein and residual protein A detection.** Walk-away 96 samples in under 2 hours with a fully-automated workflow.
- **Protein quality.** Profile molecules based on differences in glycosylation and binding affinities.

fortebio.com | 888-OCTET-75

fortéBIO® A Division of Pall Life Sciences

PALL® Life Sciences

AAAS Travels

BALI & SULAWESI

February 25–March 10, 2016

Total Solar Eclipse March 9, 2016!

Indonesia is a nation of thousands of islands with a fascinating rich, cultural heritage! Combine Eclipse viewing on Sulawesi with sites on other islands that are biologically and culturally world class. On Borneo explore the world's finest orang-utan reserve, see Bali and the World Heritage Site of Borobudur on Java. $5,895 pp + air.

For a detailed brochure, call (800) 252-4910

All prices are per person twin share + air

BETCHART EXPEDITIONS Inc.
17050 Montebello Rd, Cupertino, CA 95014
Email: AAASInfo@betchartexpeditions.com
www.betchartexpeditions.com

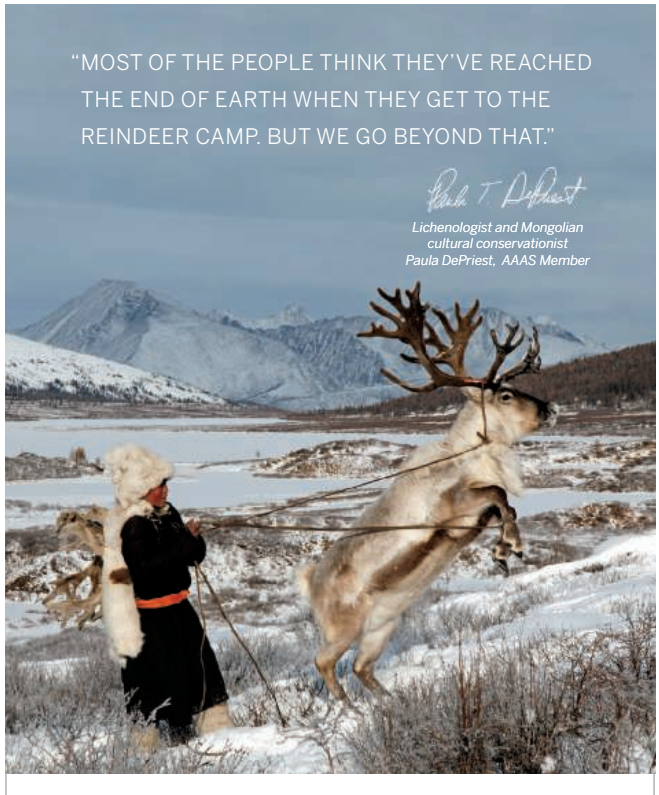

Every scientist has a *story*

Read her story at membercentral.aaas.org

AAAS MEMBERCENTRAL

myIDP: A career plan customized for you, by you.

For your career in science, there's only one Science

my IDP
ScienceCareers

Recommended by leading professional societies and the NIH

Features in myIDP include:

- Exercises to help you examine your skills, interests, and values.
- A list of 20 scientific career paths with a prediction of which ones best fit your skills and interests.
- A tool for setting strategic goals for the coming year, with optional reminders to keep you on track.
- Articles and resources to guide you through the process.
- Options to save materials online and print them for further review and discussion.
- Ability to select which portion of your IDP you wish to share with advisors, mentors, or others.
- A certificate of completion for users that finish myIDP.

Visit the website and start planning today!
myIDP.sciencecareers.org

ScienceCareers In partnership with:

advancing the life sciences 1912-2012 FASEB Federation of American Societies for Experimental Biology

UCSF University of California San Francisco

Medical College of Wisconsin

Burroughs Wellcome Fund

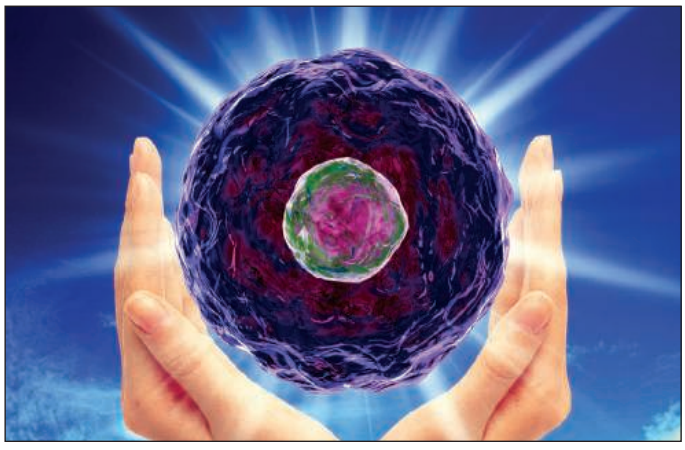

Single-cell biology: The power of one

Pick a paper, any paper. If it involves the protein, nucleic acid, or metabolite content of bacterial or eukaryotic cells, there's likely a section detailing how those cells were grown in culture. Cell culture is how researchers expand cells to harvest macromolecules or to interrogate their responses to changing conditions or chemical treatment. Inherent in such work is the assumption that all the cells in a dish are identical—by growing them in culture, the researcher is simply amplifying the signal. But that isn't always true. Subtle differences at the molecular level can yield significant variation in cellular behavior, but until recently researchers had no way to probe that variability. Today, they do. **By Jeffrey M. Perkel**

Akos Vertes, professor of chemistry at **George Washington University** in Washington, DC, uses mass spectrometry methods to quantify metabolites at the single-cell level. He offers a simple justification for the work: "Cell populations are heterogeneous. And these differences between individual cells in large populations sometimes become very important."

Consider cancer stem cells, for instance. Or drug-resistant bacteria. Or the many subtly different neuronal cell types in the brain. It's possible to detect those subpopulations in a bulk analysis, but it isn't easy: Their signals tend to be swamped by the general population. And in any event, such analyses blur cell-to-cell distinctions, making it impossible to know which cells contribute what to the population. The only way to untangle that skein of competing signals is to make measurements cell by cell.

Other researchers turn to single-cell methods because they have no other choice. In microbiology, for instance, the vast majority of microbes cannot be cultivated in the lab, says Ramunas Stepanauskas, director of the **Bigelow Laboratory Single Cell Genomics Center** in East Boothbay, Maine. "We really don't know much about them, although they are the drivers of the global biogeochemical cycles; they inhabit every conceivable environment, including our own bodies, and they are a largely untapped source of novel natural products, bioenergy, and other applications." The best way to tap these organisms' capabilities, he says, is to sequence them one at a time, letting their genetic material tell researchers what Petri dishes cannot.

Fundamentally, the process of single-cell research isn't difficult at all. Simply isolate a single cell, lyse it, collect its molecular innards, and analyze what you get. Of course, it's not nearly so straightforward in practice.

"There are all kinds of pitfalls in single-cell analysis," says Jim Eberwine, codirector of the **Penn Program in Single Cell Biology** at the University of Pennsylvania School of Medicine, who has taught a course on single-cell analytical techniques at the Cold Spring Harbor Laboratory since 2012 and has been studying single-cell gene expression in his own lab since the 1990s. According to Eberwine, whether a researcher is interested in a cell's DNA, RNA, protein, or metabolites, the fundamental issue is always the same: "Can you detect your signal over the noise." Researchers have devised a number of clever strategies to do just that.

Of single cells and amplification

The key to single-cell biology, of course, is isolating a single cell. This typically is accomplished using micromanipulation, microfluidics, or fluorescence-activated cell sorting (FACS), the method Stepanauskas favors.

One alternative, developed in the laboratory of Nancy Allbritton, chair of the joint biomedical engineering department at the University of North Carolina at Chapel Hill (UNC-CH) and North Carolina State University (NCSU), is the microraft array (MRA).

An MRA is an array of tiny transparent, magnetic, polystyrene elements, each small enough to fit into a tiny well on a plate or slide. Commercialized by **Cell Microsystems**, MRAs typically contain about 10,000 wells, Allbritton says, though some measure in the millions. Researchers plate their cells such that there are, on average, zero or one cells per element. They can then image the array immediately, or allow the cells to grow and develop complex phenotypes. Cells of interest are gently isolated using a microneedle to pierce the bottom of the array and dislodge the MRA element. Because they are magnetic, these elements are easily captured, at which point they can be analyzed or clonally expanded.

According to Allbritton, the system enables isolation strategies that might otherwise be impossible, such as isolating cytotoxic T lymphocytes based on their ability to kill target cells. In one study, UNC-CH collaborator Scott Magness, working with Allbritton, used an MRA to study intestinal stem cells. Among other things, the team used the platform to investigate whether intestinal stem cells must

IMAGE: © KLSS/FIORE/SHUTTERSTOCK.COM

Upcoming Features

Cell-Sorting Technologies—December 4 ■ *Automated Sample Preparation—January 15* ■ *Genomics—February 12*

physically contact other cells in order to reach their full potential. "What he showed quite clearly is they really need to be touching a Paneth cell to grow, prosper, and divide and get the highest outgrowth rates," Allbritton says.

Vertes takes a lower-throughput approach to metabolomics. Using a sharpened capillary and a micromanipulator—a tool typically used in patch clamping and embryonic manipulation—his team aspirates a fraction of a picoliter of material from adherent cells stuck to the bottom of a culture dish and injects it directly into a mass spectrometer.

In that way, Vertes says, his team can quantify some 22 metabolites and 54 lipids from each of about 30 cultured hepatocytes—not the whole metabolome, of course, but enough to reveal for instance, the cells' adenylate energy charge—a measure of cellular health. It was always possible to measure such variables at the population level, Vertes notes. But by going to the single-cell level, he can observe the distribution of energy states, and correlate those values with such parameters as morphology or metabolic activity. "For every cell, we can tell [if it] was a healthy cell, a cell half-dead, or a cell programming itself to die," he says.

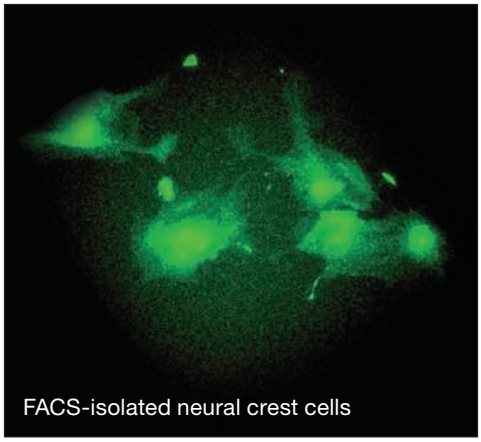

FACS-isolated neural crest cells

The key to single-cell biology, of course, is isolating a single cell.

Single-cell transcriptomics

Jonathan Sweedler, the James R. Eiszner Family Chair in Chemistry at **the University of Illinois at Urbana-Champaign**, has developed another novel approach to cellular isolation and analysis. His team disperses some 10,000 cells onto a microscope slide. They then stain the nuclei of those cells, localize them with a fluorescent microscope, and pass those coordinates to a laser for mass spectral analysis. Because the cells are widely dispersed, there's never a question of whether a laser is hitting one cell or another, as can occur in traditional mass spec imaging. "We can actually do 100,000 cells this way in an afternoon if we wanted."

Sweedler's approach thus trades cellular context and interaction for throughput. He can quantify many more discrete cells than he otherwise might, but he loses any sense of where those cells were in relation to one another. That's a common problem with single-cell approaches, Eberwine says, because it also potentially alters cell biology. "You're removing the cells from their natural microenvironment, where they have the adjacent cell connections and the influence of the cellular environment."

Indeed, using a method called "transcriptome in vivo analysis" (TIVA), Eberwine and his colleagues compared the gene-expression patterns in pyramidal neurons in intact mouse brain slices and dissociated cells. They found that neurons in intact tissues expressed 12,000 transcripts on average, compared to 16,000 when dissociated. That finding suggests that a cell's capacity to express a gene is modulated by the physical signals it receives from its neighbors. The local microenvironment "act[s] as a brake for gene expression," Eberwine says.

TIVA employs a caged, photoactivatable double-stranded oligonucleotide coupled to a cell-penetrating peptide and biotin moiety. When this "TIVA tag" crosses the cell membrane, the peptide is removed, locking the molecule within the cell. Laser irradiation then causes the two strands to separate ("uncaging"), revealing a sequence for capturing polyadenylated messenger RNAs (mRNAs) in the targeted cells. Finally, the biotinylated RNA-RNA hybrids are isolated on streptavidin beads, amplified, and analyzed via RNA sequencing (RNA-seq), allowing the team to quantify gene expression from locales ranging from specific cells to subcellular compartments. "We can activate it in the cell soma, we can activate it in the dendrites or in the nucleus of the cell, and we can do it in one or multiple cells," Eberwine says.

At **Harvard University**, Xiaowei Zhuang, a Howard Hughes Medical Institute investigator and David B. Arnold Professor of Science, who invented the superresolution method of stochastic optical reconstruction microscopy (STORM), has also developed a technique for in situ single-cell transcriptome analysis. But unlike TIVA, her imaging-based method retains information on precisely where in the cell the transcripts were located. "We know that RNA are not uniformly distributed inside the cell," Zhuang explains. "The local distributions of RNA are actually quite important for the establishment and maintenance of local cellular structures."

Multiplexed error-robust fluorescence in situ hybridization (MERFISH) is an in situ hybridization-based approach for quantifying thousands of transcripts simultaneously. In one specific implementation, each transcript is assigned a unique binary code. The trick is to read that code bit by bit.

To do that, oligonucleotides complementary to each transcript are flanked by readout sequences corresponding to the different bits. This pool, which may comprise 100,000 oligos or more, is hybridized to the mRNAs in the fixed cells, "convert[ing] each cellular RNA into a combination of readout sequences," Zhuang explains. Then, the cell is interrogated bit by bit using oligonucleotides complementary to the readout sequences. After each hybridization round, the cells are imaged, the fluorescent probes quenched, and the process repeats. Each fluorescent signal in any given round represents an RNA whose code reads "1" at that position in the corresponding binary code. By mapping these points over 16 rounds of hybridization and quenching, the system can quantify numerous RNAs in the cell, and map their subcellular location. continued>

S SINGH ET AL., J BIOMED BIOTECHNOL. 2005; 2005(3): 232–237. LICENSED UNDER CC BY

Featured Participants

Bigelow Laboratory Single Cell Genomics Center
scgc.bigelow.org

Cell Microsystems
www.cellmicrosystems.com

Fluidigm
www.fluidigm.com

George Washington University
www.gwu.edu

Harvard University
www.harvard.edu

Stanford University
www.stanford.edu

UNC-CH/NCSU Joint Department of Biomedical Engineering
www.bme.unc.edu

University of Illinois at Urbana-Champaign
www.illinois.edu

University of Pennsylvania Program in Single Cell Biology
www.med.upenn.edu/ppscb

University of Zürich
www.uzh.ch

But according to Zhuang, multiplexing is only half the story. FISH has a low but measurable error rate, Zhuang says. Over 16 rounds of hybridization, that can add up. So, taking a cue from telecommunications, her team designed its codes such that each code differs from every other one by up to four bits. "That means you have to make four errors in one RNA in order to convert it to a different RNA," she explains. Thus, even if a particular transcript is read out with a single error, the software can determine its correct identity, although RNAs containing two or more errors can be detected but no longer corrected, as it is no longer possible to unambiguously identify them. "We can actually do both error detection and error correction," Zhuang says, "and that's how we get very highly accurate measurements."

Using this strategy, Zhuang's team quantified as many as 1,000 transcripts in individual cells. But there's no reason that number of transcripts cannot go higher, she adds. A 32-bit code, for instance, could easily encode 30,000 genes. Now she hopes to apply the technology to map the different cell types in the human brain and in cancer, as well as the subcellular distribution of RNAs within them.

Single-cell proteomics

Bernd Bodenmiller, assistant professor for quantitative biology at the **University of Zürich**, Switzerland, and Sean Bendall, assistant professor of pathology and immunology at the **Stanford University** School of Medicine, are both former postdocs of Garry Nolan, also at Stanford, who champions mass cytometry, a cross between flow cytometry and mass spectrometry that overcomes one of the key shortcomings of the former technique.

Traditional flow cytometry, constrained by overlapping fluorescent channels, is limited to about 18 simultaneous signals, or markers, though in practice, the real limit is even lower. Mass cytometry can theoretically resolve more than 100 channels, but is currently limited to about 44—the result of conjugation chemistry needing to catch up with the instrumentation itself.

Like flow cytometry, mass cytometry, commercialized by DVS Sciences as the CyTOF (recently acquired by **Fluidigm**), is a flow-based method that uses heavy metal-conjugated antibodies rather than fluorescent dyes to achieve its high information content. But in a pair of papers published in 2014, Bodenmiller and Bendall simultaneously demonstrated methods to turn a CyTOF analyzer into a mass spec imager, enabling a kind of high-throughput single-cell proteomics spatial analysis. "We built what you could call a mass cytometry-based microscope," Bodenmiller explains, enabling "spatial systems biology or spatial proteomics."

As with advanced mass spec imaging systems, this approach allows researchers to measure protein content cell by cell in situ. But, unlike traditional mass spec imaging, which typically detects the most abundant proteins, mass cytometry allows researchers to actually preselect the proteins they want to image.

Bodenmiller used his mass cytometry microscope to study the impact of tumor microenvironment on metastasis—for instance, the impact of macrophage infiltration. "I think here is the sweet spot of our imaging mass cytometry approach, because it's antibody-based, so we can exploit prior knowledge to detect different immune cells or stromal cells, and we can use many antibodies to learn what these cells are actually doing." Bendall and Nolan used their multiplexed ion beam imaging (MIBI) system to probe the histology of breast cancer sections.

Separately, Bendall and Nolan used traditional CyTOF mass cytometry to map the single-cell trajectories of B-cell development, using a set of 42-marker molecular profiles—everything from extracellular markers associated with B-cell development to intracellular signaling factors—and a novel algorithm called "Wanderlust" to trace how molecular signatures change as a lymphocytic stem cell differentiates into a mature B cell.

Though 40-plus parameters are impressive, researchers like Bendall and Bodenmiller hope to ultimately push that number even higher. All that's required is efficient chemistry to conjugate the ions to the antibodies. Bendall jokes of a creeping condition among flow and mass cytometrists that he calls "PDS," or "parameter dependency syndrome." "At first you ask yourself, 'Well, what the heck am I going to do with 40 parameters?' And then after you've done this for a while, you're like, 'How am I [going to] fit everything I want to measure into 40 parameters?'" To put it another way, researchers never say no to more data.

Of course, those data describe just one particular aspect of single-cell biology. And therein lies one of the field's primary challenges, says Eberwine. What's needed now, he says, are methods for integrating these different datasets to gain a comprehensive, quantitative, and reproducible view of the cell. Work on that front is ongoing. "I think the information will be incredible," he says.

Jeffrey M. Perkel is a freelance science writer based in Pocatello, Idaho.

DOI: 10.1126/science.opms.p1500099

Whole Transcriptome Assays

Whole Transcriptome Single Cell Precise Assays enable absolute and direct molecular counting of the entire transcriptome from single cells without any specialized equipment or training. Whole Transcriptome Single Cell Precise Assays are unique because they are the first commercial RNA sequencing (RNA-seq) assay to enable thousands of cells to be sequenced per run at a cost far lower than existing alternatives. In addition, no expensive dedicated laboratory equipment is needed to run the assays, and the sequencing library is compatible with any Illumina sequencer. Based on the patented Molecular Indexing technology, Precise assays offer absolute quantization and bias-free expression information. The assays allow the examination of large numbers of standard or low-input messenger RNA (mRNA) samples from precious samples, or whenever absolute quantitation is required. The Precise assays combine molecular and sample indexing in 96- and 384-sample formats, enabling customers to sequence up to 4,608 samples on one sequencing run without investment in new equipment or extensive training.

Cellular Research
For info: 650-752-6144
www.cellular-research.com

Automated Single-Cell Analysis

The ICELL8 Single-Cell System creates a new standard for single-cell analysis. The system includes an imaging station for rapid image capture and CellSelect software for automatic selection of cells of interest for further processing for RNA sequencing. The system also allows researchers to run multiple samples on a single chip, enabling applications that require investigation under uniform conditions. The ICELL8 Single-Cell System delivers greater cell isolation capabilities, control over the selection of isolated cells, and the ability to run multisample experiments. The system provides power with a Poisson distribution for unbiased isolation of up to 1,800 single cells on a single chip, control with CellSelect software, and insight by enabling the analysis of up to eight samples on a single chip, so that complex experimental designs can now be accomplished in single-cell research.

WaferGen Biosystems
For info: 877-923-3746
www.wafergen.com

Cell Sorter

The easy-to-use S3e Cell Sorter (488/640 nm) is the latest addition to the series of S3e Cell Sorters and incorporates the fluorescence wavelengths commonly used by immunologists. Immunologists customarily use the 640 nm wavelength to excite and detect red fluorophores, such as allophycocyanin (APC) and APC-Cy7. The new S3e Cell Sorter possesses the 488/640 nm laser combination, thus extending the convenience of benchtop cell sorting to immunologists. Like all instruments in the S3e series, the S3e Cell Sorter (488/640 nm) offers a hands-free startup sequence that automatically aligns the stream to optics and optimizes the droplet/side stream. This capability, along with the instrument's other features, allows scientists to begin sorting more quickly than they could with more complex systems. In addition, the S3e Cell Sorter's ability to prevent tubes from running dry or overfilling ensures that precious sample is never lost.

Bio-Rad
For info: 800-424-6723
www.bio-rad.com/S3ePR2

High-Throughput Oligonucleotide Microarray

The GenetiSure Pre-Screen Kit is a high-throughput oligonucleotide microarray for screening aneuploidy and other genomic aberrations in the 5- to 10-megabase (Mb) range from single cells in three- and five-day embryos. The kit allows for a turnaround time of less than eight hours from DNA extraction to data analysis—an industry first. The kit consists of a microarray that can run up to 14 samples and two reference samples simultaneously, so more embryos can be screened without significantly increasing costs. The GenetiSure Pre-Screen array is based on Agilent's market-leading technology for high-resolution oligonucleotide comparative genomic hybridization. The kit contains all the necessary reagents to enable whole-genome amplification and labeling of single cells. The microarray is compatible with Agilent's CytoGenomics software (version 3.0 or higher) for easy data analysis.

Agilent Technologies
For info: 800-227-9770
www.agilent.com

RNA Assay

The PrimeFlow RNA Assay is the first and only flow cytometry assay capable of simultaneous detection of RNA and protein within millions of cells at single-cell resolution. With the novel PrimeFlow assay, researchers can now incorporate the simultaneous analysis of RNA transcripts and proteins to elevate their understanding of single-cell dynamics. The assay enables high-throughput detection of RNA and protein expression; thus it can be used to mechanistically and phenotypically characterize coexpression of RNAs with functional proteins at the single-cell level. This assay, with a user-friendly protocol that has many similarities to standard antibody-staining procedures and data acquisition of flow cytometry, is an invaluable tool for any immunology lab performing translational research. Its major advantage is the ability to detect, with high sensitivity, messenger RNAs (mRNAs) for which flow cytometry antibodies against the corresponding proteins perform poorly or are not available.

Affymetrix
For info: 888-362-2447
www.affymetrix.com

Electronically submit your new product description or product literature information! Go to www.sciencemag.org/products/newproducts.dtl for more information.

Newly offered instrumentation, apparatus, and laboratory materials of interest to researchers in all disciplines in academic, industrial, and governmental organizations are featured in this space. Emphasis is given to purpose, chief characteristics, and availability of products and materials. Endorsement by Science or AAAS of any products or materials mentioned is not implied. Additional information may be obtained from the manufacturer or supplier.

AAAS Marion Milligan Mason Award for Women in the Chemical Sciences

Marion Milligan Mason was a chemist and a proud AAAS member. Her will provided for the creation of a fund with a $2.2 million bequest to support research by early-career women in the chemical sciences. AAAS is grateful for philanthropic gifts like Dr. Mason's bequest, which make it possible for us to support promising scientists early in their careers.

The online application site will open
November 16, 2015

Proposals are due on or before
March 1, 2016

Awards will be announced on or before
January 2017

Apply today!

www.aaas.org/masonaward

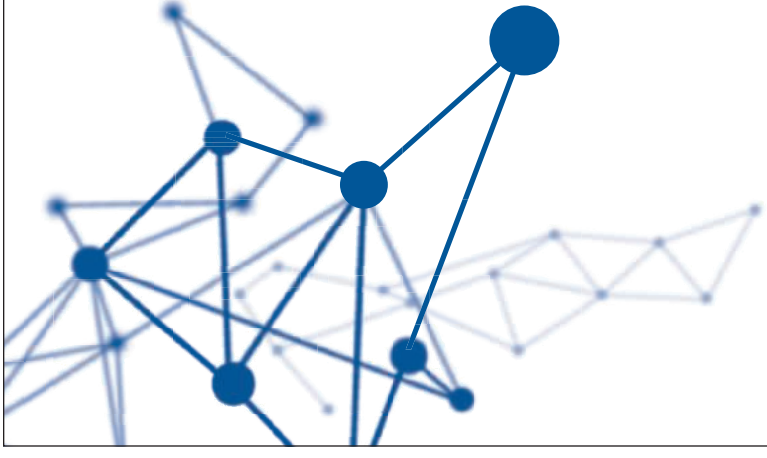

Congratulations to the 2015 Recipients

ALISON FOUT
Assistant Professor of Chemistry
University of Illinois at Urbana-Champaign

Nitrite Reduction in a Non-Heme System: Evidence for an Alternative Mechanism

KATHERINE MACKEY
Assistant Professor, Department of Earth System Science
University of California Irvine

Aerosol Trace Metal Chemistry in a Changing Ocean

KRISTIN PARENT
Assistant Professor of Biochemistry and Molecular Biology
Michigan State University

Cryo-electron tomography of large and challenging biological specimens

LUISA WHITTAKER-BROOKS
Assistant Professor of Chemistry
The University of Utah

Exploration of scalable polymer-metal for thermoelectric applications

AAAS
ADVANCING SCIENCE, SERVING SOCIETY

R&D SYSTEMS
a bio-techne brand

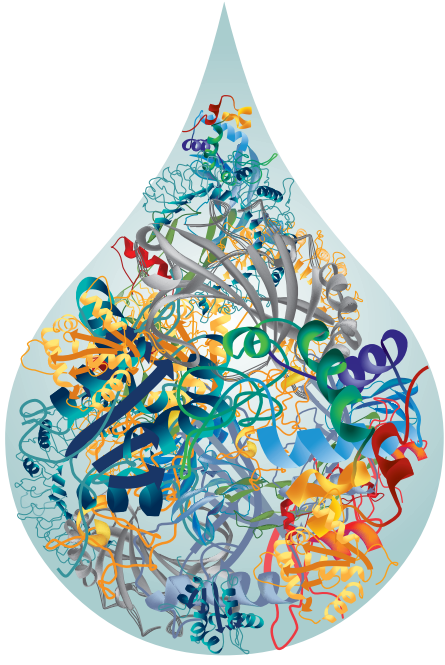

What's in Your Sample?

Find Your Answers!

rndsystems.com/
Immunoassays

Science Careers Advertising

For full advertising details, go to ScienceCareers.org and click For Employers, or call one of our representatives.

Tracy Holmes
Worldwide Associate Director
Science Careers
Phone: +44 (0) 1223 326525

THE AMERICAS

E-mail: advertise@sciencecareers.org

Fax: +1 (202) 289 6742

Tina Burks
Phone: +1 (202) 326 6577

Nancy Toema
Phone: +1 (202) 326 6578

Online Job Posting Questions
Phone: +1 (202) 312 6375

EUROPE / INDIA / AUSTRALIA / NEW ZEALAND / REST OF WORLD

E-mail: ads@science-int.co.uk

Fax: +44 (0) 1223 326532

Sarah Lelarge
Phone: +44 (0) 1223 326527

Kelly Grace
Phone: +44 (0) 1223 326528

Online Job Posting Questions
Phone: +44 (0) 1223 326528

JAPAN

Katsuyoshi Fukamizu (Tokyo)
E-mail: kfukamizu@aaas.org
Phone: +81 3 3219 5777

Hiroyuki Mashiki (Kyoto)
E-mail: hmashiki@aaas.org
Phone: +81 75 823 1109

CHINA / KOREA / SINGAPORE / TAIWAN / THAILAND

Ruolei Wu
Phone: +86 186 0082 9345
E-mail: rwu@aaas.org

All ads submitted for publication must comply with applicable U.S. and non-U.S. laws. *Science* reserves the right to refuse any advertisement at its sole discretion for any reason, including without limitation for offensive language or inappropriate content, and all advertising is subject to publisher approval. *Science* encourages our readers to alert us to any ads that they feel may be discriminatory or offensive.

ScienceCareers
FROM THE JOURNAL SCIENCE AAAS

ScienceCareers.org

Department of Biology
University of Nevada, Reno

Neurobiology Faculty (2 tenure-track and 1 lecturer)

The Department of Biology at the University of Nevada, Reno, seeks two **tenure-track** assistant professors in **NEUROBIOLOGY**. We seek faculty in the broad area of neuroscience whose expertise might include integrative approaches spanning cells to systems, optogenetics, plasticity, neurophysiology, or behavior. Optogenetics is the focus area for one of these positions. Highly competitive startup funds are available. In addition, there is potential support from existing and pending NIH COBRE career development grants. Our faculty are expected to develop nationally recognized, extramurally funded research programs, to train PhD students, and to participate in undergraduate teaching. The department is also hiring one neurobiology **lecturer**.

The department has about 330 Neuroscience majors, 1050 Biology majors, 60 graduate students, 24 state-funded tenure ladder faculty and 7 state-funded lecturers. Extramural awards average ~ $4.5 million/yr. Reno is located in the Sierra Nevada mountains near Lake Tahoe. Reno has been rated one of the best small cities in the US for outdoor recreation and overall quality of life.

Go to **http://jobs.unr.edu** to submit application materials, including an application letter, CV, statement of teaching interests, and contact information for three references. For the tenure-track positions submit a statement of research interests as well. Applications received by **December 1, 2015** will receive full consideration.

EEO/AA Women, under-represented groups, individuals with disabilities, and veterans are encouraged to apply.

GRAVITATING TOWARD
Higher Levels of Success

www.qu.edu.qa

73%
of employers favor QU graduates.

45%
Consistent success rate in National Priorities Research Program.

85%
student satisfaction with skills and knowledge acquired for the job market.

38.8%
Compound annual growth rate in research, making QU the fastest in growing research in the region.

92%
of graduates would recommend QU to family and friends.

US$240 million
in accumulated grants.

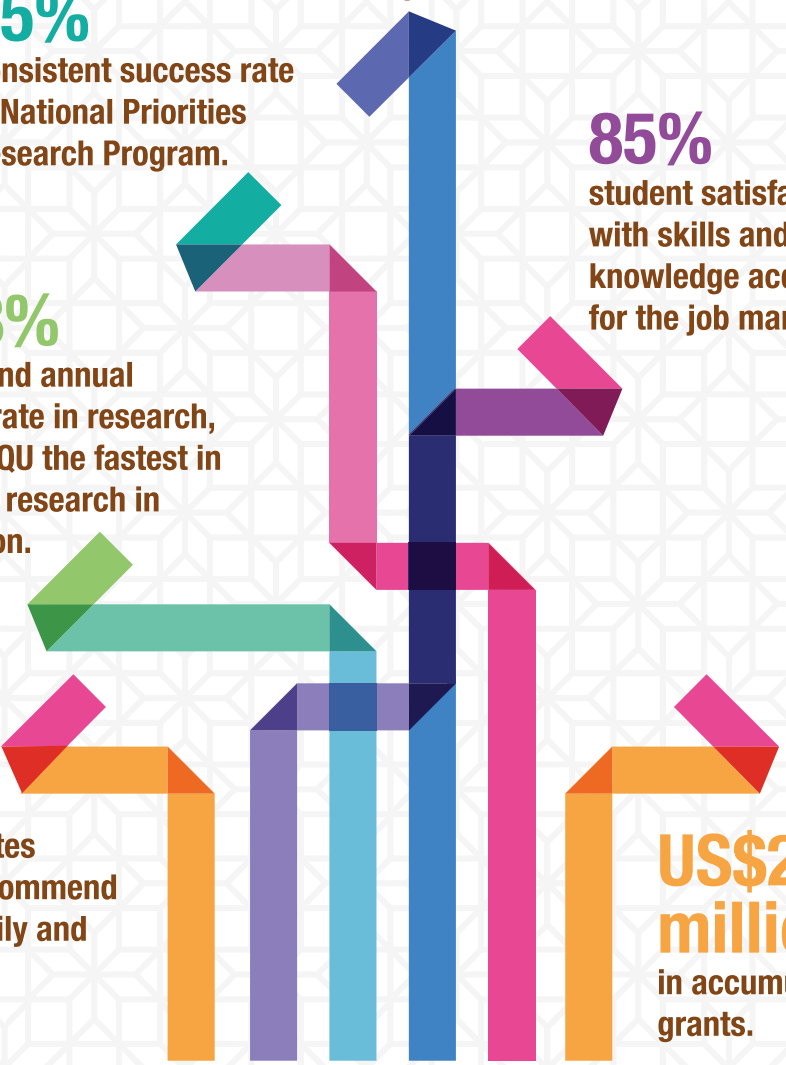

جامعة قطر
QATAR UNIVERSITY

Science Careers online @sciencecareers.org

2016 Lasker Awards

ALBERT AND MARY LASKER FOUNDATION

Call for Nominations:

• Basic Medical Research
• Clinical Research
• Special Achievement in Medical Science

Submit a nomination at **www.laskerfoundation.org**
Deadline: February 1, 2016

COLUMBIA UNIVERSITY
IN THE CITY OF NEW YORK

The 2016 Louisa Gross Horwitz Prize for Biology or Biochemistry

NOMINATIONS
All materials must be written in the English language and submitted electronically at:
http://www.cumc.columbia.edu/research/horwitz-prize

Deadline date: January 22, 2016

Renominations are by invitation only.
Self-nominations are not permitted.

The Louisa Gross Horwitz Prize was established under the will of the late S. Gross Horwitz through a bequest to Columbia University and is named to honor the donor's mother. Louisa Gross Horwitz was the daughter of Dr. Samuel David Gross (1805–1889), a prominent surgeon of Philadelphia and author of the outstanding *Systems of Surgery* who served as president of the American Medical Association.

Each year since its inception in 1967, the Louisa Gross Horwitz Prize has been awarded by Columbia University for outstanding basic research in the fields of biology or biochemistry. The purpose of this award is to honor a scientific investigator or group of investigators whose contributions to knowledge in either of these fields are deemed worthy of special recognition.

The Prize consists of an honorarium and a citation, which are awarded at a special presentation event. Unless otherwise recommended by the Prize Committee, the Prize is awarded annually. Dr. S. Lawrence Zipursky, at the University of California, Los Angeles, was the 2015 awardee.

QUALIFICATIONS FOR THE AWARD
The Prize Committee recognizes no geographical limitations. The Prize may be awarded to an individual or a group. When the Prize is awarded to a group, the honorarium will be divided among the recipients, but each member will receive a citation. Preference will be given to work done in the recent past.

NOMINATIONS SHOULD INCLUDE
1) A summary of the research on which this nomination is based (no more than 500 words).
2) A summary of the significance of this research in the fields of biology or biochemistry (no more than 500 words).
3) A brief biographical sketch of the nominee, including positions held and awards received by the nominee.
4) A key publication list of up to ten of the nominee's most significant publications relating to the research noted under item 1.
5) A copy of the nominee's curriculum vitae.

WE ARE SEEKING OUTSTANDING RESEARCHERS IN MOLECULAR MEDICINE

The **Wallenberg Centres for Molecular Medicine** are key elements in a national effort to reposition Sweden as a world-leading life science nation. The initiative was taken by the Knut and Alice Wallenberg Foundation, and is a joint venture with the Universities and University Hospitals of Gothenburg, Lund, Umeå and Linköping. SciLifeLab in Stockholm and Uppsala serves as a research partner and unique core facility for the four Centres.

Through **repeated calls in the upcoming years** with **tenure track research positions** we will recruit up to **sixty new research groups**, centred around internationally recruited young scientists of outstanding potential and funded at a globally competitive level through **very generous four-year starting packages**. Each of these groups will synergize with pre-existing excellent research environments as well as strong clinical collaborators, promoting ground-breaking research in molecular and translational medicine. Together, we will rise to future challenges within molecular life science in order to improve human health.

www.wcmm.se

UNIVERSITY OF GOTHENBURG · LUND UNIVERSITY · Umeå University · LINKÖPING UNIVERSITY

UNIVERSITY OF GOTHENBURG:

Up to three tenure track research positions as Assistant Professors are currently advertised in Molecular Medicine with a focus on **translational neuroscience or metabolic diseases**. Successful candidates will become part of strong research environments with excellent infrastructure and enjoy close collaboration with AstraZeneca and clinical/translational research platforms at one of the largest University hospitals in northern Europe. **www.wcmtm.gu.se**

LUND UNIVERSITY:

Focusing on eight research fields within **regenerative medicine**, up to three tenure track research positions will be advertised in early 2016. In close integration with Skåne University Hospital, a clinical researcher will be part of each team. We have access to state-of-the-art infrastructure facilities such as MAX IV and the future ESS - You will be in a great position to conduct translational and inventive research at one of Scandinavia's largest full-scale universities. **www.med.lu.se/wcmm**

UMEÅ UNIVERSITY:

Up to four tenure track research positions are currently advertised in the areas of **cancer, infection biology, metabolism/diabetes and neuroscience**. The positions are at Assistant Professor level that can be combined with a clinical position. The successful candidates will work in association with strong research environments and have access to excellent research infrastructures including unique collections of longitudinal samples in existing biobanks. **www.wcmm.umu.se**

LINKÖPING UNIVERSITY:

With a **medicine-technology interface** and extending from a **biomedical engineering** profile, onwards to **basic biomedical** and **clinical research**, we plan to currently recruit up to four tenure track faculty members, at the level of Assistant/Associate Professor. The successful candidates will be expected to develop a dynamic, extramurally funded, internationally recognized research program, and to integrate with existing strengths in medical technology, materials science and bioengineering. **www.liu.se/wcmm**

WALLENBERG CENTRES FOR MOLECULAR MEDICINE SWEDEN

Knut och Alice Wallenbergs Stiftelse

Careers at HKUST

Faculty Positions
Division of Life Science

Job Posting Details

The Division of Life Science at The Hong Kong University of Science and Technology seeks applications for tenure-track positions at ranks of Assistant Professor and above.

Applicants should have a doctoral degree and preferably at least 2 years of postdoctoral experience. They will be expected to establish an independent and internationally recognized research program and to contribute to the missions of the Division in undergraduate and graduate education. The Division of Life Science (life-sci.ust.hk) currently has 37 faculty members working in diverse research areas. We encourage application from candidates whose research programs can complement or enhance the existing strengths of the Division. The University has a vibrant research environment and is consistently ranked as one of the top universities in Asia. New faculty is provided with competitive start-up funding. The medium of instruction is English.

Starting salary (with full 12-months' coverage) will be commensurate with qualifications and experience. Fringe benefits including medical and dental benefits, annual leave and housing will be provided where applicable. Initial appointment will normally be on a 3-year contract. A gratuity will be payable upon successful completion of contract.

Application Procedure

Application materials including a cover letter, curriculum vitae, research proposal (maximum 3 pages), teaching statement (maximum 1 page), and contact information of three referees should be sent to the **Chair of Life Science Search and Appointments Committee (lifssearch@ust.hk)**. Review of applications will start in November 2015.

(Information provided by applicants will be used for recruitment and other employment-related purposes.)

Human Resources Office

UTHEALTH NORTHEAST
The University of Texas Health Science Center at Tyler

The Department of Cellular and Molecular Biology at UT Health Northeast invites applications from outstanding scientists for state funded faculty positions at all levels to conduct independent research. The research of the applicant should be in various research areas of biochemistry or cell biology with an emphasis of cell motility and cytoskeletal regulation. Investigators working on cellular and molecular biology using electron microscopy are encouraged to apply.

The mission of the research program at UT Health Northeast is to create an outstanding research community that links basic science and clinical science. UT Health Northeast has established research programs in lung injury/repair, cell motility and cytoskeletal rearrangement, and pulmonary infectious diseases and the successful candidate is encouraged to interact with researchers in these areas. A strong track record is required. Applicants at the level of Associate Professor or higher need extramural funding. Teaching in the biotechnology graduate program is encouraged and voluntary.

Our institution is growing rapidly and substantive resources have been allocated to build its basic and translational research portfolio. The Department has recently set up a state-of-the-art cellular and molecular imaging facility including a custom made single molecule total internal reflection fluorescence (TIRF) microscope, ultrafast super-resolution microscope which can visualize dynamic movement of the molecules in living cells, a spinning disc confocal microscope and a scanning confocal microscope with a white light laser system.

Applicants should submit their CV, a statement of accomplishment, future research plans and the names of three references to: **Dr. Mitsuo Ikebe, Chair of Department of Cellular and Molecular Biology, The University of Texas Health Science Center at Tyler, 11937 US Highway 271, Tyler TX 75708-3154**; e-mail: **kasandra.harris@uthct.edu**

UT Health is an Equal Opportunity and Affirmative Action Employer and seeks to build a diverse employee community. It is the policy of The University to promote and ensure equal employment opportunity for all individuals without regard to race, color, religion, sex, national origin, age, sexual orientation, disability, or veteran status. Women and minorities are encouraged to apply.

CANCER INSTITUTE DIRECTOR

New York City Suburbs

The North Shore-LIJ Health System and **Cold Spring Harbor Laboratory** jointly seek a **Director for the Cancer Institute**, headquartered at the **Center for Advanced Medicine** in **Lake Success, New York**. This individual will be an internationally renowned physician-scientist and thought-leader with an exceptional track record of building teams and leading translational research programs.

The North Shore-LIJ Health System – a fully integrated health care system, and Cold Spring Harbor Laboratory – a National Cancer Institute designated Cancer Center, recently formed a strategic affiliation focusing on basic and translational cancer research, and advancing these discoveries into the clinic.

The Director of the Cancer Institute will be responsible for the development and growth of a comprehensive program spanning basic, clinical and population research activities. The ideal candidate must have the following:

- A vision for translating fundamental diagnostic and therapeutic discovery research through clinical development within the partnership.
- A commitment to changing the paradigm of cancer care delivery to decrease the physical, as well as emotional and financial burden.
- The leadership skills to create a vision, manage and grow a cancer center within an integrated healthcare system.

The North Shore-LIJ Health System, one of the largest not-for-profit health systems in the country, treats over 19,000 unique patients with cancer annually. The North Shore-LIJ Cancer Institute is composed of over 200 members, and growing, who participate in at least one of twelve interdisciplinary disease specific Centers of Excellence that oversee clinical care, quality, research and educational initiatives.

This position will include academic appointments at both the Hofstra North Shore-LIJ School of Medicine and Cold Spring Harbor Laboratory.

Please send cover letter and curriculum vitae to: **Dr. Lawrence Smith, Dean, Hofstra North Shore-LIJ School of Medicine and Physician-in-Chief at North Shore-LIJ Health System, lscreeney@nshs.edu, (516) 823-8874.** EOE M/F/D/V.

North Shore LIJ

HOFSTRA NORTH SHORE-LIJ SCHOOL of MEDICINE

CSH Cold Spring Harbor Laboratory

PRINCETON UNIVERSITY

Princeton University seeks distinguished candidates for a senior and a junior appointment in the field of environmental science or environmental engineering. The positions will be given to scholars with a demonstrated record of excellence in scholarship and teaching who work in fields such as, but not limited to, environmental chemistry, environmental microbiology, hydrology, biogeochemistry and ecology. The successful candidates will be jointly appointed in the departments best suited to their research and in the **Princeton Environmental Institute**. The senior position will be filled at the tenured level and the junior position is a tenure-track position at the rank of Assistant Professor. Fields of specialization are open.

Applicants should apply online at **https://jobs.princeton.edu** (**requisition number 1500904 for the senior position** and **requisition number 1500903 for the junior position**) and should submit a letter of interest along with a vitae, and a list of three potential referees. The letter of interest should include the candidate's vision of the field and identify major unanswered questions. Evaluation of applicants will begin on **December 15, 2015** and continue until the position is filled.

This position is subject to the University's background check policy. Princeton University is an Equal Opportunity Employer and all qualified applicants will receive consideration for employment without regard to race, color, religion, sex, sexual orientation, gender identity, national origin, disability status, protected veteran status, or any other characteristic protected by law.

IPP International Postdoctoral Programme

cnic

Opportunities for POSTDOCTORAL RESEARCHERS in Biomedical Research at the Spanish National Centre for Cardiovascular Research, CNIC, Madrid - Spain

The CNIC is dedicated to excellence in cardiovascular research and to translating new knowledge into real improvements in clinical practice.

The scientific project of the centre has been structured in three research areas:

- Vascular Pathophysiology
- Myocardial Pathophysiology
- Cell & Developmental Biology

To be eligible, candidates must:

- Hold a PhD degree that must have been awarded no more than six years ago (exceptions will be made for documented career brakes and candidates with children)
- Have, at least, one publication as first author in an international peer reviewed journal
- Candidates must not have resided or carried out their main activity in Spain for more than twelve months in the last three years

The CNIC offers EIGHT (8) fellowships in this call:

- A 3-year contract
- An internationally competitive salary
- State of the art infrastructure and latest generation of technological equipment
- Scientific-technical support and complementary training

Deadline for submission of proposals: 23 December 2015

CNIC is an inclusive, equal opportunity employer, irrespective of nationality, ethnic origin, gender, marital or parental status, sexual orientation, creed, disability, age or political belief. Confidentiality is guaranteed throughout the selection process and all current regulations relating to the protection of personal data will be strictly adhered to.

For further information and applications please visit www.cnic.es

cnic

WESTERN MICHIGAN UNIVERSITY

Tenure Track Faculty Position
Anatomy or Physiology

The Department of Biological Sciences at Western Michigan University seeks applications for a position at the Assistant/Associate Professor level beginning in Fall 2016, pending budgetary approval. The successful candidate will pursue research that complements existing strengths within the department, establish an extramurally funded research program, teach graduate level courses in their area of expertise, participate in the training of Master and Ph.D. students and serve on departmental and University committees. The successful candidate will also be required to teach an undergraduate course in anatomy or physiology and demonstrate commitment to support the success of students from underrepresented groups. A Ph.D. and relevant post-doctoral experience are required. Competitive salary and startup funding will be offered. Information concerning the Biological Sciences Department's programs and faculty can be obtained at www.wmich.edu/biology/.

Western Michigan University is a learner centered, discovery driven and globally engaged university with high research activity, provides Master's and Ph.D. degrees, and offers a unique opportunity for individuals seeking a balanced research and teaching career. Applicants have to apply at **http://www.wmich.edu/hr/jobs**. Please have three letters of reference sent to **Cindy Linn, Ph.D. (cindy.linn@wmich.edu), Anatomy/Physiology Search Committee, Department of Biological Sciences, Western Michigan University, Kalamazoo, MI 49008-5410**. Review of applications will begin on **December 1, 2015**, but will be considered until position is filled.

WMU is an Equal Opportunity/Affirmative Action Employer. Minorities, women, veterans, individuals with disabilities and all other qualified individuals are encouraged to apply.

UNIVERSITY OF MINNESOTA
Neuroscientist to Lead a Medical Discovery Team on Addiction

We are seeking a world-renowned neuroscientist in the field of addiction who has the vision to link basic research to novel therapeutic approaches for prevention or treatment of addiction. The state of Minnesota has appropriated significant funds over the next ten years for the University of Minnesota Medical School to create a world-class, neuroscience-based program for the study and treatment of addiction.

The first charge of the team leader will be to identify and address opportunities for growth through the targeted hires of at least six additional faculty. Second, the leader will bring together existing faculty and infrastructure at the University of Minnesota invested in addiction research and patient outcomes. Third, building on the synergy between new hires and existing strengths, the team leader will promote research by aggressive targeting of federal funding.

The team leader will be able to leverage the University of Minnesota's current faculty and research strengths in addiction. The National Institute on Drug Abuse (NIDA)-based research funding currently stands at ~$15M per year. Funded research includes studies of psychostimulants, nicotine, and opioids. We serve as the NorthStar Node of the NIDA Clinical Trials Network—a newly established national platform for pragmatic clinical effectiveness trials in addiction. A recently funded program is developing a vaccine against opioid addiction for clinical trials. In addition, addiction-based research is funded by the National Institute on Alcohol Abuse and Alcoholism (NIAAA), the National Cancer Institute (NCI) and the National Heart, Lung, and Blood Institute (NHLBI) at ~$12M per year. The University of Minnesota has had a strong history of collaborative and transdisciplinary research in addiction research.

Additional strengths at the University of Minnesota include the internationally-recognized Center for Magnetic Resonance Research - at the forefront of the Human Connectome project; the Institute for Therapeutics Discovery and Development with the resources and expertise to develop new drug therapies; and the Clinical and Translational Science Institute, which provides resources to implement new treatment strategies and a conduit to promote the community-wide understanding and application of scientific discoveries.

The state of Minnesota is the home of multiple biomedical research companies where development of therapeutic approaches to addiction is a priority. Minnesota is also the home for world-renowned hospitals and treatment centers for addiction. Leveraging university relationships with these resources throughout of the state of Minnesota will be a priority of the team leader.

Review of applications will begin **mid-November 2015** and continue until the position is filled. The University of Minnesota is committed to diversifying its faculty and encourages applications from women and minorities. Applicants should include a curriculum vitae, a brief statement of research interests containing future plans, and a 1-2 page vision statement for the Discovery Team. Electronic versions should be emailed to Kathleen Beterams (**kbeteram@umn.edu**). Applicants also need to complete the online application. This may be found at **http://www1.umn.edu/ohr/employment/index.html** by searching for **Job ID 305675** under keywords. Additional questions can be directed to Dr. Timothy Ebner (**ebner001@umn.edu**)

The University of Minnesota is an Equal Opportunity Educator and Employer.

香港中文大學
The Chinese University of Hong Kong

Applications are invited for:-

Department of Microbiology
Research Assistant Professor
(Ref. 1516/089(665)/2) (Closing date: November 30, 2015)

The Department invites applications for a Research Assistant Professorship. The Department has a wide range of research facilities and access to a large comprehensive teaching hospital. The establishment provides a good environment for basic as well as clinical research and facilitates collaboration with other disciplines. Further information about the Department is available at http://www.cuhk.edu.hk/med/mic/.

Applicants should have (i) a PhD degree or equivalent; and (ii) a strong research track record in the field of microbiology or virology. Experience in tumour virology, microbial genomics and antibiotic resistance will be advantageous, though not a pre-requisite.

The appointee will (a) apply for competitive research grants and related funding; and (b) conduct high-standard research projects independently and in collaboration with other parties.

Appointment will initially be made on contract basis for up to three years commencing as soon as possible, renewable subject to mutual agreement.

Salary and Fringe Benefits
Salary will be highly competitive, commensurate with qualifications and experience. The University offers a comprehensive fringe benefit package, including medical care, plus a contract-end gratuity for an appointment of two years or longer, and housing benefits for eligible appointee. Further information about the University and the general terms of service for appointments is available at https://www2.per.cuhk.edu.hk/. The terms mentioned herein are for reference only and are subject to revision by the University.

Application Procedure
Application forms are obtainable (a) at https://www2.per.cuhk.edu.hk/, or (b) in person/by mail with a stamped, self-addressed envelope from the Personnel Office, The Chinese University of Hong Kong, Shatin, Hong Kong.

Please send the completed application form and/or full curriculum vitae, together with copies of qualification documents, a publication list and/or abstracts of selected published papers, and names, addresses and fax numbers/e-mail addresses of three referees to whom the applicants' consent has been given for their providing references (unless otherwise specified), to the Personnel Office by post or by fax to (852) 3942 0947 by the closing date.

Please quote the reference number and mark 'Application – Confidential' on cover. The Personal Information Collection Statement will be provided upon request.

Faculty Position in Experimental Biophysics
University of Pittsburgh
Department of Physics and Astronomy

The Department of Physics and Astronomy at the University of Pittsburgh invites applications for a new faculty member in experimental biophysics. This tenure-stream position will be at the Assistant Professor level, starting on or after September 1, 2016, subject to budgetary approval.

We are seeking candidates with strong physics backgrounds who will complement current research strengths in experimental biophysics. We are particularly interested in candidates with expertise in epigenetics, cellular dynamics, and novel experimental techniques, but we will consider candidates with any area of specialization within biophysics. In addition to research accomplishments and future promise, candidates must show potential for a high degree of teaching effectiveness at both the graduate and undergraduate levels.

To ensure full consideration, complete applications should be received by **November 30, 2015**. However, applications will be accepted until the positions are filled. Applicants can apply online at: **https://facultysearch.as.pitt.edu/apply/index/MTI0**. Candidates should submit a letter of application, CV, research statement, publication list, teaching statement and at least three letters of reference. For each reference, you will have the opportunity to input a personal email address or an email address generated through Interfolio's Online Application Delivery. In both cases, an email notification will be sent to the designated address with instructions about uploading the letters to our system.

University of Pittsburgh is an Affirmative Action, Equal Opportunity Employer. Women and members of minority groups under-represented in academia are especially encouraged to apply.

GW Cancer Center

Faculty Positions in Cancer Biology

The George Washington University invites applications from outstanding scientists interested in contributing to the research program of the recently established George Washington Cancer Center (GWCC).

The GWCC (http://smhs.gwu.edu/cancercenter/) brings together the resources of the George Washington University, the GW Medical Faculty Associates, and the GW University Hospital to expand current research efforts in the fight against cancer and to position our institution as the premier cancer care provider in the Washington, D.C. area.

Applications are welcome from scientists with expertise in the broad area of cancer biology. Areas of particular interest are cancer epigenetics, cancer immunology and immunotherapy, and viral/microbial oncology. Examples include gene regulation, signal transduction, cancer genetics, and functional genomics and proteomics. Tenured/tenure-track appointments will be made in one of the School's departments at a rank (Assistant, Associate, or Full Professor) and salary commensurate with experience, publication record, and potential to maintain an externally-funded research program. Successful candidates will also receive a competitive start-up package and will participate in the teaching mission of their department.

Basic Qualifications: Applicants must hold a Ph.D. and/or M.D. degree (or equivalent) in an appropriate discipline and have an established research program, as evidenced by extramural funding and publications.

Application Process: To be considered, please complete an online faculty application at: **http://www.gwu.jobs/postings/29926** and upload a current CV, cover letter, and statement of current and future research interests (three-page limit). Review of applications will begin on **December 2, 2015** and will continue until the positions are filled. Only complete applications will be considered. Employment offers are contingent on the satisfactory outcome of a standard background screening.

The George Washington University and the George Washington University Medical Faculty Associates are an Equal Employment Opportunity/Affirmative Action Employer that does not unlawfully discriminate in any of its programs or activities on the basis of race, color, religion, sex, national origin, age, disability, veteran status, sexual orientation, gender identity or expression, or on any other basis prohibited by applicable law.

For recruitment in science, there's only one Science

Looking to hire cell biologists?

Why choose this cell biology feature for your advertisement?

- Relevant ads lead off the career section with special cell biology banner
- Bonus distribution to the American Society for Cell Biology meeting, December 12–16 in San Diego, CA.

SCIENCECAREERS.ORG

Science Careers AAAS

To book your ad: **advertise@sciencecareers.org**
The Americas 202-326-6582
Europe/RoW +44(0)1223-326500
Japan +81-3-3219-5777
China/Korea/Singapore/Taiwan +86-186-0082-9345

PURDUE
UNIVERSITY

Head and Professor, Department of Biological Sciences

Purdue University invites applications for the position of Head of the Department of Biological Sciences to start August 2016. The Department seeks a dynamic leader with creative vision and an outstanding record of teaching, research, and administrative accomplishments.

The Department is undergoing a period of exciting development. Departmental strengths include Biology Education; Cell & Molecular Biology; Ecology and Evolutionary Biology; Microbiology & Infectious Disease; Neuroscience & Physiology; and Structural Biology. The University has recently announced two large investment areas in life science research, Neuroscience and Immunology/Infectious Disease, in which this Department will play a leading role. http://www.purdue.edu/newsroom/releases/2015/Q4/purdue-makes-major-new-investments-in-the-life-sciences.html

The Department is comprised of over 60 faculty members and 30 post-doctoral researchers, along with 160 graduate students and over 850 undergraduate biology majors. Further information about the Department is available at www.bio.purdue.edu. Department faculty are involved in University-wide multidisciplinary research through Discovery Park (see www.discoverypark.purdue.edu) and the Purdue Center for Cancer Research (see www.cancerresearch.purdue.edu).

Qualifications: The successful candidate will have a Ph.D. in biology or a related discipline, an outstanding record of scholarly achievement and a history of extramurally funded research commensurate with the rank of full professor at Purdue, exceptional and proven leadership abilities, a vision for the Department in the university, state, and nation, a commitment to excellence in undergraduate and graduate education, an enthusiasm for engagement, and a dedication to diversity. Faculty in the department have teaching loads determined by the head. The successful candidate will be expected to teach when the term of office is complete.

Applications: Interested candidates should submit a cover letter, curriculum vitae, and a one-page statement that includes a description of past leadership experience and a vision for the future of biology research and education along with the names and e-mail addresses of three references to **http://hiring.science.purdue.edu**. Inquiries should be directed to **Biology Head Search Committee, Department of Biological Sciences, Purdue University, 915 W. State St., West Lafayette, IN 47907-2054** or **search@bio.purdue.edu**. Review of applications will begin **December 14, 2015** and will continue until the position is filled. A background check is required for employment in this position.

Purdue University is an EEO/AA Employer. All individuals, including minorities, women, individuals with disabilities, and protected veterans are encouraged to apply.

Join the Conversation!

Twitter is a great way to connect with AAAS members and staff about the issues that matter to you most. Be a part of the discussion while staying up-to-date on the latest news and information about your personal member benefits.

Follow us @AAASmember and join the conversation with #AAAS

AAAS MemberCentral
MemberCentral.aaas.org

UCDAVIS
UNIVERSITY OF CALIFORNIA

FACULTY POSITION ANNOUNCEMENT

Associate/Full Professor of Postharvest Physiologist

Department of Plant Science at the University of California, Davis

The University of California at Davis is pleased to announce the recruitment for a tenure-track faculty position in Posthavest Physiologist. The successful candidate will join the Department of Plant Sciences in the College of Agricultural and Environmental Sciences at the rank of Associate/Full Professor.

Qualifications: Ph.D. in plant physiology, biology, horticulture, biochemistry or related discipline with experience and documented central focus in postharvest plant physiology. International development experience is desirable.

Salary: Commensurate with qualifications and experience.

To Apply: The complete position description and application instructions can be viewed at **http://apptrkr.com/700371.** For questions regarding the application, processes please send e-mail to kgeer@ucdavis.edu. Review of applications will begin December 1, 2015. The position will remain open until filled.

UC Davis is an affirmative action/equal employment opportunity employer and is dedicated to recruiting a diverse faculty community. We welcome all qualified applicants to apply, including women, minorities, veterans, and individuals with disabilities.

COLUMBIA | ENGINEERING
The Fu Foundation School of Engineering and Applied Science

Faculty Position in "Sensors and Systems" in the Department of Mechanical Engineering

Columbia Engineering is pleased to invite applications for faculty positions in the Department of **Mechanical Engineering** at Columbia University in the City of New York City. Applications at the assistant professor, and in exceptional cases, at the associate professor and full professor levels, will be considered.

Applications are specifically sought in interdisciplinary areas related to the design, analysis, and fabrication of unique sensors, especially at small length scales; and deployment of such sensors into large scale monitoring systems utilizing big data analysis. Candidates must have a Ph.D. or its professional equivalent by the starting date of the appointment. Applicants for this position at the Assistant Professor and Associate Professors without tenure must demonstrate the potential to do pioneering research and to teach effectively. Applicants for this position at the tenured level (Associate or Full Professor) must have a demonstrated record of outstanding research accomplishments, excellent teaching credentials and established leadership in the field.

The successful candidate is expected to contribute to the advancement of their field and the department by developing an original and leading externally funded research program, and contributing to the undergraduate and graduate educational mission of the Department. Columbia fosters multidisciplinary research and encourages collaborations with academic departments and units across Columbia University. **This position particularly seeks candidates whose research focus intersects with the field of data sciences and can take full advantage of the Data Science Institute at Columbia University**. Opportunities exist for collaboration with a broad range of research centers and activities at Columbia University, including but not limited to centers in Materials Science, Photonics, and Neuroscience. The Department is especially interested in qualified candidates who can contribute, through their research, teaching, and/or service, to the diversity and excellence of the academic community.

For additional information and to apply, please see: **http://academicjobs.columbia.edu/applicants/Central?quickFind=61656**. Applications should be submitted electronically and include the following: curriculum-vitae including a publication list, a description of research accomplishments, a statement of research and teaching interests and plans, contact information for three experts who can provide letters of recommendation, and up to three pre/reprints of scholarly work. All applications received by **December 31, 2015** will receive full consideration.

Applicants can consult **www.me.columbia.edu** for more information about the department.

Columbia is an Affirmative Action/Equal Opportunity Employer with a strong commitment to the quality of faculty life.

Science Careers online @sciencecareers.org

POSITIONS OPEN

TWO FACULTY POSITIONS IN OCEANOGRAPHY

The Graduate School of Oceanography at the University of Rhode Island invites applications for 2 tenure track faculty members. We seek applications for (1). Assistant Professor specializing in the chemistry or biogeochemistry of seafloor vent and/or seep systems (posting number SF00162); and (2). Assistant Professor specializing in autonomous systems and data processing for ocean observation (posting number SF00165).

Located on the water's edge at URI's Narragansett Bay Campus, GSO is the state's center for marine studies, research and outreach. The new hires will have the unique opportunity to participate in the active sea-going community of GSO and the Ocean Exploration Trust utilizing platforms such as the R/V Endeavor and E/V Nautilus. The new faculty members will be expected to develop strong externally funded research programs, advise graduate students, and teach undergraduate and graduate courses.

Application review will begin January 7, 2016 and continue until the positions are filled. Visit website: **https://jobs.uri.edu** and search individual posting number (**#SF00162 & #SF00165**) to read full position descriptions, required and preferred qualifications, and application instructions. Applications must be submitted online only.

The University of Rhode Island is an Affirmative Action/Equal Employment Opportunity Diversity Employer. Women, persons of color, protected veterans, individuals with disabilities, and members of other protected groups are encouraged to apply.

TENURE TRACK ASSISTANT PROFESSOR in CELL BIOLOGY

The Department of Biological Sciences at the University of Arkansas invites applications for a tenure-track **FACULTY POSITION** in cell biology (Position F117P). Requirements include: Ph.D. and post-doctoral experience, and a strong research record. Preferred research focus is in biomedical aspects of cell biology; such as immunology, neurobiology, pathogenesis, cancer, and -omics approaches. Expectations: establish an externally funded research program, contribute to undergraduate/graduate education, and service. Application materials include letter of application, curriculum vitae, research and teaching statements and email contacts for three referees. Application and further position details are through website: **https://jobs.uark.edu/postings/10217**. For information about the department see website: **http:/biology.uark.edu**. For full consideration, applications must be received by **15 December 2015**. Search committee chair is **Dr. Douglas Rhoads (e-mail: drhoads@uark.edu).** Review will continue until the position is filled. *The University of Arkansas is an Equal Opportunity, Affirmative Action Institution. All applicants are subject to public disclosure under the Arkansas Freedom of Information Act and persons hired must have proof of legal authority to work in the United States.*

FACULTY POSITION
University of North Carolina at Greensboro
Department of Biology

The Department of Biology invites applications for a tenure-track Assistant Professor position in the field of Developmental Biology. We seek individuals whose biological research addresses environmental impacts upon development, with use of any model organism. Successful applicants will be expected to develop a strong, externally funded research program and train a diverse group of undergraduate and graduate students. Candidates must hold or anticipate a Ph.D. in Biology or a related discipline by August 1, 2016, postdoctoral experience is preferred. The position will start August 2016. University of North Carolina Greensboro is especially proud of the diversity of its student body and is an Equal Employment Opportunity/Affirmative Action Employer with a strong commitment to increasing faculty diversity. Equal Opportunity Employer Affirmative Action/Military/Female/Disabled/Veteran. To apply, visit website https://jobsearch.uncg.edu and click on "Faculty" (position 999417).

POSITIONS OPEN

Vice Chair for Research
Pennsylvania State University

An opportunity exists for a Vice Chair for Research and Director of the Division of Musculoskeletal Sciences within the Department of Orthopaedics and Rehabilitation at The Pennsylvania State University College of Medicine. This is a tenure or tenure track faculty positon at the rank of Associate or Full Professor. This position will provide administrative oversight of the Department's research programs and includes a highly competitive salary and start-up funds. This is a unique opportunity to join and direct a well-established, highly interactive research group consisting of engineers, material, clinical and basic scientists focusing on musculoskeletal research. A joint academic appointment will include a primary appointment in the College of Medicine at the Hershey, PA campus and a secondary appointment in an appropriate department at Penn State University main campus at State College, PA.

The professional qualifications for this position include: The ideal candidate will have an advanced degree of Ph.D., M.D., or M.D./Ph.D. Will have established an independent and extramurally funded research program in the area of musculoskeletal sciences or engineering. Demonstrated strong leadership skills; have experience in teaching and mentoring junior investigators, postdoctoral fellows, graduate and medical students; and have a record of strong publications in peer-reviewed journals. Will be an individual who can apply modern biomedical science and engineering concepts to the study of musculoskeletal tissues and lead others in developing their own research programs.

As part of one of the country's pre-eminent universities, our 551-bed tertiary medical center is the central Pennsylvania's region's only level I adult and pediatric trauma center and academic medical center. Also home to Penn State Children's Hospital, we are considered a resource for the most complex adult and pediatric cases. Hershey, PA, and the surrounding area offer a pleasant alternative to the pressures of urban living with a mix of well-maintained communities with quiet tree-lined streets, safe shopping districts, beautiful farmland, and state parks and game lands. It's the best of both worlds, with cultural events and nightlife both within Hershey and driving distance to Harrisburg; Philadelphia; the Pocono Mountains; Baltimore; Washington, D.C.; and New York City. The area is home to two professional sports teams, an amusement park, golf courses, professional and amateur theater, symphonies, and opportunities for hunting, fishing, and mountain biking.

Apply to job 58934 at website: http://apptrkr.com/690803

CAMPUS SECURITY CRIME STATISTICS: For more about safety at Penn State, and to review the Annual Security Report which contains information about crime statistics and other safety and security matters, please go to website: **http://www.police.psu.edu/clery/**, which will also provide you with detail on how to request a hard copy of the Annual Security Report.

Penn State is an Equal Opportunity, Affirmative Action Employer, and is committed to providing employment opportunities to all qualified applicants without regard to race, color, religion, age, sex, sexual orientation, gender identity, national origin, disability or protected veteran status.

Post Your Jobs
1 million candidates*
151,000 job applications*
Reach Scientists.
Fill Positions.
*Jan–Dec 2014
ScienceCareers
employers.sciencecareers.org

POSITIONS OPEN

ASSISTANT PROFESSOR in PLANT EVOLUTIONARY BIOLOGY

The Department of Biological Sciences at the University of Arkansas invites applications for a **TENURE-TRACK FACULTY POSITION** in plant evolutionary biology (Position 2163). Requirements include: Ph.D. and post-doctoral experience in land plant evolution and a strong research record. Candidates studying phylogenetically based comparative biology, evolutionary ecology, or the genetics of adaptation and speciation are preferred. Expectations: establish an externally funded research program, contribute to undergraduate/graduate education, and service. Application materials include a letter of application, curriculum vitae, research and teaching statements and contact information for three referees. Application and further position details are available at website: **http://jobs.uark.edu/postings/10034**. The names, titles, email addresses, and contact numbers of three professional references willing to provide letters of reference will be requested during the application process. Additional inquiries should be directed to the search committee chair, **Dr. Jeffrey Silberman (e-mail: jeff@uark.edu).**

The University of Arkansas is Affirmative Action/Equal opportunity Employer/Veterans/Disabled.

AAAS is here –
helping scientists achieve career sucess.

Every month, over 400,000 students and scientists visit ScienceCareers.org in search of the information, advice, and opportunities they need to take the next step in their careers.

A complete career resource, free to the public, *Science* Careers offers hundreds of career development articles, webinars and downloadable booklets filled with practical advice, a community forum providing answers to career questions, and thousands of job listings in academia, government, and industry. As a AAAS member, your dues help AAAS make this service available to the scientific community. If you're not a member, join us. Together we can make a difference.

To learn more, visit
aaas.org/plusyou/sciencecareers

AAAS + U = Δ

SEARCH JOBS ON THE GO!
Download the App
ScienceCareers
apps.sciencemag.org

UNIVERSITY OF LOUISVILLE

Tenure Track Faculty Positions in Biomedical Basic Sciences
University of Louisville School of Medicine

The University of Louisville School of Medicine invites applicants for tenure track faculty positions at all ranks in the Basic Sciences Departments of **Anatomical Sciences & Neurobiology**, **Microbiology & Immunology**, and **Biochemistry & Molecular Genetics**. The U of L School of Medicine provides an excellent research environment with many basic science faculty belonging to numerous Research Centers and Institutes including the Center for Predictive Medicine for Biodefense and Emerging Infectious Diseases (CPM), the Institute for Cellular Therapeutics, the Brown Cancer Center, Center for Genetics and Molecular Medicine, Kentucky Spinal Cord Injury Research Center, or the Kentucky Lions Eye Center. Applicants must have a Ph.D. and/or M.D. degree and a strong record of research achievement commensurate with rank.

Successful candidates are expected to develop or maintain an independent and externally funded research program, and to teach in professional and graduate programs. All applicants should apply electronically (**see Job ID # below**) and submit a cover letter describing a statement of their research interests, curriculum vitae, and the names of four references. Review of applications will begin immediately and continue until the positions are filled.

The **Department of Anatomical Sciences and Neurobiology** invites applications at the Assistant or Associate Professor level. The ideal candidate should utilize the mouse as a model system and have a research program in one of the following areas: sensory systems, neural development, or neural injury and repair. Information about the department and faculty can be found at http://louisville.edu/medschool/anatomy. Interested candidates can apply electronically at https://highereddecisions.com/uofl/current_vacancies.asp (**Job ID# 435**)

The **Department of Microbiology and Immunology** invites applications at all ranks in the area of Virology. The ideal candidate will have an active and productive research program in virus-host interactions. Both BSL-3 and ABSL-3 research can be accommodated by the university's state-of-the-art facilities. Information about the department can be found at http://louisville.edu/medicine/departments/microbiology. Applicants can apply electronically at https://highereddecisions.com/uofl/emp_apply_login.asp (**Job ID# 457**)

The **Department of Biochemistry & Molecular Genetics** invites applications at all ranks. The ideal candidate should have research interests in metabolism, metabolic related diseases, molecular genetics and personalized medicine. Information about the department is available at www.louisville.edu/medschool/biochemistry. Apply on-line at (**Job ID# 31321**) http://highereddecisions.com/uofl/current_vacancies.asp.

The University of Louisville is an Affirmative Action, Equal Opportunity, Americans with Disabilities Employer, committed to diversity and in that spirit, seeks applications from a broad variety of candidates.

AAAS

ADVANCING SCIENCE, SERVING SOCIETY

EDITOR-IN-CHIEF

SCIENCE Family of Journals

The American Association for the Advancement of Science (AAAS), an international non-profit organization dedicated to advancing science, engineering, and innovation throughout the world, has initiated a search for a new **Editor-in-Chief** for its international journal *Science* and the *Science* family of research journals (*Science Translational Medicine*, *Science Signaling*, the open-access *Science Advances*, and forthcoming journals *Science Immunology* and *Science Robotics*). One of the premier journals in the world, Science is published weekly and includes reviews and reports of research across the spectrum of science and engineering, with an emphasis on those with cross-disciplinary impact and interest. The journal also serves as a forum for the presentation and discussion of the latest news and other issues surrounding science, with particular emphasis on the interactions among science, technology, government, and society.

In selecting an Editor-in-Chief, the AAAS Chief Executive Officer/Executive Publisher and the AAAS Board of Directors will give weight to evidence of significant achievement in scientific research, editorial experience and creativity, awareness of leading trends broadly in science and scientific communication, and managerial abilities. This position requires a full level of commitment and engagement.

Applications or nominations should be accompanied by complete curriculum vitae, including refereed publications, and should be sent to:

Andrew Black, Chief of Staff
AAAS
1200 New York Avenue, NW
Washington, DC 20005
or ablack@aaas.org

Salary is negotiable based on qualifications and experience. Application materials will be reviewed beginning **November 15, 2015**, and continue until position is filled.

AAAS is an Equal Opportunity Employer.

ScienceCareers online @sciencecareers.org

By **Rachel Bernstein**

Improving student advising

In the midst of his graduate chemistry studies at the Massachusetts Institute of Technology (MIT), Carl Brozek stumbled into a new challenge: a yearlong campaign to improve advising for graduate students. His effort began 2 years ago, after the head of the chemistry department called a town hall meeting to discuss the results of a departmental survey that identified areas of dissatisfaction. Brozek felt the department was proposing good plans to address most of the problems raised. But when it came to students' concerns that their advisers weren't giving them the mentorship they needed, he was struck by the lack of ideas. "I realized it was a very, very, difficult challenge," recalls Brozek, who is now a postdoc at the Clean Energy Institute at the University of Washington, Seattle.

But he also saw a possible solution, or at least a step in the right direction. Though he didn't have complaints about his own advising experience, he decided to pursue the issue in part because "I've always been interested in these kinds of social justice causes," Brozek says. "I saw little failures of advising here and there that were just so obviously due to problems with communication." He reckoned that one way to start addressing the problem would be by documenting what graduate students and their advisers expect from the system so that at least everyone would be on the same page.

"My goal was to have one good, meaningful meeting with an administrator once a week."

Brozek began by reaching out to graduate students from across the university, and to the postdoc association. Over snacks and wine, the participants brainstormed about what they saw as their rights and responsibilities, and those of their advisers. He shared the list with as many students as he could for further input. The only rule was no deleting.

Next he sought out university administrators, including heads of divisions, the chancellor, and the chair of the faculty policy committee. He asked them whether his effort was helpful and how to move forward with it. And he requested their input about the role of advisers and their feedback about the students' comments. "My goal was to have one good, meaningful meeting with an administrator once a week for the summer of 2014," he says. He ended up taking the result to MIT's Committee on Graduate Programs, which institutes and oversees policies and procedures related to graduate education. Last February, after some fine-tuning of the language, the MIT dean of graduate education approved his two-part document.

The first part concisely lays out existing policies related to graduate student treatment, such as protection from discrimination and harassment, which had previously been scattered across many sources. The second goes a step further to promote "common values" to guide the behavior of both students and their advisers. "Faculty members and their graduate students are strongly encouraged to build their relationship by establishing common expectations on the major elements of their professional interactions," the first item reads. The remaining guidelines emphasize the importance of clear communication for building a productive relationship.

"It isn't a battle cry, or a shield, or a last resort," Brozek explains. Nor is it a directive. "A lot of the items are pretty vague, and we deliberately kept them vague, because what works for one adviser may not work for another." The document has been distributed at various MIT events, and Brozek has anecdotal evidence that it has made an impact. "I hear stories from students saying, 'Carl, what have you done? My adviser keeps asking me if he or she is a good adviser; what's happening?'"

The work required to create the document provided a welcome outlet after long days in the lab, Brozek says. "At the end of the day, even if I was exhausted with working on my project, I still had a little energy that wasn't really meant for research. I could expend that reserve energy on going to the gym, or on sending a couple of emails, or thinking about what my next step should be." Overall, he says, "it was a great experience, learning what it takes to make something like this happen." ■

Rachel Bernstein is the editor of Science *Careers. For more on life and careers, visit sciencecareers.org. Send your story to SciCareerEditor@aaas.org.*

ILLUSTRATION: ROBERT NEUBECKER

Downloaded from www.sciencemag.org on November 5, 2015

Published by AAAS